

NASA Technical Memorandum 89871

Advances in Planetary Geology

John A. Grant III and Susan S. Nedell

JUNE 1987

NASA

NASA Technical Memorandum 89871

Advances in Planetary Geology

John A. Grant III and Susan S. Nedell

NASA Office of Space Science and Applications
Washington, D.C.



National Aeronautics
and Space Administration

Scientific and Technical
Information Office

1987

TABLE OF CONTENTS

Part I:	The Geomorphic Evolution of Eastern Margaritifer Sinus, Mars	v
Part II:	Sedimentary Geology of the Valles Marineris, Mars and Antarctic Dry Valley Lakes	269

PRECEDING PAGE BLANK NOT FILMED

PART I

THE GEOMORPHIC EVOLUTION OF EASTERN MARGARITIFER SINUS, MARS

by

John A. Grant III

PRECEDING PAGE BLANK NOT FILMED

PAGE iv INTENTIONALLY BLANK

ABSTRACT

Geomorphic mapping, crater counts on selected surfaces, and a detailed study of drainage basins, were used to trace the geologic evolution of the Margaritifer Sinus Quadrangle (0°-30°S, 0°-45°W). Relative ages are given as the cumulative number of craters $> 1 \text{ km} \cdot 10^6 \text{ km}^{-2}$. The oldest features and dominant structural controls in MC19 are three multi-ringed impact basins, Ladon, Holden and Noachis. The oldest dated surface covering these basins (1,000,000-850,000) evolved during the period of intense bombardment. Since that time four resurfacing events have occurred. The first three (300,000-100,000, 70,000-40,000, and 14,000-8200) were all of regional extent, while the fourth (6000-2000), occurred locally, filling basins. Valley networks, incised in the third event unit, are always buried by the fourth event unit when present.

A peak in geomorphic activity occurred from 10,000-5000. Events during this period included the formation of Uzboi/Ladon Valles with deposition in Ladon Basin (11,000-6200), and the formation of Samara and Parana/Loire Valles in MC19SE (8500-4600). Flow out of Ladon Basin and to a lesser extent Samara and Parana/Loire Valles created etched terrain at their confluence (9000-4500) that was synchronous with initiation of Margaritifer and Iani Chaos (10,000-2300). The range of dates for the chaos may be due to periodic collapse.

The extensive, well integrated nature of Samara and Parana/Loire Valles (combined drainage area = 84% of the Colorado River, USA) requires the existence of a long period of favorable climatic conditions to allow their formation. Development of these two systems was probably through sapping processes because of: 1) similarities in general setting and morphology to terrestrial systems formed by sapping; and 2) drainage densities well below any observed for terrestrial systems formed by surface runoff.

ACKNOWLEDGMENTS

I would like to thank my major professor, Dr. J.C. Boothroyd, and the other members of my graduate committee, Drs. D.P. Murray, E. Laine and especially D.U. Wise, for providing me with the technical skills, guidance and support that resulted in a successful graduate education.

The process of obtaining images used in this study was simplified enormously by help from J. Swann and numerous other individuals at the USGS Astrogeology Branch in Flagstaff, Az.

Computer programs used for data analyses in this study were written by B. Fessler at the Lunar and Planetary Institute in Houston, TX. Revisions of the programs was made easy with the help of D. Halloway at the URI Academic Computer Center and M. Stam at the University of Massachusetts.

Financial support for this project was provided almost entirely through NASA, Planetary Geology and Geophysics Program, Grant No. NSG-7414 (Jon C. Boothroyd, Principal Investigator) with additional support from Sigma Xi.

PRECEDING PAGE BLANK NOT FILMED

TABLE OF CONTENTS

ABSTRACT	1
ACKNOWLEDGMENTS	3
LIST OF TABLES	7
LIST OF FIGURES	9
LIST OF APPENDICES	11
INTRODUCTION	13
PHYSICAL SETTING	15
Location and Description	15
Physical Processes	15
METHODS	21
RESULTS	23
Geologic/Geomorphic Mapping	23
Description of Units	23
Channel Features	23
Channels and Valley Networks	23
Etched Terrain	41
Chaotic Features	44
Chaotic Terrain	44
Fretted Terrain	44
Positive Relief Chaotic Deposits	44
Smooth Plains	44
Smooth Plains Deposits	44
Relict Polar Deposits	45
Craters	45
Multi-Ringed Basins, Heavily Cratered Deposits	46
Hilly and Heavily Cratered Terrain	46
Ancient Multi-Ringed Impact Basins	46
Mount Material	46
Other Features	46
Grabens	46
Flow Modified Grabens	47

Ridges	47
Eolian Deposits	47
Mass Movement Deposits	47
Drainage Basins	47
Drainage Basin Mapping	47
Drainage Basin Areas	58
Drainage Densities	64
DISCUSSION	67
Interpretation of Map Units	67
Channel Features	67
Channels and Valley Networks	67
Etched Terrain	67
Chaotic Features	67
Chaotic Terrain	67
Fretted Terrain	67
Positive Relief Chaotic Deposits	68
Smooth Plains	68
Smooth Plains Deposits	68
Relict Polar Deposits	68
Multi-Ringed Basins, Heavily Cratered Deposits	68
Hilly and Heavily Cratered Terrain	68
Ancient Multi-Ringed Impact Basins	68
Mount Material	68
Other Features	69
Grabens	69
Flow Modified Grabens	69
Ridges	69
Eolian Deposits	69
Geometry and Relationship of Large Scale Features	69
Drainage Basin Evolution	81
Period of Formation	81
Valley Network Drainage Densities	94
Valley Network Genesis	96
Geologic/Geomorphic Evolution	101
Oldest Features and Terrain	101
Periods of Resurfacing	102
Peak Geomorphic and Tectonic Activity	103
Meso-Scale Outflow Channels	103
Valley Network Formation	106
Tectonic Activity	106
Chaotic Terrain Formation	107
Post Channel and Valley Formation Activity	111
CONCLUSIONS	113
REFERENCES	117
APPENDICES	125

LIST OF TABLES

Table

1. Geologic/Geomorphic Map Explanation.....	29
2. Crater Counts: Location, Age and Quality.....	30
3. Samara and Parana/Loire Valles Sub-Basins and Internal Drainage Basins: Names and Location.....	59
4. Samara, Parana/Loire Valles Drainage Basins and Internal Drainage Basins: Areas and Densities.....	65
5. Samara and Parana/Loire Valles Sub-Basins: Areas and Densities.....	66
6. Stereo Pairs: Images Used for Drainage Basin Mapping and the Location of Overlap.....	266

LIST OF FIGURES

Figure

1. General geologic map of Mars and location of the Margaritifer Sinus quadrangle.....	17
2. Shaded relief map of the Margaritifer Sinus quadrangle with topographic lines to show the regional slope.....	19
3. Geologic/Geomorphic map of the Margaritifer Sinus quadrangle.....	25-28
4. Crater count location diagram.....	33-36
5. Summary of crater count results.....	38
6. Geologic/Geomorphic map unit correlation.....	40
7. Photomosaic of the central portion of the Margaritifer Sinus quadrangle.....	43
8. Footprints of stereo pairs used for drainage basin mapping.....	49-52
9. Drainage basins and inferred flow directions in the Margaritifer Sinus quadrangle.....	54-57
10. Photomosaic of the LP3 sub-basin and I2, I3a, and I3b internal drainage basins.....	61
11. Valley segments measured for the calculation of drainage densities for Samara and Parana/Loire Valles.....	63
12. Photomosaic of terraces in Ladon Valles and the relationship of the system to the rings of the Holden and Ladon multi-ringed impact basins.....	72
13. Photograph of Jones crater and portions of Samara and Loire Valles that have been buried by Jones crater Ejecta.....	75
14. Photograph of the channel split in Samara Valles as it crosses an ancient ridge in MC19SE.....	77
15. Photomosaic showing the relationship between Parana Valles, Parana Basin, and Loire Vallis.....	80
16. Photograph of relict polar material in MC19NE....	83

17. Photomosaic of post valley formation resurfaced areas and associated valley burial in the LP3 sub-basin.....	85
18. Photograph of post valley formation resurfaced areas and associated valley burial in the Clota Valles and S1 sub-basins.....	87
19. Sketch maps of the area in Fig. 9 --	
a. Sketch of LP3 sub-basin and I2, I3a, I3b internal basins with the position of the geologic contact between Sp ₄ and Sp ₃ , and crater Gb and its ejecta in relation to existing valley segments.....	90
b. Sketch of drainage reconstruction within, and extent of, the LP3 sub-basin prior to post valley formation resurfacing and the crater Gb impact event.....	91
20. Photograph of an area east of mid to upper Loire Vallis where possible differential erosion of layers in the substrate has occurred.....	93
21. Photomosaic of northern Uzboi Vallis and Holden crater with small interior connecting channel...	105
22. Photograph of flow modified graben and associated valley networks in MC19SE.....	109
23. Cumulative crater size-frequency plots --	
a. Cumulative crater size-frequency plot of all craters present in an area centered on 12S, 16W.....	129
b. Cumulative crater size-frequency plot of craters generally between 10 and 30 km in diameter in an area centered on 12S, 16W.....	130
c. Cumulative crater size-frequency plot of craters generally between 1 and 2 km in diameter in an area centered on 15S, 17W.....	131
d. Cumulative crater size-frequency plot of craters generally between 2 and 6 km in diameter in an area centered on 14S, 15W.....	132
24. Idealized drawing of a hypothetical cratered surface and possible crater count locations.....	135
25. Plot of the Martian standard crater curve.....	141

LIST OF APPENDICES

Appendix

1. CRATER COUNTING METHODOLOGY..... 125
2. COMPUTER PROGRAMS USED TO DERIVE LOGARITHMIC
CUMULATIVE CRATER SIZE-FREQUENCY PLOTS..... 143
3. CRATER COUNTS: LOGARITHMIC CUMULATIVE CRATER
SIZE-FREQUENCY PLOTS..... 153
4. STEREO PAIRS USED FOR DRAINAGE BASIN MAPPING.... 262

INTRODUCTION

A broad range of channel and valley features are displayed on the surface of Mars. There is as great a range in morphology as in scale, from huge macro- and smaller meso-scale outflow channels such as Kasei Vallis and Ladon Valles respectively, to small scale valley networks such as Nirgal Vallis and Parana/Loire Valles. The Margaritifer Sinus quadrangle of Mars contains examples of all these types of systems, and has one of the best integrated and highest concentrations of valley networks on the entire planet (Carr 1979a; 1980b; Pieri 1979; Baker 1982). The quadrangle also displays a variety of other interesting geologic and geomorphic features, such as etched, chaotic and fretted terrain; ancient multi-ringed impact basins (Schultz et al. 1982b); possible relict polar deposits (Schultz 1984); ancient heavily cratered uplands; and smooth plains that display various crater densities.

Several possible Earth analogs have been examined in an effort to explain the origin of the various different scale channels seen of the Martian surface. The morphology and scale of the Channeled Scabland in eastern Washington is strikingly similar to the Martian outflow channels (Baker 1982). A catastrophic flood hypothesis similar in effect to that which formed the Channeled Scabland has been evoked as one possible mechanism for the creation of the outflow channels (Baker 1982; Murray et al. 1981; Carr 1979b; 1981; Masursky 1973). Boothroyd and Timson (1983) showed that braided rivers on the Arctic North Slope that frequently switch active channels, due to ice jams during ice drives, can result in morphologic features similar to those found within Martian meso-scale outflow channels such as Ladon Valles.

The smaller valley networks are the most diverse and least studied of the channel and valley features (Baker 1982). Several different theories have attempted to explain their formation, ranging from lava erosion (Carr 1974) to rainfall and surface runoff at an earlier time in Martian history (Masursky 1973; Masursky et al. 1977). Many workers (Sharp and Malin 1975; Sagan and Pieri 1979; Mutch et al. 1976; Carr 1979a; 1980a; 1981; Carr and Clow 1981; Pieri 1980a; 1980b; Murray et al. 1981; Baker 1982; Laity 1985; Laity and Pieri 1980; Mars Channel Working Group 1983; Higgins 1982; 1984) now feel that a combination of wet-sapping and resultant downstream fluvial action, after Sharp and Malin (1975), were the most probable formative processes.

The purpose of this paper is to: 1) present a larger scale (1:2,000,000), more detailed geologic map of the Margaritifer Sinus quadrangle than presently exists (Saunders 1979); 2) use crater counts and cross-cutting

relationships to consider the timing of various channel and valley forming events, their drainage basin evolution, and the interplay and relationship of the channels and valleys to each other and other geomorphic features in the quadrangle; 3) use crater counts to determine when peak periods of geomorphic and tectonic activity occurred in the region; 4) advance the theory of valley network formation through wet-sapping and downstream fluvial action by providing a detailed, quantitative and qualitative study of their drainage basins, densities, morphology and geologic setting, and comparing them to terrestrial drainage systems formed by similar processes; 5) develop a reasonable hypothesis for the geologic/geomorphic evolution of the quadrangle.

PHYSICAL SETTING

Location and Description

The Margaritifer Sinus quadrangle is located at the eastern end of Valles Marineris, approximately 1000 km NE of Argyre Planitia, between 0° and 30°S, 0° and 45°W (Fig. 1). The quadrangle is located within a broad trough known as the Chryse Lowland (Frey 1974; Saunders 1979), and has a distinct northward slope (Fig. 2). Surface materials consist mainly of heavily cratered terrain and intercrater or smooth plains (Mutch et al. 1976; Scott and Carr 1978; Saunders 1979), two of the older units on the Martian surface (Scott and Carr 1978; Saunders 1979; Murray et al. 1981). The quadrangle includes: (1) some of the best integrated and highest concentrations of valley networks on the planet (eg Samara, Parana/Loire Valles in the SE quadrangle) (Carr 1979a; 1980b; Baker 1982); (2) Eos Chasma (12S, 39W) and Capri Chasma (8S, 40W), marking the eastern end of Valles Marineris; (3) several meso-scale outflow channels, Ladon, Uzboi and Margaritifer Valles (22S, 28W); (4) Chaotic terrain (many locations) and fretted terrain (3S, 20W); (5) several ancient multi-ringed impact basins (Schultz and Glicken 1979; Saunders 1979); and (6) possible ancient polar deposits (Schultz 1984).

Physical Processes

The Margaritifer Sinus quadrangle is presently undergoing only minor morphologic modifications resulting mainly from eolian (Carr 1981; 1984; Greeley et al. 1982; Murray et al. 1981), cratering and mass movement events. A wide range of processes, including tectonism, cratering, volcanism, and channeling, have operated within the quadrangle at a much greater rate and scale in the past (Saunders 1979; Neukum and Hiller 1981; Schultz et al. 1982; Scott and Carr 1978). The result is that features formed at a relatively early period in the history of the planet can still be observed and studied today.

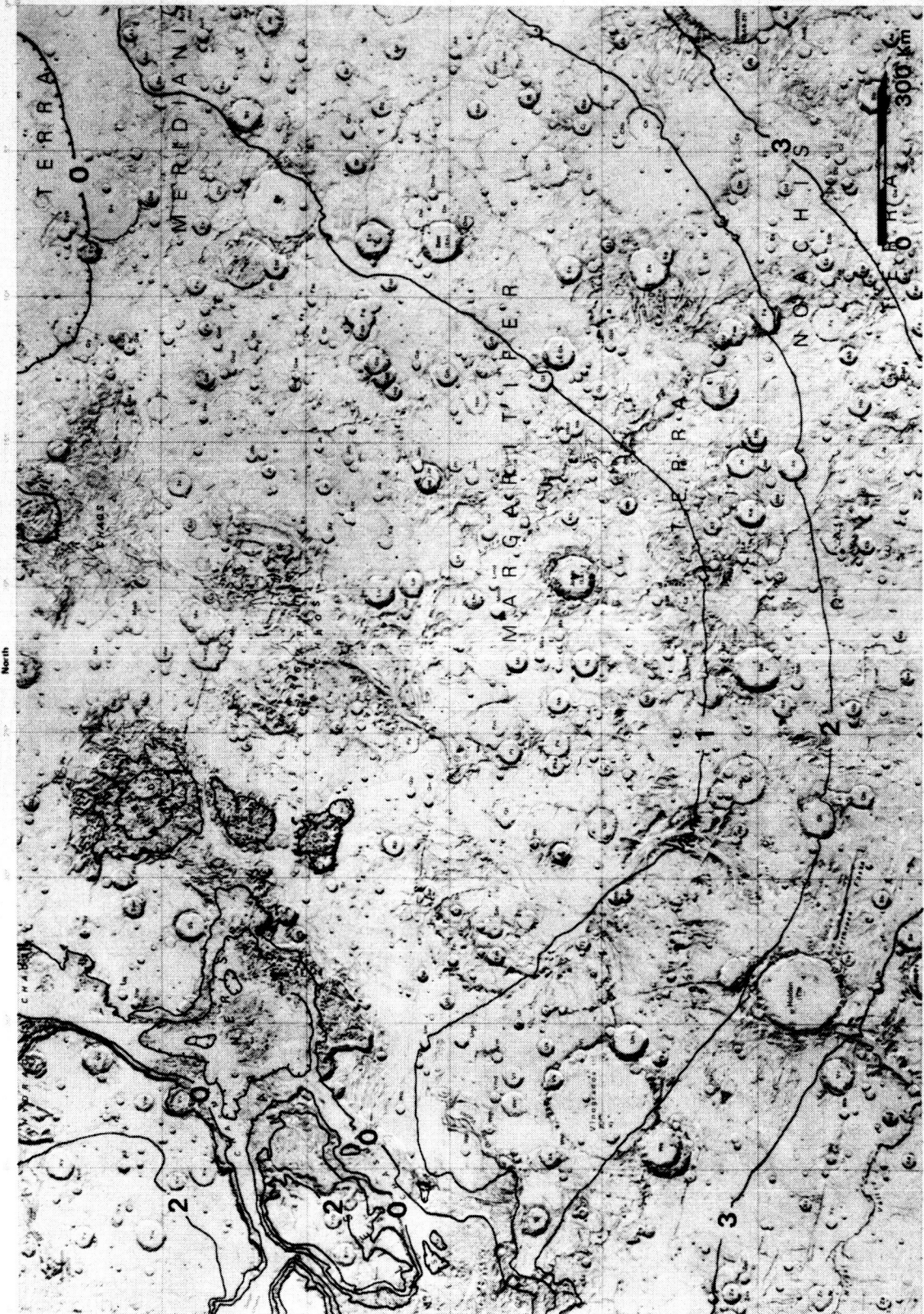
Fig. 1. Simplified geologic map of Mars between 65N and 65S showing the location of the Margaritifer Sinus quadrangle, selected channels, and other major features. Map modified from Baker (1982).

Fig. 2. Shaded relief map of Margaritifer Sinus with contours illustrating the distinct northward slope of the region and convergence towards the center of the quadrangle along the axis of the Chryse lowland trough. Contours from the topographic map of the Margaritifer Sinus quadrangle (USGS 1976). The contour interval is 1 km.

ORIGINAL PAGE IS
OF POOR QUALITY

M 58 15 22 RV 1960
1:250,000

Prepared for the
NATIONAL AERONAUTICS AND SPACE ADMINISTRATION



METHODS

Using approximately 400, mainly orthographic, Viking Orbiter Image negatives of the study area, contact prints were made to determine negative quality and precise location. All but the poorest quality were then printed to a scale of 1:2,000,000 and stereo pairs were selected. Certain high resolution sequences (about 50 m/pixel) were printed to a scale of 1:500,000 and assembled into mosaics. High quality negatives (200 m/pixel) of the area surrounding Samara and Parana/Loire Valles, in the Margaritifer Sinus SE and Argyre NE quadrangles, were printed to a scale of 1:1,000,000 and assembled into a mosaic. All of the above were then used in conjunction with published 1:2,000,000 photomosaics (USGS 1979a; 1979b; 1979c; 1979d; 1979e), and 1:5,000,000 geologic (Saunders 1979), shaded relief (USGS 1975; 1980), and topographic (USGS 1976) maps of the region to complete the 1:2,000,000 geologic map of the quadrangle. All work completed in the area since it was mapped by Saunders (1979), (Carr 1979b; 1980a; 1980b; Schultz and Glicken 1979; Shultz and Lutz-Garihan 1982; Schultz 1984; Pieri 1980a; Boothroyd 1983; Boothroyd and Grant 1984; 1985; Grant and Boothroyd 1984; Parker and Pieri 1985a; 1985b) was incorporated into the map. Methods employed for mapping were after Baker and Kochel (1979), Saunders (1979), Baker (1980a; 1980b; 1982), Boothroyd and Timson (1981), and Wise (1979).

Stereo pairs used for geologic mapping were also used to delineate drainage basin boundaries, after Boothroyd (1982). Work began in the Margaritifer Sinus SE and Argyre NE quadrangles along a major N-S trending basin boundary located at 9W (Boothroyd and Grant 1984), and extended towards the NW, encompassing all of Samara and Parana/Loire Valles, their associated sub-basins and internal-basins. Work continued westward to the Margaritifer Sinus SW quadrangle, mapped by Boothroyd (1982). A Bausch and Lomb zoom stereoscope was used for the mapping. The areas of the drainage basins were then measured using a polar planimeter and a table digitizer. All valley lengths visible within the basins at 1:1,000,000 scale and 200m/pixel resolution were measured using a table digitizer. Drainage densities, for Samara and Parana/Loire Valles, sub-basins, internal-basins, and selected areas within the drainage basins, were calculated and compared to values obtained for other Martian systems (Baker 1985) and terrestrial systems (Gregory and Gardiner 1975; Abrahams 1984). A further comparison, based on morphology, density, and geologic setting was made to terrestrial systems formed mainly by sapping processes (Higgins 1974; 1982; D'Amore 1983; 1984; Laity 1985; Laity and Pieri 1980; Pieri, Malin and Laity 1980).

1:1,000,000 and 1:2,000,000 photographs, various orthographic negatives, stereo pairs and crater counts were

used to determine the relative ages of units surrounding/covering Samara/Parana/Loire Valles, Margaritifer Chaos (10S, 21W), and Ladon Basin (18S, 30W). The possibility of flow out of Samara and Parana/Loire and the Ladon Basin into/through the Margaritifer Chaos was also examined in this manner.

After consideration of many papers concerning various approaches to methods of crater counting and the presentation of results (Hartmann 1965; 1969; Marcus 1968; Chapman et al. 1969; Murray et al. 1971; Soderblom et al. 1974; McGill 1977; McGill and Wise 1972; Crater Analysis Techniques Working Group 1978; Masursky et al. 1980; Neukum and Wise 1976; Neukum and Hiller 1981; Neukum et al. 1979; Hiller and Neukum 1979; 1980; Wise 1984; 1985; Wise and Milkowski 1980; Wise et al. 1979; Wise, personal communication 1984) the D.U. Wise method of dating local surfaces was chosen to complete the crater counts. This method utilizes small, homogeneous crater populations and is described fully in Appendix 1. The relative ages of surfaces are presented as the cumulative number of craters $\geq 1 \text{ km} \cdot 10^6 \text{ km}^{-2}$, derived by comparison to the standard curve of Neukum and Hiller (1981). Absolute ages were derived from the Lunar cratering vs. age curve (Neukum and Hiller 1981). The counts were completed using a table digitizer linked to a DEC VAX 11/780 computer at the Lunar and Planetary Institute, Houston, TX.. A program called 'STAMMER' written by Brian Fessler at the Lunar and Planetary Institute, was used for calculation of cumulative crater/size frequency plots (Appendix 2). Plots were obtained on a Digital VT 125 graphics terminal, and compared to the standard curve to obtain relative ages for the various surfaces. Edits and final copies of the plots were made using an updated version of the 'STAMMER' program (Appendix 2). The updated version was designed to run on a Prime/850 computer and a CalComp 1051 plotter at the University of Rhode Island Computer Center was used to plot the final cumulative crater size-frequency curves.

RESULTS

Geologic/Geomorphic Mapping

On the basis of its high valley network density and overall geomorphic diversity, the Margaritifer Sinus quadrangle was selected as the site for this study. A detailed geologic/geomorphic map of the entire quadrangle was completed at a scale of 1:2,000,000 (Figs. 3a-d). For the purposes of this paper, the map has been reduced and divided into quarters. A copy of the original map, in the form of a clear overlay and at a scale of 1:2,000,000, can be obtained from the author. The map explanation is presented in Table 1.

Relative ages have been assigned to selected surfaces within the quadrangle based on 102 crater counts completed (Table 2, Figs. 4a-d, a reduced version of the original 1:2,000,000 Fig., shows crater count locations). The individual crater counts are presented in Appendix 3 and a summary of all results is given in Figure 5. The results of the crater counts were used, where possible, to help define and correlate units and to locate contacts. The map unit correlation is shown in Figure 6. Relative ages are always given as the cumulative number of craters $>1\text{km} \cdot 10^6 \text{ km}^{-2}$ obtained by projection of the Neukum and Hiller Martian standard curve (1981). Tentative absolute ages have been assigned by simple comparison with the lunar standard curve. An introduction to, and general description of, the various units and terrain types described below can be found in Mutch et al. (1976), Murray et al. (1981), and Baker 1982.

Description of Units

Channel Features

Channels and Valley Networks (Ch)-Examples of varying scale include: macro-scale features such as Eos and Capri Chasma (see USGS 1980); meso-scale outflow channels, Uzboi and Ladon Valles (see USGS 1980); and various valley networks ranging in size and morphology from Nirgal Vallis to Parana/Loire Valles (see USGS 1980) to numerous small, poorly-integrated valley features found throughout the quadrangle.

Morphological descriptions of Eos and Capri Chasma can be found in Boothroyd and Timson (1981), Baker (1982), and Carr (1981; 1984). Descriptions of the meso-scale features, Uzboi and Ladon Valles are found in Florenski et al. (1975), Carr (1979b), Carr and Clow (1981), Pieri (1980a), Boothroyd (1983), Parker and Pieri (1985a; 1985b), and later in this paper. A further description of these features is not presented here.

Figs. 3a-d. Geologic/Geomorphic map of MC19. Approximately one quarter of the quadrangle is displayed in each of 3a-d: MC19NW in 3a; MC19SW in 3b; MC19SE in 3c; and MC19NE in 3d. The map explanation is given in Table 1. A copy of the original map at 1:2,000,000 can be obtained from the author.

Fig. 3a

Fig. 3b

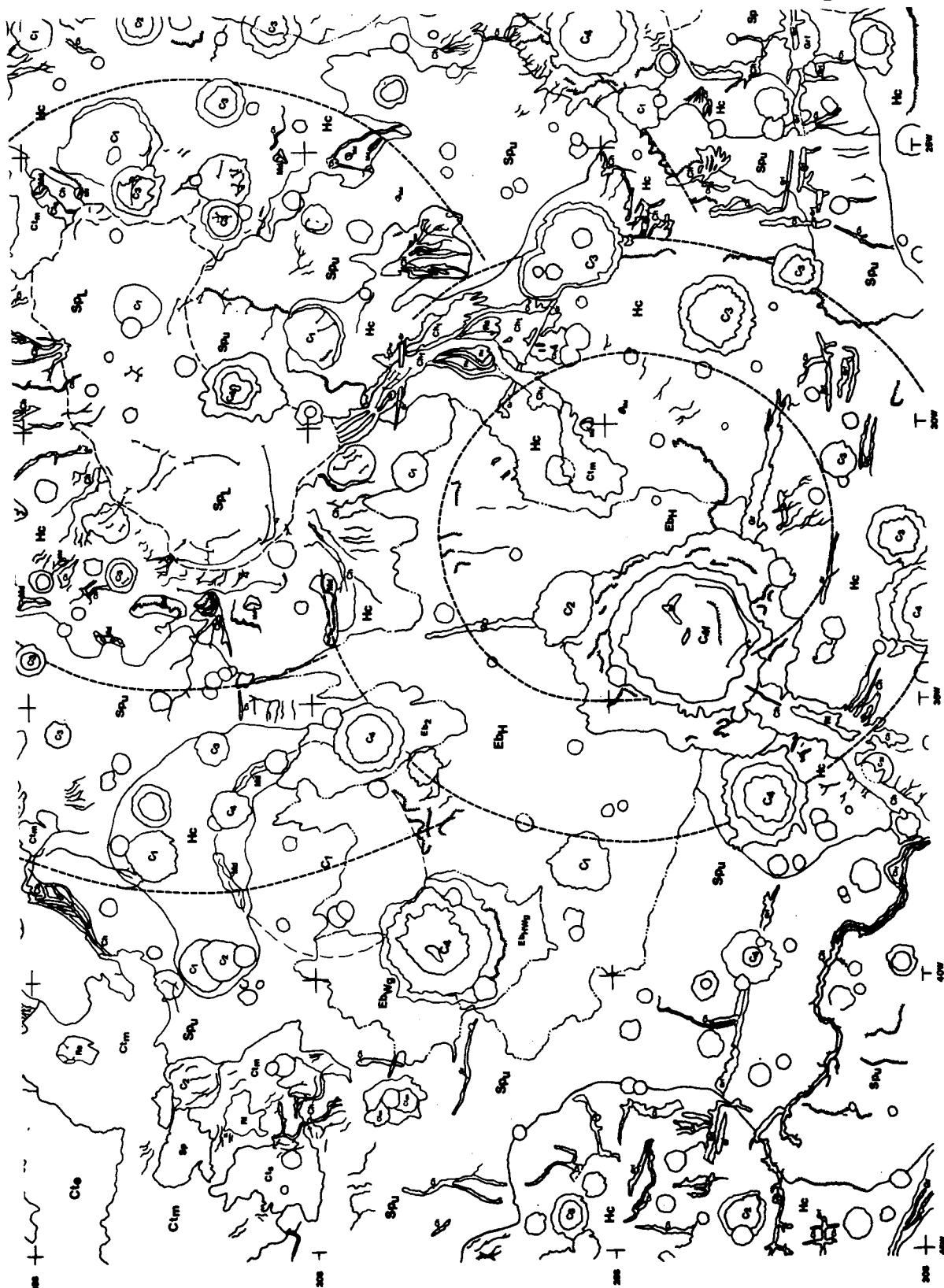


Fig. 3c

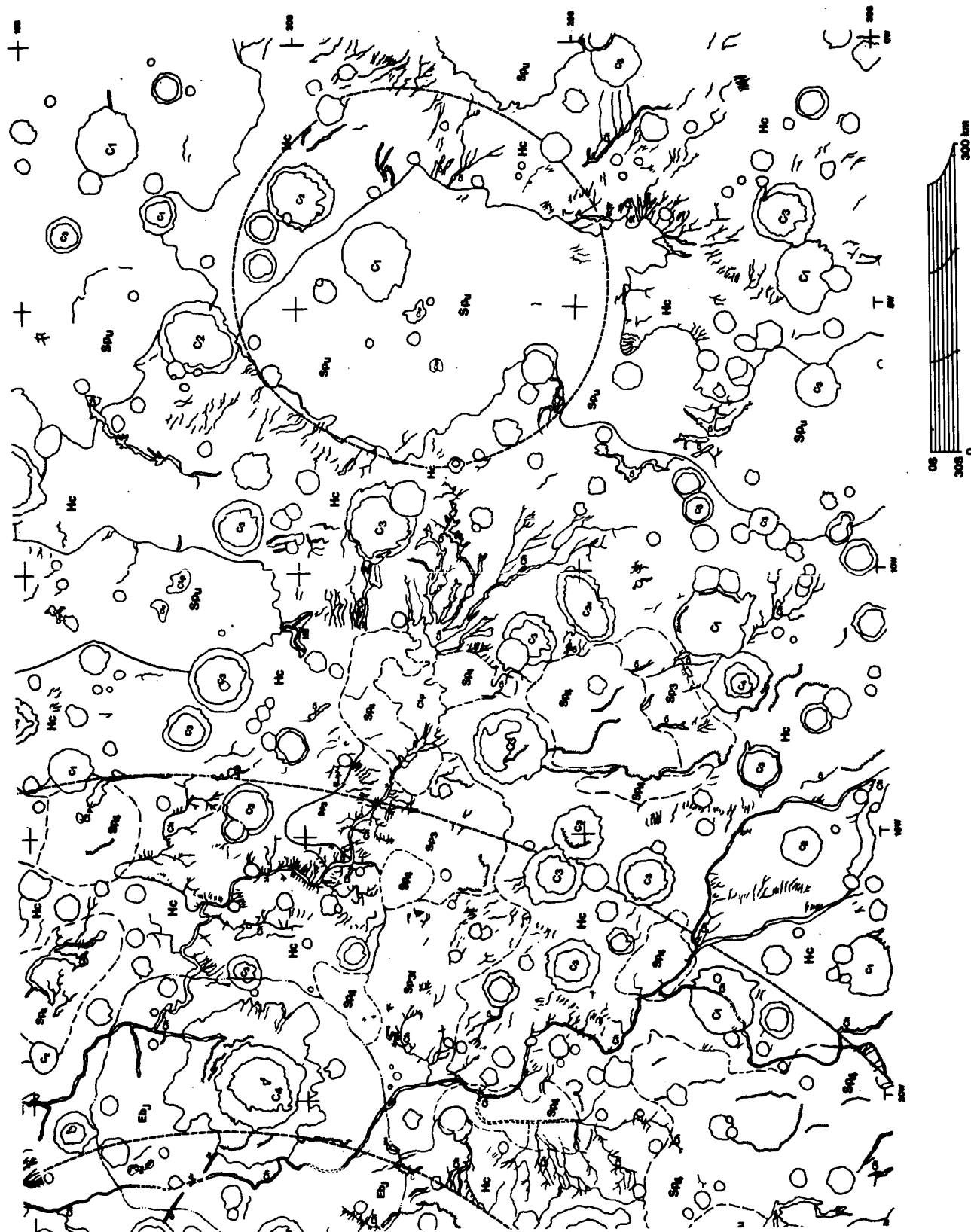


TABLE 1
GEOLOGIC/GEOMORPHIC MAP EXPLANATION

CHANNELS AND VALLEYS

Ch Valley networks and channel features
 Small valley networks
 Ch_w Channel walls
 Ch_f Channel floor
 Ch_t Terraces
 R_l Remnants, large
 R_s Remnants, small
 R_l_f Remnants, large, flow modified
 R_s_f Remnants, small, flow modified

CHAOTIC TERRAIN

Ct_e Extreme collapse
 Ct_m Moderate collapse
 Ct_s Slight collapse
 Ct_p Positive relief chaotic deposits
 Ct_f Fretted terrain


SMOOTH PLAINS DEPOSITS

Sp₄ Fourth resurfacing event (6000-2000)
 Sp₃ Third resurfacing event (14,000-8100)
 Sp_u Smooth plains, undifferentiated
 Sp_L Floor of Ladon Basin
 Sp_f Smooth plains, grooved
 Sp_p Relict polar deposits

CRATERS

C₄ Youngest, fresh
 C₃ Subdued
 C₂ Degraded
 C₁ Extremely degraded
 C_f Craters, flow modified
 C_J Jones crater
 C_H Holden crater
 E_b Ejecta blanket, as labelled

MULTI-RINGED BASINS AND HEAVILY CRATERED TERRAIN

Hc Hilly and heavily cratered terrain
 Ancient multi-ringed impact basins (AMIB)
 Md Mount material

OTHER FEATURES



Gr Grabens
 Gr_f Grabens, flow modified
 Ridges
 Ed Eolian deposits (mantled areas and dunes)
 Mml Mass movement deposits
 Fractures

Table 2.-- CRATER COUNTS: location, age and quality
(count refers to the image or photomosaic derived from)

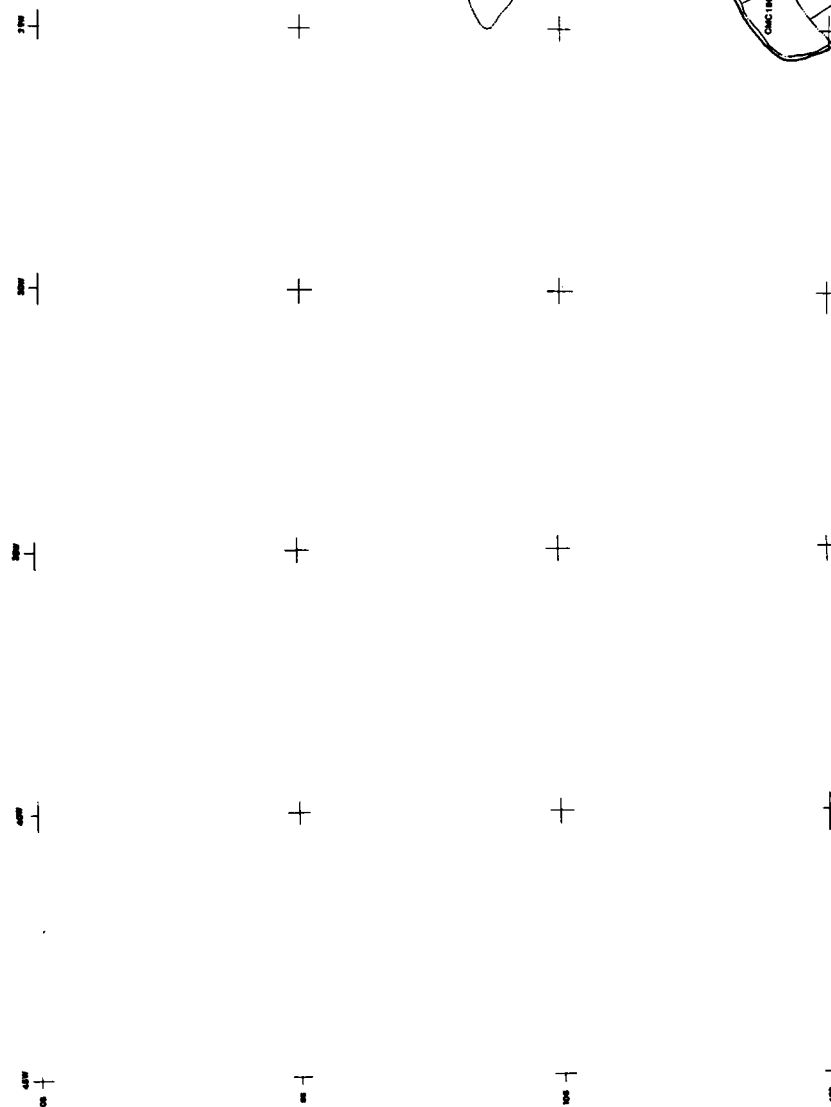
Crater Count	Location		Relative age (# >1km/10 ⁶ km ²)	Count quality	Number of Craters
	S Lat	W Long			
C084A38.001	28.5	21	5500	GOOD	18
C084A38.002	29	22	12500	FAIR	5
C084A39.01B	30	20.5	2000	GOOD	12
C084A39.01C	29	21	1600	GOOD	13
C084A40.01B	27	21	5400	FAIR	10
C084A40.002	27	18	3300	POOR	10
C084A40.003	27	21	3500	GOOD	12
C084A40.004	26	20	4000	POOR	9
C084A40.005	29	20	2200	POOR	20
C084A42.001	26	18	8700	GOOD	8
C084A42.01B	26	18	2600	GOOD	14
C084A42.02B	27	17	5200	POOR	10
C084A43.001	27	13.5	2500	POOR	22
C084A43.01B	26	3	4900	FAIR	10
C084A45.01B	25	13	3950	FAIR	15
C084A45.002	27	11	9000	FAIR	7
C084A45.02B	27	12	13800	FAIR	7
C084A46.01B	22	13	5200	GOOD	11
C084A46.01D	22	14	10800	FAIR	7
C084A46.01E	21	13	10000	FAIR	8
C084A46.02B	23	13	12500	POOR	6
C084A47.01B	24	8	11500	POOR	28
C084A47.002	25	7.5	9500	FAIR	9
C084A47.02B	24	8.5	9000	POOR	15
C084A47.003	23	11	9500	POOR	15
C451A06.001	3	17	10000	POOR	5
C451A06.002	1N	17	6000	POOR	8
C451A07.001	2N	17	7000	POOR	4
C451A07.01B	2N	17	5000	POOR	5
C451A08.001	4	18	8000	POOR	6
C615A24.001	10	22	7100	POOR	9
C615A24.002	11	21	9000	POOR	8
C615A42.001	19	21	3400	POOR	4
C615A42.01B	20	22	3000	POOR	8
C615A43.001	21	18	3000	POOR	13
C615A43.002	23	18	10000	FAIR	11
C615A46.001	16	15	34000	POOR	5
C615A46.002	15	15	10000	FAIR	13
C615A46.003	17	14	5800	FAIR	7
C650A13.001	17	31	8500	POOR	7
C650A13.002	18	28	8900	POOR	18
C650A13.003	15.5	28	11000	POOR	18
C650A13.004	16	27	6200	POOR	15
C651A61.01B	9	23	7000	FAIR	6
C651A61.002	11	23	6700	FAIR	10
C651A63.001	14	22	4600	POOR	9
C651A63.01B	15	23	9000	GOOD	11
C651A64.001	16	27	10500	GOOD	7
C651A64.02B	16	25	8500	FAIR	9

Table 2 (cont'd)

C651A67.001	23	15	16000	FAIR	10
C651A67.002	22	18	7000	FAIR	8
C651A68.001	24	22	9000	FAIR	12
C651A68.002	25	21	9800	POOR	6
C651A85.001	10	21	5500	GOOD	7
C651A85.002	9	18	5000	FAIR	15
C651A86.01B	9	23	2375	POOR	5
C651A86.002	10	21	5000	POOR	8
C651A87.001	12	16	105000	POOR	111
C651A87.01B	13	16	110000	FAIR	17
C651A87.002	15	17	3100	FAIR	21
C651A87.003	14	15	13900	FAIR	29
C651A92.001	23	15	9000	POOR	23
CNC19SEMOS.001	MC19SE		8700	FAIR	64
CNC19SEMOS.002	16	23	11000	POOR	20
CNC19SEMOS.003	14	18	15300	POOR	8
CNC19SEMOS.004	22	23	10100	POOR	21
CNC19SEMOS.005	28	20	10000	FAIR	29
CNC19SEMOS.006	23	15	9500	FAIR	13
CNC19SEMOS.007	22	19	11000	POOR	9
CNC19SEMOS.008	25	6	11500	FAIR	6
CNC19SEMOS.009	20	10	9100	FAIR	16
CNC19SEMOS.010	25	10	10000	POOR	18
CNC19SEMOS.011	35	10	14000	FAIR	8
CNC19SEMOS.012	34	15	20000	POOR	10
CNC19SEMOS.013	34	7	11000	FAIR	10
CNC19SEMOS.014	31	7	15500	POOR	7
CNC19SEMOS.015	32	12	10000	POOR	12
CNC19SEMOS.016	29	13	10000	FAIR	28
CNC19SEMOS.017	31.5	18	11700	GOOD	13
CNC19SEMOS.018	28	16	12300	POOR	10
CNC19SEMOS.BK1	16	15	50000	GOOD	6
CNC19SEMOS.BK2	20	12	56000	POOR	8
CNC19SEMOS.BK3	25	9	48000	POOR	10
CNC19SEMOS.BK4	14	22	41000	POOR	12
CNC19SEMOS.BK5	22	22	47000	POOR	6
CNC19SEMOS.BK6	29	16	57000	FAIR	20
CNC19SEMOS.BK7	34	11	65000	POOR	9
CNC19SEMOS.BK8	27	21	40000	POOR	21
CNC19SEMOS.BK9	21	16	43000	FAIR	11
CNC19SEMOS.BK0	18	22	67000	POOR	7
CNC19SEMOS.BU1	MC19SE		120000	FAIR	18
CNC19SEMOS.BU2	MC19SE		92000	FAIR	26
CNC19SEMOS.BU3	18	22	170000	POOR	7
CNC19SEMOS.BU4	34	14	220000	GOOD	7
CNC19SEMOS.BU5	28	9	170000	POOR	26
CNC19SEMOS.BR1	18	12	1000000	GOOD	7
CNC19SEMOS.BR2	28	16	950000	FAIR	17
CNC19SEMOS.BR3	34	7	1000000	GOOD	7
CNC19SEMOS.BR4	18	22	850000	FAIR	9
CNC19SEMOS.RD1	27	10	300000	GOOD	39
CNC19SEMOS.RD2	26	20	198000	GOOD	16
CNC19SEMOS.RD3	16	19	210000	GOOD	18

Figs. 4a-d. Crater count locations in MC19. Approximately one quarter of the quadrangle is displayed in each of 4a-d: MC19NW in 4a; MC19SW in 4b; MC19SE in 4c; and MC19NE in 4d. The map explanation is given at the bottom of Fig. 4b. A copy of the original diagram at 1:2,000,000 can be obtained from the author.

FIG. 4 CRATER COUNT LOCATIONS



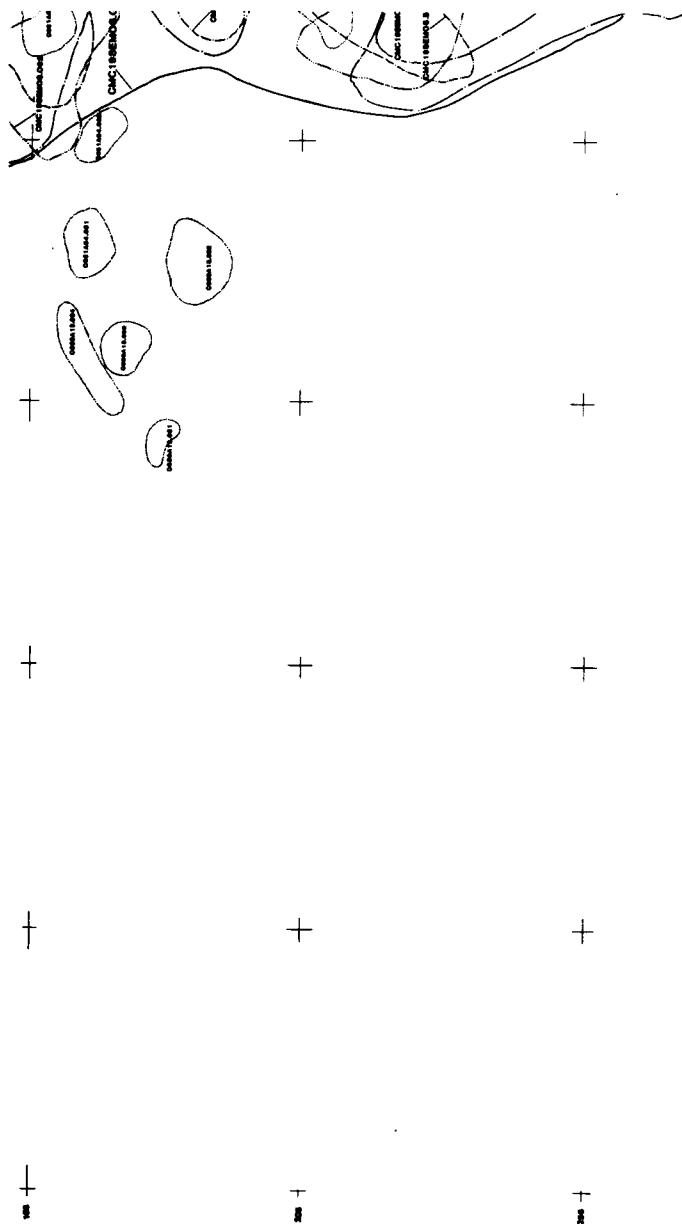
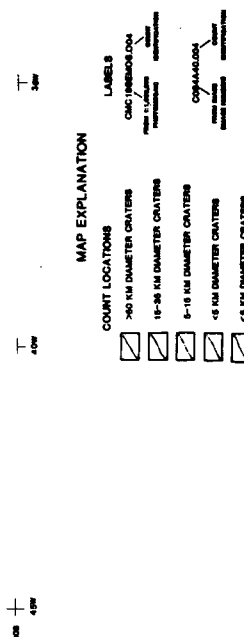
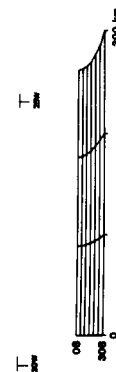


Fig. 4b



ORIGINAL PAGE IS
OF POOR QUALITY

ORIGINAL PAGE IS
OF POOR QUALITY

Fig. 4c

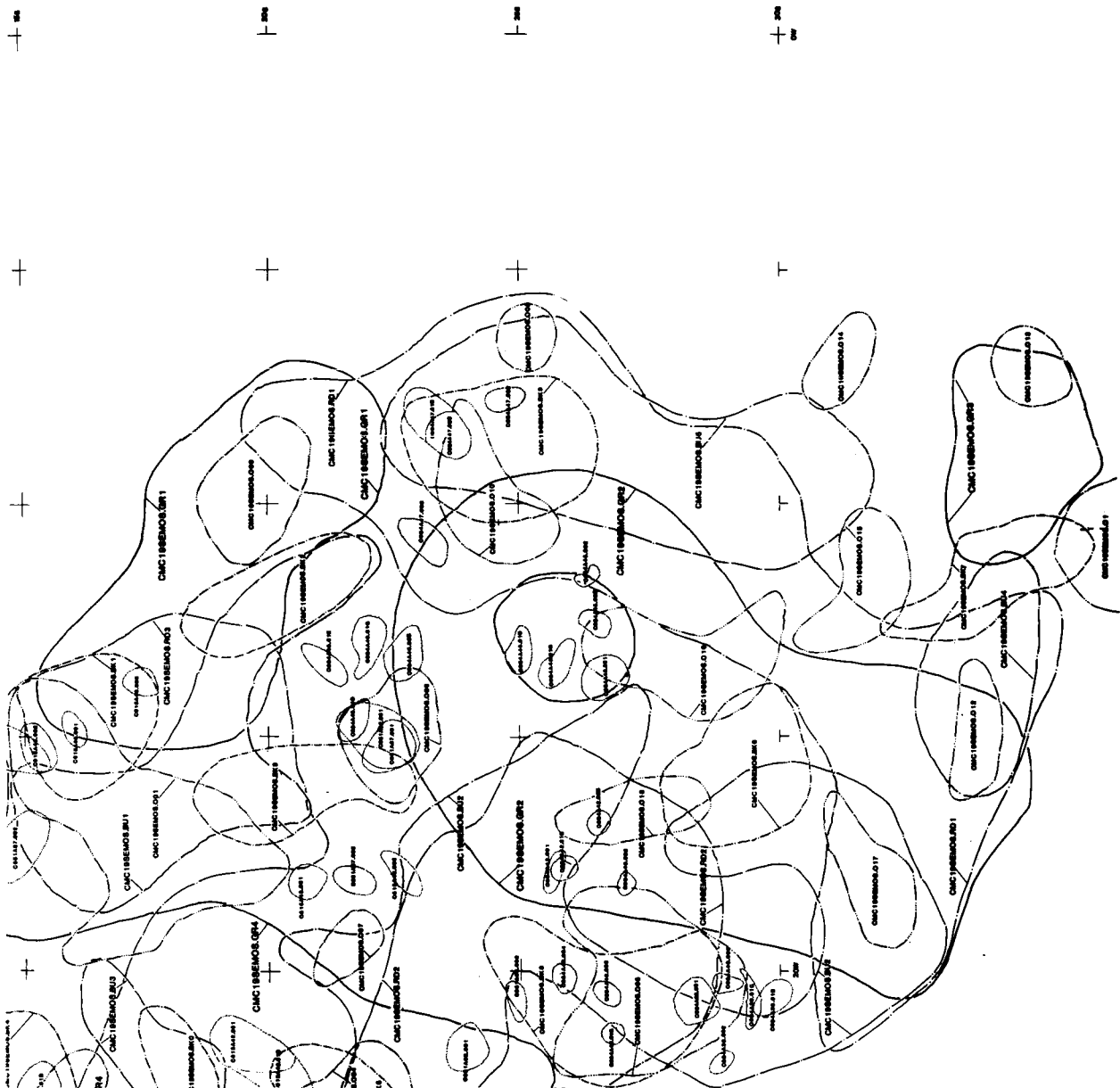


Fig. 4d

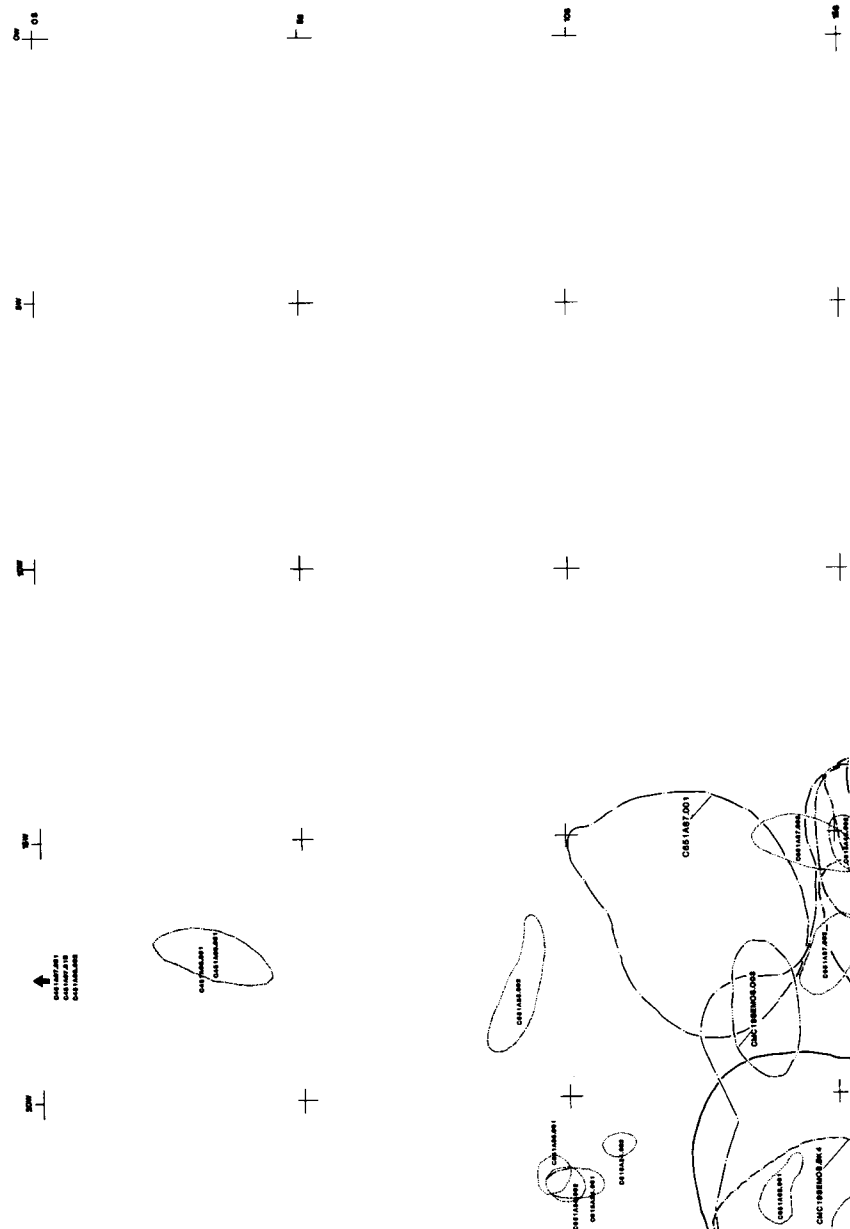
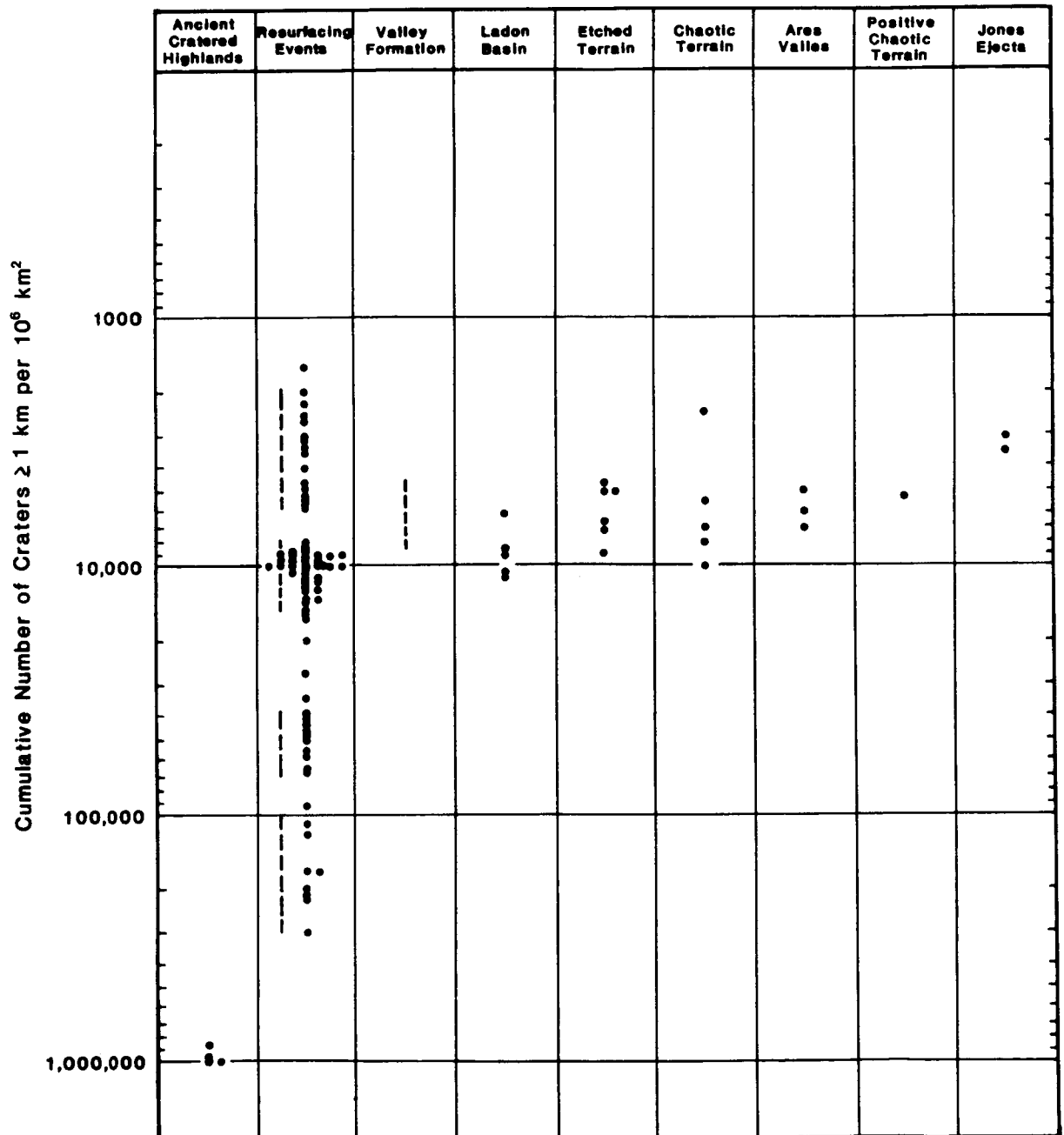


Fig. 5. Summary of all useable crater count data. Each point plotted represents the relative age of one crater count performed in the terrain indicated (see Table 2 and Appendix 3 for individual cumulative crater size-frequency curves, locations, and assigned relative ages). Time intervals of formation of various features and terrain were determined by using the range of relative ages obtained for that feature. Most likely times of resurfacing (dashed vertical lines) were determined by identifying distinct clusters of the relative age values that were obtained by performing crater counts on various homogeneously cratered surfaces (in a specific crater size range). The time of valley formation in the region (dashed vertical line) was determined by the cross cutting relationship of various dated surfaces incised by, and covering, the valleys.

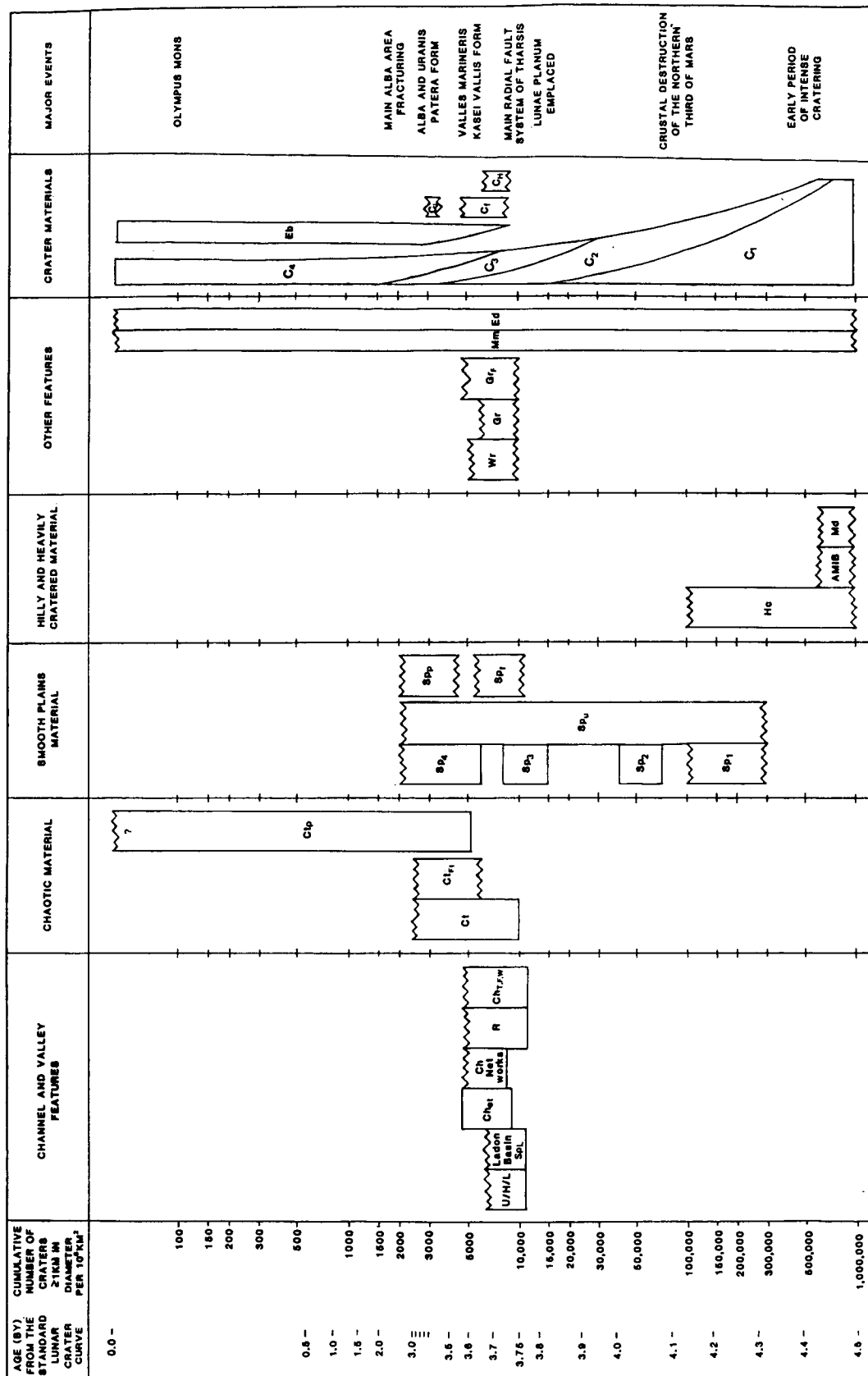
Figure 5



ORIGINAL PAGE IS
OF POOR QUALITY

Fig. 6. Correlation of map units on the geologic/geomorphic map of MC19 (Figs. 3a-d), and comparison to the timing of major events across the planet. Correlations were made using the relative ages determined for various surfaces by crater counting, and cross-cutting relationships. Relative ages are given as the cumulative number of craters $> 1\text{km-}10^6\text{ km}^{-2}$.

Figure 6



ORIGINAL PAGE IS
OF POOR QUALITY

The morphology of the valley networks is similar to that observed across the planet, as described by the Mars Channel Working Group (1983). Valley walls appear cliff-like and most valley floors are flat, especially in the case of Nirgal and Loire Valles. The network tributaries usually have steep, cusped headward ends, best developed in Nirgal and Parana Valles. Valley widths average about 3 to 5 km for the larger systems, and range up to about 20 km at the widest point of Nirgal Vallis. Valley lengths range from about 10 km for small valleys and tributaries to 900 km for the Parana/Loire system to over 1200 km for the Samara Valles system. Some networks show interior channels, possibly indicating differential erosion of layered deposits and/or multiple flow events.

A relative age of 8,500 to 4,600 has been determined for the valley network systems in MC19SE on the basis of crater densities observed on surfaces incised by the networks and those covering them. This age is inferred for the other valley networks incised in surfaces for which no age was derived and is in general agreement with the age determined for valley networks by other workers (Carr 1979b; 1980a; Hiller and Neukum 1979; and Neukum and Hiller 1981; Baker and Partridge 1984b).

The meso-scale outflow channel features have a relative age of 11,000 to 6200 based on crater densities found in Ladon Basin. Chasma flow features are probably of a similar, but slightly younger age than the other flow features because some valley systems have been beheaded by the Chasma wall (Schultz 1982; Boothroyd 1982; 1983). With the exception of the Chasma, most other channel and valley features are located within the hilly and heavily cratered terrain. Two notable exceptions to this are Nirgal Vallis and a large unnamed valley network in MC19NE (Fig 3d) at 9S, 14W. It is important to note however, that both of these systems head in the hilly and heavily cratered terrain.

Where possible, sub-units have been assigned to further define features within the channels and valleys. Sub-units include: the bounding channel walls; the channel floor, to distinguish that part of the channel that was actually occupied by fluid; terraces, to indicate various locations and elevations occupied by fluid as downcutting progressed; and large (long axis greater than 50km) and small (long axis less than 50km) remnants. Remnants have been further subdivided into those that have been submerged and modified by flow over the top, and those not modified by flow.

Etched Terrain (Ch_{et})-Etched terrain is present in the central part of the quadrangle near the foot of Samara, Parana/Loire, and Margaritifer Valles (Fig. 7). Crater densities display a wide range of values from 9,000 to 4,600. Numerous remnants are seen across the unit some of

Fig. 7. Photomosaic of etched terrain, with numerous remnants (R), in MC19 centered at 12S, 22W. Shows the relationship of Samara and Loire Valles, entering from the south, and Margaritifer Valles, to the etched terrain and Margaritifer Chaos to the north. The presence of distributaries (D) and flow modified remnants clearly associated with Margaritifer Valles, and the lack of same visibly associated with Samara and Loire Valles, suggests that flow out of Ladon Basin was the dominant factor in the formation of the etched terrain (651A61, 63, 64, 85, 86, 88).

ETCHED TERRAIN

SOUTHERN VALLES

SAMARA VALLES

100 km

N

which may have been submerged and flow modified. Some low areas in the unit show slight collapse. The boundary along the west side and northeast corner is very subtle and its exact position is subject to question. Type locality: 11.5S, 21W and Figure 7.

Chaotic Features

Chaotic Terrain (Ct)—Chaotic terrain is located mainly in MC19NW (Fig 3a) and the eastern part of MC19NE (Fig. 3d, see also USGS 1980, and Fig. 7) where it appears as disordered areas of flat-topped, angular and occasionally rounded or flow modified blocks of material showing high local relief. A trend from flat-topped blocks towards the edge to angular and rounded blocks in the center is common. The terrain is located in depressions, that are sometimes closed, and are either scarp bounded or gradational with channel floors, fretted terrain or adjacent uplands. The deposits surrounding the chaotic terrain occasionally displays many fractures. Crater densities within Iani and Margaritifer Chaos display a range of values from 10,000 to 2375. Type localities: 0 to 10S and 15 to 30W.

Fretted Terrain (Ct_f)—A small area of fretted terrain exists in MC19NE at 3S, 19W (Fig. 3d). It grades into the adjacent uplands to the west and the chaotic terrain to the east. The fretted terrain occurs as undissected outliers of the adjacent uplands separated from each other by steep, flat-floored chasms or channels that are roughly aligned parallel to the east-southeast, west-northwest structural grain that is seen the area. Type locality: 3S, 19W.

Positive Relief Chaotic Deposits (Ct_p)—Positive relief chaotic deposits occur as small, commonly rounded, isolated patches mostly in MC19SE. These are best developed in Parana Basin between Parana and Loire Valles (22.5S, 12W, Fig. 3c). The chaos consists of numerous fairly flat-topped blocks that commonly display an outward facing scarp that forms the boundary with the adjacent terrain. The chasma between adjacent blocks are less well developed than in the fretted terrain and they do not appear to show a preferred orientation. A very tentative crater density of 5200 (based on a single count) was obtained for the positive chaotic deposits in the region of 22.5S, 12W, making it younger than the valleys in that area.

Smooth Plains

Smooth Plains Deposits (Sp)—Located throughout the quadrangle, smooth plains are seen as smooth to rolling surfaces that sometimes contain channels. These deposits are also present on many crater floors.

Crater densities, mainly from MC19SE (Figs. 3c, 4c), indicate that four resurfacing events occurred in the region. The earliest (300,000 to 100,000), was of wide regional extent and resulted in the first modification of the cratered highlands in the area. The second (70,000 to 40,000) and third (14,000 to 8,100) events were also of regional extent. The surface created by the third event, labelled Sp₃, is the youngest surface in the quadrangle dissected by the valley networks. It was dated mainly in MC19SE (Fig. 3c), but is probably of regional extent as surfaces displaying similar crater densities occur across the quadrangle. The youngest surface (6,000 to 2,000), labelled Sp₄, was also dated mainly in MC19SE (Fig. 3c). It occurs locally, filling basins, and always covers valley networks when present. Similar fill, not dated, occurs in other basins throughout the area. The Ladon Basin unit, mapped as Sp_L in Fig. 3b, displays a relative age of 11,000 to 6,200 based on the crater density of its surface. Areas mapped as smooth plains outside MC19SE and the Ladon basin are inferred to be associated with one or more of the above events and, unless otherwise specified, are labelled Sp_u (undifferentiated). Where two plains units are superimposed, only the top surface has been labelled. Grabens, wrinkle ridges, and fractures are located predominately within the smooth plains units. Type localities: 29S, 41W and 12S, 17W.

Relict Polar Deposits (Sp_r)—Relict polar deposits (described by Schultz 1984) occur as a distinct unit in the extreme northeastern corner of the quadrangle mapped as Sp_r (Fig. 3d). This unit partially and completely buries craters, and always covers valley networks that extend into the region. Inverted topography and pedestal craters are common.

Craters

Craters are classified on the basis of their morphology. For a given size range of craters, decreasing crater class number implies increasing age. However, within a given class, craters of differing sizes can be of differing ages (after Wise 1979). This is because smaller craters are more easily modified by resurfacing events than larger craters. Craters smaller than 10 km were not mapped and craters smaller than 30 km were not classified.

The youngest craters (C₄) are very fresh in appearance and usually display a central peak and a locally defineable ejecta blanket. The next class of craters (C₃) is subdued in appearance. This class of craters usually lacks a defineable central peak and proximal ejecta blanket. Their floors are usually quite smooth and show low local relief. Degraded craters (C₂) have been extensively modified and have floors that are only slightly lower than the adjacent

terrain. This class is the oldest/most modified that display complete rims. The oldest and/or most modified class of craters (C₁) are extremely degraded in appearance and display incomplete rims. Craters whose appearance has been modified by flow have the subscript 'f' following the usual classification, as is the case for Holden crater (Fig 3b, see also USGS 1980). Asymmetric craters, such as the one located at 25S, 11W (Fig. 3c), are the result of low angle (<10 degrees) impact events (Schultz and Lutz-Garihan 1982). They are denoted by the subscript 'a' following the normal classification.

Ejecta Blankets (Eb)—Ejecta blankets are mapped around some larger C₄ craters. Where defined, they are labeled according to the crater they are associated with.

Multi-Ringed Basins and Hilly and Heavily Cratered Deposits

Hilly and Heavily Cratered Terrain (Hc)—This terrain is located mainly in the southwest (Fig. 3b), southeast (Fig. 3c) and northeast (Fig. 3d) quarters of the quadrangle. Most valley networks are located within this unit. Large numbers of craters, approximately 50 km and larger, and of all morphologies are present. Very high calculated crater densities (1,000,000 to 100,000) characterize the unit. Areas that display numerous hills and scarps associated with ancient multi-ringed impact basins (Schultz et al. 1982) have been included in this unit. Grabens; ancient volcanic flows; and some channel, eolian, and mass movement deposits are also present. Type locality: 25S, 16W.


Ancient Multi-Ringed Impact Basins (—)—These features have been best described by Schultz et al. (1982). Three basins occur within the limits of the quadrangle: Ladon Basin, centered at 18S, 30W; Holden Basin at 26S, 32W (both in Fig. 3b); and Noachis/Newcomb A Basin located at 22.5S, 3W (Fig. 3c). The rings of these basins, identified by Schultz and Glicken (1979), Saunders (1979) and Schultz et al. (1982), are indicated on the map.

Mount Material (Md)—Mount material exists as isolated, degraded, generally elongate hills. They usually appear in somewhat arcuate patterns and often form the rings of multi-ringed impact basins. Type locality: 16 to 17S, 32 to 33W.

Other Features

Grabens (Gr)—Features interpreted as grabens occur mainly in MC19SW (Fig. 3b), the eastern edge of MC19SE (Fig. 3c), and the southern part of MC19NW (Fig. 3a). Their average trend is 100 degrees with a range between 90 and 110 degrees. The grabens are roughly parallel to the Valles Marineris system and radial to the Syria rise.

Flow modified grabens (Gr_f)-Many of the grabens have valley networks associated with them and have been flow modified.

Ridges ()-Almost all ridges mapped fall into two distinctly different categories. The first, and oldest, are those that define isolated arcuate sections of degraded multi-ringed impact basin rings, described by Schultz et al. (1982). Examples of this type of ridge are located at 26S, 25W and 20S, 21W (Fig. 3b, USGS 1980).

The second type of ridge strongly resembles lunar, volcanic, wrinkle ridges. These ridges occur throughout the quadrangle within smooth plains units. They are oriented predominantly N-S ± 10 degrees and are roughly concentric to the Tharsis region.

Eolian Deposits (Ed)-These deposits exist in numerous locations both as mantling deposits and dune fields. Many locations appear to be partially to completely buried by mantling deposits (e.g. the region just east of Osuga Valles, see USGS 1980). Dune fields occur mainly on crater floors (26S, 33.5W, Fig. 3b) and on the floors of Eos and Capri Chasma (Fig. 3a).

Mass Movement Deposits (Mml) All mapped locations consist of deposits derived from landslides, although other types of mass movement deposits probably exist. Landslide deposits have been observed on crater floors (27.5S, 36.5W, Fig. 3b) and on the floor of Eos and Capri Chasma (Fig. 3a).

Drainage Basins

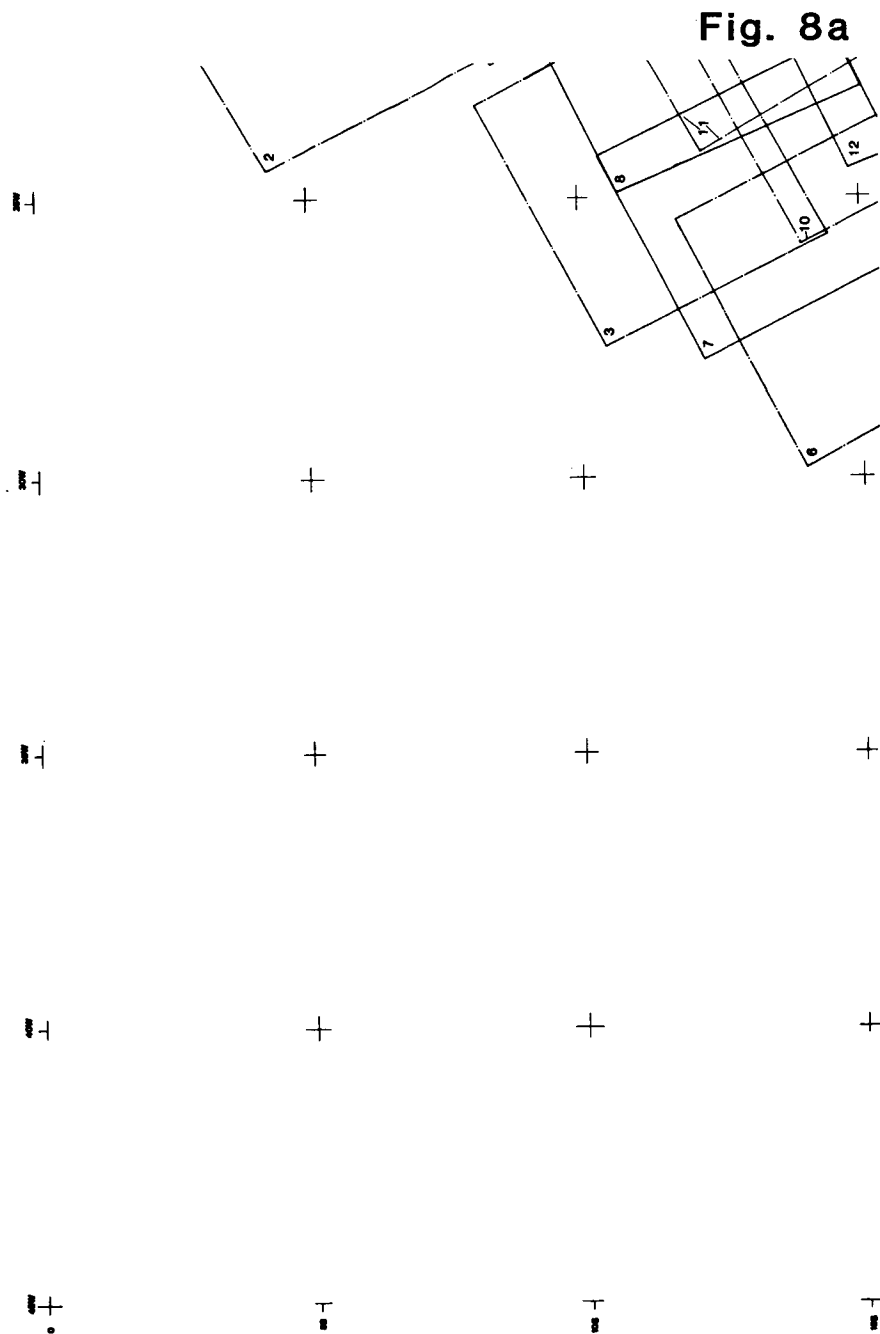
Drainage Basin Mapping

Drainage basin mapping, using stereo pairs of Viking Orbiter images after Boothroyd (1982), was conducted in MC19SE and MC26NE in the Samara and Parana/Loire Valles areas. Stereo pairs used for the drainage-basin mapping are shown in Appendix 4 (Table 6, Figs. 8a-d). The mapped area incorporates the entire drainage network of both systems, including sub-basins of major tributaries, and internal drainage basins between the major networks. Figures 9a-d shows the mapped region in MC19SE and MC26NE from a major N-S trending drainage divide at 9W (Figs. 9c,d), discussed by Boothroyd and Grant (1984; 1985) and Grant and Boothroyd (1984), westward to, and including, the locations in MC19SW (Fig. 9a,b) mapped by Boothroyd (1982). A copy of the original drainage basin map of the entire area, in the form of a clear overlay and at a scale of 1:2,000,000, can be obtained from the author.

Both Samara Valles and Parana/Loire Valles are fairly well integrated and extensive systems. Both have numerous

Figs. 8a-d. Stereo pairs used for drainage basin mapping in MC19. The footprints of the images making up the stereo pairs used are shown. Actual stereo pairs are listed in Table 6. Approximately one quarter of the quadrangle is displayed in each of 8a-d: MC19NW in 8a; MC19SW in 8b; MC19SE in 8c; and MC19NE in 8d. The map explanation is given at the bottom of Fig. 8b. A copy of the original diagram at 1:2,000,000 can be obtained from the author.

FIG 8 STEREO PAIR FOOTPRINT LOCATIONS



ORIGINAL MAP
OF POOR QUALITY

Fig. 8b

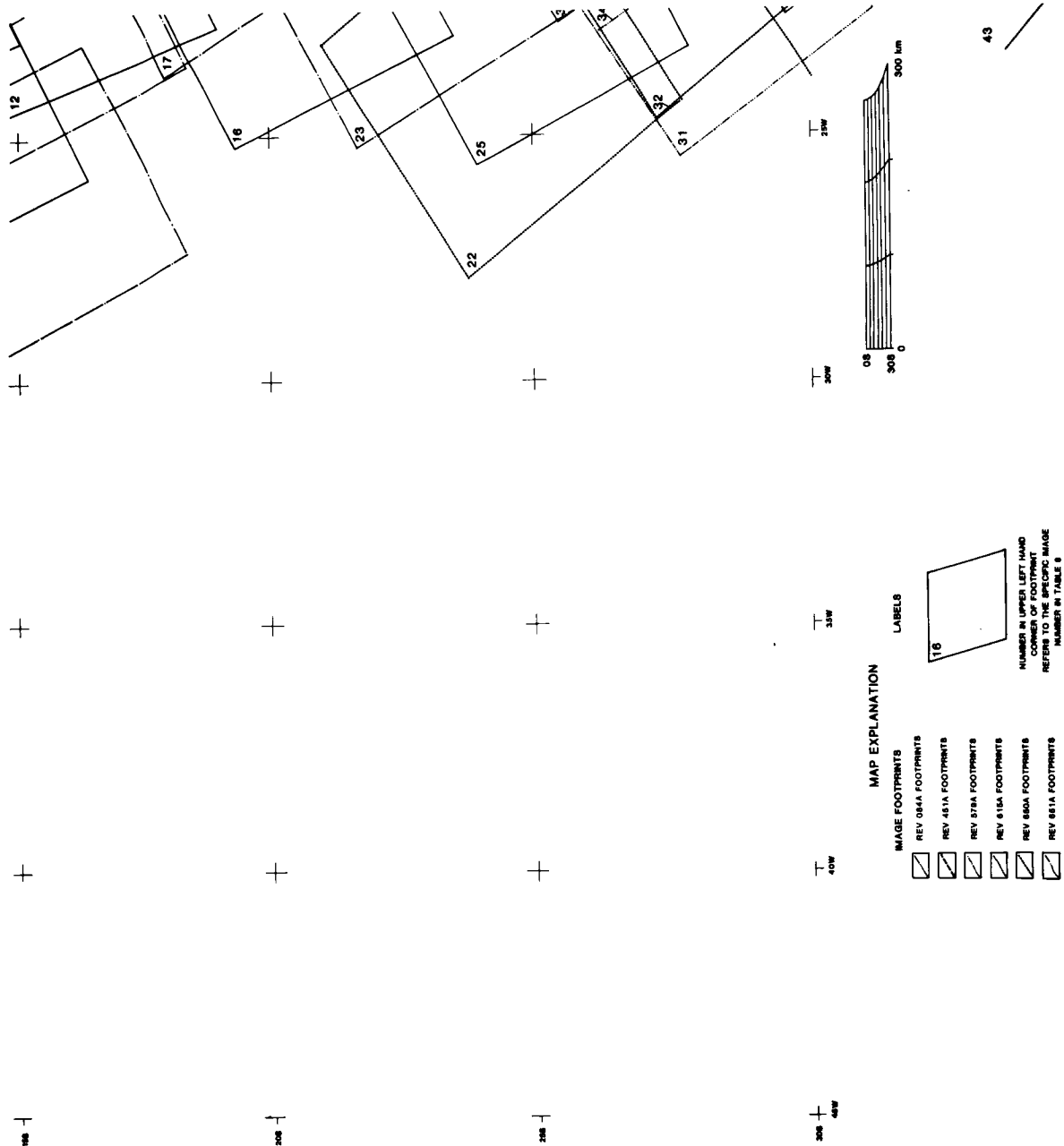


Fig. 8c

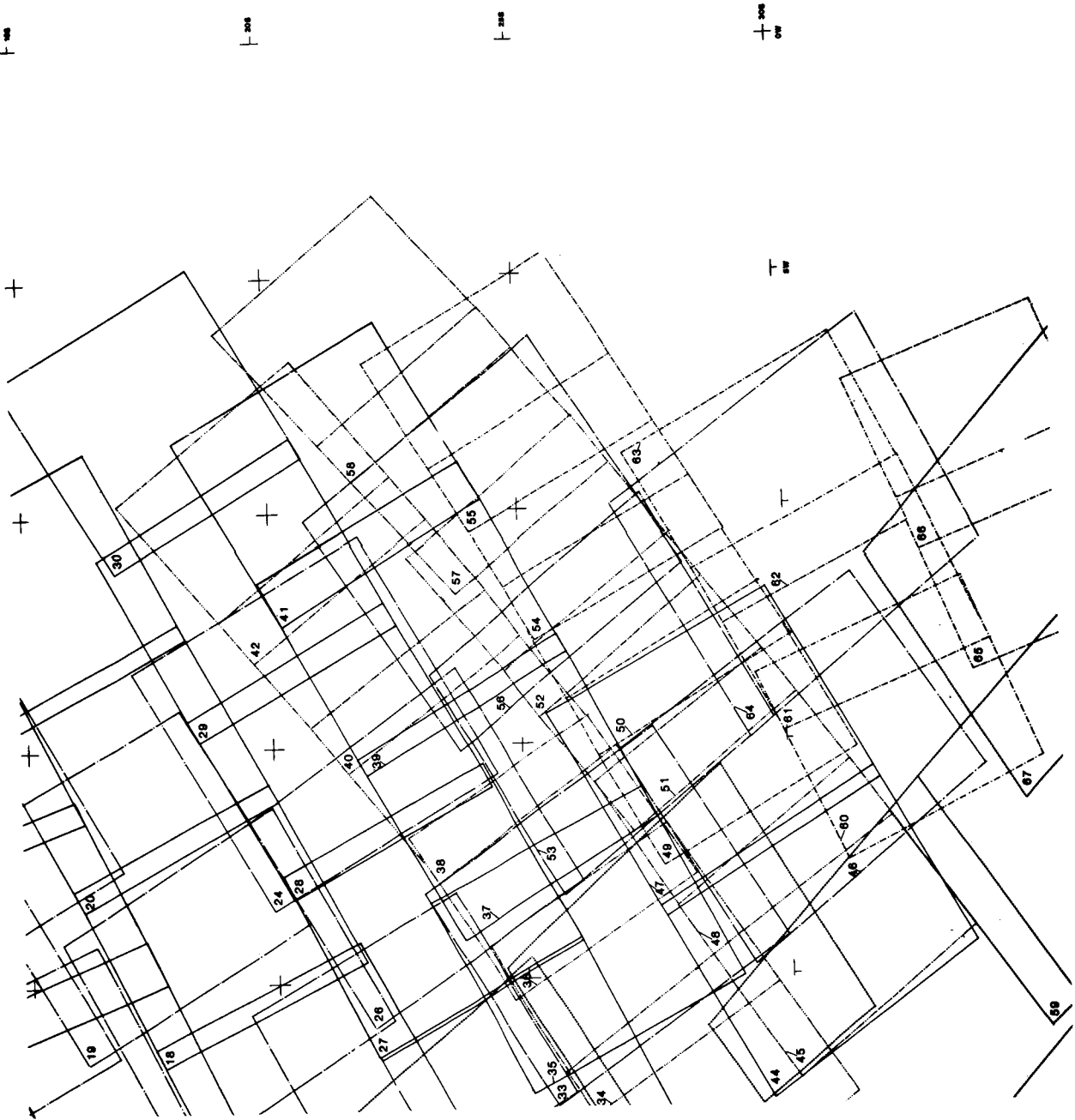
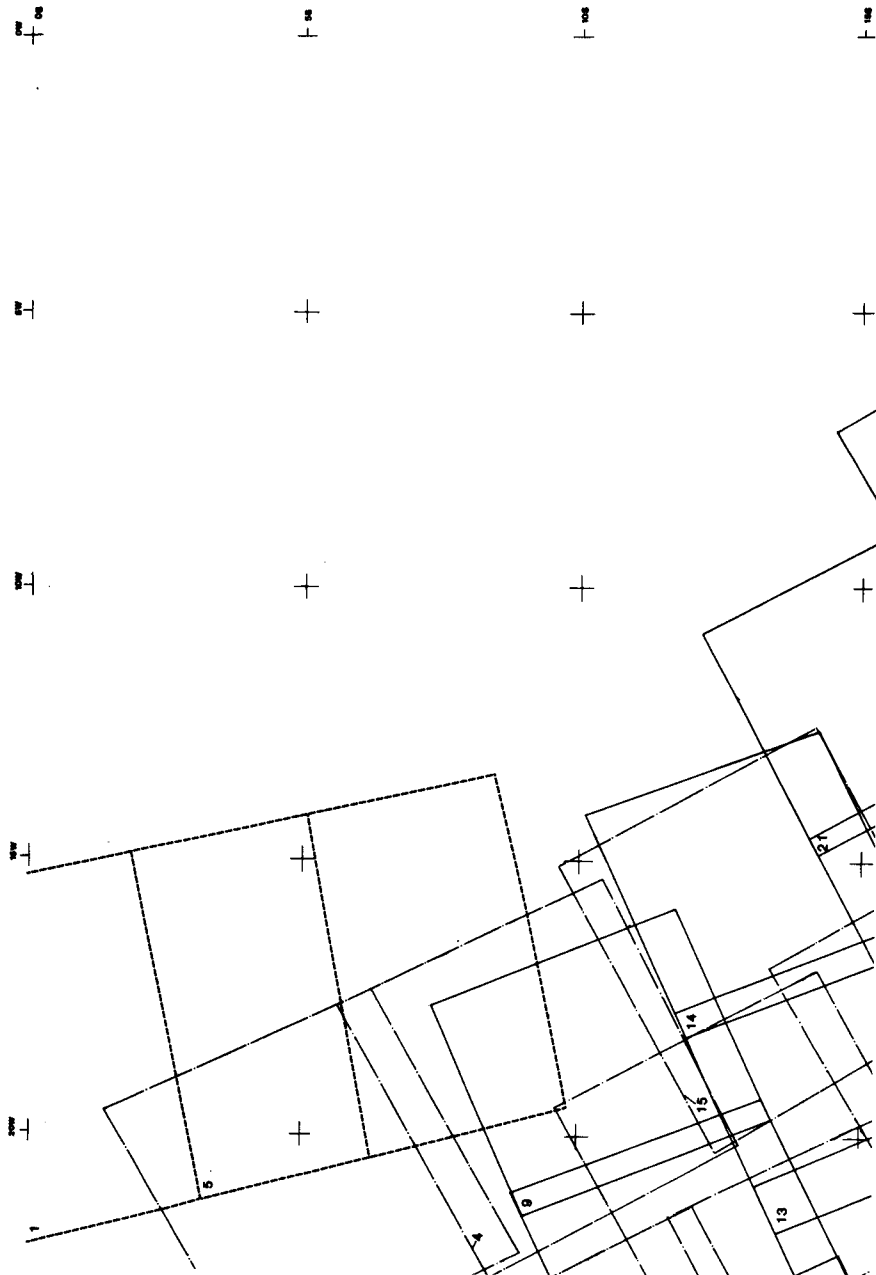


Fig. 8d



Figs. 9a-d. Drainage basins in MC19. Approximately one quarter of the quadrangle is displayed in each of 9a-d: MC19NW in 9a; MC19SW in 9b; MC19SE in 9c; and MC19NE in 9d. The map explanation is given at the bottom of Fig. 9b. A copy of the original diagram at 1:2,000,000 can be obtained from the author.

FIG 9 DRAINAGE BASINS IN MC19

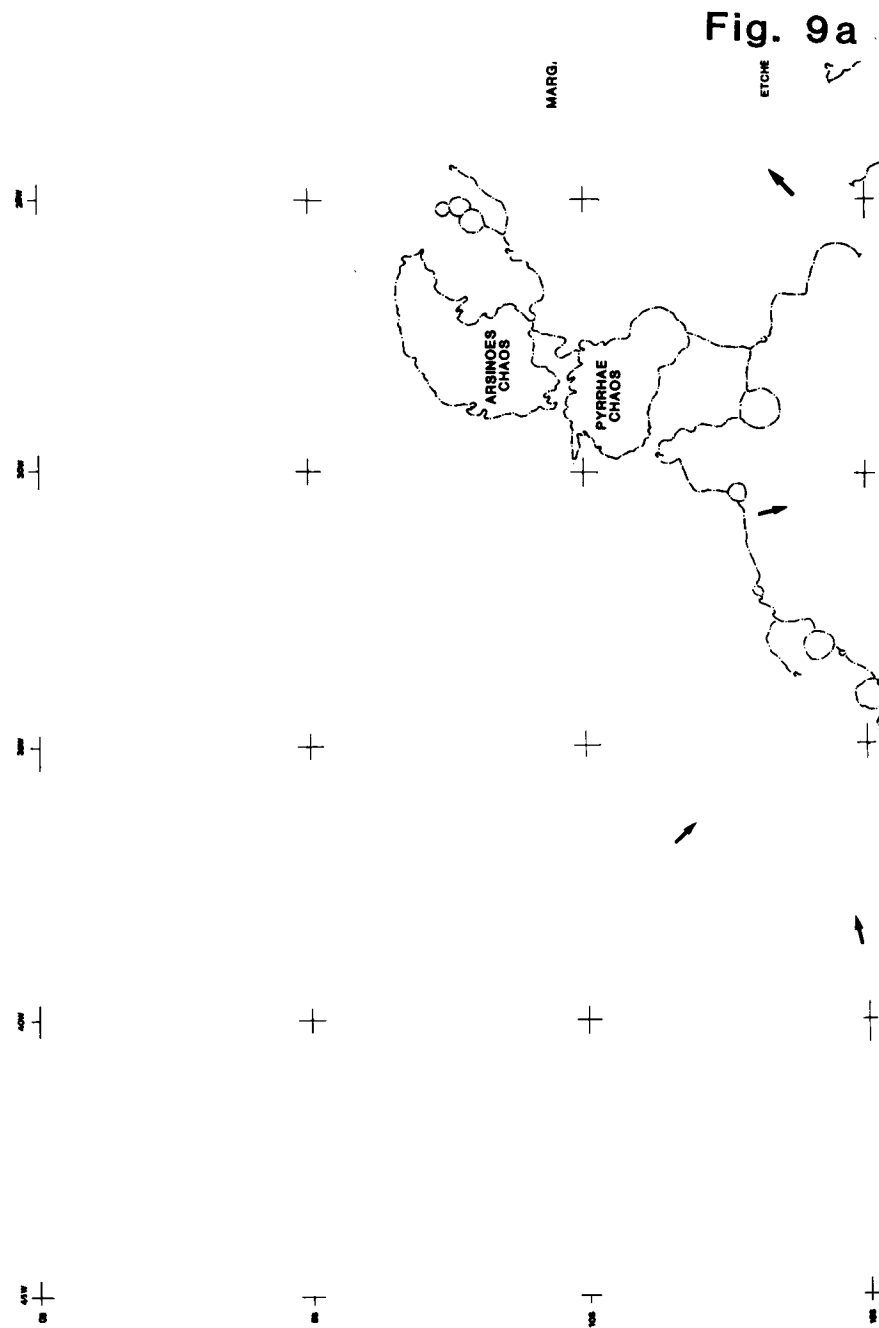


Fig. 9b

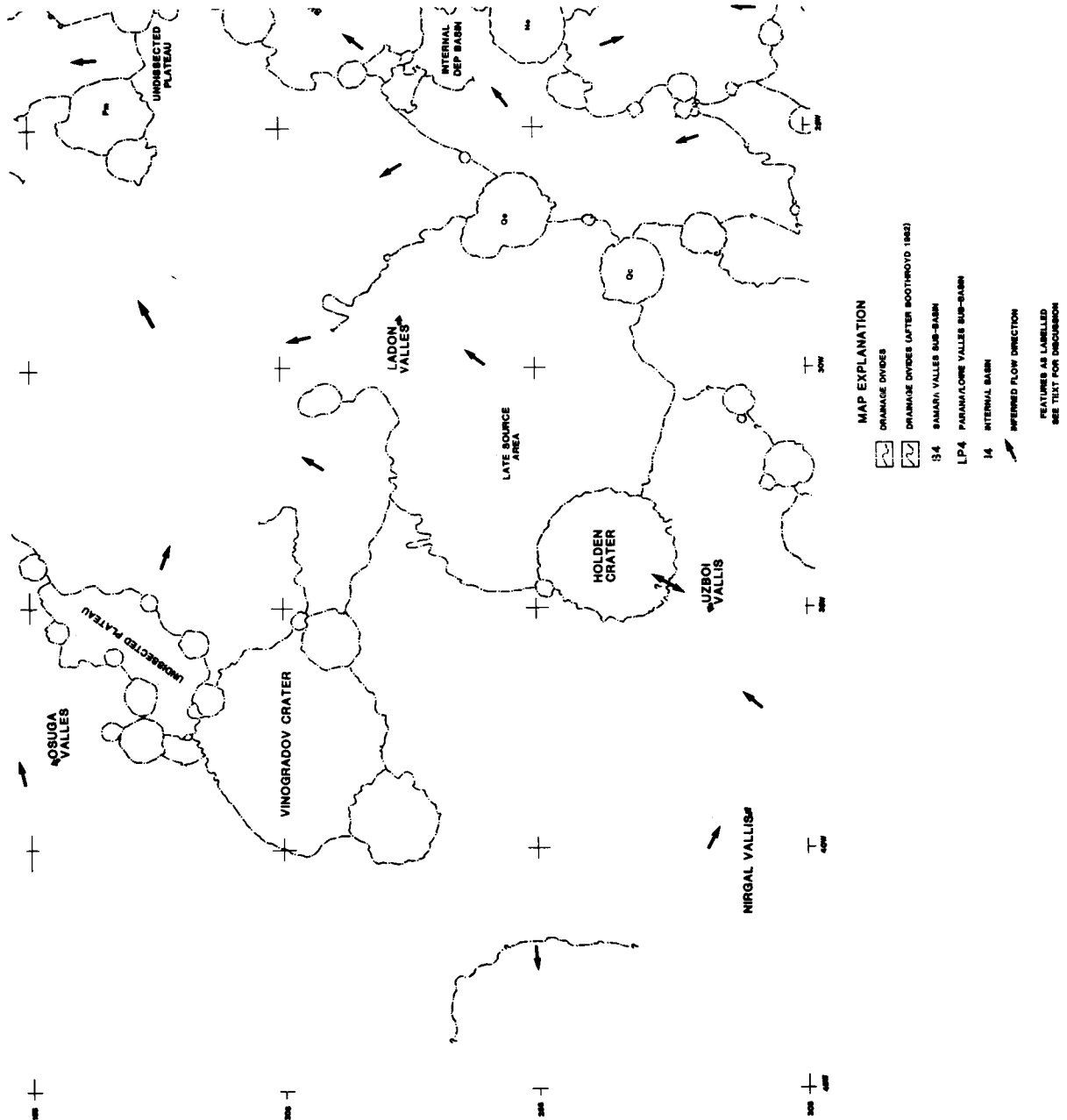


Fig. 9c

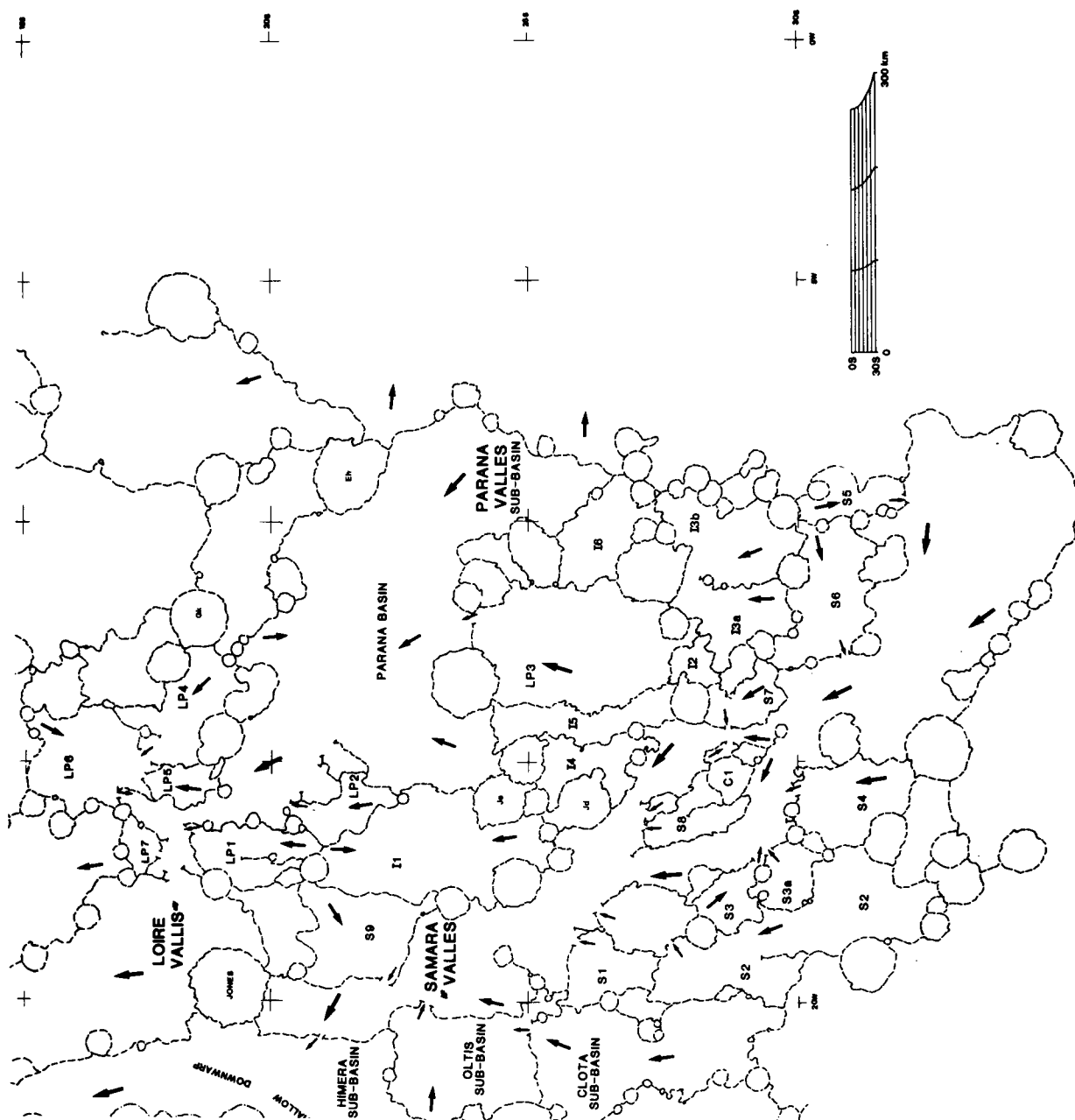
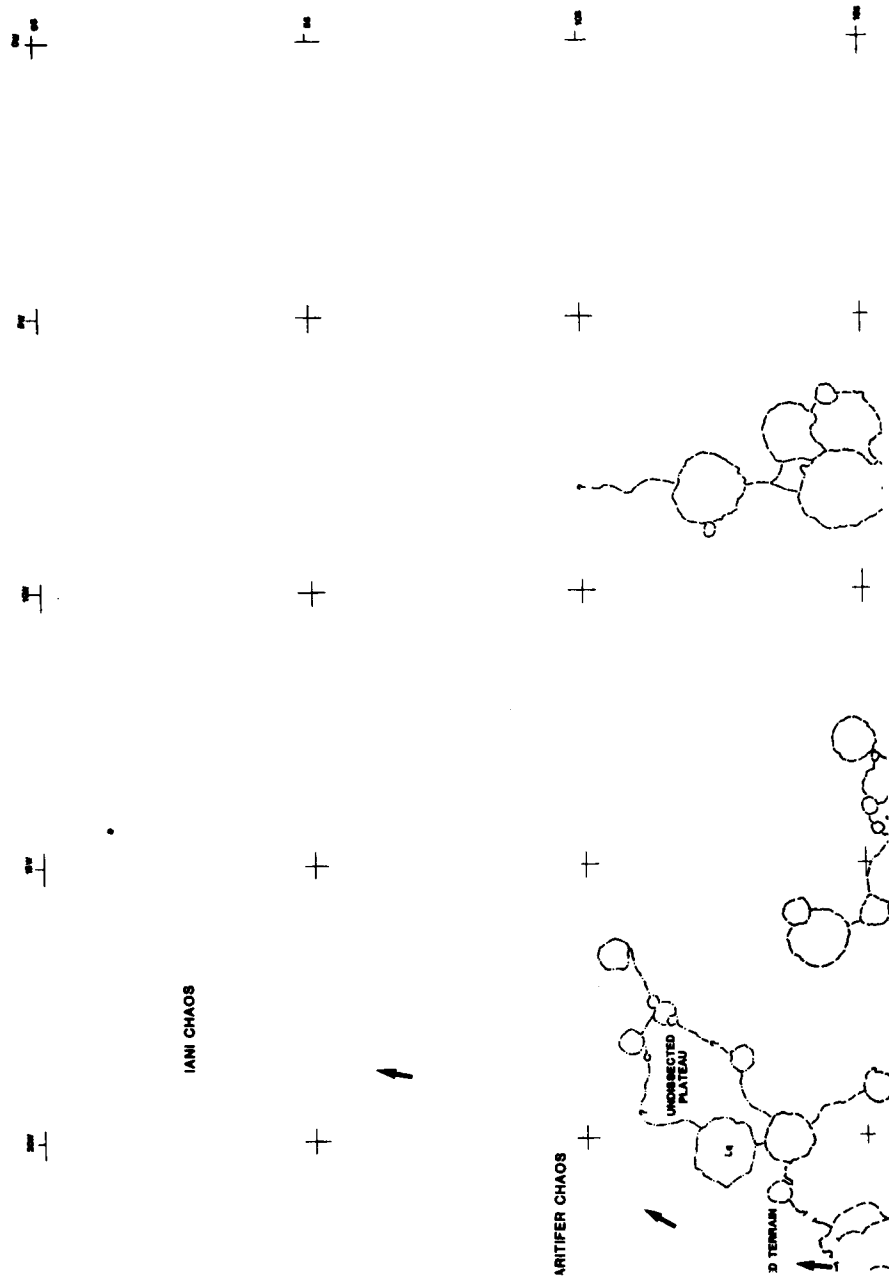


Fig. 9d



sub-basins, many of which are occupied by third or fourth order tributary valleys (Strahler stream order classification; Strahler 1952) that empty into the main trunk valley system. The locations of the major sub-basins and associated internal basins of these systems are given in Table 3, and are shown in Figs. 9c,d. The LP3 sub-basin and I2, I3a, and I3b internal basins are shown in Figure 10. Some sub-basins, notably southern Clota, S1, S5, S6, and LP3 (Fig 9c), have undergone post valley formation resurfacing that has partially to completely buried the existing valleys within them.

Drainage divides between basins and sub-basins are located: 1) along the rims of craters, such as the divide along the western side of the LP4 sub-basin; 2) along the crest of inferred wrinkle ridges, as for the divide around the western side of the LP3 sub-basin; 3) along the crest of rings of the ancient multi-ringed impact basins, as seen along the eastern Himera sub-basin divide; and 4) as poorly defined lines crossing regions of low local relief as is the case for the divide along the southern edge of the Clota Valles sub-basin.

Drainage basin areas of Samara and Parana/Loire valleys, their major sub-basins and internal basins, were measured from the 1:1,000,000 photomosaic constructed for the region. The lengths of all valleys able to be identified at 200 m/pixel resolution were also measured (a reduced copy of the 1:1,000,000 photomosaic showing the measured valley segments is given in Fig. 11). Values obtained for total valley lengths were divided by the encompassing drainage basin area to obtain the drainage densities of the two systems, their major sub-basins, internal basins, and selected sections along the trunk valleys. Basin areas and densities are displayed in Table 4.

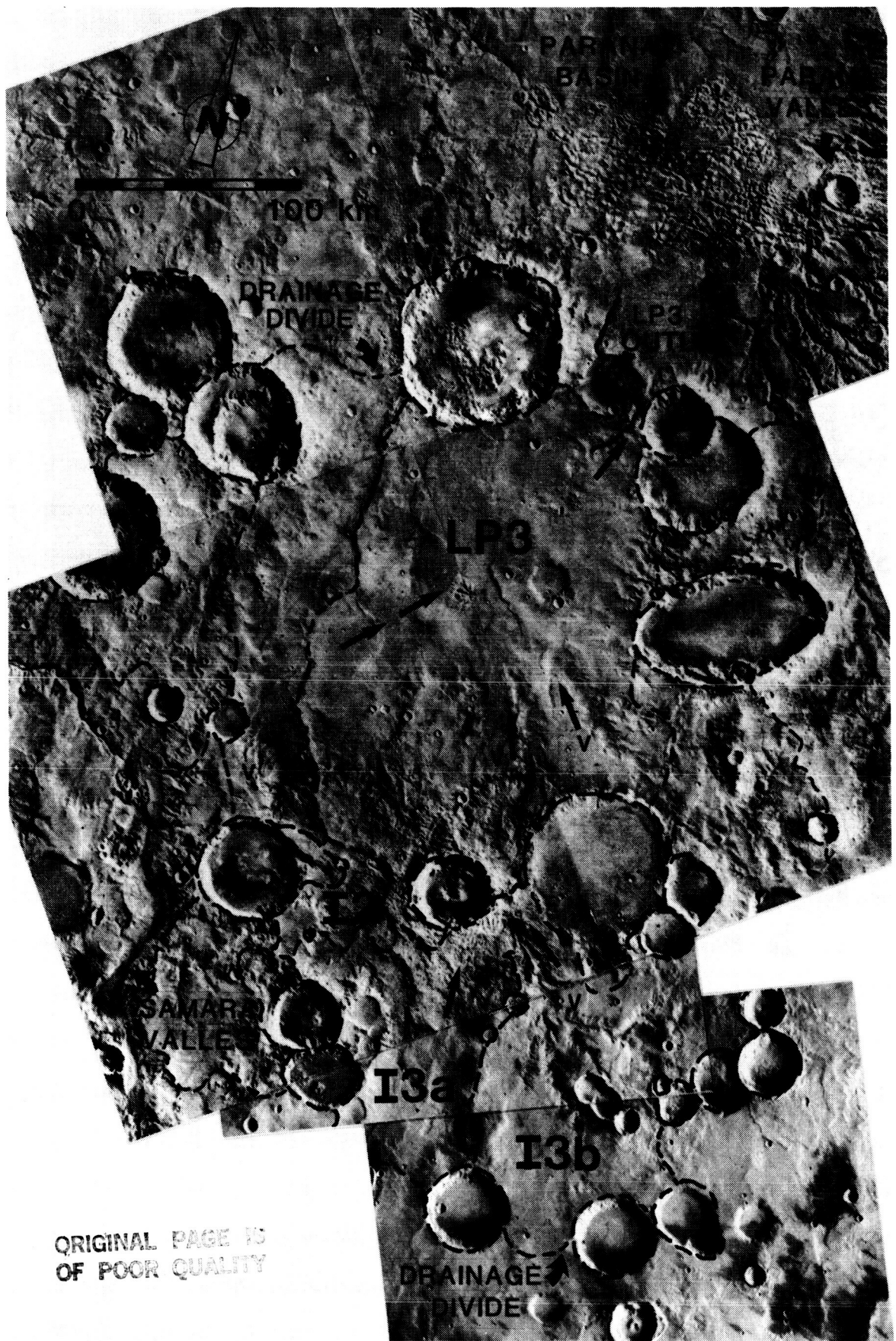
Drainage Basin Areas

From Table 4, the total drainage area of Samara Valles (313,295 km²) and Parana/Loire Valles (222,255 km²) are, respectively, approximately 0.5 and 0.33 that of the Colorado River, USA. Samara Valles sub-basins (Table 5) range in area from 52,528 km² for Himera and 28,406 km² for S2 to 3,601 km² for S3 and 3,351 km² for S7. Sub-basins in Parana/Loire Valles (Table 5) range from 40,420 km² for Parana and 27,696 km² for LP3 to 3,690 km² for LP5 and 2,620 km² for LP7. Internal drainage basins (Table 4) range from 21,966 km² for I1 to 2,313 km² for I2. The majority of the Samara and Parana/Loire Valles sub-basins and associated internal basins are under 10,000 km², tending towards the lower end of the range of values presented above.

Table 3.-- SUB-BASINS, names and locations

SAMARA			PARANA/LOIRE			INTERNAL BASINS		
Sub-basin	Location		Sub-basin	Location		Sub-basin	Location	
	S Lat	W Long		S Lat	W Long		S Lat	W Long
Himera	21	22	Parana	23	9	I1	22	16.5
Oltis	23.5	21	LP1	19.5	16.5	I2	28	12.5
Clota	26.5	21	LP2	21.5	16	I3a	29	12
S1	26.5	19	LP3	26	13	I3b	29	10
S2	28.5-31	18-19.5	LP4	18.5	13.5	I4	26	15
S3	28.5	18	LP5	18	15	I5	26	14
63a	29.5	17.5	LP6	16	15	I6	26	10
S4	31	16	LP7	17.5	16.5	C1	29	15
S5	31.5	9						
S6	31	11.5						
S7	29	13.5						
S8	28	16						
S9	21	18						

Fig. 10. Section of MC19SE centered at 27S, 12W. Dashed lines outline sub-basin LP3 of Parana Loire Valles. A drainage divide along the rim and ejecta blanket of crater Gb at the southern edge of LP3, separates drainage in the sub-basin from drainage in three internal basins to the south (I2, I3a, I3b). Several short valley segments are present in the southern half of LP3 (V) and well developed northward flowing segments exist in I3a and I3b (V). Paleoflow (arrows) was to the north out into Parana Basin. (0B4A43, 44, 45, 46, 579A44, 45).

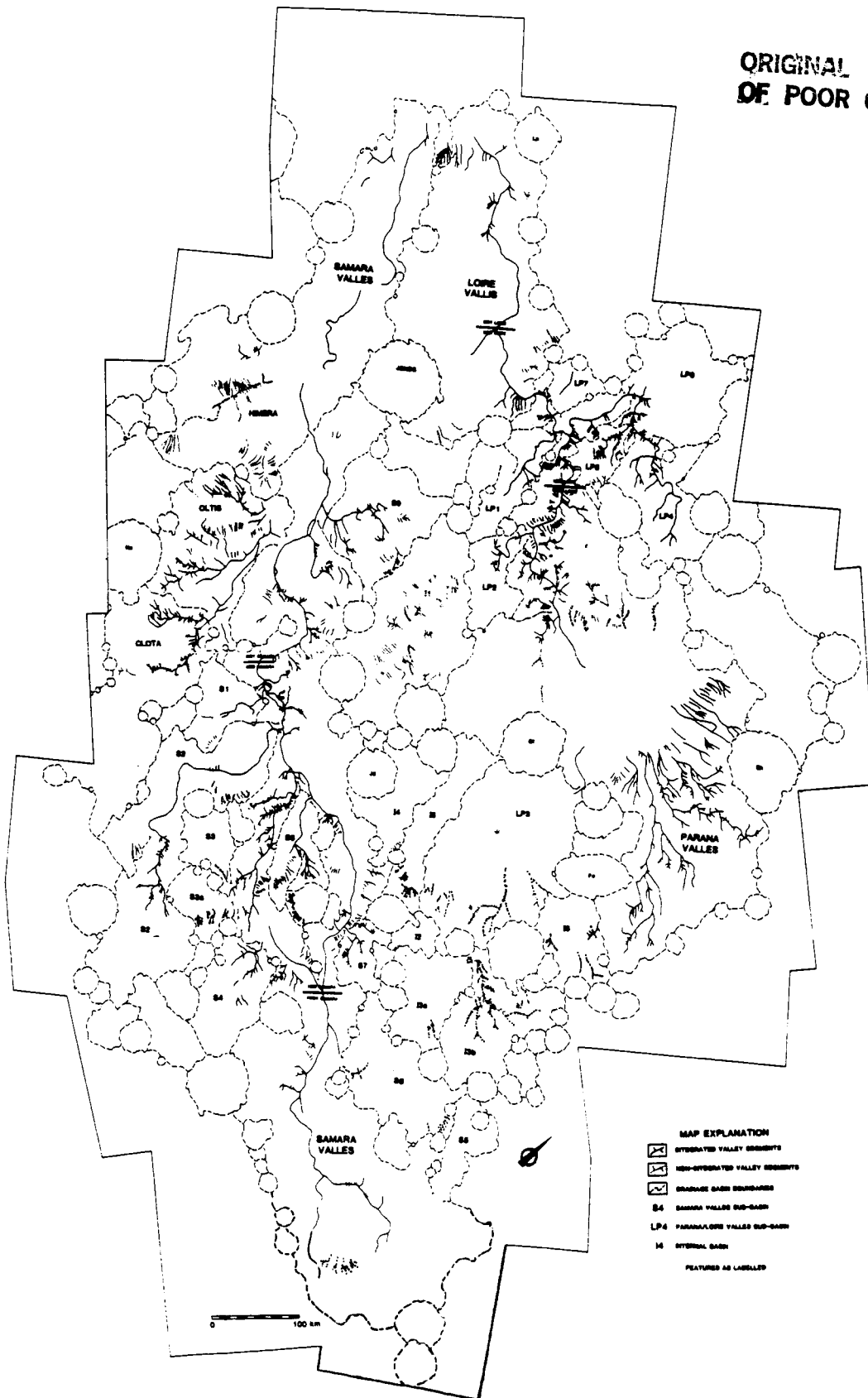


ORIGINAL PAGE IS
 OF POOR QUALITY

Fig. 11. All valley segments measured for use in the calculation of drainage densities for Samara and Parana/Loire Valles, portions of their trunk valleys, all sub-basins and internal basins. Integrated valley segments are indicated by a solid line. Non-integrated valley segments are assumed to have been integrated in the past, and are indicated by a dashed line. Post valley formation resurfacing and valley burial was probably responsible for the present disintegrated appearance of some segments. A copy of the original figure at 1:1,000,000 can be obtained from the author.

FIG 11 VALLEY SEGMENTS MEASURED FOR DRAINAGE DENSITY CALCULATIONS

ORIGINAL PAGE IS
OF POOR QUALITY



Drainage Densities

Overall drainage densities of Samara and Parana/Loire Valles (Table 4) are quite similar with Samara Valles having an average density of $0.034 \text{ km} \cdot \text{km}^{-2}$ and Parana/Loire Valles an average density of $0.039 \text{ km} \cdot \text{km}^{-2}$. Loire Valles has a density of $0.032 \text{ km} \cdot \text{km}^{-2}$ and Parana Valles has a density of $0.070 \text{ km} \cdot \text{km}^{-2}$. Sections along the trunk portions of these large systems display a range of densities. The highest values, 0.043 and $0.067 \text{ km} \cdot \text{km}^{-2}$, are found along central portions, between the third and fourth rings of Ladon Basin. Slightly lower values, eg 0.016 and $0.022 \text{ km} \cdot \text{km}^{-2}$, are found in proximal and distal reaches. Samara Valles sub-basins (Table 5) have an average density of $0.039 \text{ km} \cdot \text{km}^{-2}$, with a range from $0.075 \text{ km} \cdot \text{km}^{-2}$ for S8 to $0.013 \text{ km} \cdot \text{km}^{-2}$ for S6. Parana/Loire sub-basins display slightly higher drainage density values (Table 5), averaging $0.054 \text{ km} \cdot \text{km}^{-2}$ and ranging from $0.107 \text{ km} \cdot \text{km}^{-2}$ in LP5 to $0.018 \text{ km} \cdot \text{km}^{-2}$ in LP1.

TABLE 4.-- DRAINAGE SYSTEMS, areas and densities

Location (basin)	Area (km ²)	Integrated Channels (km)	Integrated Density (km/km ²)	Additional Channels (km)	Total Density (km/km ²)
COMPLETE DRAINAGE SYSTEMS					
Samara	313,295	8616.7	0.028	2033.1	0.034
Parana/Loire	222,255	7378.1	0.033	1247.0	0.039
Loire	181,835	4547.5	0.025	1247.0	0.032
Parana	40,420	2830.6	0.070	--	0.070
SAMARA TRUNK VALLEY SECTIONS					
Proximal	56,874	834.5	0.015	84.3	0.016
Mid	33,300	2220.0	0.067	--	0.067
Mid/Dist	28,465	948.8	0.033	196.4	0.040
Dist	52,528	509.6	0.010	1002.1	0.028
LOIRE TRUNK VALLEY SECTIONS					
Proximal	22,023	1408.9	0.022	25.9	0.022
Mid	19,255	670.8	0.035	162.4	0.043
Distal	32,898	707.5	0.034	476.3	0.045
INTERNAL DRAINAGE BASINS					
I1	21,966	--	--	596.9	0.027
I2	2,313	--	--	18.4	0.008
I3A	8,081	--	--	57.4	0.007
I3B	11,583	--	--	608.1	0.053
I4	6,529	--	--	41.3	0.006
I5	7,471	--	--	127.1	0.017
I6	5,304	--	--	140.0	0.026
C1	2,136	--	--	95.2	0.045

AVERAGE INTERNAL BASIN DRAINAGE DENSITY = 0.0236

TABLE 5.-- SUB-BASINS, areas and densities

Location (sub- basin)	Area (km ²)	Integrated Channels (km)	Integrated Density (km/km ²)	Additional Channels (km)	Total Density (km/km ²)
SAMARA VALLES SUB-BASINS					
Himera	52,528	509.6	0.010	1002.1	0.028
Oltis	18,090	1149.5	0.064	91.7	0.069
Clota	23,509	631.3	0.027	38.1	0.029
S1	6,794	113.0	0.016	25.1	0.020
S2	28,406	602.6	0.021	147.5	0.026
S3	3,601	--	--	--	--
S3a	3,544	--	--	189.4	0.053
S4	8,320	236.6	0.028	--	0.028
S5	5,578	--	--	--	--
S6	9,009	--	--	118.3	0.013
S7	3,331	242.9	0.073	--	0.073
S8	7,077	533.4	0.075	--	0.075
S9	12,997	379.5	0.029	140.2	0.040
PARANA/LOIRE SUB-BASINS					
Parana	40,420	2830.6	0.070	--	0.070
LP1	7,686	136.5	0.018	--	0.018
LP2	5,225	191.1	0.037	--	0.037
LP3	27,696	71.2	0.003	526.0	0.022
LP4	9,910	396.4	0.040	--	0.040
LP5	3,690	338.9	0.092	56.4	0.107
LP6	12,589	333.0	0.027	--	0.027
LP6a	2,708	212.8	0.079	--	0.079
LP7	2,620	21.9	0.083	--	0.083
Average Samara Sub-Basin Drainage Density = 0.0386					
Average Parana/Loire Sub-Basin Drainage Density = 0.0537					
Average Internal Basin Drainage Density = 0.0236					

DISCUSSION

Interpretation of Map Units

Channel Features

Channels and Valley Networks (Ch)—All the various scale channel and valley features have been shaped by fluid erosion. The source of this fluid varied for the different scale features. For the macro-scale features within Eos and Capri Chasma, the source was most likely the adjacent chaotic terrain (Carr 1979; Carr and Clow 1981; Murray et al. 1981; Baker 1982). Parker and Pieri (1985b) suggested that the catastrophic flow of water out of Argyre Planitia carved the Uzboi/Holden/Ladon system. Valley network formation by sapping processes and associated downstream fluvial activity was first hypothesized by Sharp and Malin (1975). As summarized by the Mars Channel Working Group (1983) this is currently the popular theory of formation held by most workers today, and will be further discussed in this study.

Etched Terrain (Ch_e)—The etched topography was created by the removal of surface material through fluidal activity. This flow was associated with discharge mainly from Margaritifer Valles and, to a lesser extent, Samara and Parana/Loire Valles. The eroded material was transported downslope to the north and east.

Chaotic Features

Chaotic Terrain (Ct)—The chaotic terrain represents the remains of a previously overlying surface that collapsed after water was catastrophically released from below and removed support (Saunders 1979; Carr 1979b). Carr (1979b) suggested that extremely high pore pressure in confined aquifers could lead to breakout and the catastrophic release of water, thus forming the chaotic terrain. He demonstrated that this process could repeat itself several times over an extended period of time. This would help explain the wide range of crater densities observed in the terrain. Errors in the measurement of crater densities, due to poor negative resolution (<260 km/pixel for much of Iani and Margaritifer Chaos) and difficulties in determining whether a crater is within the chaotic terrain, or on the pre-collapse surface, may be partially responsible for the large range of density values for the chaotic terrain.

Fretted Terrain (Ct_f)—The fretted terrain in MC19NE (Fig. 3d) is not typical of the fretted terrain described elsewhere by Sharp (1973). It is most probably the incompletely developed edge of the adjacent chaotic terrain to the east, and was formed in a similar manner.

Positive Relief Chaotic Deposits (Ct_r)—As previously suggested by Boothroyd and Grant (1985) the positive relief chaotic features may be similar to very large scale terrestrial pingos. It is unclear whether or not these features are still evolving at present.

Smooth Plains

Smooth Plains Deposits (Sp)—Volcanic, fluid and eolian deposits of various ages that partially to completely cover the Hc unit. Locations mapped as smooth plains that display high crater densities (about 100,000) have a deficiency of small diameter craters, and large craters display almost exclusively C₁, C₂, and occasionally C₃ morphology. Other areas, partially buried by resurfacing, that display mainly C₂, C₃, and C₄ class craters and high cumulative crater densities (greater than 100,000), are labelled as part of the Hc unit. Deposition of channel eroded material in the area within Ladon Basin was responsible for the formation of the smooth plains unit there. Smooth plains units mapped are equivalent to unit P mapped by Saunders (1979).

Relict Polar Deposits (Sp_r)—The location mapped as relict polar deposits was classified as such by Schultz (1984) on the basis of its: 1) layered nature; 2) numerous pedestal craters; 3) location adjacent to an area of low thermal inertia; and 4) position relative to asymmetric crater orientations around the planet (Schultz and Lutz-Garihan 1982). Schultz (1984) suggested that the polar wandering which resulted in the deposits was the result of a relatively rapid mass redistribution somewhere on the planet. The development of the Syria Rise may represent such a situation (Schultz, personal communication 1984).

Multi-Ringed Basins and Hilly and Heavily Cratered Deposits

Hilly and Heavily Cratered Terrain (Hc)—The terrain that comprises this unit is the oldest in the quadrangle. The unit is quite thick and intensely brecciated by impact events. It is also locally volatile rich. The surface of the unit shows impact crater saturation in some locations, and incorporates terrain associated with the multi-ringed impact basins (Schultz et al. 1982). Similar to unit pc mapped by Saunders (1979) and units hc and Uic mapped by Wise (1979).

Ancient Multi-ringed Impact Basins (—)—These features are multi-ringed topographic basins formed by large meteorite impacts. Cross cutting relationships indicate that they are the oldest recognizable features in the quadrangle.

Mount Material (Md)—These generally elongate hills are the extremely degraded remnants of concentric ridges (rings)

created during the formation of the multi-ringed impact basins (Schultz et al. 1982).

Other Features

Grabens (Gr)-All grabens in Margaritifer Sinus are tensional features. Parker and Pieri (1985) have associated their formation with the development of the fault system radial to Tharsis and the initiation of formation of Valles Marineris, thus giving them a relative age of about 10,000 to 5,500 from Wise et al. (1979).

Flow Modified Grabens (Gr_f)-Development of these grabens was synchronous with development of the other grabens. Flow modification associated with valley network development was immediately post graben formation, based on cross-cutting relationships and the relative ages of the two features.

Ridges (~~~~~)-The first type of ridge is associated with multi-ringed impact basin rings. The second type of ridge, of compressional origin, is probably associated with Tharsis evolution. Parker and Pieri (1985a) suggested that the preferential location of the second type of ridge within smooth plains units was due regional compression that caused buckling in the relatively rigid plains deposits overlaying less competent regolith. Wise et al. (1979) derived a relative age of 10,000 to 5,000 for similar features located in the Tharsis region.

Eolian Deposits (Ed)-All post Sp₄ mantled and buried surfaces appear to be a result of eolian deposition. All dune fields also appear to be of eolian origin.

Geometry and Relationship of Large Scale Features

The NW portion of the quadrangle (see USGS 1980) is dominated by Eos and Capri Chasma and related chaotic terrain (Carr 1979; Carr and Clow 1981; Murray et al. 1981; Baker 1982). These workers have suggested that the catastrophic release of fluid from the chaotic terrain caused the flow features observed in the chasma and the connected outflow channels further to the north. Recession of the southern wall of Eos Chasma has caused the beheading of several southward flowing valley networks along the chasma edge (Schultz et al. 1982, Boothroyd 1983). The position of the chaotic terrain throughout the area (see Fig. 3a,b and USGS 1980) is probably controlled by a structural zone of weakness that enhanced permeability and collapse, associated with the region of overlap of the rings of the Ladon and Chryse multi-ringed impact basins (Schultz and Glicken 1979, Schultz et al. 1982).

The Ladon and Holden multi-ringed impact basins (Shultz et al. 1982) are clearly the dominant structural controls in

the SW portion of the quadrangle (Fig. 3b). Almost all mount material in the region is associated with the basins (Saunders 1979; Schultz and Glicken 1979; Schultz et al. 1982), and valley networks located there tend to show an exterior radial centripetal pattern (after Pieri 1980a) with segments of the systems commonly being deflected parallel to a ring just before crossing it. The drainage pattern in most of MC19SW is roughly centered on the Ladon impact basin, the largest of the three, and which has been the site of considerable fluvial deposition (Boothroyd 1982; Parker and Pieri 1985a).

A large segmented system consisting of Uzboi, Holden and Ladon Valles crosses the quadrangle from the SW to the NE. Ladon Valles (Fig. 12) has isolated terraces at different levels that were abandoned as the channel downcut (Boothroyd 1982; 1983; Parker and Pieri 1985a). Where Ladon Valles passes one of the impact basin rings before debouching into Ladon Basin, its course is changed from the NE to the NW indicating the structural influence of the Ladon impact basin on the system (Parker and Pieri 1985b).

The entire Uzboi/Holden/Ladon system was initially through flowing into Ladon Basin (Florenski 1975; Pieri 1975; Boothroyd 1982), however, Holden crater, now superimposed on the central part of the system, appears to have interrupted the late stage flow. Close examination of Margaritifer Valles at the NE margin of Ladon Basin (Fig. 7) shows that it drains the basin, and empties into the etched terrain just south of Margaritifer Chaos (as had been suggested by Florenski et al. 1975, and Boothroyd and Grant 1984). This indicates that the Uzboi/Holden/Ladon system may once have been through flowing to the northeast.

Nirgal Vallis (see USGS 1980), a tributary network to Uzboi Vallis, has received considerable attention because of its conspicuous sinuosity and unusual morphology (Milton 1973; Schumm 1974; Weihs 1974; Sharp and Malin 1975; Baker 1980b; 1982). Schultz et al. (1982) suggested a source area for the system along a ring of the Holden Basin. Milton (1973) described the lower half of Nirgal Vallis as being most similar to a sinuous lunar rille, with the upper half similar to the entrenched arroyo systems in the southwestern USA. Because the system is internally coherent Milton felt a two-fold method of genesis, e.g. lava tube collapse and subsequent headward extension by fluvial processes was unlikely. Sharp and Malin (1975) hypothesized that because Nirgal Vallis is probably not located in a region of youthful volcanic features, and because the overall morphology resembles that of terrestrial systems formed by sapping and runoff, sapping and associated fluidal activity was most likely the principal agent of formation. This is the generally accepted theory today.

Fig. 12. Ladon Valles (MC19SW centered at 22.5S, 29W) is part of a large, segmented, northward flowing system comprised of Uzboi/Holden and Ladon Valles. The system empties into Ladon Basin to the north of Ladon Valles, and may have been through flowing out of Ladon Basin into the etched terrain (Fig. 7) further to the NE. At least five different levels of terraces can be indentified in Ladon Valles (1 is oldest, 5 is youngest) that were created as the system evolved. A small region of chaotic terrain to the SW of Ladon Valles probably served as a late source area after interruption of the Uzboi/Holden flow by the Holden impact event. The course of Ladon Valles changes from the NE to the NW as it crosses the first (FRH) and second (SRH) rings of the Holden, and the second (SRL) ring of the Ladon multi-ringed impact basins. This is a result of the structural influence imparted on the system by the multi-ringed basins. Figure is slightly modified from that of Boothroyd (1982; 1983) (611A32, 650A16).



The influence of the Ladon impact event extends well out into MC19SE (Fig. 3c and USGS 1980), where a fourth poorly defined ring may be present (Schultz and Glicken 1979; Schultz et al. 1982; Schultz, personal communication 1985). The fourth ring is defined by widely spaced ridges concentric about the center of the basin. Other evidence favoring the existence of a fourth ring comes from morphological changes in Samara and Parana/Loire Valles (Fig. 3c), observed as they cross its hypothesized position (Schultz et al. 1982). Between the fourth and third rings of Ladon Basin, Samara and Parana/Loire Valles display many short tributaries that usually enter the trunk valley at very large junction angles, commonly 90 degrees (Schultz et al. 1982). The drainage density along this reach is the greatest that the two systems display (Tables 4 and 5). This is also the zone where tributaries with the highest drainage densities (with the exception of Parana Valles) enter the systems (Fig. 9c,d, Table 5). The plains and cratered terrain between the Ladon third and fourth rings in MC19SE are highly dissected by numerous short, poorly-integrated valleys, giving the area a grooved appearance. Inside the third ring and outside the fourth ring Samara and Parana/Loire Valles display a subdued morphology with relatively low densities and poorly integrated tributaries. Schultz et al. (1982), and Schultz (personal communication 1985) postulated that the observed change in valley number and density between the two rings was due to the presence of a thick blanket of volatile rich ejecta emplaced during the Ladon impact event. In the immediate vicinity of crater Jones, both Samara and Parana/Loire valleys are partially to completely buried by ejecta from the Jones impact event (Fig. 13).

Samara and Parana/Loire Valles are classified as well integrated longitudinal stem valley networks after Pieri (1980a). Samara heads in the Argyre NE quadrangle (MC26NE) and flows across MC19SE. Just before crossing the fourth ring of Ladon basin, Samara Valles splits as it crosses an ancient ridge (Fig. 14), rejoining at the edge of the fourth ring. The more western of the two Samara valleys is higher than the eastern. This may be due to an impact crater in the western valley that appears to have dammed the flow, resulting in deposition upstream, and forcing flow to be diverted into the deeper eastern Samara valley. At the point that the two valleys diverge, several incised interior channels described by Pieri (1980a) can be seen in eastern Samara Valles (Fig. 14).

After crossing the fourth and third rings of Ladon Basin, Samara Valles enters a gentle northward trending downwarp known as the Himera Basin. At this point Himera Valles joins the system (Boothroyd and Grant 1985). After entering Himera Basin, Samara Valles trends in a more northerly direction along the axis of the Chryse lowland trough (Fig.

Fig. 13. Jones Crater, located just outside the third ring of the Ladon multi-ringed impact basin (TRL) at 19S, 20W. Ejecta from the crater has partially buried sections (P) of Samara and Loire Valles and completely buried sections (C) of Samara Valles and a graben located NW of the crater (651A65).

ORIGINAL PAGE IS
OF POOR QUALITY

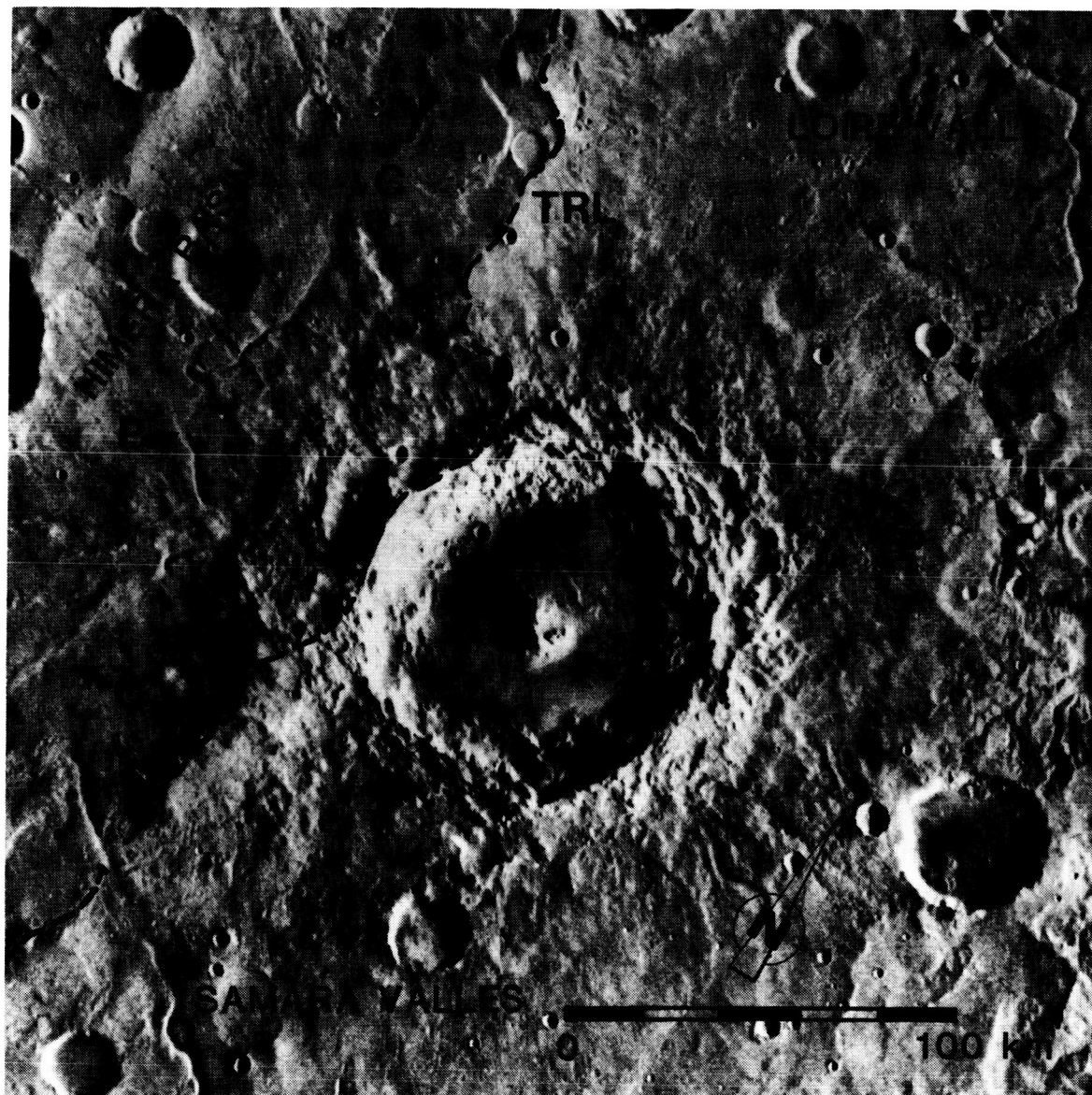
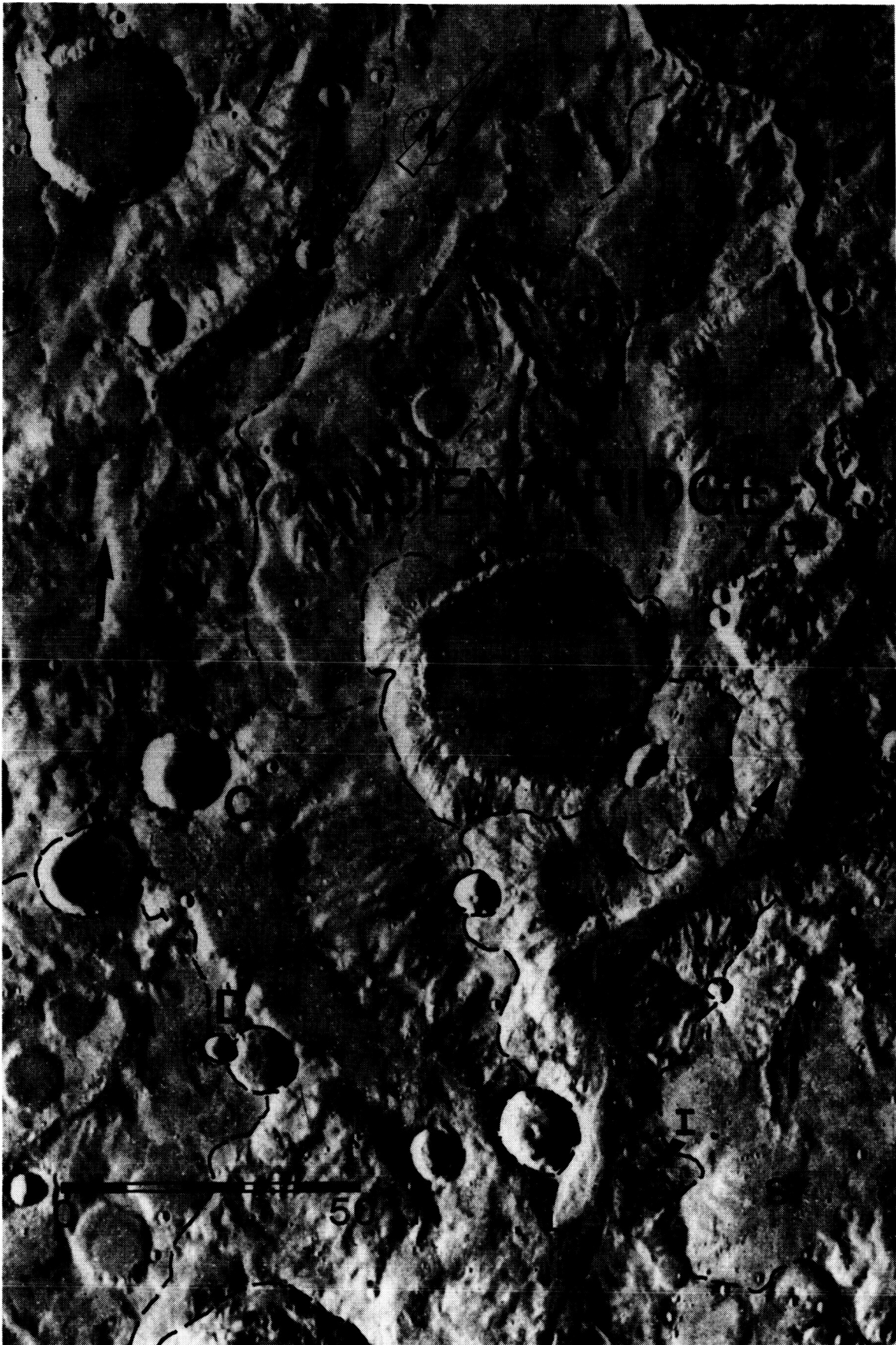


Fig. 14. Split in Samara Valles as it crosses an ancient NE trending ridge centered at 28.5S, 15W. The eastern valley is deeper than the western valley, possibly due to damming of the western channel by the crater at (C), resulting in deposition behind it (D), and the diversion of all flow into the eastern valley. The eastern valley shows several interior terraces and a deep central channel (I) at 29.5S, 14W. This may be due to multiple flow events and/or the differential erosion of the underlaying units at that location. The material comprising the ancient ridge (dated by crater counting) is some of the oldest terrain in the quadrangle (relative age 1,000,000 to 850,000). Drainage basins are depicted by dashed lines, and large arrows indicate the flow direction. Positive relief chaotic deposits (Ct_p) exist along the eastern valley (084A41).



2). The system debouches into etched terrain just south of Margaritifer Chaos, close to Margaritifer Valles.

The Parana/Loire Valles system parallels Samara Valles to the northeast. This system is comprised of two separate, but connected sub-systems, Parana Valles and Loire Vallis, and is treated as one system (Boothroyd and Grant 1985). Parana Valles (Fig. 15 and USGS 1980) is a digitate network (after Pieri 1980; Mars Channel Working Group 1983) bounded to the east by the Noachis/Newcomb A multi-ringed impact basin (22.5S, 3W), described by Schultz et al. (1982). Parana Valles shows one of the highest drainage densities on the Martian surface (Baker 1982). This may in part be due to the presence of a thick volatile rich layer associated with the ejecta lithofacies of Noachis/Newcomb A basin to the east, similar to that between the third and fourth rings of the Ladon Basin (Schultz et al. 1982; Schultz, personal communication 1985). Parana Valles drains to the northwest into Parana basin, located within a very degraded impact basin (Fig. 15) that displays positive relief chaos features similar to very large scale pingos (Boothroyd and Grant 1985).

Loire Vallis heads in Parana basin (Fig. 15), thus Parana and Loire Valles are connected and were probably through flowing (Boothroyd and Grant 1985). Loire Valles is a longitudinal stem valley that drains in a northwesterly direction along its entire course, finally debouching into etched terrain at the axis of the Chryse lowland trough close to Samara Valles and Margaritifer Valles (Figs. 2, 7). Between the third and fourth rings of the Ladon impact basin, Loire Valles displays a wide flat-bottomed profile with tighter incised meander bends than Samara Valles. Short high angle tributaries entering into Loire Vallis along this section tend to be more numerous and better developed than along the same section of Samara Valles (Fig. 3c).

The etched terrain that Margaritifer Valles and Samara and Parana/Loire Valles empty into is shown in detail in Figure 7. The unit lies along the axis of the Chryse lowland trough and is bounded on the west, south and east by relatively higher terrain (Fig. 7). The northern boundary has been engulfed by collapse features associated with Margaritifer Chaos. Remnants appear to be unmodified by flow over their tops. However, fluidal erosion from flow out of the three systems was probably responsible for removal of the material between the remnants.

Margaritifer Chaos and Iani Chaos (Fig. 7 and USGS 1980) lie to the north of the etched terrain; Ares Valles outflow channel heads along the northern edge of chaotic terrain. The relationship between Ares Valles, the chaotic terrain,

Fig. 15. Relationship between Parana Valles, Parana Basin and Loire Vallis. Parana Valles heads along a drainage divide (dashed line) located at the crest of a ring of the Noachis multi-ringed impact basin. It drains to the NW, emptying into Parana Basin (22S, 12W). Loire Vallis heads in Parana Basin with paleoflow to the NW, roughly parallel to Samara Valles. Because Loire Vallis heads in Parana Basin, and because the relative ages of the two valley networks are similar (based on crater counts), they can be treated as one system. Positive relief chaotic features (Ctp) are present in Parana Basin (084A46, 47, 48, 615A45).



ORIGINAL PAGE IS
OF POOR QUALITY

etched terrain and flow out of Ladon Basin, Samara and Parana/Loire Valles will be discussed later in the paper.

Besides Margaritifer and Iani Chaos, MC19NE shows several large unnamed valley networks (Fig. 3d and USGS 1980). These networks drain to the north and west and may possibly empty into Iani Chaos. Poor image resolution and thick mantling in the region by relict polar deposits prevent definitive mapping.

The northeastern most corner of MC19NE (Fig. 3d) is the site of a thick blanket of relict polar deposits (Schultz 1984) that completely covers all valley networks and some very large craters (Fig. 16). The deposit may have been created by migration of the pole relative to the stationary spin axis of the planet (Schultz 1984). Because the relict polar deposits always cover the valley networks, Schultz (1984) determined they are younger than the networks. He suggests that by basal melting and/or trapping by impact ejecta or flood basalts, volatiles in the deposits could accumulate in the underlying megaregolith.

Drainage Basin Evolution

Period of Formation

The period of formation for the major valley networks in the quadrangle, Samara and Parana/Loire Valles, was between 8,500 and 4,600 based on the crater densities of surfaces incised by the valleys and those covering them. Figures 9a-d shows the drainage basins for these two systems. The combined drainage area of Samara and Parana/Loire valles is 84% that of the Colorado River in the southwest USA (Table 4). Coupled with the fact that each major sub-basin is drained by at least a third or fourth order system (Strahler stream order classification, Strahler 1952), and the extensive, well integrated nature of these networks becomes evident.

Several of the sub-basins of the two systems underwent extensive resurfacing after formation by the fourth or youngest dated resurfacing event that partially to completely buried parts of the networks. Examples are Clota Valles, S1, S3a, 55, 56, and LP3 (Figs. 17, 18). The formation of some impact craters has also deranged and buried valley segments that were probably once integrated parts of the larger valley network systems.

Figure 10 shows an area in MC19SE centered at 275, 12W. A sub-basin of the Parana/Loire system (LP3) is in the central portion of the figure. The southern half shows several internal drainage basins (I2, I3a and I3b) separated from LP3 by a drainage divide running E-W along the rim of a

Fig. 16. An example of the typical appearance of relict polar material located in the NE corner of MC19NE described by Schultz (1984). Figure is centered at 1N, 1.5W. Pedestal craters (P) are common, indicating the removal of material around them since their formation (615A36).

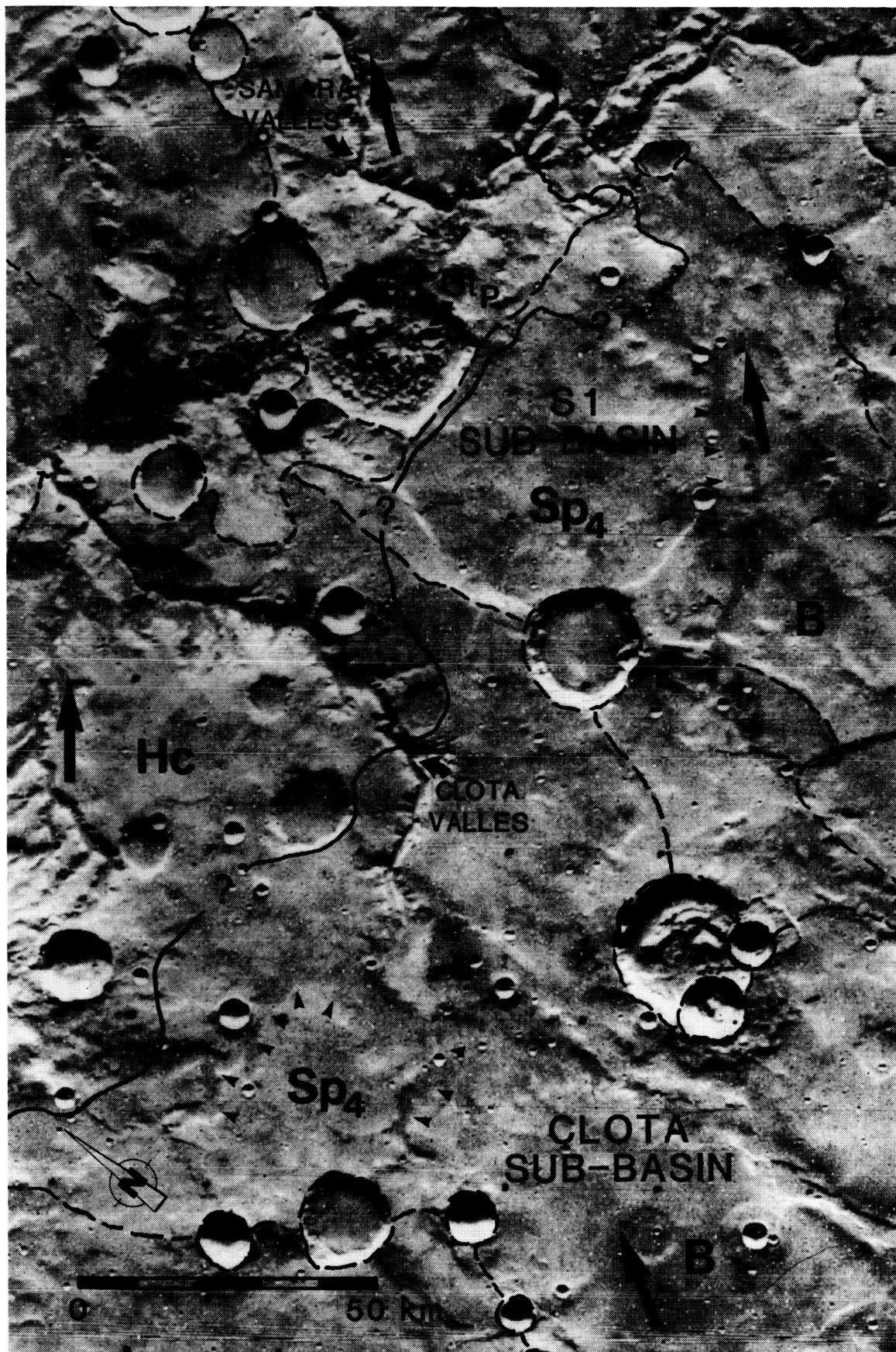
ORIGINAL PAGE IS
OF POOR QUALITY



Fig. 17. LP3 sub-basin of the Parana/Loire drainage system, centered at 26S, 13W. The area shown is the same as the central portion of Figure 10. Valley segments (VS) and some craters (C) are present in the southern 1/3 of the sub-basin that have been partially to completely buried by material associated with the Sp₄ resurfacing event in the northern 2/3 of the sub-basin. The contact between the Sp₃ and Sp₄ material was located using crater counts and is shown as a solid line. Dashed lines show the location of drainage divides. Flow in the sub-basin (large arrows) was to the north and out into Parana Basin via the small, partially filled, outlet shown (084A43, 45).



Fig. 18. Clota Valles and S1 sub-basins of Samara Valles centered at 27S, 21W. Valley segments (small arrows) in both sub-basins have been partially buried by material associated with the Sp₄ resurfacing event. The contact between the Sp₄ and the older material to the north was located using crater counts and is drawn as a solid line. Any valley segments in the southern part of either of these two sub-basins (B) have been completely buried by Sp₄ material. The dashed lines represent the position of drainage divides and the large arrows indicate the flow direction. Positive relief chaotic features are labelled Ct_p (084A40).



class C₄ crater. The regional slope of the area shown in the figure is to the north, determined by stereographic mapping. Figure 19a, a sketch of the area in Fig. 10, shows numerous short northward flowing valley segments incised into the Sp₃ surface (14,000 to 8,100) can be seen in the southern third of LP3 (Figs. 10, 19a) that are completely buried by the Sp₄ unit (6,000-2,000) further to the north (Fig. 19a). A short segment of almost completely buried valley marks the outlet of LP3 into Parana Basin. The I3a and I3b internal drainage basins are also occupied by fairly well developed valley segments indicating paleoflow to the north, that terminate at the southern edge of class C₄ crater Gb where buried by its ejecta (Fig. 19a).

It seems likely that the valley segments in LP3 were once part of a more extensive integrated valley system that drained the entire area and emptied into Parana Basin (Fig. 19b). This drainage has since been completely mantled, except along the southern edge of LP3, by basin fill associated with the last resurfacing event (Sp₄). It also seems likely that internal basins I3a and I3b were once connected to and a part of the LP3 drainage before interruption by the crater Gb impact event. Figure 19b shows a reconstructed drainage pattern for LP3, I3a and I3b before valley burial by the fourth resurfacing event in the northern part of LP3, and before the crater Gb impact event. Drainage was probably much more extensive and better integrated in the past than observed today (Fig. 19b). Similar modifications, mainly burial after valley formation (6,000-2,000), have affected other sub-basins and sections of the trunk systems. Locations include Clota Valles (Fig. 18), S3a, the headward section of Samara Valles, S5, S6, and the northern edge of Parana Basin (Fig. 15).

The presence of several terrace levels in Samara Valles at 29.55, 14.5W (Fig. 14), first identified by Pieri (1980a), indicate that multiple flow events may have occurred there, each resulting in incision below a given terrace level. Another possibility is that the terraces represent differential erosion of material deposited by various resurfacing events. This could have happened as the channel was downcut continuously or during multiple flow events. A stronger case for differential erosion of the strata deposited by resurfacing events can be made for an area on the eastern side of Loire Valles at 20S, 15W (Fig. 20). At this location, headward erosion by small tributaries of Loire Vallis was at different rates on different levels, with the headwall receding more rapidly than any beds below it. Differential erosion may have been due to differences in the composition, porosity and thickness of the various beds.

Samara and Parana/Loire Valles and their associated sub-basins are extensive and well integrated systems, and may

Figs. 19a-b. Figures 19a, b are sketch maps of the area shown in Figure 10, containing the LP3 sub-basin of Parana/Loire Valles and I2, I3a, and I3b internal basins. Several short valley segments are present in the southern half of LP3 (V) and well developed, northward flowing, valley segments exist in I3a and I3b (V) (Fig. 19a). Drainage in LP3 was to the north out into Parana Basin. Much post valley resurfacing (Sp₄) has occurred in the northern 2/3 of LP3 (Fig 19a). The resurfacing appears to have buried all valley segments in that area. Surviving valley segments in the southern 1/3 of the sub-basin are incised into the Sp₃ surface. Valleys in I3a and I3b terminate where buried at the edge of ejecta (E) from crater Gb (Fig. 19a). Figure 19b is a reconstruction of drainage in Parana/Loire sub-basin LP3 before partial valley burial in the northern section by Sp₄ material and interruption of the southern drainage by crater Gb. Existing valley segments in Figure 19b are shown as solid lines, dotted segments are inferred. Drainage divides in Figs. 19a, b are depicted as dashed lines. Arrows show paleoflow direction. See text for further discussion.

Figure 9A

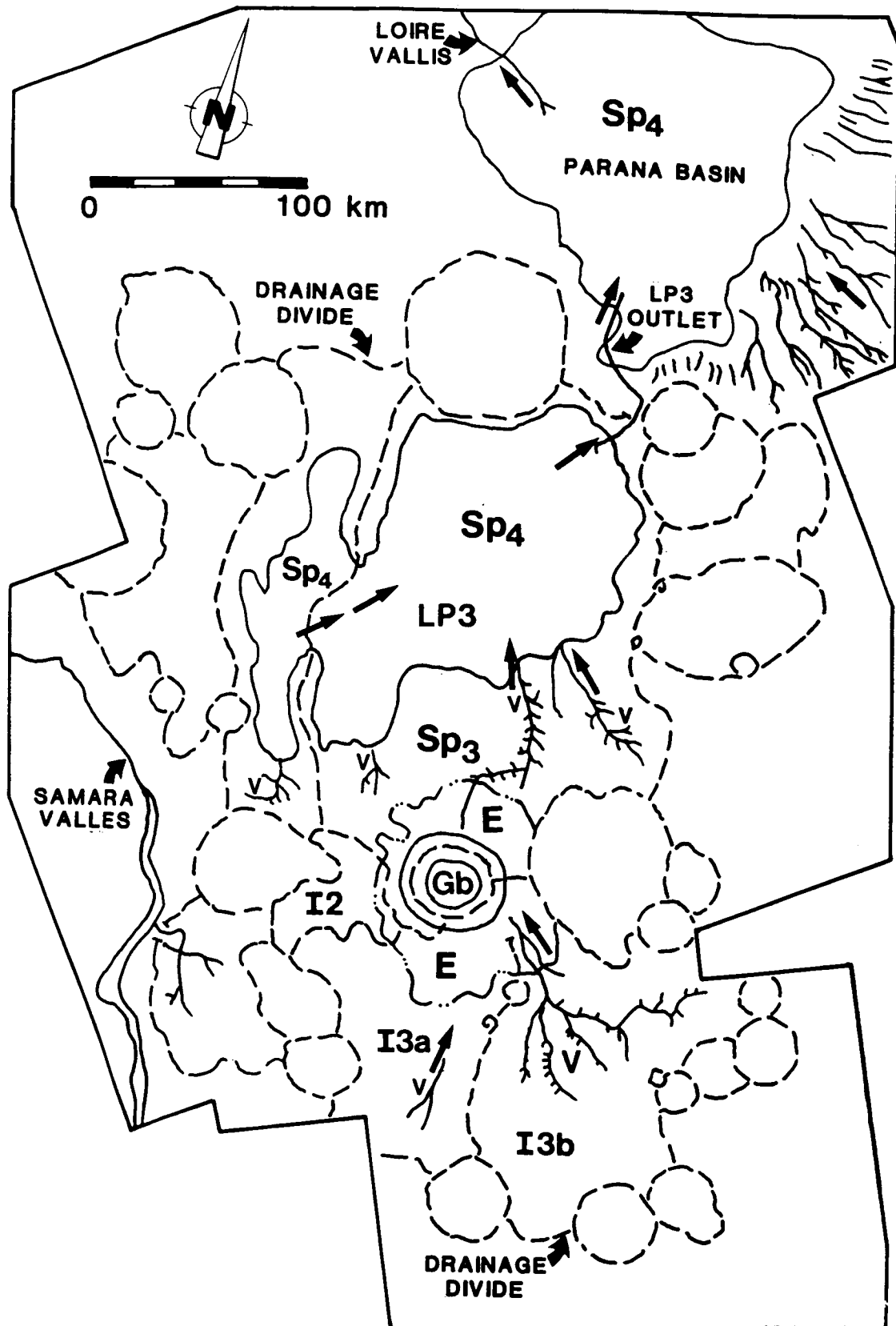


Figure 9B

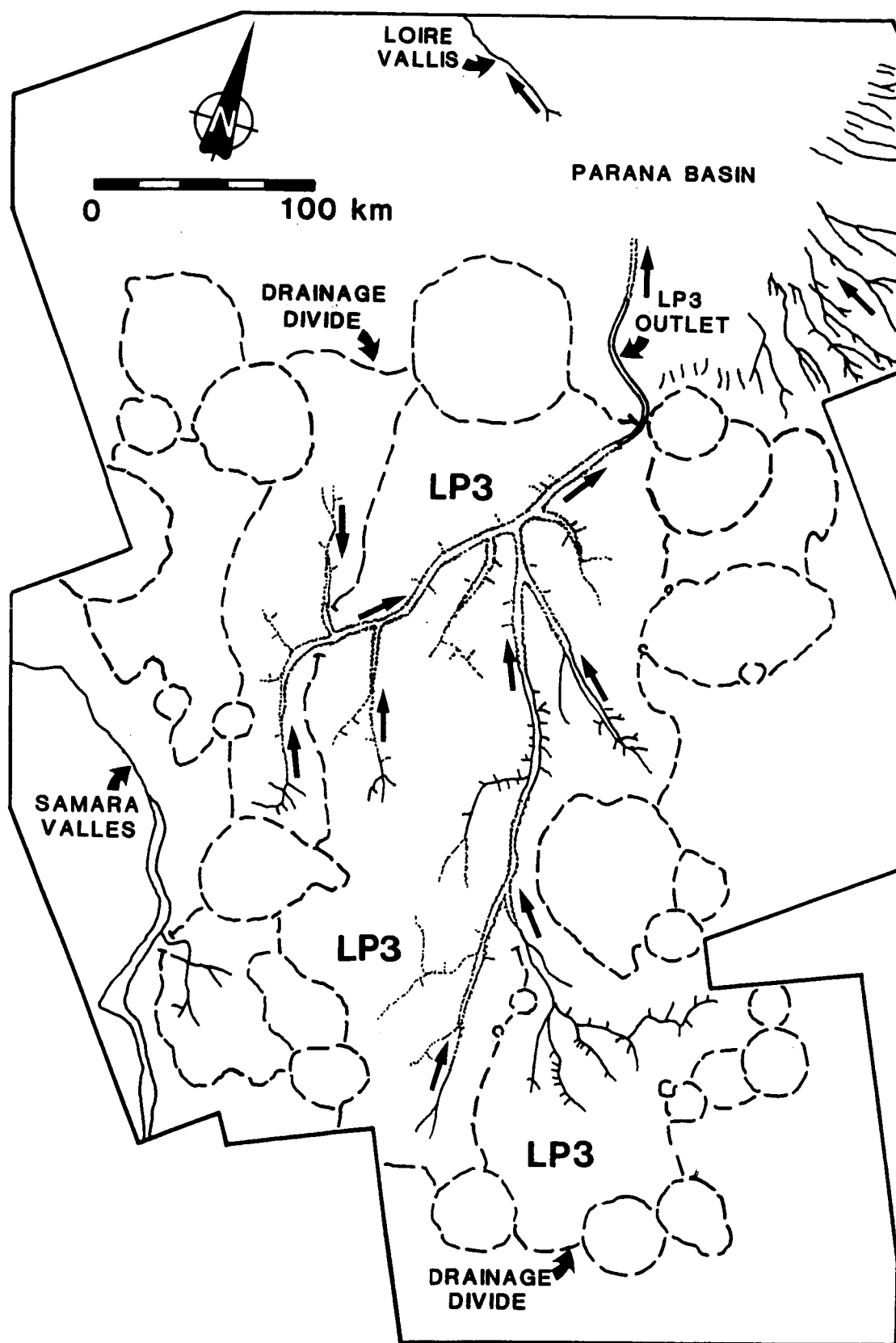


Fig. 20. Headward and middle portions of Loire Vallis with Parana Basin to the SE. The arrowheads in the north central part of the figure show the location where differential erosion of layers in the substrate may have occurred. The geomorphic contact between smooth plains and the heavily cratered terrain is shown by the solid line. The geologic contact between Sp₃ and Sp₄ (in Parana Basin and along the western edge of the photograph), as determined by crater counts, is shown by the dashed/dotted line (615A45).



have been even more extensive and better integrated in the past. Because of this, a relatively long period during which climatic conditions were favorable for network formation must have existed to permit their development. This implies that valley formation, once initiated, was probably more or less continuous throughout the 8,500 to 4,600 (3.73 to 3.6 BYBP) period determined for their formation.

Evidence for an extended period of conditions favorable to valley formation argues against the possibility that a single catastrophic event was responsible for their formation. It seems unlikely that events such as the creation of Argyre Planitia, though huge in scale, could have modified conditions regionally or possibly planetwide for such an extended period of time (probably on the order of 100 million years based on crater counts). A more appealing scenario would be one where a sustained event, capable of affecting conditions on such a large scale, was responsible for the period of valley formation. A possibility of such an event was the period of activity in the Tharsis region associated with the creation of the Syria Rise. This appears to have been mainly a tectonic event that began at about 15,000 and peaked in activity from 10,000 to 5,000 (Wise et al. 1979). The timing of this event is right, however any relationship to the valleys and the creation of conditions favorable to their formation remains unclear and may warrant further investigation.

Valley Network Drainage Densities

Drainage density, the measure of the total valley length/basin area (Gregory and Walling 1973; Baker 1982), is one of the most useful variables in the analysis of drainage basins because it measures the stream density, a fundamental feature of fluvial drainage basins (Gregory and Gardiner 1975; Baker 1982; Abrahams 1984). Simplistically, drainage density is the measure of the basin efficiency in removing excess precipitation in the form of surface runoff (Patton and Baker 1976). Despite its value, few studies have focused on drainage density for several reasons, including the time consuming nature of derivation (Gregory and Gardiner 1975). Only one study besides this one has quantitatively examined the drainage density of Martian valley networks (Baker and Partridge 1984a; Baker 1985), and to date, no drainage density data has been located for terrestrial systems formed by sapping processes.

At the macroscale relevant for Mars (Baker 1985), terrestrial drainage densities are climate controlled (Gregory and Gardiner 1975; Abrahams 1984) and are dependent on mean annual precipitation, its seasonality (Gregory and Gardiner 1975) and intensity (Gregory 1976). Drainage densities are lowest in arid regions (mean annual

precipitation <180 mm), increase to a maximum in semiarid regions (mean annual precipitation >180mm but <380mm), decrease again in humid areas due to vegetation cover (mean annual precipitation >500mm but <1,000mm) and finally increase to a second maximum in superhumid areas (mean annual precipitation >1,500mm but <3,000mm) (Abrahams 1984).

The drainage densities determined for Samara and Parana/Loire Valles (Table 4) are remarkably similar for both systems ($0.034 \text{ km} \cdot \text{km}^{-2}$ for Samara and $0.039 \text{ km} \cdot \text{km}^{-2}$ for Parana/Loire). This suggests that the mechanism that created the valleys was operating at similar rates during formation of both systems. It further suggests that the substrate beneath the two systems is of fairly uniform composition and that equivalent amounts of fluid, whether of meteoric or subsurface origin, were available to both during formation.

The range of drainage density values observed for the sub-basins and various trunk portions of Samara and Parana/Loire Valles (Table 4 and 5) is probably due to local variations in the amount of resurfacing that has occurred since valley formation and/or local variations in the substrate and amount of fluid available. The Clota Vallis sub-basin shows extensive post valley resurfacing limited mainly to the southern 2/3 of the basin. The observed drainage density of the entire sub-basin is $0.029 \text{ km} \cdot \text{km}^{-2}$, however, if only the northern third of the basin is considered, the density becomes $0.049 \text{ km} \cdot \text{km}^{-2}$. Other sub-basins and portions of the trunk valleys displaying low density values may have been affected in a similar manner.

Mid trunk portions of Samara and Loire Valles and all of Parana Valles may be incised into thick, volatile rich lithofacies associated with ejecta from the multi-ringed impact basins (Schultz et al. 1982; Schultz, personal communication 1985). As discussed above, the presence of this material may be responsible for the higher density values.

The drainage density values calculated for Samara and Parana/Loire Valles are almost an order of magnitude lower than values reported by Baker and Partridge (1984a) and Baker (1985) for 24 Martian valley networks. This difference is due to differences in the technique used to derive the values. Baker and Partridge (1984a) and Baker (1985) used the headward extent of tributaries to define the limit of the drainage basins of the valley networks, not the topographic limit. Because of this, undissected basin between tributaries and above the headward extent of the tributaries was not included in the basin area and resulted in the higher drainage density values. Because the topographic drainage basin areas were utilized for density calculations in this study, the values obtained can be

compared better to terrestrial examples than those obtained by Baker and Partridge (1984a) and Baker (1985).

All drainage density values obtained for the Martian systems are well below those observed for terrestrial systems formed by surface runoff in even the most arid climates (Gregory and Gardiner 1975; Abrahams 1984), suggesting that other processes, such as spring sapping, were responsible for their formation. Unfortunately, drainage density values for terrestrial systems formed by sapping process are unavailable for comparison to Martian values.

Valley Network Genesis

The general characteristics of the valley networks in MC19 are similar to those described by others for networks elsewhere on the planet. The networks in MC19 all head in, and in most cases are located completely within, old heavily cratered terrain. Pieri (1979) and Carr (1979a) noted a similar distribution of networks in MC19 and elsewhere; Carr and Clow (1981) calculated that over 99% of all valley networks were located within heavily cratered terrain. Tributary valleys either hang or appear as deep and wide as trunk valleys; the interfluvial areas between valleys are broad, flat, and undissected. Valley junction angles tend to show wide variability, but in general are low, a characteristic that has been well documented (Pieri 1980a; 1980b; Pieri and Sagan 1979) for other Martian systems. Drainage densities in MC19 and elsewhere are quite low (Baker 1982; 1985; this study), and all the valleys are scale variant (Mars Channel Working Group 1983). In summary, the valley networks in MC19 are morphologically typical of most Martian valley networks.

Pieri and Sagan (1979) compared all of the above mentioned Martian valley characteristics, plus sinuosity, presence of drainage basins, and drainage patterns among others, to characteristics of terrestrial systems. On this basis they concluded that genesis by headward sapping and associated down valley fluvial activity was most consistent with the observed Martian valley morphology. Formation of Martian valley networks by sapping and downstream fluvial activity was first suggested by Sharp and Malin (1975) and is the most popular theory for their formation today (Pieri and Sagan 1979; Pieri 1980a; 1980b; Pieri et al. 1980; Laity and Pieri 1980; Laity 1983; Laity and Malin 1985; Higgins 1982; Mars Channel Working Group 1983).

Laity and Malin (1985) define sapping as the process resulting in undermining and collapse of valley head and side walls, as a result of the reduction or complete loss of basal support due to enhanced weathering and erosion by concentrated fluid flow at a site of seepage. Examples of

terrestrial systems formed mainly by sapping are not easily located. This may be because many drainage systems whose early development was dominated by sapping processes have later been modified by surface runoff and can no longer be recognized (Higgins 1982; 1984). Baker (1982) suggests that systems formed by sapping simply have not received much attention in recent geomorphic research. Laity and Malin (1985) point out that most work that has been done on drainages formed by sapping has focused on small and micro scale systems (Higgins 1974; 1982; D'Amore 1983; 1984), although Higgins (1982; 1984) has suggested that the sapping process is scale independent.

Dunne (1980) developed a model for drainage networks formed by spring sapping. He cited the presence of a sloping water table with drainage towards a hydraulic sink (stream or sea level) as the most important conditions necessary for the initiation of sapping processes. Baker (1982) examined volcanic valleys in Hawaii that have formed by sapping. He noted that the high permeability of the surface materials there has inhibited network development by fluvial action and has thus allowed sapping processes to dominate.

One of the best examples of a terrestrial drainage system formed by sapping processes exists in the Glen Canyon region of the Colorado Plateau, southwestern USA. Because the region contains numerous canyons that are strikingly similar in appearance and scale to Martian valley networks it has recently been studied as a possible analog (Laity and Pieri 1978; Pieri et al. 1980; Laity 1983; Laity and Malin 1985). In addition to conditions outlined by Dunne (1980) and Baker (1982), Laity and Malin (1985) stated that the presence of beds dipping in accordance with the slope was very important in the development of valleys that most closely resemble those seen on Mars. Valleys in the Glen Canyon region that formed where the beds dipped away from the regional slope more closely resemble valleys formed by surface runoff. They also stated the importance of a relatively easily weathered lithology. This allows rapid undermining of the headwall by groundwater, and facilitates the removal of talus following collapse. Laity and Malin (1985) concluded that gross geomorphic processes similar to those forming drainages on the Colorado Plateau may have operated during formation of the Martian valley networks.

Fanale (1976), Carr (1979b) and Baker (1982) among others, have suggested that a thick permafrost layer covers the surface of Mars to a depth of 1 to 2 km. This is supported by numerous occurrences of inferred permafrost features. Saunders (1979) stated that in MC19 the ancient heavily cratered terrain was probably highly brecciated to a depth of at least 1 km. Locations undergoing later resurfacing have had a layer(s) of material deposited on top

of the ancient terrain. These overlaying units are probably thin in most locations, in comparison to the thickness of the ancient brecciated terrain beneath, and may consist of highly permeable lava and ash deposits. In MC19SE, the area between the third and fourth rings of Ladon basin probably contains an even thicker zone of intensely brecciated volatile rich regolith than surrounding areas. This is due to the probable presence of ejecta from the Ladon impact event (Schultz et al. 1982; Schultz, personal communication 1985).

Samara and Parana/Loire Valles in MC19SE have features indicating paleoflow directions accordant with the present regional slope in the area. This suggests that the Chryse lowland trough developed prior to the period of network formation. Material emplaced during resurfacing events prior to trough development would have been tilted to dip in accordance with the regional slope as the trough was formed.

It is apparent from the above discussion that the general conditions described by Dunne (1980), Baker (1982) and Laity and Malin (1985) as necessary for the initiation of sapping processes may be present on a regional scale in MC19SE. Creation of the Chryse lowland trough provided the necessary slope and hydraulic gradient towards the axis of the trough. It also caused the dip of beds on the flanks of the trough to be accordant with the regional slope. The presence of thick intensely brecciated regolith would provide the required permeability for ample groundwater flow. Even higher permeabilities would be expected between the third and fourth rings of Ladon Basin, the site of the most extensively developed sections for the networks. The intensely brecciated nature of the regolith probably also provided the required lithology for high erodeability and easy removal of debris. Regional thawing of the permafrost layer in locations with sufficient ground ice would probably have provided the necessary water to drive the system, although it remains unclear what process or event caused thawing to occur. Once started, sapping would have continued until conditions favoring their formation changed or until the groundwater supply was exhausted (assuming no recharge).

Samara and Parana/Loire Valles, in MC19SE, have extremely low drainage densities that argue strongly against formation by surface runoff. A morphological comparison of the two systems to terrestrial systems show that Samara and Parana/Loire most closely resemble terrestrial systems (e.g. the Glen Canyon region and the Gifl Kebir plateau in southwest Egypt) formed by sapping and associated downstream fluvial activity (Pieri and Sagan 1979). Geologically, the setting of Samara and Parana/Loire Valles appears to meet the general conditions described by Dunne (1980), Baker (1982), and Laity and Malin (1985) as important for network

development by sapping processes. Coupled with drainage density measurements and morphological evidence, and a strong case in favor of development by some sort of sapping process can be presented for Samara and Parana/Loire Valles. Similarities in scale, morphology and setting between Samara and Parana/Loire Valles and other valley networks in the region suggests that sapping processes may have been the dominant mechanism of valley formation throughout the region.

Finally, as pointed out by Baker (1985) caution must be exercised when directly comparing terrestrial and Martian valleys. He states that caution is necessary because: the origin of terrestrial systems is not fully understood; conditions creating the Martian valleys were probably unique; only morphologic parameters can be examined in the case of the Martian networks; and the fact that terrestrial studies have focused on channel networks, whereas Martian studies examine relict valleys. This requires that any conclusion concerning valley genesis and formation must remain speculative in nature.

Geologic/Geomorphic Evolution

The: 1) geologic/geomorphic map constructed of the area (Figs. 3a-d); 2) crater counts, summarized in Figure 5; 3) geologic/geomorphic map unit correlation (Fig. 6); 4) cross-cutting and morphologic relationships; and 5) results of drainage basin mapping and density determination (Figs. 9a-d, 11, Tables 3, 4 and 5); were used to trace the geologic/geomorphic evolution of the Margaritifer Sinus quadrangle.

The Oldest Features and Terrain

The oldest recognizable features present (about 4.5 BYBP) in Margaritifer Sinus are the three multi-ringed impact basins, Ladon, Holden and Noachis, first described by Schultz and Glicken (1979) and Saunders (1979). The formation of these basins resulted in large topographic basins (e.g. Ladon Basin) and deep seated fracture systems that have persisted to the present. Schultz and Glicken (1979) and Schultz et al. (1982) also proposed that a structural zone of weakness associated with an area of overlap of the Ladon and Chryse Basin rings and of the presence of a thick volatile rich ejecta blanket from Ladon Basin may have led to collapse and formation of the chaotic terrain in MC19NW (Figs. 3a,d and USGS 1980). The impact basins have had considerable influence on some of the drainage patterns. A thick blanket of volatile rich ejecta beginning at the limit of excavation of Ladon Basin (Schultz et al. 1982) may be responsible for the relatively higher drainage densities along central portions of Samara and Loire Valles (between the third and fourth rings of the Basin). A similar situation may exist around Noachis/Newcomb A Basin in the area of Parana Valles. Thus the multi-ringed impact basins probably exert the dominant structural control in Margaritifer Sinus.

The oldest dated surface in the quadrangle (1,000,000 to 850,000 or about 4.4 to 4.5 BYBP) was created during the period of early intense bombardment that appears to have affected the entire inner solar system 4.5 to 4.0 BYBP before present (Murray et al. 1981). Where recognized (Figs. 4a-d), the surface is expressed by numerous, large (>50km) craters of various classes. Of the locations where the surface has been dated (Figs. 4a-d), it is best preserved along a broad ridge trending roughly SW-NE from central Samara Valles (29S, 16W to southern Parana Valles (24S, 11W), and in the area to the west of Jones Crater from about 14S to 20S. The surface has been labelled Hc on the basis of its large diameter craters and very high crater densities.

Periods of Resurfacing

Towards the end of the period of intense bombardment, the first dated resurfacing event occurred (4.3 to 4.1 BYBP). The event was probably volcanic in origin and appears to have been the earliest regional modification of the cratered highlands in MC19. Of the locations dated (Figs. 4a-d), the surface is best preserved: 1) along a wide swath through medial and distal Loire Vallis; 2) from Parana Valles SW into MC267NE; and 3) in central areas of MC19NE (from crater count C651A87.01B, Table 2, Appendix 3). Because the event took place during the period of intense bombardment, the surfaces created display high crater densities (300,000 to 100,000) with numerous large diameter craters (20 to 40 km), though smaller in size and fewer in number than the cratered uplands. Thus, the surface is usually mapped as unit Hc where present. Crater densities observed on this surface are similar to those noted by Wise et al. (1979) for the ancient cratered highlands in the Tharsis region.

The next dated resurfacing event took place at the end of the period of intense bombardment (just over 4.0 BYBP). The surface displays moderately high crater densities (70,000 to 40,000) with craters predominantly 5 to 15 km in diameter. This event was also volcanic in origin and regional in extent. The surface is best preserved in the area around 27S, 22W and at the foot of Samara and Loire Valles. At some locations the unit has been almost completely buried by later events. The creation of this surface was concurrent with the end of the crustal destruction of the northern part of Mars (Wise et al. 1979). The unit has been mapped as Hc where superimposed on older, incompletely buried, higher density surfaces, and as Sp₂ where the older material has been completely buried.

The third period of resurfacing was the last to occur before development of the valley networks and was the last to affect the quadrangle on a regional scale. Whenever this unit is present, valley networks are always incised into it. The surface displays crater densities of 14,000 to 8,100 (about 3.75 to 3.8 BYBP) and has been dated at numerous locations in MC19SE, and MC26NE (Fig. 4c). Where thick enough to bury older terrain completely it is labelled as Sp₃. Emplacement of this unit coincided with creation of the Lunae Planum lava plains (from Wise et al. 1979).

Development of the Chryse lowland trough was prior to the initiation of valley network and channel formation (before about 3.8 BYBP). This can be inferred by observing that the paleoflow indicators of direction in the major channels and valleys are generally concordant with the present day regional slope of the area, as first pointed out by Saunders (1979). Several exceptions to this are the interior and

exterior radial centripetal drainage systems on hills surrounding multi-ringed impact basins.

Peak Geomorphic and Tectonic Activity

A peak in geomorphic and tectonic activity occurred in MC19 from 10,000 to 5,000 (3.75 to 3.6 BYBP), concurrent with peak Tharsis tectonic activity (Wise et al. 1979). This period saw the development of major channels and valleys, the etched terrain, and chaotic terrain. Development of grabens and wrinkle ridges also occurred at this time.

Meso-scale Outflow Channels - Channel and valley formation in the quadrangle may have begun with the development of the Uzboi/Holden/Ladon system between 11,000 and 6,200 (about 3.75 to 3.65 BYBP) and associated deposition in Ladon Basin. This event has been associated with flow out of Argyre Planitia (Parker and Pieri 1985b). The age of the system is not well constrained, being based on only five 'average' and 'poor' crater counts from the floor of Ladon Basin. The system may have developed contemporaneously with channel and valleys elsewhere in the region (8,500-4,600), or slightly earlier than the other systems. Earlier development may have been favored by local conditions associated with the Argyre impact event that hastened the release of fluid from that area. This may have occurred before conditions favorable to channel and valley formation were fully developed elsewhere in Margaritifer Sinus.

Flow in the Uzboi/Holden/Ladon system was interrupted as a result of the Holden crater impact event. The floor of Holden crater does show some evidence of flow modification and a relatively small valley crosses the southern crater rim from Uzboi Vallis into the crater (Fig. 21). The flow direction in this small valley has not been determined and it is possible that flow was out of Holden Crater southward into Uzboi Vallis due to a change in local slope associated with Holden crater. There is no evidence that the Uzboi/Holden/Ladon system was through flowing following the Holden impact event. No valleys breaching the northeast side of the crater and connecting with Ladon Valles are present, indicating that Holden Crater probably formed during the late stages of flow, between 9,000 and 6,000 (about 3.74 to 3.65 BYBP). Boothroyd (1982; 1983) and Parker and Pieri (1985b) have suggested that an area of chaotic terrain to the northeast of crater Holden (25.5S, 31W, Fig. 12) served as a late source area for Ladon Valles after interruption of the system by the Holden impact event.

Flow out of Ladon Basin to the northeast, via Margaritifer Valles appears to have been the dominant factor in development of the etched terrain centered at 12S, 22W

Fig. 21. Northern Uzboi Vallis, Holden crater, and small valley cutting across the rim of Holden crater (27.5S, 35W). The floor of Holden crater shows some evidence of flow modification (F), however, due to limited resolution, low slope, and high adjacent local relief, flow direction in the interior connecting channel could not be determined. It is possible that late flow in the channel was southward out of Holden crater, a result of a possible local change in slope associated with the impact. Flow in Uzboi Vallis further to the south (large arrows) is northward (467A18, 19, 20).

ORIGINAL PAGE IS
OF POOR QUALITY



(Fig. 7). This is based on: 1) the large size of the meso-scale outflow channel in comparison to Samara and Parana/Loire Valles; 2) the relatively unmodified nature of several large distributaries clearly associated with Margaritifer Valles; and 3) the position of remnants throughout the system (Fig. 7). There is an apparent lack of distributary channels at the mouth of Samara and Parana/Loire Valles. Crater densities from within the etched terrain indicate a time of formation of 9,000 to 4,600, suggesting that flow out of Ladon Basin occurred at this time. This would mean that development of the Uzboi/Holden/Ladon/Margaritifer system actually may have been more contemporaneous with channel and valley formation elsewhere in the region (8,500 to 4,600) if flow was simultaneous in all segments of the system. But, if ponding in Ladon Basin occurred, release may have been associated with later flow into the Basin from the numerous small valley systems located mainly along its northern edge (see USGS 1980).

Valley Network Formation - The formation of the major valley systems in the quadrangle, Samara and Parana/Loire Valles, was between 8,500 and 4,600 (3.73 to 3.6 BYBP) and probably occurred over much of the time span. This age is based on numerous crater counts and is much better constrained than the age of the Uzboi/Holden/Ladon system. All valleys associated with Samara, Parana/Loire Valles and their tributaries are clearly incised into the unit associated with the third resurfacing event (14,000 to 8,100). A fourth unit, associated with a younger resurfacing event (6,000 to 2,000), and also well dated, always covers the valleys when present. The period of network formation can thus be narrowly constrained based upon the stratigraphic relationship of the networks to the two units. Flow out of Samara and Parana/Loire was into/through the etched terrain and out to the north. However, the lack of features in the etched terrain that can be confidently associated with flow from these valley networks further suggests that the terrain was shaped primarily by flow out of Ladon Basin.

It is possible that valley formation had ended completely by the time of the first occurrence of the fourth smooth plains unit (Sp₄, 6,000), however, because of the range of dates on this surface, and its local occurrence, a more intermediate value, such as 4,600, for the cessation of valley formation is probably more realistic. This suggests that the waning stages of valley formation in the region may have alternated with the initial phases of the last resurfacing event.

Tectonic Activity - The region was also tectonically active during the period 10,000 to 5,000. Almost all features labelled as grabens are approximately parallel to

Valles Marineris and radial to the Syria rise. Parker and Pieri (1985a) have associated these features with early development of Valles Marineris and are therefore probably part of the radial fault system of Tharsis. This would make them similar to grabens described by Wise et al. (1979) in the Tharsis area, thus assigning them an age of 10,000 to 5,500. The only exceptions to the graben orientation described above are a N-S trending graben associated with the Holden impact event (24S, 28.5W, Fig. 3b) and a graben system to the north of Ladon Basin (14S, 31W, see USGS 1980) that is arcuate in form and concentric about the center of Ladon Basin. It probably formed at the same time as the other grabens, but its trend was controlled by the Ladon fracture system.

Many grabens have valley networks associated with them and have been flow modified (Fig. 22). Valley network development was definitely post, but probably just after graben formation, as the valleys always cut cross the grabens. Evolution of grabens at the same time that conditions favored valley formation would have created numerous seepage faces from which the valleys could then evolve through spring sapping and the headward extension of valleys, as suggested by numerous authors (Higgins 1974; 1982; Sharp and Malin 1975; Laity and Pieri 1980; Pieri et al. 1980; Mars Channel Working Group 1983; Laity 1983; Laity and Malin 1985).

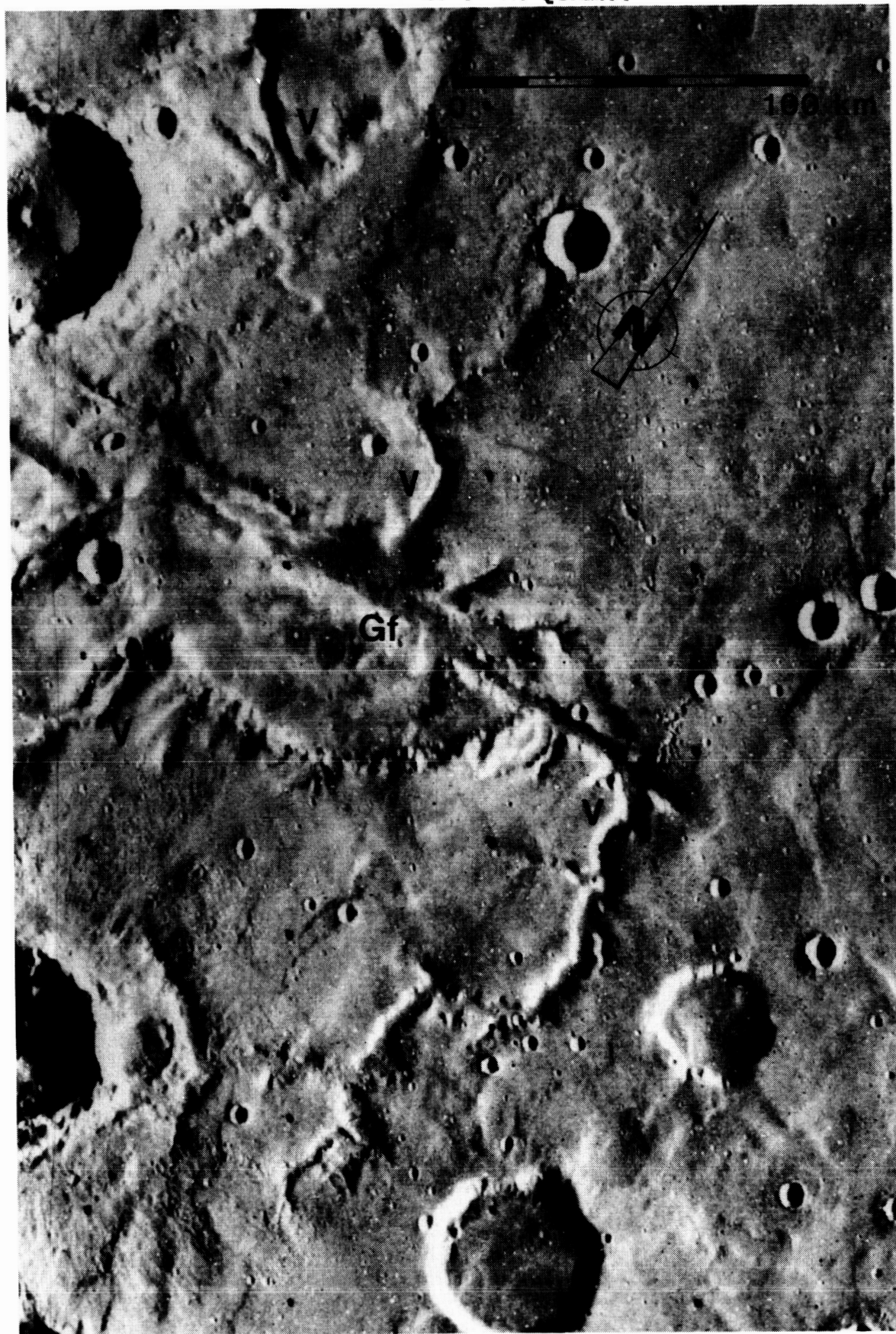
Features interpreted as wrinkle ridges are oriented roughly N-S and are compressional features that may have formed when buckling occurred in rigid volcanic layers overlaying less competent regolith as described by Parker and Pieri (1985a). Because these features are oriented semi-concentric to the Tharsis region, they are inferred to be part of the semi-concentric system of wrinkle ridges described by Wise et al. (1979). This would assign an age of 10,000 to 5,000 to the wrinkle ridges in Margaritifer Sinus by analogy with those dated by Wise et al. (1979) closer to Tharsis.

Chaotic Terrain Formation - Development of the chaotic terrain in MC19NW and MC19NE (Figs. 3a,d and USGS 1980) was between 10,000 and 2,300 (3.75 to 3.1 BYBP). Initial development was post, but probably essentially synchronous with major channel and valley development and the formation of the etched terrain. The relative ages are based on cross-cutting relationships, as the chaotic terrain always interrupts valleys or etched terrain where they occur.

Chaotic terrain is located predominantly between the third and fourth rings of Ladon Basin, the proposed site of a thick layer of intensely brecciated, volatile rich regolith associated with the ejecta facies of Ladon Basin (Schultz et al. 1982). The region is also postulated to be

Fig. 22. Flow modified graben (Gf) and associated valley networks located at 28S, 23W. All valleys (V) drain into the graben and appear to have originated either along its walls or the walls of the degraded crater bisected by the graben (084A38).

ORIGINAL PAGE IS
OF POOR QUALITY



a structural zone of weakness due to overlap of the rings of Chryse and Ladon multi-ringed impact basins and their associated deep seated fracture systems (Schultz and Glicken 1979 and Schultz et al. 1982). The nature of the regolith and presence of numerous fractures would have greatly improved permeability. Later development and thickening of a permafrost layer, after flow through the etched terrain during channel and valley formation, would have substantially increased the pore pressure in the regolith (Carr 1979b), further reducing support in this already structurally weak area. The result would have been the rapid collapse of the surface and the catastrophic outflow of fluid from the region (after Carr 1979b), resulting in the observed downslope flow features and outflow channels to the north. Collapse and outflow would have continued until pore pressures were reduced and the area became more stable, or until outflow had decreased to the point that freezing could occur thus resealing the aquifer (Carr 1979b).

It is possible that development of the chaotic terrain was periodic in nature. A period(s) of collapse may have been associated with each of the following events: 1) discharge from Ladon Basin via Margaritifer Valles (11,000 - 6,200); 2) discharge from Samara and Parana/Loire Valles (8,500 - 4,600); and 3) the continued eastward development of Valles Marineris toward Margaritifer Sinus, probably between 5,000 and 4,000 from Wise et al. (1979). Any chronological combination of these events may reflect reality, however, insufficient data precludes determination of the precise age relationships of these systems/features. Thus, the actual combination of events resulting in collapse, and the number of periods of collapse remains obscure. Following a period of collapse, redevelopment of the permafrost layer and/or later recharge of the aquifer by downslope migration of additional groundwater could have resulted in additional collapse unrelated to the above events (Carr 1979b).

Development of the positive relief chaotic features (5,200?) may also have begun during the period of peak geomorphic and tectonic activity (10,000 to 5,000). The nature and origin of these features, and whether or not they are actively evolving at present, remains obscure. As suggested by Boothroyd and Grant (1985) these features resemble large scale pingos and may or may not have formed in similar manner.

The fretted terrain in MC19NE (Fig. 3d) is inferred to be the incompletely developed edge of the chaotic terrain. It probably occurred during the waning stages of collapse and outflow, either during the initial period of collapse or a possible later period of collapse.

The orientation of the chasma or channels between undissected remnants in the fretted terrain appears to be somewhat structurally controlled (Fig. 3d). However, the orientation of fractures associated with the multi-ringed basins, and the orientation of fractures inferred to be associated with the early opening of Valles Marineris (10,000 to 5,000) is similar. It can not be determined, therefore, which, if either, set of fractures controls the chasma orientation.

A fourth period of resurfacing, between 6,000 and 2,000 (about 3.65 to 2.5 BYBP) began as the period of channel and valley formation was nearing its end. This event was probably of volcanic origin and occurred locally, filling basins. The unit is the youngest dated in the quadrangle and is mapped as Sp₄. Emplacement coincided with the building of Alba and Uranis Patera (Wise et al. 1979), and at the time of enlargement of Valles Marineris eastward.

Post Channel and Valley Formation Activity

Following the period of channel formation the relict polar deposits described by Schultz (1984) in the NE corner of MC19NE (Figs. 3d, 16) were emplaced. The relationship of those deposits to the adjacent Iani Chaos is unknown due to poor image coverage and resolution. Although undated, an age between 4,500 and 2,000 (3.5 to 2.5 BYBP) appears reasonable, based on the stratigraphic relationship of the unit to the valleys and other smooth plains units.

Jones Crater (19S, 20W) was formed sometime after the peak period of geomorphic and tectonic activity. Ejecta associated with the crater partially to completely covers all valleys and grabens present (Fig. 13). Two tentative crater counts performed on the Jones ejecta blanket have yielded an age of 3,500 to 3,000 (about 3.4 BYBP) for the crater, making it one of the youngest dated features in the quadrangle.

Eolian mantling following the Sp₄ event may account for significant deposits around the quadrangle. Numerous locations display a subdued appearance as a result of this mantling, and in some locations the complete burial of features may have occurred. Thus, eolian mantling, occurring after the Sp₄ event, may represent a separate, undated, resurfacing event in some locations. Eolian dune formation and mass movement have probably occurred throughout the history of the planet. Present day locations of these features include crater floors and the floors of Eos and Capri Chasma. Dunes probably exist in other locations not mapped, such as on the plains units, and mass movement has probably occurred anywhere there was sufficient relief.

CONCLUSIONS

1) The oldest recognizable features in Margaritifer Sinus, based on cross-cutting relationships, are the three multi-ringed impact basins, Ladon, Holden, and Noachis, first described by Schultz and Glicken (1979) and Saunders (1979). These basins have remained as the dominant structural control in Margaritifer Sinus to the present.

2) The oldest dated surface in Margaritifer Sinus (1,000,000 - 850,000 craters $> 1 \text{ km} \cdot 10^6 \text{ km}^{-2}$) was created during the period of early intense bombardment (4.5 to 4.0 BYBP). Since that time numerous events, including four resurfacing events of volcanic, fluid or eolian origin, have occurred.

a) The earliest resurfacing event (300,000 - 100,000) was of regional extent and was the first modification of the ancient highlands in the area.

b) The second event (70,000 - 40,000) was also of regional extent and coincides with the crustal destruction of the northern third of Mars.

c) The third event (14,000 - 8200) was the last of regional extent and is the youngest surface dissected by valley networks. This event coincided with the end of emplacement of the Lunae Planum lava plains.

d) Following the third event, the peak period of geomorphic activity occurred from 10,000 - 5000 (3.75 - 3.6 BYBP) concurrent with peak Tharsis tectonic activity.

e) The fourth resurfacing event (6000 - 2000) occurs locally, filling basins, and always covers valley networks when present. Emplacement was contemporaneous with the opening of Valles Marineris.

f) Following the last resurfacing event, geomorphic activity has resulted in: 1) eolian deposits that mantle, and sometimes completely bury, features in some locations; 2) the formation of relict polar material; 3) the possible continued development of positive relief chaotic features; 4) the Jones impact event; and 5) mass movement and eolian dune deposits.

3) During the peak period of geomorphic activity the following events related to fluid release occurred: a) the development of Uzboi/Holden/Ladon Valles with deposition in Ladon Basin (11,000 - 6,200); b) the formation of Samara and Parana/Loire Valles in MC19SE (8,500 - 4,600); c) flow out of Ladon Basin via Margaritifer Valles and, to a limited extent, flow out of Samara and Parana/Loire Valles that created etched terrain (9,000 - 4,500) at their confluence;

and d) initial development of Margaritifer and Iani Chaos (10,000 - 2,300), which was immediately post channel and valley formation.

4) Channel and valley formation may have begun with development of the Uzboi/Holden/Ladon system (11,000 - 6,200). However, if ponding in Ladon Basin did not occur and flow in Uzboi/Holden/Ladon was continuous into the etched terrain, dates within the etched terrain (9,000 - 4,600) suggest that development actually was contemporaneous with channel and valley formation elsewhere (8,500 - 4,600).

5) Development of Margaritifer and Iani Chaos (10,000 - 2,300) may have been periodic in nature. A period of collapse associated with each of the following events is possible: a) discharge from Ladon Basin; b) discharge from Samara and Parana/Loire Valles (8,500 - 4,600); and c) development of Valles Marineris into Margaritifer Sinus (around 5,000 - 4,000). Any chronological combination of these events may reflect reality, however, insufficient age data prevents the actual combination of events and number of periods of collapse from being determined. Additional periods of collapse, unrelated to these events, may have occurred in the manner described by Carr (1979b).

6) Samara and Parana/Loire Valles are extensive well-integrated fluvial systems with a combined drainage area of 535,550 km², 84% of that of the Colorado River in the southwestern USA. As a result of resurfacing episodes after valley formation and impact events, some valley burial and network derangement has occurred indicating that these systems were more extensive in the past.

7) The extensive, well-integrated nature of Samara and Parana/Loire Valles and their sub-basins requires a relatively long period of favorable climatic conditions to have existed to allow their evolution. Once initiated, valley creation was probably continuous throughout the interval (8,500 - 4,600).

8) Development of Samara and Parana/Loire Valles was most likely a result of sapping processes because: a) the geologic setting of the two systems appears to meet the general conditions described by Dunne (1980), Baker (1982) and Laity and Malin (1985) as important for the initiation of terrestrial network development by sapping processes; b) drainage densities for Samara (0.034 km·km⁻²) and Parana/Loire Valles (0.039 km·km⁻²) are well below those observed for terrestrial systems formed by surface runoff; and c) morphologically, Samara and Parana/Loire Valles most closely resemble terrestrial systems formed by sapping and associated downstream fluvial activity (Pieri and Sagan 1979).

9) The similarity in drainage density values between Samara and Parana/Loire valleys suggests that the mechanism that created the valleys was operating at similar rates during formation of the two systems. It further suggests that the substrate beneath the two systems is of fairly uniform composition and that equivalent amounts of fluid, whether of meteoric or subsurface origin, were available to both systems on a regional scale.

10) The range of density values that is observed for the sub-basins and various trunk portions of Samara and Parana/Loire Valles is probably because of: a) local variations in the amount of resurfacing that has occurred after valley formation thus masking original higher drainage densities; and b) variations in substrate and the amount of fluid available on a local scale.

REFERENCES CITED

- ABRAHAMS, A.D., 1984, Channel networks: A geomorphological perspective: Water Res. Research, v. 20, p. 161-188.
- BAKER, V.R., 1980a, Geomorphic mapping of dry valley systems on Mars: Reports of the Planetary Geology Program, NASA Tech. Memo. 81776, p. 54-56.
- BAKER, V.R., 1980b, Nirgal Vallis: Reports of the Planetary Geology Program, NASA Tech. Memo. 82385, p. 345-347.
- BAKER, V.R., 1982, The channels of Mars: Austin, Texas, University of Texas press, 198p.
- BAKER, V.R., 1985, Paleohydrologic implications of valley networks on Mars: Reports of the Planetary Geology Program, NASA Tech. Memo. 87563, p. 313-315.
- BAKER, V.R. AND KOCHER, R.C., 1979, Martian channel morphology: Maja and Kasei Valles: Jour. Geophys. Research, v. 84, p. 7961-7983.
- BAKER, V.R. AND PARTRIDGE, J.B., 1984a, Morphometry of small valley networks on Mars: p. 23-24, in Lunar and Planetary Science XV, Lunar and Planetary Institute, Houston, Texas.
- BAKER, V.R. AND PARTRIDGE, J.B., 1984b, Pristine and degraded segments of small valley networks on Mars: p. 25-26, in Lunar and Planetary Science XV, Lunar and Planetary Institute, Houston, Texas.
- BOOTHROYD, J.C., 1982, Ancient fluvial drainage systems: Margaritifer Sinus area, Mars: Reports of the Planetary Geology Program, NASA Tech. Memo. 85127, p. 209-212.
- BOOTHROYD, J.C., 1983, Fluvial drainage systems in the Ladon Basin area: Margaritifer Sinus area, Mars: Geol. Soc. America Abstracts with Programs, v. 15, p. 530.
- BOOTHROYD, J.C. AND TIMSON, B.S., 1981, Geomorphic mapping of Capri Chasma: Reports of the Planetary Geology Program, NASA Tech. Memo. 84211, p. 302-304.
- BOOTHROYD, J.C. AND TIMSON, B.S., 1983, The Sagavanirktok and adjacent river systems, Eastern North Slope, Alaska: An analog for ancient fluvial terrain on Mars: p. 74-79, in Permafrost: Fourth International Conference, Proceedings, National Academy Press, Washington, DC, 1524p.

- BOOTHROYD, J.C. AND GRANT, J.A., 1984, Fluvial drainage systems: Margaritifer Sinus and Argyre (NC,NE) quadrangles, Mars: Reports of the Planetary Geology Program, NASA Tech. Memo. 86246, p. 182-184.
- BOOTHROYD, J.C. AND GRANT, J.A., 1985, Fluvial drainage basins and valley networks: Eastern Margaritifer Sinus, Mars: Reports of the Planetary Geology Program, NASA Tech. Memo. 87563, p. 316-318.
- CARR, M.H., 1974, The role of lava erosion in the formation of Lunar rilles and Martian channels: *Icarus*, v. 22, p. 1-23.
- CARR, M.H., 1979a, Distribution of small channels on Mars: Reports of the Planetary Geology Program, NASA Tech. Memo. 80339, p. 337.
- CARR, M.H., 1979b, Formation of Martian flood features by the release of water from confined aquifers: *Jour. Geophys. Research*, v. 84, p. 2995-3007.
- CARR, M.H., 1980a, Fluvial history of Mars: Reports of the Planetary Geology Program, NASA Tech. Memo. 82385, p. 342-344.
- CARR, M.H., 1980b, Survey of Martian fluvial features: Reports of the Planetary Geology Program, NASA Tech. Memo. 81776, p. 265-267.
- CARR, M.H., 1981, The surface of Mars: New Haven, Conn., Yale University Press, 232p.
- CARR, M.H., 1984, Mars: p. 207-263, in Carr, M.H. (ed.), The geology of the terrestrial planets, NASA SP-469: NASA, Washington, D.C., 317p.
- CARR, M.H. AND CLOW, G.D., 1981, Martian channels and valleys: Their characteristics, distribution and age: *Icarus*, v. 48, p. 91-117.
- CHAPMAN, C.R., POLLACK, J.B. AND SAGAN, C., 1969, Analysis of the Mariner-4 cratering statistics: *The Astronomical Journal*, v. 74, p. 1039-1051.
- CRATER ANALYSIS TECHNIQUES WORKING GROUP, 1978, Standard techniques for presentation and analysis of crater size-frequency data: NASA Tech. Memo. 79730, 21p.
- D'AMORE, D.W., 1983, Hydrogeology and geomorphology of the Great Sanford Outwash Plain, York County, Maine: Tech. Report No. 3, Boston, Mass., Boston University Dept. of Geology.

- D'AMORE, D.W., 1984, Branch Brook in York County Maine: Formation and maintenance of a drainage network by groundwater sapping: p. 370-380, in Hanson, L.S. (ed.), *Geology of the coastal lowlands*, Boston, MA, to Kennebunk, ME: 76th Annual NEIGC Guidebook, 1984.
- DUNNE, T., 1980, Formation and controls of channel networks: *Progress in Phys. Geog.*, v. 4, p. 211-239.
- FANALE, F.P., 1976, Martian volatiles: Their degassing history and geochemical fate: *Icarus*, v. 28, p. 179-202.
- FLORENSKI, C.P., BASILEUSKI, A.T., KUZMIN, R.O. AND CHERNAYA, I.M., 1975, Geomorphic analysis of some Martian surface images from the Mars 4 and 5 automatic stations: *Icarus*, v. 26, p. 219-229.
- FREY, H., 1974, Surface features on Mars: Ground-based albedo and radar compared with Mariner-9 topography: *Jour. Geophys. Research*, v. 79, p. 3907-3916.
- GRANT, J.A. AND BOOTHROYD, J.C., 1984, Geomorphic mapping and delineation of drainage basin boundaries: Margaritifer Sinus (SE) quadrangle, Mars: *Geol. Soc. America Abstracts with Programs, Northeastern Section*, v. 16, p. 19.
- GREELEY, R., LEACH, R.N., WILLIAMS, S.H., WHITE, B.R., POLLACK, J.B., KRINSLEY, D.H. AND MARSHALL, J.R., 1982, Rate of wind abrasion on Mars: *Jour Geophys. Research*, v. 87, p. 10,009-10,024.
- GREGORY, K.J., 1976, Drainage networks and climate: p. 289-315, in Derbyshire, E. (ed.), *Geomorphology and climate*: London, John Wiley and Sons Press, 514p.
- GREGORY, K.J. AND WALLING, D.E., 1973, Drainage basin form and process: A geomorphological approach: New York, John Wiley and Sons, 458p.
- GREGORY, K.J. AND GARDINER, V., 1975, Drainage density and climate: *Z. Geomorph. N.F.*, v. 19, p. 287-298.
- HARTMANN, W.K., 1965, Terrestrial and Lunar flux of large meteorites in the last two billion years: *Icarus*, v. 4, p. 157-165.
- HARTMANN, W.K., 1973, Martian cratering, 4, Mariner 9 initial analysis of cratering chronology: *Jour. Geophys. Research*, v. 78, p. 4096-4116.
- HIGGINS, C.G., 1974, Model drainage networks developed by ground-water sapping: *Geol. Soc. America Abstracts with Programs*, v. 6, p. 794-795.

- HIGGINS, C.G., 1982, Drainage systems developed by sapping on Earth and Mars: *Geology*, v. 10, p. 147-152.
- HIGGINS, C.G., 1984, Piping and sapping: Development of landforms by groundwater outflow: p. 18-58, in LaFleur, R.G. (ed.), *Ground water as a geomorphic agent, The Binghamton Symposia in Geomorphology: International Series*, no. 13: Boston, Mass, Allen and Unwin, Inc., 389p.
- HILLER, K. AND NEUKUM, G., 1979, Ages of Martian volcanoes and erosional features: *Reports of the Planetary Geology Program, NASA Tech. Memo. 80339*, p. 173-175.
- HILLER, K. AND NEUKUM, G., 1980, Time sequence of martian geologic features: *Reports of the Planetary Geology Program, NASA Tech. Memo. 81776*, p. 119-121.
- LAITY J.E., 1983, Diagenetic controls on groundwater sapping and valley formation, Colorado Plateau, revealed by optical and electron microscopy: *Physical Geography*, v. 4, p. 103-125.
- LAITY J.E. AND PIERI, D.C., 1980, Sapping processes in tributary valley systems: *Reports of the Planetary Geology Program, NASA Tech. Memo. 81776*, p. 295-297.
- LAITY, J.E. AND MALIN, M.C., 1985, Sapping processes and the development of theater-headed valley networks on the Colorado Plateau: *Geol. Soc. America Bull.*, v. 96, p. 203-217.
- MARCUS, A.H., 1968, Martian craters: Number density: *Science*, v. 160, p. 1333-1335.
- MARS CHANNEL WORKING GROUP, 1983, Channels and valleys on Mars: *Geol. Soc. America Bull.*, v. 94, p. 1035-1054.
- MASURSKY, H., 1973, An overview of geological results from Mariner 9: *Jour. Geophys. Research*, v. 78, p. 4009-4030.
- MASURSKY, H., DIAL, A.L., Jr. AND STROBELL, M.E., 1980, Martian channels - A late Viking view: *Reports of the Planetary Geology Program, NASA Tech. Memo. 82385*, p. 184-187.
- MASURSKY, H., BOYCE, J.M., DIAL, A.L., SCHABER, G.G. AND STROBELL, M.E., 1977, Classification and time of formation of Martian channels based on Viking data: *Jour. Geophys. Research*, v. 82, p. 4016-4038.

- MCGILL, G.E., 1977, Craters as "fossils": The remote dating of planetary surface materials: Geol. Soc. America Bull., v. 88, p. 1102-1110.
- MCGILL, G.E. AND WISE, D.U., 1972, Regional variations in degradation and density of Martian craters: Jour. Geophys. Research, v. 77, p. 2433-2441.
- MILTON, D.J., 1973, Water and processes of degradation in the Martian landscape: Jour. Geophys. Research, v. 78, p. 4037-4047.
- MURRAY, B.C., MALIN, M.C. AND GREELEY, R., 1981, Earthlike planets: San Francisco, Calif., W.H. Freeman press, 387p.
- MURRAY, B.C., SODERBLOM, L.A., SHARP, R.P. AND CUTTS, J.A., 1971, The surface of Mars: 1. Cratered terrains: Jour. Geophys. Research, v. 76, p. 313-330.
- MUTCH, T.A., ARVIDSON, R.E., HEAD, J.W., III, JONES, K.L. AND SAUNDERS, R.S., 1976, The geology of Mars: Princeton, New Jersey, Princeton University Press, 400p.
- NEUKUM, G. AND WISE, D.U., 1976, Mars: A standard crater curve and possible new time scale: Science, v. 194, p. 1381-1387.
- NEUKUM, G. AND HILLER K., 1981, Martian ages: Jour. Geophys. Research, v. 86, p. 3097-3121.
- NEUKUM, G., HILLER, K. AND HENKEL, J., 1979, Martian absolute time scales: Reports of the Planetary Geology Program, NASA Tech. Memo. 80339, p. 170-172.
- PARKER, T.J. AND PIERI, D.C., 1985a, Geomorphology and geology of the southwestern Margaritifer Sinus and Argyre regions of Mars-1: Geological and geomorphological overview: Reports of the Planetary Geology and Geophysics Program, NASA Tech. Memo. 87563, p. 361-363.
- PARKER, T.J. AND PIERI, D.C., 1985b, Geomorphology and geology of the southwestern Margaritifer Sinus and Argyre regions of Mars-3: Valley types and distribution: Reports of the Planetary Geology and Geophysics Program, NASA Tech. Memo. 87563, p. 367-368.
- PATTON, P.C. AND BAKER, V.R., 1976, Morphometry and floods in small drainage basins subject to diverse hydrogeomorphic controls: Water Res. Research, v. 12, p. 941-952.
- PIERI, D.C., 1979, Global distribution of Martian valley systems: Reports of the Planetary Geology Program, NASA Tech. Memo. 80339, p. 353-356.

- PIERI, D.C., 1980a, Geomorphology of Martian valleys: p. 1-60 in *Advances in Planetary Geology*, NASA Tech. Memo. 81979, 326p.
- PIERI, D.C., 1980b, Geomorphology of valley networks on Mars: Speculations on their origins: p. 82-87, in *Planetary Water: Proceedings of the Third Colloquium on, Niagra Falls, N.Y., October, 27-29, 1980*, 189p.
- PIERI, D.C. AND SAGAN, C., 1979, Origin of Martian valleys: Reports of the Planetary Geology Program, NASA Tech. Memo. 80339, p. 349-352.
- PIERI, D.C., MALIN, M.C. AND LAITY, J.E., 1980, Sapping: Network structure in terrestrial and martian valleys: Reports of the Planetary Geology Program, NASA Tech. Memo. 81776, p. 292-294.
- SAUNDERS, S.R., 1979, Geologic map of the Margaritifer Sinus quadrangle of Mars: USGS Map I-1144 (MC-19).
- SCHULTZ, P.H., 1984, Polar wandering on Mars and the distribution of water-ice through time: p. 71-73, in *"Water on Mars" Workshop Abstracts Volume*, 1984.
- SCHULTZ, P.H. AND GLICKEN, H., 1979, Impact crater and basin control of igneous processes on Mars: *Jour. Geophys. Research*, v. 84, No. B14, p. 8033-8047.
- SCHULTZ, P.H. AND LUTZ-GARIHAN, A.B., 1982, Grazing impacts on Mars: A record of lost satellites: *Jour. Geophys. Research*, v. 87, p. A84-A96.
- SCHULTZ, P.H., SCHULTZ, R.A. AND ROGERS, J., 1982, The structure and evolution of ancient impact basins on Mars: *Jour. Geophys. Research*, v. 87, No. B12, p. 9803-9820.
- SCHUMM, S.A., 1974, Structural origin of large Martian channels: *Icarus*, v. 22, p. 371-384.
- SCOTT, D.H. AND CARR, M.H., 1978, Geologic map of Mars: USGS Map I-1083.
- SHARP, R.P., 1973, Mars: troughed terrain: *Jour. Geophys. Research*, v. 78, p. 4063-4072.
- SHARP, R.P. AND MALIN, M.C., 1975, Channels on Mars: *Geol. Soc. America Bull.*, v. 86, p. 593-609.
- SODERBLOM, L.A., CONDIT, C.D., WEST, R.A., HERMAN, B.M. and KRIEDLER, T.J., 1974, Martian planetwide crater distributions: Implications for geological history and surface processes: *Icarus*, v. 22, p. 239-263.

- STRAHLER, A.N., 1952, Hypsometric (area-altitude) analysis of erosional topography: Geol. Soc. America Bull., v. 63, p. 1117-1142.
- U.S. GEOLOGICAL SURVEY, 1975, Shaded relief map of the Argyre quadrangle Mars: USGS Map I-923 (MC-26).
- U.S. GEOLOGICAL SURVEY, 1976, Topographic map of the Margaritifer Sinus quadrangle Mars: USGS Map I-975 (MC-19).
- U.S. GEOLOGICAL SURVEY, 1979a, Controlled photomosaic of the Argyre NE quadrangle Mars: USGS Map I-1193 (MC-26NE).
- U.S. GEOLOGICAL SURVEY, 1979b, Controlled photomosaic of the Margaritifer Sinus SW quadrangle of Mars: USGS Map I-1209 (MC-19SW).
- U.S. GEOLOGICAL SURVEY, 1979c, Controlled photomosaic of the Margaritifer Sinus SE quadrangle of Mars: USGS Map I-1210 (MC-19SE).
- U.S. GEOLOGICAL SURVEY, 1979d, Controlled photomosaic of the Margaritifer Sinus NW quadrangle of Mars: USGS Map I-1381 (MC-19NW).
- U.S. GEOLOGICAL SURVEY, 1979e, Controlled photomosaic of the Margaritifer Sinus NE quadrangle of Mars: USGS Map I-1382 (MC-19NE).
- U.S. GEOLOGICAL SURVEY, 1980, Shaded relief map of the Margaritifer Sinus quadrangle Mars: USGS Map I-1293 (MC-19).
- WEIHAUPT, J.G., 1974, Possible origin and probable discharges of meandering channels on the planet Mars: Jour. Geophys. Research, v. 79, p. 2073-2076.
- WISE, D.U., 1979, Geologic map of the Arcadia quadrangle of Mars: USGS Map I-1154 (MC-3).
- WISE, D.U., 1984, Kasei Vallis of Mars: Dating the interplay of tectonics and geomorphology: Geol. Soc. America Abstracts with Programs 1984, v. 16, no. 6, p. 699.
- WISE, D.U., 1985, Kasei Vallis of Mars: Dating the interplay of tectonics and geomorphology: Reports of the Planetary Geology Program, NASA Tech. Memo. 87563, p. 512.

WISE, D.U. AND MILKOWSKI, G., 1980, Dating methodology of small, homogeneous crater populations applied to the Tempe-Utopia Trough region of Mars: Reports of the Planetary Geology Program, NASA Tech. Memo. 81776, p. 122-124.

WISE, D.U., GOLOMBECK, M.P. AND MCGILL, G.E., 1979, Tharsis province of Mars: Geologic sequence, geometry, and a deformation mechanism: Icarus, v. 38, p. 456-472.

APPENDIX 1

Crater Counting Methodology

Theory

The D.U. Wise method of dating local surfaces was employed to complete crater counts on various surfaces within MC19. This method uses relatively small areas displaying a homogeneous distribution of craters in some size range (Wise et al. 1979; Wise and Milkowski 1980). Most other methods of crater counting utilize relatively larger areas in an effort to build a large statistical base (Wise and Milkowski 1980). These other methods are effective when applied to single age surfaces, however, the method becomes ineffective in regions affected by multiple resurfacing events (Wise et al. 1979).

Lava flooding, mantling or erosion, occurring as resurfacing events, preferentially destroys smaller craters, due to their small volume and area, and usually only partially destroys larger craters. The result is an alteration in the crater size frequency distribution on surfaces affected by a resurfacing event(s), the extent of which being dependent on flow magnitude, thickness and frequency of occurrence, so that it represents at least two crater populations (Figs. 23a-d) (Neukum and Hiller 1981; Wise and Milkowski 1980). Each resurfacing event will affect crater populations in a similar manner, completely burying small craters and sometimes all craters in some locations, and leaving larger craters or patches of larger craters partially buried that represent an older surface and show through the cover material.

As pointed out by Neukum and Wise (1976) Neukum and Hiller (1981) and Wise and Milkowski (1980) a cumulative crater size-frequency plot performed on a large area affected uniformly by a resurfacing event will show flattening in the smaller crater sizes (Fig. 23a) or yield a curve with two segments parallel to the standard curve, but separated by a distinct bump. In the second case, one segment represents all the larger craters that survived the resurfacing event. Projection of the Martian standard curve (Neukum and Hiller 1981) through this segment to 1 km may yield a valid cumulative crater number for the older surface. The other segment represents the crater history of the surface following the resurfacing event. Projection to 1km for this section will yield only an approximate age for the resurfacing event. A crater size-frequency plot derived from an area affected by multiple resurfacing events will display numerous bumps that will prevent reliable ages for the various surfaces from being determined.

Even in an area affected by only one resurfacing event problems arise. If resurfacing did not uniformly affect the area, as often is the case, the larger surviving craters may only be visible in patches. A crater size frequency plot from such a location would result in a curve that is flat

Fig. 23. Fig 23a is a cumulative crater size-frequency plot obtained by counting all craters present in an area centered on 12S, 16W (see Fig. 4 and Table 2 for the location of count C651AB7.001). The curve is noticeably flat for craters less than 10 to 15 km in diameter, and it displays several bumps and different slopes. This is most likely the result of one or several periods of resurfacing. Comparison with the Martian standard curve (Fig. 25) would yield only one age for this curve, based on the largest craters, as that portion of the plot most closely matches the slope of the standard curve. Close examination of the region shows that three distinct size ranges of craters are present. Using the method of dating local surfaces and the three crater size ranges present, three plots (Fig. 23b-d), each representing a period of resurfacing, have been generated. Each curve yields a relative age that corresponds to events dated elsewhere in the quadrangle: Fig. 23b to the Sp₁ event (age 110,000); Fig. 23c to the Sp₄ event (age 3,100); and Fig. 23d to the Sp₃ event (age 13,900).

Fig. 23a

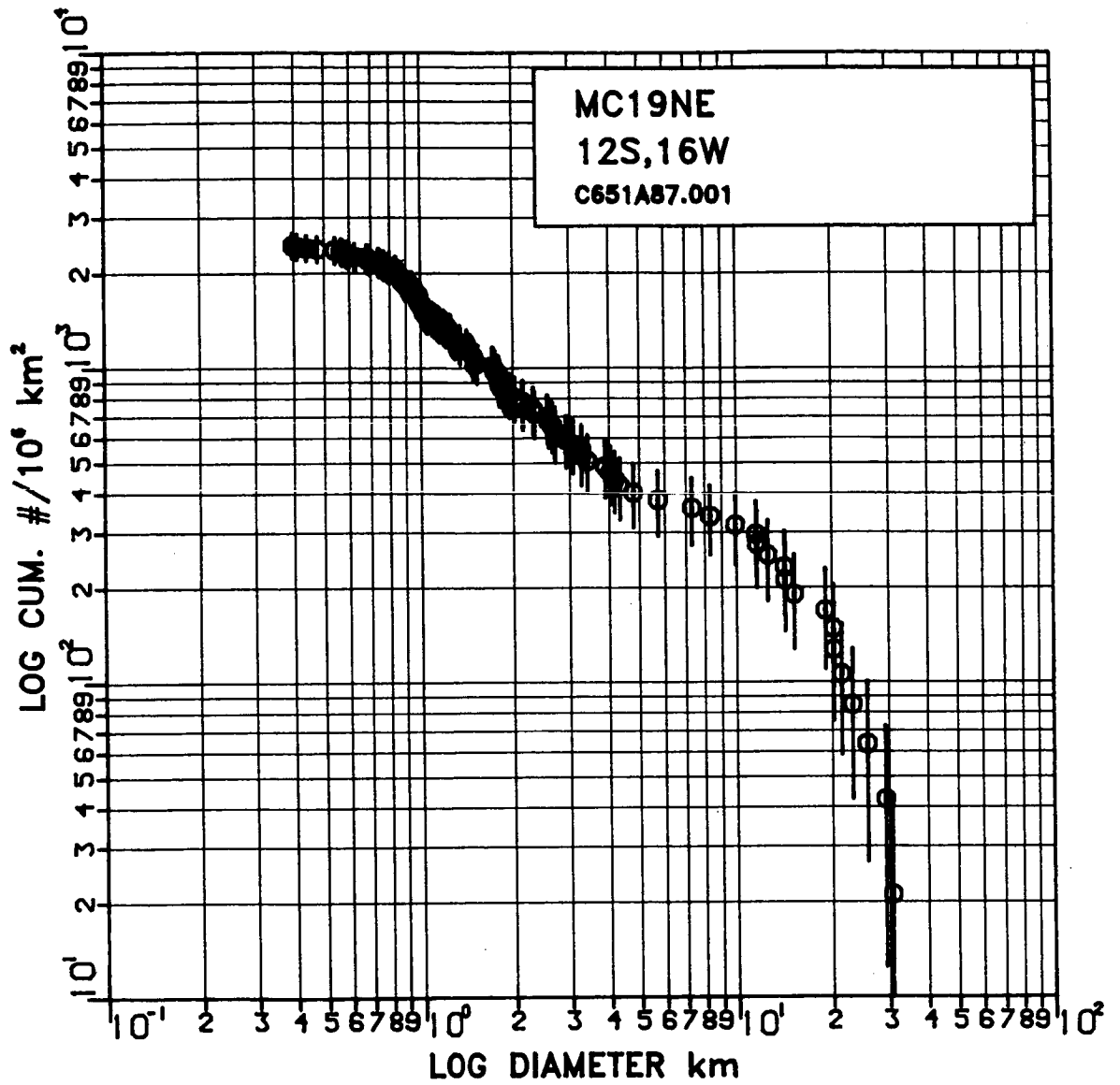


Fig. 23b

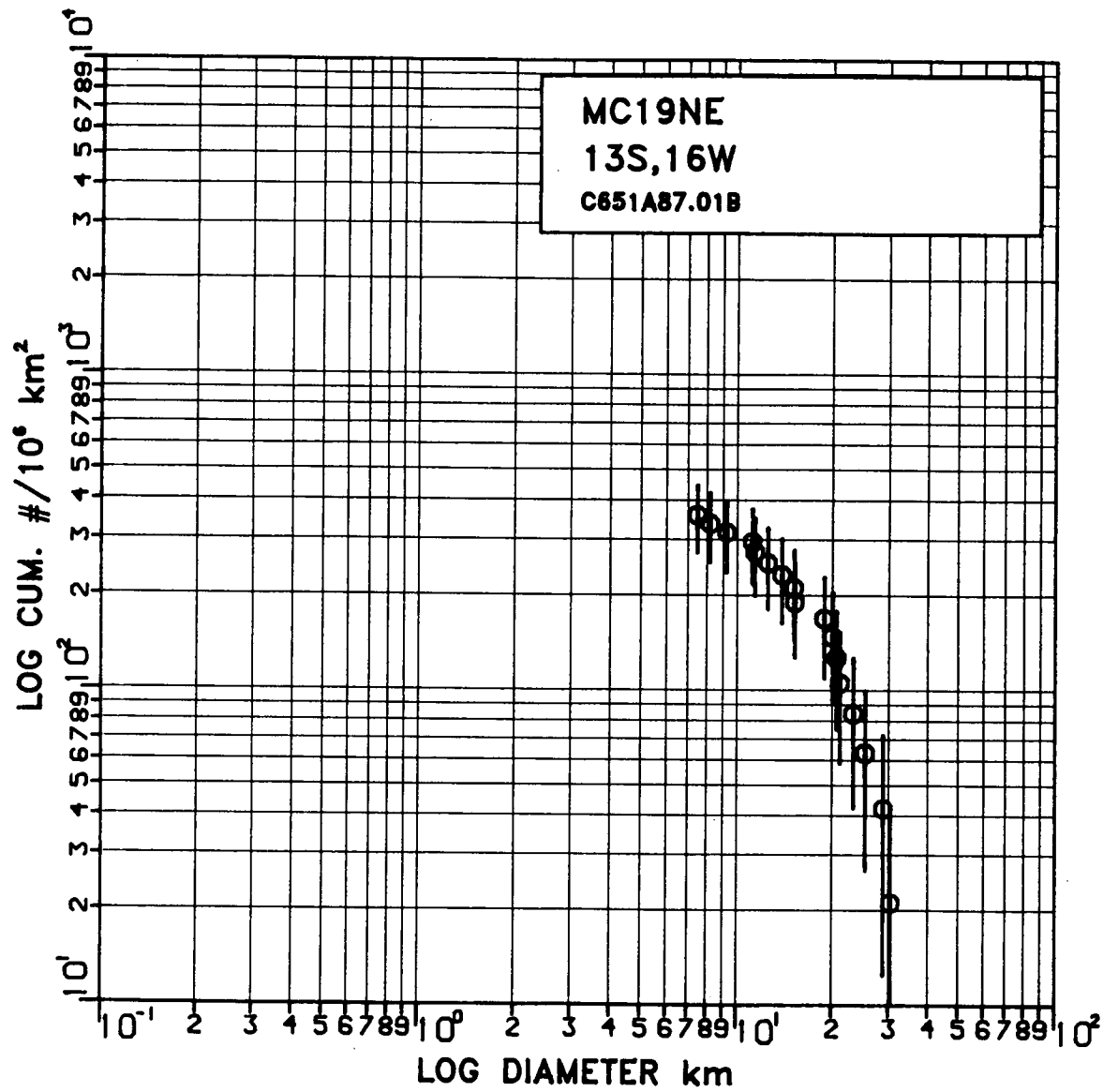


Fig. 23c

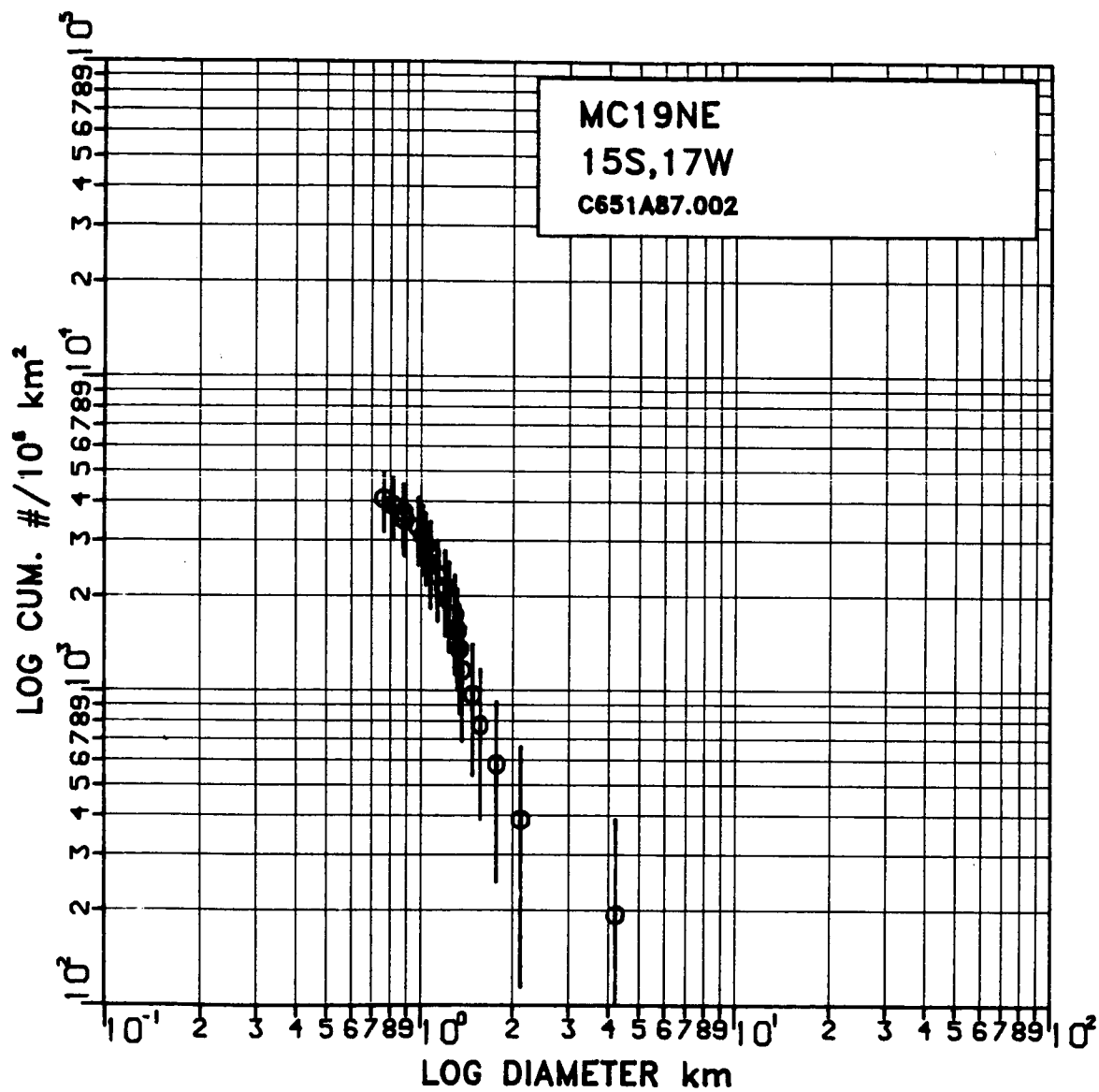
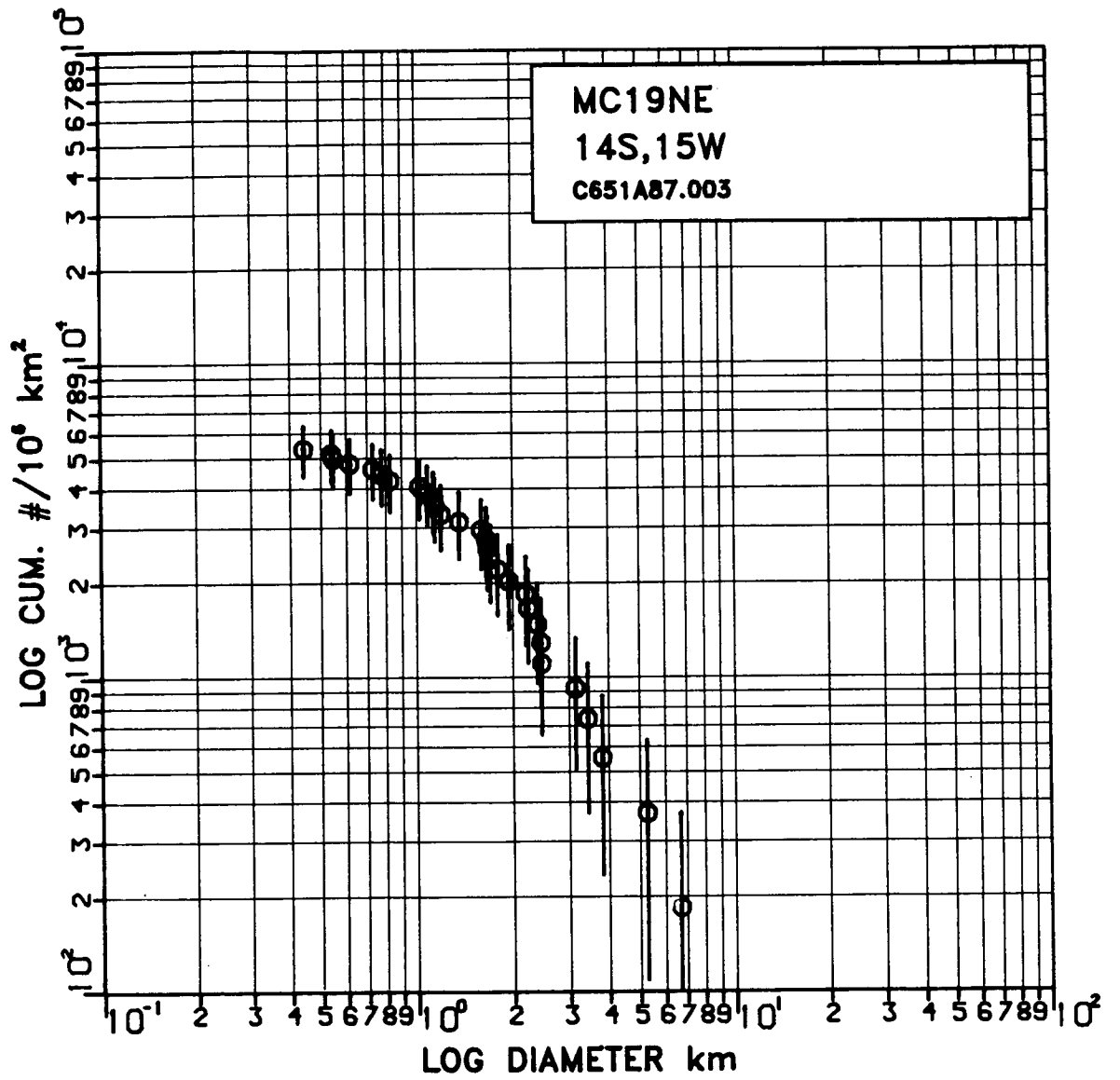


Fig. 23d



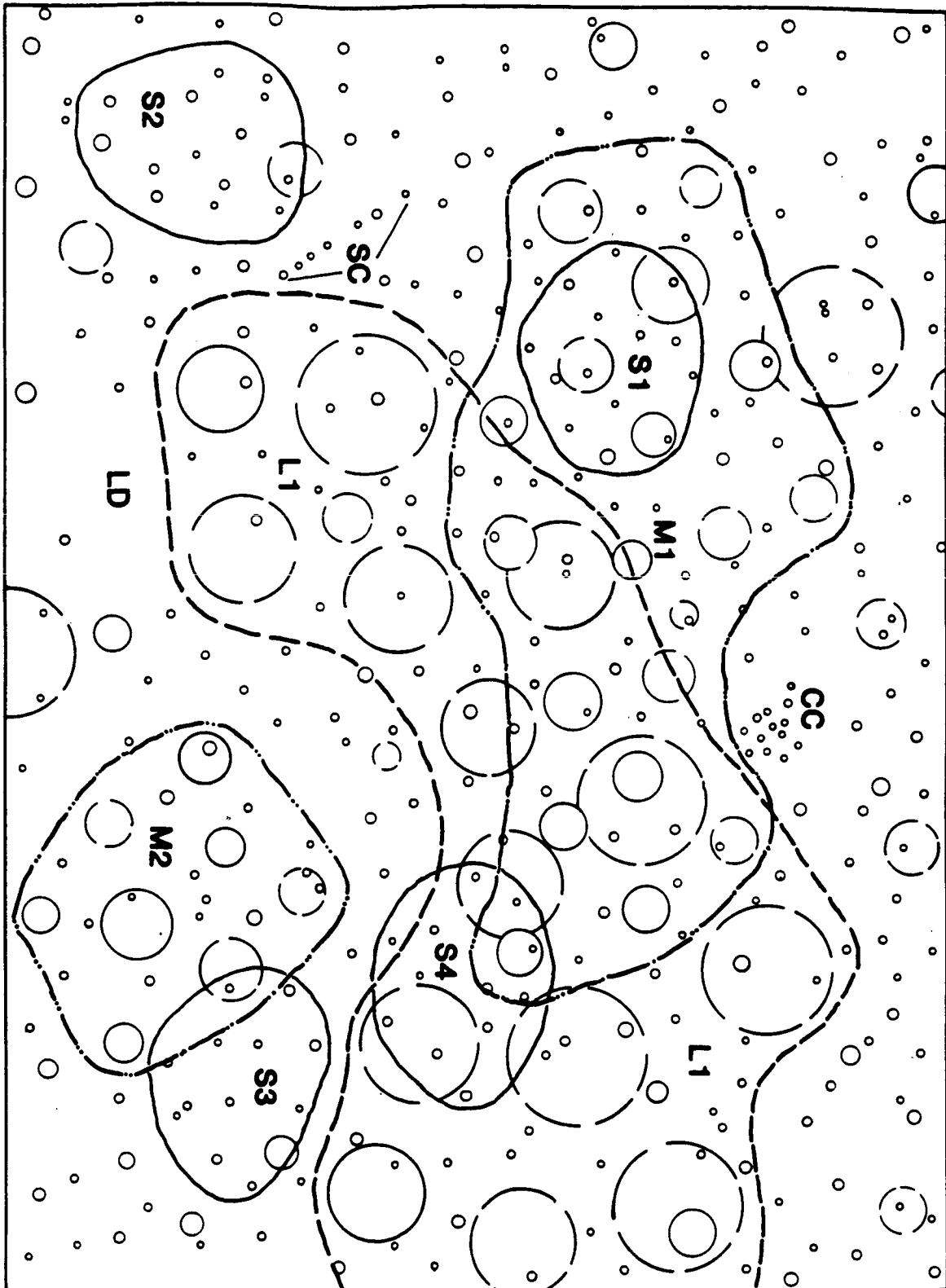
even for the larger diameter craters because local distributions of the larger craters would end up being averaged over the entire area of the count. This may prevent derivation of a reliable age for the older, partially buried surface. In both cases where a single resurfacing event affects an area the age determined for the time of resurfacing by projection through the segment parallel to the standard curve in the smaller crater diameters will be artificially high. Because the large craters from the old surface have been included in the plot, they become part of the cumulative frequency, causing all the smaller diameter craters to plot at artificially large cumulative values.

The method of dating local surfaces differs from the method described above in that small (on average 40 \pm 30 craters per count), homogeneous populations of craters in a given size range are utilized (Wise and Milkowski 1980). A homogeneously cratered area is one that would yield similar crater counts for randomly selected sub-areas within it (Wise et al. 1979). Areas that should be avoided when employing this method include those with: 1) anomalous crater concentrations, both high and low; 2) locations displaying numerous potential secondary craters; 3) linear rays of craters; and 4) some multiple craters. Figure 24 shows an idealized drawing of a hypothetical area that is homogeneously cratered in various locations by several size ranges of craters. Outlined are locations in the various size ranges that would be selected to perform crater counts. Figure 24 also shows areas that should not be counted due to the presence of anomalous crater distributions. The selected areas show the craters chosen for each count. Care must be taken to avoid counting craters partially buried and not incised into the surface being considered. Where not apparent, this is accomplished by examining the morphological characteristics of the crater such as crater class, rim characteristics, etc.. The presence of craters from older surfaces in a cumulative size-frequency plot of an area would shift the curve vertically upwards as a result of contamination from older crater populations.

By selecting areas to be counted in this manner, each cumulative crater size-frequency plot completed will be related to a specific geologic unit (Wise and Milkowski 1980). This technique allows the dating of the different periods of resurfacing by examining the locations of different homogeneous size populations of craters in an area. Each count will result in a cumulative crater size-frequency curve that is parallel to the standard curve and can be projected to a 1 km crater number using the standard curve of Neukum and Wise (1976). By projection to a 1km crater number, numerous curves from different size ranges of craters can be compared on a common base and the ages of the various surfaces determined. The method of local surfaces

Fig. 24. Idealized sketch of a hypothetical cratered surface. Three size ranges of craters are present, designated as small (S), medium (M), and large (L). Craters of subdued morphology are designated by a dashed outline. Only the small crater size range is present uniformly across the figure. As a result, a crater count performed over the entire area might resemble the one in Figure 23a. Areas that might be selected for crater counts using the method of local surfaces are shown for each size range. The large craters are homogeneously distributed over the area labelled L1 and enclosed by the dashed line. The medium size range of craters is homogeneously distributed in two separate areas (M1 and M2), so two counts could be performed, each enclosed by a dashed and dotted line. Numerous locations show a homogeneous distribution of craters in the small size range. Possible count locations in this size range (S1-S4), enclosed by a solid line, are only a few of those possible. Only craters on the surface represented by each size range should be included in a count on that surface. Areas to avoid include crater clusters (CC), low crater density areas (LD) and possible secondary craters (SC).

Figure 24



avoids the problem of smearing of the data, such as can occur when using large areas, due to an unequal distribution of various size crater populations across an area counted. The problem is eliminated by defining count locations on the basis of the presence of a homogeneous distribution of craters in some size range(s).

Because the number of craters in any one count completed using this method is small, individual counts are not statistically significant (Wise and Milkowski 1980), and should not be heavily relied on. However, when numerous counts are performed at various locations on the surface of the same unit, a consistently recurring age is a good indicator of the correct age.

As pointed out by Wise and Milkowski (1980), this method of crater counting requires that the geologic analyses and crater measurements be done simultaneously in an effort to explain the appearance of each plot. Each curve should also be re-examined to determine if the craters selected are actually on the surface in question, on an older partially buried surface, or part of a younger surface covering the area. This technique allows the surfaces of various specific units to be dated when it is not possible to do so by counting craters of various size populations over a large area (Wise and Milkowski 1980). A further discussion of the method of dating local surfaces can be found in Wise and Milkowski (1980), Neukum and Wise (1976), Neukum and Hiller (1981) and Wise et al. (1979).

Figure 23a shows count number C651A87.001, performed in MC19NE. This area has been affected by at least one resurfacing event. For all crater sizes < 10 - 15 km the curve is noticeably flattened and has several bumps in it. Comparison of this plot to the Martian standard curve would yield the relative age of the oldest surface in the area at best. Closer examination of this location shows that three size ranges of craters are present. Three separate counts (Figs. 23b-d), using the method of local surfaces, were performed in the same region as Figure 23a. Each count considered only craters in one of the three size ranges present, and only in the areas where they were homogeneously distributed. Interpretation of these three curves revealed that three resurfacing events have affected this area. Comparison with the standard curve of Neukum and Wise (1976) shows that these events correspond to the Sp₁ (Fig. 23b, age 110,000), Sp₃ (Fig. 23c, age 13,900), and Sp₄ (Fig. 23d, age 3100) events.

Technique

Areas were selected across MC19 that, when dated, would show the age relationships between the channel and valley features, the etched terrain at their confluence and

Margaritifer and Iani Chaos further to the north. For the Uzboi/Holden/Ladon system the floor of Ladon Basin was selected for crater counts and relative age determinations. Numerous locations, mainly in MC19SE and MC19NE, were selected in an effort to determine the relative ages of Samara and Parana/Loire Valles based on the ages of surfaces that the valleys were incised into and those covering the networks. Other counts were performed in this same area to determine the age of the ancient cratered highlands and the timing and extent of the resurfacing events that have occurred. All counts were used to help determine the geologic evolution of MC19. Crater counts were also performed in the etched terrain, within Margaritifer and Iani Chaos and on the floor of Ares valles to determine their age relationships to to each other and to other features in Margaritifer Sinus.

After selecting the types of terrain and the features where counts would be performed, the highest quality orthographic images of them (Table 2) were selected (resolution about 200m/pixel). These images, along with the 1:1,000,000 photomosaic of MC19SE were then checked to determine scale accuracy using the following spherical trigonometric formula:

$$\cos(a) = \cos(90 - \delta_2) \cos(90 - \delta_1) + \sin(90 - \delta_2) \sin(90 - \delta_1) \cos(\lambda_2 - \lambda_1)$$

where $\cos(a)$ is the cosine of distance between adjacent corners of the photograph or image in degrees, δ_1 = the latitude and δ_2 = the longitude of two adjacent corners of the photograph or image. To get $\cos(a)$ into degrees, its inverse was taken. This was then multiplied by the average number of km/degree on Mars (calculated to be 59.07 km/degree) to derive the actual distance between corners of the image or photograph in kms. This was then compared to the bar scale given on the images to determine the percent error in scale. All images examined were found to have less than 1% error in scale. The assembled 1:1,000,000 photomosaic of MC19SE was found to have a scale error of generally less than 1%. The 1% error in the scale of the images and photographs was considered negligible, therefore the scale on the images was utilized for crater and area measurements. The calculated scale was used for crater and area measurements done from individual negatives because of the large scale enlargement.

The 1:1000,000 photomosaic was then examined for specific areas with homogeneous crater populations in some size range(s). Measurements in areas displaying homogeneous populations of craters 5 km and larger in diameter were done directly from the 1:1,000,000 photomosaic. Some measurements were also made from the photomosaic in areas showing a homogeneous crater distribution in the range of 2

to 5 km in diameter. Measurements taken off individual images used for crater counts were made for areas showing a homogeneous crater distribution in diameters less than 5 km in diameter.

To perform crater counts in areas located on individual images, the following procedure was used. The images were enlarged using an overhead projector so that small diameter craters (about 0.75 to 5 km) could more accurately be measured. The projector was placed at least 7-8 m from a wall where a piece of tracing paper had been taped. An image was then taped in the center of the projector and projected onto the tracing paper. The scale of the enlarged image was determined by measuring the distance between the same two corners of the enlarged negative that were used in the original scale calculation and comparing it to the calculated value. Distortion due to the projector was considered and found to be 1% or less. A tracing of all craters on the image and/or the area of interest on the photomosaic was then made and the position of valleys, grabens, chaos, etc, were marked for later ease of location identification. Craters of various sizes partially buried by resurfacing events, and craters of questionable quality (see Theory section), were marked accordingly for later identification. This procedure was repeated for all the images used. The image tracings were then examined to locate those areas displaying homogeneous crater populations in some size range(s).

Locations selected to perform crater counts on both the 1:1,000,000 photomosaic and tracings of the individual negatives were defined by a loosely fitting line drawn around the selected craters that was placed in an effort to preserve the homogeneous crater distribution (Table 2, Fig. 24). This was done by placing the line about one half the observed distance between craters beyond the outermost craters in the group to be counted (Fig. 24). Placement of the line was such that narrow embayments and peninsulas were not created as this would not reflect a homogeneous crater distribution. For count locations chosen on the photomosaic the placement of the line averaged about 0.5 to 1.5 cm beyond the limit of the craters to be counted. Locations on the negative tracings have the line placed 1 to 3 cm beyond the outermost craters. This difference in the distance of line placement is due to the much larger scale of the negative tracings.

The last step before actual area and crater measurement was the labeling of all areas to be counted so that they could be easily referred to later. Individual craters within the count area were, in most cases, also numbered to prevent them from being overlooked or counted twice.

Measurement of the area of each crater count location was done at least twice and then averaged to derive a more accurate value. Areas were derived using both a Digital Polar Planimeter and a plane table digitizer. Measurement of individual crater diameters was performed twice on each crater across two different diameters approximately 90 degrees apart. These two values were then averaged to derive an accurate diameter for each crater. Diameter values were obtained using a plane table digitizer or by hand measurement and were calculated to the nearest 0.1 mm.

The values obtained for the area and crater diameters for each crater count location were used in a program called 'STAMMER' written by Brian Fessler at the Lunar and Planetary Institute, Houston, TX, USA, to derive a logarithmic plot of the cumulative crater size-frequency distribution (Figs. 23a-d, Appendix 3). Each plot has been normalized so that it displays the log of the cumulative number of craters $\cdot 10^6 \text{ km}^{-2}$ vs. log of the crater diameter (obtained by dividing 1,000,000 km by the actual area of the count and multiplying it times the cumulative frequency of each crater in the area measured). The counts were normalized to allow easy comparison of the plots to the Martian standard crater curve (Neukum and Hiller 1981) so that relative ages could be derived, and to provide a common base for inter-comparison of the plots. Each point on a plot represents the cumulative number of craters of that diameter and larger for that count. The confidence interval for each point on the plot was calculated using the following formula and is explained below:

Confidence interval = (cum.freq \pm square root of the cum.freq.) $\times 10^6 \text{ km}^2$ / Area of the count

The value for the cumulative frequency of each crater within the area measured \pm the square root of that value, was multiplied times the quantity (1,000,000 km^2 divided by the actual measured area of the crater count). This derives the confidence interval based on the normalized area (1,000,000 km^2) of the count.

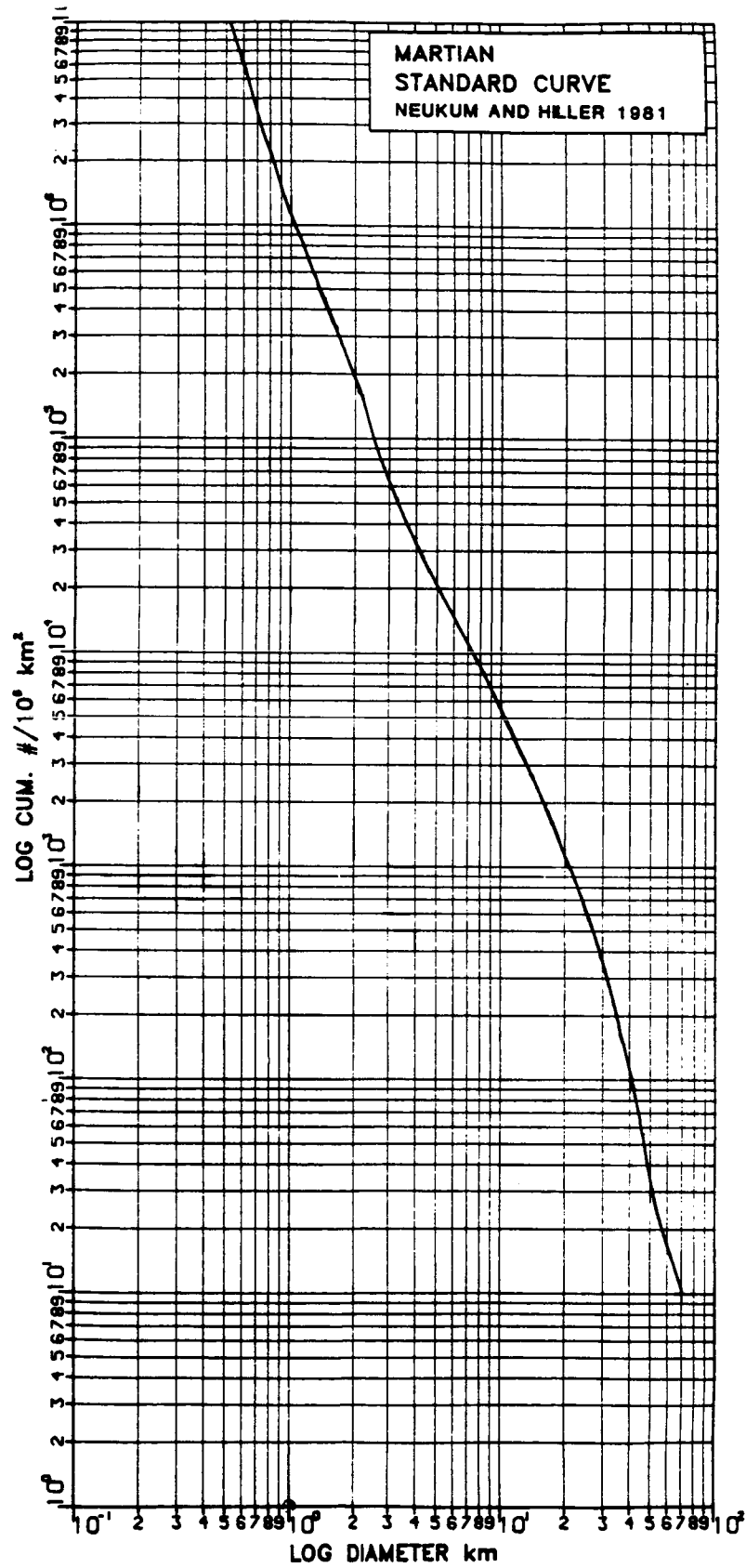
The Martian standard crater curve (Neukum and Hiller 1981, Fig. 25) was used to project the data to obtain a 1 km crater number. This was done for each plot and the resultant cumulative number of craters $\geq 1 \text{ km} \cdot 10^6 \text{ km}^{-2}$ has been used as a relative time standard throughout the study (after Neukum and Wise 1976; Wise 1979; Wise et al. 1979; Wise and Milkowski 1980; and Neukum and Hiller 1981).

Each crater count was compared to photographs of the count location. This was done to locate any errors in crater selection and to see how the derived relative age of the count compared to the geology of the region and other counts located on similar and different surfaces. Anomalous

Fig. 25. The Martian standard crater curve reproduced from Neukum and Hiller (1981). A copy of the standard curve at the same scale as the plots in Appendix 3, included in the original thesis, can be obtained from the author.

Figure 25

ORIGINAL PAGE IS
OF POOR QUALITY



curves due to error in crater selection or measurement were edited and replotted. Anomalous curves with no identifiable cause for their abnormalities (such as strange slope, numerous bumps in the curve, or poor relative age determination) were discarded altogether. All replotted curves were generated using a second version of the 'STAMMER' program set up to run on the Prime computer with CalComp graphics subroutines. All useable counts were eventually replotted using the updated program to create a common format for all counts (Appendix 3).

All counts considered as useable (total of 102) are listed in Table 2, Figure 4a-d, and presented in Appendix 3. A point representing the relative age of each count vs the terrain where the count was performed (e.g. smooth plains, chaotic, etc,) was plotted in Figure 5 in an effort to determine periods of resurfacing and the time of formation of the various units and landforms present. Emphasis was placed on the relative ages determined for the best counts. For specific types of terrain (Ladon Basin, etched, chaotic, etc) the full range of ages derived for the unit have been used to assign the period during which the feature most likely formed. Periods during which resurfacing events occurred were defined by distinct clusters of relative ages (Fig. 5) for counts completed at locations inferred to have been resurfaced, and that could be correlated with geologically distinct units.

Absolute ages were assigned to the units by comparison of their relative ages with the lunar standard crater curve (Neukum and Hiller 1981). The lunar curve is probably a reasonable estimate of the crater flux at Mars and was therefore used for the age determinations.

APPENDIX 2

Computer Programs

Used to Derive Logarithmic

Cumulative Crater Size-Frequency Plots

Two versions of the same program called 'STAMMER', were used to derive cumulative crater size-frequency plots for each crater count location. Each version is presented in the following pages. Both programs are written in Fortran 77 and both create data files containing all calculations performed during execution that allow for later examination. The first version was written by Brian Fessler at the Lunar and Planetary Institute, Houston, TX. USA. It is designed to run on a Digital Vax 11/780 mainframe computer. Graphics for this version were written using DEC ReGIS (Remote Graphics Instruction set) graphics subroutines. Output was reviewed on a Digital VT125 Graphics terminal and hardcopies were obtained from a Digital Letterwriter 100 printer. Initial plots and edits were obtained at the Lunar and Planetary Institute in January 1985.

The second version of the 'STAMMER' program, listed after the first in the following pages, was a modification of the original that allowed the program to operate on the Prime/850 computer at the University of Rhode Island. Modifications were almost entirely within the graphics section of the program, the actual calculation part of the text was unaltered. The new version used Primos/Rev.19.3 Calcomp graphic subroutines to obtain hardcopies of the plots on a Calcomp 1051 printer. Source changes were completed by Dan Halloway at the URI Academic Computer Center and by the author. All final edits of the program and final copies of each log cumulative crater size-frequency plots are shown in Appendix 3.

PRECEDING PAGE BLANK NOT FILMED

```

C      ORIGINAL VERSION OF PROGRAM STAMMER
C      FOR CALCULATION OF CUMULATIVE CRATER
C      SIZE-FREQUENCY PLOTS
C      WRITTEN BY BRIAN FESSLER
C      AT THE LUNAR AND PLANETARY INSTITUTE
C      HOUSTON, TX, USA

```

PROGRAM STAMMER

```

REAL    DIAM(1000),DIAMCUM(1000),DIAMNUM(1000),NEWD,OLDD
REAL    FACTOR,AREA,CUMPER1D6(1000),CONFID(2,1000),Y(2)
REAL    MAXDIAM
REAL    LENGTH1,LENGTH2,LENGTH(200),MM,KM
CHARACTER INFILE*40,OUTFILE*40,TITLE*40

      WRITE(6,*) 'ENTER INPUT FILENAME:'
      READ(5,5) INFILE
5      FORMAT(A)

C      OPEN(UNIT=1,FILE=INFILE,STATUS='OLD',READONLY)

      WRITE(6,*) ' '
      WRITE(6,*) 'ENTER OUTPUT FILENAME:'
      READ(5,5) OUTFILE
C      OPEN(UNIT=2,FILE=OUTFILE,STATUS='NEW')

C      WRITE(6,*) ' '
C      WRITE(6,*) 'ENTER TITLE FOR GRAPH:'
C      READ(5,5) TITLE

      MAXDIAM=100.0

      READ(1,6) MM,KM      /* READ MAP SCALE (mm:km)
6      FORMAT(F2.0,1X,F)
      CONST=KM/MM

      CALL GETVALUE(AREA1,*99) /* GET AREA ESTIMATES AND AVERAGE
      CALL GETVALUE(AREA2,*99)
      AREA=((AREA1+AREA2)/2.0)*CONST**2

      N=0
7      CALL GETVALUE(LENGTH1,*8) /* GET LENGTH ESTIMATES AND AVERAGE
      CALL GETVALUE(LENGTH2,*99)
      N=N+1
      LENGTH(N)=((LENGTH1+LENGTH2)/2.0)*CONST
      GOTO 7

8      CALL SORT(LENGTH,N) /* SORT LENGTHS INTO DESCENDING ORDER

10     DO I=1,N             /* DETERMINE NUMBER OF CRATER DIAMETERS

```

```

NEWD=LENGTH(I)
IF (I.EQ.1) THEN
  OLDD=NEWD
  ICTR=1
  DIAM(ICTR)=NEWD
ENDIF
IF (NEWD.EQ.OLDD) THEN
  DIAMNUM(ICTR)=DIAMNUM(ICTR)+1.0
ELSE
  OLDD=NEWD
  ICTR=ICTR+1
  DIAM(ICTR)=NEWD
  DIAMNUM(ICTR)=1.0
ENDIF
ENDDO

```

```

20  WRITE(2,*) 'DIAMETER    CUMULATIVE FREQUENCY    NO. OF CRATERS'

DO I=1,ICTR                      /* COMPUTE CUMULATIVE FREQUENCY
  IF (I.EQ.1) THEN                /* OF CRATERS
    DIAMCUM(I)=DIAMNUM(I)
  ELSE
    DIAMCUM(I)=DIAMNUM(I)+DIAMCUM(I-1)
  ENDIF
  WRITE(2,*) DIAM(I), '      ', DIAMCUM(I), '      ', DIAMNUM(I)
ENDDO

WRITE(2,*) ' '
WRITE(2,*) 'DIAMETER    CUM.FREQ.*1.E6/AREA    CONFIDENCE INTERVAL'

```

```

FACTOR=1.0D6/AREA

```

```

DO I=1,ICTR                      /* COMPUTE CUMULATIVE FREQUENCY
  CUMPER1D6(I)=FACTOR*DIAMCUM(I) /* OF CRATERS PER 10**6 KM**2
  CONFID(1,I)=FACTOR*(DIAMCUM(I)+SQRT(DIAMCUM(I))) /* COMPUTE CONFID
  CONFID(2,I)=FACTOR*(DIAMCUM(I)-SQRT(DIAMCUM(I))) /* INTERVAL
  IF (CONFID(2,I).EQ.0.0) CONFID(2,I)=1.0
  WRITE(2,*) DIAM(I),CUMPER1D6(I),CONFID(1,I),CONFID(2,I)
ENDDO

```

```

CALL INIT_GRAPHICS()
CALL CLEAR_TEXT
CALL CLEAR_SCREEN
CALL DRAW_GRAPHPPAPER('LOG',5,1,'LOG',5,1,'GRAY3')
CALL LNAXIS('XT',INFILE,,,)
CALL LNAXIS('XB','LOG(DIAMETER (km))',0.001,MAXDIAM,.FALSE.)
CALL LNAXIS('YL','LOG(CUM.#/10**6 km**2)',
*1.0,100000.0,.TRUE.)

```

```

DO I=1,ICTR
  Y(1)=DIAM(I)
  Y(2)=DIAM(I)
  CALL PLOT_POINT(Y(1),CUMPER1D6(I),'L',7)
  CALL PLOT_DATA(2,Y,CONFID(1,I),'L','GRAY3',,1,,)
ENDDO

```

```

80      WRITE(6,*) 'ENTER HARDCOPY OPTION: 1) SMALL, 2)LARGE, 3)NONE'
      READ(5,*) IOPT

      IF (IOPT.EQ.1) THEN
        CALL COPY_VIEWPORT
        GOTO 80
      ELSE IF (IOPT.EQ.2) THEN
        CALL ZOOM(2,2)
        CALL COPY_VIEWPORT
        CALL NOZOOM
        GOTO 80
      ENDIF

      CALL CLEAR_SCREEN
      STOP

99      WRITE(6,*) '***UNEXPECTED END OF DATA***'
      STOP
      END

```

SUBROUTINE GETVALUE(VAL,*)

```

      REAL VAL
      CHARACTER LINE*80,NUM*10

1      READ(1,5,ERR=25,END=35) LINE
5      FORMAT(A)
      NUM(1:6)=LINE(33:38)
      NUM(7:10)=LINE(41:44)
      DECODE(10,15,NUM(1:10),ERR=25) VAL
15     FORMAT(E10.3)
      IF (VAL.EQ.0.0) GOTO 1
      RETURN

25     WRITE(6,*) '***ERROR DURING READ OR DECODE***'
      WRITE(6,*) LINE
      WRITE(6,*) NUM
35     RETURN 1
      END

```

SUBROUTINE SORT(ARRAY,N) /* DESCENDING

```

      REAL ARRAY(200)
      LOGICAL SORTED
      SORTED=.FALSE.

      DO WHILE (.NOT.SORTED)
        SORTED=.TRUE.
        DO I=1,N-1
          IF (ARRAY(I).LT.ARRAY(I+1)) THEN
            SORTED=.FALSE.

```

```
        TEMP=ARRAY(I)
        ARRAY(I)=ARRAY(I+1)
        ARRAY(I+1)=TEMP
    ENDIF
ENDDO
RETURN
END
```

```

C      UPDATED VERSION OF PROGRAM STAMMER
C      FOR CALCULATION OF CUMULATIVE CRATER
C      SIZE-FREQUENCY PLOTS
C      CHANGED TO OPERATE ON
C      THE PRIME/850 COMPUTER WITH
C      CALCOMP GRAPHICS SUBROUTINES
C      CHANGES IMPLEMENTED BY
C      DAN HALLOWAY AND JOHN GRANT

```

PROGRAM STAMMER

```

REAL    DIAM(1002),DIAMCUM(1000),DIAMNUM(1000),NEWD,OLDD
REAL    FACT,AREA,CUMPER(1002)
REAL    CONFID1(1000),CONFID2(1000)
REAL    MAXDIAM,XARRY(1002),BLOG(10)
REAL    LENGTH1,LENGTH2,LENGTH(200),MM,KM
CHARACTER INFILE*40,OUTFILE*40,PLOTFILE*40
CHARACTER*1 TEXT1(24),TEXT2(24),TEXT3(24)

      WRITE(*,*) 'ENTER INPUT FILENAME:'
      READ(*,5) INFILE
5      FORMAT(A)

      OPEN(UNIT=101,FILE=INFILE,STATUS='OLD')

      WRITE(*,*) ' '
      WRITE(*,*) 'ENTER OUTPUT FILENAME:'
      READ(*,5) OUTFILE

      OPEN(UNIT=102,FILE=OUTFILE,STATUS='NEW')

      WRITE(*,*) ' '
      WRITE(*,*) 'ENTER PLOTFILE FILENAME:'
      READ(*,5) PLOTFILE

      MAXDIAM=100.0
      DIAMNUM(1)=0.0
      DIAMCUM(1)=0.0

      READ(101,6) MM,KM      /* Read map scale (mm:km)
6      FORMAT(F3.0,1X,F6.3)
      CONST=KM/MM

      CALL GETVALUE(AREA1,*99) /* Get area estimates and average
      CALL GETVALUE(AREA2,*99)
      AREA=((AREA1+AREA2)/2.0)*CONST**2

      N=0
7      CALL GETVALUE(LENGTH1,*8) /* Get length estimates and average
      CALL GETVALUE(LENGTH2,*99)

```

```

N=N+1
LENGTH(N)=((LENGTH1+LENGTH2)/2.0)*CONST
GOTO 7

8      CALL SORT(LENGTH,N)      /* Sort lengths into descending order

10     DO 991 I=1,N              /* Determine number of crater diameters

        NEWD=LENGTH(I)

        IF (I.EQ.1) THEN
            OLDD=NEWD
            ICTR=1
            DIAM(ICTR)=NEWD
        ENDIF

        IF (NEWD.EQ.OLDD) THEN
            DIAMNUM(ICTR)=DIAMNUM(ICTR)+1.0
        ELSE
            OLDD=NEWD
            ICTR=ICTR+1
            DIAM(ICTR)=NEWD
            DIAMNUM(ICTR)= 1.0
        ENDIF
991    CONTINUE

20     WRITE(102,*) 'DIAMETER    CUMULATIVE FREQUENCY    NO. OF CRATERS'

        DO 992 I=1,ICTR          /* Compute cumulative frequency
            IF (I.EQ.1) THEN      /* of craters
                DIAMCUM(I)=DIAMNUM(I)
            ELSE
                DIAMCUM(I)=DIAMNUM(I)+DIAMCUM(I-1)
            ENDIF
            WRITE(102,*) DIAM(I),'    ',DIAMCUM(I),'    ',DIAMNUM(I)
992    CONTINUE

        WRITE(102,*) ' '
        WRITE(102,*) 'DIAMETER    CUM.FREQ.*1.E6/AREA    CONFIDENCE INTERVAL'

        FACT=1.0D6/AREA

        DO 993 I=1,ICTR          /* Compute Cumulative frequency
            CUMPER(I)=FACT*DIAMCUM(I)
            CONFID1(I) = FACT*(DIAMCUM(I)+SQRT(DIAMCUM(I)))
            CONFID2(I) = FACT*(DIAMCUM(I)-SQRT(DIAMCUM(I)))
            IF (CONFID2(I).EQ.0.0) CONFID2(I)=1.0

C      Output Diameter, Cumulative frequency and Confidence intervals

        WRITE(102,*) DIAM(I),CUMPER(I),CONFID1(I),CONFID2(I)
993    CONTINUE

C
C      Minimum values stored into data arrays at ICTR+1 locations.

```



```

C      Used to insure constant scaling when using packaged SCALG routines.
C      ICTR then incremented to accommodate extra elements.
C      Added minimum data point will NOT be plotted.
C
      CUMPER(ICTR+1) = 100.00
      DIAM(ICTR+1) = 0.10
      ICTR = ICTR + 1

C
C
C      Source changes to operate on PRIME/850--PRIMOS/REV.19.3
C      Calcomp graphic subroutine calls to create log. plot
C
C      Open plotfile for output

      CALL OPEN(120,PLOTFILE,20,'OUTPUT')
      CALL PLOTS(0,0,120)

C      Call Automatic Scaling Routines

      CALL SCALG(CUMPER,6.0,ICTR,1)
      CALL SCALG(DIAM,6.0,ICTR,1)
      CALL NEWPEN(3)

C      Draw and Annotate X-Axis

      CALL LGAXS(0.0,0.0,' ',-1,6.0,+0.0,DIAM(ICTR+1),0.5)
      CALL CENTER(STX,.14,';LOG DIAMETER #KM',17,6.0)
      CALL CHARS(STX,-0.50,.14,';LOG DIAMETER #KM',0.0,17)

C
C      Draw and Annotate Y-Axis

      CALL LGAXS(0.0,0.0,' ',1,6.0,90.0,CUMPER(ICTR+1),0.5)
      CALL CENTER(STX,.14,';LOG CUM. ># C;/10^6 #KM;"2',27,6.0)
      CALL CHARS(-0.40,STX,.14,';LOG CUM. ># C;/10^6 #KM;"2',90.0,27)

C
C      Complete a Box with X and Y Axis
C

      CALL PLOT(0.0,6.0,3)
      CALL PLOT(6.0,6.0,2)
      CALL PLOT(6.0,0.0,2)

C
C      Draw Grid on Log. Axis
C

      CALL NEWPEN(1)
      ETO10 = 0.4342945
      DO 11 I=1,9
11      BLOG(I) = ALOG(FLOAT(I))*ETO10

      FXMN = INT( ETO10 * ALOG(CUMPER(ICTR+1))+100.0001)-100
      BLMN = (ETO10 * ALOG(CUMPER(ICTR+1))-FXMN)/.5-.0001
      FJ = 0.0

```

```

X = 0.0
DO 13 J = 1,3
  DO 12 I = 1,9
    Y = (BLOG(I)+FJ)/0.5
    IF (( Y .GT. 4.9 ) .AND. ( Y .LE. 5.9 )) THEN
      CALL PLOT(X,Y,3)
      CALL PLOT(X+2.75,Y,2)
      CALL PLOT(5.9,Y,3)
      CALL PLOT(6.0,Y,2)
    ELSE
      CALL PLOT(X,Y,3)
      CALL PLOT(X+6.0,Y,2)
    ENDIF
12    CONTINUE
    FJ = FJ + 1.0
13  CONTINUE

FJ = 0.0
Y = 0.0
DO 14 J = 1,3
  DO 15 I = 1,9
    X = (BLOG(I)+FJ)/0.5
    IF (( X .GE. 2.75 ) .AND. ( X .LE. 5.9 )) THEN
      CALL PLOT(X,Y,3)
      CALL PLOT(X,Y+4.9,2)
      CALL PLOT(X,5.9,3)
      CALL PLOT(X,6.0,2)
    ELSE
      CALL PLOT(X,Y,3)
      CALL PLOT(X,Y+6.0,2)
    ENDIF
15    CONTINUE
    FJ = FJ + 1.0
14  CONTINUE

C
C   Annotate Graph in Upper-right corner
C
C   Draw a Box to enclose the annotation
C
      CALL NEWPEN(3)
      CALL PLOT(2.75,5.9,3)
      CALL PLOT(2.75,4.9,2)
      CALL PLOT(5.9,4.9,2)
      CALL PLOT(5.9,5.9,2)
      CALL PLOT(2.75,5.9,2)
C
C   Prompt User for Annotation Information
C
      WRITE(*,102)
102    FORMAT(' ', ' Enter First-Text Array')
      READ(*,104)(TEXT1(I),I=1,24)
104    FORMAT(24A1)

```

```

        WRITE(*,103)
103    FORMAT(' ',' Enter Number of Chars in Text Array')
        READ(*,*)N

        CALL CHARS(3.0,5.60,.15,TEXT1,0.0,N)
C
C    Prompt User for Second Line of annotation
C
        WRITE(*,105)
105    FORMAT(' ',' Enter Second-Text Array')
        READ(*,104)(TEXT2(I),I=1,24)
        WRITE(*,103)
        READ(*,*)N

        CALL CHARS(3.0,5.30,.15,TEXT2,0.0,N)
C
C    Prompt User for Third Line of annotation
C
        WRITE(*,106)
106    FORMAT(' ',' Enter Third-Text Array')
        READ(*,104)(TEXT3(I),I=1,24)
        WRITE(*,103)
        READ(*,*)N

        CALL CHARS(3.0,5.05,.100,TEXT3,0.0,N)
C
C    Plot data points with confidence interval attribute
C
        XMIN = ET010 * ALOG(DIAM(ICTR+1))
        YMIN = ET010 * ALOG(CUMPER(ICTR+1))

        CALL NEWPEN(2)
        DO 88 I = 1,ICTR-1
            CUMPER(I) = ALOG(CUMPER(I))*ET010
            DIAM(I) = ALOG(DIAM(I))*ET010
            XPAGE = (DIAM(I)-XMIN)/0.5
            YPAGE = (CUMPER(I)-YMIN)/0.5
C
C    Plot symbols at data points
C
        CALL SYMBOL( XPAGE, YPAGE, 0.100, 1, 0.0, -1 )
C
C    Plot line representing confidence-interval
C
        YNEW = ((ET010*ALOG(CONFID1(I)))-YMIN)/0.5
        CALL PLOT( XPAGE, YNEW, 3 )
        YNEW = ((ET010*ALOG(CONFID2(I)))-YMIN)/0.5
        IF( YNEW .LT. 0 ) YNEW = 0.0
        CALL PLOT( XPAGE, YNEW, 2 )
C
88    CONTINUE
C    Close plotfile

```

```

        CALL PLOT(0.0,0.0,999)
        CALL CLOSE(120)

C      Close Data and Output files

        CLOSE(UNIT=101)
        CLOSE(UNIT=102)
        STOP

C
C      Abnormal termination error message
C

99      WRITE(*,*) '***UNEXPECTED END OF DATA***'
        STOP
        END

SUBROUTINE GETVALUE(VAL,*)

    REAL VAL
    CHARACTER LINE*80,NUM*10

1      READ(101,5,ERR=25,END=35) LINE
5      FORMAT(A)
        NUM(1:6)=LINE(33:38)
        NUM(7:10)=LINE(41:44)
        DECODE(10,15,NUM(1:10),ERR=25) VAL
15     FORMAT(E10.3)
        IF (VAL.EQ.0.0) GOTO 1
        RETURN

25     WRITE(*,*) '***ERROR DURING READ OR DECODE***'
        WRITE(*,*) LINE
        WRITE(*,*) NUM
35     RETURN 1
        END

SUBROUTINE SORT(ARRAY,N) /* Descending

    REAL ARRAY(200)
    LOGICAL SORTED
    SORTED=.FALSE.

97     IF (.NOT.SORTED) THEN
        SORTED=.TRUE.
        DO 991 I=1,N-1
            IF (ARRAY(I).LT.ARRAY(I+1)) THEN
                SORTED=.FALSE.
                TEMP=ARRAY(I)
                ARRAY(I)=ARRAY(I+1)
                ARRAY(I+1)=TEMP
            
```

```
991      ENDIF  
          CONTINUE  
          GO TO 97  
      ENDIF  
      RETURN  
      END
```

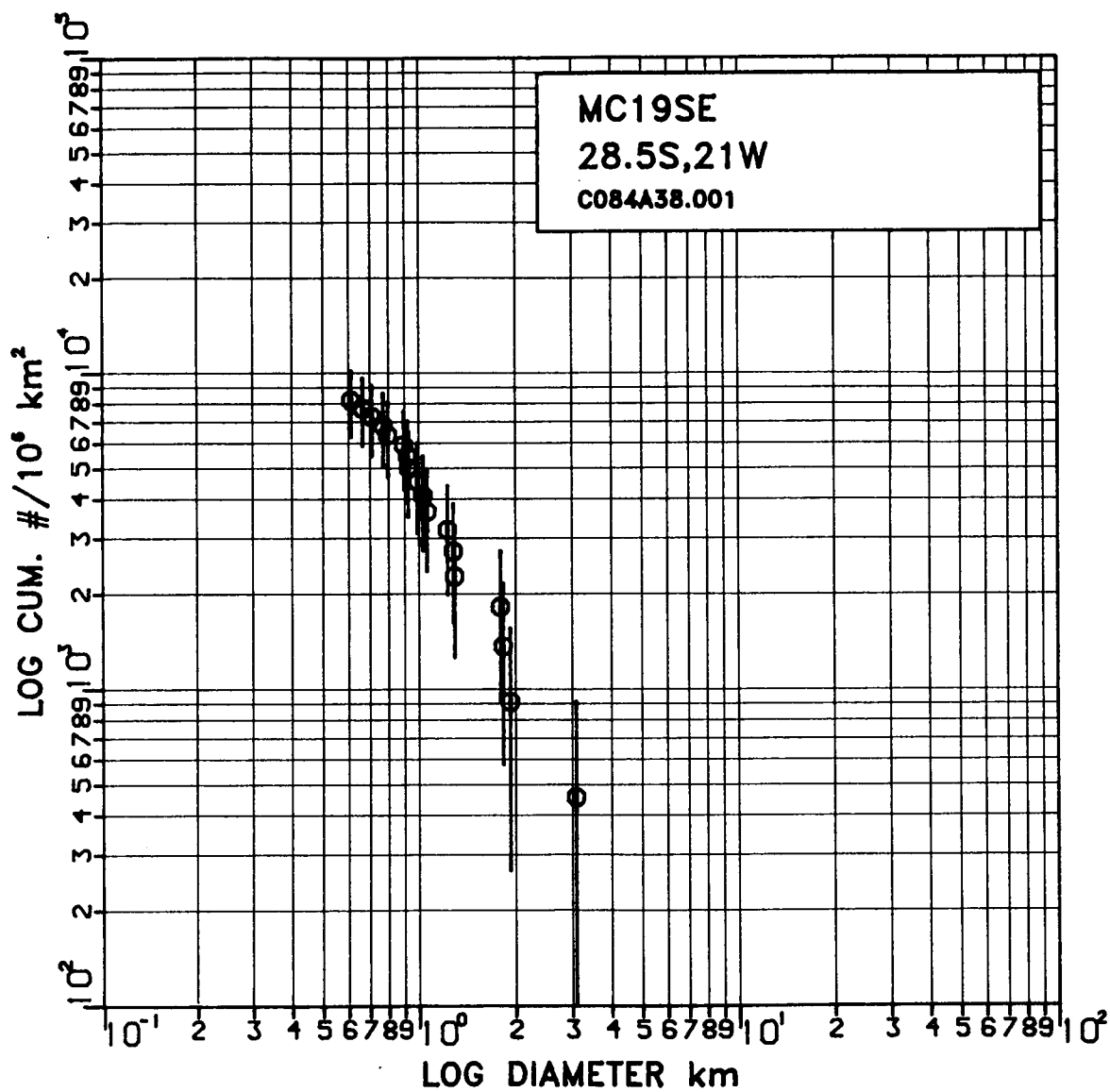
APPENDIX 3

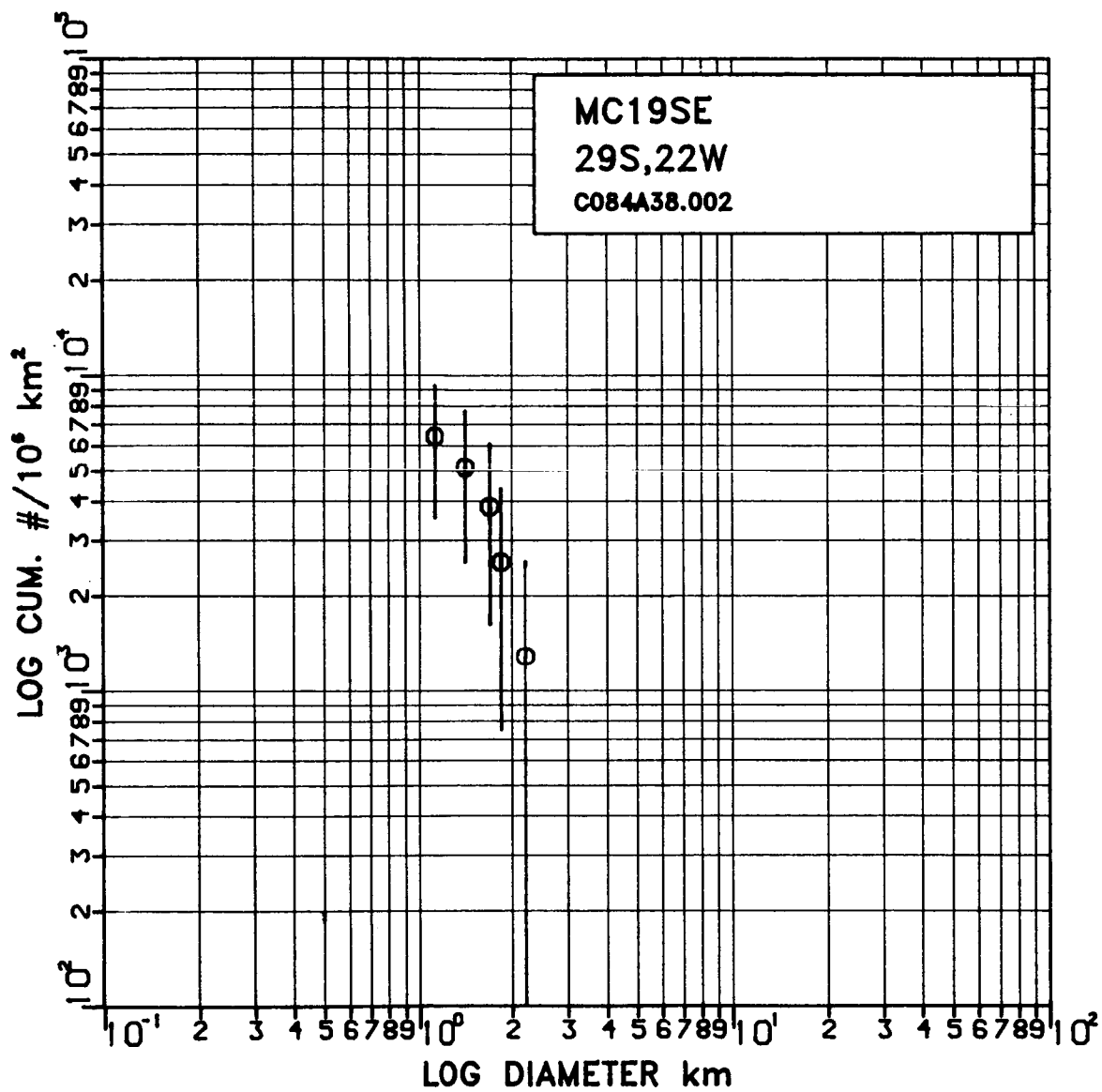
Crater Counts:

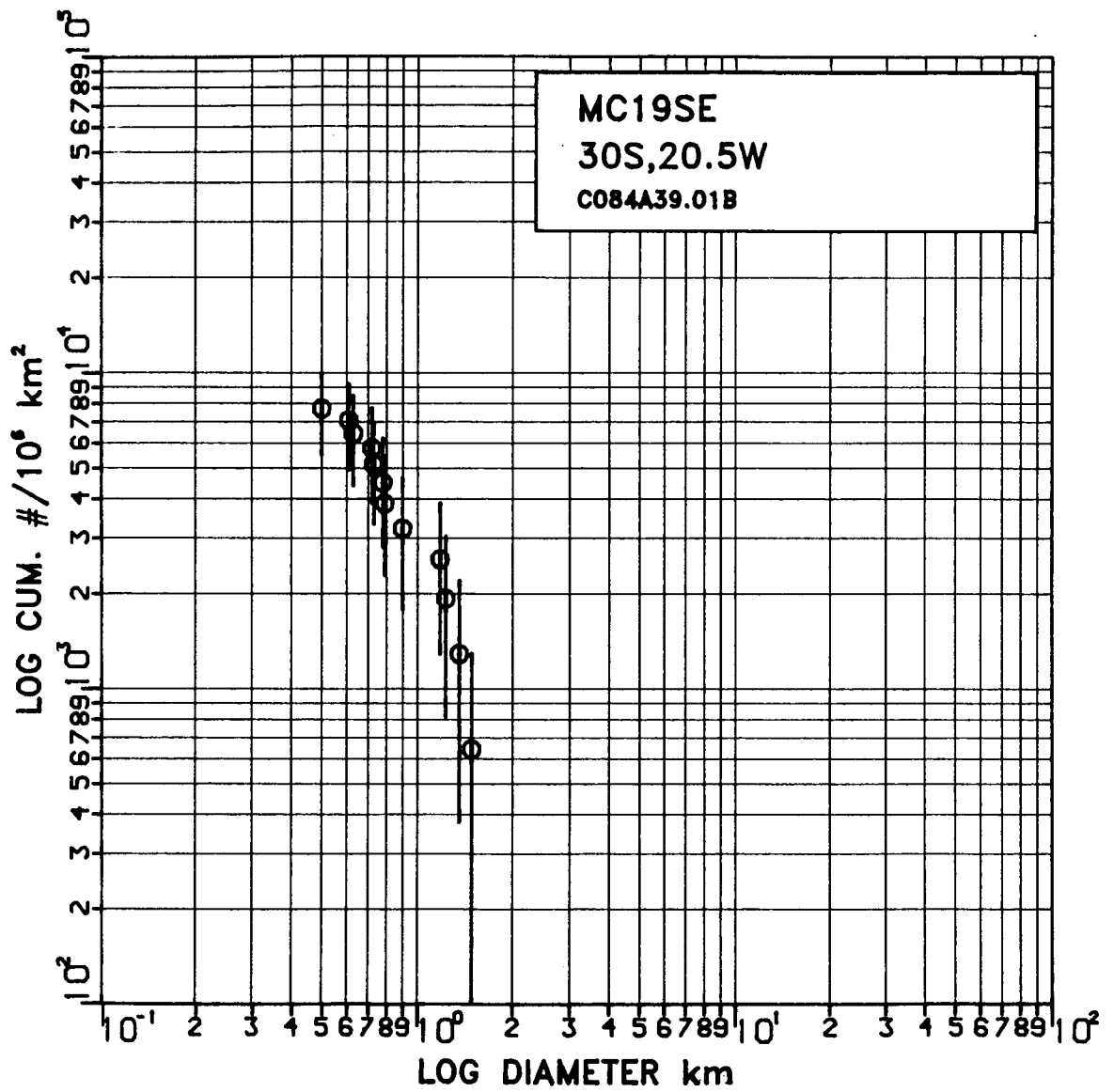
Logarithmic Cumulative Crater Size-Frequency Plots

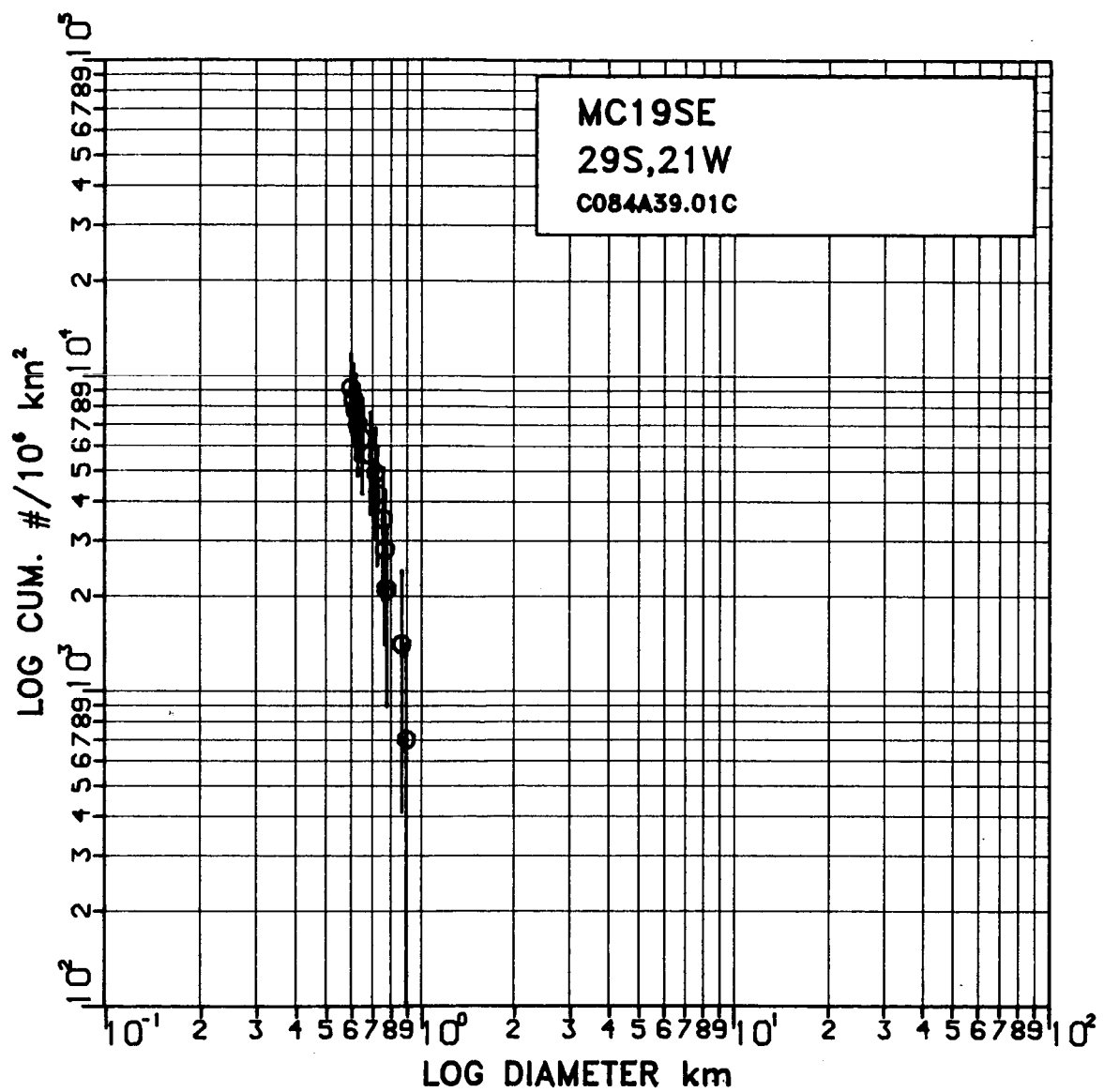
Each count is labelled in the top right hand corner of the plot. The first line of annotation refers to the quarter of MC19 or MC26 that the count was performed in. The second line describes the specific location of the count (place name) followed by the latitude and longitude of its center. The third line refers to the specific negative used for the count and the count number on the negative (e.g. C084A38.002 refers to count number two on the negative 084A38). Plots with CMC19SEMOS at the beginning of the third line of annotation refer to those counts taken from the 1:1,000,000 photomosaic constructed of MC19SE. The last three characters on the third line of these plots refers to the general size range of craters measured from the 1:1,000,000 photomosaic that were used to create the plot. See Table 2, Figs. 4a-d and the individual plots for the specific location and crater size range of individual counts.

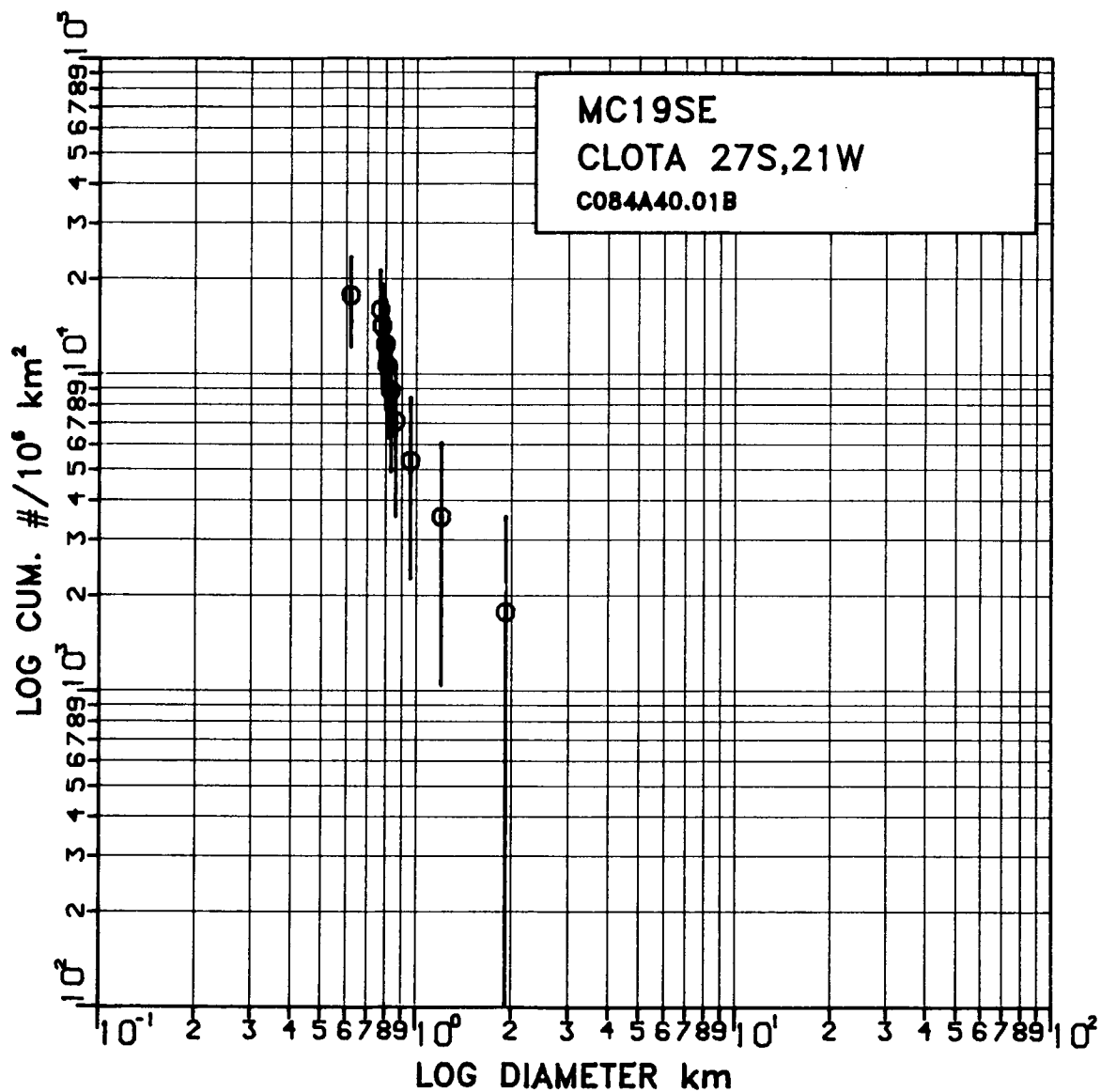
PRECEDING PAGE BLANK NOT FILMED

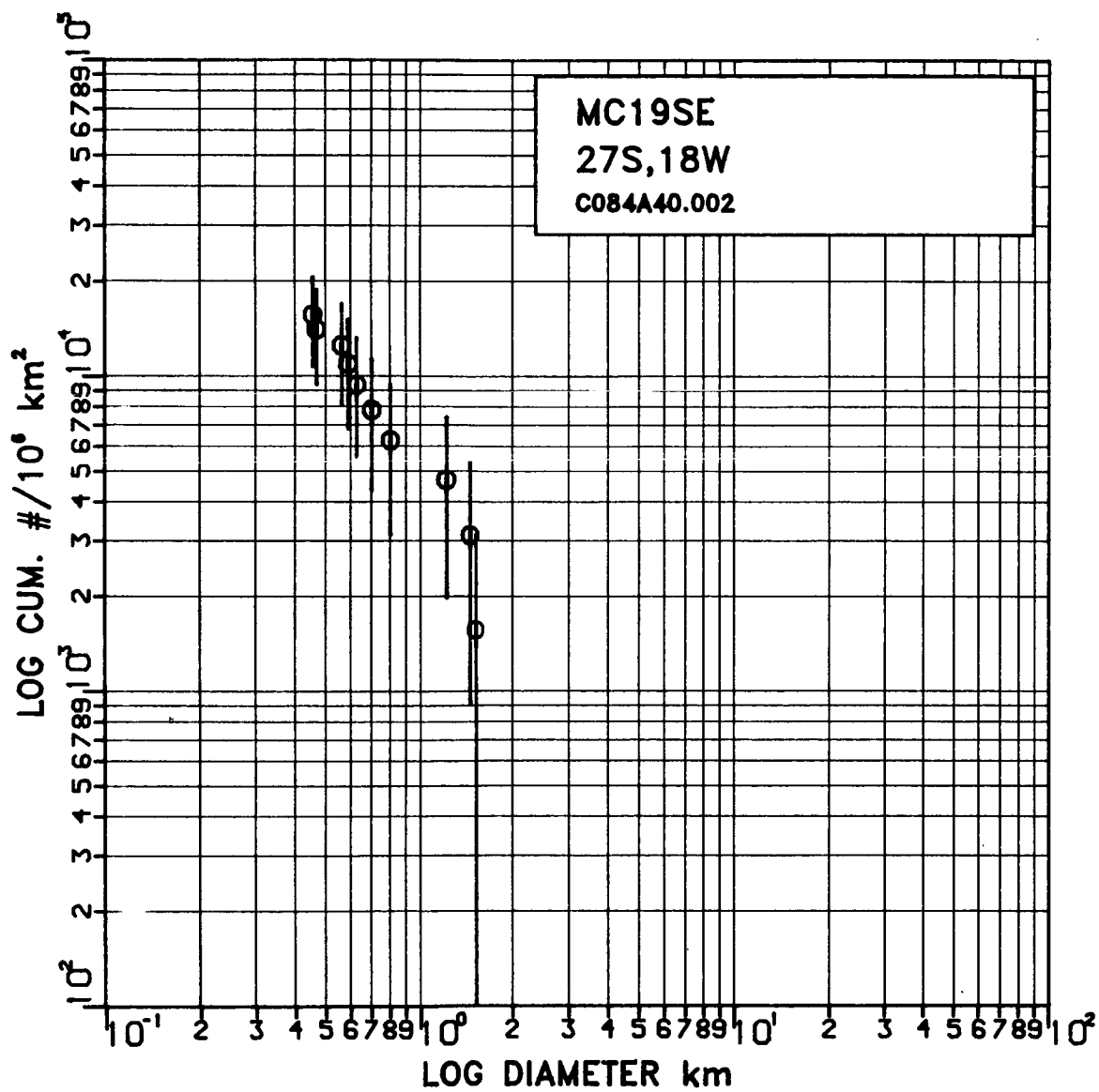


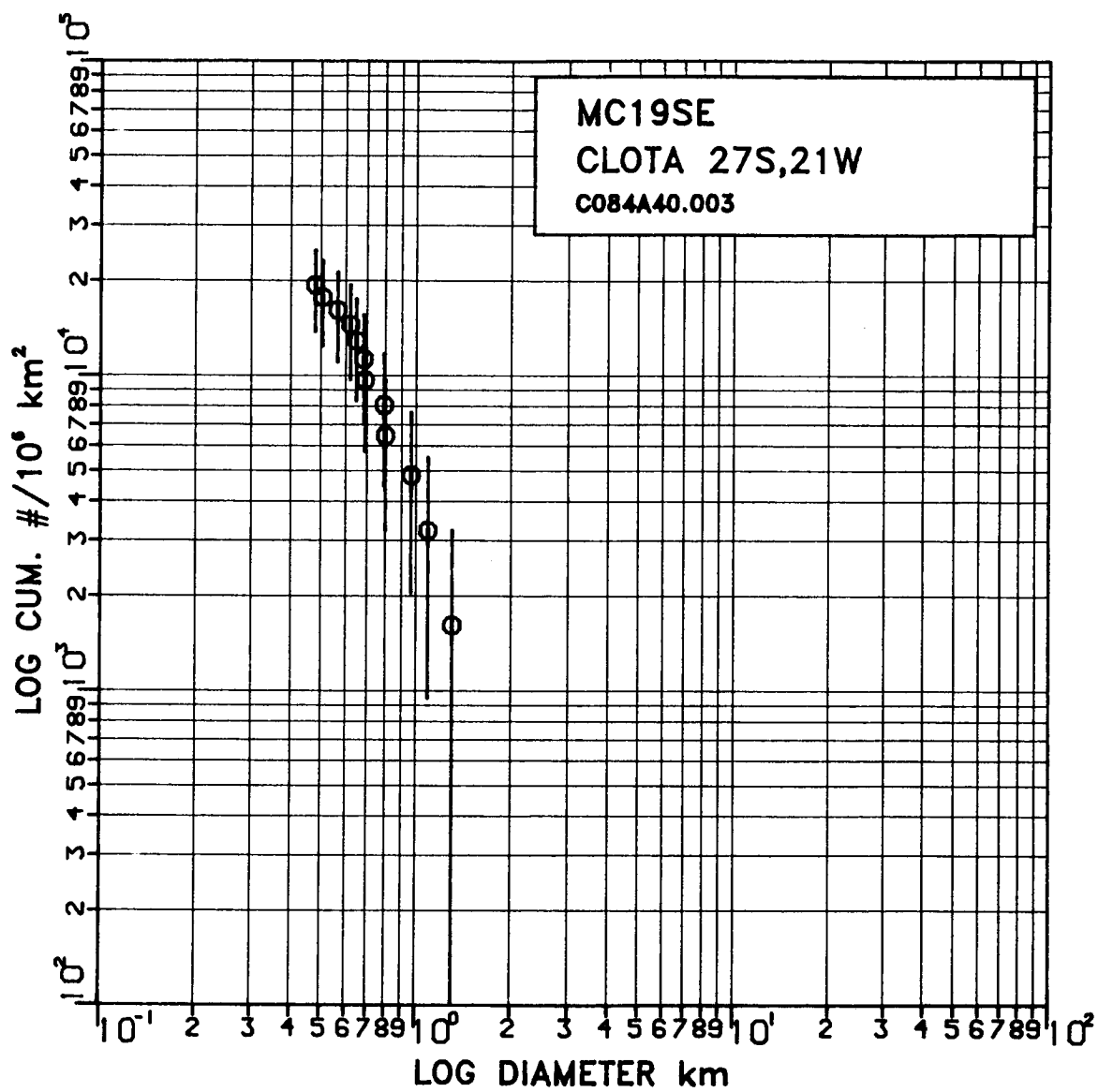


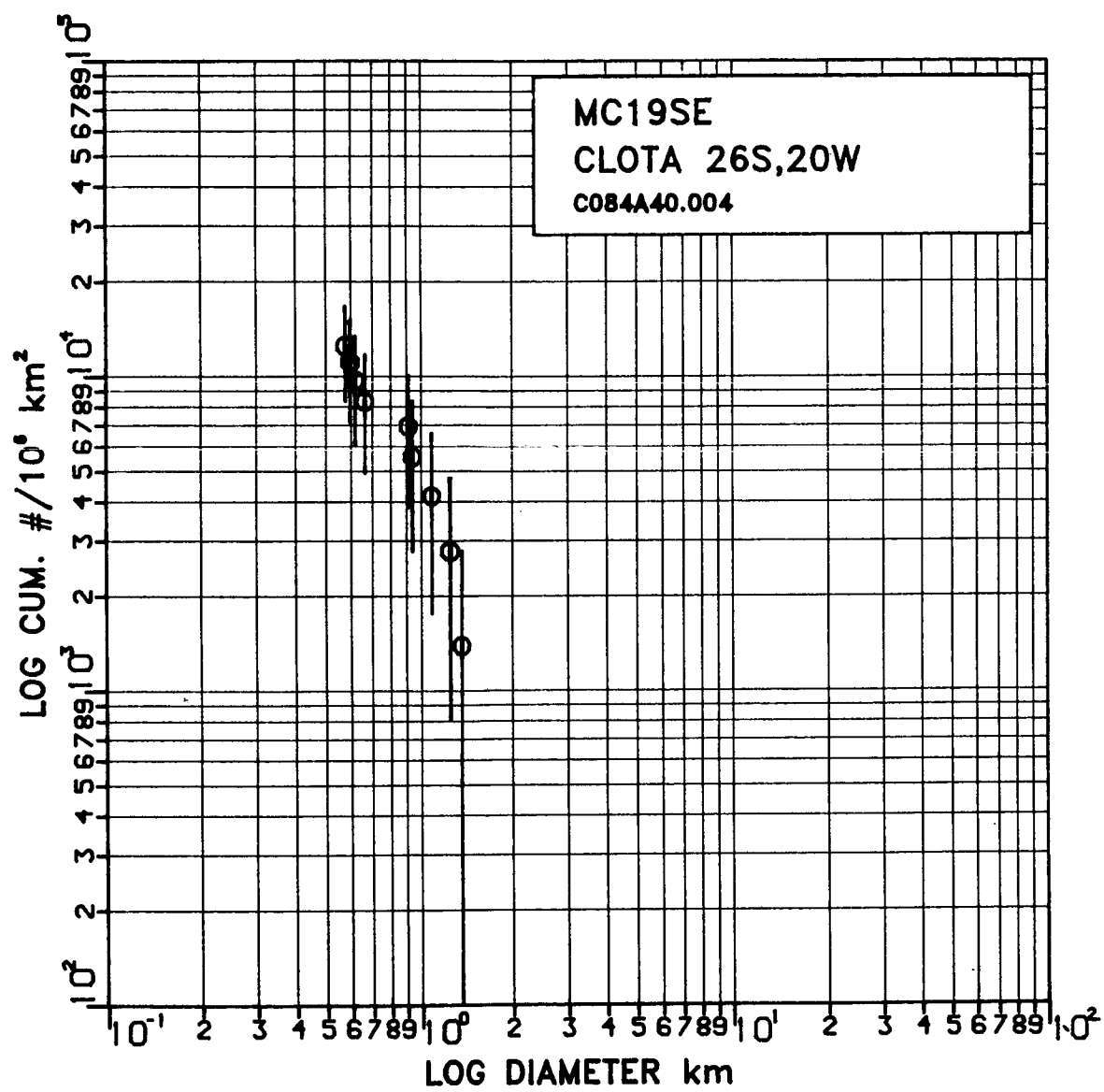


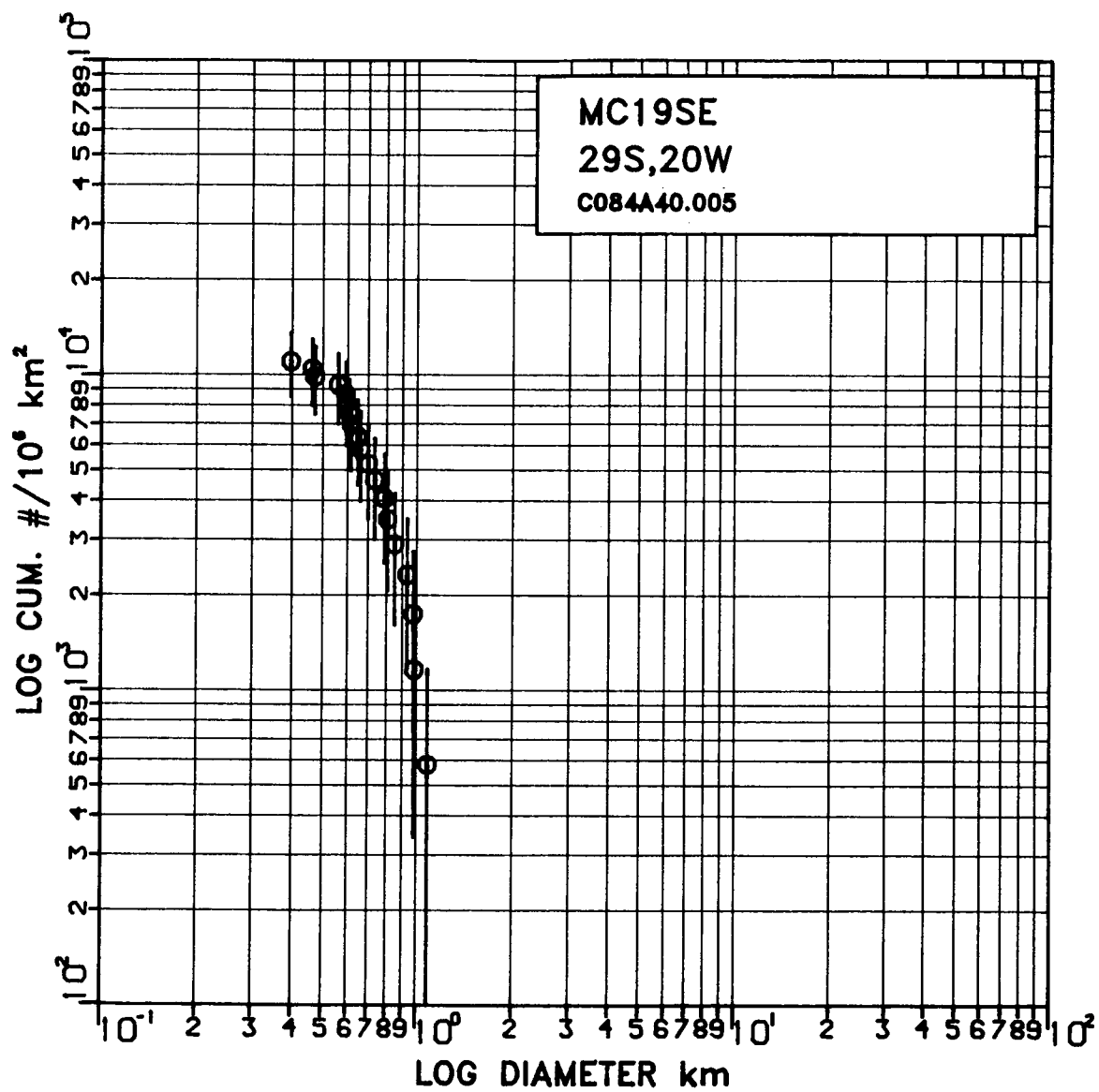


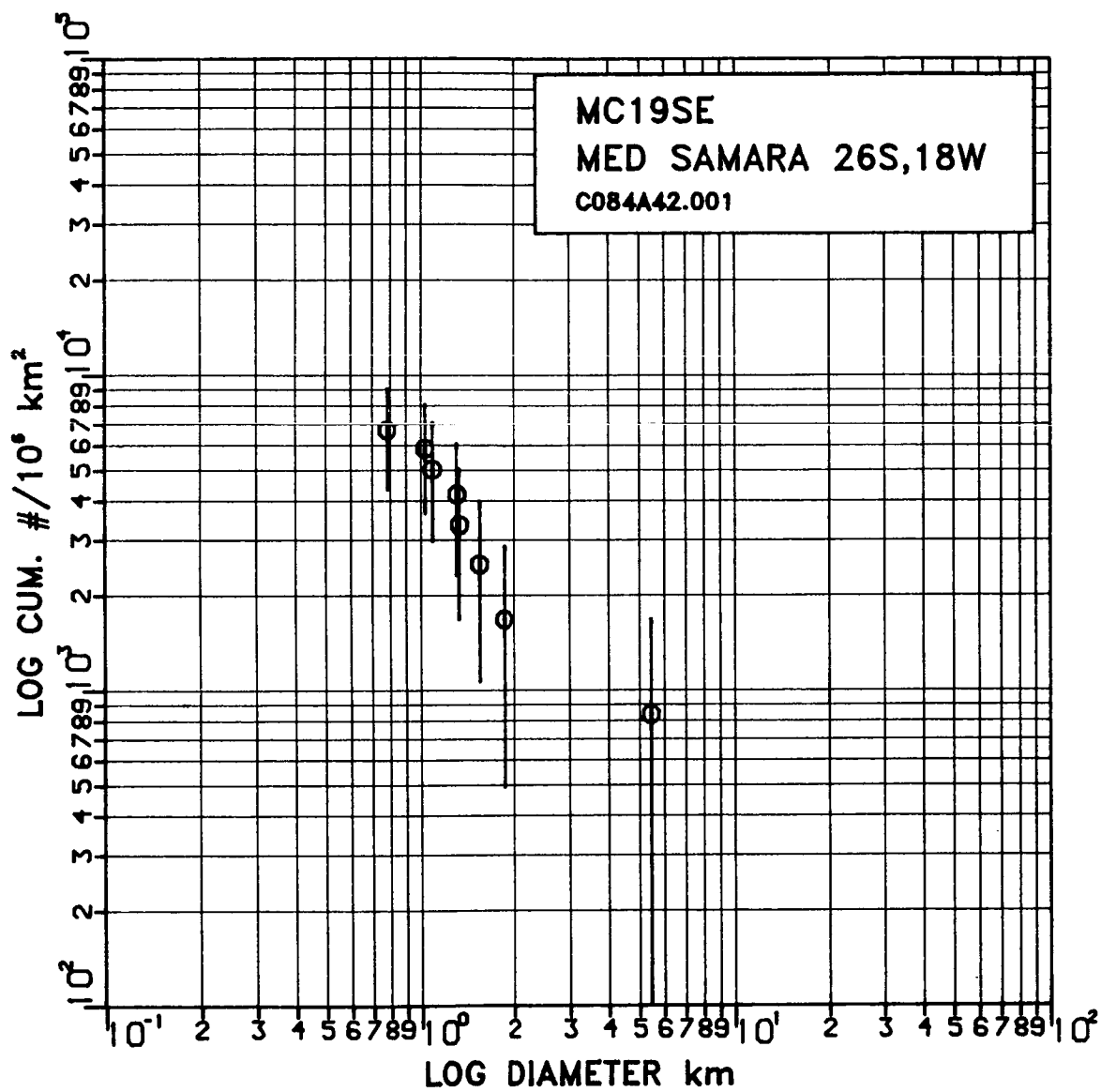


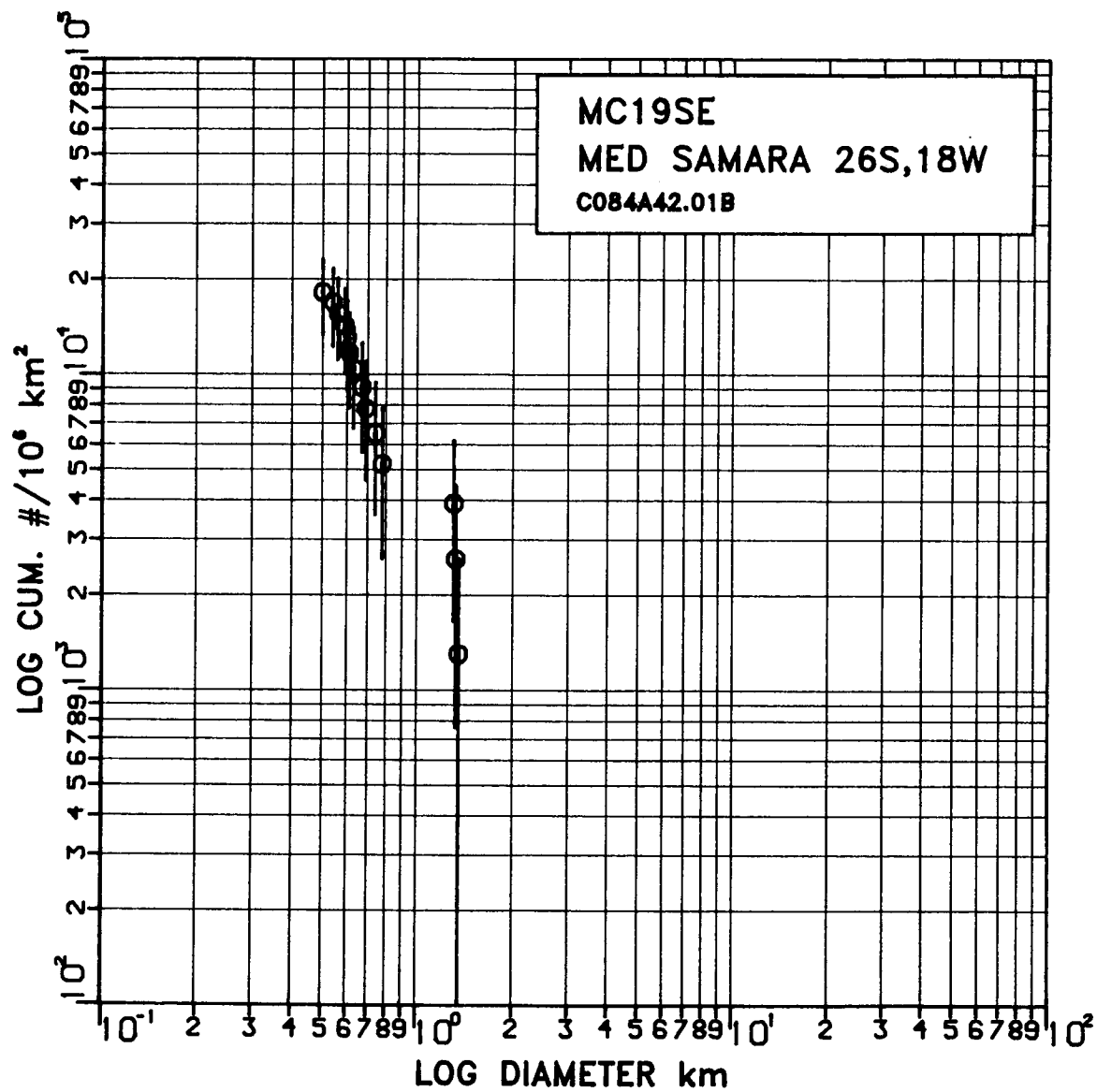


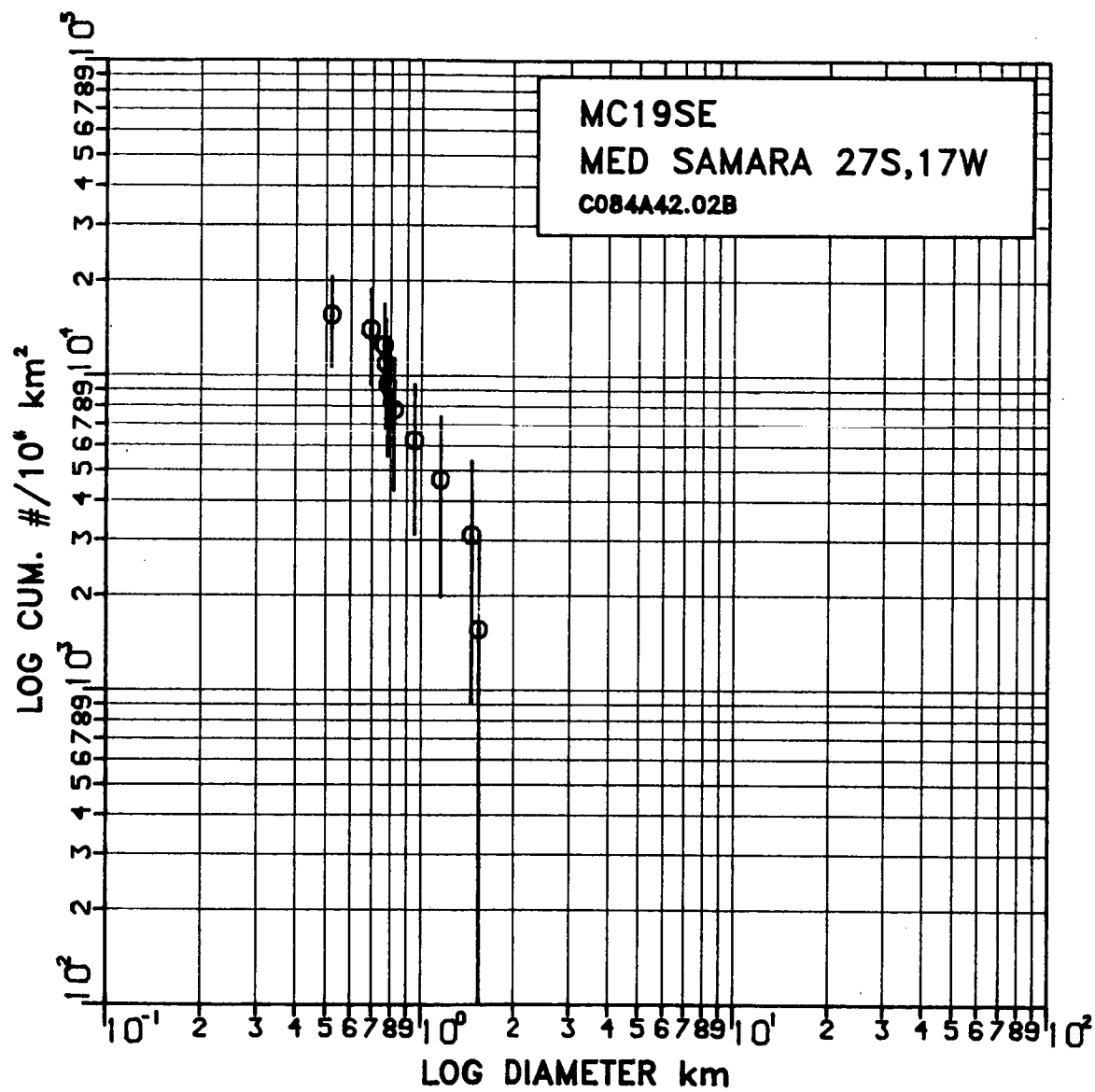


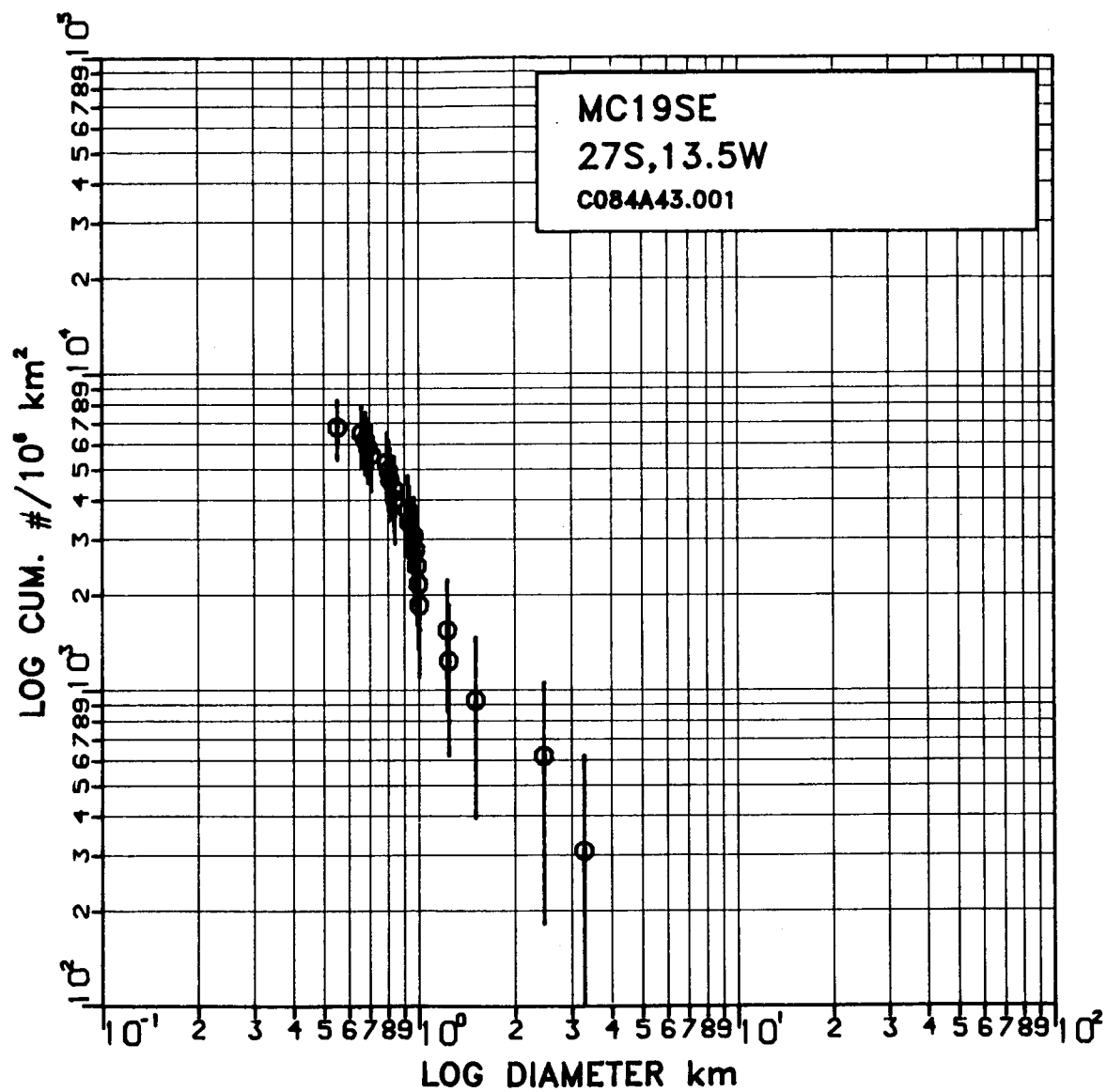


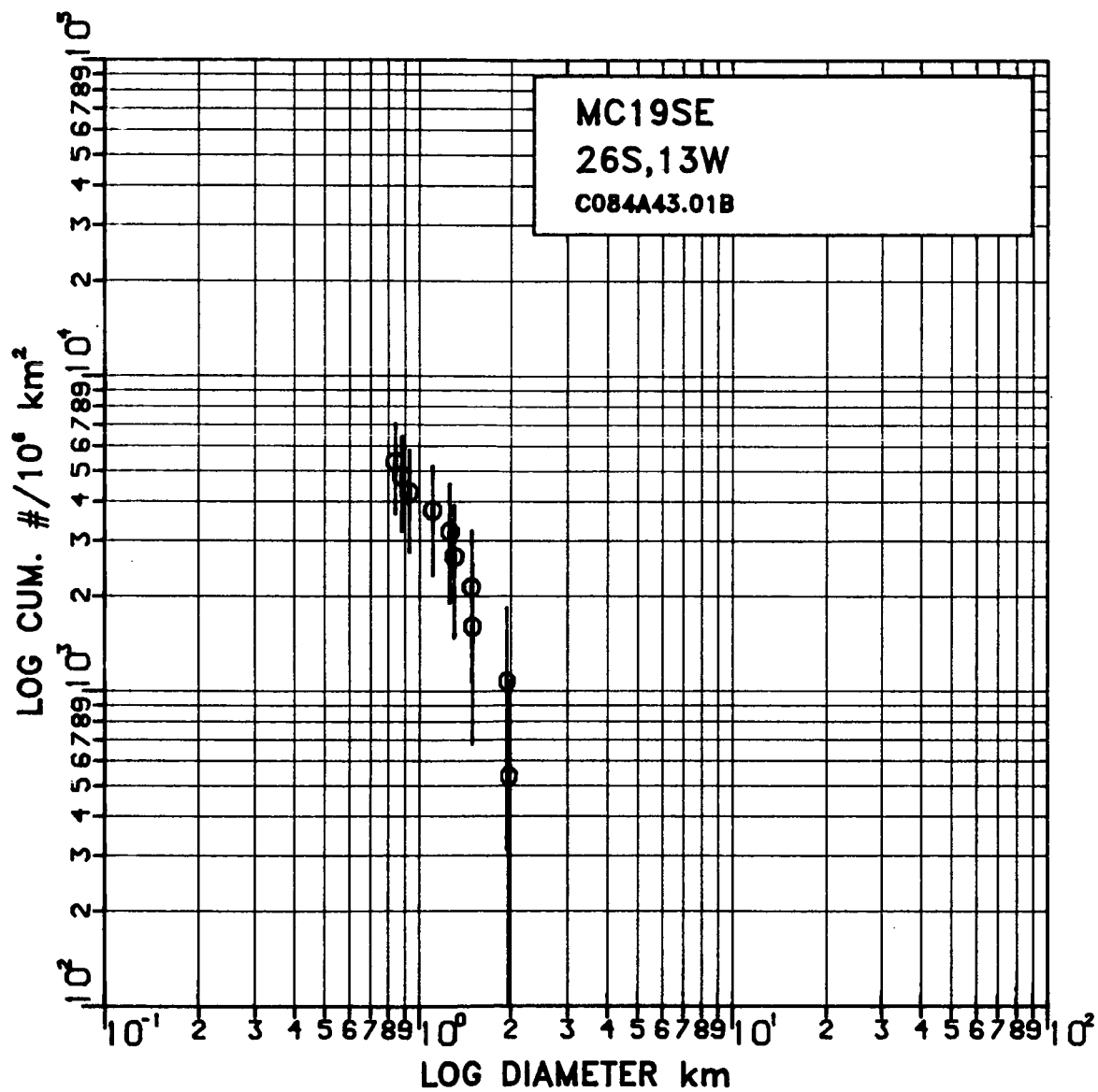


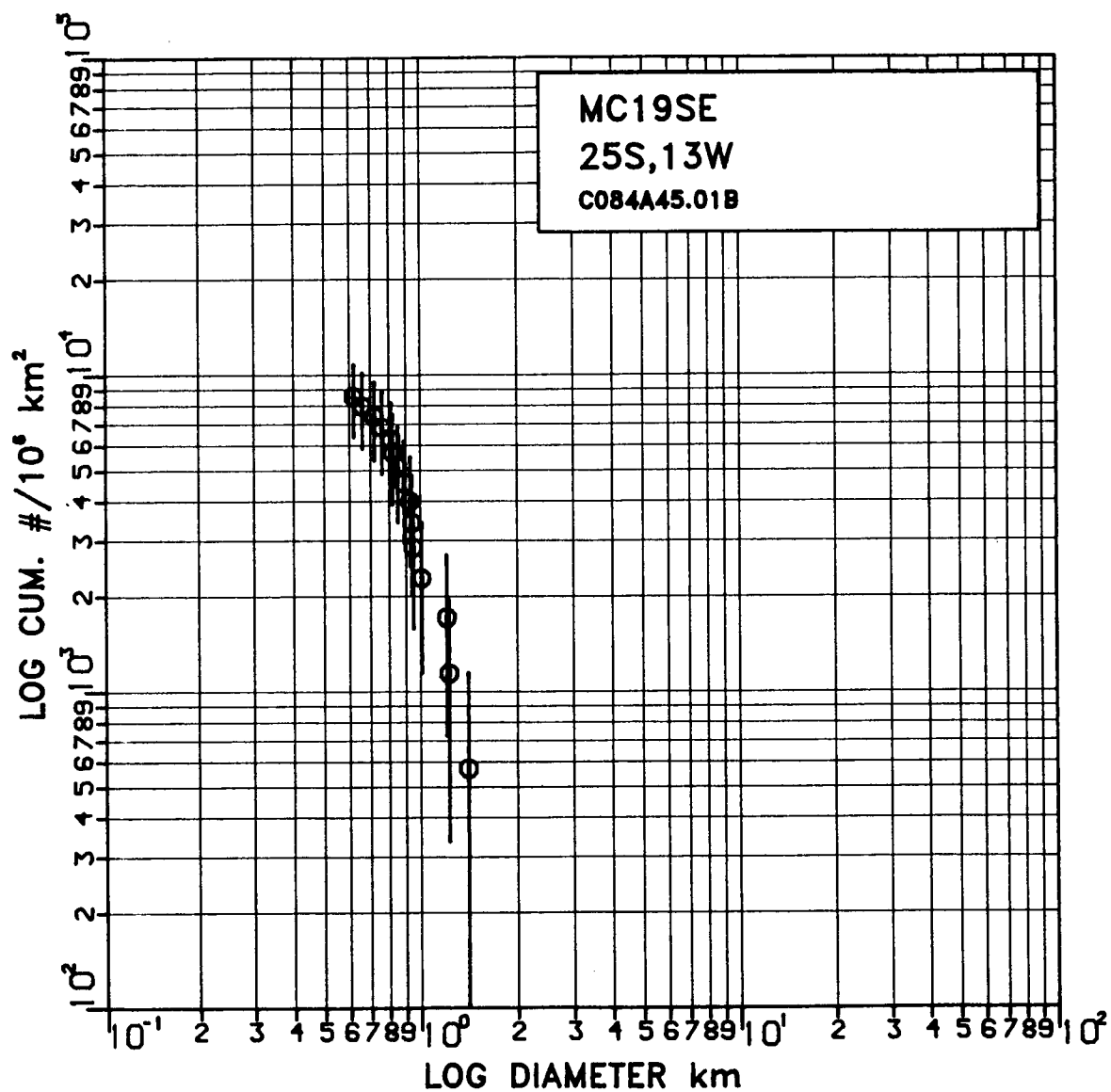


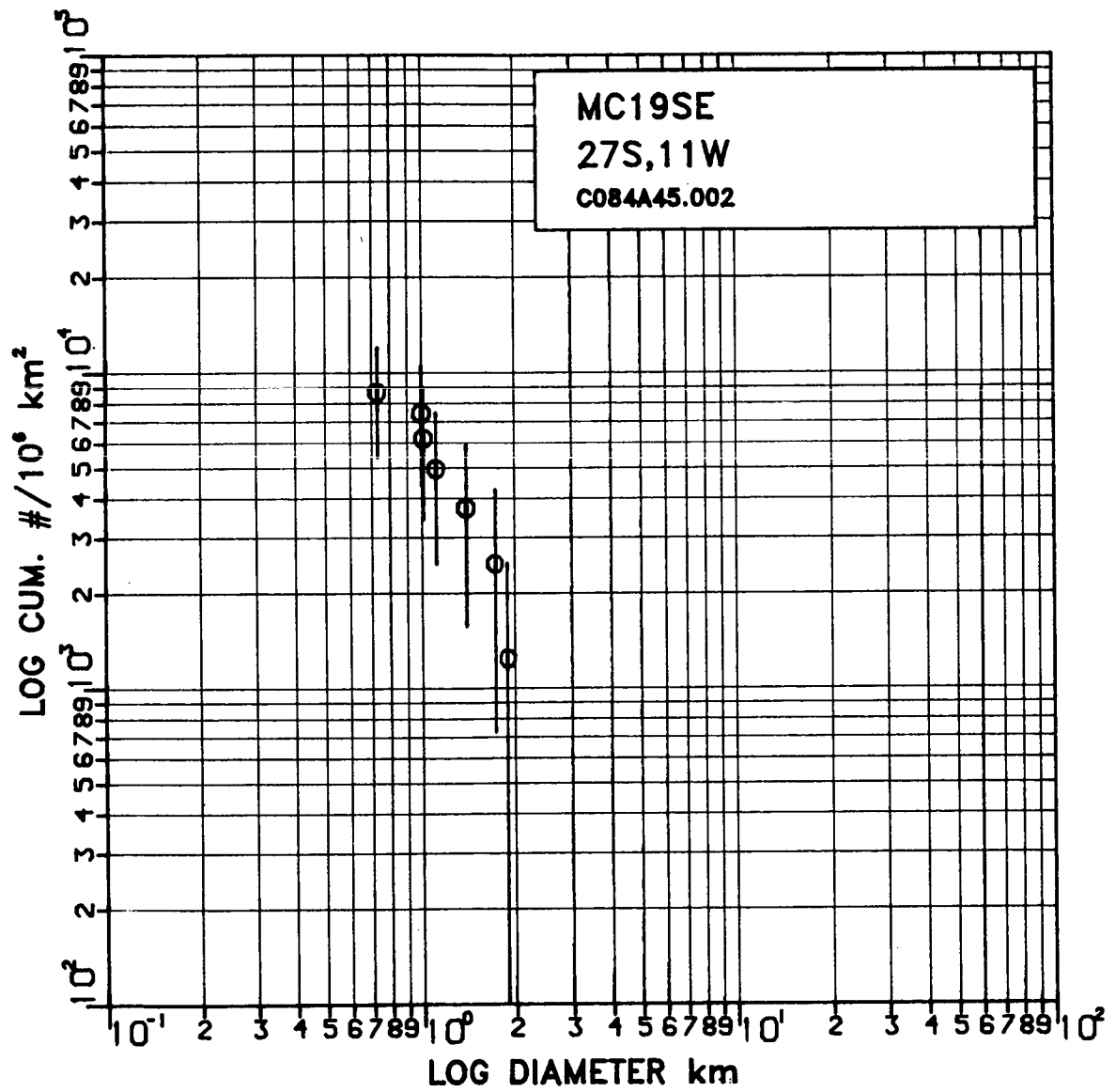


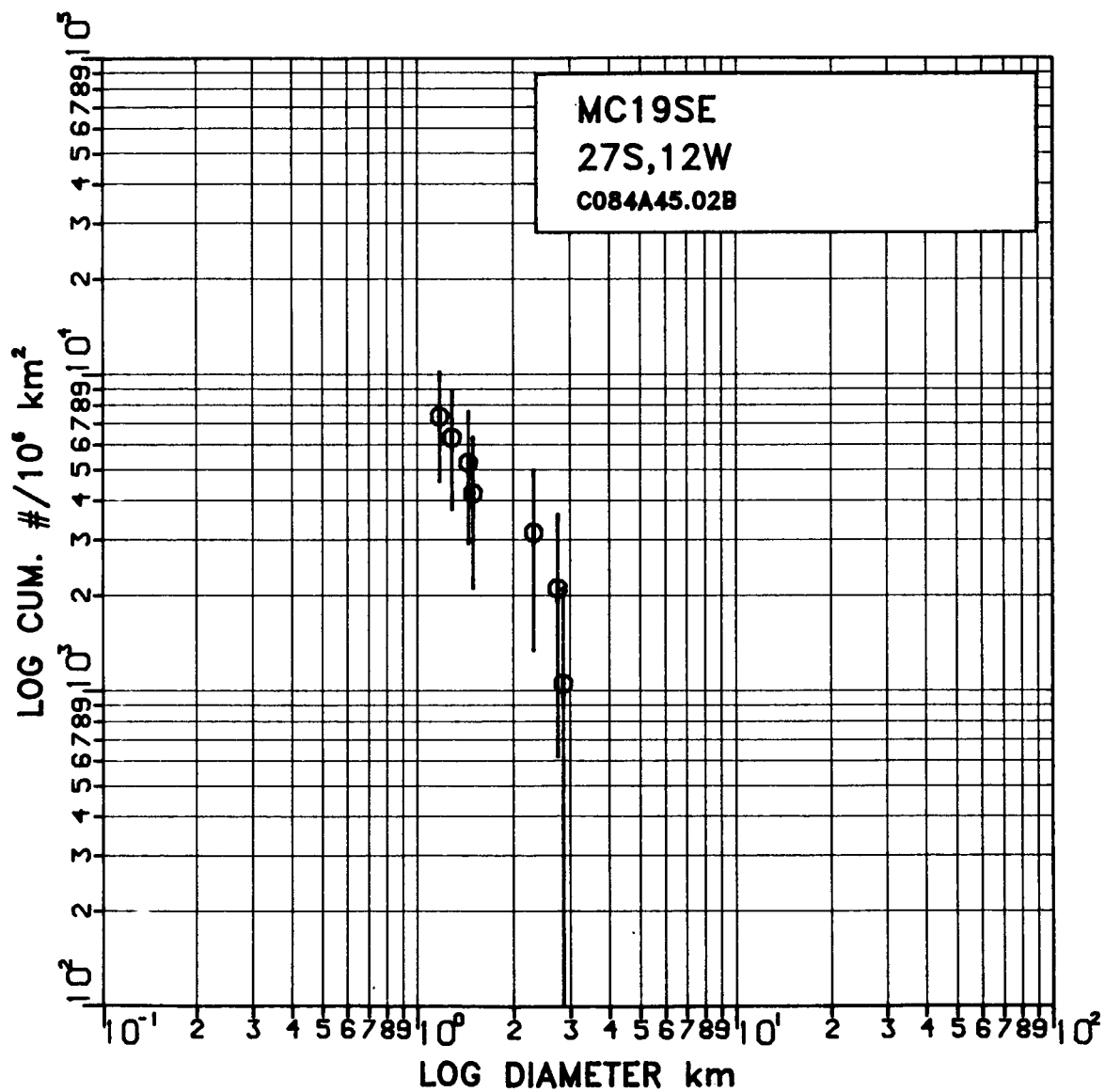


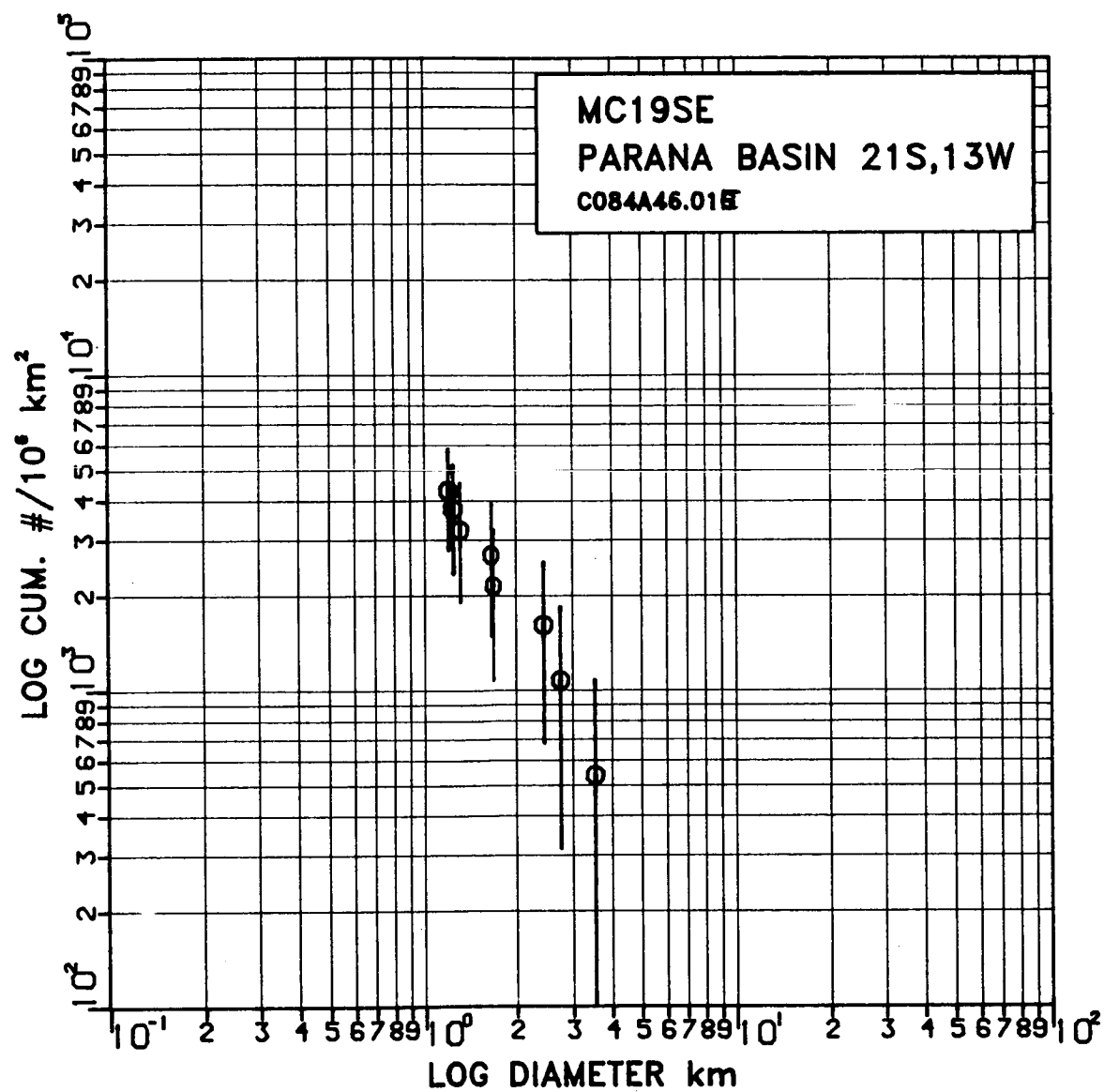


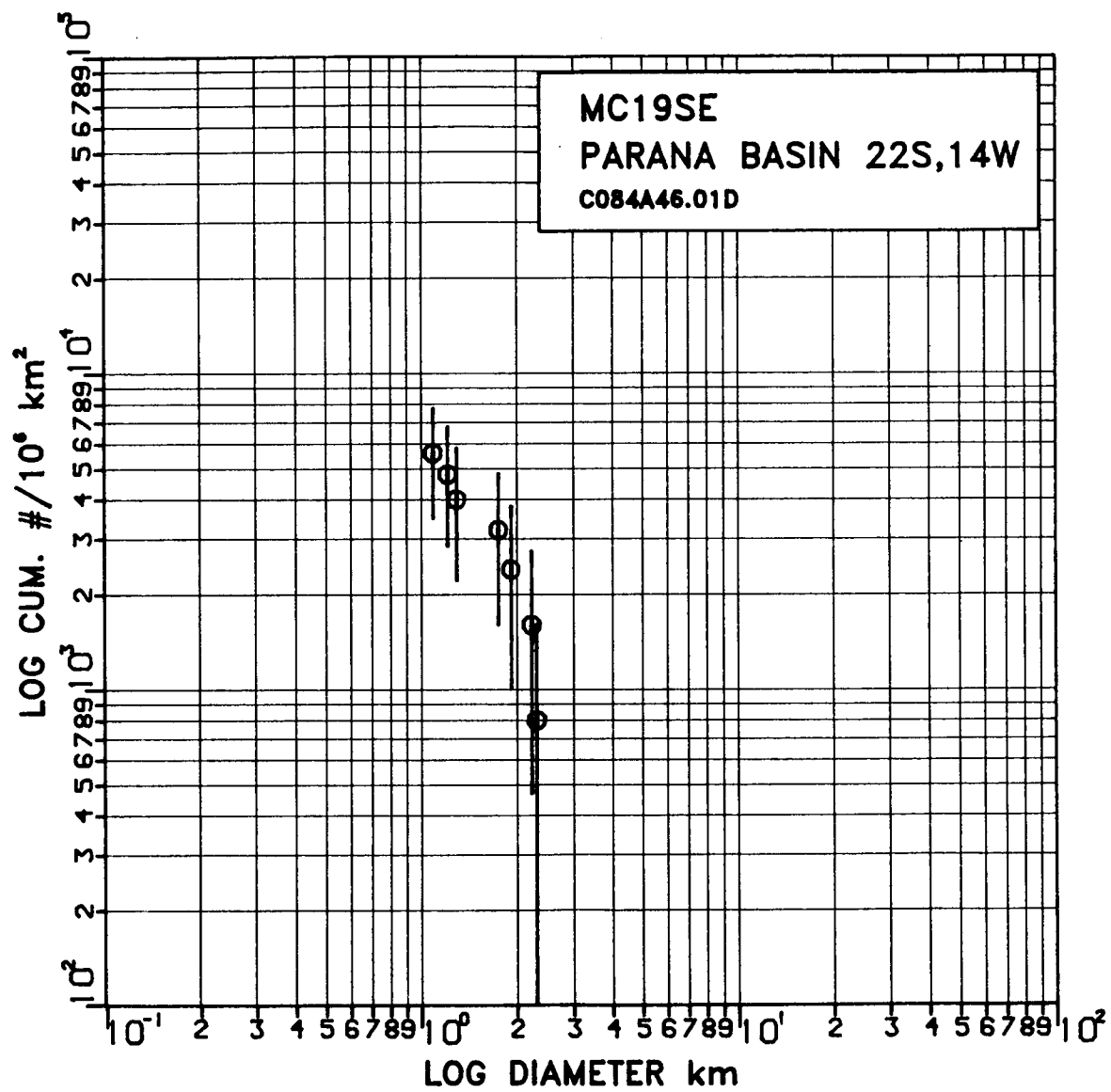


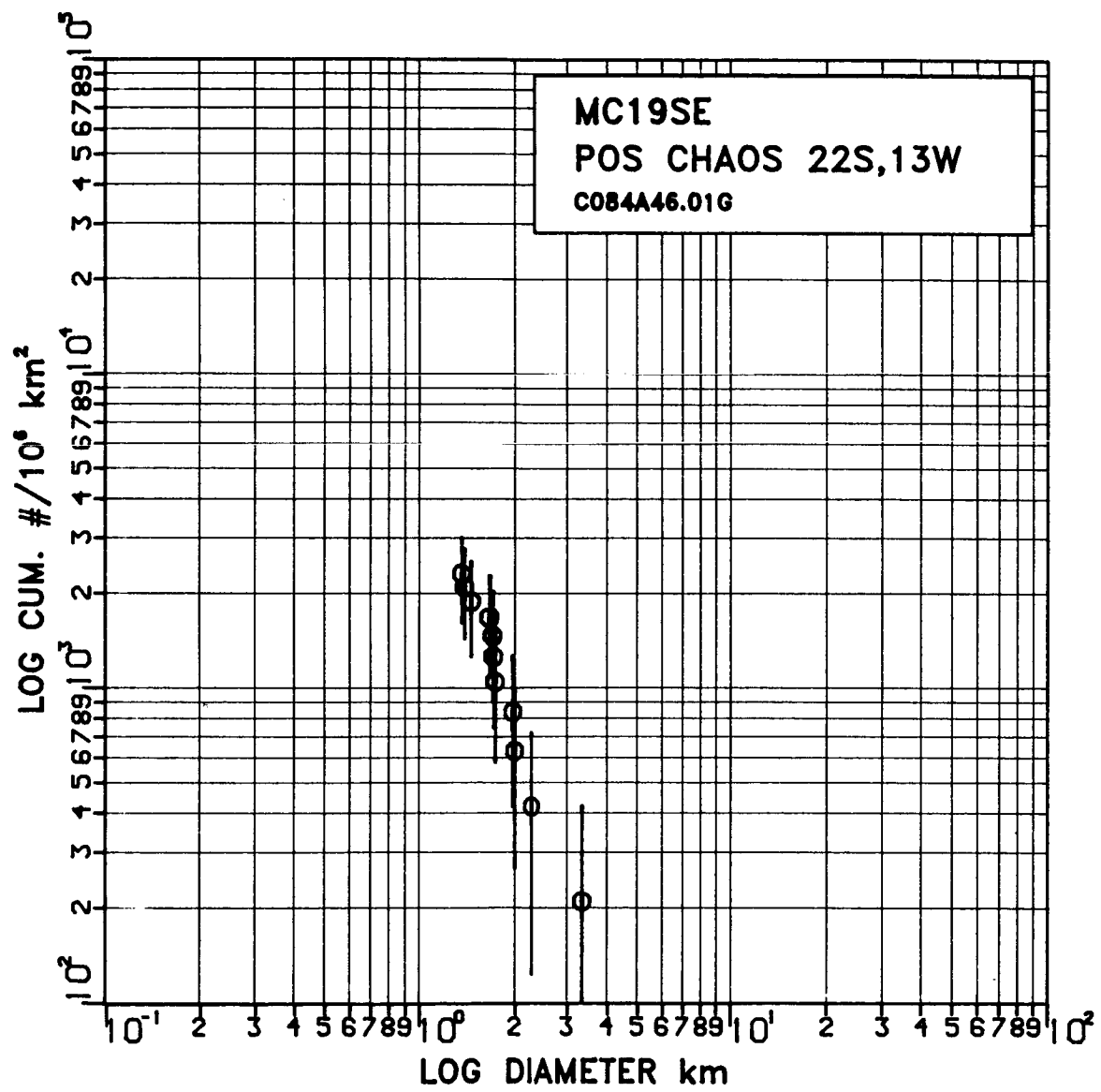


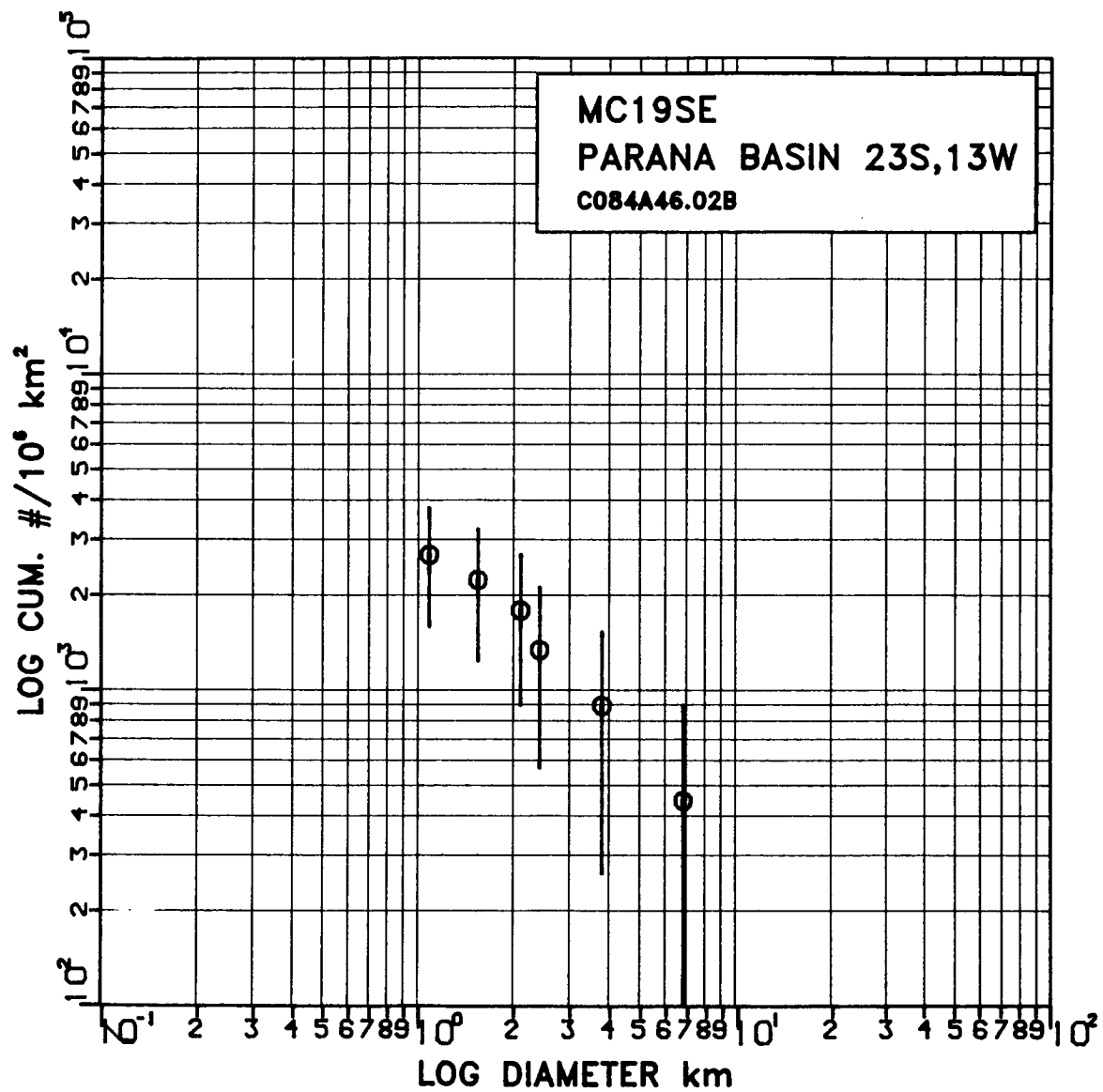


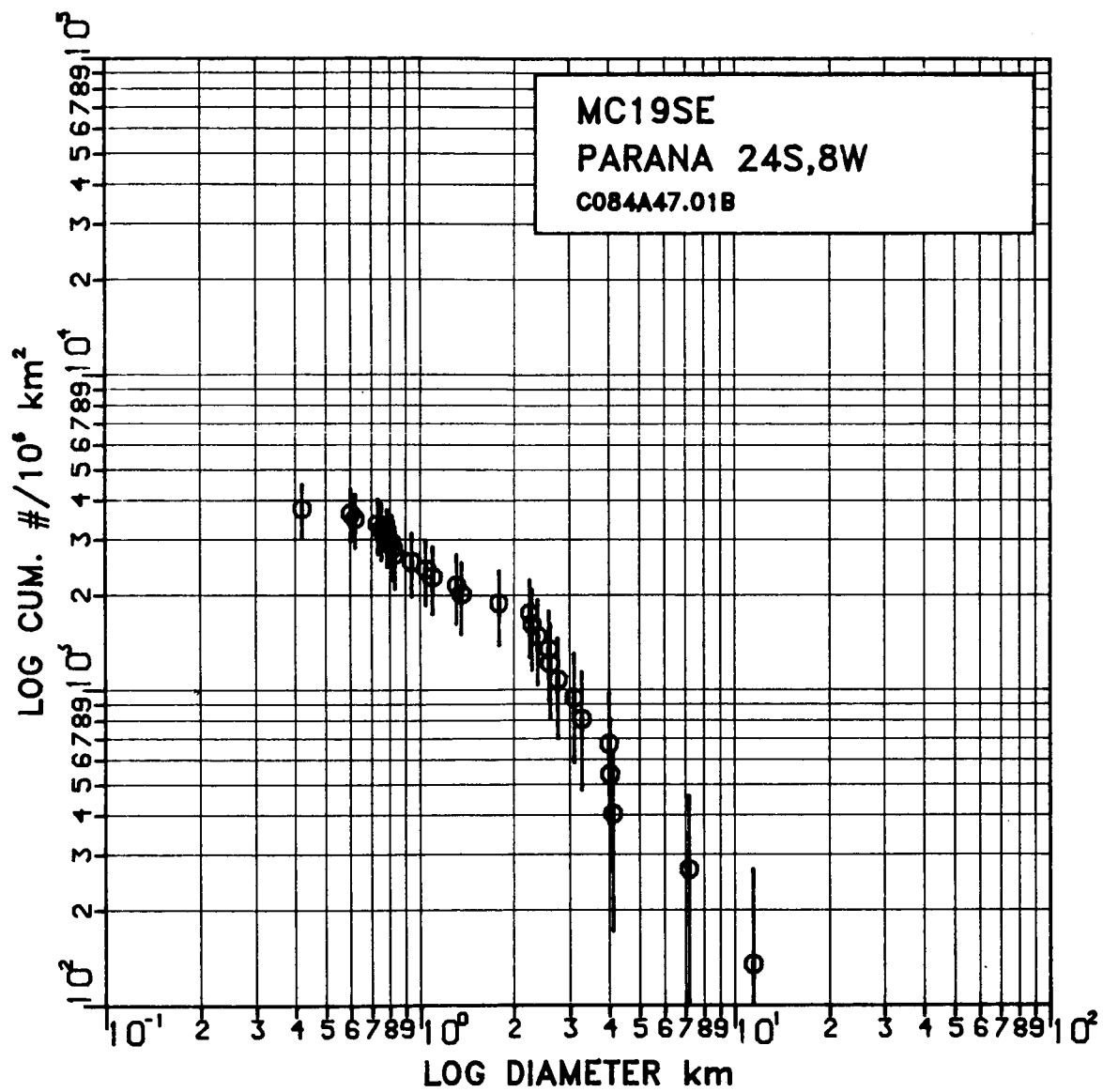


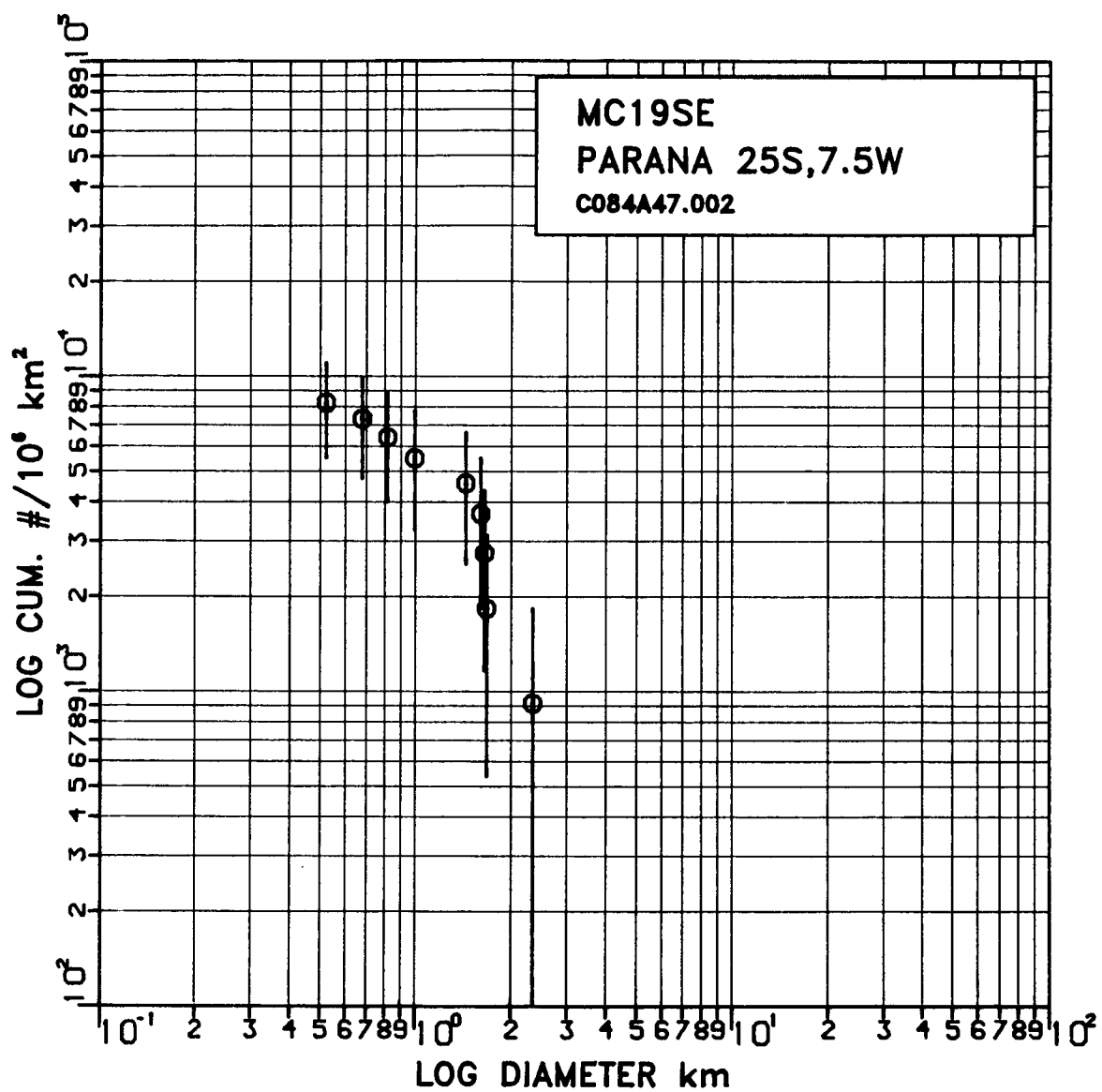


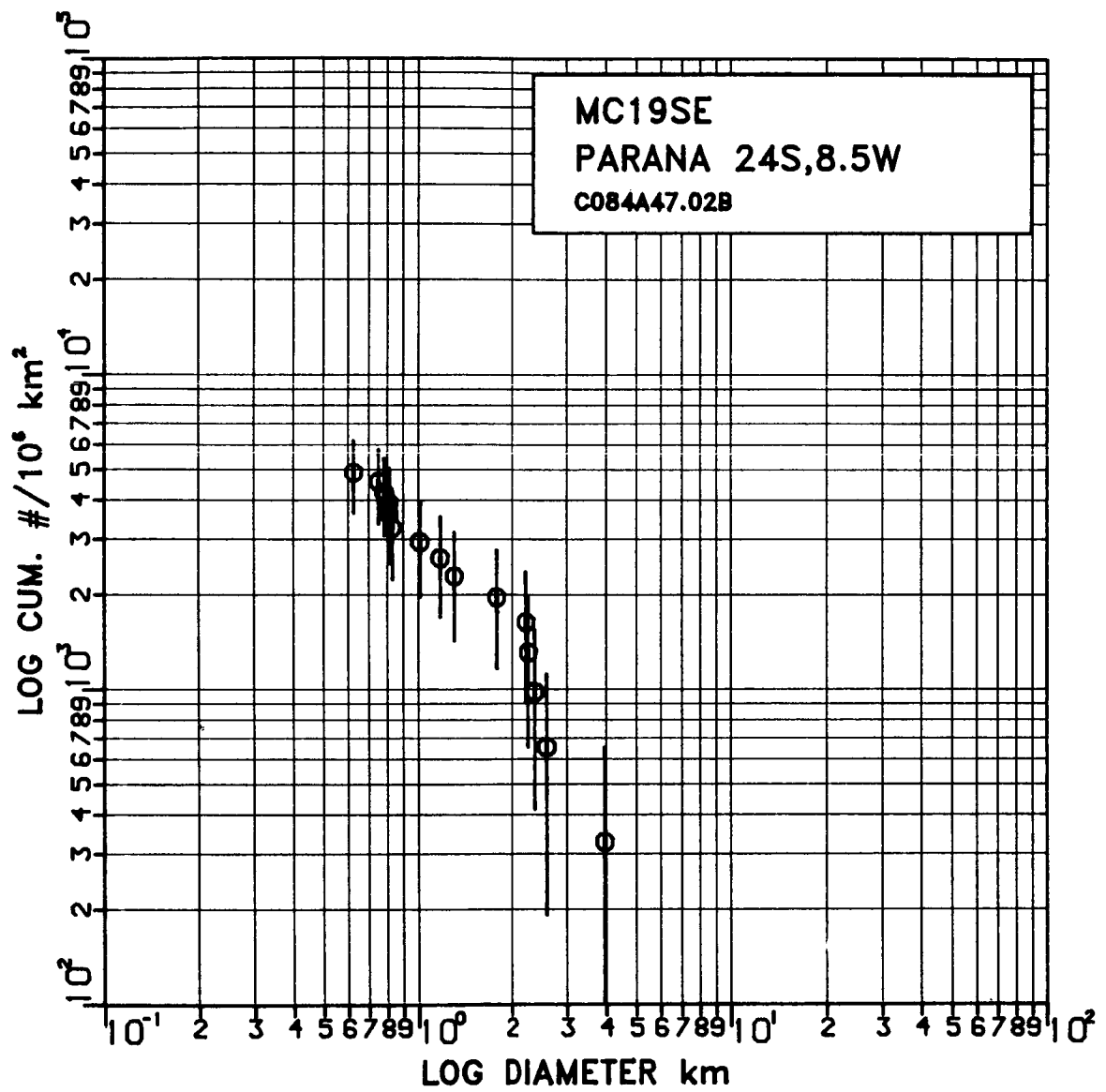


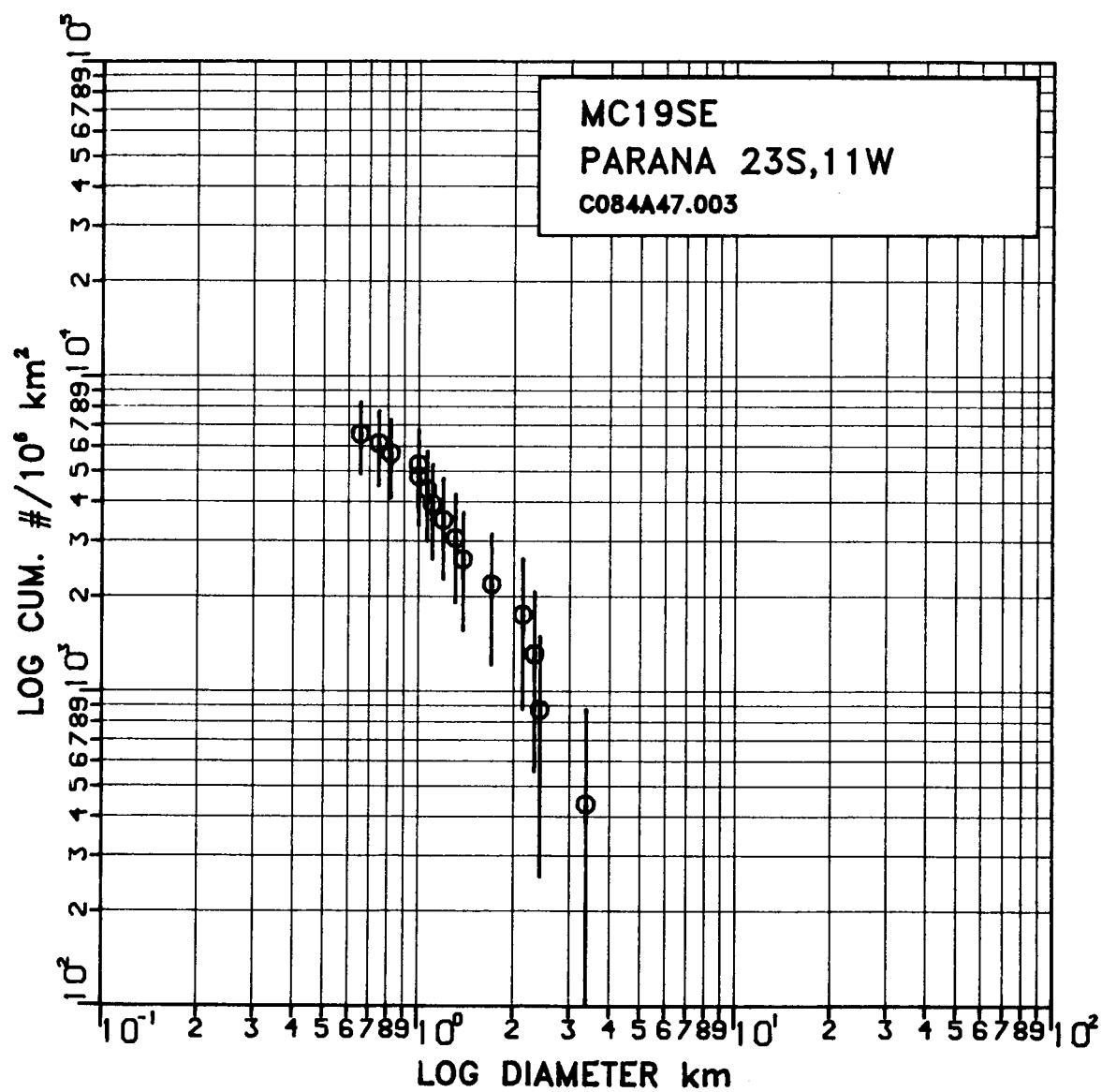


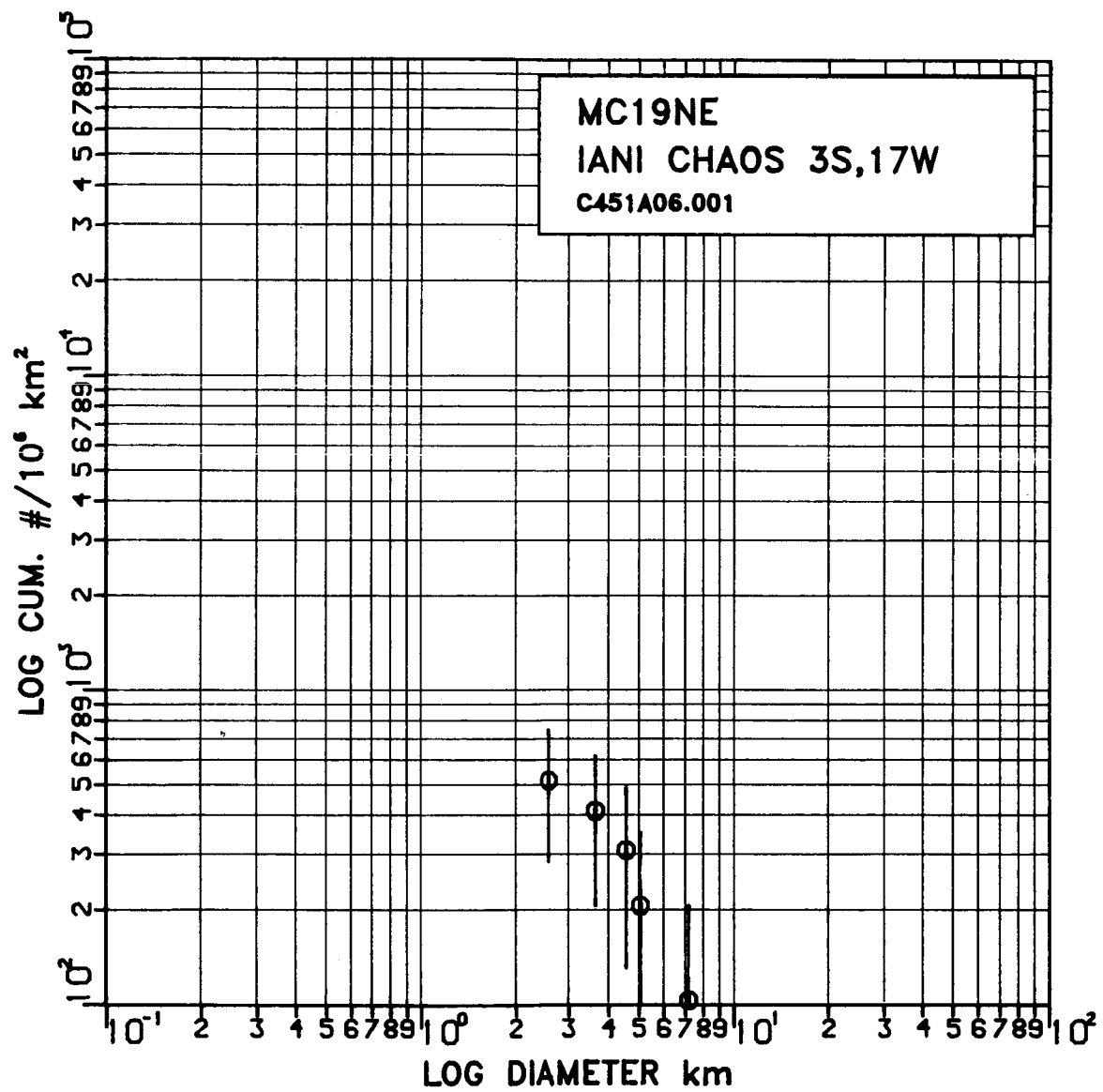


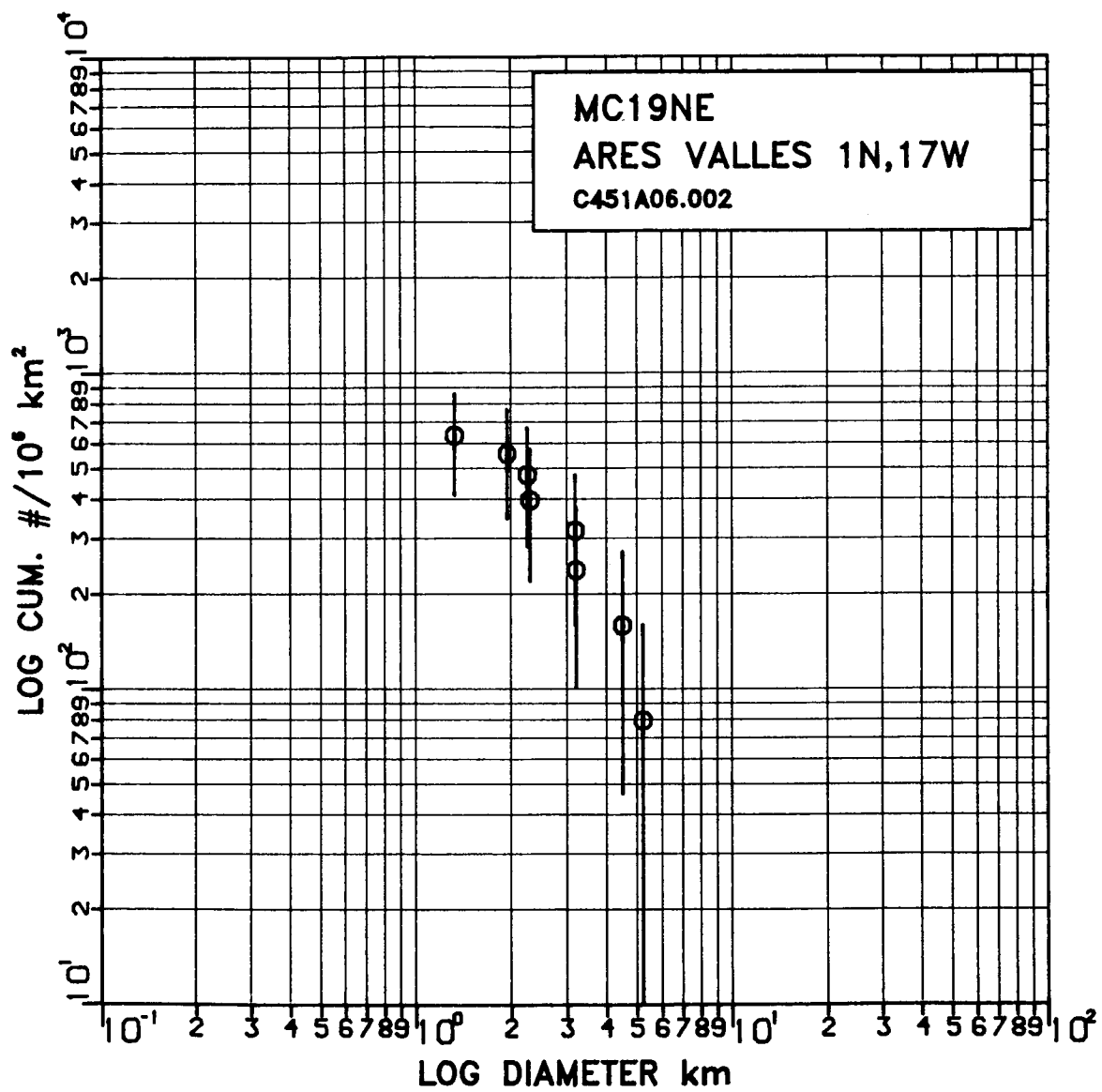


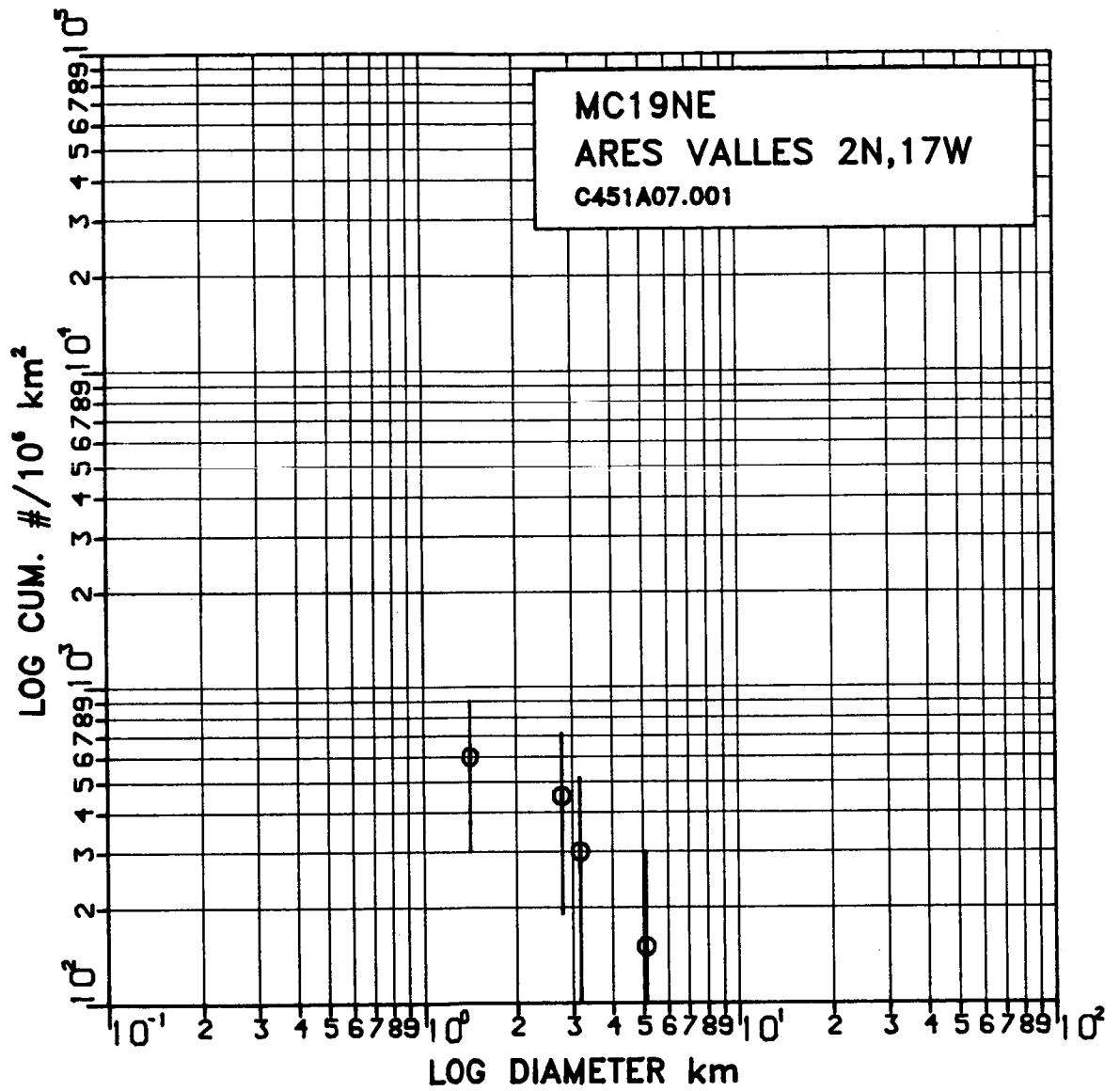


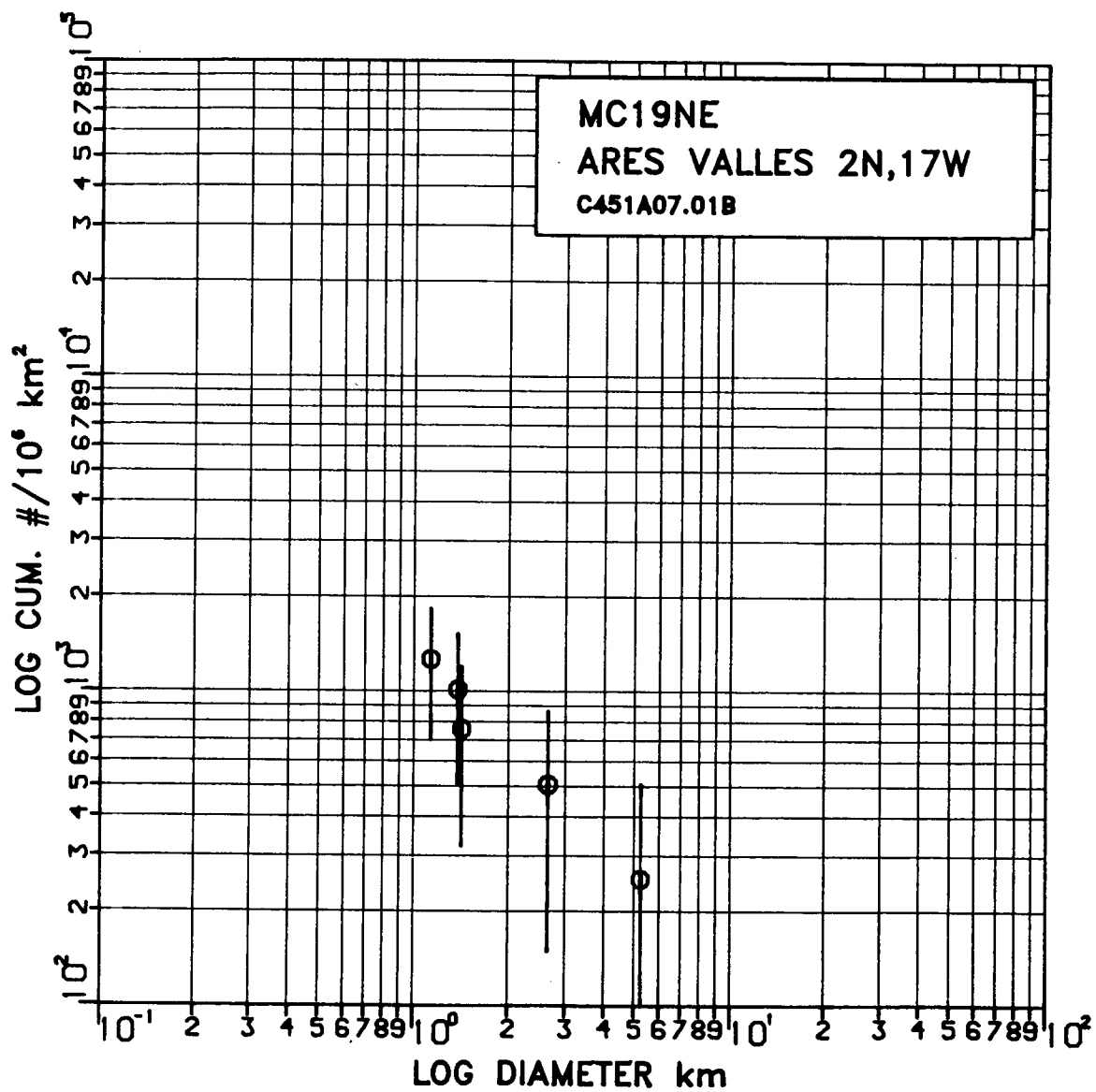


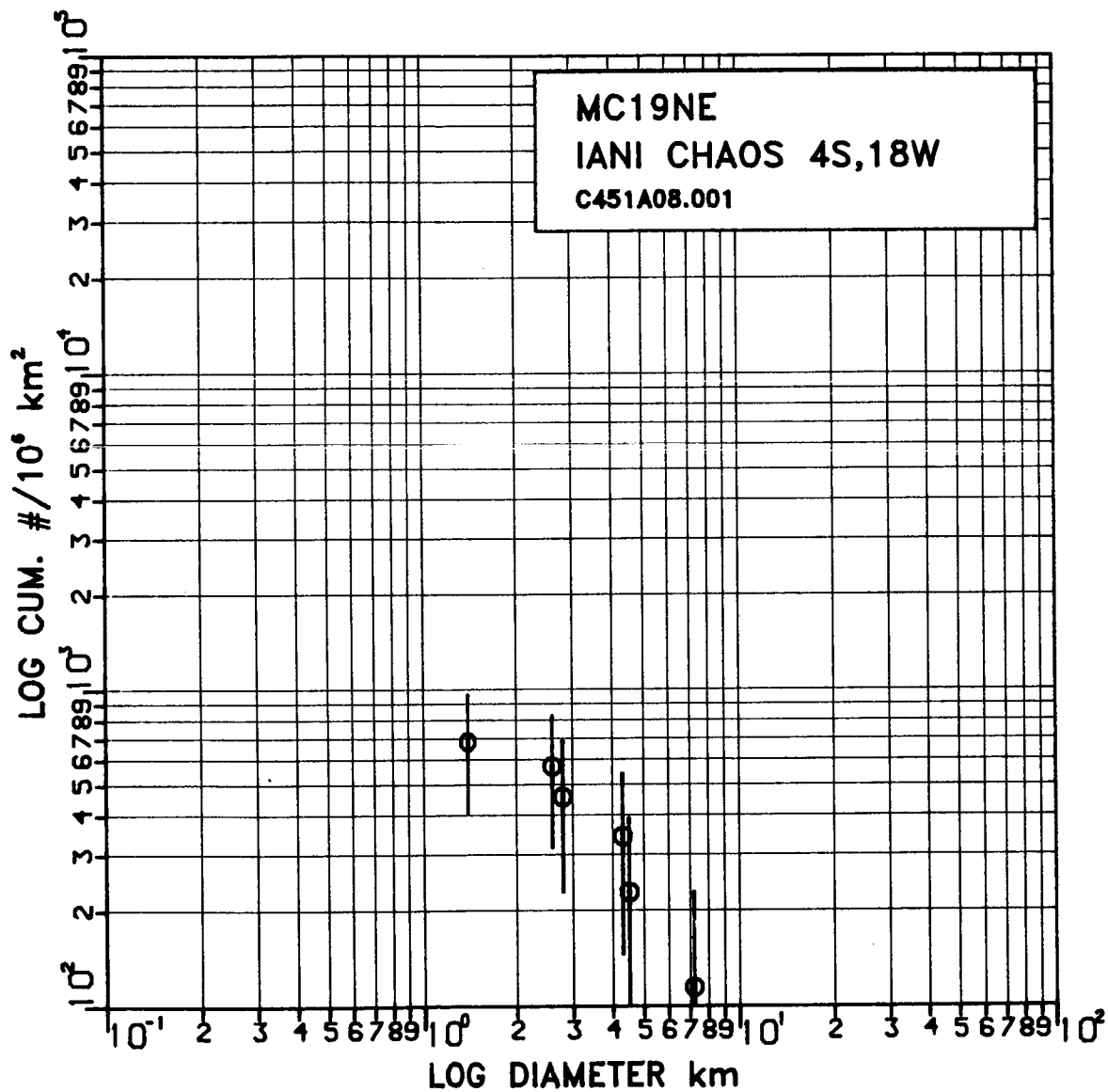


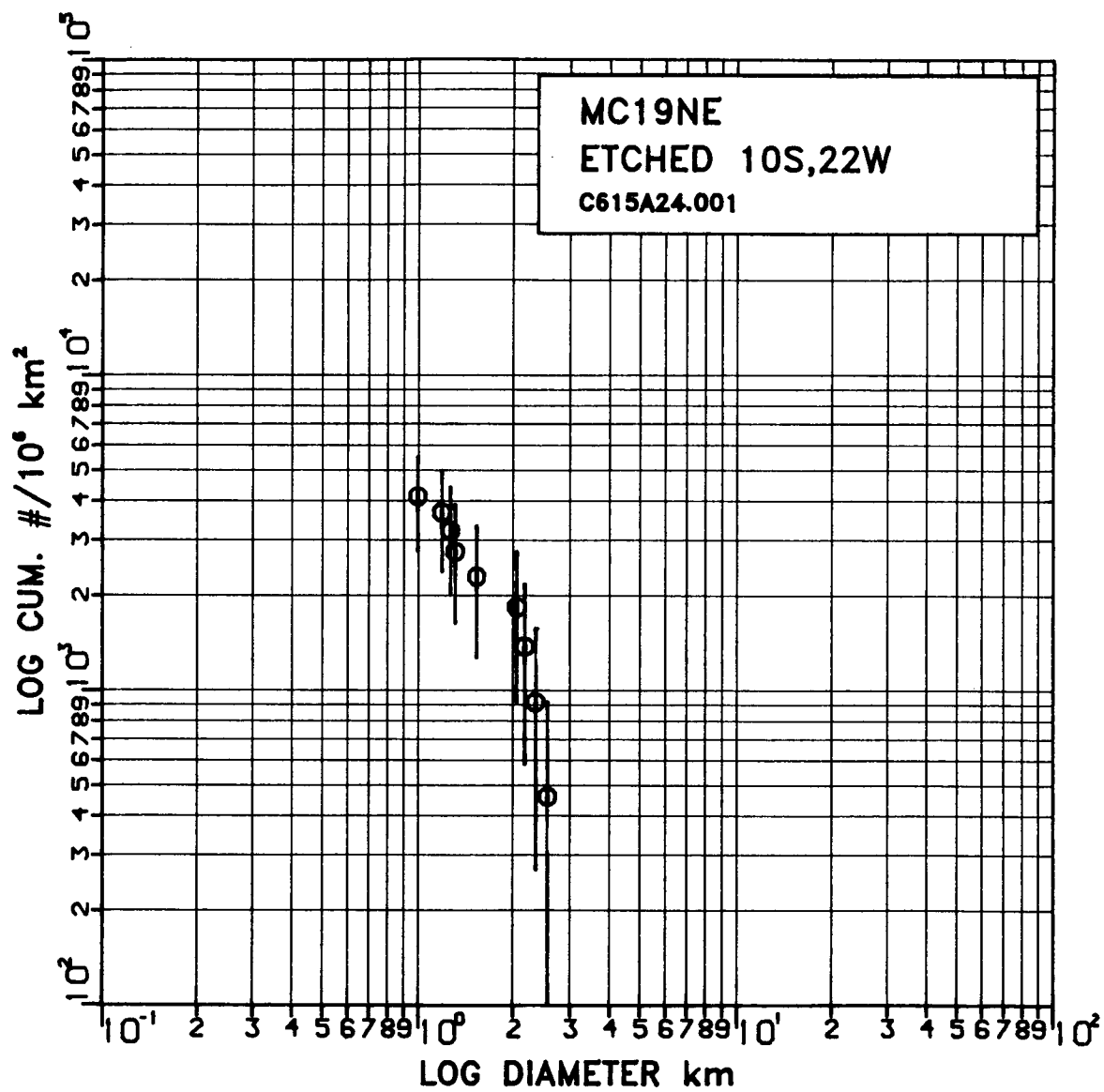


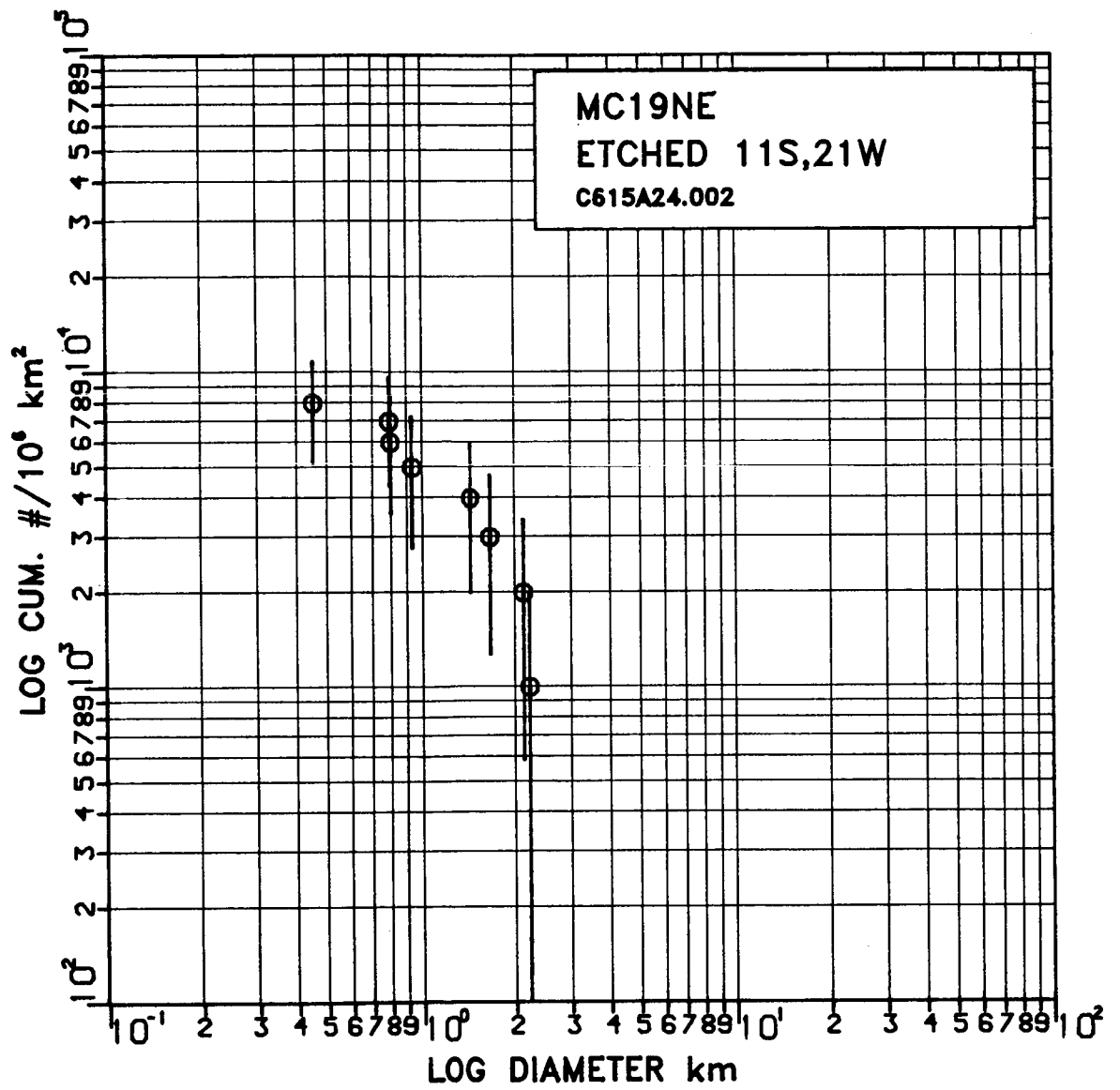


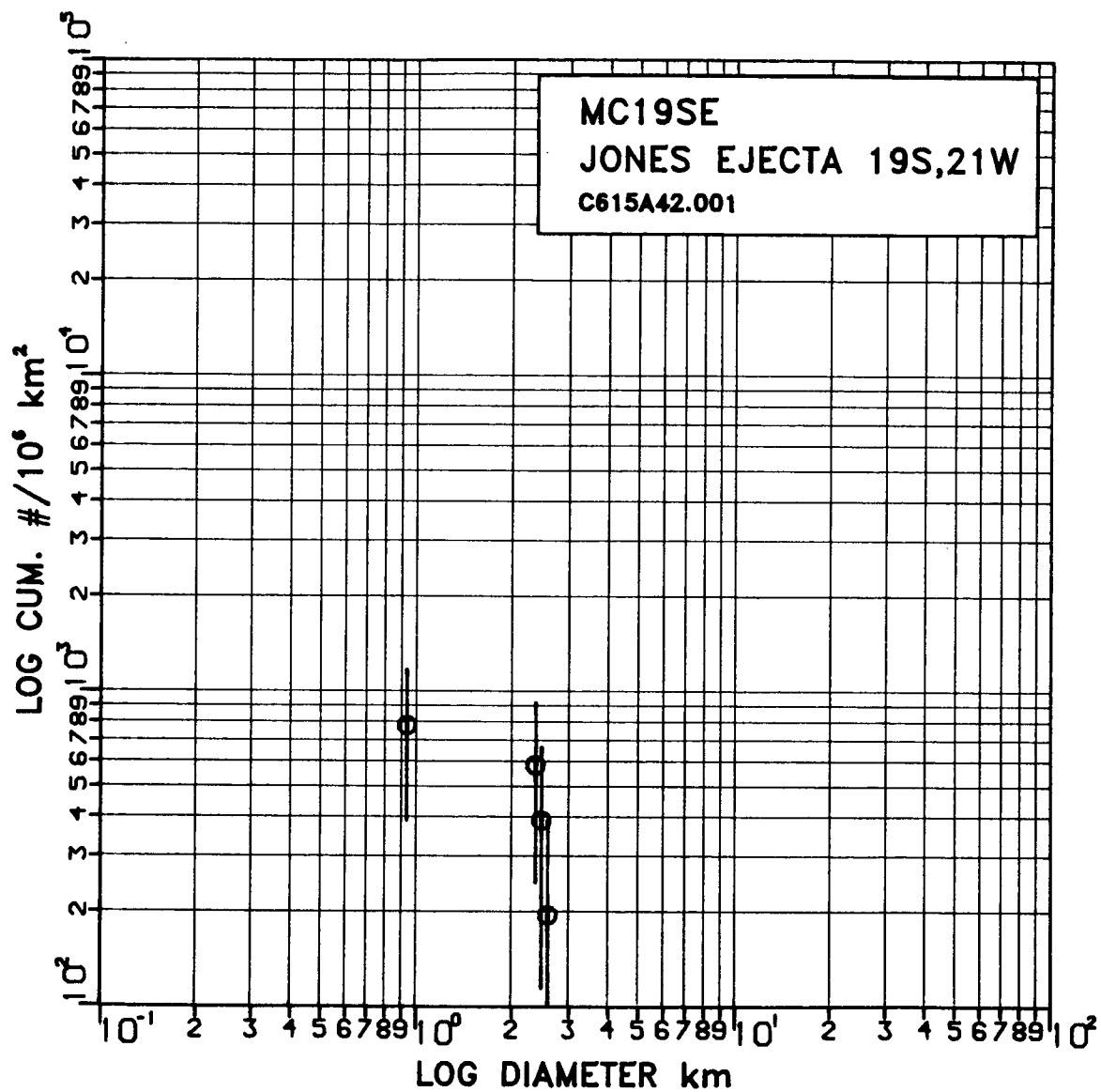


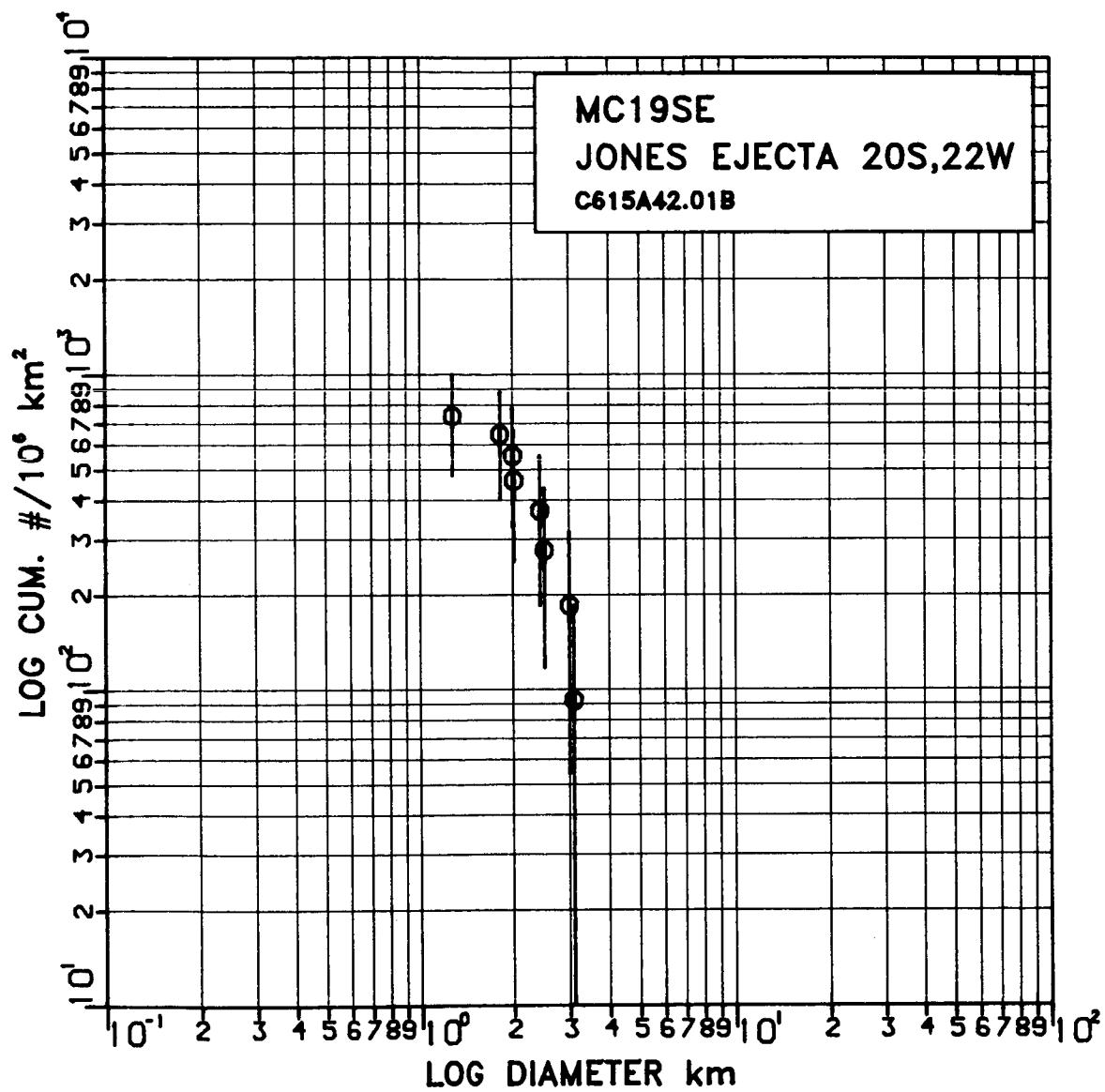


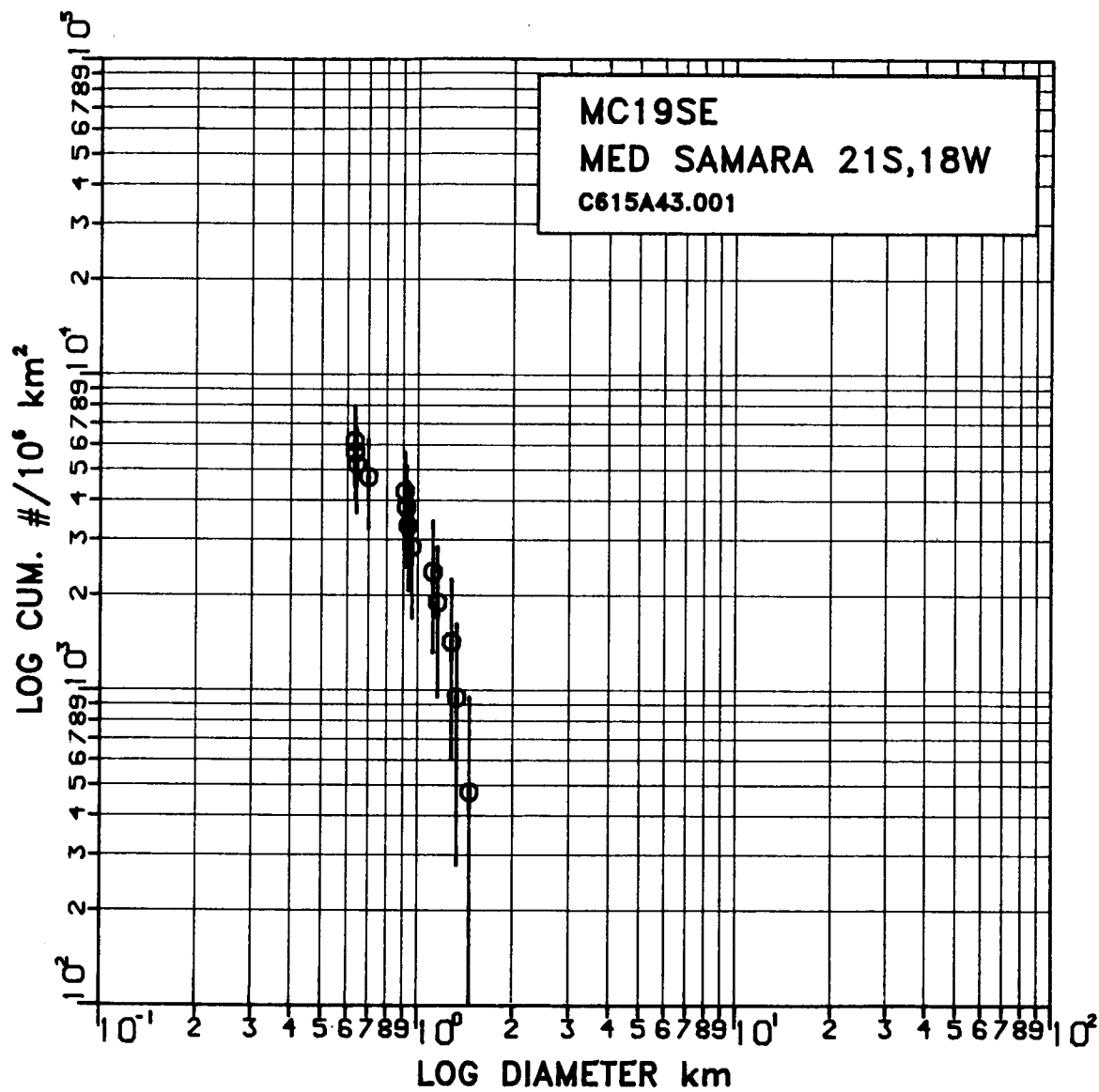


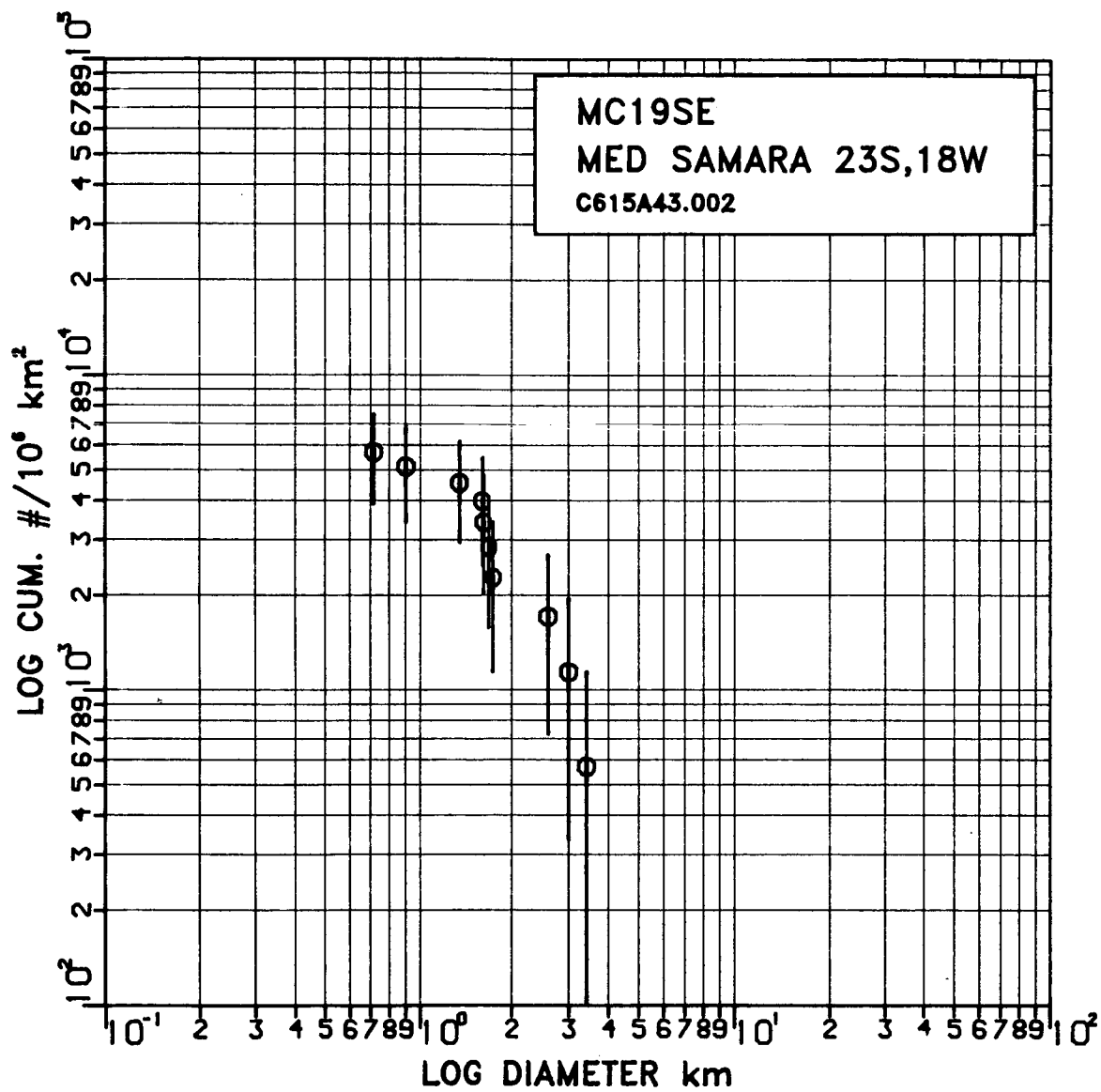


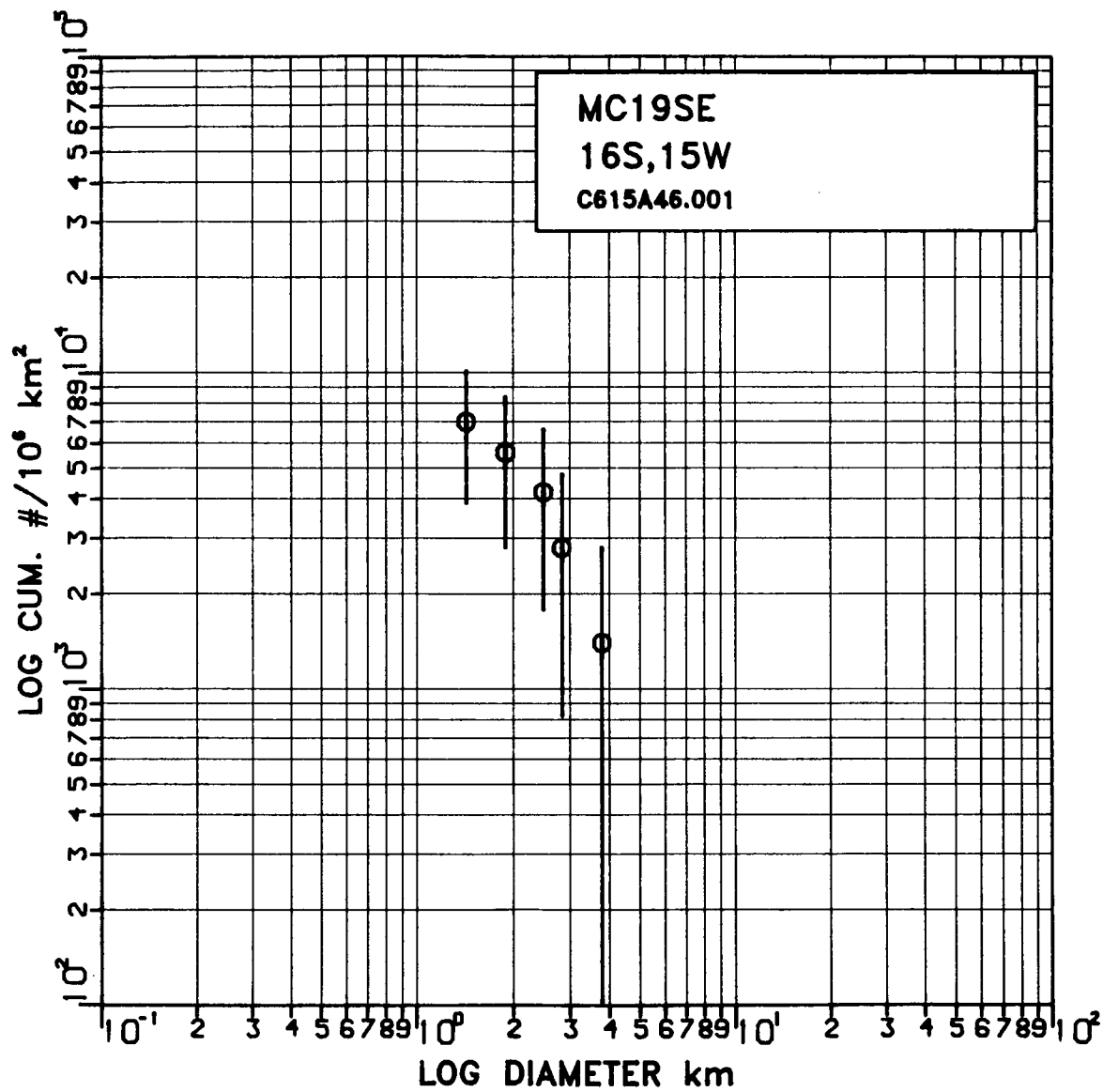


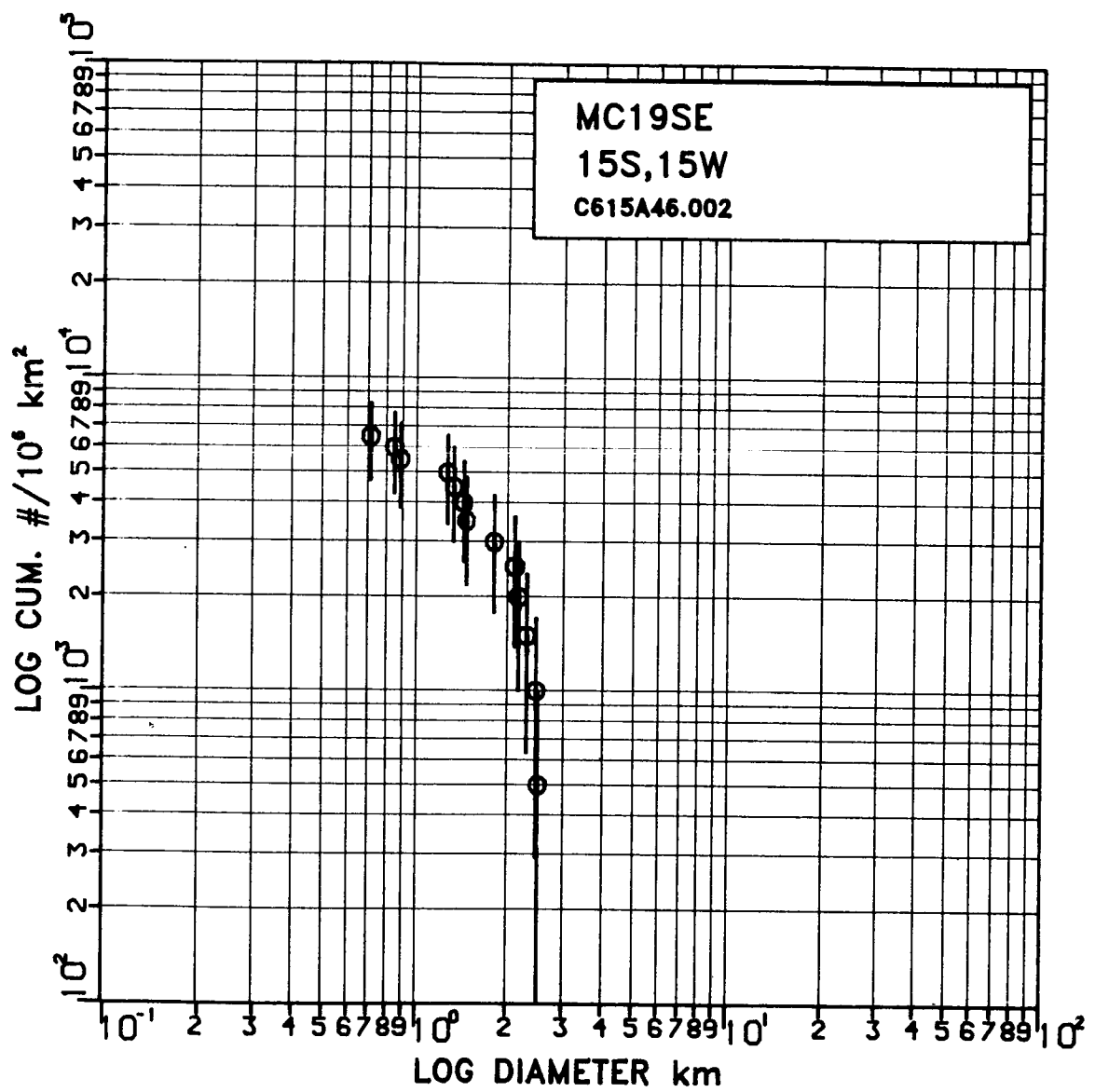


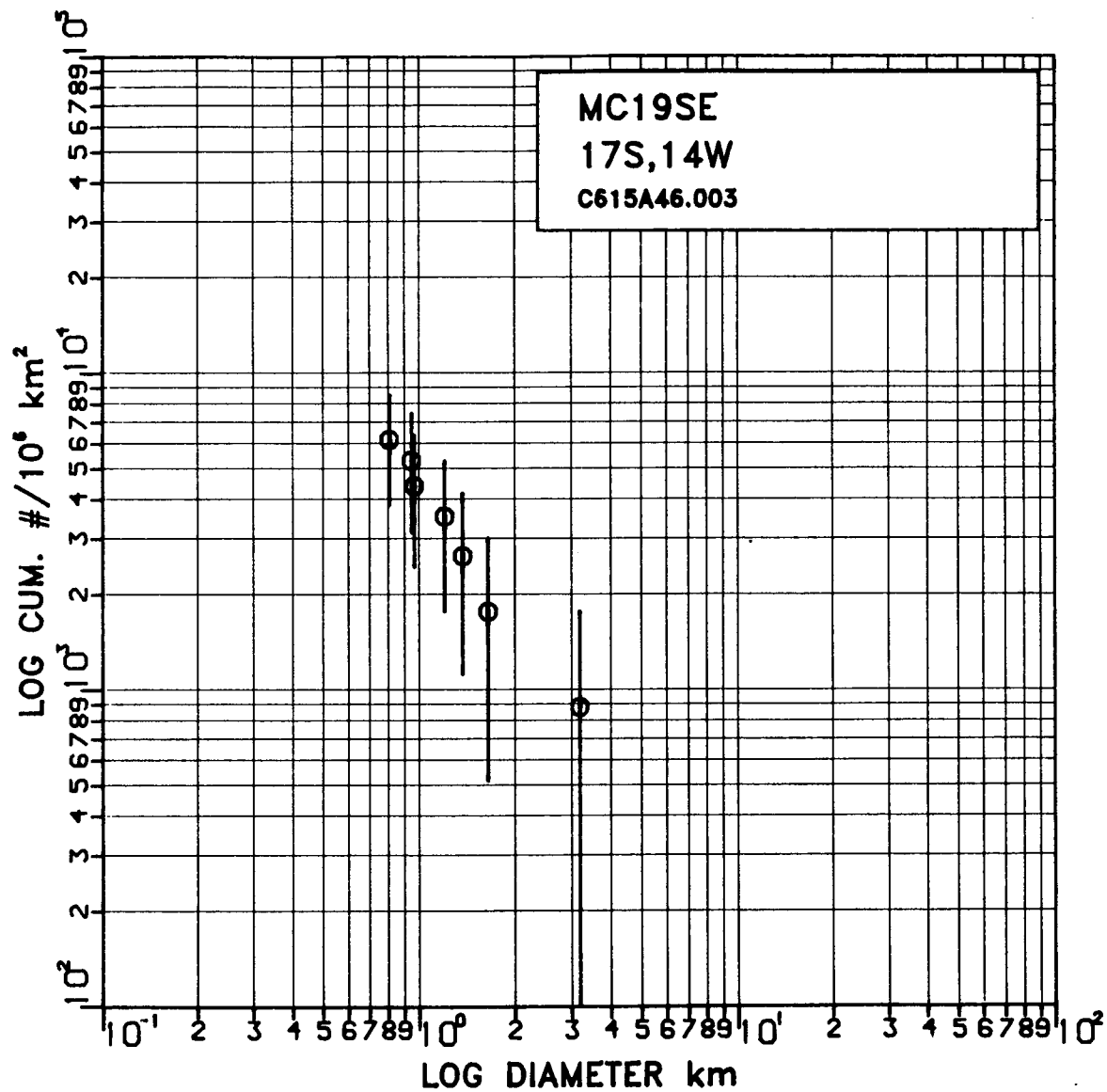


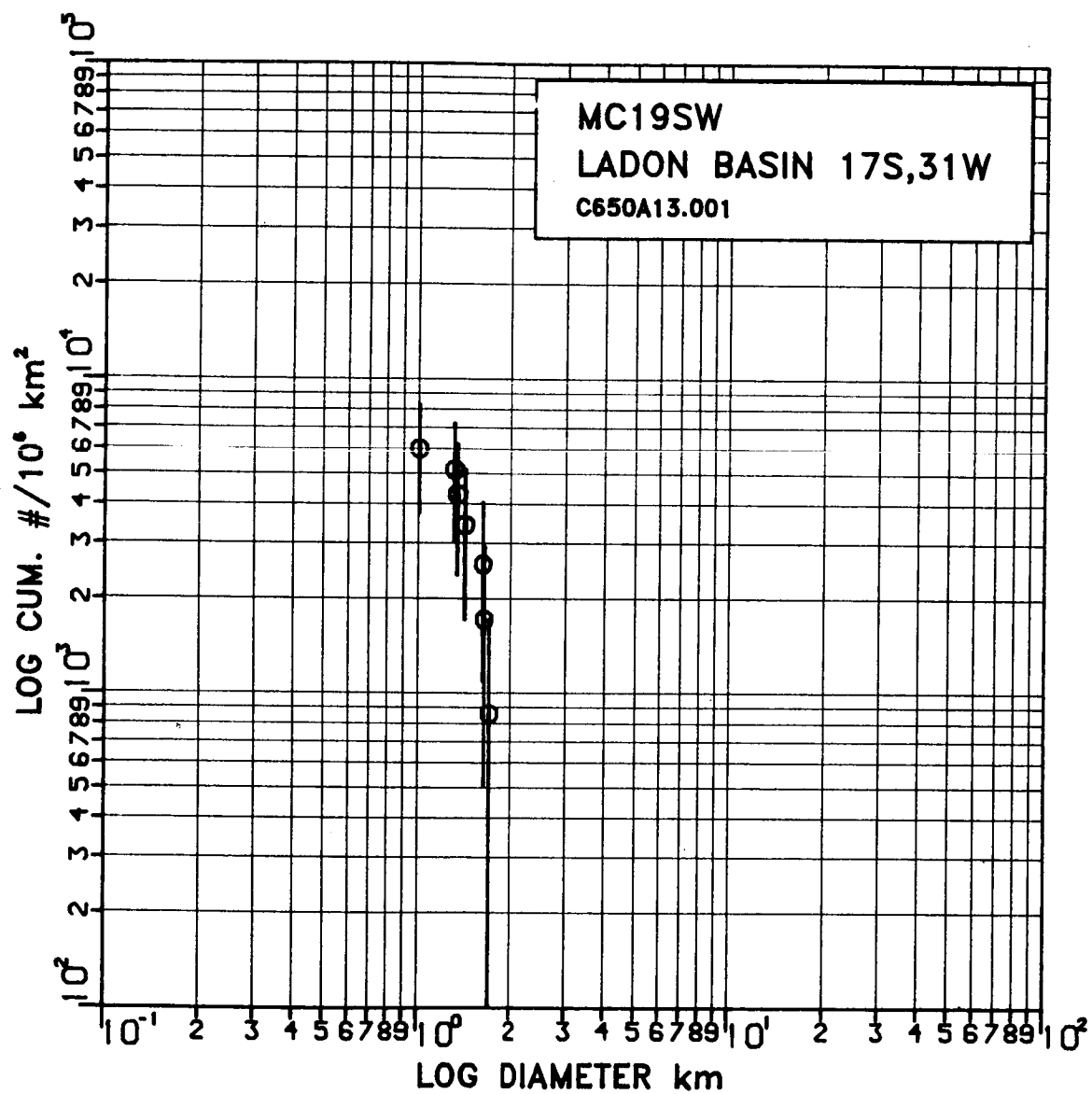


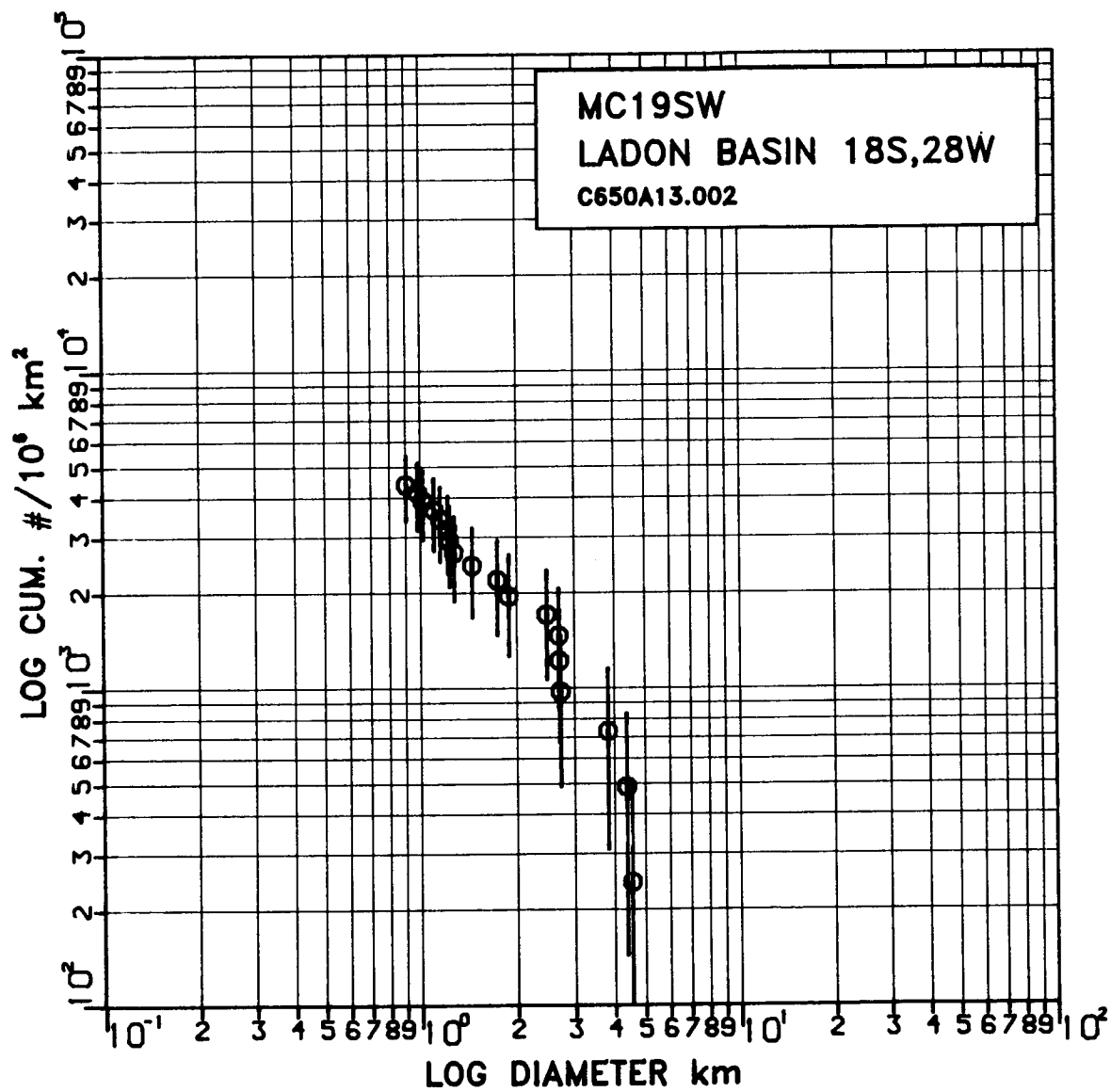


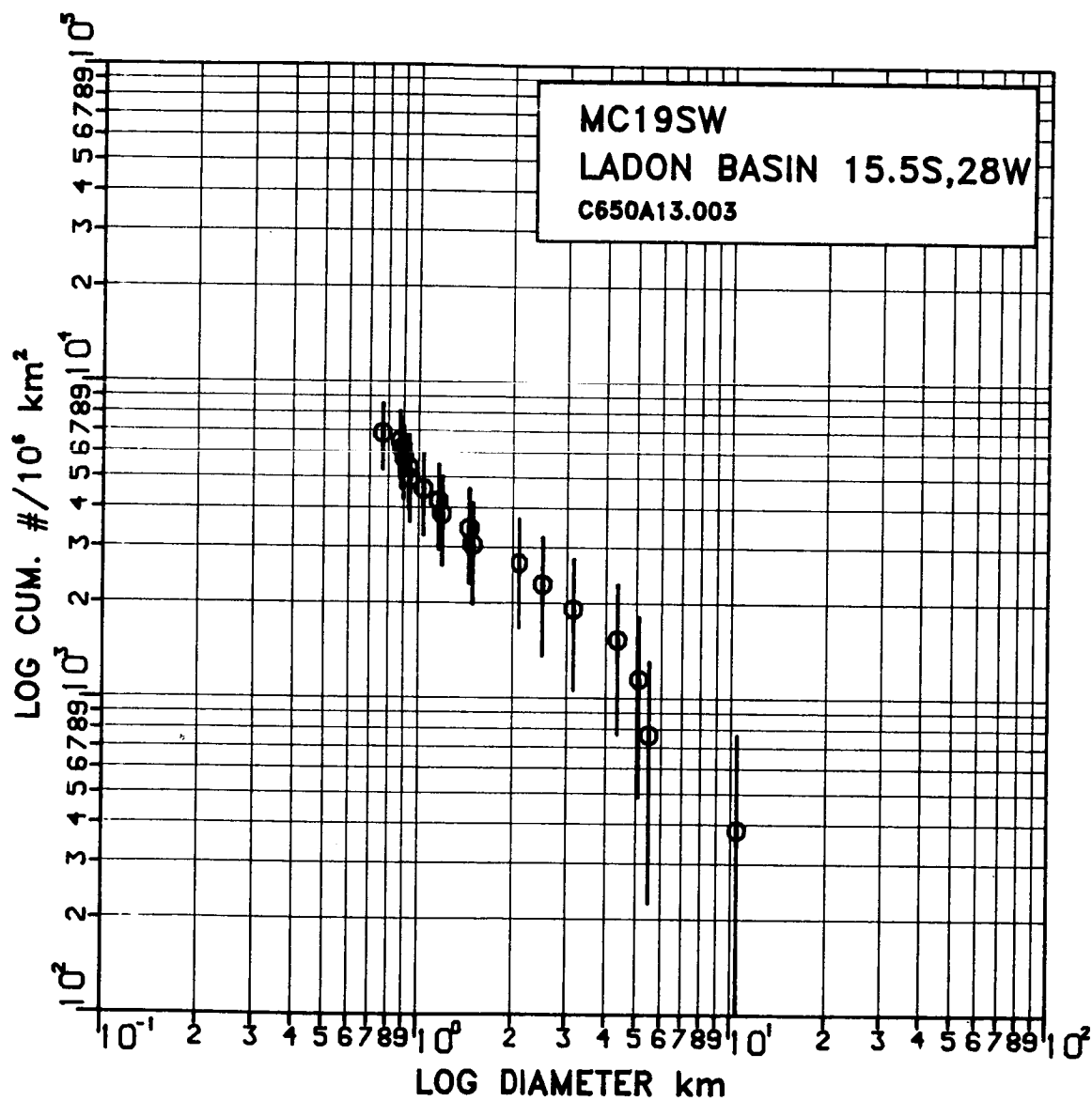




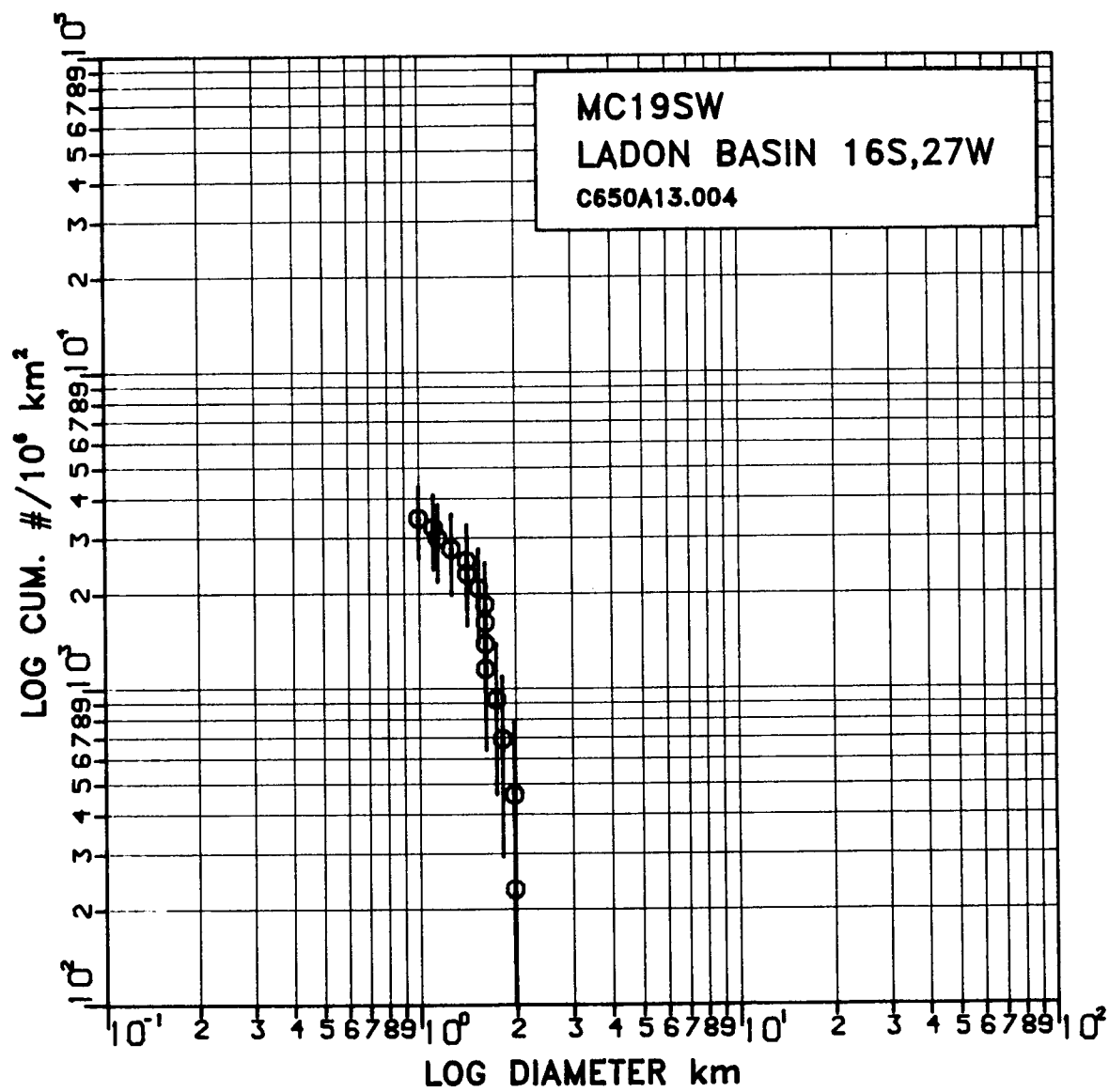


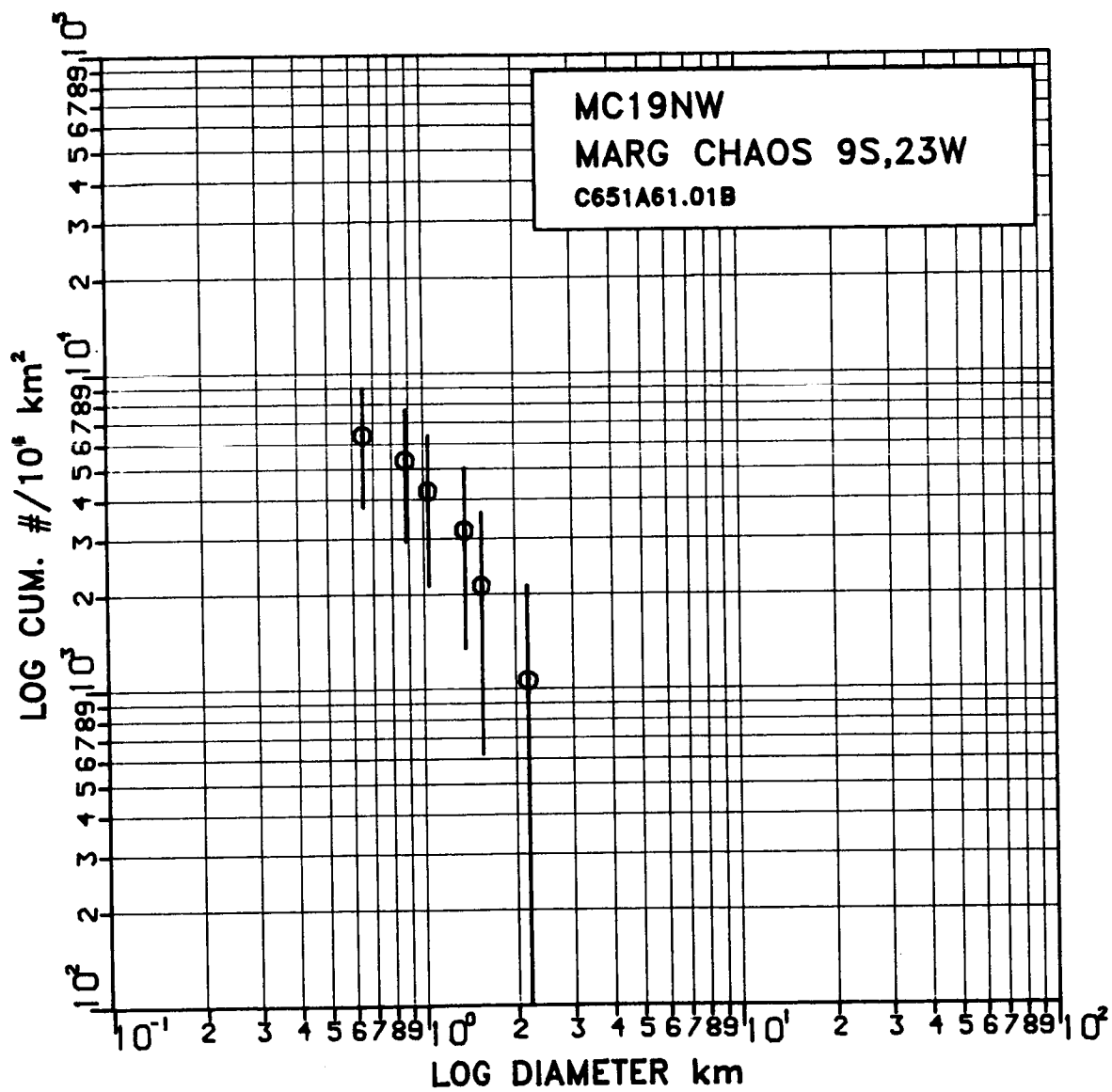


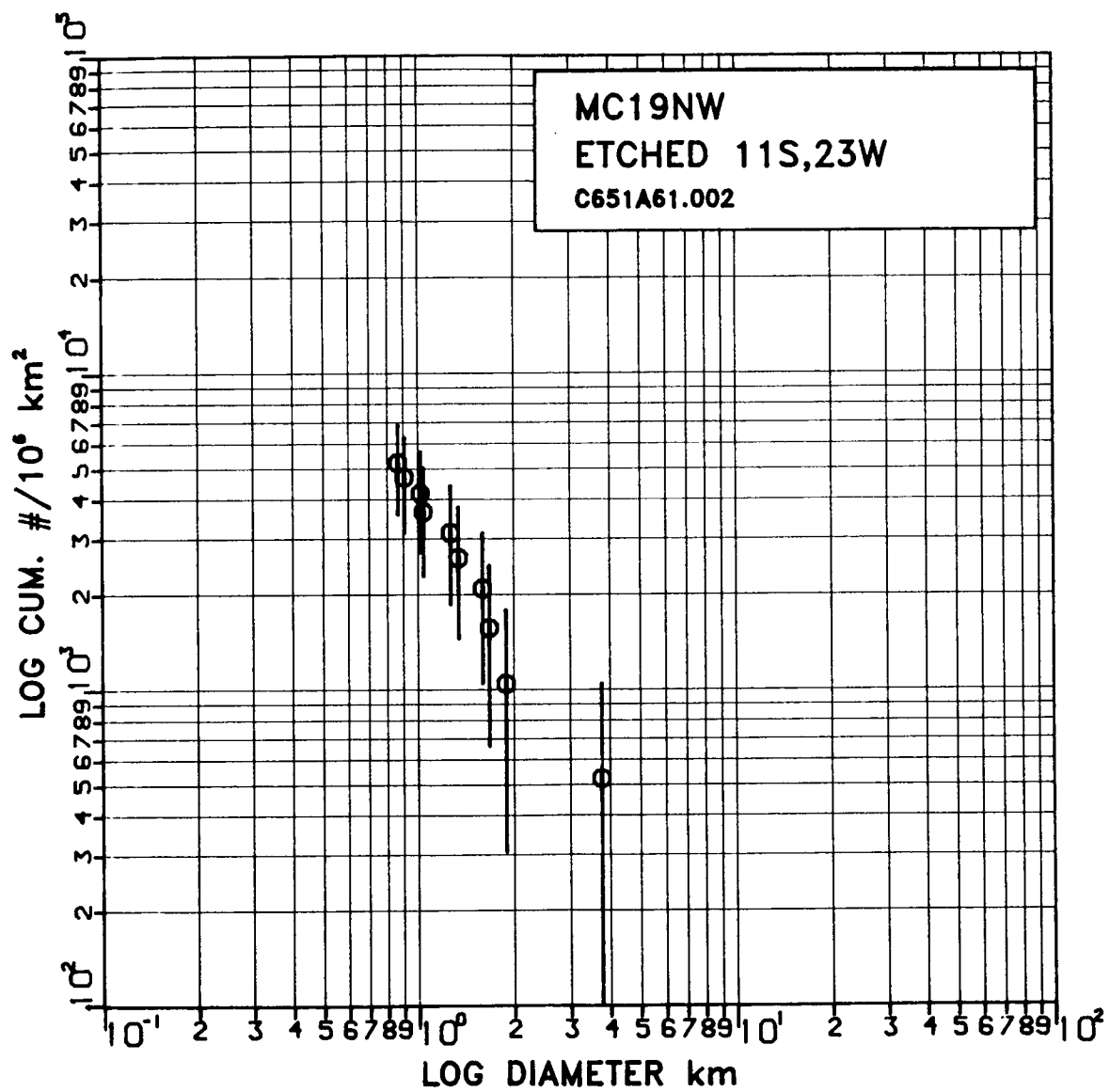


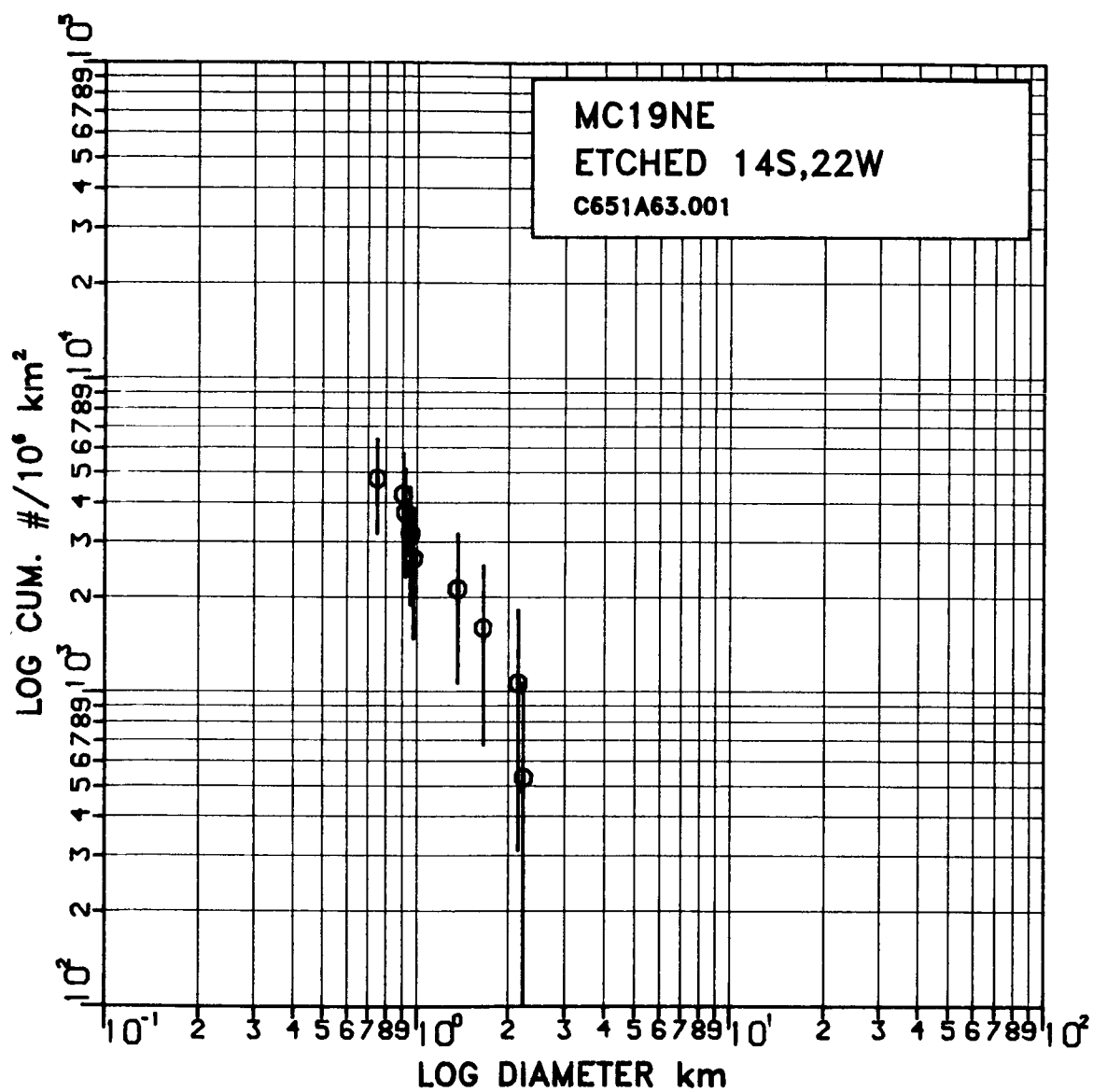


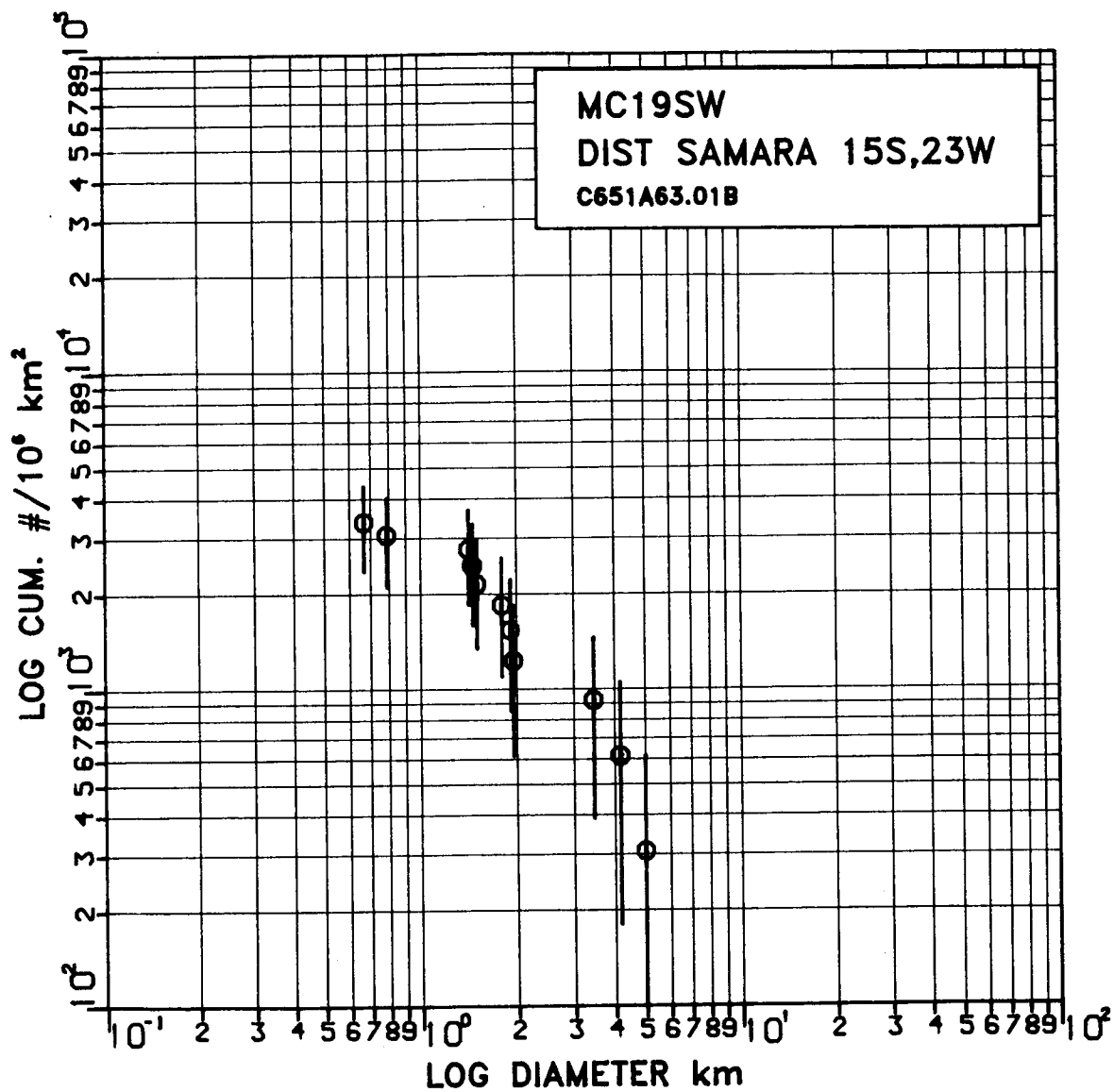
C-3

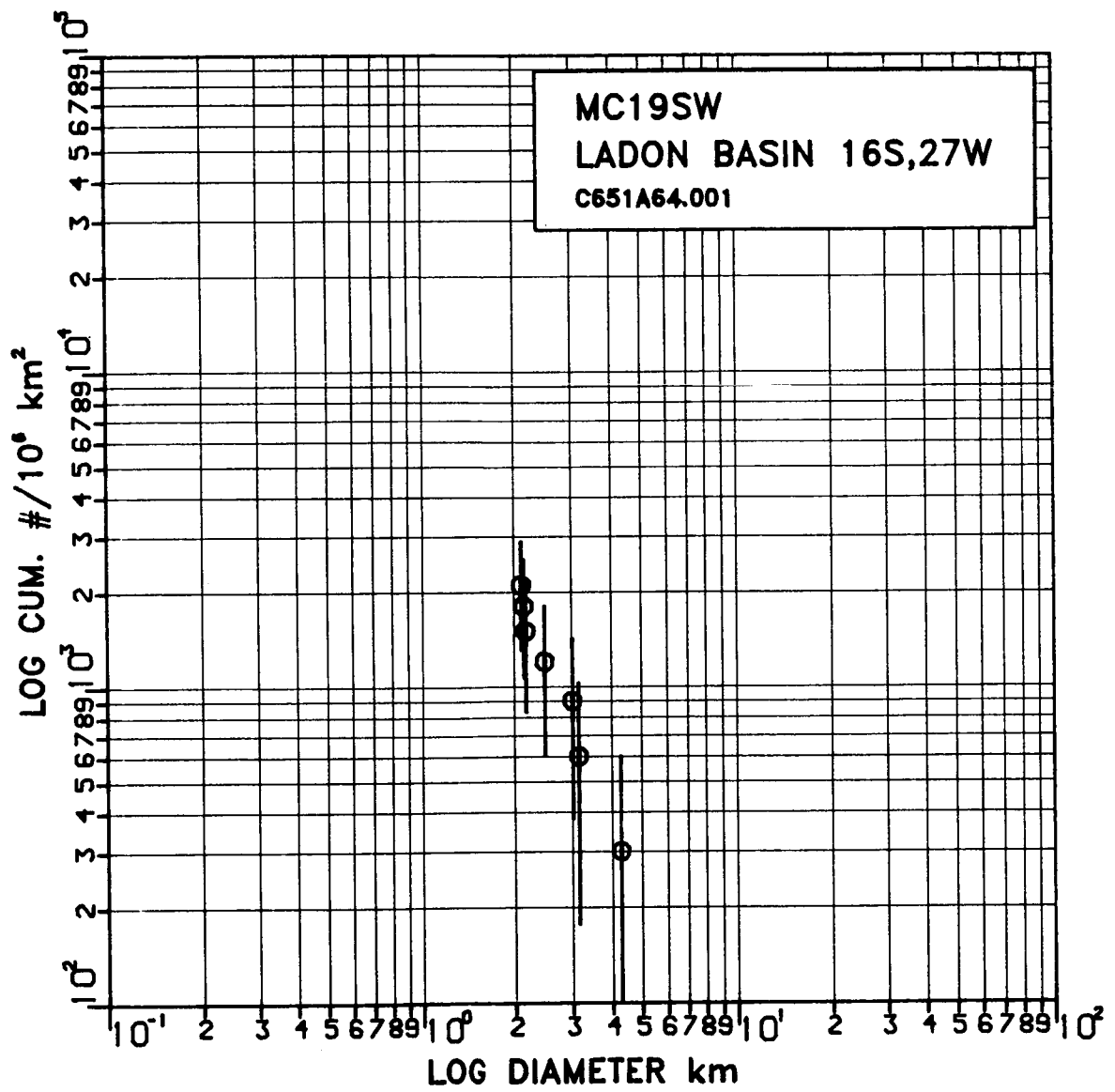


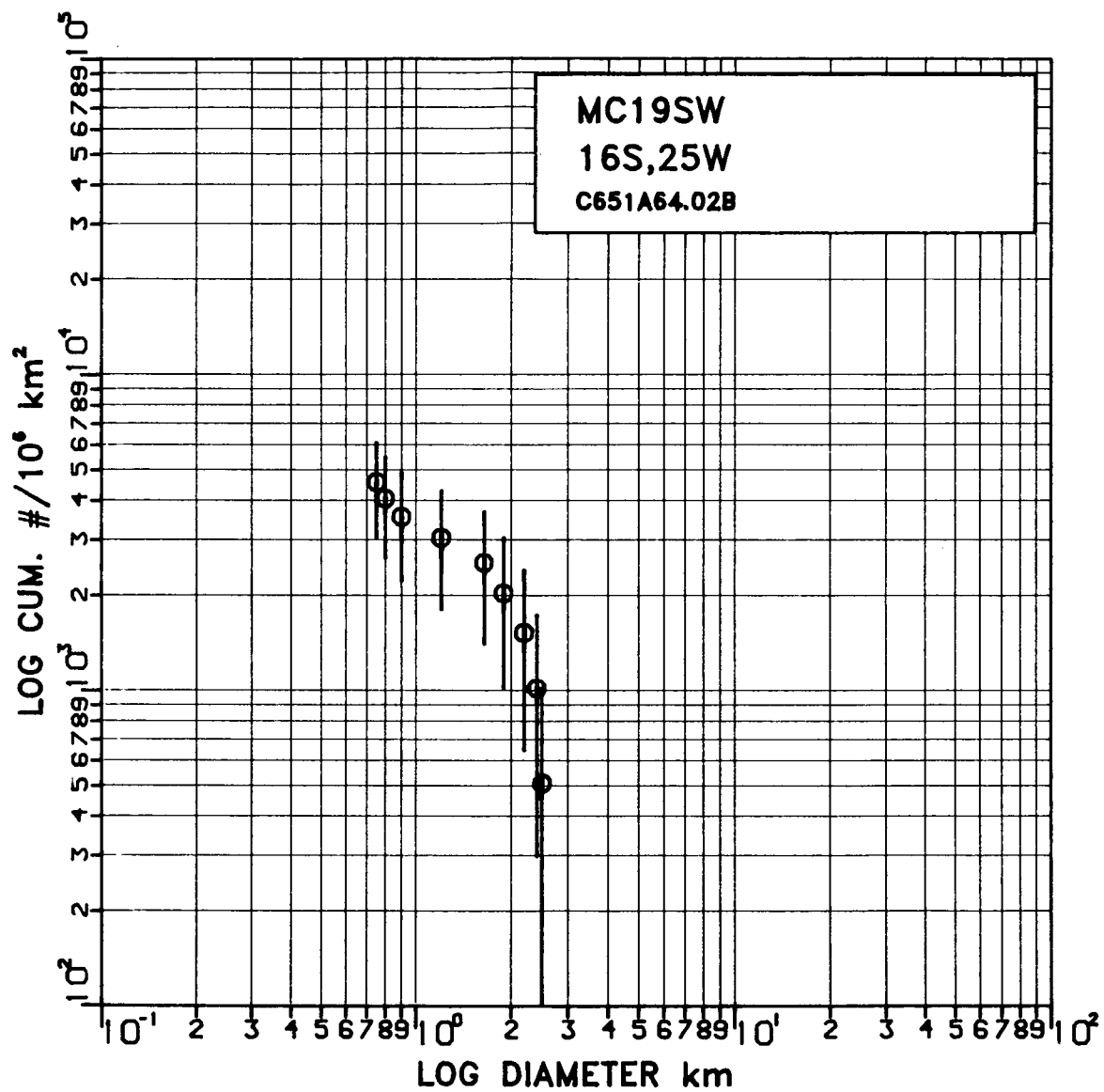


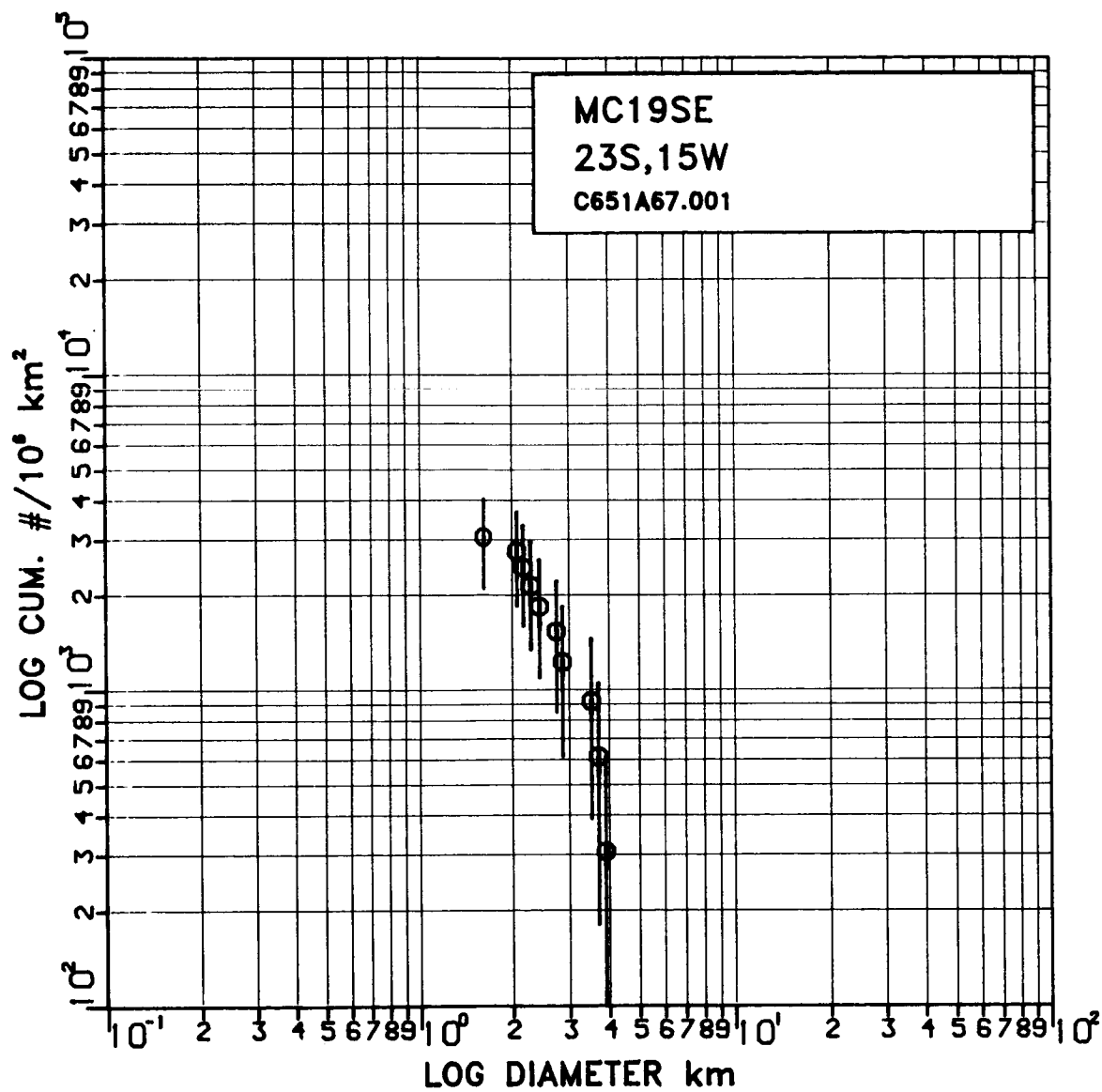


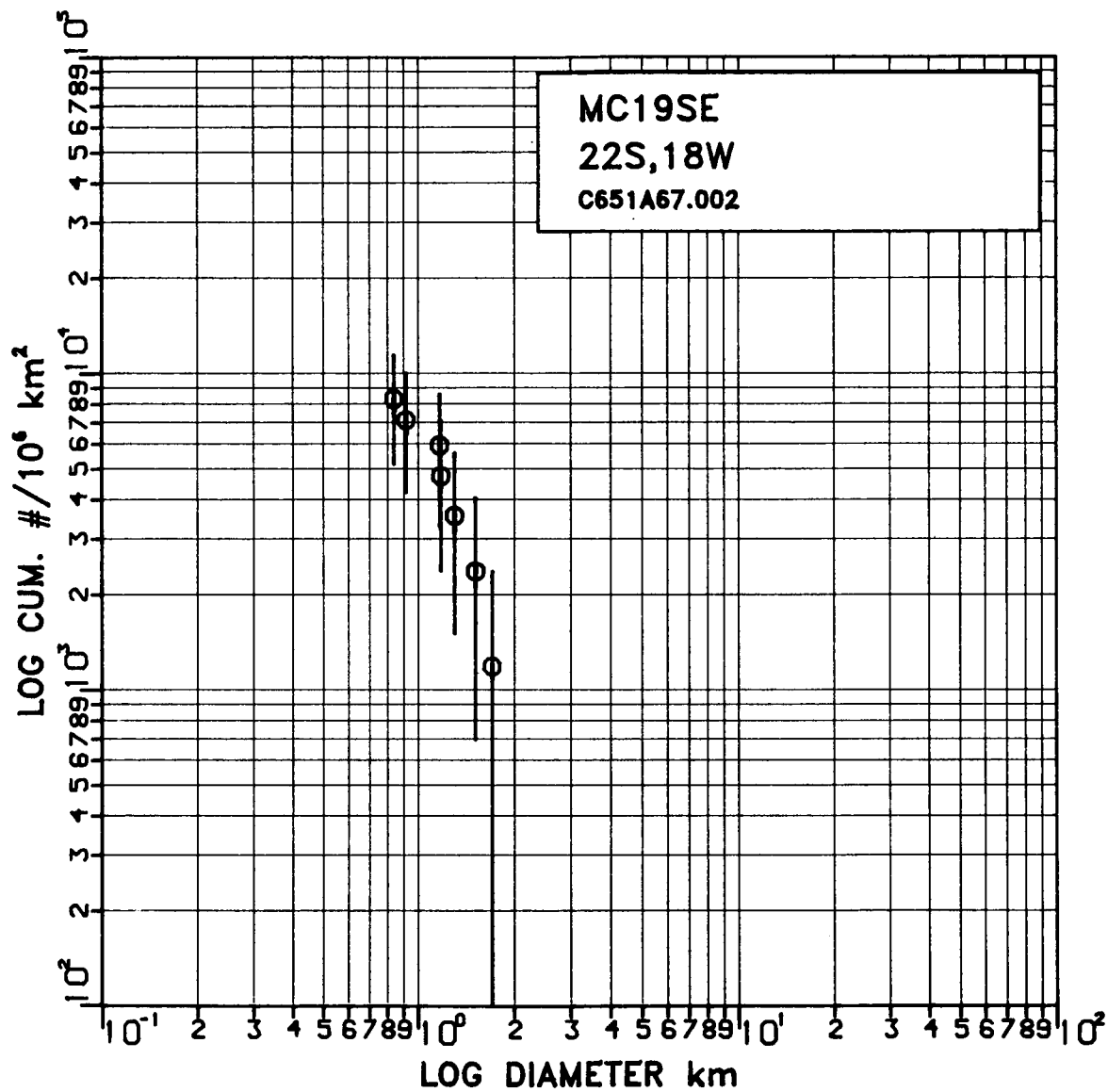


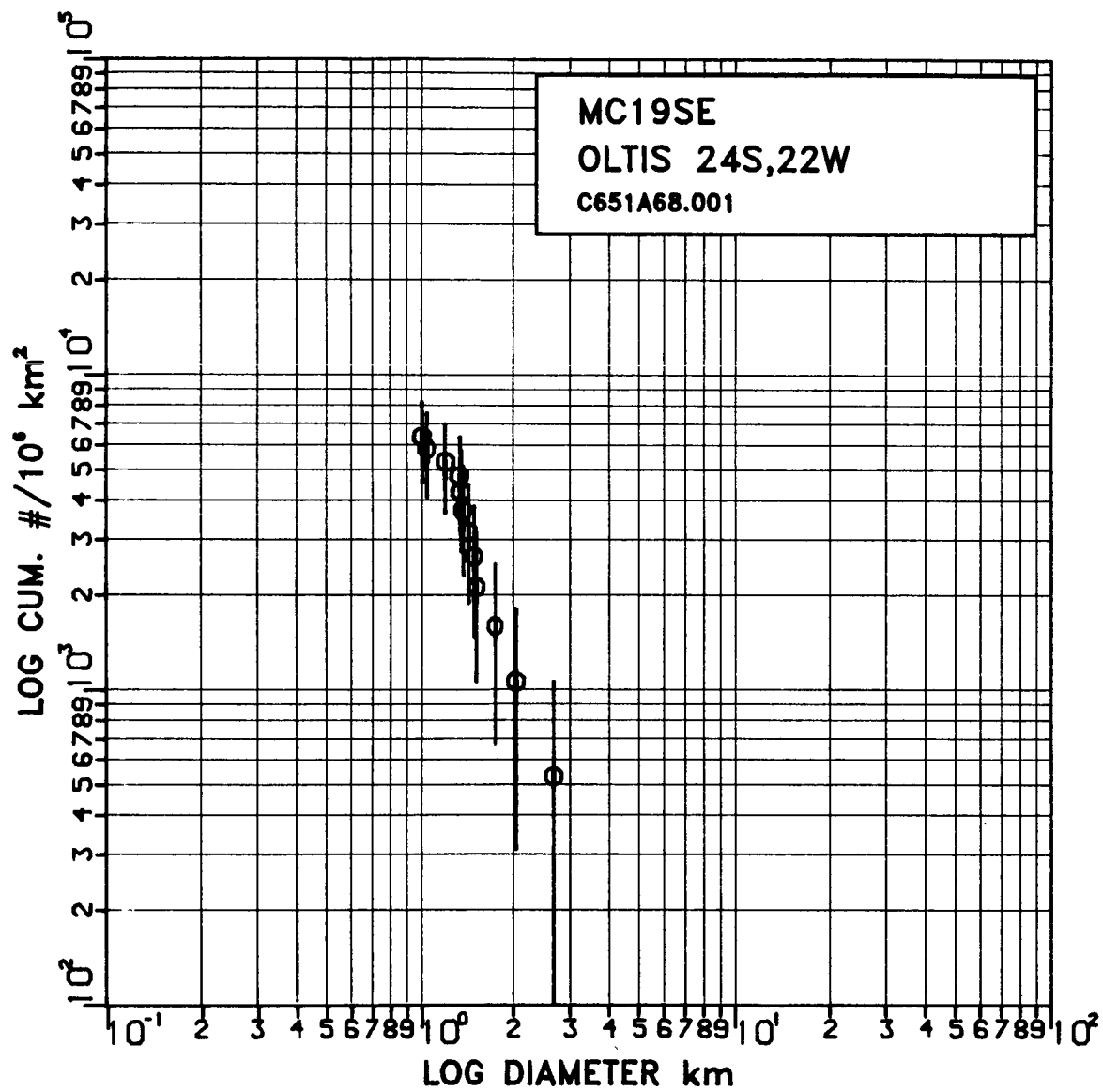


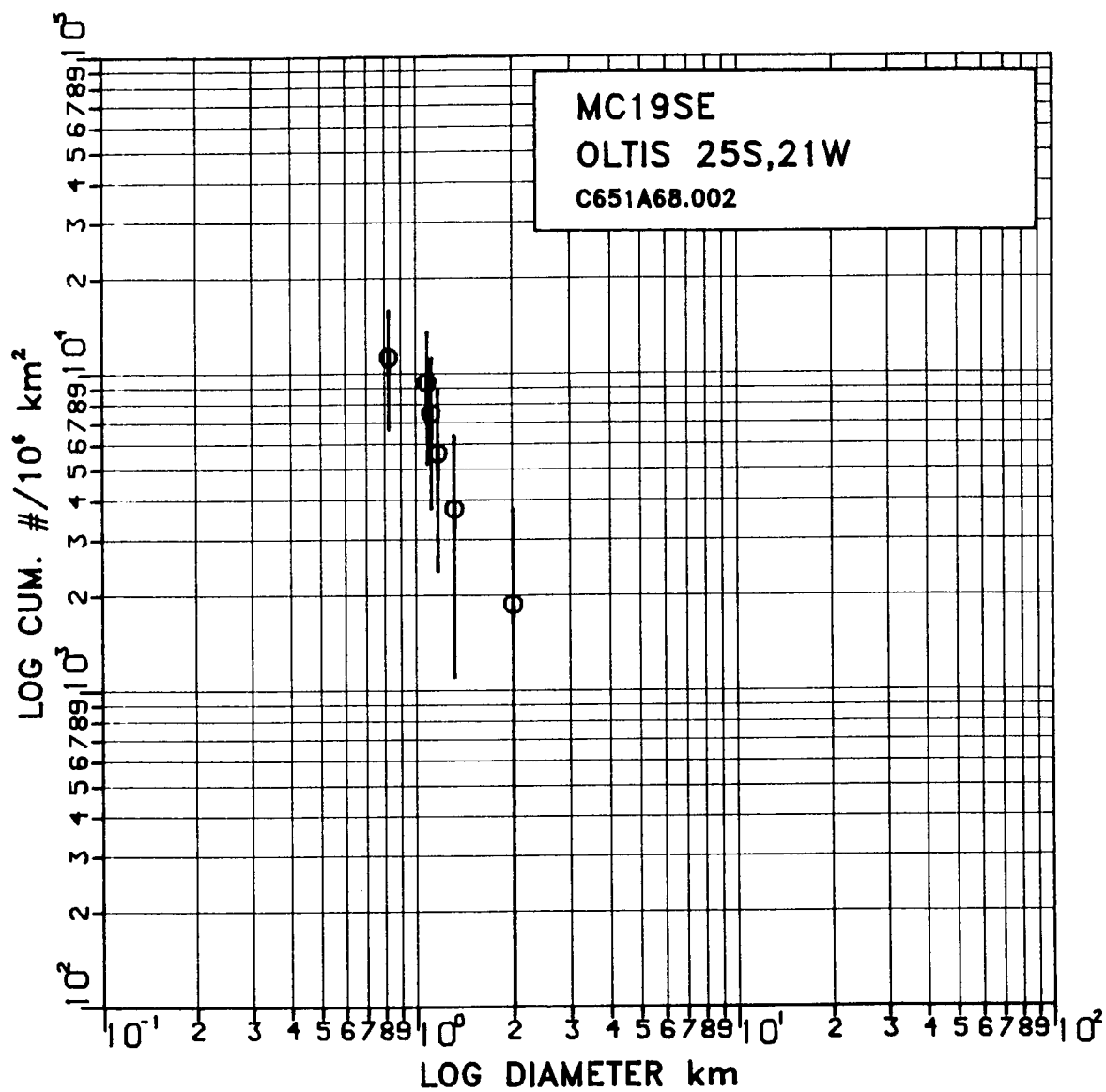


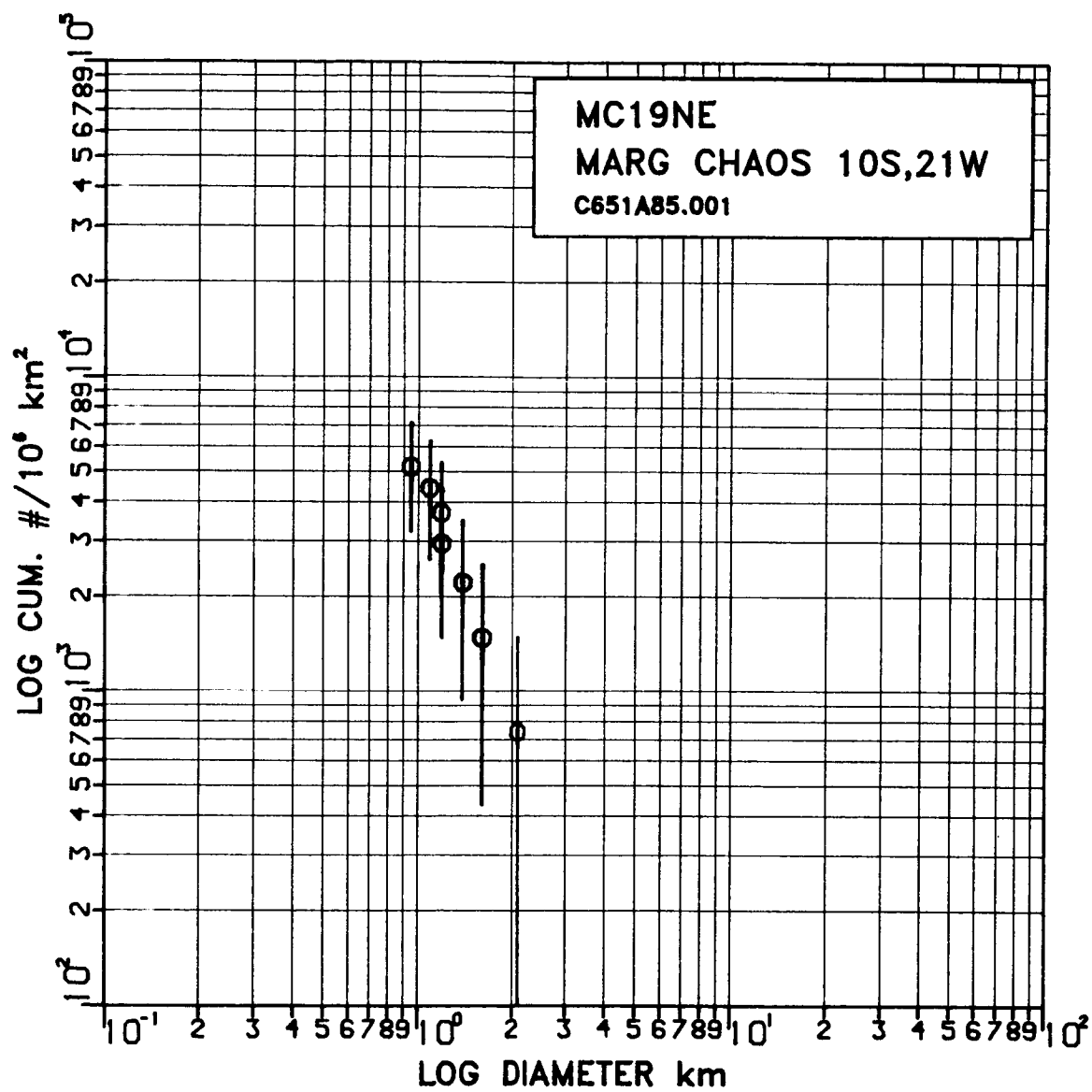




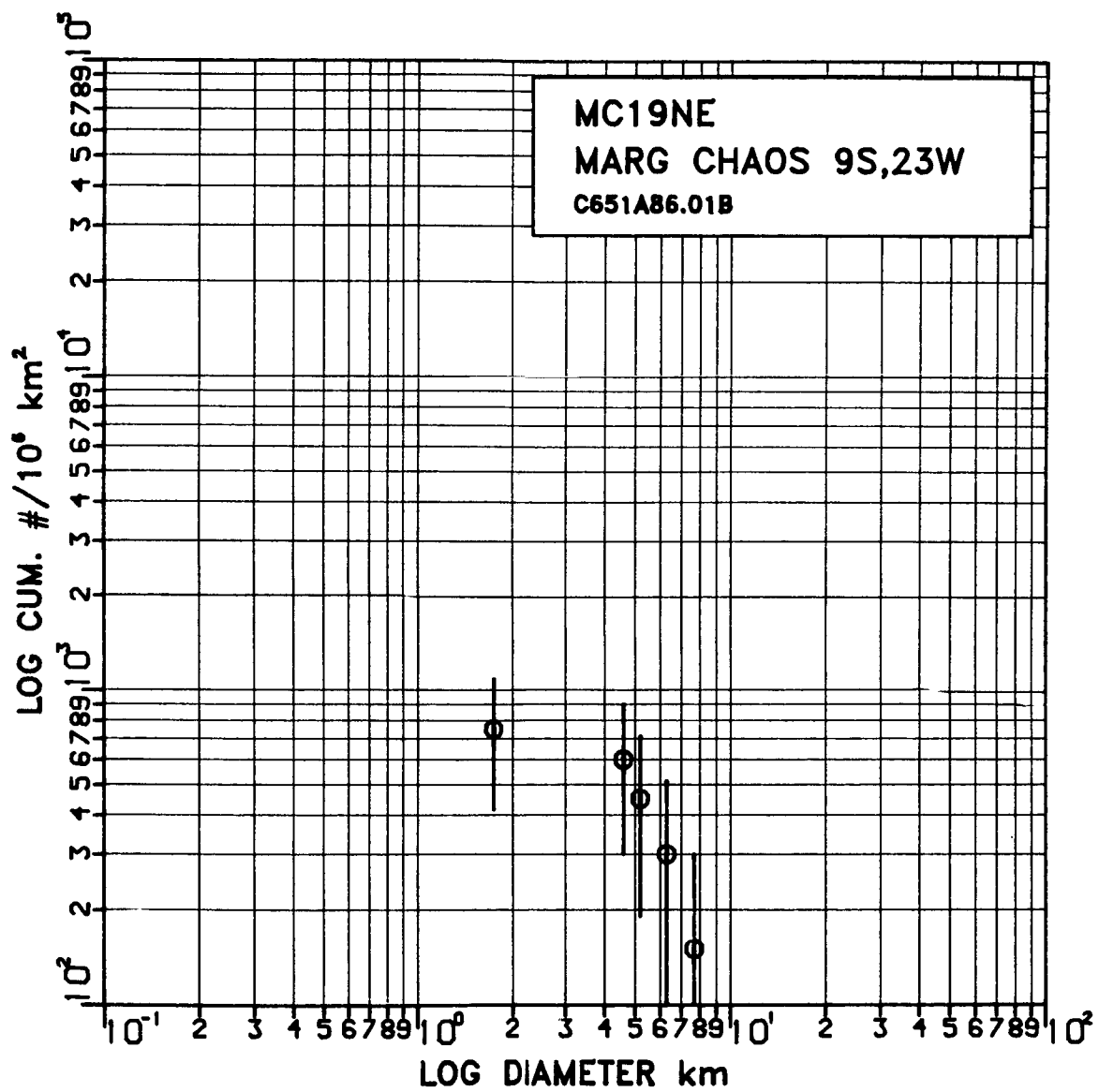


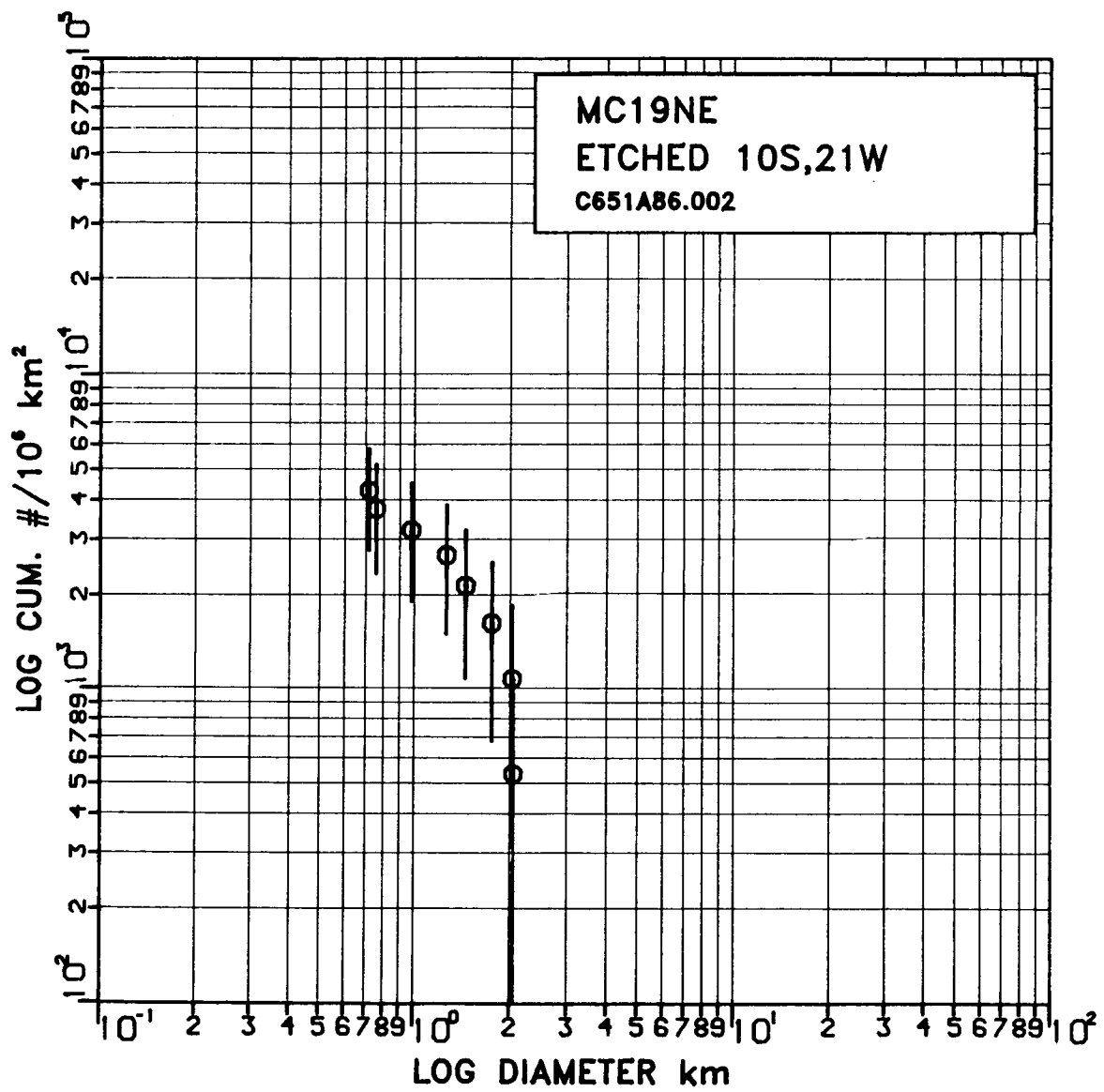


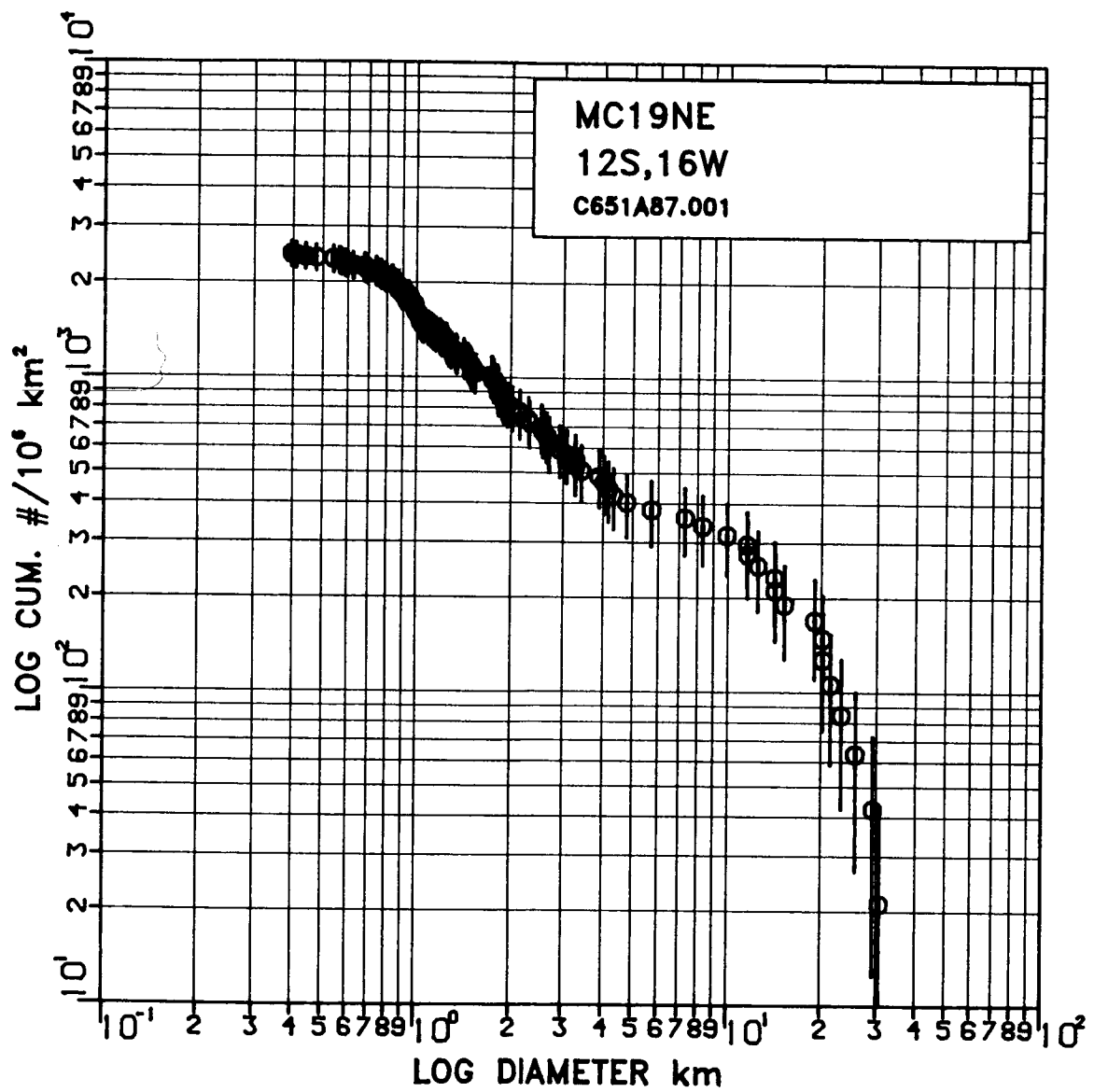


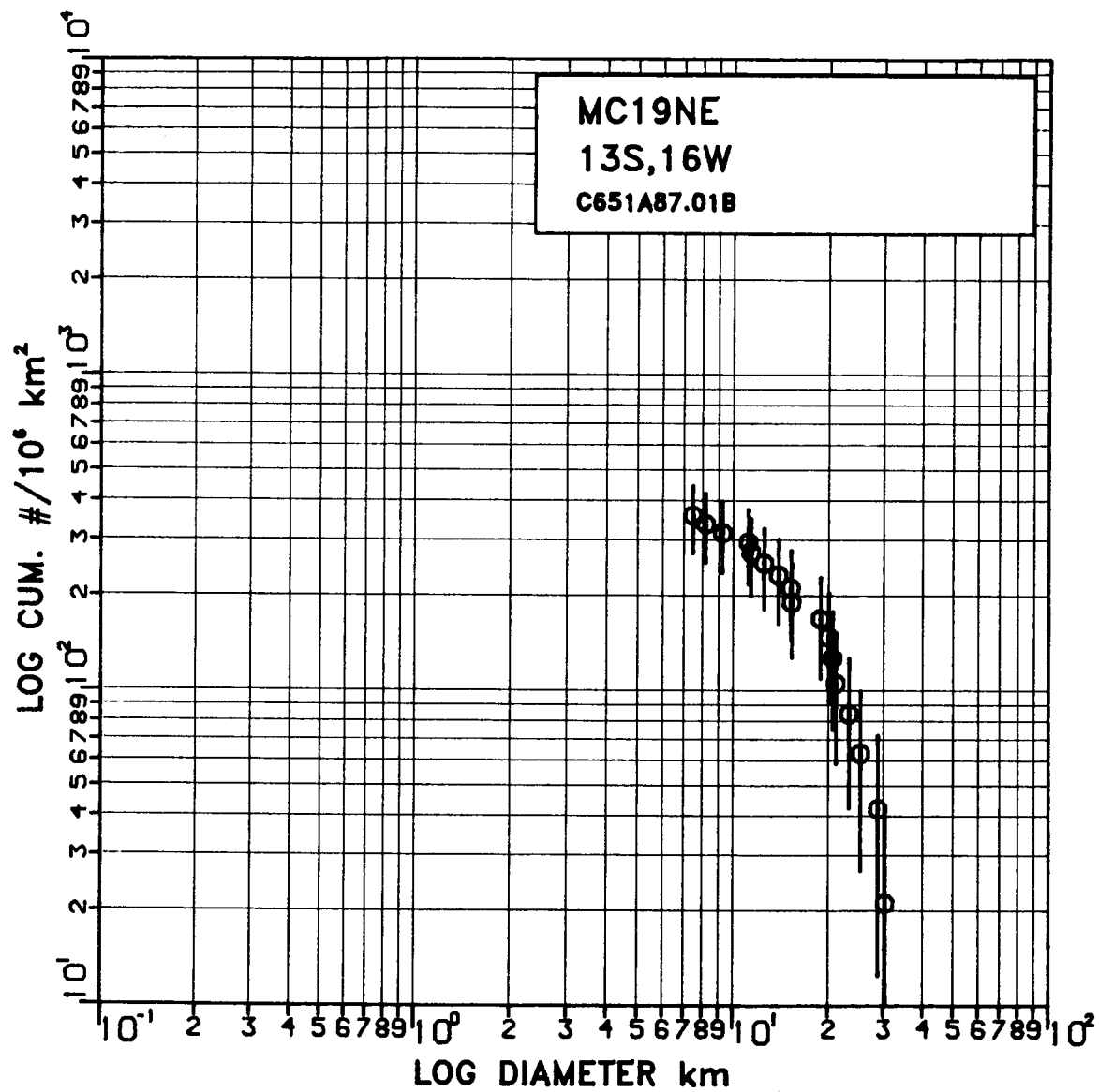


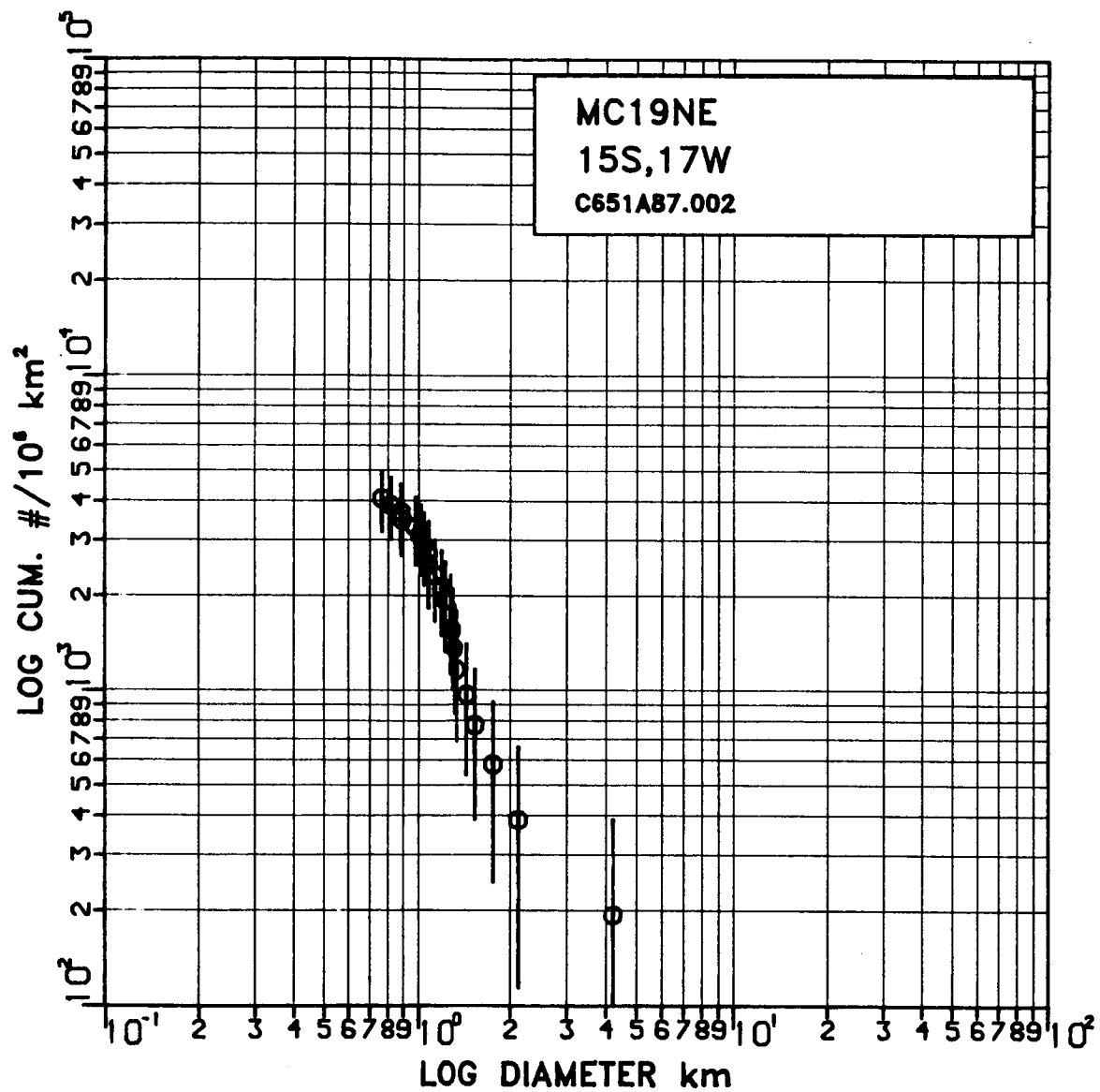


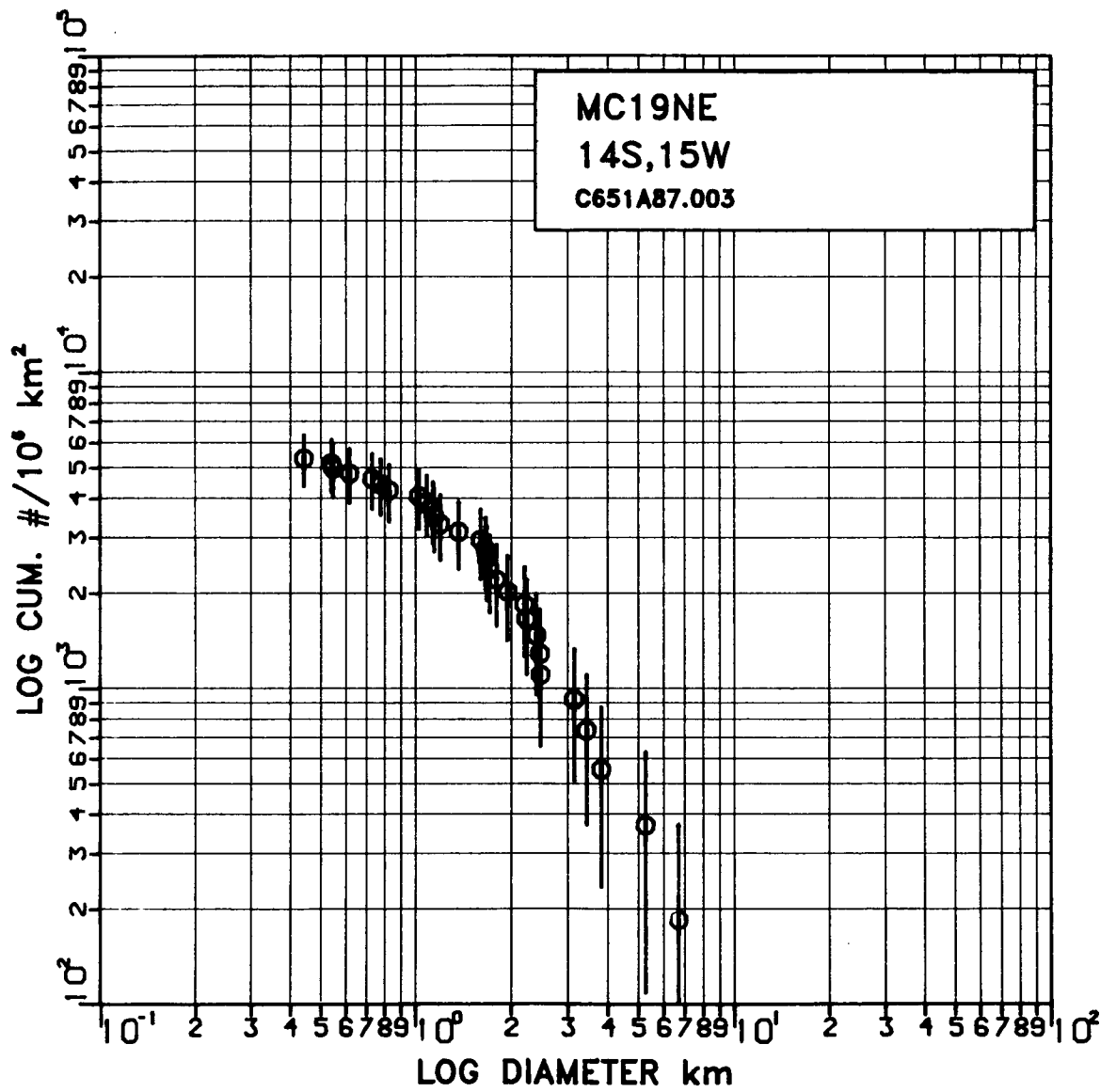


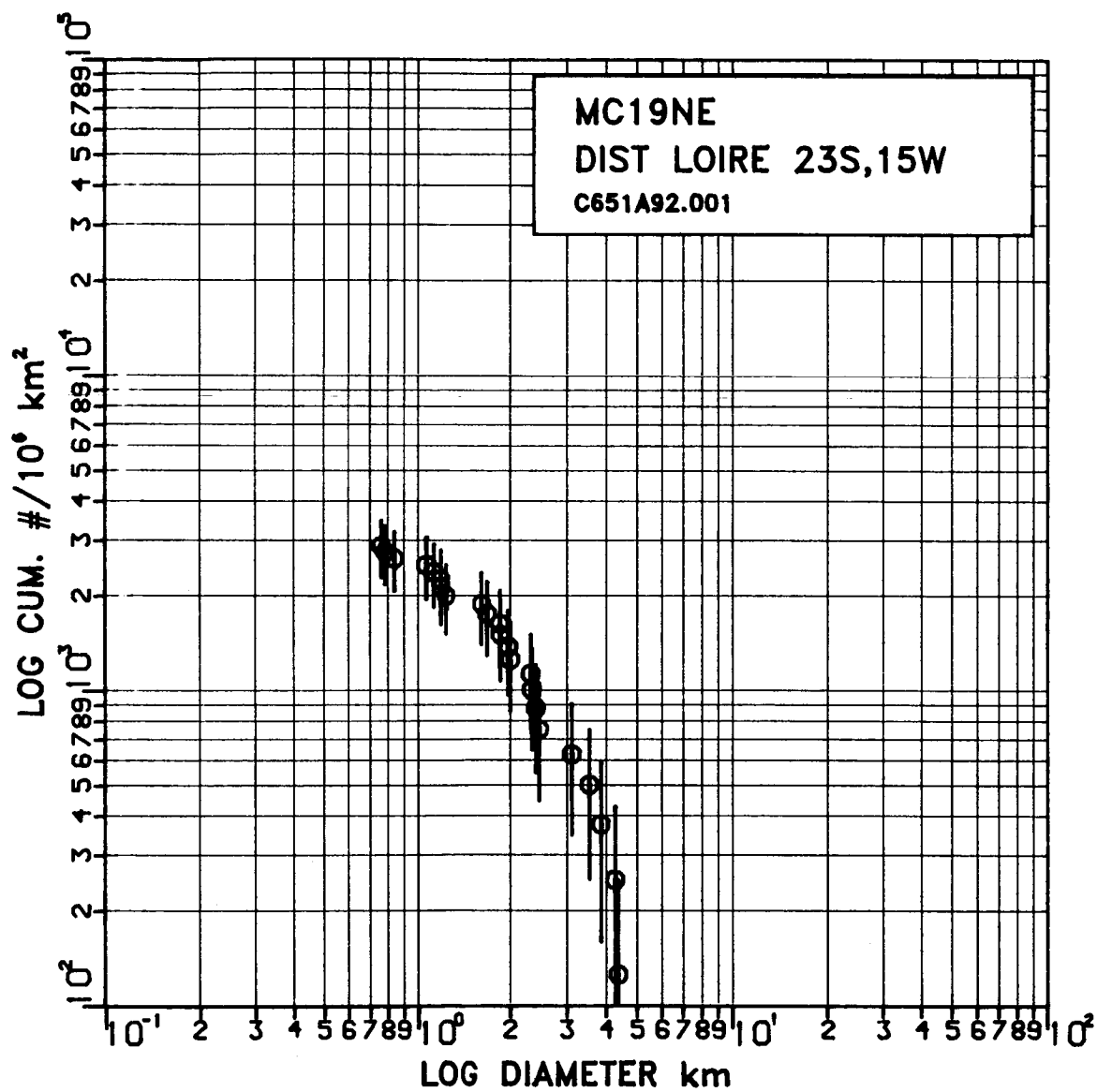


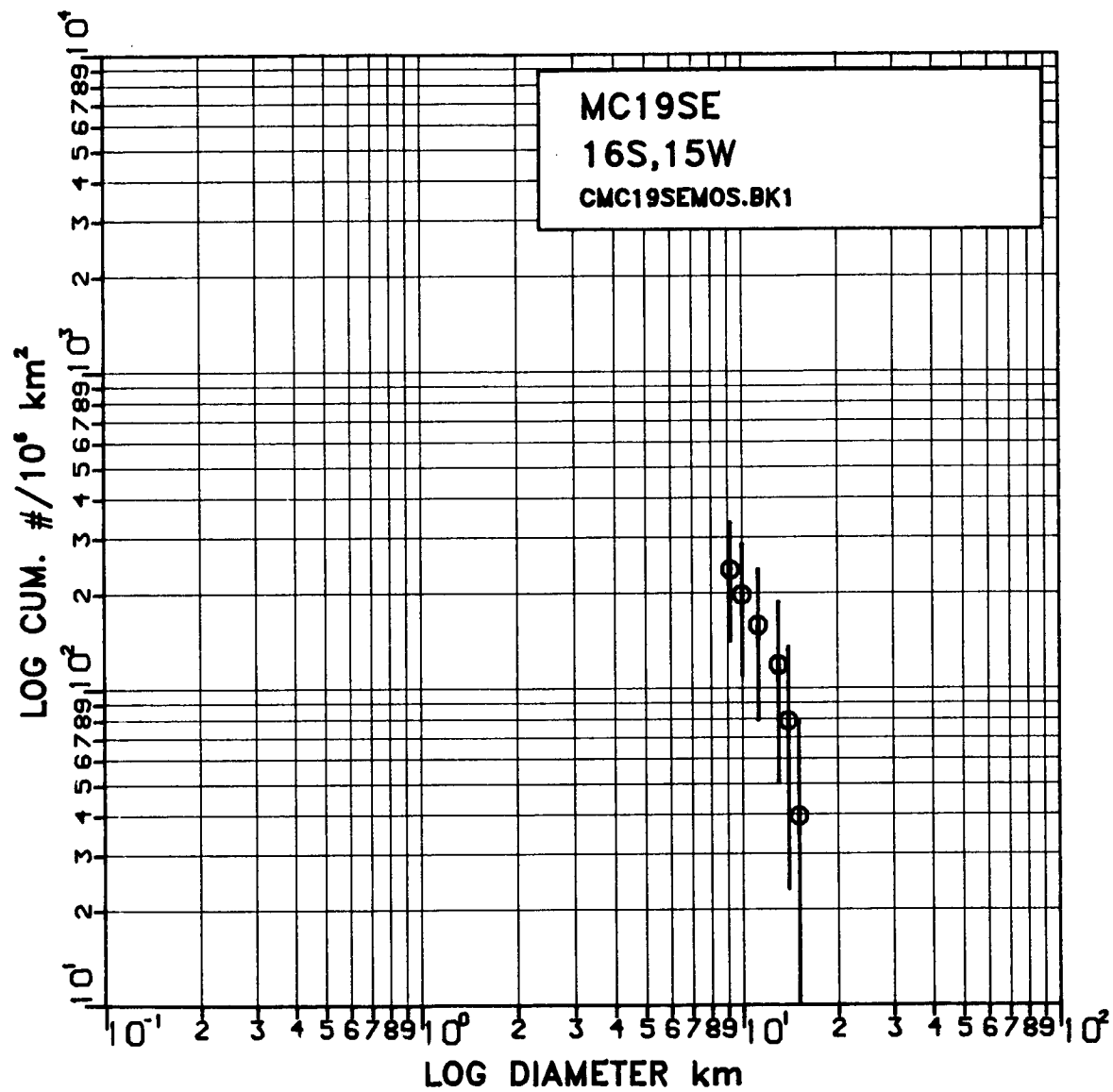


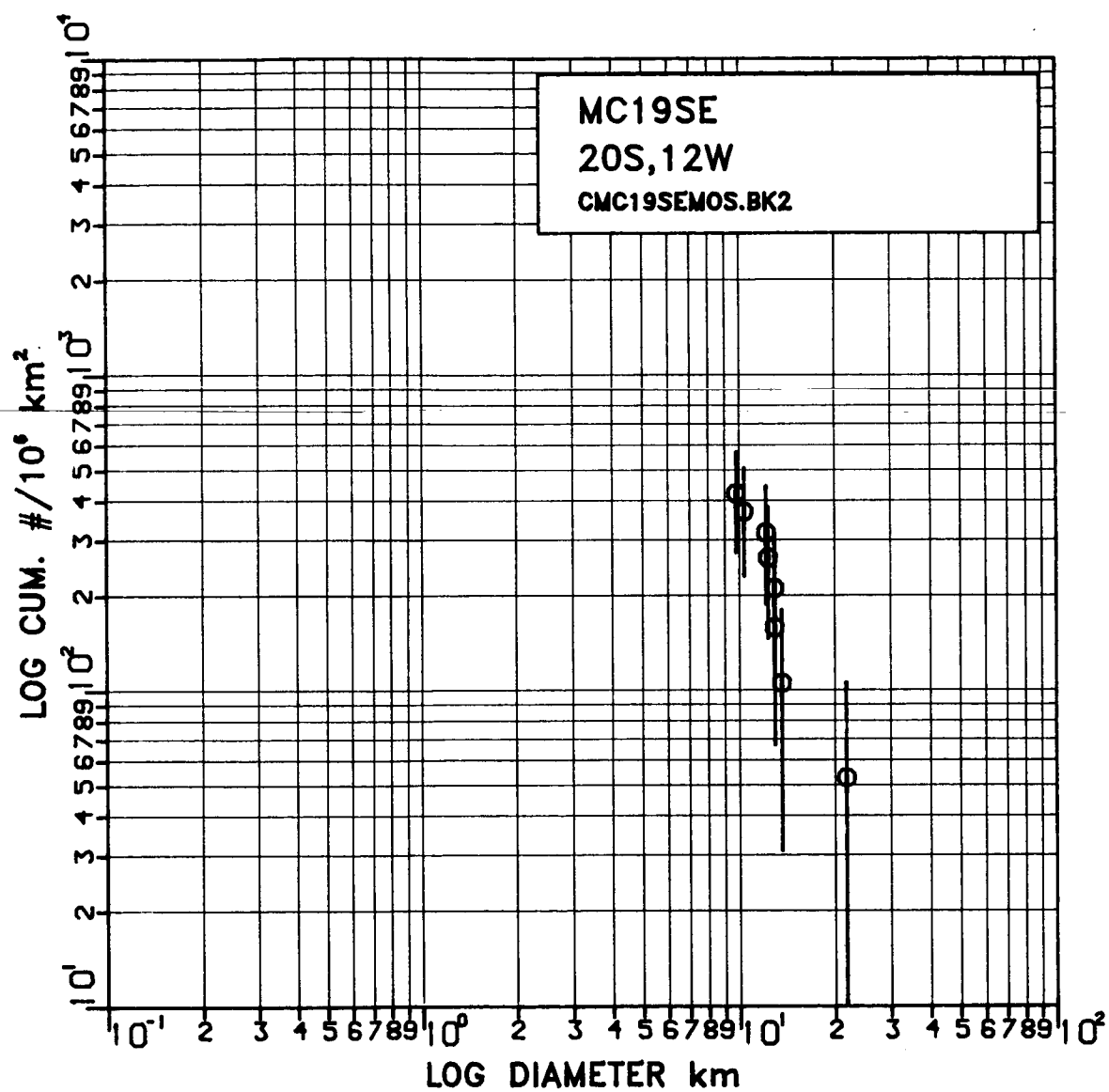


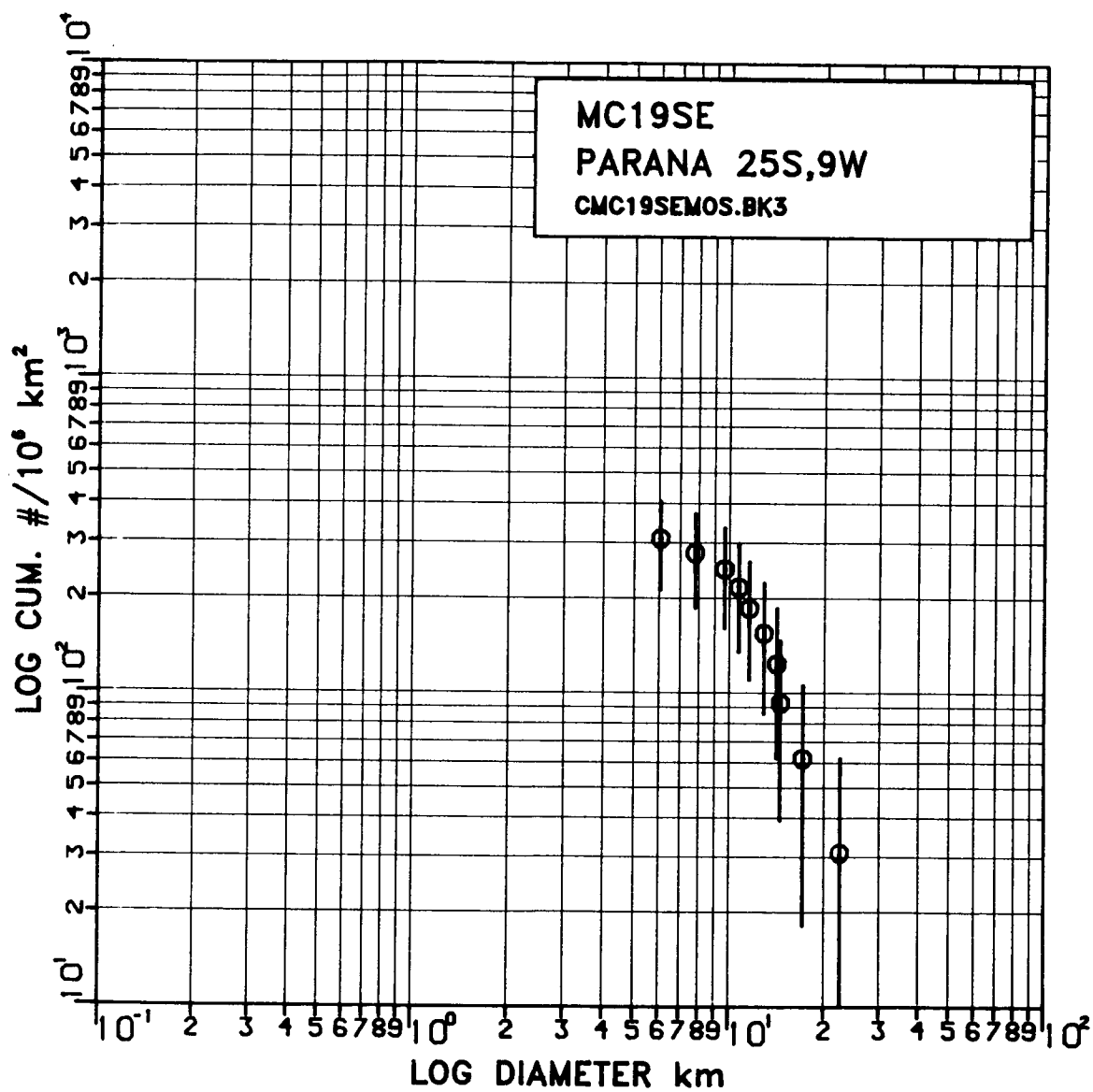


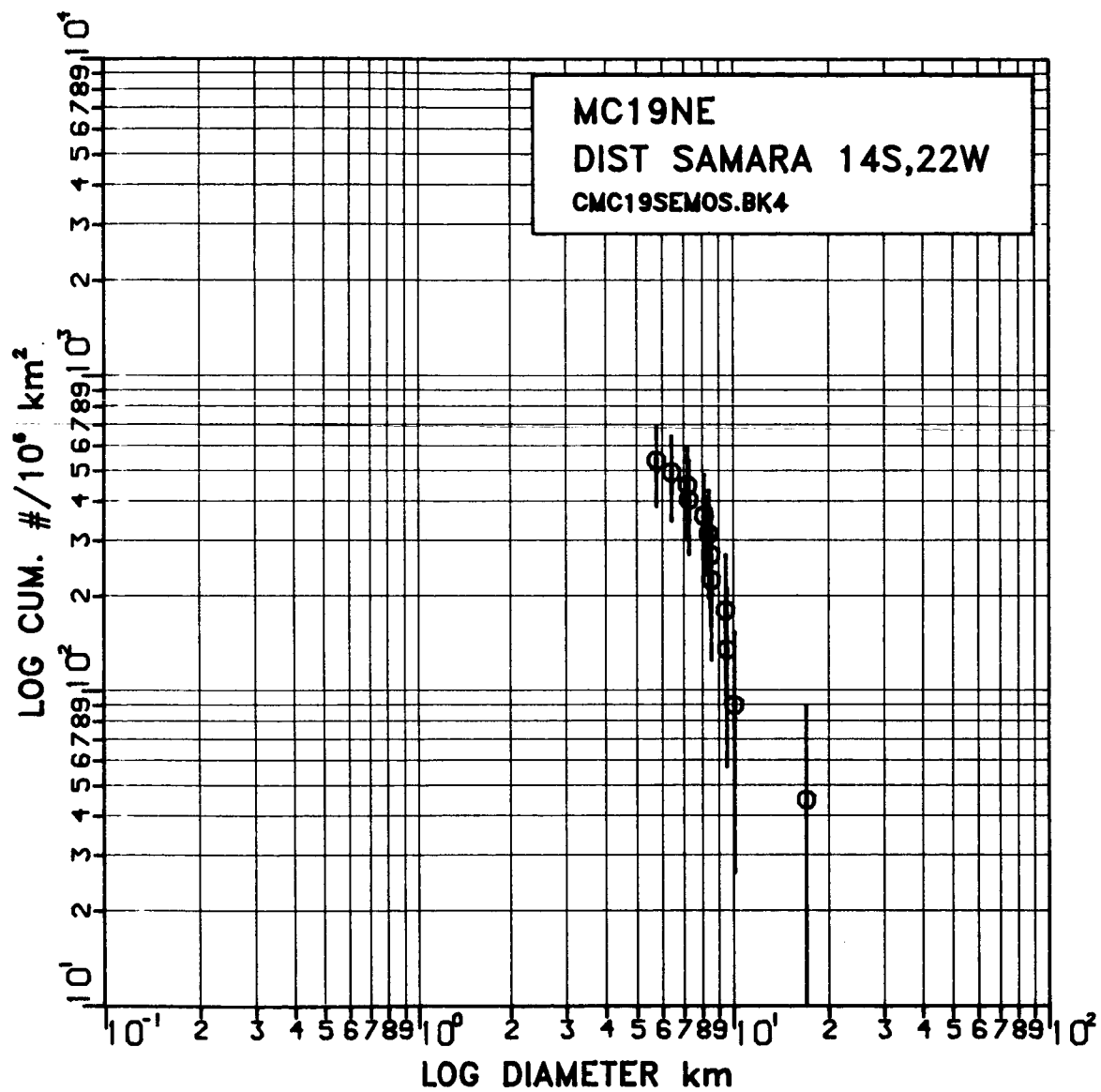


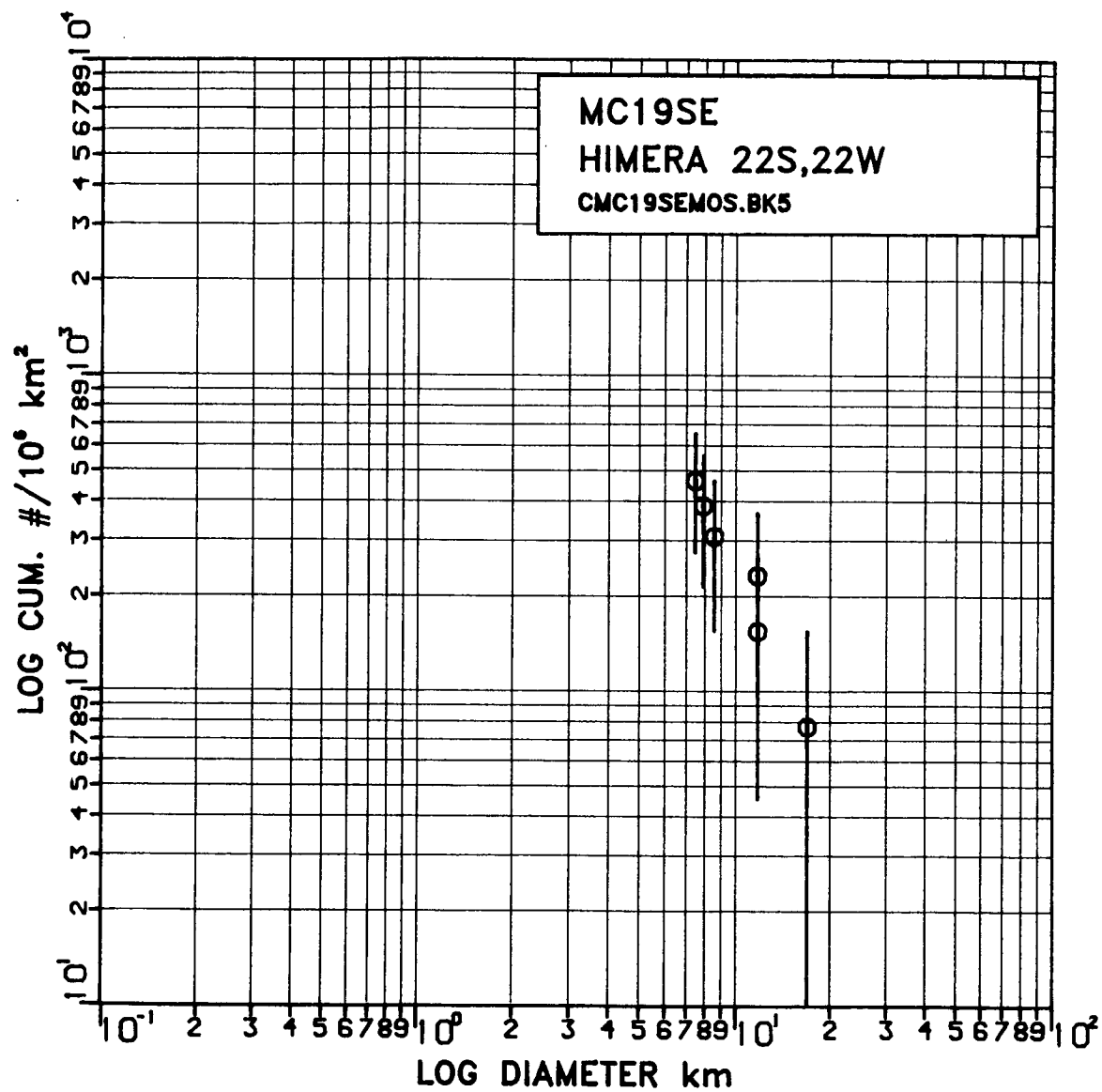


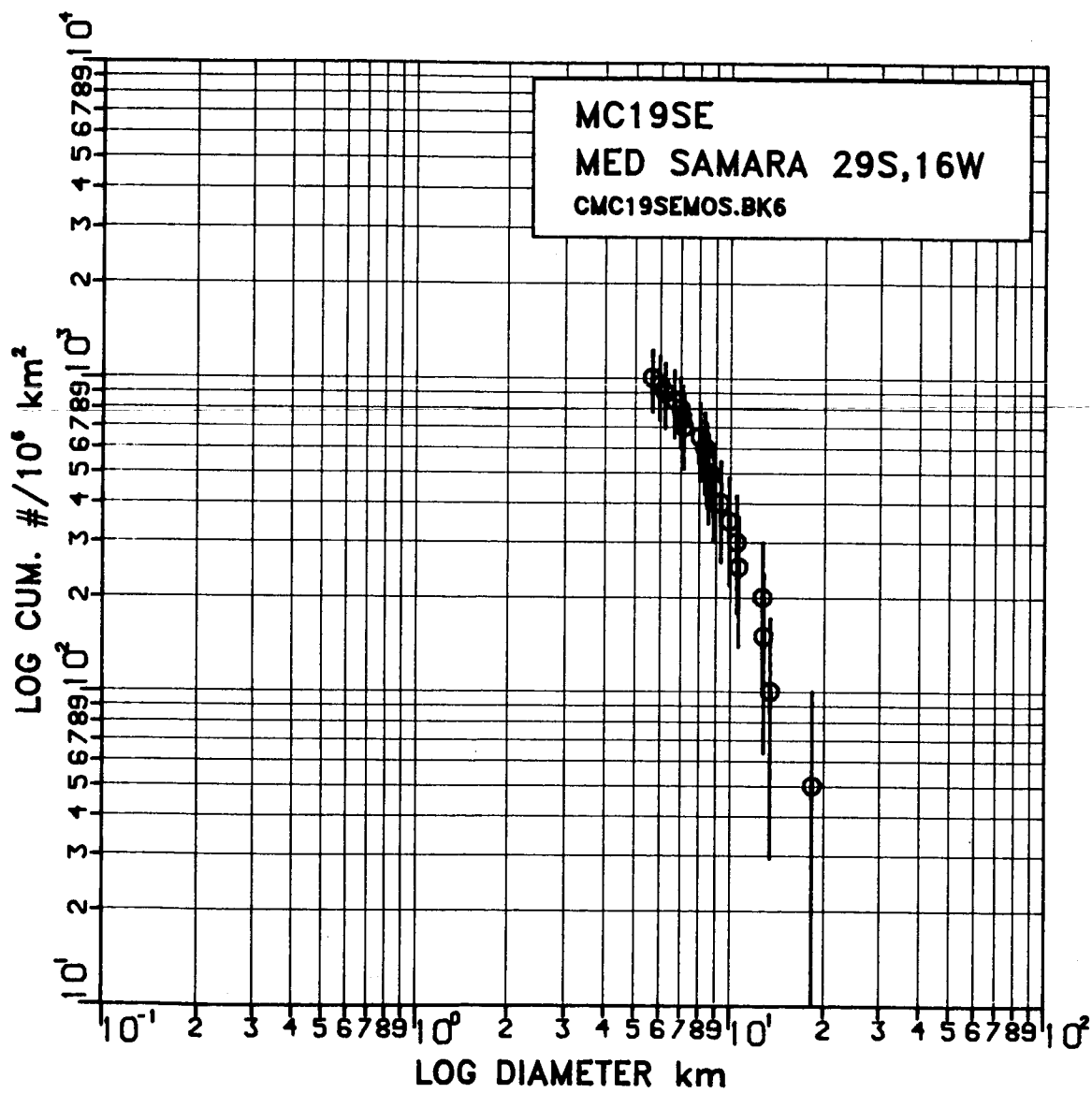


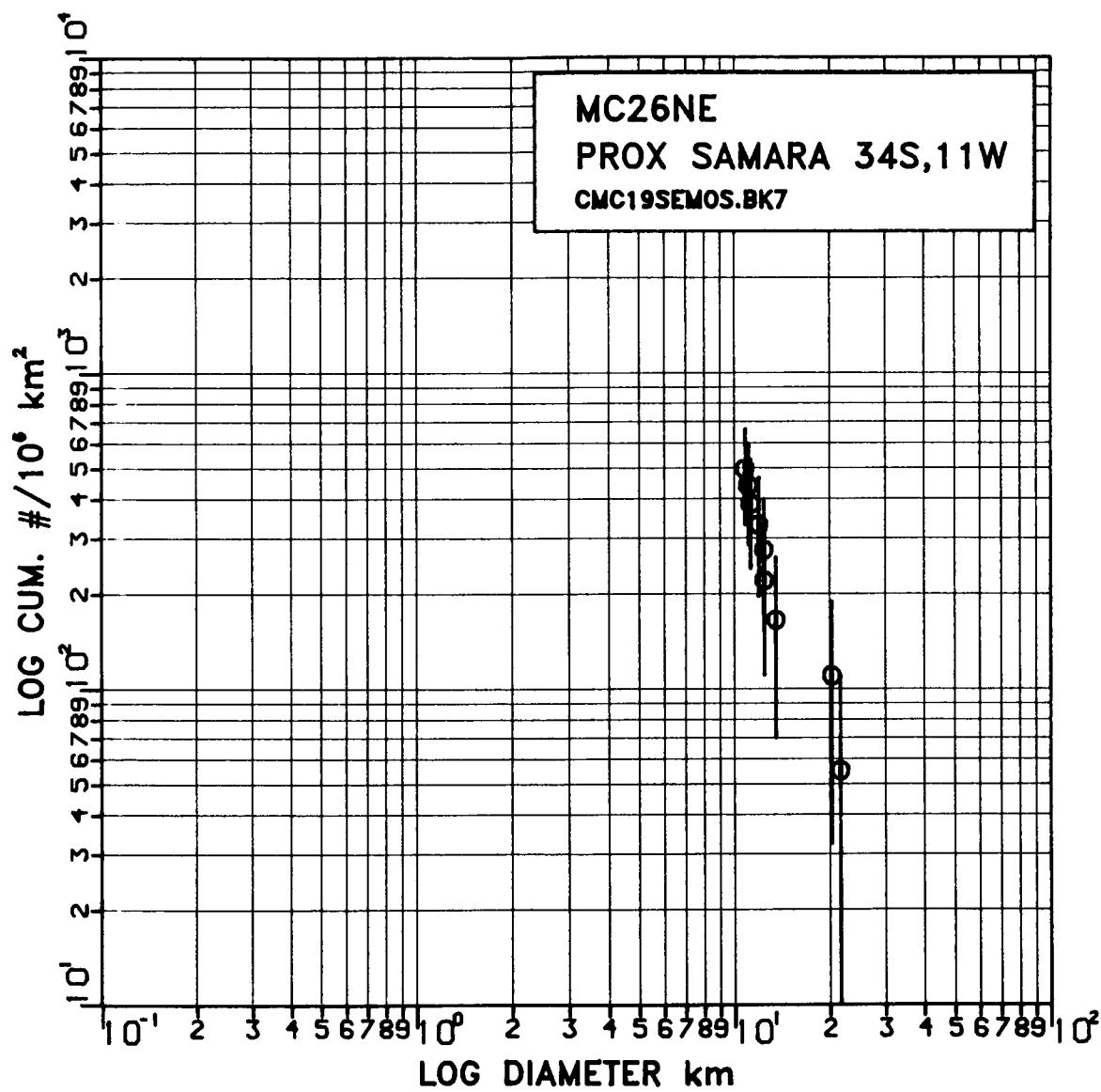


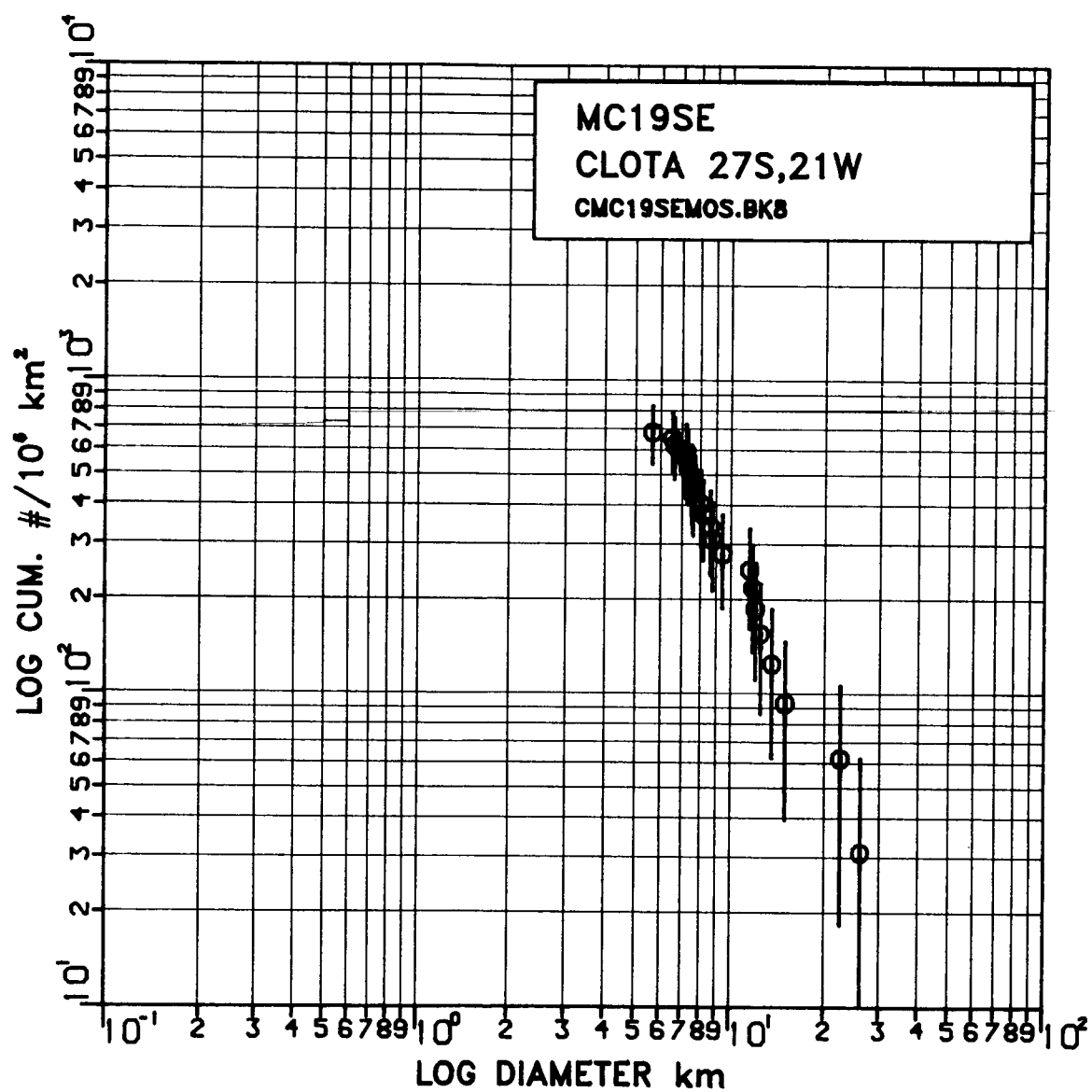


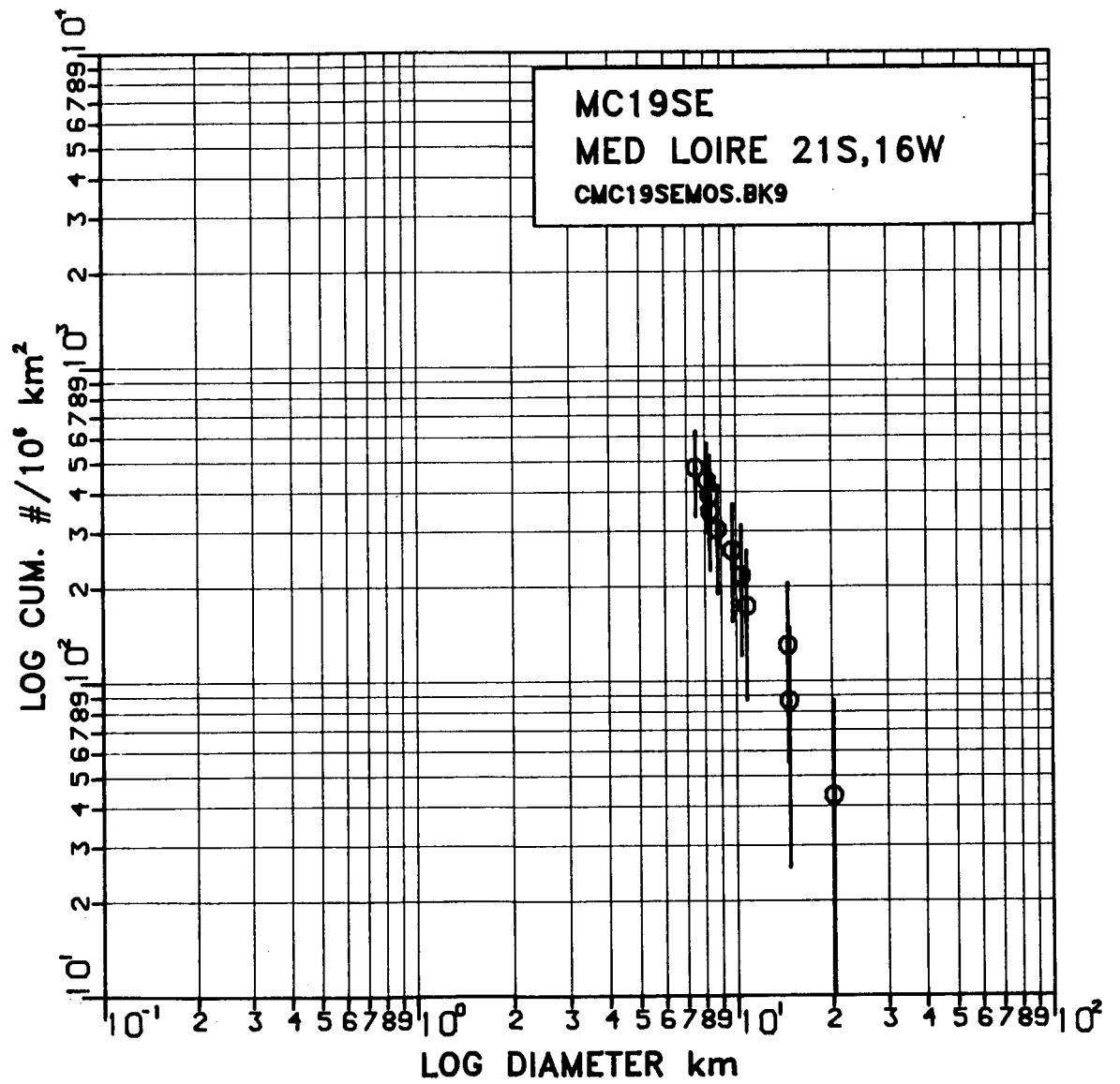


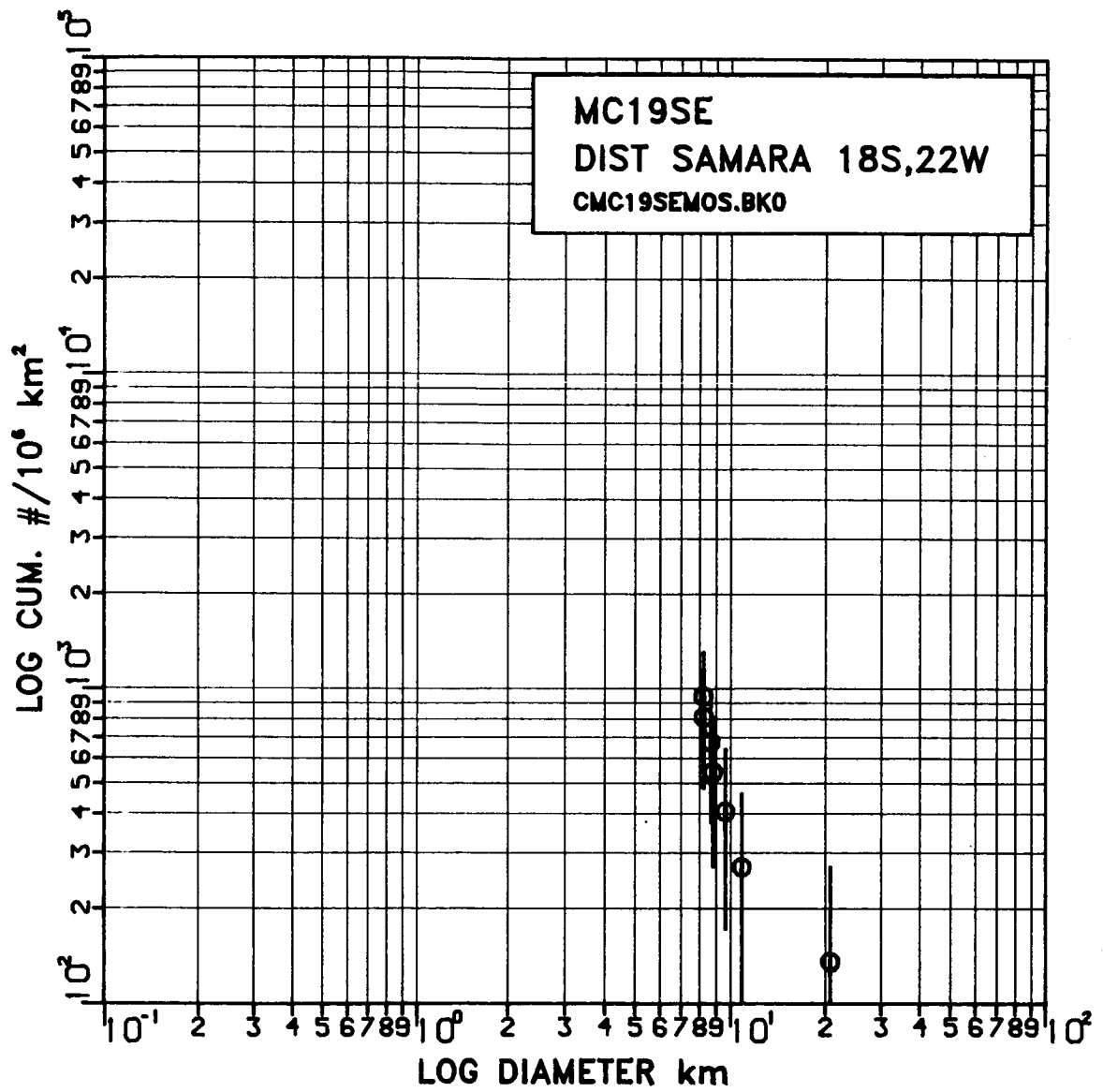


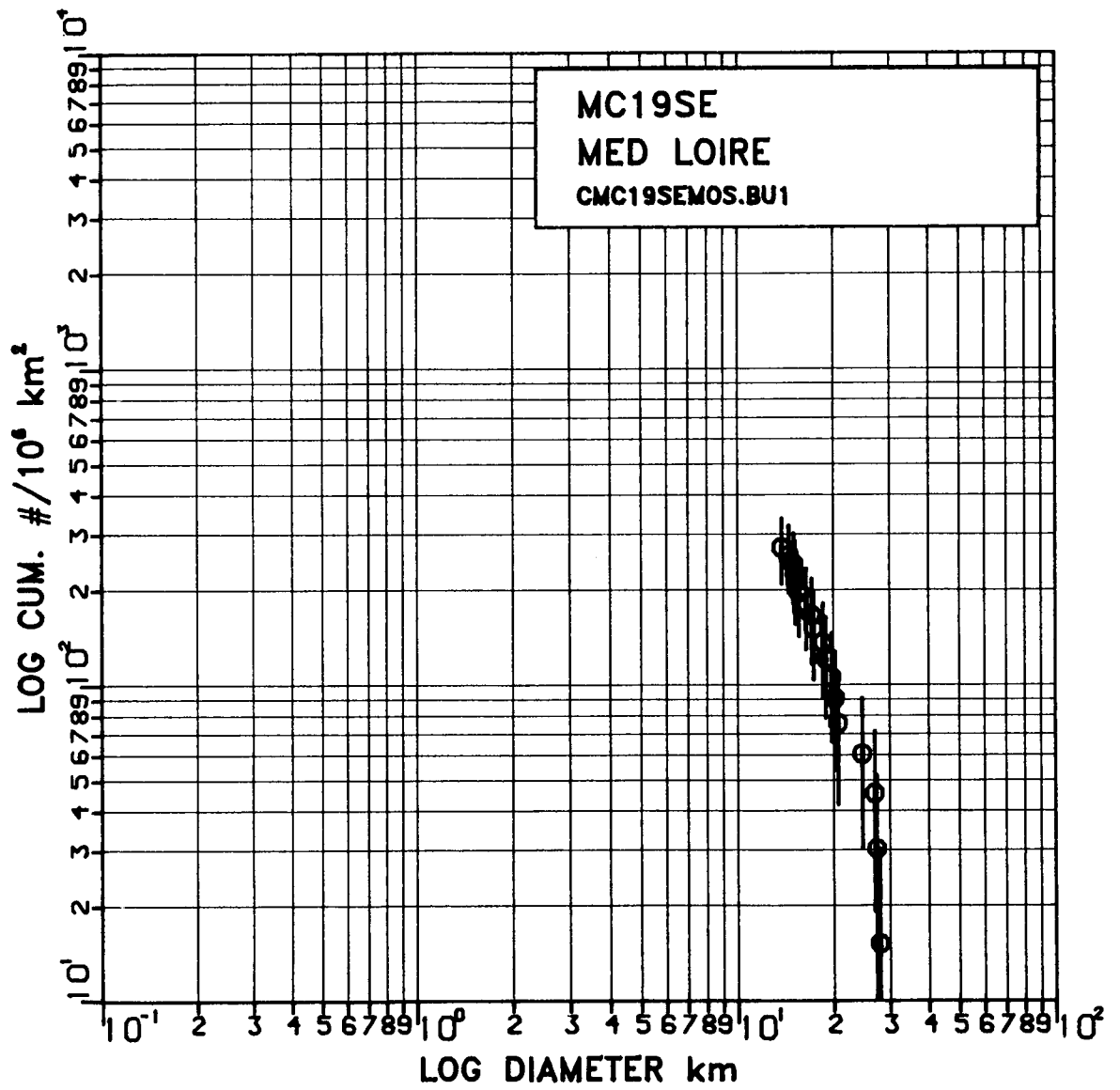


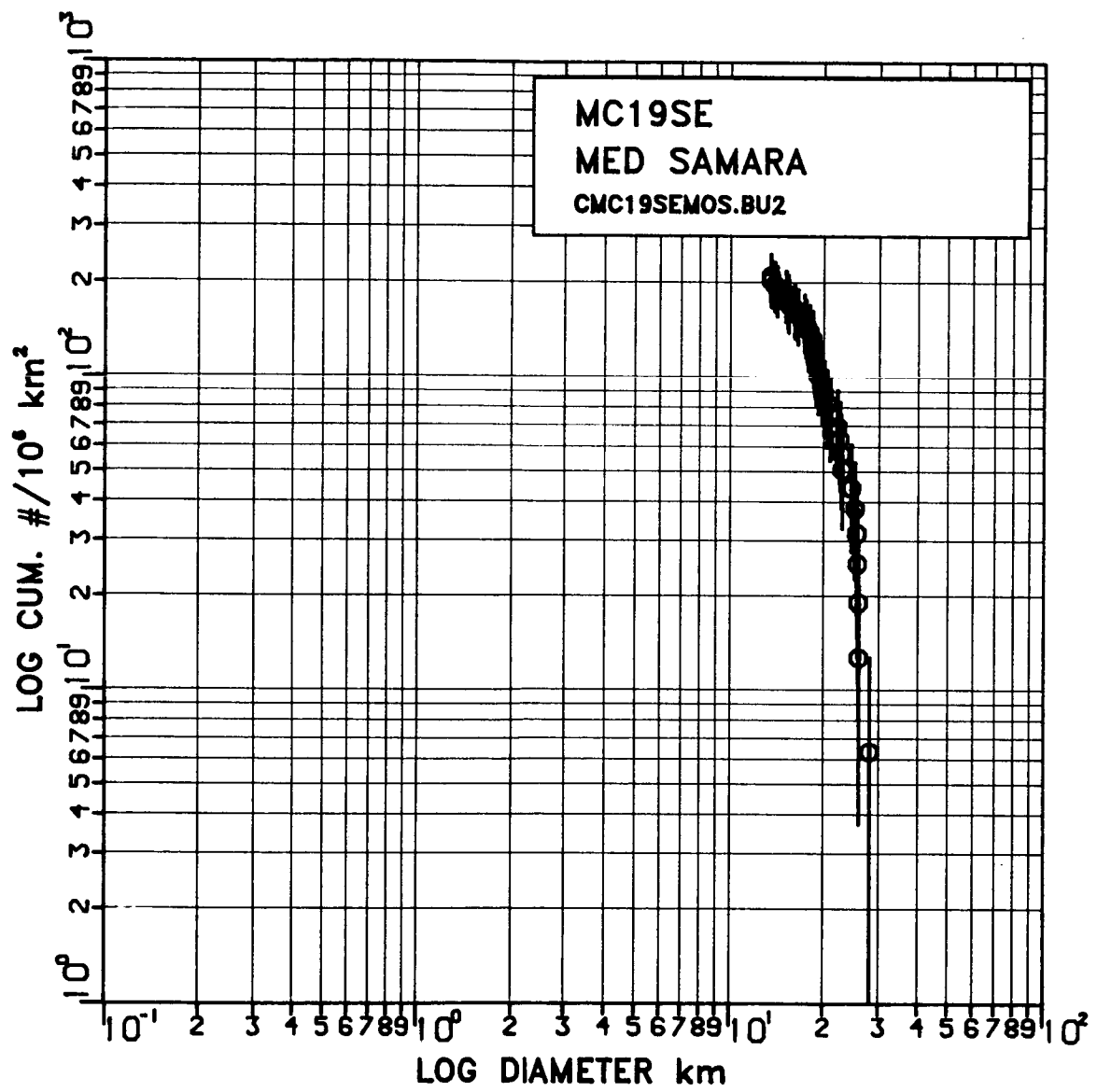


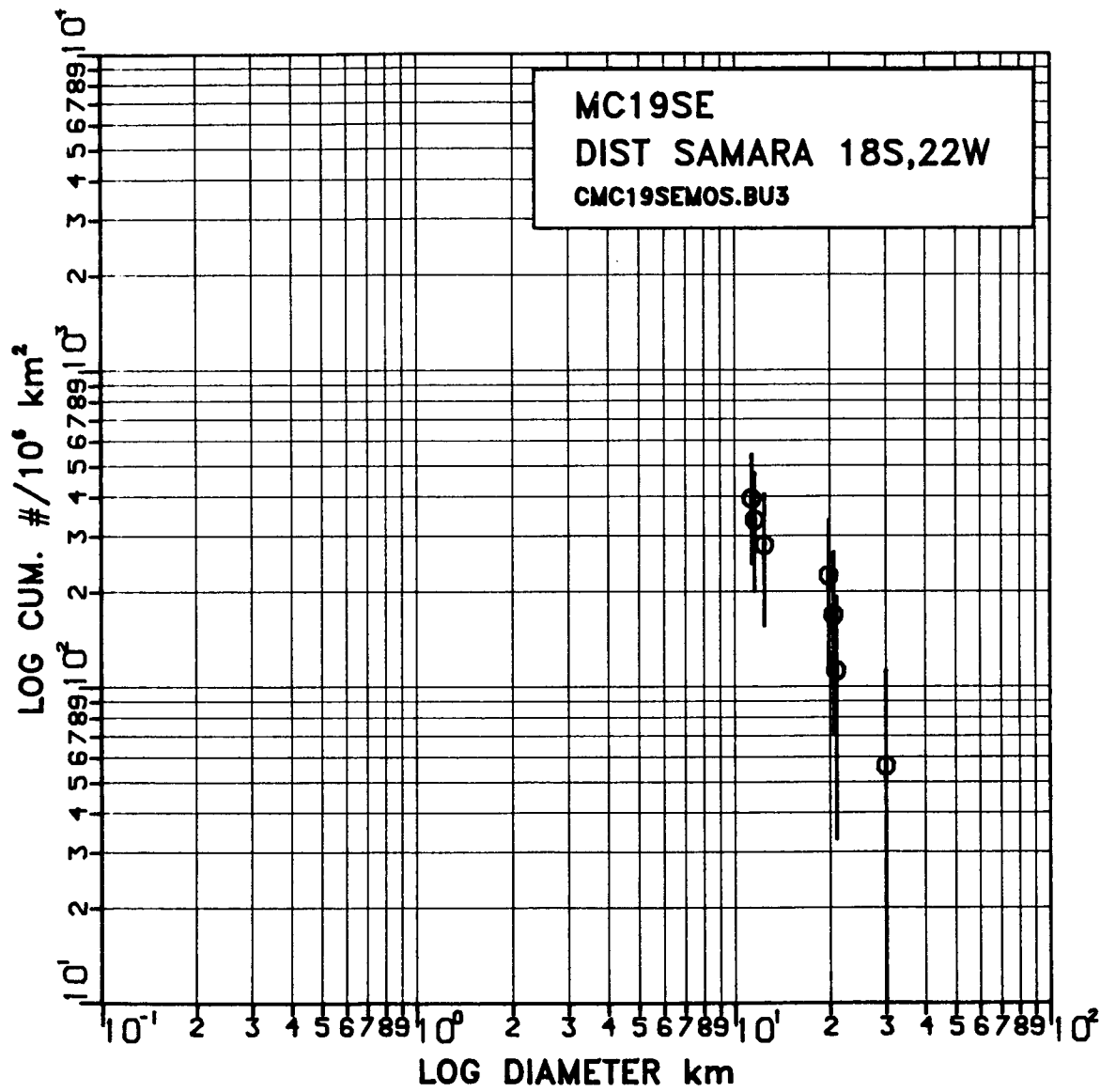


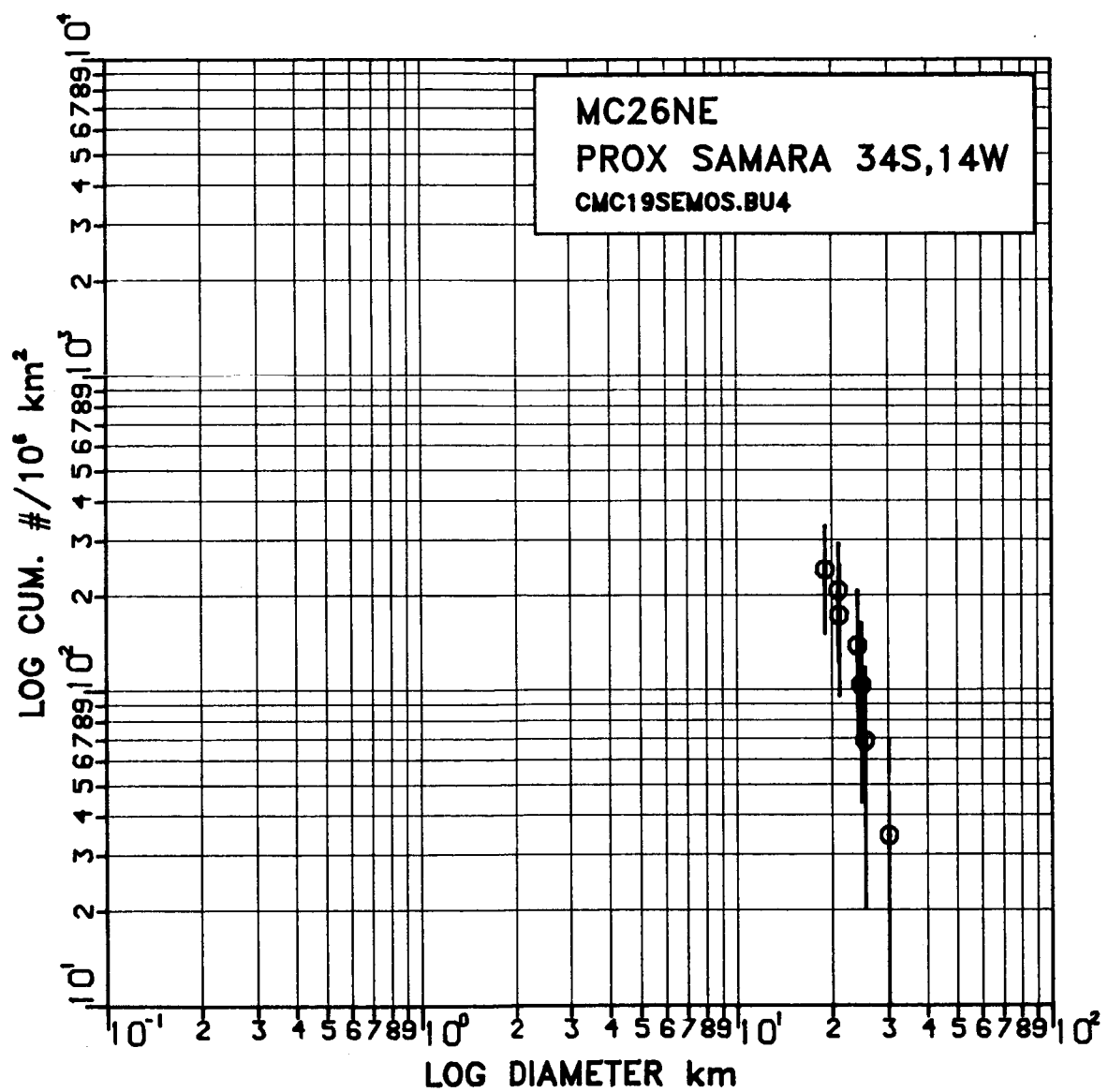


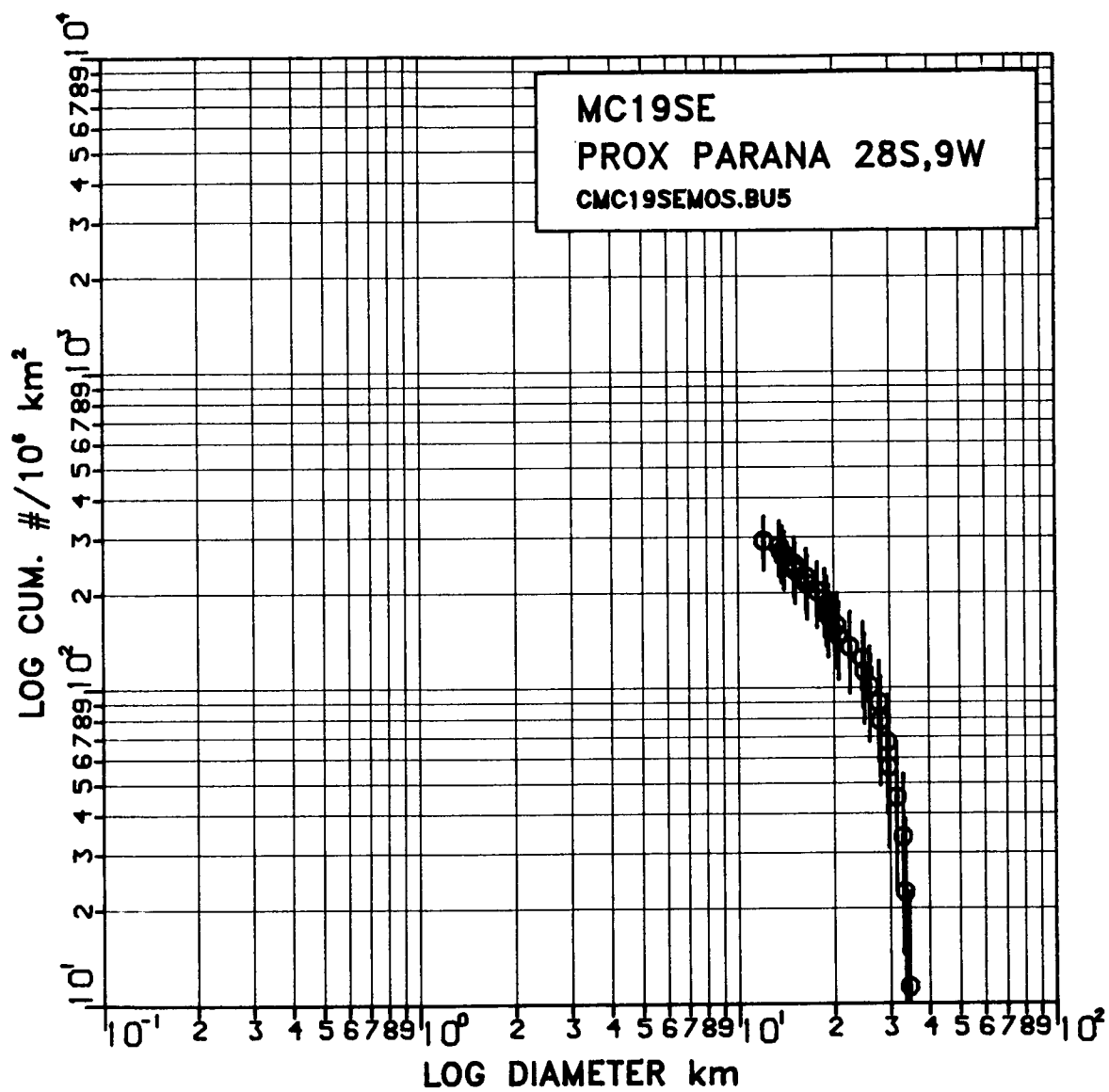


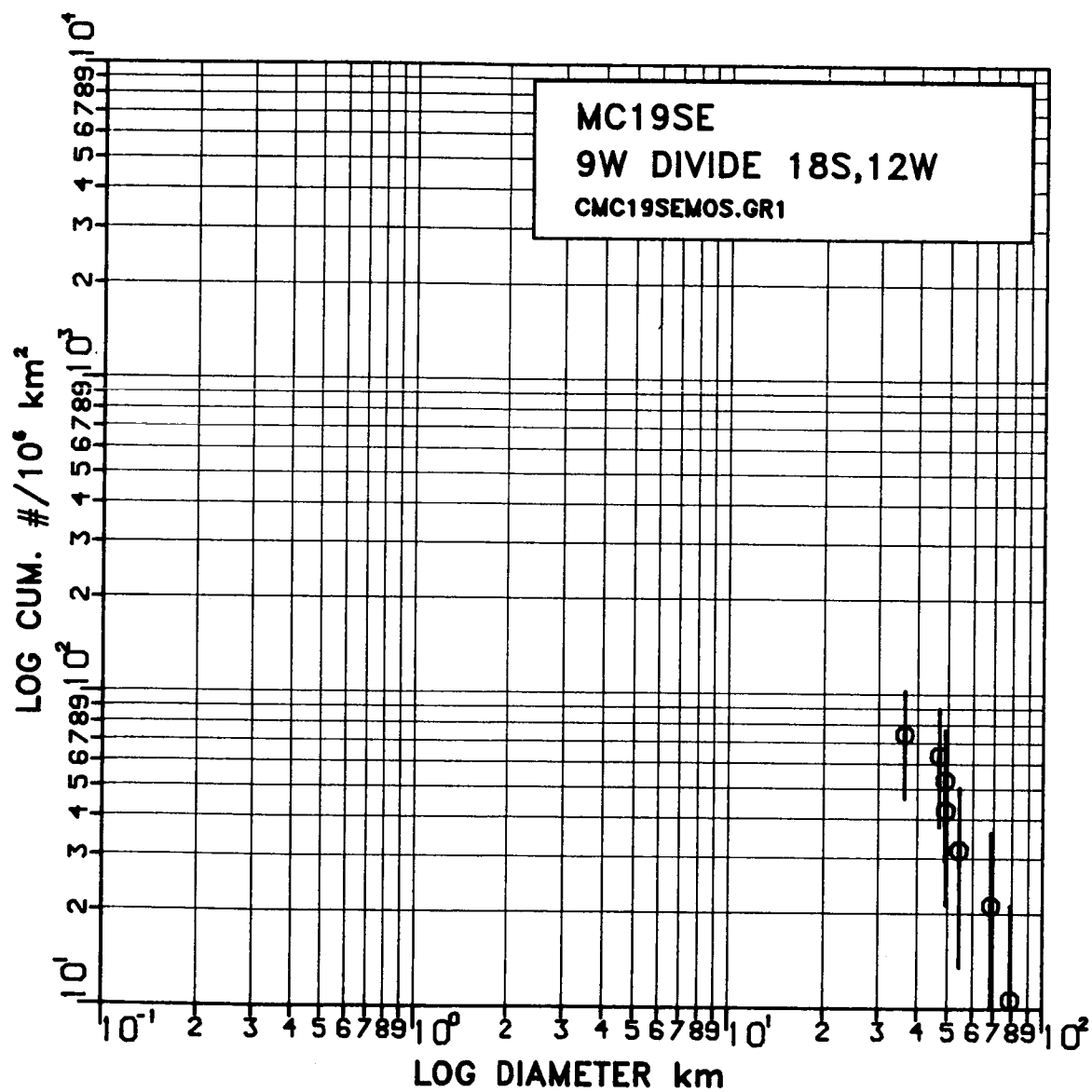


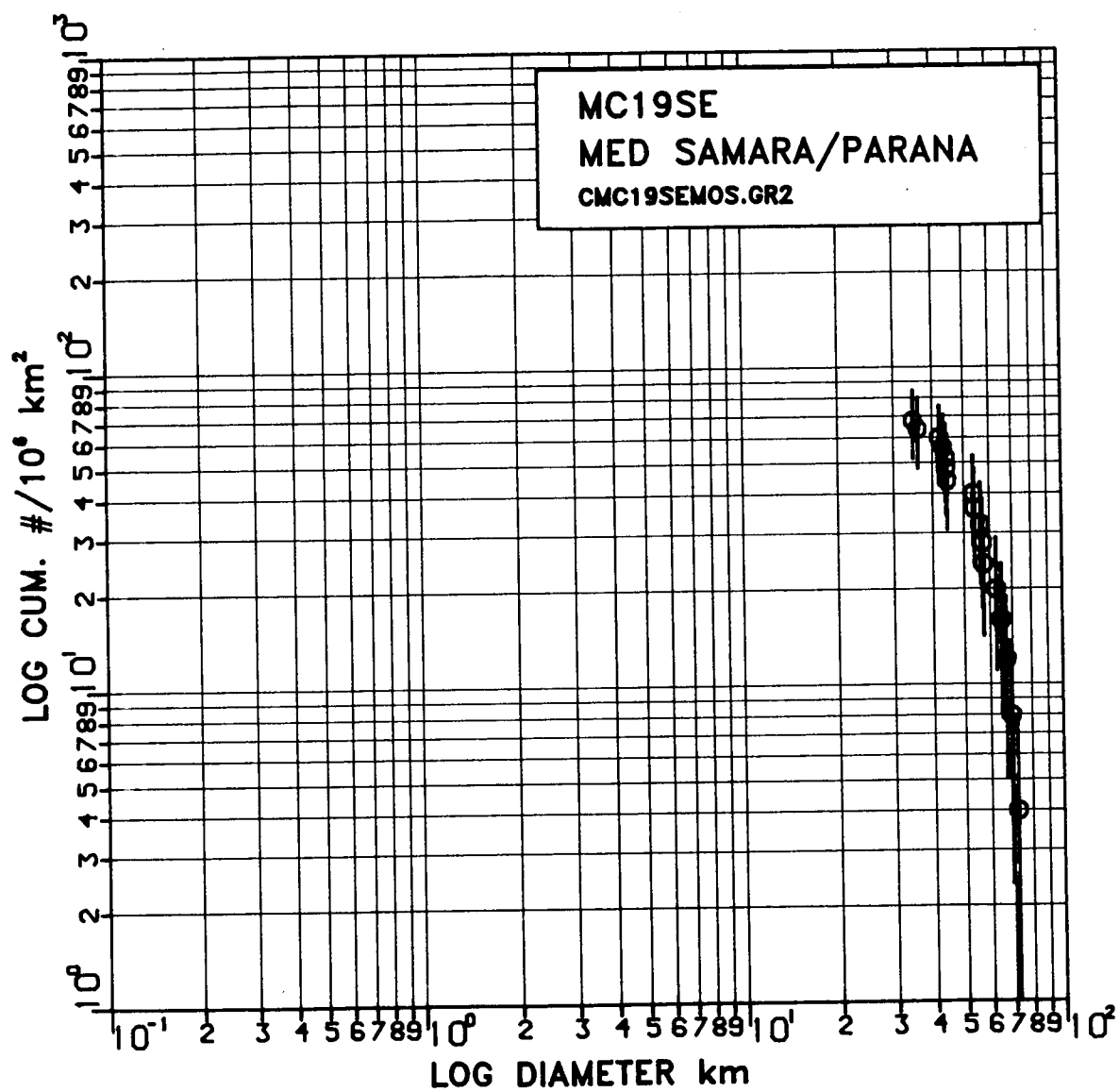


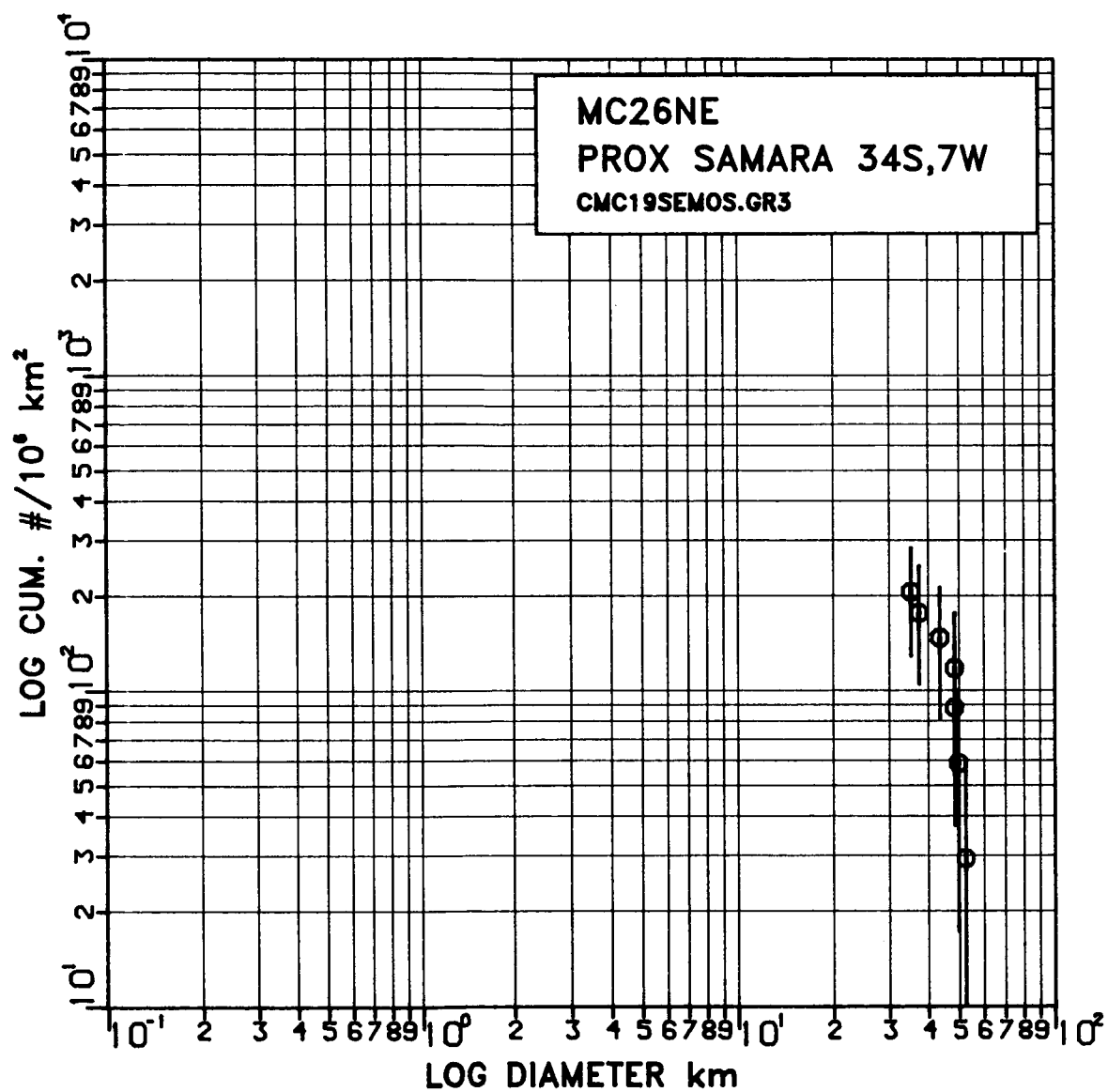


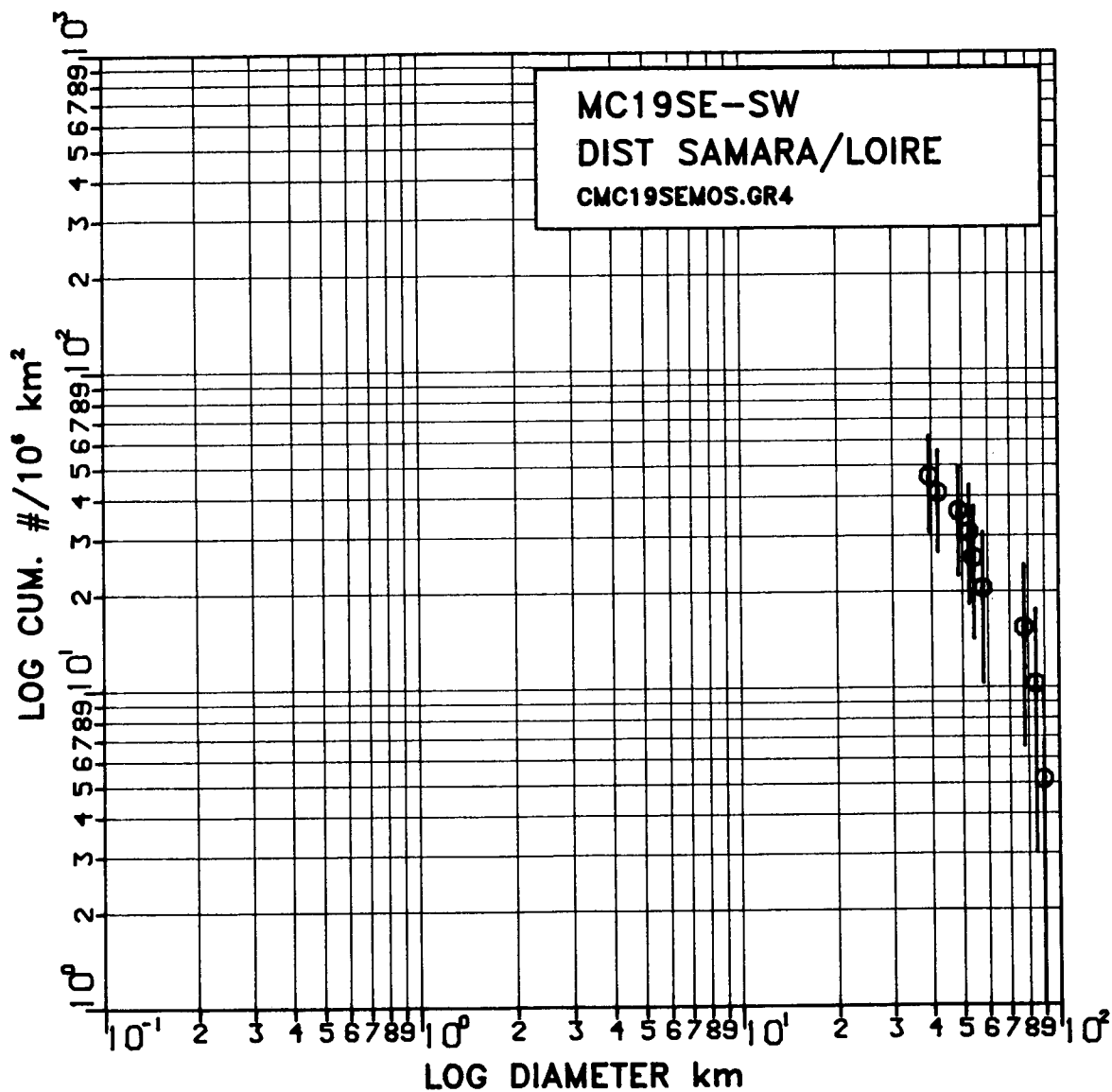


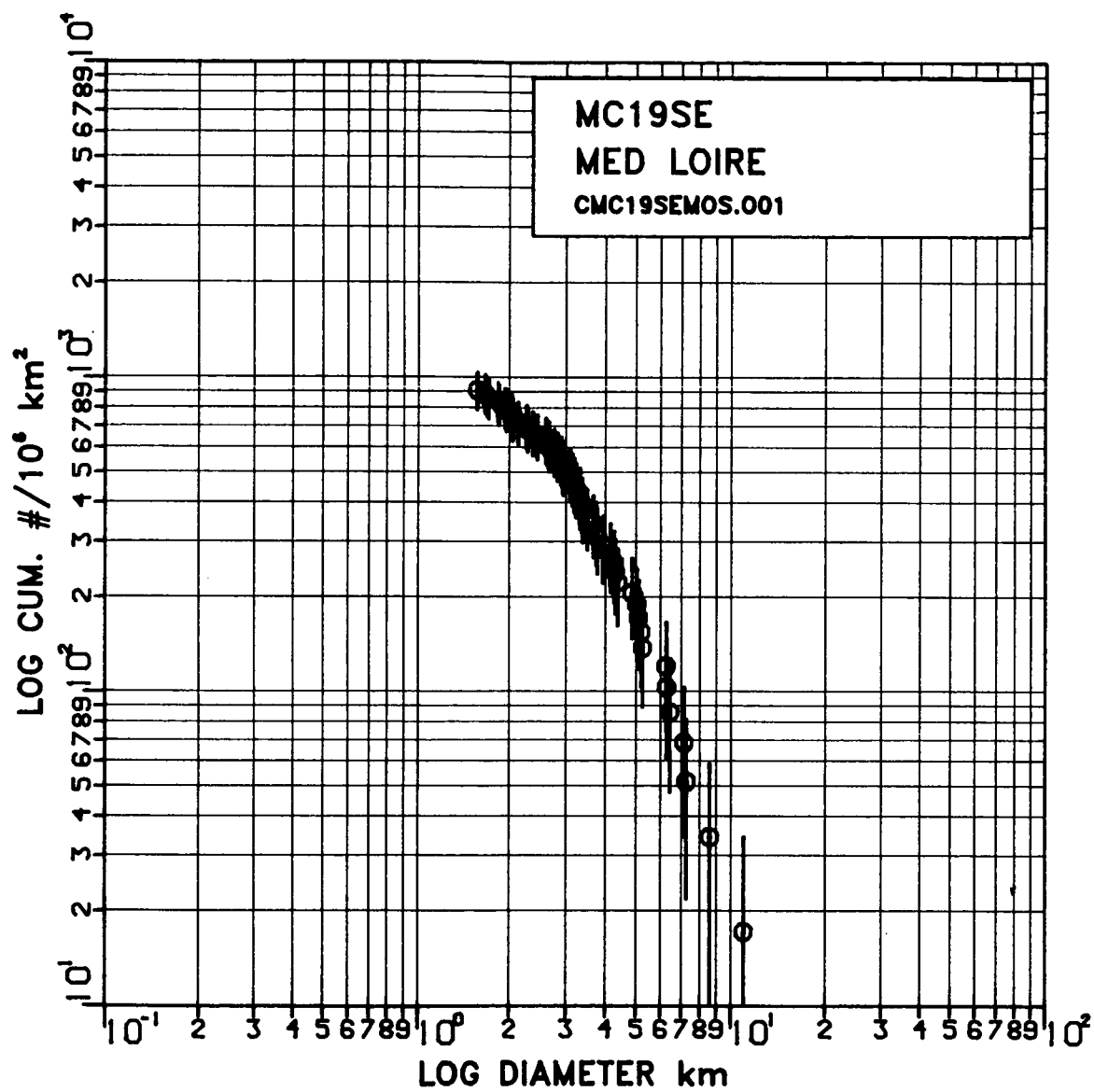


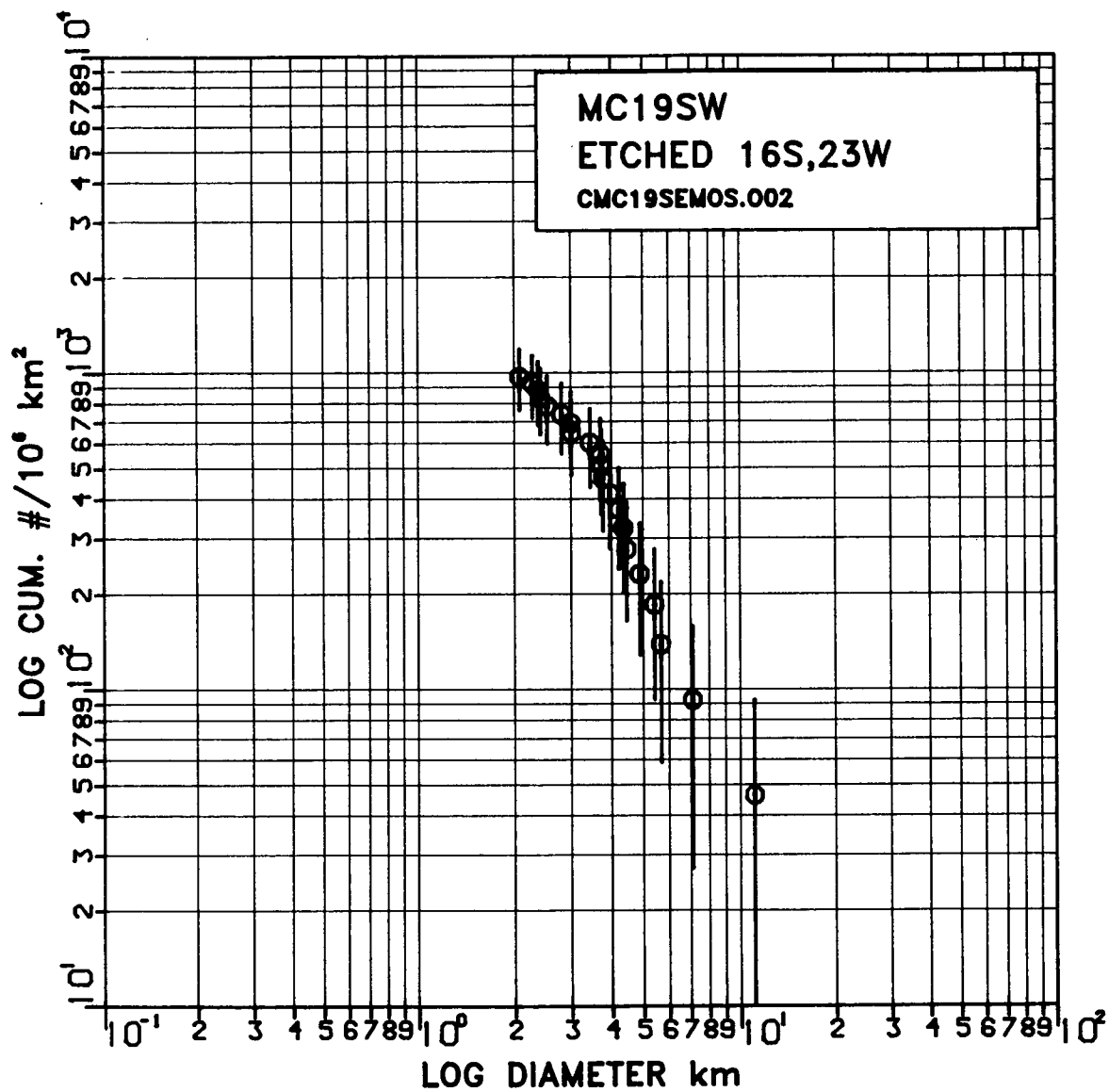


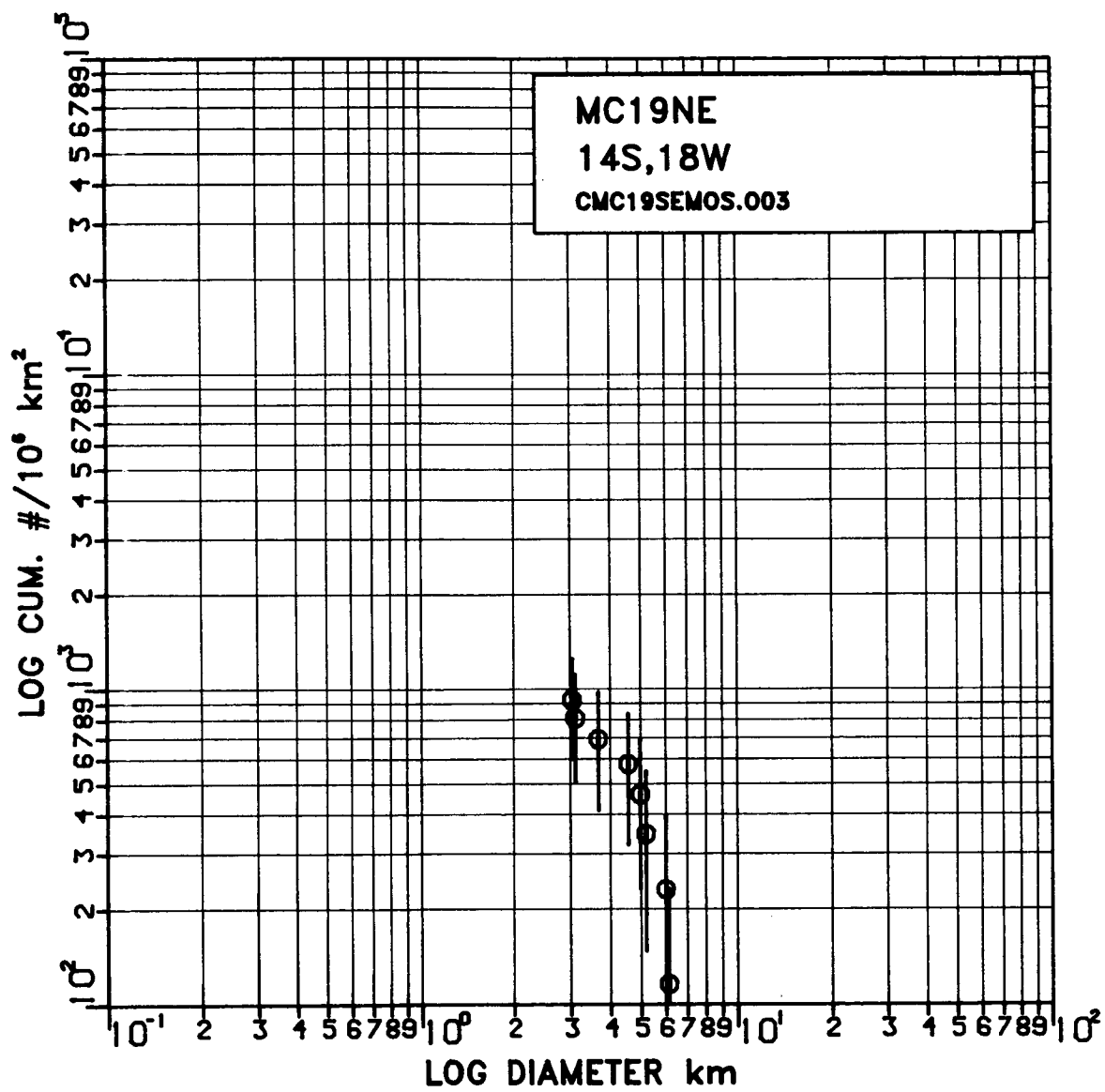


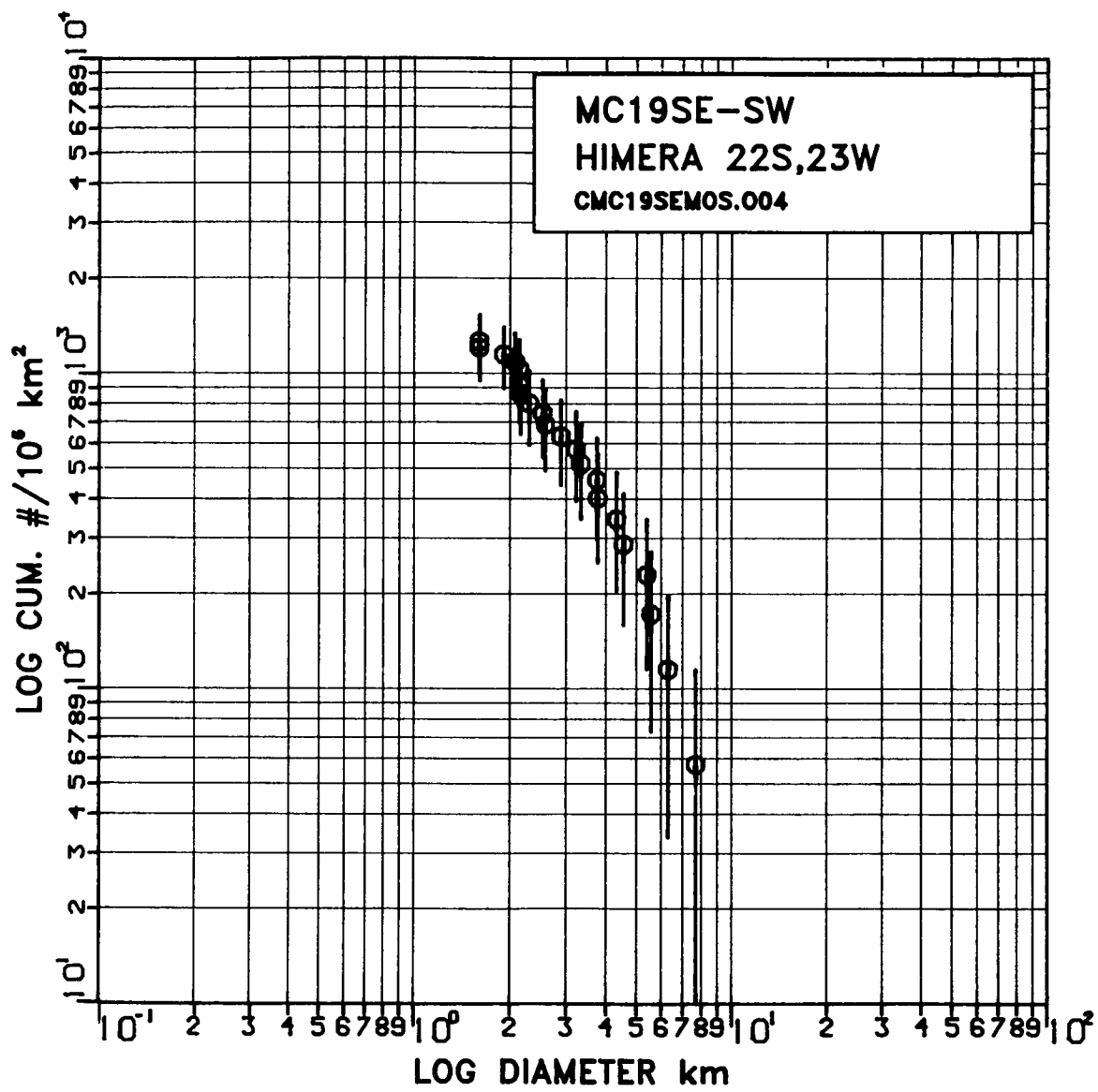


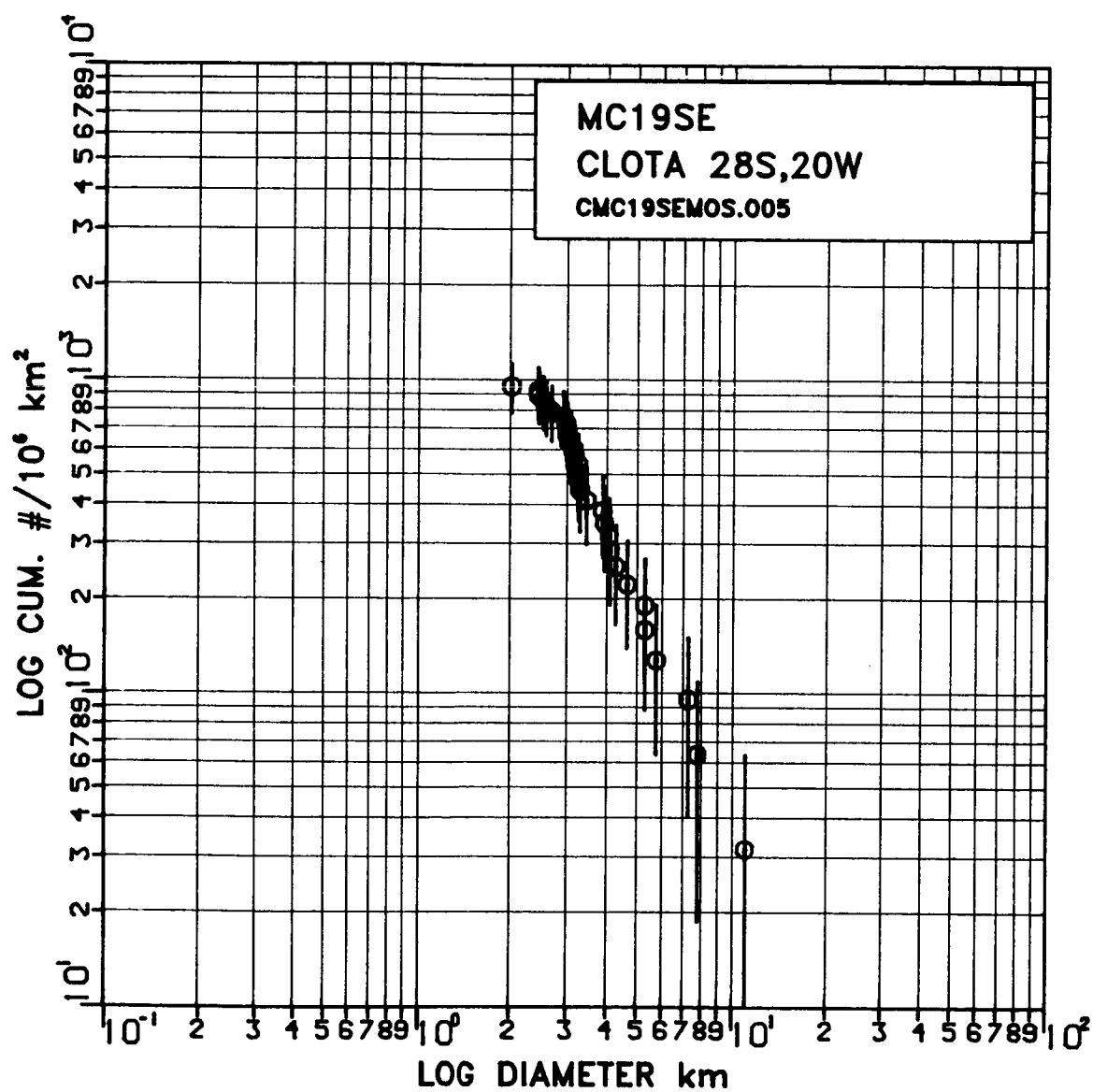


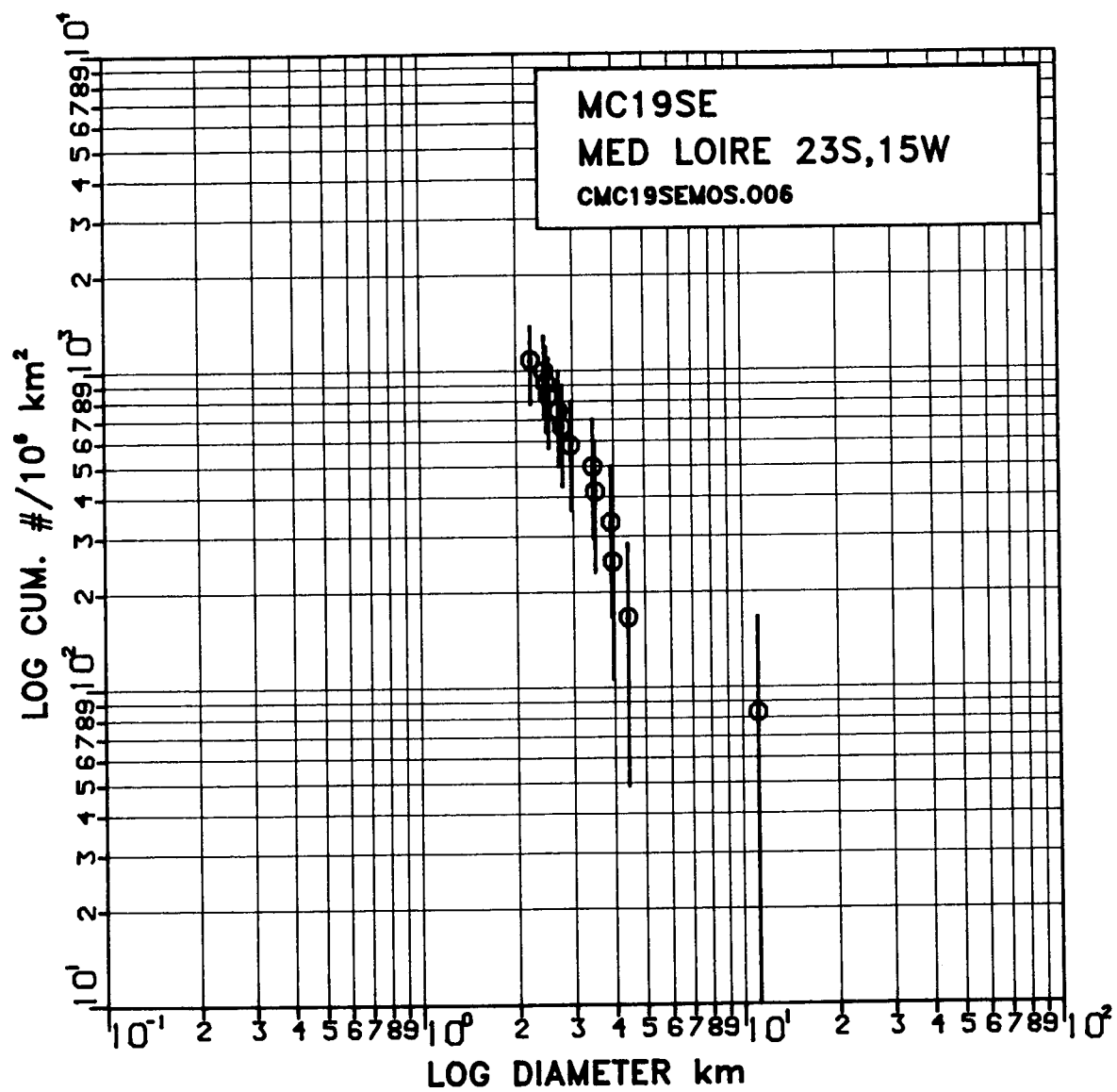


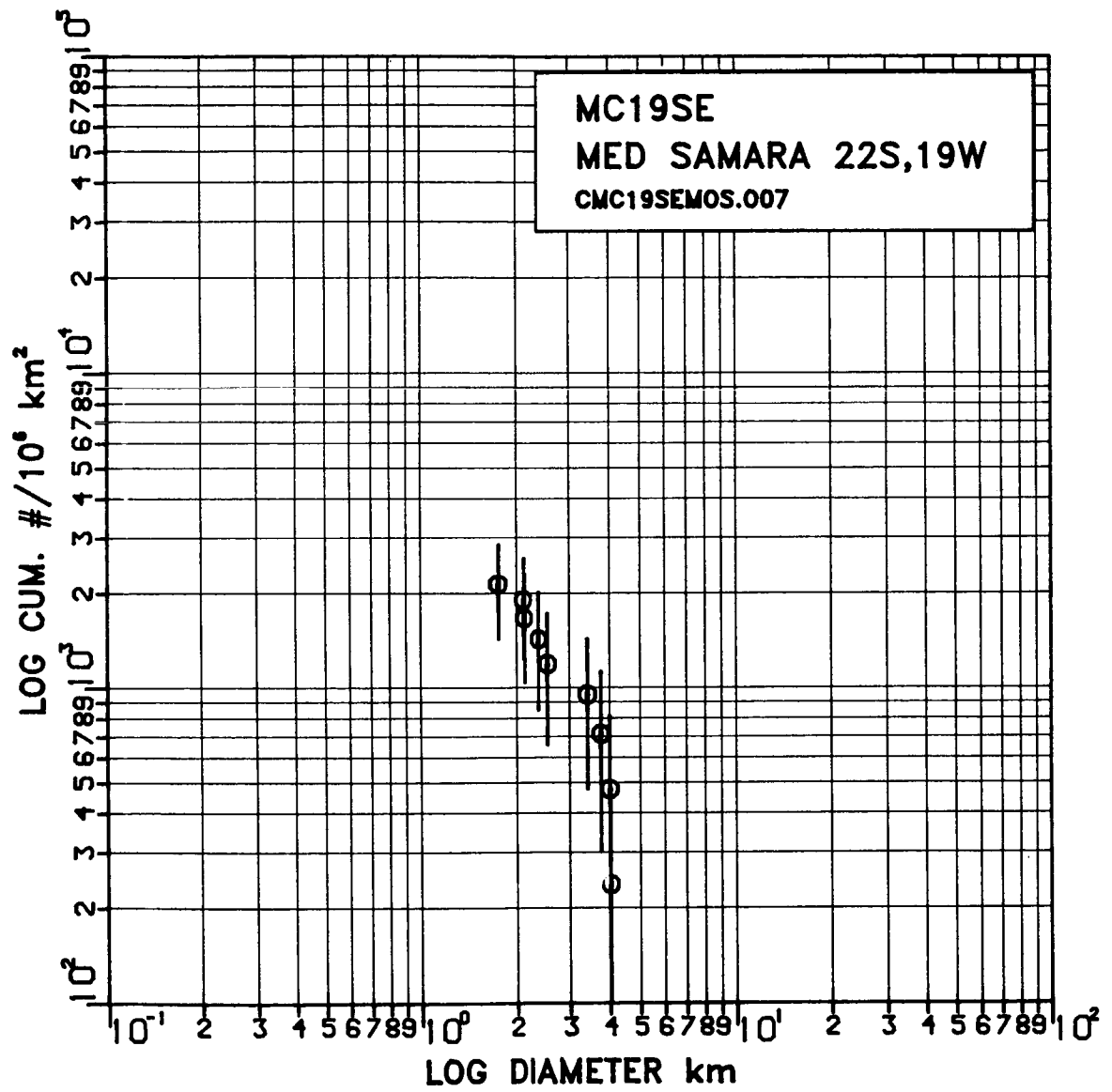


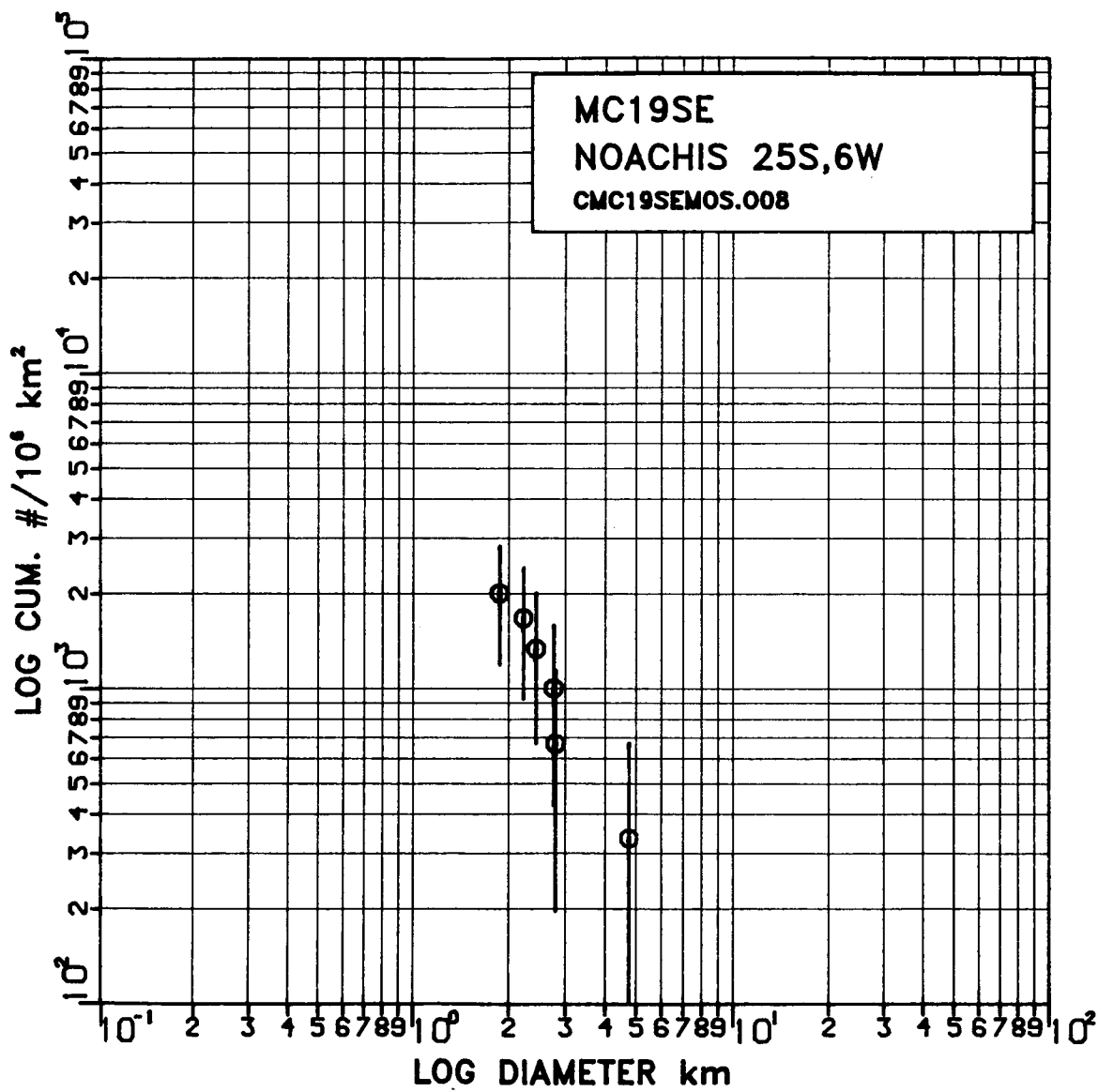


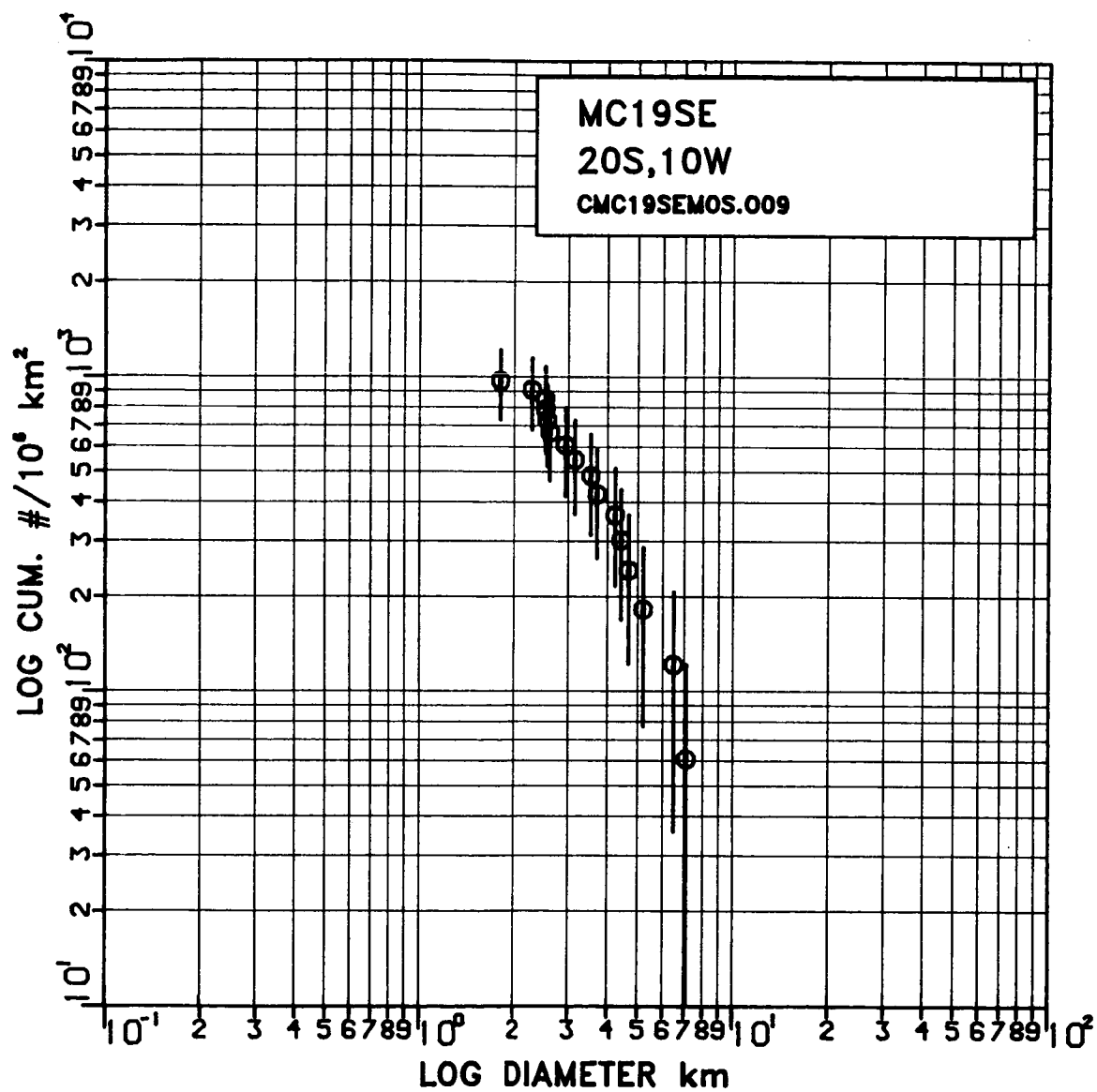


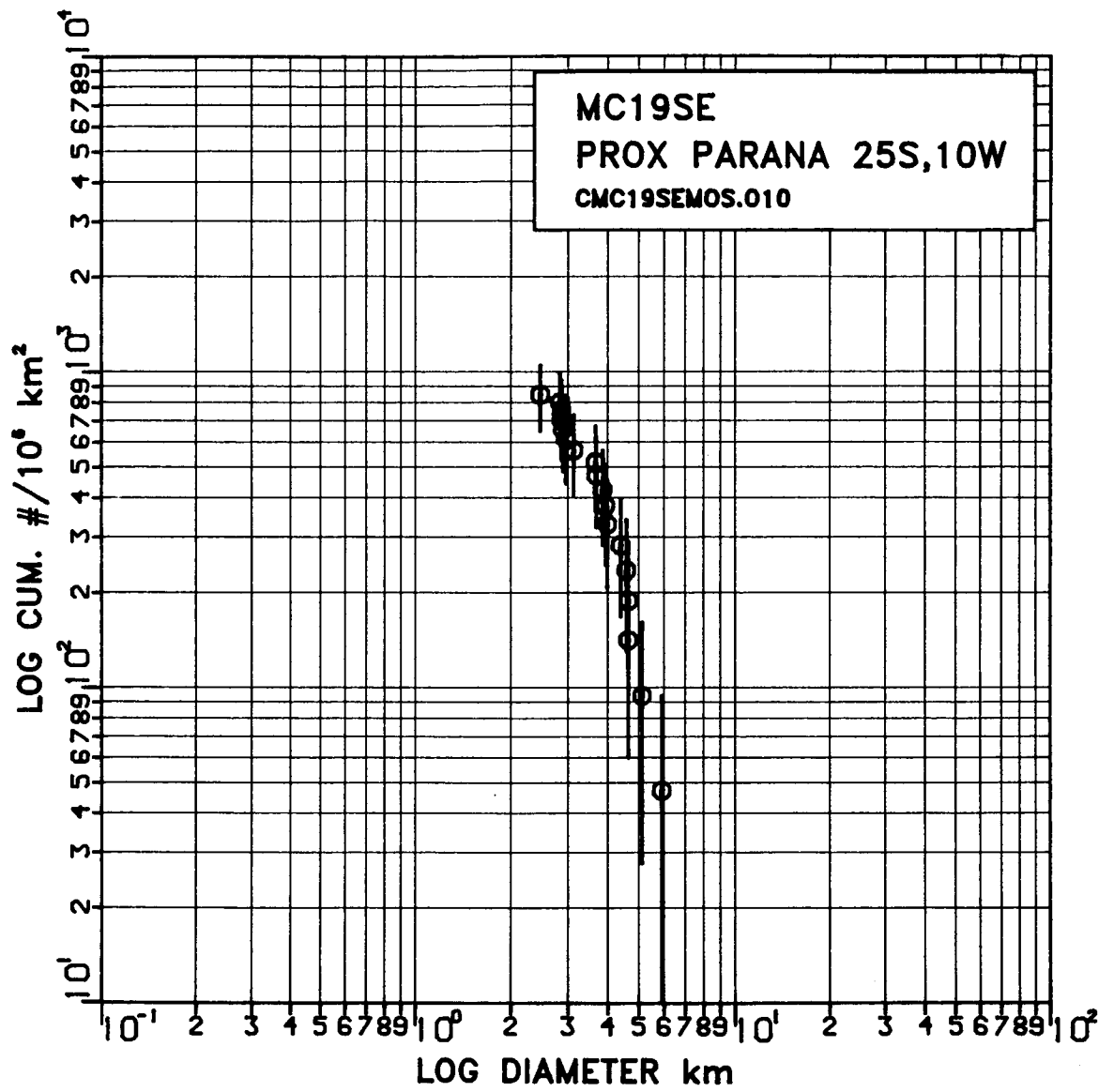


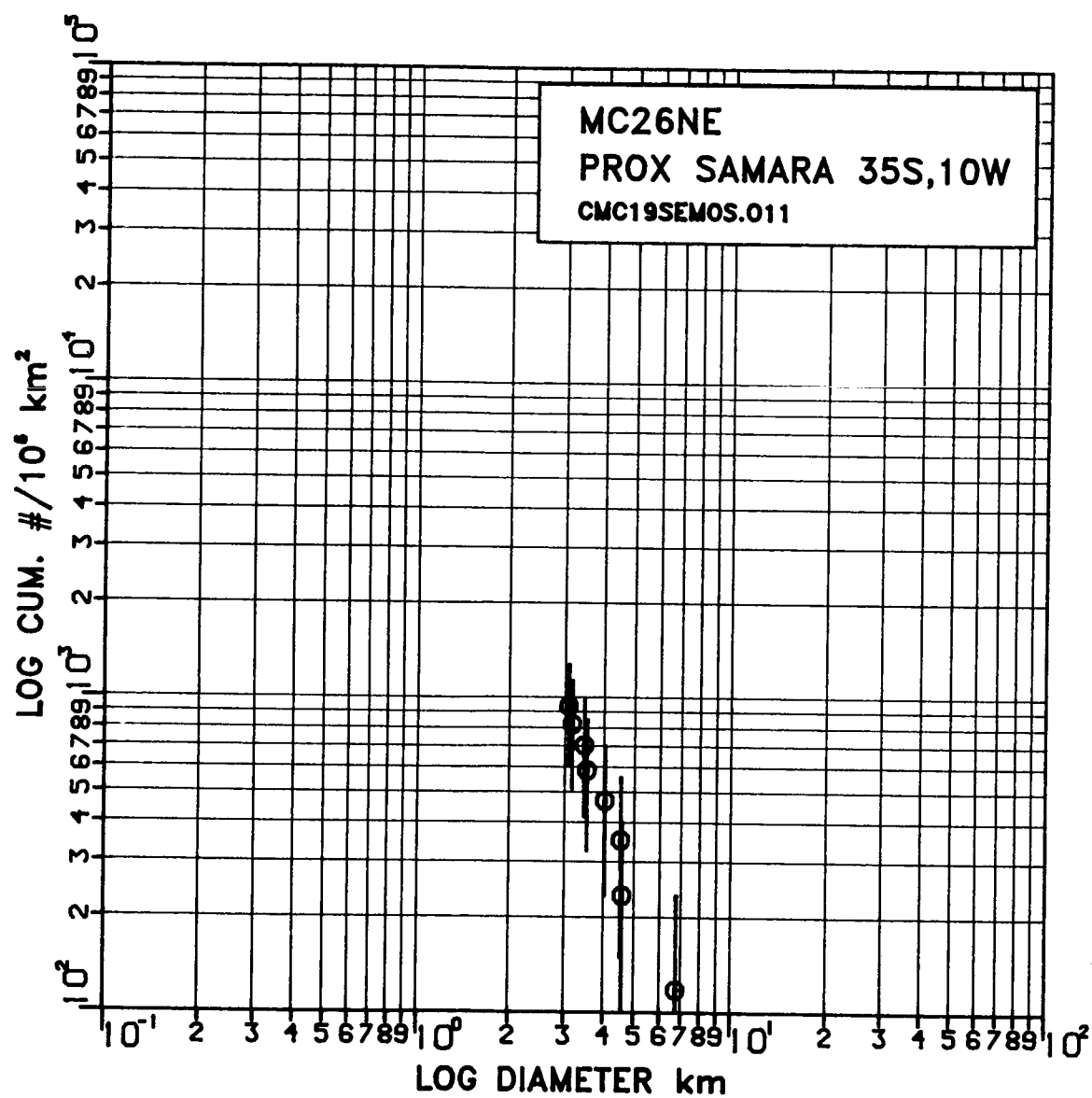


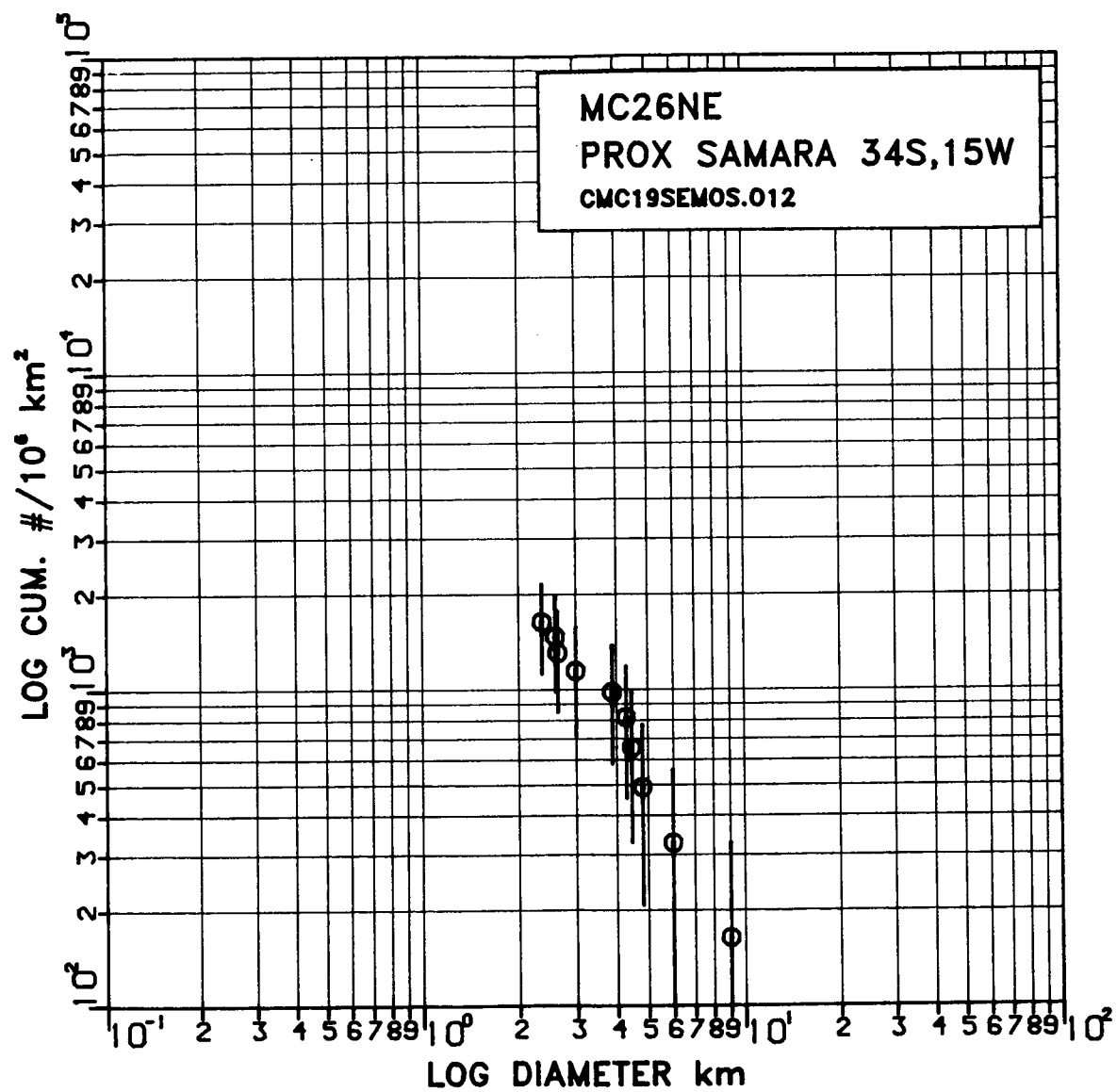


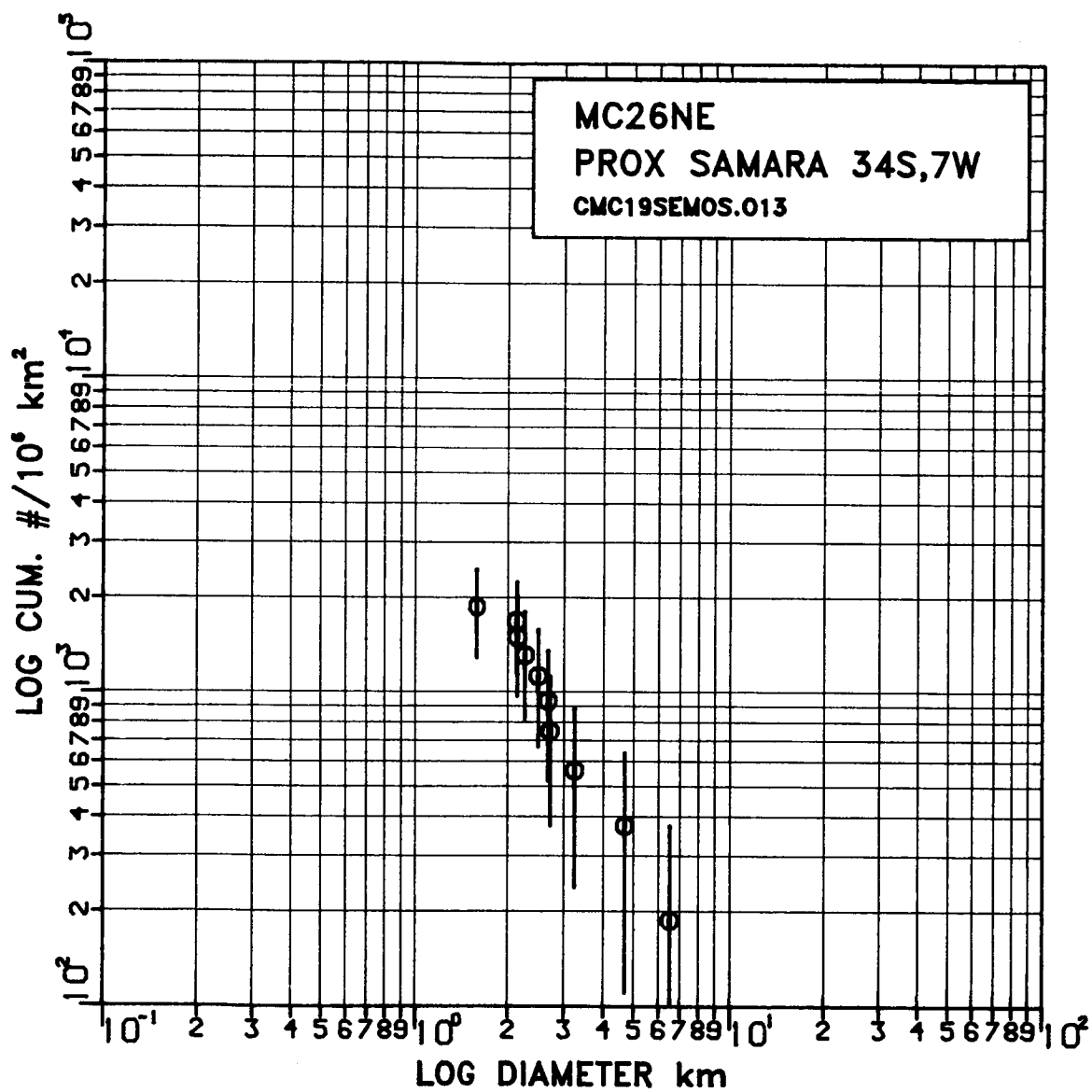


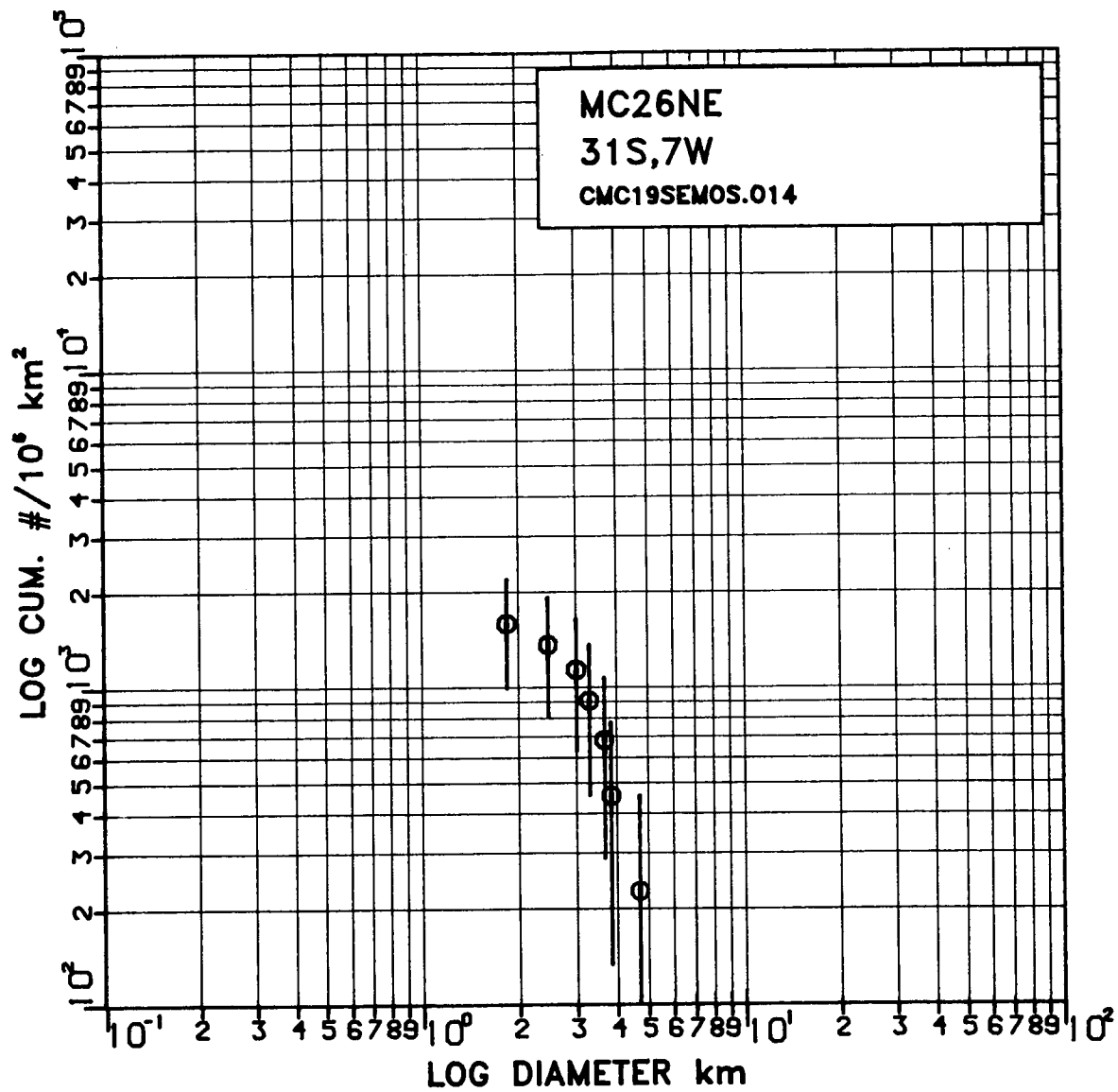


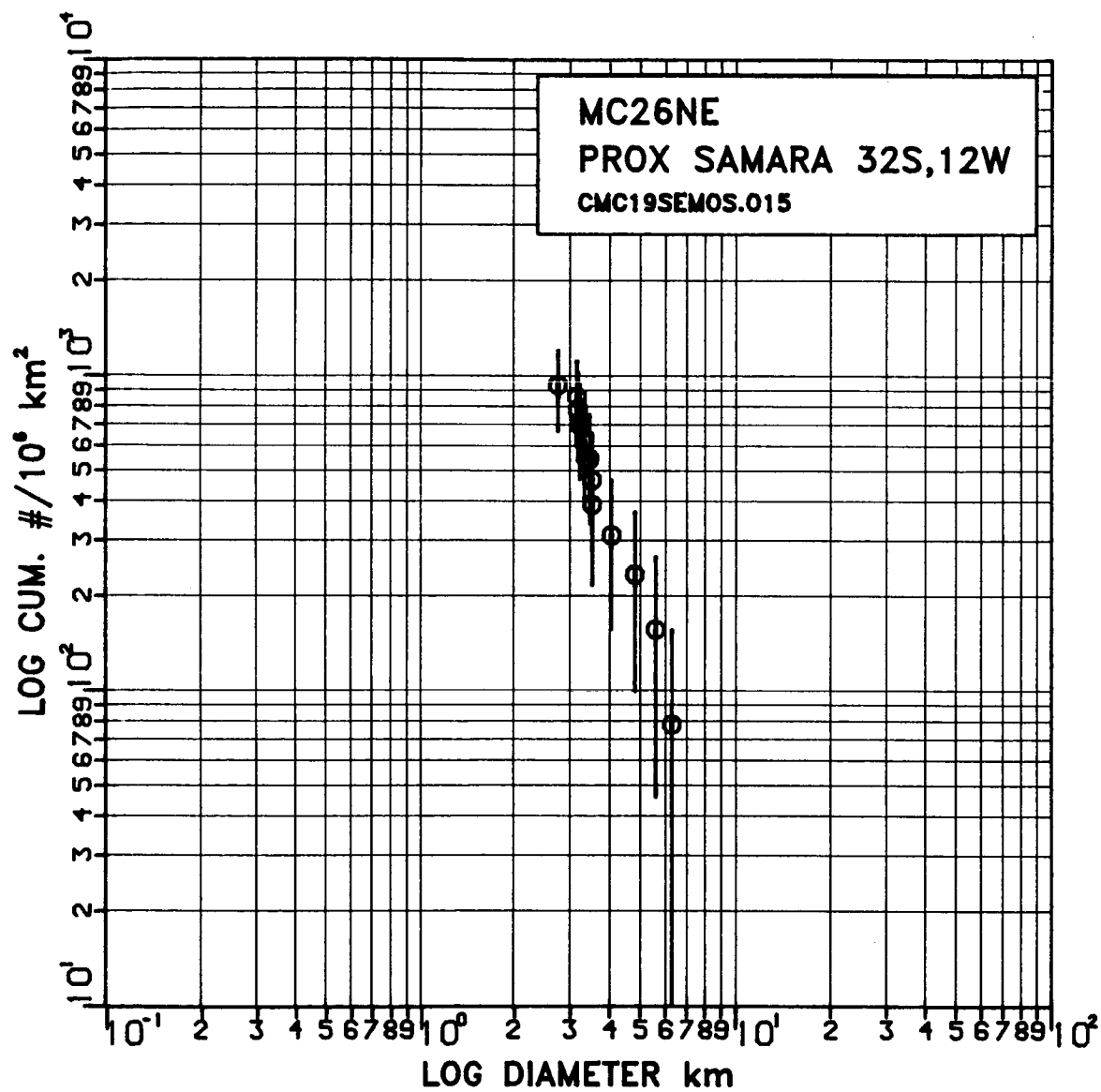


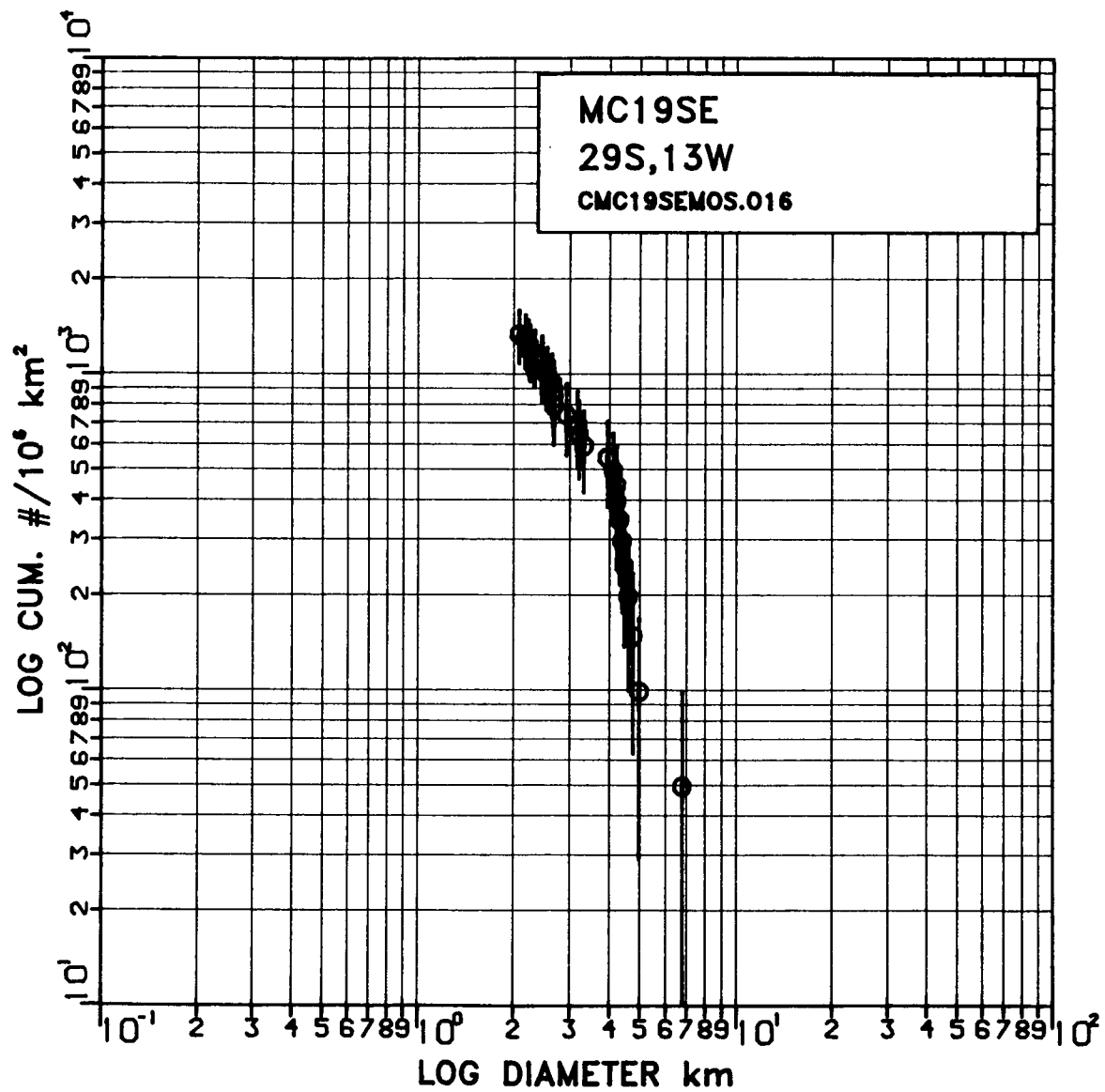


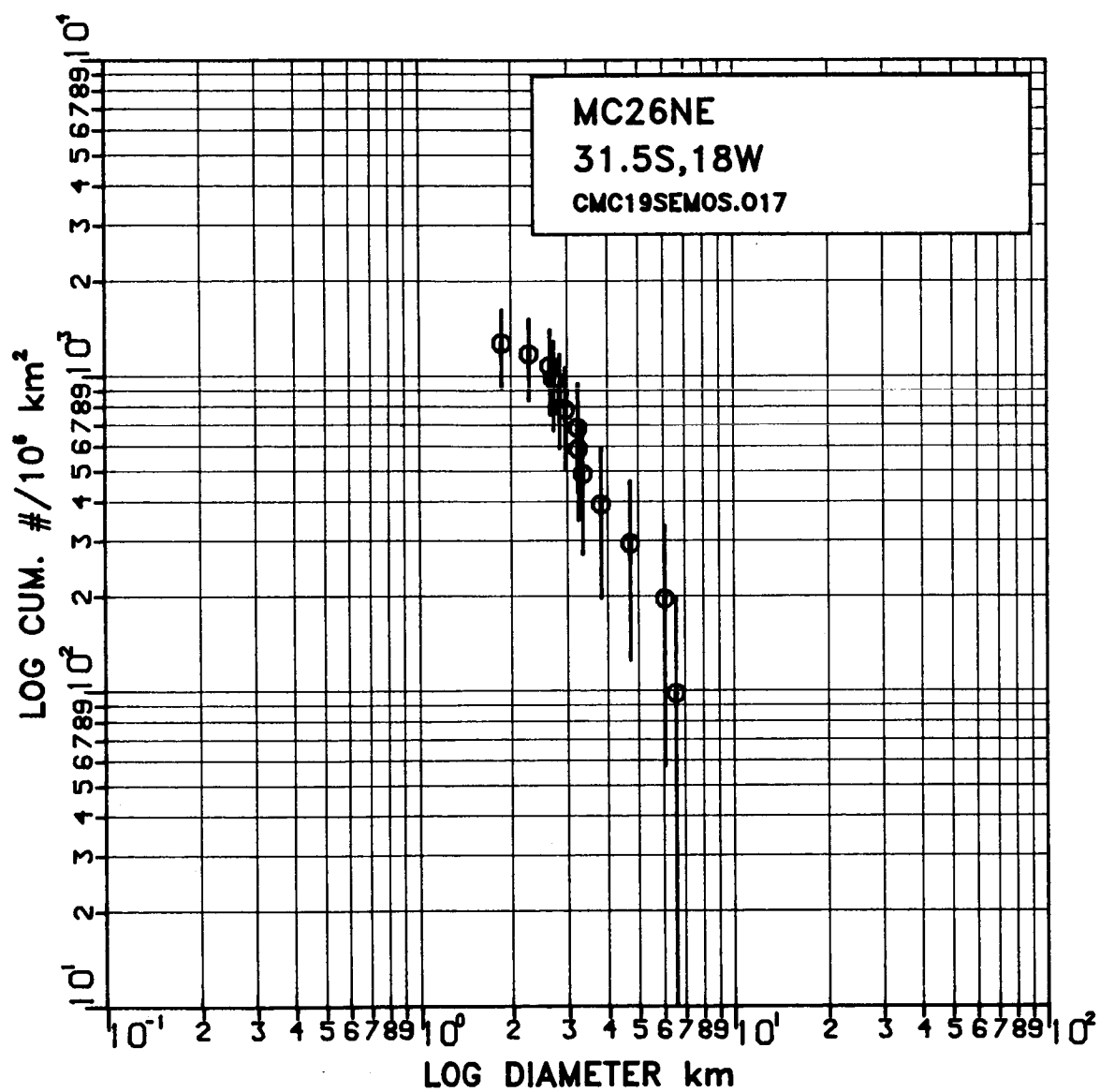


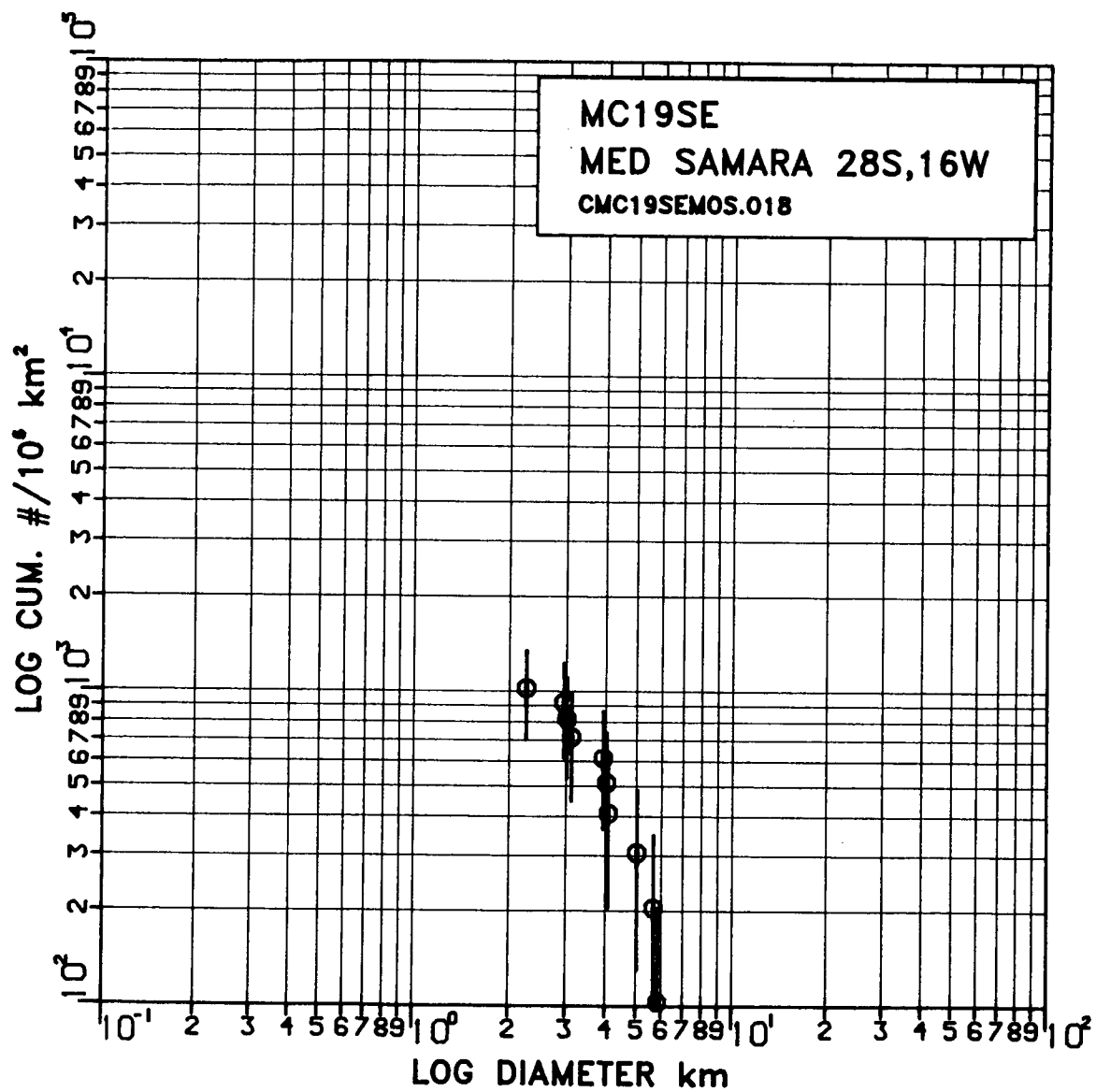


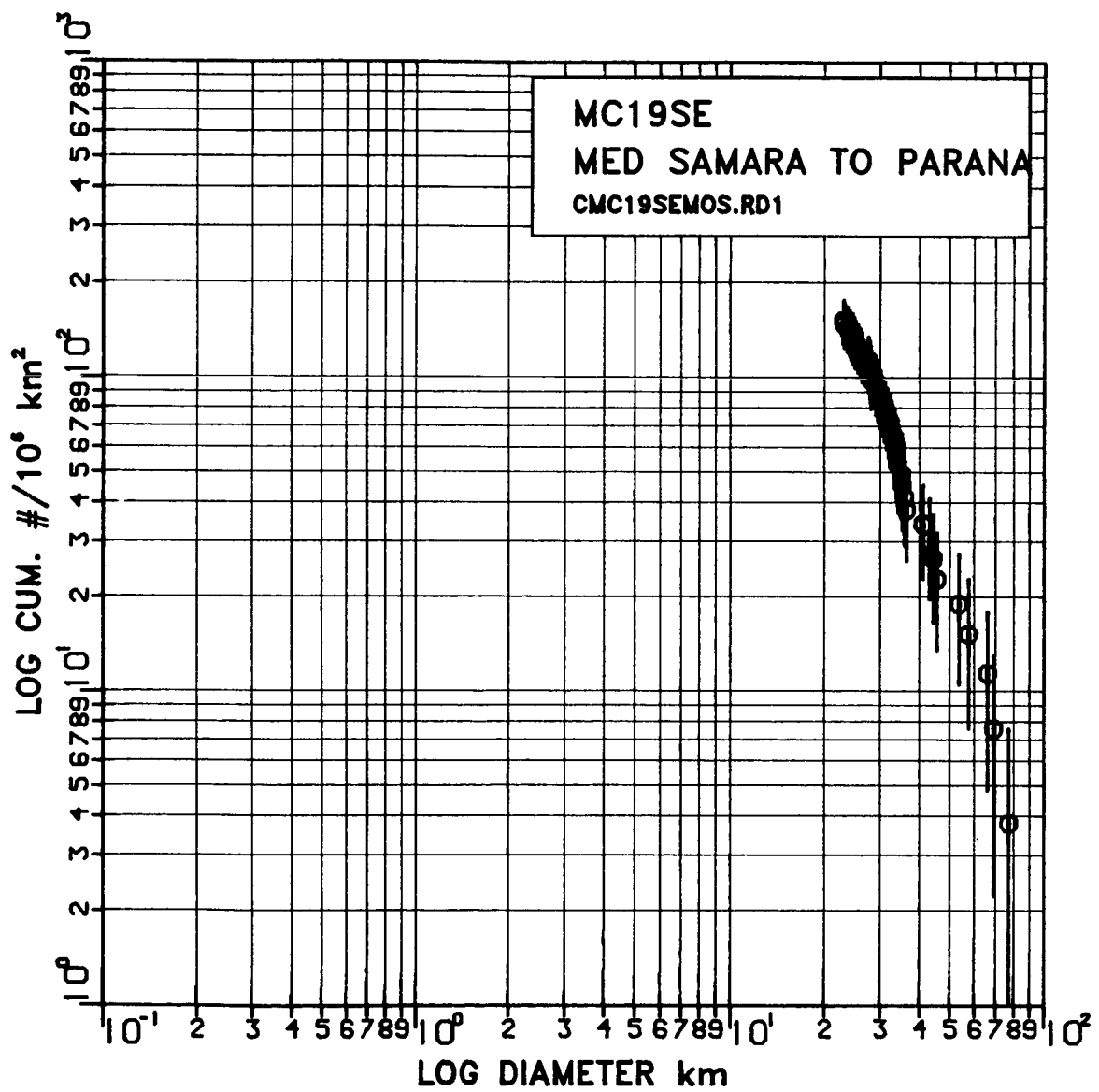


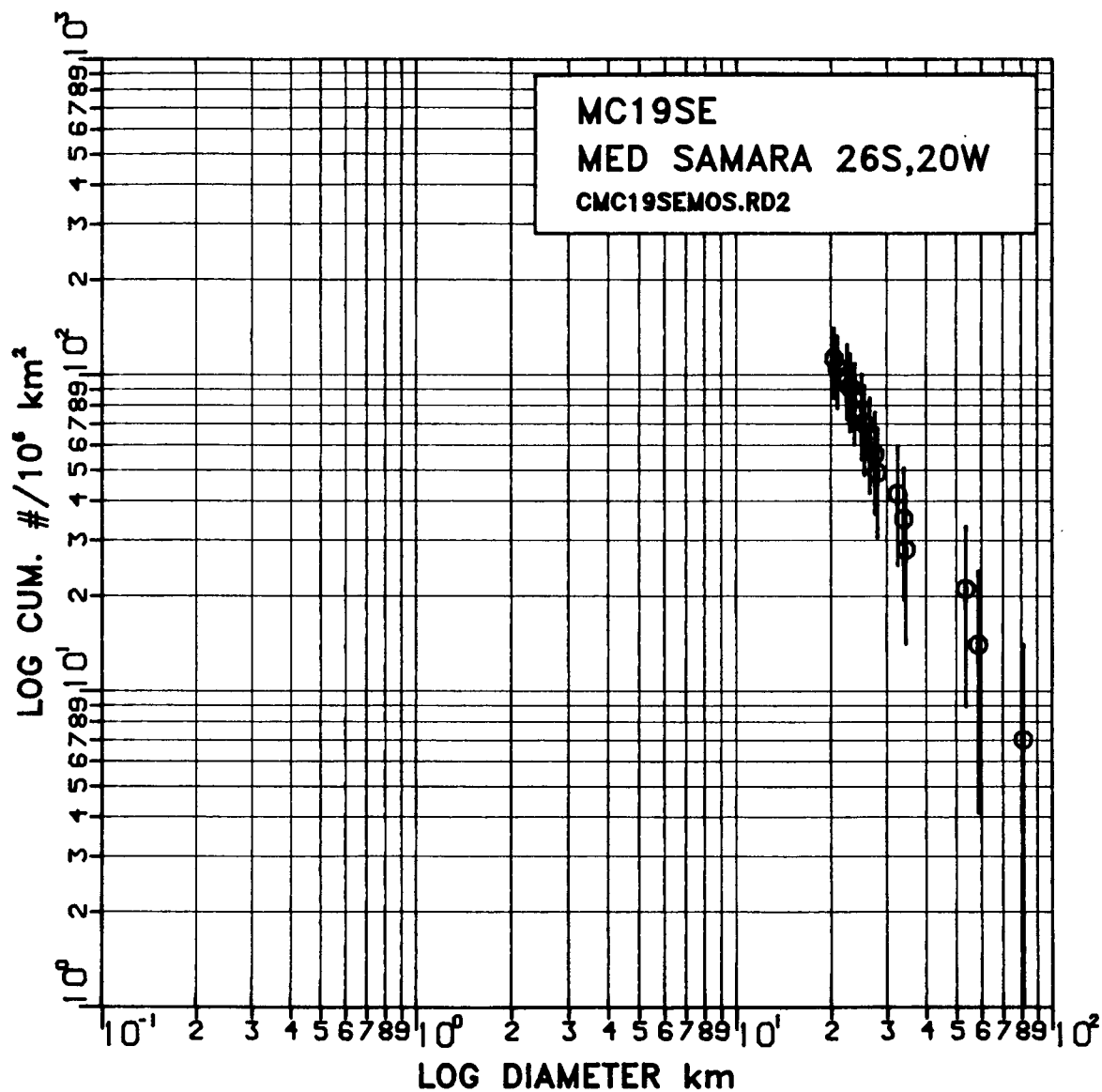


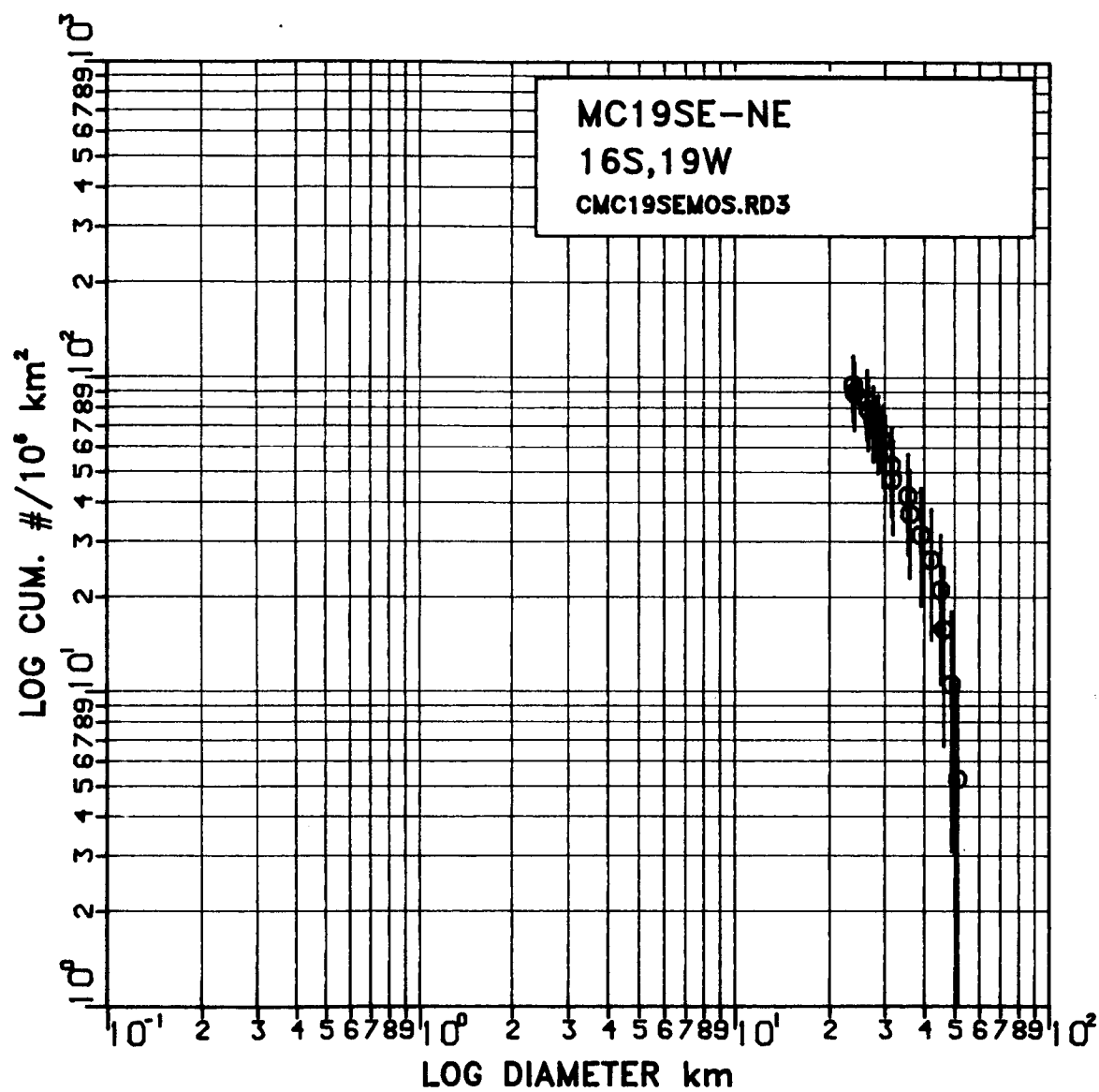












APPENDIX 4

STEREO PAIRS
USED FOR
DRAINAGE BASIN MAPPING

PRECEDING PAGE BLANK NOT FILMED

PAGE 262 INTENTIONALLY BLANK

Table 6 is a list of all stereo pairs used for drainage basin mapping. All images with >25% overlap are listed. The location given refers to the approximate center of overlap between two images. Footprints of images listed in Table 6 are given in Fig. 8. The number in () following an image number in Table 6 refers to the footprint number of that image in Fig. 8.

Table 6.-- STEREO PAIRS: images and location

(includes all images with >25% overlap)
 (* numbers in () refer to footprint locations in Fig. 26)

Stereo Pair		Location	
Image #	Image #	S Lat	W Long
MC19NW			
615A22 (7)	651A62 (3)	12	25
615A22 (7)	651A63 (10)	14.5	24
615A22 (7)	651A64 (6)	14	26
615A24 (8)	651A62 (3)	11	23
MC19NE			
451A06 (1)	451A08 (5)	4.5	18
451A06 (1)	651A83 (2)	5	20
451A08 (15)	651A83 (2)	5	20
451A08 (5)	651A85 (4)	8	18.5
615A23 (12)	651A88 (11)	14.5	21
615A24 (8)	651A62 (3)	13	22
615A24 (8)	651A88 (11)	12.5	21.5
651A25 (13)	651A87 (15)	14	18
651A25 (13)	651A88 (11)	14	19
651A26 (9)	651A85 (4)	10	19
615A26 (9)	651A87 (15)	12	18
651A27 (14)	651A87 (15)	12.5	10
MC19SW			
084A38 (31)	650A15 (32)	28	22.5
651A41 (25)	650A17 (22)	25	23
650A17 (22)	651A63 (23)	23	23
MC19SE			
084A38 (31)	650A22 (43)	29.5	22
084A38 (31)	084A40 (34)	27.5	21
084A39 (45)	084A41 (48)	29.5	18
084A39 (45)	650A15 (32)	29.5	20
084A40 (34)	084A42 (36)	27	18.5
084A40 (34)	650A15 (32)	27	19.5
084A40 (34)	615A62 (35)	27	19.5
084A40 (34)	651A70 (33)	27	18
084A41 (48)	579A42 (49)	29	15.5
084A41 (48)	615A61 (44)	29	18
084A41 (48)	615A63 (47)	29	16
084A41 (48)	650A15 (32)	28.5	18
084A41 (48)	651A69 (53)	28	15
084A41 (48)	651A70 (33)	28	17
084A41 (48)	651A72 (46)	29	16.5
084A42 (36)	615A43 (27)	24	18
084A42 (36)	615A62 (35)	26.5	18
084A42 (36)	651A67 (26)	24	18
084A42 (36)	651A69 (53)	26	16
084A42 (36)	651A70 (33)	26	18
084A43 (51)	579A42 (42)	28	14.5
084A43 (51)	615A63 (47)	28	14.5

Table 6.-- STEREO PAIRS (cont'd)

084A43 (51)	651A69 (53)	27	14
084A43 (51)	651A72 (46)	28.5	15
084A44 (38)	615A45 (28)	22.5	15
084A44 (38)	651A67 (26)	23.5	16
084A44 (38)	651A69 (53)	25	14.5
084A44 (38)	651A92 (24)	22.5	15
084A44 (38)	651A94 (56)	23.5	13.5
084A45 (52)	579A46 (54)	26	10
084A45 (52)	084A47 (25)	25	10
084A45 (52)	651A69 (53)	26	12
084A46 (40)	084A48 (42)	21.5	11.5
084A46 (40)	615A47 (29)	20.5	12
084A46 (40)	651A92 (24)	22	13.5
084A46 (40)	651A94 (56)	23	12
084A47 (57)	579A48 (55)	24.5	8
084A47 (57)	615A66 (39)	23.5	10.5
084A47 (57)	615A68 (41)	22.5	9
084A47 (57)	651A94 (56)	24.5	9.5
084A48 (42)	615A47 (29)	20	11
084A48 (42)	615A49 (30)	19	9
084A48 (42)	615A68 (41)	21	9
084A49 (58)	579A48 (55)	23.5	7
084A49 (58)	615A68 (41)	22	8
579A42 (49)	615A63 (47)	28.5	14.5
579A42 (49)	651A72 (46)	29.5	15
579A44 (50)	615A63 (47)	28	13.5
579A46 (54)	579A48 (55)	22.5	8.5
579A46 (54)	651A94 (56)	26	10
579A48 (55)	651A94 (56)	25	8.5
615A23 (12)	615A25 (13)	15.5	20.5
615A23 (12)	651A63 (23)	15.5	22
615A23 (12)	651A65 (17)	18	21
615A23 (12)	651A88 (11)	15	21
615A23 (12)	651A90 (19)	16.5	20
615A25 (13)	651A90 (19)	15.5	18.5
615A27 (14)	651A90 (19)	15	17.5
615A41 (25)	615A62 (35)	25.5	20.5
615A41 (25)	650A17 (22)	25	22.5
615A41 (25)	651A63 (23)	23.5	22
615A42 (16)	651A63 (23)	21	22
615A42 (16)	651A65 (17)	19.5	21.5
615A43 (27)	651A67 (26)	23	18.5
615A44 (18)	651A65 (17)	19	19
615A44 (18)	651A90 (19)	18	18.5
615A45 (28)	615A66 (39)	22	13
615A45 (28)	651A67 (26)	22	16
615A45 (28)	651A92 (24)	22.5	14
615A46 (20)	651A92 (24)	18.5	14.5
615A46 (20)	651A90 (19)	17	16.5
615A47 (29)	615A68 (41)	20.5	10.5
615A47 (29)	651A92 (24)	20.5	13
615A48 (21)	615A49 (30)	17	10
615A63 (47)	651A69 (53)	27	14.5

Table 6.-- STEREO PAIRS (cont'd)

615A63 (47)	651A72 (46)	29.5	15.5
615A64 (37)	651A69 (53)	25.5	15.5
615A66 (39)	615A68 (41)	22	11
615A66 (39)	651A92 (24)	22	13.5
615A66 (39)	651A69 (53)	24.5	13
615A68 (41)	651A94 (56)	23	9.5
650A15 (32)	651A72 (46)	29	18
651A65 (17)	651A90 (19)	18.5	19
651A67 (26)	651A92 (24)	22	16
651A69 (56)	579A44 (50)	27	12.5
651A69 (56)	579A46 (54)	27	11.5
651A69 (56)	651A94 (56)	26.5	12
651A88 (11)	651A90 (19)	15	19

MC26NE

084A39 (45)	650A22 (43)	31	19.5
084A39 (45)	615A61 (44)	30.5	19
084A39 (45)	651A72 (46)	31	17.5
084A41 (40)	615A61 (44)	30	17.5
579A24 (65)	579A26 (66)	34	9.5
579A26 (66)	651A71 (64)	32.5	9
579A41 (60)	579A43 (61)	31.5	13.5
579A41 (60)	651A72 (46)	32	15
579A43 (61)	579A45 (62)	31	10.5
579A43 (61)	650A23 (67)	32.5	12
579A43 (61)	651A71 (64)	31	12
579A43 (61)	651A72 (46)	31	13.5
579A45 (62)	651A72 (46)	30	4
615A61 (44)	650A22 (43)	31	20
650A23 (67)	579A24 (65)	34	11
650A23 (67)	650A24 (59)	35	14
650A23 (67)	579A26 (66)	34	8.5

7-175

D2-91

N 87-25257

PART II

SEDIMENTARY GEOLOGY OF THE VALLES MARINERIS, MARS AND ANTARCTIC
DRY VALLEY LAKES

by

Susan S. Nedell

ACKNOWLEDGEMENTS

My greatest appreciation goes to my advisors, Drs. Steven W. Squyres and David W. Andersen for freely giving their patience, time and guidance. I would like to thank Dr. Christopher P. McKay and Dr. George M. Simmons for presenting the opportunity to do field work in Antarctica. It was a privilege to work with them and Dr. Robert A. Wharton on the science of the Dry Valley lakes. F. Gordon Love was very helpful in relating his observations of the Dry Valley lakes. Dr. June A. Oberdorfer was also on my thesis committee, and gave helpful and prompt attention while reviewing this thesis.

A number of people at the U.S. Geological Survey provided assistance. Dr. Michael H. Carr made available the Viking images and a work space in which to study them. Drs. Gerald G. Shaber and Sherman S.C. Wu promptly prepared stereophotogrammetric measurements for locations in the Valles Marineris. Gary Clow introduced me to relevant techniques of data analysis. Robert Oscarson taught me how to use the scanning electron microscope (SEM). Drs. Theodore Bunch and Delbert Philpott at NASA Ames also provided SEM analysis.

This investigation was supported by the NASA Planetary Geology Program. Funds for the support of this study have been allocated by the NASA-Ames Research Center, Moffett Field, California, under interchange No. NCA2-1R675-402.

PRECEDING PAGE BLANK NOT FILMED

TABLE OF CONTENTS

List of Illustrations	277
List of Tables	281
ABSTRACT	283
INTRODUCTION	287
Geologic Setting	287
Previous Work	294
Scope of Investigation	298
GEOLOGY OF THE LAYERED DEPOSITS IN THE VALLES MARINERIS	301
Mapping	301
Slope and Bedrock Material	301
Layered Chasma Deposits	306
Possible Layered Chasma Deposits	318
Landslide Material	322
Chasma Floor Material	322
Thickness, Topography, and Volume of the Layered Chasma Deposits	331
Thickness of Individual Layers	331
Regional Slopes	338
Total Thickness and Volume of Deposits	341
Stratigraphic Relationships and History of the Valles Marineris	344
Origin of the Layered Deposits	349
Eolian Hypothesis	349
Canyon Wall Hypothesis	349
Volcanic Hypothesis	350
Lacustrine Hypothesis	354
ANTARCTIC DRY VALLEY LAKES	357
Purpose of Investigation	357
Location and General Geography	357
Climate	359
General Geology	360

Description of Lakes	361
Wright Valley: Lake Vanda	361
Taylor Valley Lakes	367
Lake Bonney	367
Lake Hoare	368
Lake Fryxell	375
Grain Size Analysis	376
Purpose and Procedure	376
Results and Discussion	384
Mineralogy	386
Procedure	386
Results and Discussion	387
Microscopic Analysis of Quartz Grain Textures	390
Purpose and Procedure	390
Results	391
Estimation of Sediment Flux	396
Interpretation	398
Processes of Sedimentation Through Ice	398
Grains Melting Through Ice	399
Percolation Through Vertical Channels or Cracks	400
Remaining Questions	401
SEDIMENTATION PROCESSES ON MARS	403
Transport of Sediment Through Ice Cover	403
Solar Warming	403
Vertical Melt-Channels in Ice	404
Foundering	405
Rayleigh-Taylor Instability	408
Eolian Deposition onto the Ice Surface	413
Subaqueous Volcanism	416
Transport of Sediment from Canyon Walls	417

DISCUSSION AND SUMMARY	423
Formation of the Layered Deposits in the Valles Marineris .	423
Analogy to the Antarctic Dry Valley Lakes	425
Recommendations for Future Work	426
REFERENCES CITED	431

LIST OF ILLUSTRATIONS

Figure

1. Index Map of the Valles Marineris, Mars	288
2. Index Map of the U.S.G.S. Quadrangle Locations	289
3. Western Portion of the Valles Marineris	291
4. Central Portion of the Valles Marineris	292
5. Eastern Portion of the Valles Marineris	293
6. Ophir Chasma Showing Morphology of Chasma, Layered Deposits, and "Moat"	303
7. V-shaped Tributary Canyons in the Southern Wall of Ius Chasma	304
8. Landslide Scarps and Deposits in Western Ius Chasma	305
9. Hebes Chasma with Central Plateau of Layered Deposits	307
10. Plateaus of Layered Deposits in Candor Chasma	308
11. Plateaus of Layered Deposits in Juventae Chasma	309
12. Plateaus of Layered Deposits in Gangis Chasma	310
13. Irregularly-shaped Plateaus of Layered Deposits in Candor Chasma	311
14. Layered Deposits in Melas Chasma Showing Plateau Roughly Parallel to Canyon Walls	312
15. Individual Layer within Plateau of Layered Deposits in Southern Melas Chasma Showing Greatest Lateral Extent	313
16. Partially Buried Canyon Wall in Ophir Chasma	315
17. Etched Layered Deposits in Ophir Chasma	316
18. Eolian Flutes on Layered Deposits in Southern Candor Chasma .	317
19. Flutes Superimposed on Layering in Southeast Candor Chasma .	319
20. Mottled Pattern on Layered Deposits in Melas Chasma	320
21. Possible Redeposited Layered Deposits in Eos and Capris Chasmata	321
22. Landslide Diverted by a Plateau of Layered Deposits	323
23. Chasma Floor Material in Melas Chasma	325
24. Chasma Floor Material in Western Candor Chasma	326
25. Chasma Floor Material in Southern Melas Chasma	327

26.	Chasma Floor Material in Ius Chasma	328
27.	"Moat" Between Candor Mensa and Canyon Wall	329
28.	Polygonal Blocks Form Chasma Floor Southeast of Candor Mensa	330
29.	Chaotic Terrain of the Chasma Floor in Eos and Capri Chasmata	332
30.	Locations of Detailed Studies of Layers in Candor Chasma . .	333
31.	Data Point Locations for Stereophotogrammetry in Eastern Candor Chasma	334
32.	Data Point Locations for Stereophotogrammetry on Candor Mensa	335
33.	Isopach Map of Layered Deposits in Coprates NW Quadrangle..	342
34.	Simplified Geologic History of the Valles Marineris	348
35.	Possible Vents for Pyroclastic Flows in Amazonis Planitia . .	352
36.	Index Map of the Dry Valleys	358
37.	Bathymetric Map of Lake Vanda	362
38.	Picture of Lake Vanda and the Onyx River	364
39.	Picture of the Surface of Lake Vanda	364
40.	Picture of the Topography of the Lake Vanda Ice Cover	365
41.	Bathymetric Map of Lake Hoare	369
42.	Picture of Troughs on the Lake Hoare Ice Cover.	370
43.	An Aerial View of Lake Hoare	371
44.	Picture of a Cross-section of the Ice Cover on Lake Hoare . .	373
45.	Picture of the Shoreline of Lake Hoare	374
46.	Picture of the Inflowing Stream at Lake Hoare	374
47.	Cumulative Size-frequency Curves of the Grain-size Distributions of Samples from Lake Hoare	378
48.	Ternary Diagram Comparing the Mineralogy of Samples from Lake Hoare	389
49.	The Five Quartz Grain Types Used for Classification of Samples from Lake Hoare	392
50.	Histograms Showing the Number of Grains in Each Grain Type. .	395
51.	Geometry of the Ice Cover for the Foundering Calculation . .	407
52.	Geometry of the Ice Cover for the Rayleigh-Taylor Instability Calculation	410

53.	Plot of Temperature vs. Time Showing Growth Rates for the Rayleigh-Taylor Calculation	413
54.	Diagram of the Present Geometry of the Layered Deposits with respect to the Canyon Walls	419
55.	Hypothetical Scenario of the Formation of the Layered Deposits	420

Plate

1.	Geologic Map of the Valles Marineris	441
----	--	-----

LIST OF TABLES

Table

1. Elevation Measurements for Locations in Candor Chasma 337
2. Volume of Plateaus of Layered Deposits in Coprates NW
Quadrangle 343
3. Results of Sieving Analyses for Sediment Samples from
Lake Hoare 382
4. Statistical Analyses of Grain-size Distributions of
Samples from Lake Hoare 383
5. Mineralogical Point Count Data of Samples from Lake Hoare . . 388

PRECEDING PAGE BLANK NOT FILMED

ABSTRACT

Detailed mapping of the layered deposits in the Valles Marineris, Mars from high-resolution Viking orbiter images revealed that they form plateaus of rhythmically layered material whose bases are in the lowest elevations of the canyon floors, and whose tops are within a few hundred meters in elevation of the surrounding plateau. The total volume of the layered deposits in Coprates Quadrangle NW is $\sim 1.28 \times 10^5 \text{ km}^3$. The average thickness of individual layers, as measured in two locations in Candor Chasma, ranges between 75m and 260 m. The greatest lateral extent of one traceable layer is 50 km in Melas Chasma.

A deep "moat" most commonly separates the plateaus of layered deposits from the canyon walls. There are a few locations in Ophir and Candor chasmata where layered deposits lap directly against the canyon walls. From these and other stratigraphic relationships, it was determined that the layered deposits formed during roughly the same time period as the enlargement of the canyons to their present configuration. Failure of the canyon walls, which produced large landslide deposits at the base of the scarps, occurred after the layered deposits formed and eroded to their present geometry. Valleys that separate plateaus of layered deposits, such as in Candor Chasma, may be a result of fluvial processes.

Four hypotheses for the origin of the layered deposits were considered: (1) that they are eolian deposits, (2) that they are remnants of the same material as the canyon walls, (3) that they are explosive volcanic deposits, or (4) that they were deposited in standing bodies of water. There are serious morphologic objections to each of the first three. The deposition of the layered deposits in standing bodies of water best explains their lateral continuity, horizontality, great thickness, rhythmic nature, and stratigraphic relationships with other units within the canyons.

Our understanding of martian climatic history indicates that any ancient lakes on

Mars would have been ice-covered. Three mechanisms to deposit sediment in an ice-covered lake were considered. Material can be transported down through the ice, in from the sides, or up from the bottom. All three methods appear to be theoretically viable, but all have some limitations.

The study of sedimentation in ice-covered lakes on Earth could help to elucidate processes that may have occurred on Mars. Ice-covered lakes in Antarctica were chosen as possible analogs to ancient lakes on Mars. Textural and mineralogical similarity of sediment at the bottom of Lake Hoare with sediment in the overlying ice indicates that sediment at the lake bottom was derived from sediment in the ice cover. Although it is not yet clearly understood how sediment migrates through the ice cover in Lake Hoare, this result gives impetus for further investigation of processes that could have transported sediment through the ice on martian lakes.

Two methods for transporting sediment through a cover of ice on a martian lake appear to be theoretically feasible. A system where sediment is superposed on ice will become unstable and founder when the mass of the sediment is greater than the mass of the ice. The result would be to effectively dump sediment into the liquid-water part of the system. Calculations show that a sedimentation rate between 0.4 and 1.5 mm/yr is needed to create an unstable situation to repeatedly dump layers of the thickness observed. The other method considered for transporting sediment through an ice cover was a Rayleigh-Taylor instability. A layer of sediment deposited on the ice could create an unstable situation where the relatively denser sediment would sink around diapirs of less dense ice, resulting in the sediment penetrating the ice layer. An instability will form in tens of years when the ice temperature is near freezing and the sediment layer is 75 to 150 m thick. When the ice is at 210 K, the instability will grow on the order of 1.4×10^4 years for a 75 m layer of sediment, and 6.5×10^3 years for a 150 m layer of sediment. Although both these mechanisms appear to be geologically feasible, there are severe limitations regarding the sediment source.

Volcanic material that originated beneath the lake might also be a source for the layered deposits. If volcanism were subaqueous rather than subaerial, many of the morpho-

logic arguments against the volcanic hypothesis are weakened or eliminated. Although there is no direct evidence for it, the process of subaqueous volcanism within the Valles Marineris lakes is an attractive hypothesis.

Transporting sediment into lakes from the canyon walls might also be a source of sediment for the layered deposits. If there were significant amounts of water present, material removed from the walls would have been deposited in horizontal layers. There are also problems with this process because the apparent geometry and volume of the layered deposits are inconsistent with the volume of material that could have originated from the canyon walls. Nevertheless, it seems unavoidable that sediment derived from the canyon walls became incorporated into the layered deposits.

Based on the presently available data, along with the theoretical calculations presented in this study, it appears most likely that the layered deposits in the Valles Marineris were laid down in standing bodies of water. Evidence concerning the size, lifetime, evolution, and content of these ancient lakes lies in their preserved sediments. They should be considered an important possible site for a future Mars Sample Return mission.

INTRODUCTION

Images of Mars received during the Mariner 9 and Viking missions revealed rhythmically layered deposits within the canyons of the Valles Marineris (McCauley, 1978; Lucchitta, 1981a; Lucchitta and Ferguson, 1983). They form thick sections of light and dark, horizontally layered material that most commonly stand as isolated plateaus or mesas on the canyon floors. Layered deposits are not found on the plains surrounding the canyon system. From the time of their initial discovery, workers have speculated on the origin of the layered deposits. Malin (1976) suggested that they are erosional remnants of canyon wall materials. It has been suggested that they were formed by eolian processes (Peterson, 1981) or explosive volcanic processes (Lucchitta, 1981a; Peterson, 1981). The layered deposits have also been compared to terrestrial lake deposits (McCauley, 1978; Lucchitta, 1982). The goals of this thesis are to describe the layered deposits in the Valles Marineris in detail, and to understand the geologic processes that could have led to their formation.

Geologic Setting

The Valles Marineris form a system of equatorial canyons on Mars. The system consists of a number of large, interconnected canyons or "chasmata" (McCauley and others, 1972) that trend east-west across the planet's surface for about 3200 km between longitudes 95° W and 40° W (figs. 1, 2). Individual canyons typically are 2 to 4 km deep and 50 to 100 km wide. They generally are interpreted to be erosionally modified grabens (Carr, 1974; Sharp, 1973a; Wise and others, 1979). The surrounding plateau surface and chasma floors are inclined about 0.10° to the east (U.S. Geological Survey, 1984).

The west end of the canyon system terminates near the summit of the Tharsis bulge at Noctis Labyrinthus, which is a complex network of interconnected canyons. The

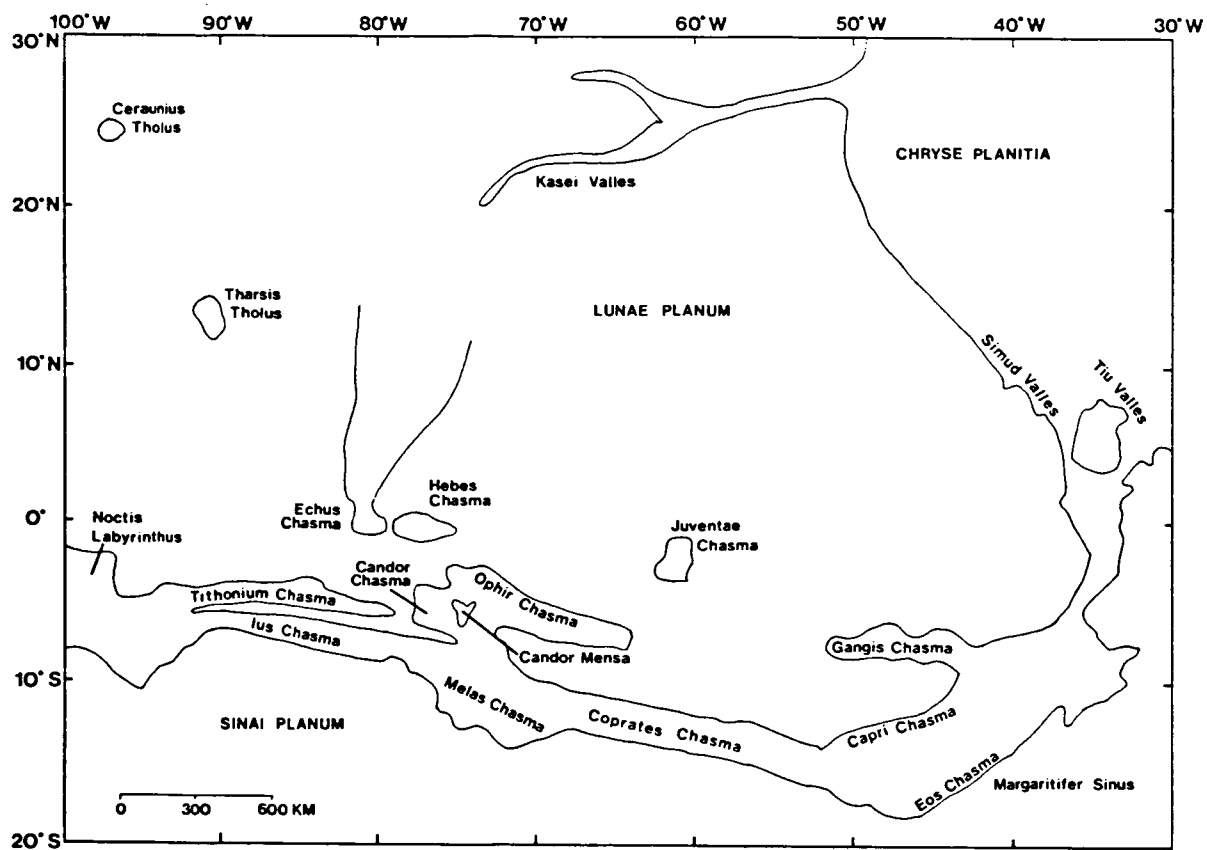


Figure 1: Index map of the Valles Marineris, Mars, and surrounding area; derived from U.S. Geological Survey shaded relief map of the western region of Mars, scale 1:15,000,000.

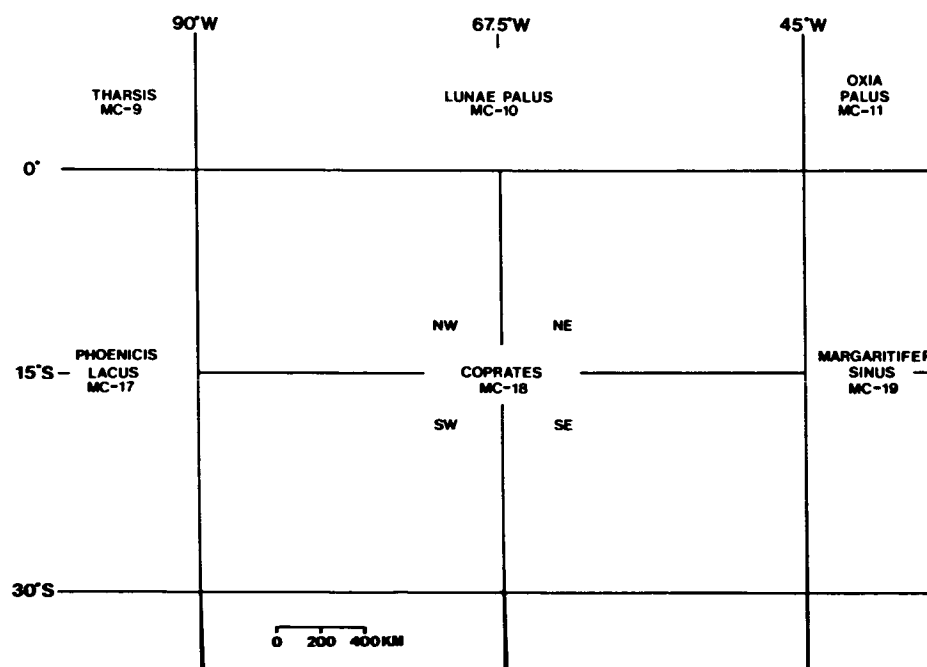


Figure 2: Index map for the U.S. Geological Survey quadrangle map.

Tharsis bulge is a topographic high, centered at approximately 10° S and 110° W, that is 5000 km to 6000 km wide at its base and 10 km high at its center. The Tharsis region is near the center of an array of radial fractures that affects the entire northern hemisphere (Carr, 1974). The Valles Marineris appear to have been partly controlled by these fractures.

The Valles Marineris system can be divided into three physiographic provinces (Carr, 1981). The western portion includes two narrow, roughly parallel canyons, Tithonium and Ius chasmata (fig. 3). Tithonium Chasma narrows to the east and ends in a line of closed depressions. Ius Chasma is composed of two troughs that merge eastward into the broad Melas Chasma. The center section is the widest part of the Valles Marineris, where Ophir, Melas, and Candor chasmata have coalesced to form a network about 700 km wide (fig. 4). Here, the canyons are 6 to 10 km deep and 100 to 150 km wide. The three central canyons are separated by eroded ridges that appear to be remnants of the surrounding plateau (McCauley, 1978). The southernmost canyon, Melas Chasma, merges eastward with Coprates Chasma. This eastern section is similar to the western section, in that it consists of narrow, parallel troughs (fig. 5). East of Coprates Chasma, the linearity and east-west trend of the canyon system are less apparent. In this third province, the canyons have irregular shapes and follow no consistent orientation. The canyon floors also change in character. They are generally smooth to the west, but, in the broad depressions to the east, the floors are very rough and blocky. The depression to the north is Gangis Chasma, and the wider depression to the south includes Capri and Eos chasmata (fig. 5).

The east end of the Valles Marineris system terminates in large areas of "chaotic terrain"—a term for ground that has apparently collapsed, forming a disordered arrangement of blocks that are at a lower elevation than their surroundings (Sharp, 1973b, fig. 5). Parts of the chaotic areas drain into large channels. To the north, Simud and Tiu valles drain into Chryse basin. The chaos merges to the east into Margaritifer Sinus (fig. 1).

Three canyons that are completely separate from the main portion of the Valles

ORIGINAL PAGE IS
OF POOR QUALITY



Figure 3: Western portion of the Valles Marineris; includes Tithonium, Ius, Echus, Hebes, and western Candor and Melas chasmata (picture no. 663A42).

ORIGINAL PAGE IS
OF POOR QUALITY

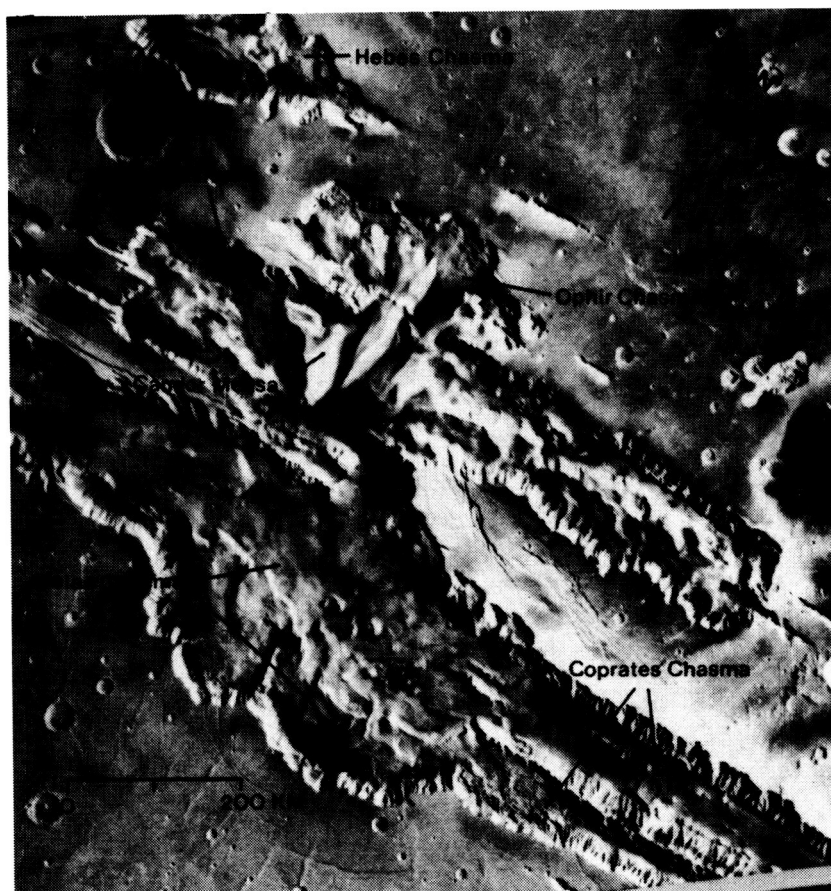


Figure 4: Central portion of the Valles Marineris; includes Hebes, Ophir, Candor, Melas, and western Coprates chasmata (picture no. 663A44).



Figure 5: Eastern portion of the Valles Marineris; includes eastern Candor, Juventae, Gangis, eastern Coprates, Eos, and Capris chasmata (picture nos. 663A46, 663A48).

Marineris lie to the north. The westernmost is Echus Chasma (fig. 3), which merges north into a broad, poorly defined depression along the west edge of Lunae Planum. Hebes Chasma lies directly to the east of Echus (figs. 3, 4). It has no inlet or outlet, and is the only closed basin in the canyon system. Further to the east lies Juventae Chasma (fig. 5), which is at the origin of another channel system that extends northward along the eastern border of Lunae Planum.

Horizontal, rhythmically layered deposits form flat-topped mesas or plateaus in the lower elevations of the canyons. The best exposures of the layering and the largest plateaus lie in Ophir and Candor chasmata, but the layered deposits exist in the other canyons as well.

Previous Work

Malin (1976) recognized layered material in Gangis Chasma from Mariner 9 images. He described the deposit as being a mesa-like structure in a 2-km-deep chasm where the summit is essentially level with the surrounding plains. Malin suggested that the layered deposits were not made of the same material as the intercrater plains because the walls of the canyon do not show the abundant layering that is seen on the mesa. He speculated that the layered deposits may represent an inhomogeneity within the plains material, because it was difficult to imagine a process that would fill the canyon to the brim with sediment, and then subsequently remove much material. He also noted that the appearance of slope gullies on the mesa suggests that the mesa may be made of loosely consolidated material that is rich in volatiles.

McCauley (1978) also speculated on the origin of the layered deposits using Mariner 9 images. He argued that no geologic process other than deposition in a low energy water environment could readily explain the apparent horizontality, lateral continuity, and competence of the individual layers. He further speculated that lakes formed from melted ground ice that collected in depressions created by tectonic subsidence, and he suggested that the divides between Ophir and Candor chasmata, and between Candor

and Melas chasmata once separated the canyons into three lakes. These divides could have been eroded and breached catastrophically, allowing water to rush through the narrow canyons to the east. He argued that overflow of these putative lakes could explain the fluvial scouring and channels that are seen in the Margaritifer Sinus and Oxia Palus regions.

In June and August of 1976, Viking Orbiters 1 and 2 arrived at Mars and began to transmit images of the Martian surface with much higher resolution that allowed features as small as 10 m to be resolved. This information confirmed what was seen in the Mariner 9 data: that plateaus of layered deposits have repeated light and dark layers exposed on their steep sides, that individual layers are continuous over large areas, and that these deposits exist throughout the Valles Marineris.

Lucchitta (1981a; 1982) studied the Valles Marineris using Viking 1 and 2 high-resolution images. Her results supported McCauley's work, in that she too concluded that the layered materials in the canyons are not erosional remnants of the surrounding plateau. She noted their fine, even bedding and suggested that their morphology was consistent with sedimentary deposition in association with water. She also noted that the canyon floor of Ophir Chasma is as much as 4,000 m above the floor of Candor Chasma, which lies directly to the south, yet the layered deposits in both canyons reach nearly the same elevation. This comparison led her to suggest that any water-related deposition might have had a common base level. She also compared the morphology of the layered deposits to sedimentary units in fault troughs of the Basin and Range province in western North America to support the hypothesis that they were deposited in lakes.

Lucchitta and Ferguson (1983) attempted to understand the origin of the outflow channels that emerge from the Valles Marineris at the east end, and to explain some of the erosional features found in the central canyons and Eos and Coprates chasmata. Outflow channels are wide, flat-floored valleys that emerge fully developed from their sources. It has been shown that they resemble large terrestrial flood features (Baker and Milton, 1974). Lucchitta and Ferguson (1983) examined the gradients on the floors

of outflow channels in Chryse Basin and Lunae Planum. The slopes were derived from six Earth-based radar-elevation profiles. Whereas some channels show gradients of 1.1 m/km and 2.5 m/km, which are similar to those of the catastrophic flood channels in the Channeled Scablands of eastern Washington State, others appear to be level. Lucchitta and Ferguson (1983) proposed that ponding in the Valles Marineris grabens, in ancient craters, and perhaps in regional lowlands took place before the outflow channels formed. As lakes overflowed, dams were breached and eroded, causing catastrophic floods carrying mixtures of water, sediment, and ice to flow through the canyon system. The floods would have had sufficient fluid potential to move across nearly level channel gradients to the east and north of the Valles Marineris. The technique of determining elevation profiles from Earth-based radar data is less accurate when the topographic relief is low, and distances are great (10-100 km). Because Lucchitta and Ferguson (1983) depended heavily on radar data for their interpretation of the history of channel formation near the Valles Marineris, their work only tentatively supports the hypothesis that ponded water once existed in the Valles Marineris, and that the erosional valleys that are associated with some of the plateaus of layered deposits may have a fluvial origin.

A study of the origin of the central plateau of layered deposits in Hebes Chasma was presented by Peterson (1981). She proposed an eolian or volcanic origin for those deposits, and by implication, the other layered deposits in the Valles Marineris. Global dust storms would have been the source of sediment if they are eolian deposits. She suggested that variations in layering could have been produced by different compositions of the dust with successive storms if the deposits are eolian in origin. If the deposits are volcanic, she suggested that they are made of dominantly ash-flow deposits, and that the source of the magma may have been related to the Tharsis volcanism. She discounted the theory that the deposits have a lacustrine origin on the basis that removal of water and sediment that may have once been in contact with the canyon walls is difficult to explain in the absence of any drainage leading out of Hebes Chasma.

A great deal of work has been done on water and ice on Mars. There is evidence, such as fretted terrain, thermokarst, lobate debris aprons, rampart craters, and

patterned ground, for large amounts of ground water or ground ice on the planet (e.g. Squyres, 1984). Fretted terrain is found along the northern lowland/southern highland boundary, and is characterized by "abrupt escarpments of complex planimetric configuration" (Sharp, 1973b). Sharp (1973b) and Soderblom and Wenner (1978) suggested that ice may have contributed to the formation of the escarpments. Thermokarst is a terrestrial feature known to result from melting of ground ice. These features on Earth have been estimated to be as much as 80-90 percent ground ice (Washburn, 1973). Similar features are seen on Mars (Carr and Schaber, 1977). Lobate debris aprons are deposits that are convex (in cross section), and are common at the bases of escarpments over latitudes from 30° to 50° in both hemispheres (Squyres, 1979). They probably were formed by gradual flow of interstitial ice, similar to terrestrial rock glaciers (Wahrhaftig and Cox, 1959). Rampart craters have ejecta deposits consisting of overlapping lobes of debris that have in some locations flowed around low-lying obstacles. Because flows have not experienced much compaction, it is speculated that interstitial liquid, mostly likely water, lubricated the flow. The source of water may have been ground ice that was partly melted during impact (Carr and others, 1977). There are a number of features on Mars that are similar to "patterned ground," which are found in high latitudes on Earth. Washburn (1973) described patterned ground as being a frost-related feature that forms by repeated freezing and thawing of ice-rich soil. Squyres and Carr (1986) found evidence for quasi-viscous relaxation of topography poleward of 30 degrees latitude in both the northern and southern hemispheres. They suggested that this relaxation may be due to creep deformation of ground ice. These features together form the geomorphic evidence that there was and may presently still be substantial amounts of water and ice in the regolith of Mars.

Carr (1979) proposed a source for the water that was responsible for creating the outflow channels, which could also be the source for possible lakes in the Valles Marineris. Carr suggested that the large volumes of water that carved the outflow channels may have been stored in confined aquifers. The older, cratered terrain may have acted as the reservoir for the liquid water. Water that flowed from the surface into the regolith during a warmer climate would have become trapped under a thick layer of permafrost

during subsequent global cooling. Water could have been released at high discharge rates if pore pressures exceeded lithostatic pressures, or if an impact or fault broke through the permafrost layer. Removal of subsurface water or ice can explain the presence of chaotic terrain at the heads of many outflow channels. Water stored deep in the Martian regolith could also account for a source of water in the Valles Marineris.

Scope of Investigation

The purpose of this thesis is to present a detailed geologic investigation of the layered deposits in the Valles Marineris using principles of planetary geologic mapping (e.g. Wilhelms 1972), and to study the origin of the layered deposits from possible terrestrial analogs.

Geologic mapping of the layered deposits includes establishing their geographic distribution, the thickness of individual layers, and the total volume occupied by the layered deposits. The time sequence in which these deposits were laid down is determined by examining the stratigraphy of all the major units within the canyons.

Four hypotheses are considered for the origin of the layered deposits: (1) that they are eolian deposits (Peterson, 1981), (2) that they are remnants of the same material that makes up the canyon walls (Malin, 1976), (3) that they are explosive volcanic deposits (Lucchitta, 1981a; Peterson, 1981), or (4) that they were deposited in standing bodies of water (McCauley, 1978; Lucchitta, 1982). The hypothesis that they were formed in ancient lakes is further considered by investigating sedimentation in perennially ice-covered lakes on Earth. Based on our present understanding of Martian climatic history, any lakes that existed on Mars would have had a permanent ice cover (e.g. Wallace and Sagan, 1979; Carr, 1983). The Dry Valley Lakes in Antarctica provide an interesting possible analog to lakes on Mars because they, too, are perennially ice-covered (McKay and others, 1985). Sedimentation in ice-covered lakes on Mars also is investigated by theoretically analyzing four mechanisms for transporting sediment through an ice cover.

In addition to the interesting geologic problem posed by these deposits, their

formation could have important exobiological significance. Life on Earth is believed to have originated in standing water. If precursors to life ever existed on Mars, a likely location would be the putative lakes in the Valles Marineris. Any evidence concerning the size, lifetime, evolution, and content of such lakes lies in their preserved sediment. This investigation of the layered deposits in the Valles Marineris will provide a thorough description of the deposits, in addition to a detailed exploration of their formation using terrestrial analogs and theoretical considerations to constrain their origin.

GEOLOGY OF THE LAYERED DEPOSITS IN THE VALLES MARINERIS

Mapping

Detailed photogeologic mapping of the layered deposits was performed using 1400 Viking Orbiter 1 and 2 high resolution images acquired with orbital altitudes less than 5000 km and having surface resolutions ranging from 125 to 20 m per picture element. The goals of the mapping were to establish the geographic distribution, thickness, and morphology of the deposits, to establish the stratigraphy of all the major geologic units within the canyons, and to choose among candidate hypotheses for the origin of the layered deposits.

Materials within the Valles Marineris were divided into five units: (1) slope and bedrock material, (2) layered chasma deposits, (3) possible layered chasma deposits (deposits with characteristic weathering such as fluting and/or a mottled surface texture like that of the layered chasma deposits), (4) landslide material, and (5) chasma floor material. Units 1,2,4, and 5 are inferred to have formed by different geologic processes, and therefore are genetically unique, rather than merely being different in appearance. Units 2 and 3 probably are the same material, but they were mapped separately in order to distinguish areas where the layering is exposed from areas where their identification as layered deposits is less certain. The geologic map of the Valles Marineris is presented in Plate 1.

Slope and Bedrock Material

The canyon walls show three major types of morphology: spurs and gullies, tributary canyons with V-shaped profiles, and steep, curvilinear recesses in the chasma wall formed by landslides (Lucchitta, 1978).

The spur and gully morphology is the most common landform of the chasma walls. One of the best examples is located on the northern wall of Ophir Chasma (fig. 6), where the face is dissected by steep gullies and intervening spurs that branch downward at acute angles (Sharp, 1973b). The average slope of this face is 18° (determined from the U.S. Geological Survey (1984) topographic map of the area). Individual spurs have gradients of 15° to 20° and intervening gullies are as steep as 30° at the south wall of Ius Chasma (Wu and others, 1973). These slopes are therefore probably near the angle of repose of for unconsolidated material. The spur and gully morphology is most likely a product of the downward movement of material by gravity, which has occurred as a slow and steady process, as opposed to a catastrophic event such as landsliding or rock fall (Lucchitta, 1978).

Tributary canyons generally are solitary canyons that dissect the surrounding plateau (fig. 7). In some areas they occur in groups, such as on the south wall of Ius Chasma. Single canyons are 30 to 130 km long, up to 10 km wide, and up to 2 km deep, or similar in size to the Grand Canyon of Arizona. Their V-shaped cross-sections may have been accentuated by additional infilling of talus (Lucchitta, 1978). Gradients of the tributary canyon floors are at most a few degrees (U.S. Geological Survey, 1976), and the tributaries slope gently toward the interior of the canyons.

Steep sections where the chasma walls are smooth and broadly curved or straight are interpreted to be old landslide scars. At the base of these scarps are hummocky piles of debris that are the landslide deposits (Lucchitta, 1978). An excellent example of an ancient landslide scar lies in northern Ius Chasma directly adjacent to a section with spur and gully topography (fig. 8). Landslide scars also expose a distinct dark, horizontal band in the canyon wall that begins at the surface of the surrounding plateau and extends downward for about one fifth of the total height of the canyon wall (fig. 8). It is most likely a layer of flood lavas that cap the surface of the surrounding plateau (McCauley, 1978). This band is prevalent in most parts of the Valles Marineris, but it is distinct from the rhythmic, light and dark banding of the layered deposits.

ORIGINAL PAGE IS
OF POOR QUALITY

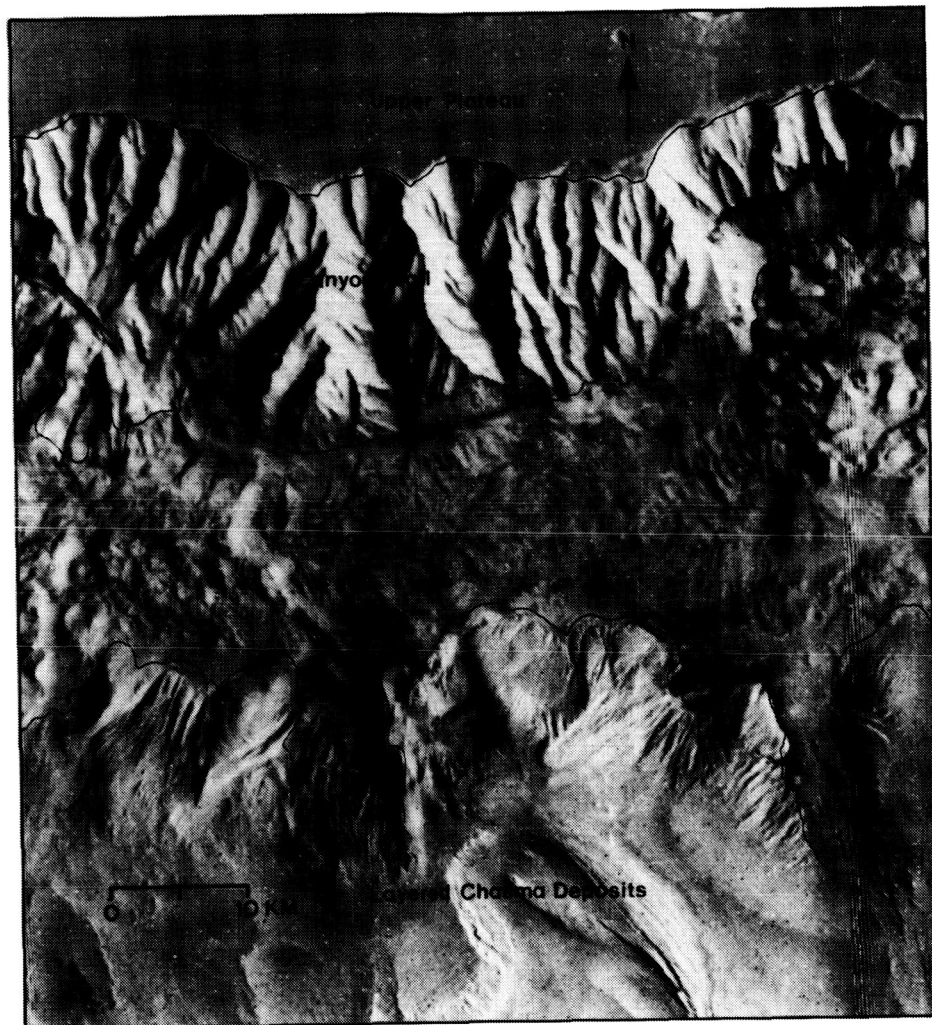


Figure 6: Northern wall of Ophir Chasma showing the spur-and-gully morphology of the canyon wall. The plateau of layered deposits show eolian fluting that is distinct from the canyon wall morphology. The "moat" that separates the layered deposits from the canyon wall has a rough texture that may have been produced by material that was sloughed off the nearby cliff faces (picture no. 914A10).

ORIGINAL PAGE IS
OF POOR QUALITY

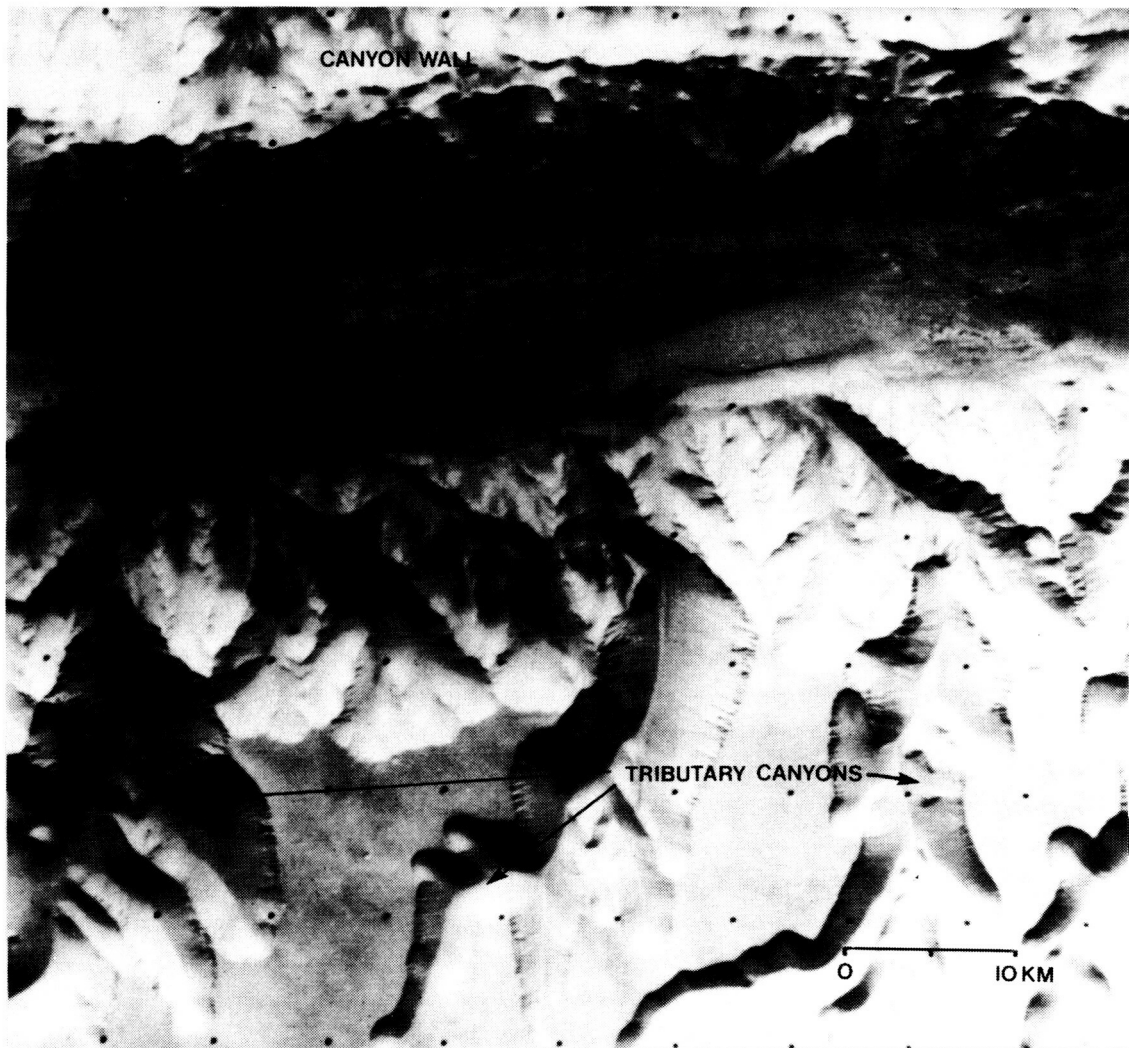


Figure 7: The southern wall of Ius Chasma has V-shaped tributary canyons. To the north is an outlier of the chasma wall material that shows the characteristic spur-and-gully morphology (picture no. 066A08).

ORIGINAL PAGE IS
OF POOR QUALITY



Figure 8: Western Ius Chasma showing landslide scarps adjacent to canyon walls with the spur-and-gully morphology. A dark band is exposed at the landslide scarps which may be a layer of flood lavas (picture no. 057A43).

Layered Chasma Deposits

The layered deposits form plateaus rising as high as 5 km above the canyon floor. The greatest total thicknesses are found in Hebes, Ophir, and Candor chasmata. In these locations, the upper surface of the layered deposit plateaus are within 500 m of the elevation of the surrounding plateau. Other occurrences are in Melas Chasma, where the plateaus are low-lying, and cover smaller areas. Two large plateaus (one each) in Juventae and Gangis chasmata appear to be similar in size to the central plateau in Hebes Chasma, based on medium resolution images. Rhythmic light and dark horizontal layers are exposed on the slopes of the plateaus that are as steep as 22 degrees. The layers are best exposed on the cliffs of plateaus in Hebes Chasma, Candor Mensa (fig. 4) in Candor Chasma, and Juventae and Gangis chasmata (figs. 9 through 12). The layers form light and dark couplets. Each couplet appears to be similar in thickness when viewed at the highest resolutions (fig. 12). Areas were mapped as "layered chasma deposits" only if the layering is clearly exposed.

The shape and sizes of the plateaus do not have any apparent systematic variation. The plateaus are all irregularly shaped, and in most cases they have essentially flat tops (fig. 10). The plateau in eastern Candor Chasma is an exception. The top of this mesa has an irregular surface, with relief up to 500 m (fig. 13). In most places, such as in Melas Chasma (fig. 14), the plateau borders facing the canyon walls are roughly parallel to the canyon walls. The plateaus vary from north to south within the central portion of the Valles Marineris. The thickest deposits are in the northern canyons (Hebes, Ophir, and western Candor), they thin to the south where the height of the canyon walls also diminishes.

Individual layers extend laterally for tens of kilometers. The most continuous exposed layer was traced for a distance of 50 km on a plateau in southern Melas Chasma (fig. 15). Layers may extend for much greater distances, but they either are obscured or can not be detected because the necessary neighboring high resolution images do not exist. Determination of the character of the individual beds also was limited because of the lack of high enough resolution.

ORIGINAL PAGE IS
OF POOR QUALITY

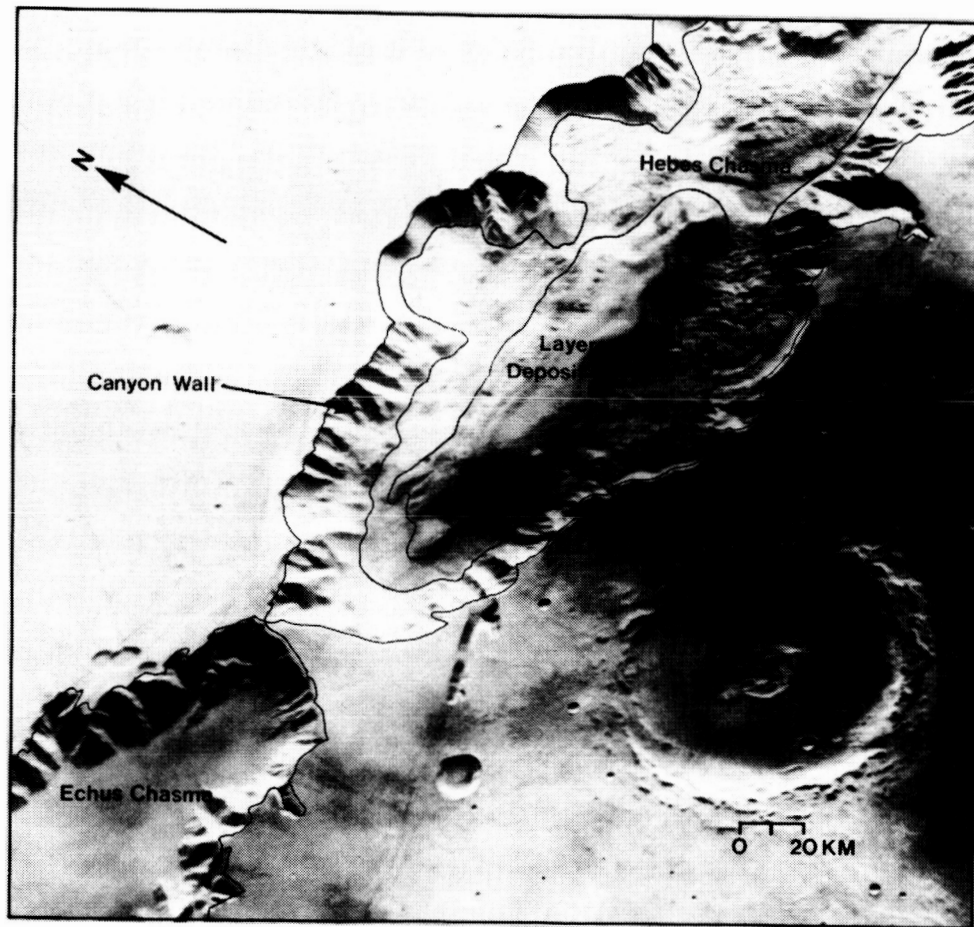


Figure 9: Hebes Chasma with a central plateau of layered deposits surrounded by a "moat", which separates the plateau from the canyon wall. Landslide deposits from the north abut against the central plateau (picture no. 645A60).

ORIGINAL PAGE IS
OF POOR QUALITY

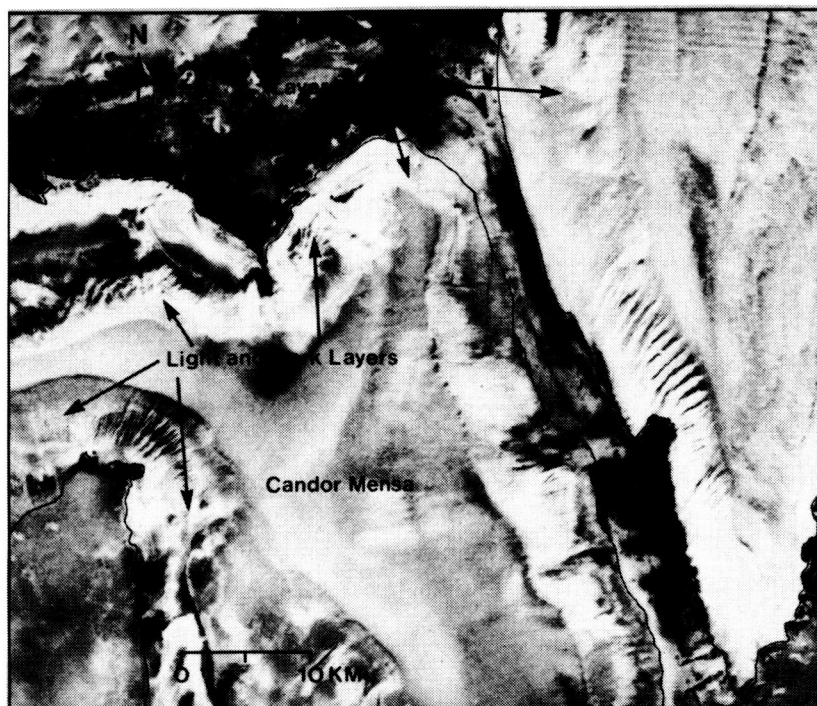


Figure 10: Two plateaus of layered deposits in Candor Chasma showing flat upper surfaces and a mottled pattern. Light and dark layers are exposed on the sides of Candor Mensa. The v-shaped valley that divides the two plateaus was probably caused by eolian and/or fluvial erosion (picture no. 066A25).

ORIGINAL PAGE IS
OF POOR QUALITY



Figure 11: Southwest Juventae Chasma showing a plateau of layered deposits (picture no. 907A05).



ORIGINAL PAGE IS
OF POOR QUALITY

Figure 12: Gangis Chasma showing a plateau of layered deposits (picture no. 610A13).

ORIGINAL PAGE IS
OF POOR QUALITY

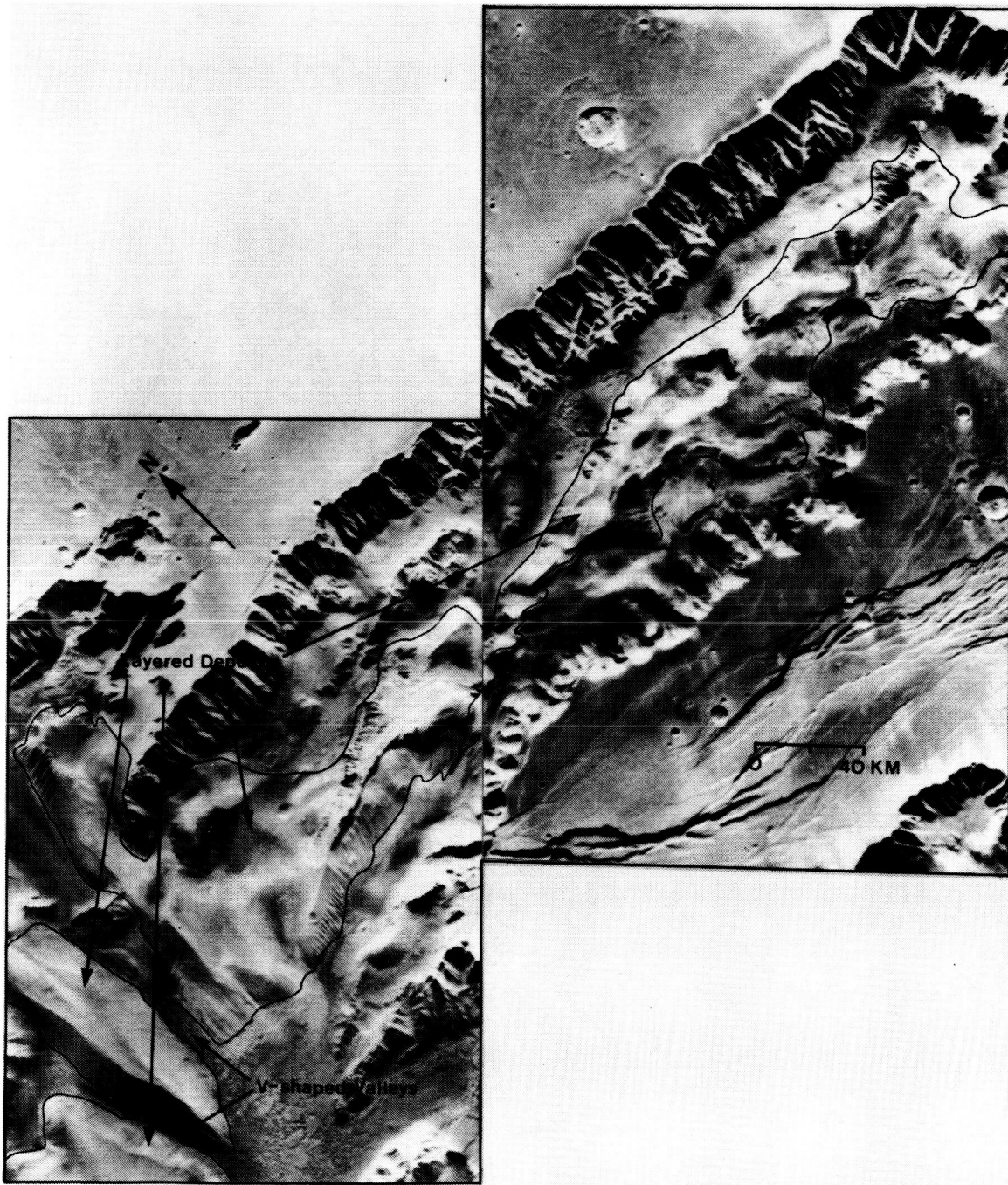


Figure 13: Plateaus of layered deposits in Candor Chasma. The upper surfaces have an undulating topography. The v-shaped valleys separating the plateaus are evidence for extensive erosion (picture nos. 608A74, 608A75).

ORIGINAL PAGE IS
OF POOR QUALITY

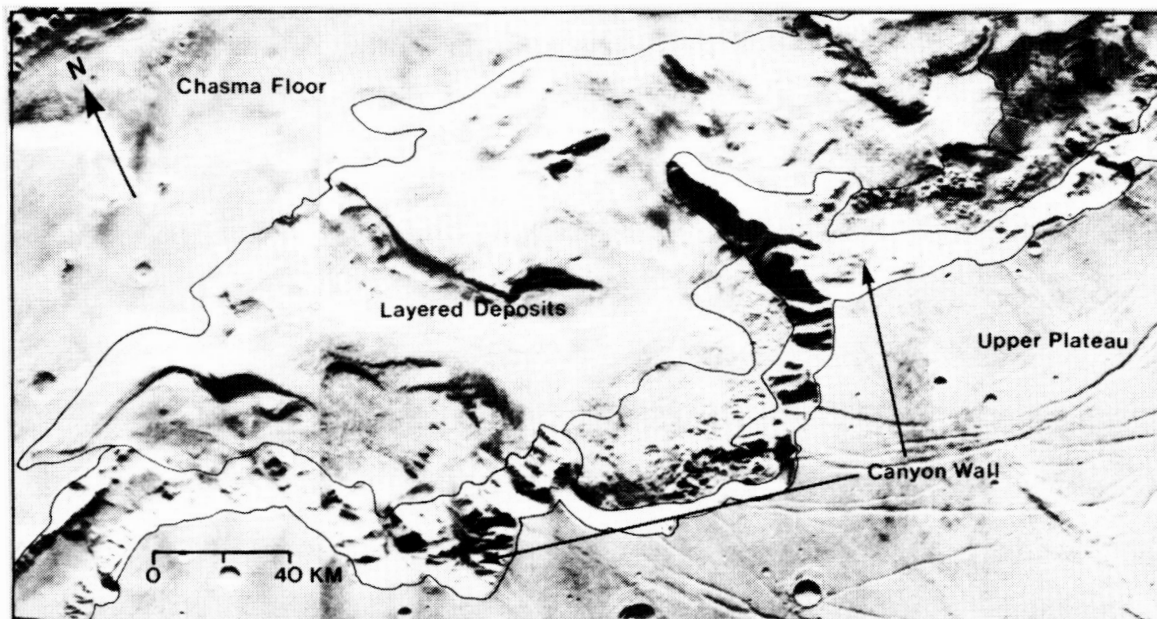


Figure 14: Layered deposits in Melas Chasma. The borders of the deposits roughly parallel the canyon wall (picture nos. 608A71, 608A72).

ORIGINAL PAGE IS
OF POOR QUALITY



Figure 15: Plateau of layered deposits in southern Melas Chasma. An individual layer (arrows) was traced laterally for 50 km. The layer may be continuous for a greater distance, but it is obscured in a valley. The upper surface shows the characteristic mottled pattern (picture no. 915A20).

A deep trough, here called a "moat," commonly separates plateaus of layered deposits from the canyon walls. In Hebes Chasma, the central mesa of layered deposits is completely surrounded by a well-developed moat (fig. 9). In other areas, the layered deposits are found in direct contact with the canyon wall. At the base of the northern canyon wall of Candor Chasma, two plateaus of the layered deposits completely encompass, and partially bury the canyon wall (fig. 16). The canyon walls can be identified by the spur-and-gully topography. A remnant of layered deposits in contact with the canyon wall also was found north of Candor Mensa. It appears that the layered deposits lap directly against the base of the spur-and-gully topography of the canyon wall in an undisturbed position. These two locations are the only ones where the layered chasma deposits were found in this context.

In some areas the layered deposits have been deeply eroded. This is most evident on a large scale in Ophir and Candor chasmata where large, V-shaped valleys divide plateaus of layered deposits (fig. 13). The floors of these valleys are up to 2 km higher than the elevation of the surrounding chasma floors and bases of the moats. The valley surfaces have streaks that are reminiscent of fluvial or eolian erosional features. A few of the plateaus such as Candor Mensa and the plateau directly to the east have a streamlined shape that is indicative of fluvial erosion (fig. 3). On a smaller scale, cliff faces in some locations have been etched in a way that makes the horizontal layering pronounced (fig. 17).

Erosion and weathering of the layered deposits also has produced fine fluting along the steeper faces of the plateaus and a light and dark mottled pattern on the subhorizontal surfaces (figs. 15, 16). The mottling may be produced by differential weathering of layers of differing albedo. This pattern has a unique appearance that can be identified on a number of surfaces within the Valles Marineris. The fluting is characterized by narrow, subparallel grooves that trend nearly perpendicular to the slope of the plateau faces, and is inferred to result from wind erosion (fig. 18). The orientation of the fluting implies that wind directions were locally up or down slope. Lucchitta (1981a) compared these landforms to terrestrial yardangs. Yardangs have

ORIGINAL PAGE IS
OF POOR QUALITY

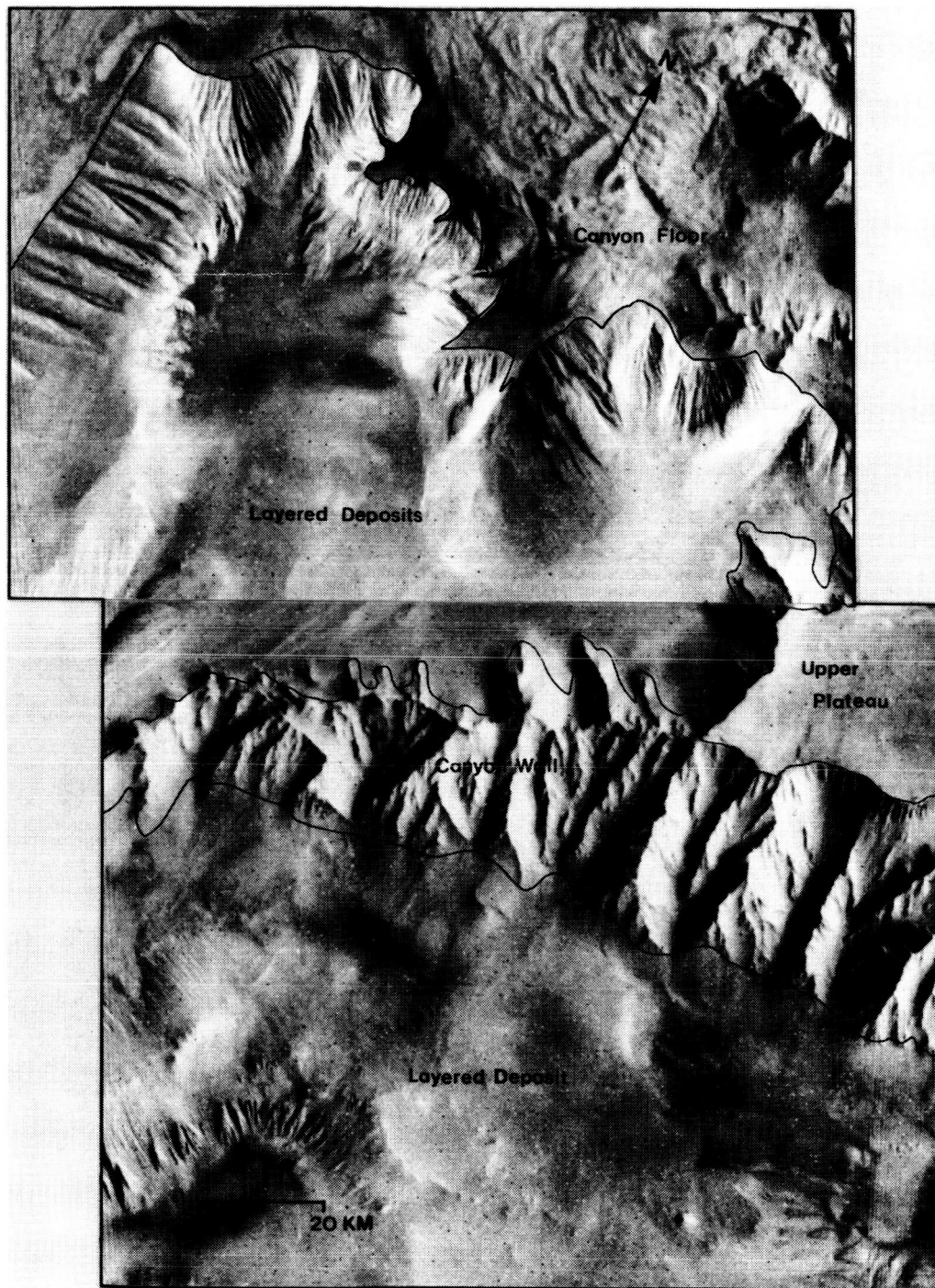


Figure 16: Spur of the canyon is partially buried by layered deposits in Candor Chasma. The top surfaces of the layered deposits have the characteristic mottled pattern (picture nos. 913A11, 913A13).

ORIGINAL PAGE IS
OF POOR QUALITY



Figure 17: Plateau of layered deposits in western Ophir Chasma. Layers have been accentuated by etching (picture no. 915A10).

ORIGINAL PAGE IS
OF POOR QUALITY

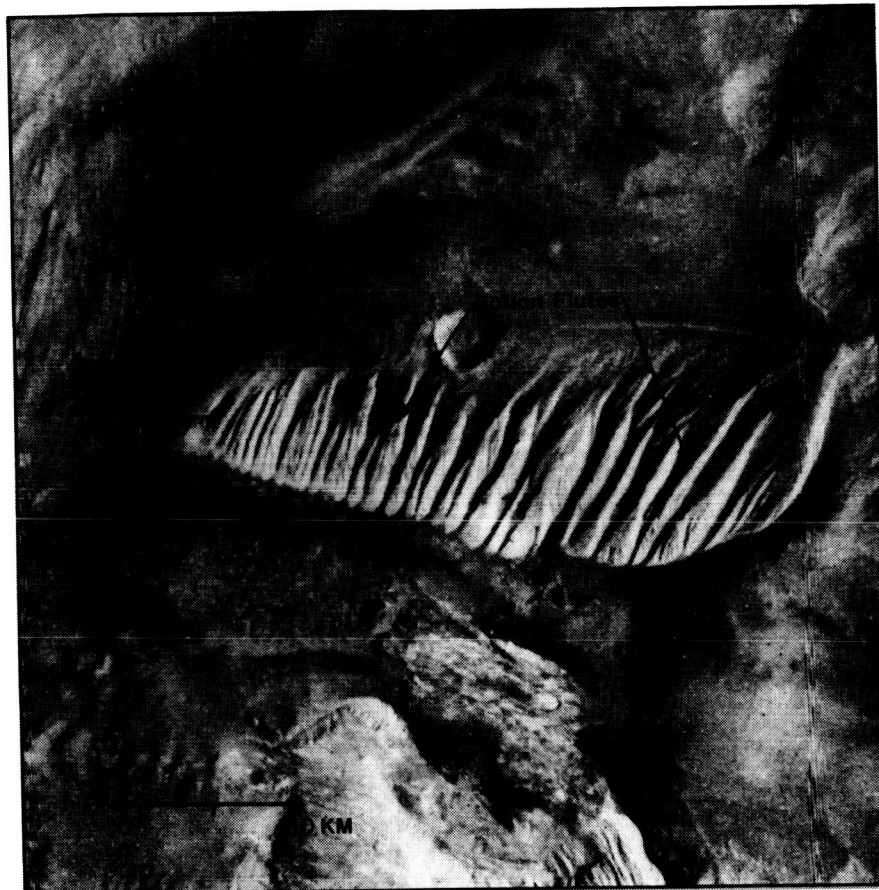


Figure 18: Eolian flutes oriented sub-perpendicular to a steep face of layered deposits in southern Candor Chasma (picture no. 914A52).

been produced by eolian erosion elsewhere on Mars (Ward, 1979). Fluting is seen on plateaus of layered deposits throughout the Valles Marineris. Some of the best localities are in Candor Chasma, where the fluting has developed on faces where the layering is clearly exposed (fig. 19). The spur-and-gully topography of the canyon walls is distinct from the eolian fluting of the layered deposits (see fig. 6 for comparison). Fluting is observed only on the layered deposits, and not on the canyon walls.

Possible Layered Chasma Deposits

The mottled, light and dark pattern on the top of the plateaus, and the presence of fluting on the cliff faces were used to identify material that was classified as "possible layered chasma deposits." Because the relationship between rhythmic layering and the mottled surface pattern was established in well-exposed remnants (fig. 10), it is inferred that layered chasma deposits may exist in areas where there is distinct mottling, but no exposed layers. For example, in Melas Chasma, only a few of the plateaus show some distinct layering, but there are many locations where the surface is mottled (fig. 20). This relationship may be valid for the association of fluting and layering. Because fluting has been observed on the layered deposits, and not on the canyon walls, landslide deposits, or the canyon floors, tentative identification of the layered deposits also can be made based on the presence of fluting. Layering may be obscured for a number of reasons. Foremost, the resolution or the sun angle of the images may not be adequate to detect layering. A surficial blanket of dust may be covering the layers, or portions of the plateau face may have crumbled enough to obscure the layers. Alternatively, some deposits may not have well-developed layering. This classification was created because it was important to separate those areas where the layers are clearly exposed from locations where only the characteristic mottling or fluting is detected.

A broad deposit that covers most of Eos and Capri Chasmata, which McCauley (1978) identified as layered chasma deposits, was mapped as possible layered chasma deposits in this report (fig. 21). The surface of this deposit has an unusual appearance. It has a gently undulating surface of uniform albedo that is similar in texture to some

ORIGINAL PAGE IS
OF POOR QUALITY



Figure 19: Flutes superimposed on layering on a southwest-facing cliff of layered deposits in Candor Chasma (picture no. 915A14).

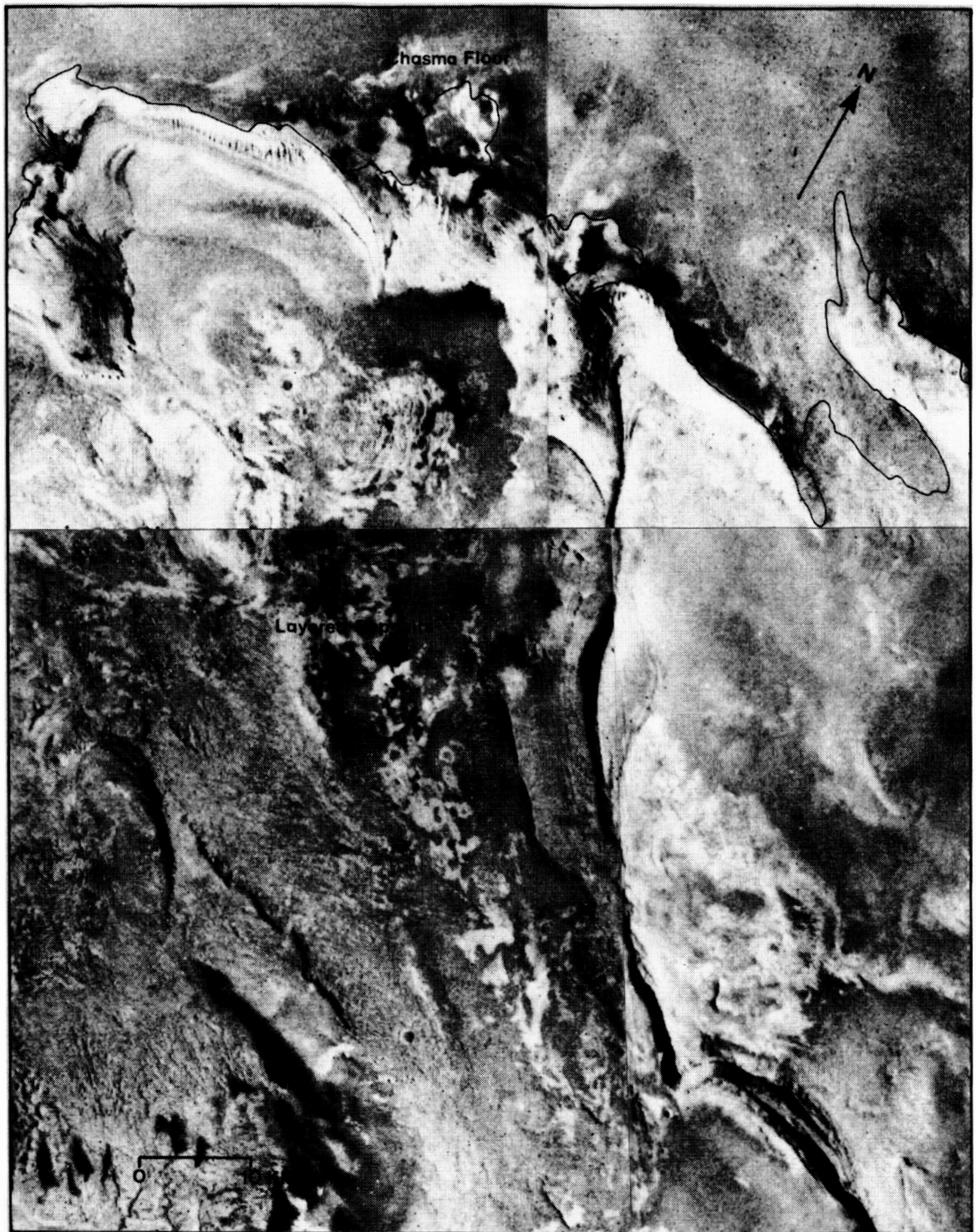


Figure 20: Plateau of layered deposits in Melas Chasma. Layers are exposed on some of the cliffs. The upper surface has the characteristic mottled pattern (picture nos. 915A19, 20, 21, 22).

ORIGINAL PAGE IS
OF POOR QUALITY

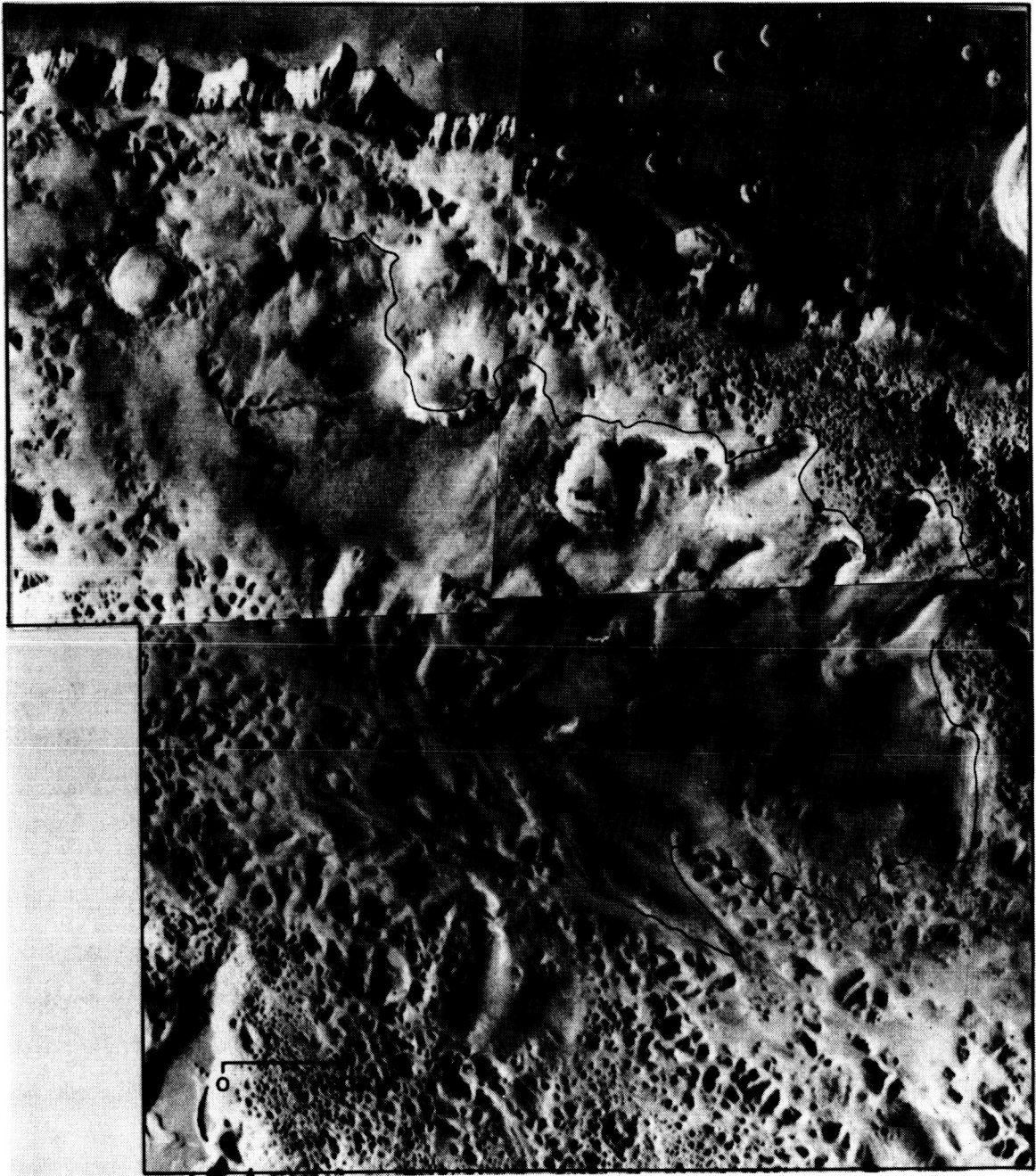


Figure 21: Material in Eos and Capri chasmata that have a surface texture similar to that of the layered deposits. See Figure 10 for comparison. This sediment may have originated as layered deposits in the western canyons and may have been redeposited in this location (picture nos. 610A30, 31, 32).

parts of the layered deposit plateaus, such as on the east side of Candor Mensa where the layering is not clearly exposed. These sediment may have originated as layered chasma deposits in the western canyons, and they may have been redeposited in Eos and Capri chasmata.

Landslide Material

Hummocky material lying at the base of landslide scars was mapped as landslide material (fig. 8). These deposits characteristically show vague alignment of ridges parallel or perpendicular to the canyon walls and they bury the walls locally up to about half their original heights. Slump blocks occur at the heads of most of the large landslides (Lucchitta, 1979).

A landslide deposit that originated on the north wall of Ophir Chasma shows curved grooves that trend away from a cliff of layered deposits to the west (fig. 22). The flow was diverted by the plateau. Lucchitta (1979) favored the theory that Martian landslides occurred as liquified debris flows or mudflows, rather than flows that moved on a cushion of air as envisioned for the Sherman landslide in Alaska (Shreve, 1966). If they were mudflows, Sharp (1973a) suggested that the water may have come from the melting of ground ice.

Most of the landslides occurred in the materials showing spur-and-gully morphology. Nowhere do landslide deposits emanate from plateaus of layered deposits. Lucchitta (1981b) also recognized this fact in the context of supporting her assertion that landslides were wet. Because landsliding only occurred on the canyon walls, she argued that the canyon walls had a higher water content than the plateaus of layered deposits, and therefore were more susceptible to catastrophic failure.

Chasma Floor Material

All other materials lying on the canyon floors were mapped as chasma floor material. This designation includes low-lying deposits between the plateaus of layered

ORIGINAL PAGE IS
OF POOR QUALITY

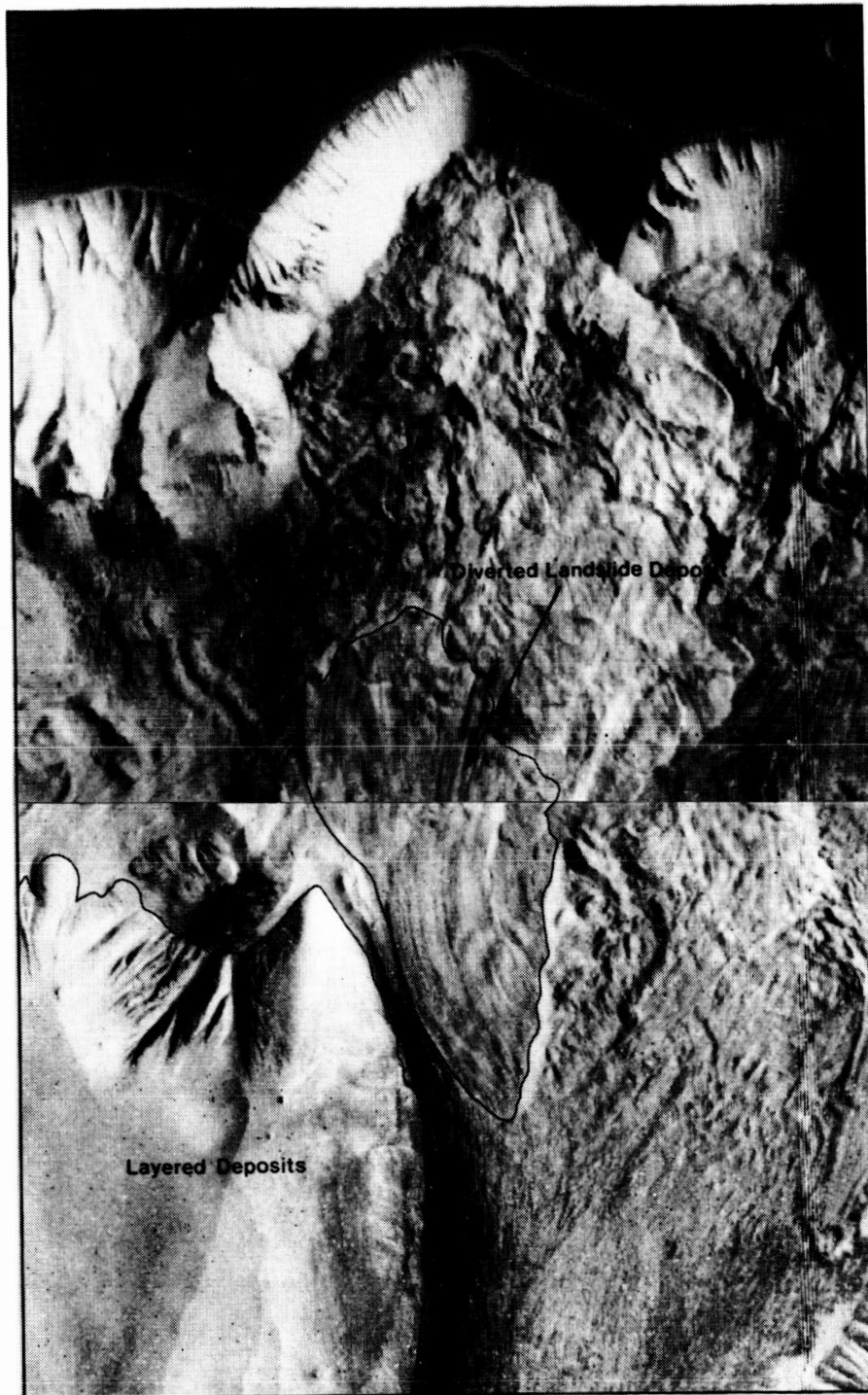


Figure 22: Deposit of a landslide that was diverted by a plateau of layered deposits, indicating that the flow was highly mobile (picture nos. 913A10, 913A12).

deposits, the floors of the moats, large stretches of the canyon floors that are virtually flat, and blocky material at the base of the spur-and-gully topography of the canyon walls.

The most common form taken by the chasma floor material is deposits with a smooth surface and uniform albedo (fig. 23). In some locations, such as in western Candor Chasma and southern Melas Chasma, the surface is smooth, but the tones range from light to dark over broad expanses, suggesting that the surface is slightly undulatory, exposing materials of differing albedos (figs. 24, 25). This pattern is distinct from the mottled surface of the layered deposits in that it occurs in topographic lows, and the spacing between the light and dark areas is wider (tens of kilometers spacing, versus 1 to 2 km spacing for the layered chasma deposits). It is possible that these areas appear to be the canyon floor, yet they are really the top surface of layered deposits that lie below. In areas close to the canyon wall, such as in western Ius Chasma, the chasma floor material has a rough texture that may have been produced by material that was sloughed off the nearby cliff faces (fig. 26).

Chasma floor material makes up the floors of most moats. The moat separating the plateau of layered deposits from the northern canyon wall in Candor Chasma is typical of the moat morphology (fig. 27). Here, the moat is flat-floored and has no discernible erosional features to suggest the manner in which it was formed. The canyon wall overlooking the moat exhibits both the spur-and-gully and landslide scar morphologies. Generally, the floor of the moat has rubbly deposits or a rough texture that may have formed by material that was sloughed off the nearby canyon wall (fig. 6).

Southeast of Candor Mensa, the canyon floor has a unique character (fig. 28). Polygonal blocks that are hundreds of meters on a side are positioned slightly above the surrounding area. The areas between the blocks are filled with rounded knobs that appear to be remnants of former polygons. The appearance is similar to that of chaotic terrain that is common elsewhere on Mars.

At the eastern extremity of the Valles Marineris, where the canyon walls taper into the surrounding plateau, the chasma floor material becomes intermingled with remnants

ORIGINAL PAGE IS
OF POOR QUALITY



Figure 23: The chasma floor material typically has a smooth surface and uniform albedo such as in this location in central Melas Chasma, where remnants of the canyon wall are surrounded by chasma floor material (picture no. 914A21).

ORIGINAL PAGE IS
OF POOR QUALITY

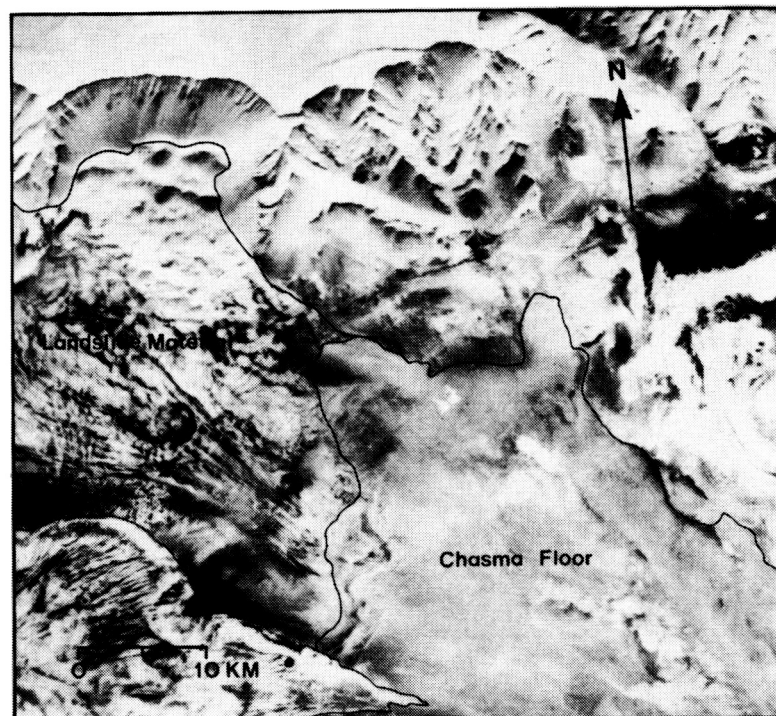


Figure 24: The albedo of the chasma floor material in western Candor Chasma is light and dark (picture no. 066A24).

ORIGINAL PAGE IS
OF POOR QUALITY

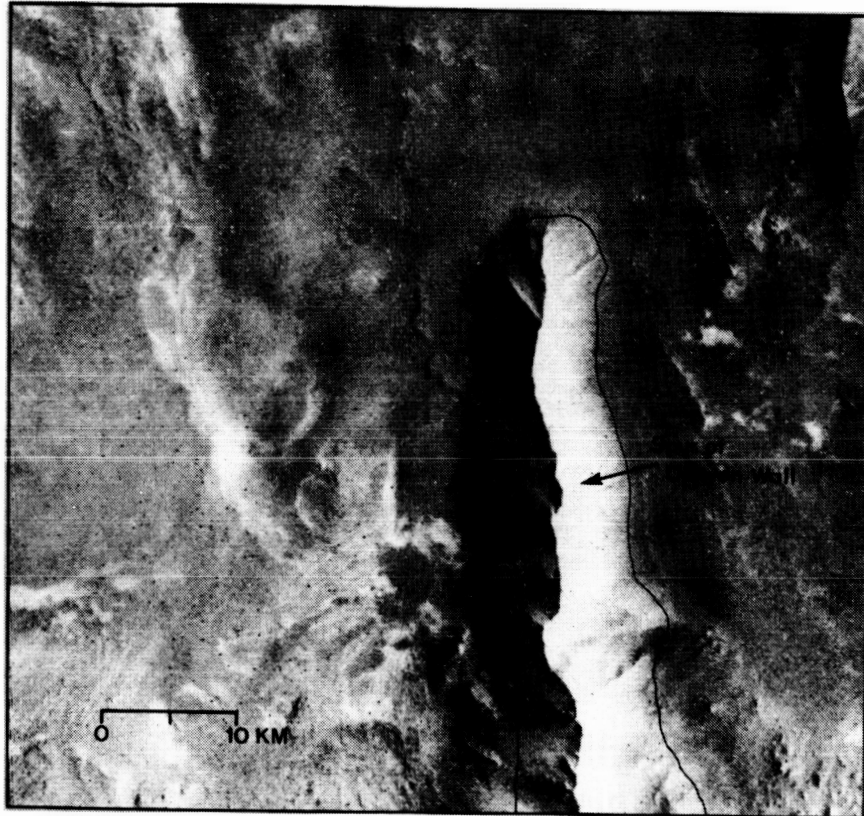
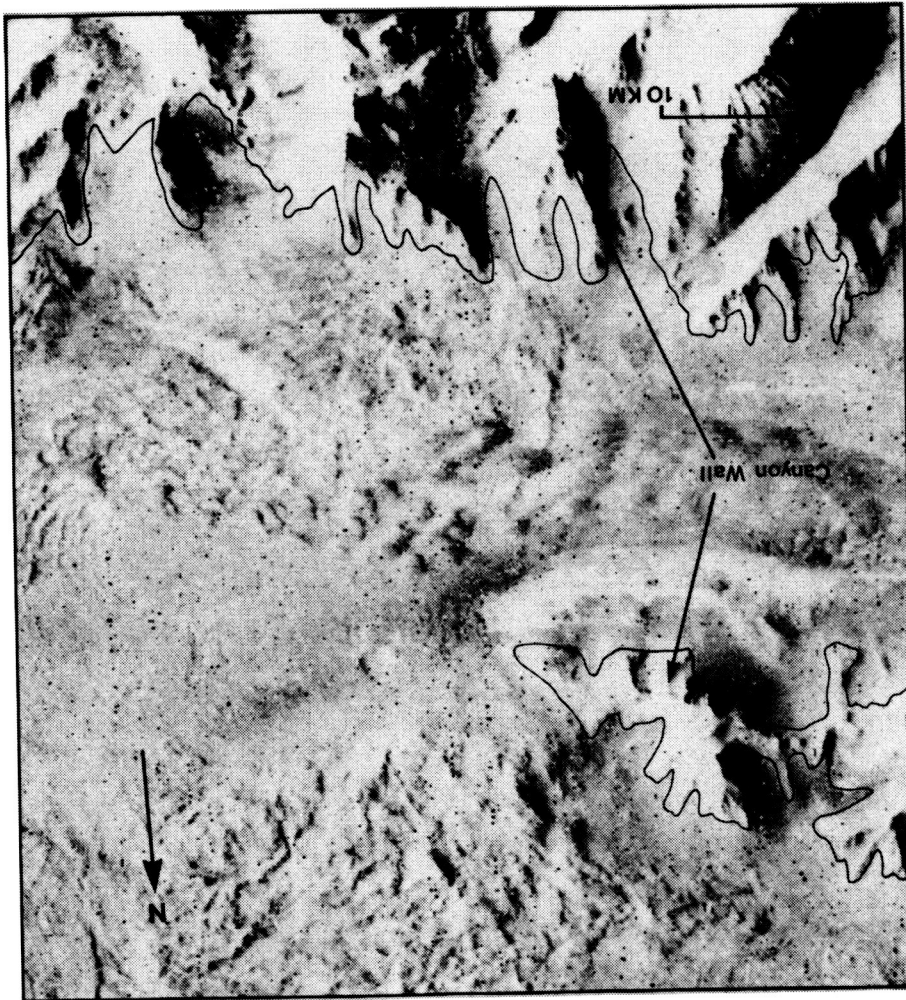


Figure 25: Chasma floor material in southern Melas Chasma has a light and dark albedo (picture no. 914A24).

Figure 26: Chasma floor material in some places shows a rough texture, such as in Ius Chasma. The hummocks may be debris that has sloughed off the nearby canyon wall (picture no. 920A17).



ORIGINAL PAGE IS
OF POOR QUALITY

ORIGINAL PAGE IS
OF POOR QUALITY



Figure 27: The "moat" between Candor Mensa and the canyon wall to the north has a flat floor, and no erosional features to suggest its mode of origin (picture no. 915A11).

ORIGINAL PAGE IS
OF POOR QUALITY

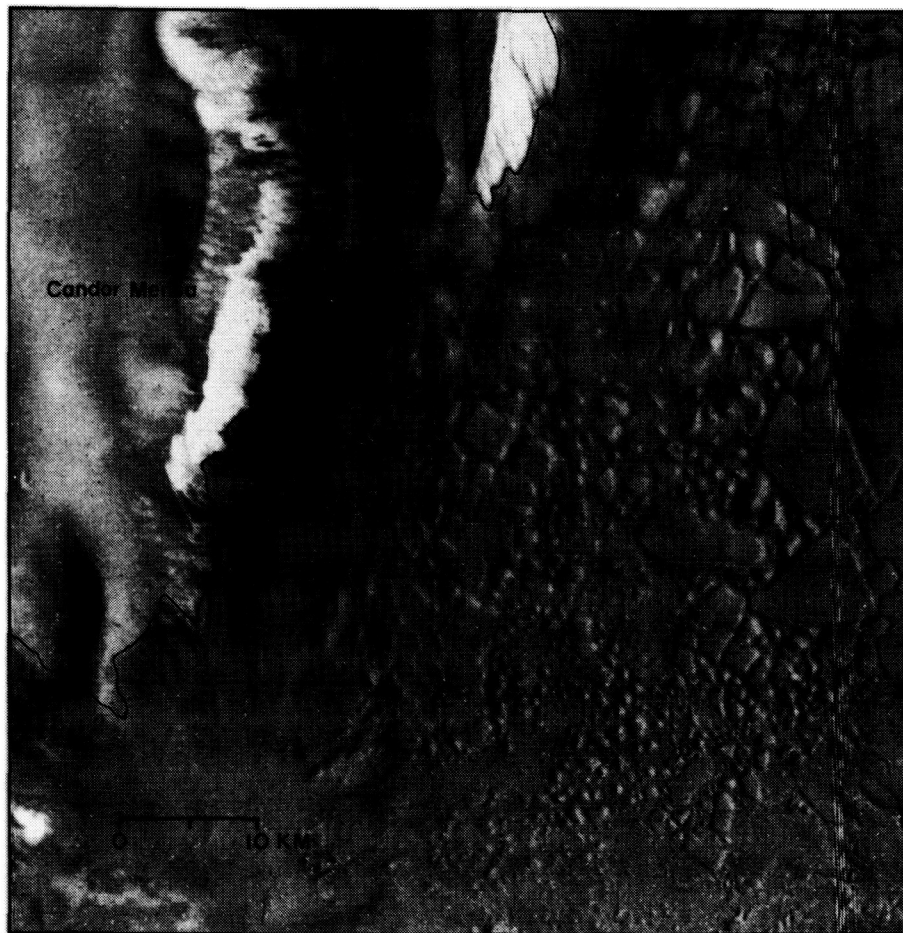


Figure 28: The chasma floor southeast of Candor Mensa is made of polygonal blocks. This texture may be related to "patterned ground" which is a frost-related feature described by Washburn (1973) (picture no. 914A16).

of the canyon wall (fig. 29). This chaotic terrain is the source for some outflow channels. In this area, the chasma floor material is hard to distinguish from the canyon walls, and therefore was mapped as an area where the canyon wall and the chasma floor are intermixed.

There are a number of dark elongate patches in the central portion of the Valles Marineris which Lucchitta (1986) identified and interpreted as mafic volcanic material. She described the dark patches as locally having feathery edges that extend either radially or in two directions from their centers. The dark patches occur along fault scarps and occasionally on top of landslide deposits. Because the dark material penetrated the slides, it is assumed to postdate them. Volumetrically, these deposits are minor, and their morphology and position within the canyons are distinct from the layered chasma deposits. In this study, the dark patches were mapped as part of the chasma floor material or landslide material, depending on the location of the occurrence.

Thickness, Topography, and Volume of the Layered Chasma Deposits

Thickness of Individual Layers

A study of the nature of the layering was performed using stereophotogrammetric measurements derived by Sherman Wu and others at the U.S. Geological Survey, Branch of Astrogeology. Candor Mensa, in Candor Chasma, and a south-facing cliff face in southeast Candor Chasma were chosen for investigation because the layering is well exposed and the images are of very high resolution (20–80 m/pixel; see fig. 30 for locations). Data points were chosen on high-resolution images at the top, bottom, and midpoints on the cliff faces. Figures 31 and 32 show the locations of all of the data points.

At each point, five elevation measurements (relative to the standard 6.1 mbar datum) were taken in order to minimize inaccuracies in the measuring technique (Moore and Wu, 1973). The mean and standard deviation were calculated for each set as outlined by Moore and Wu (1973). Table 1 shows the means and standard deviations. The thickness of a section between two data points was calculated by subtracting the mean



Figure 29: At the eastern end of the Valles Marineris, in Eos and Capri Chasmata, the chasma floor and remnants of the canyon wall produced chaotic terrain (picture no. 428A86).

ORIGINAL PAGE IS
OF POOR QUALITY

ORIGINAL PAGE IS
OF POOR QUALITY

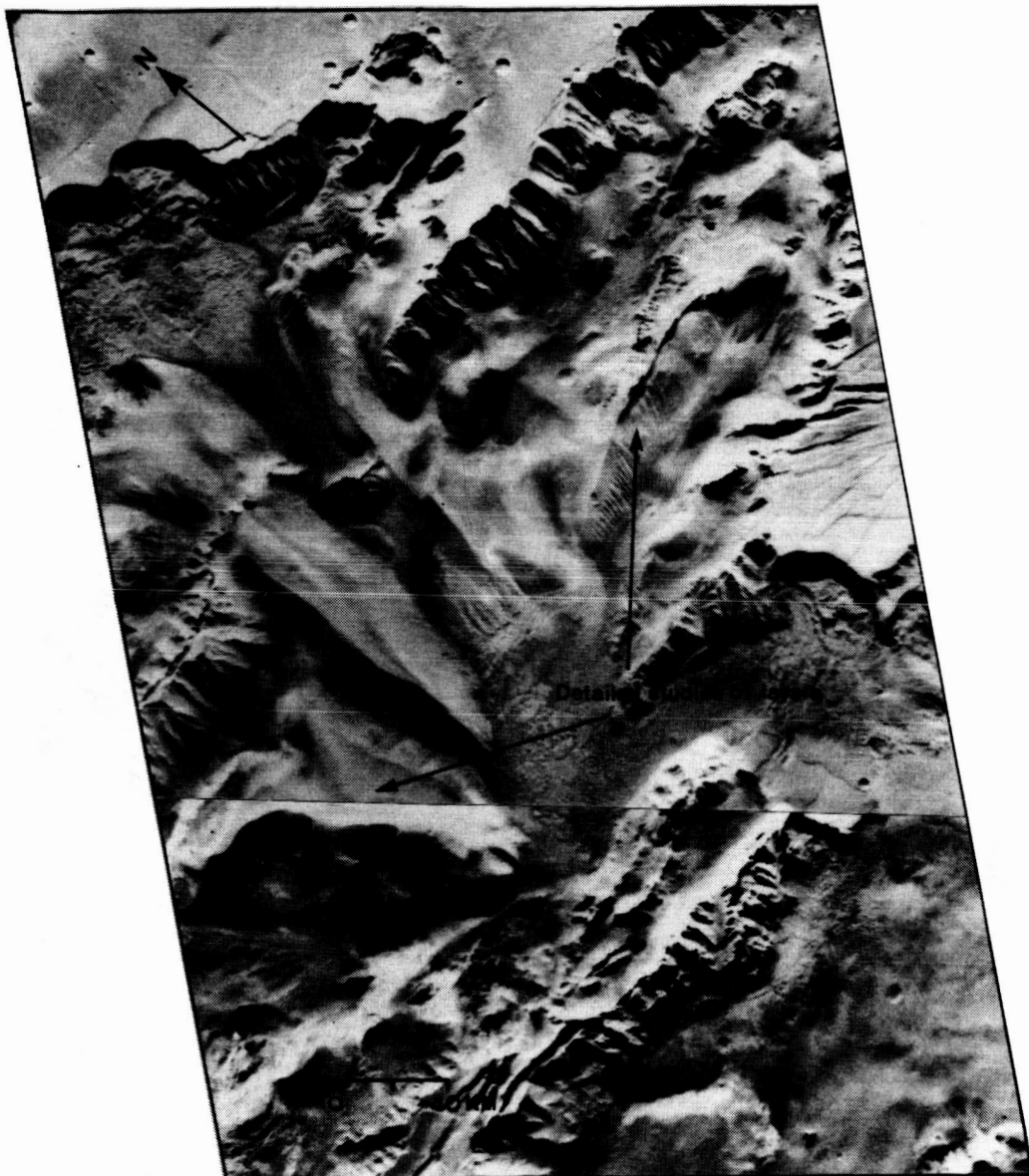


Figure 30: Locations where detailed studies of the layered deposits were performed. The plateau to the west is Candor Mensa, the plateau to the east lies in southeast Candor Chasma (picture nos. 608A72, 608A74).

ORIGINAL PAGE IS
OF POOR QUALITY

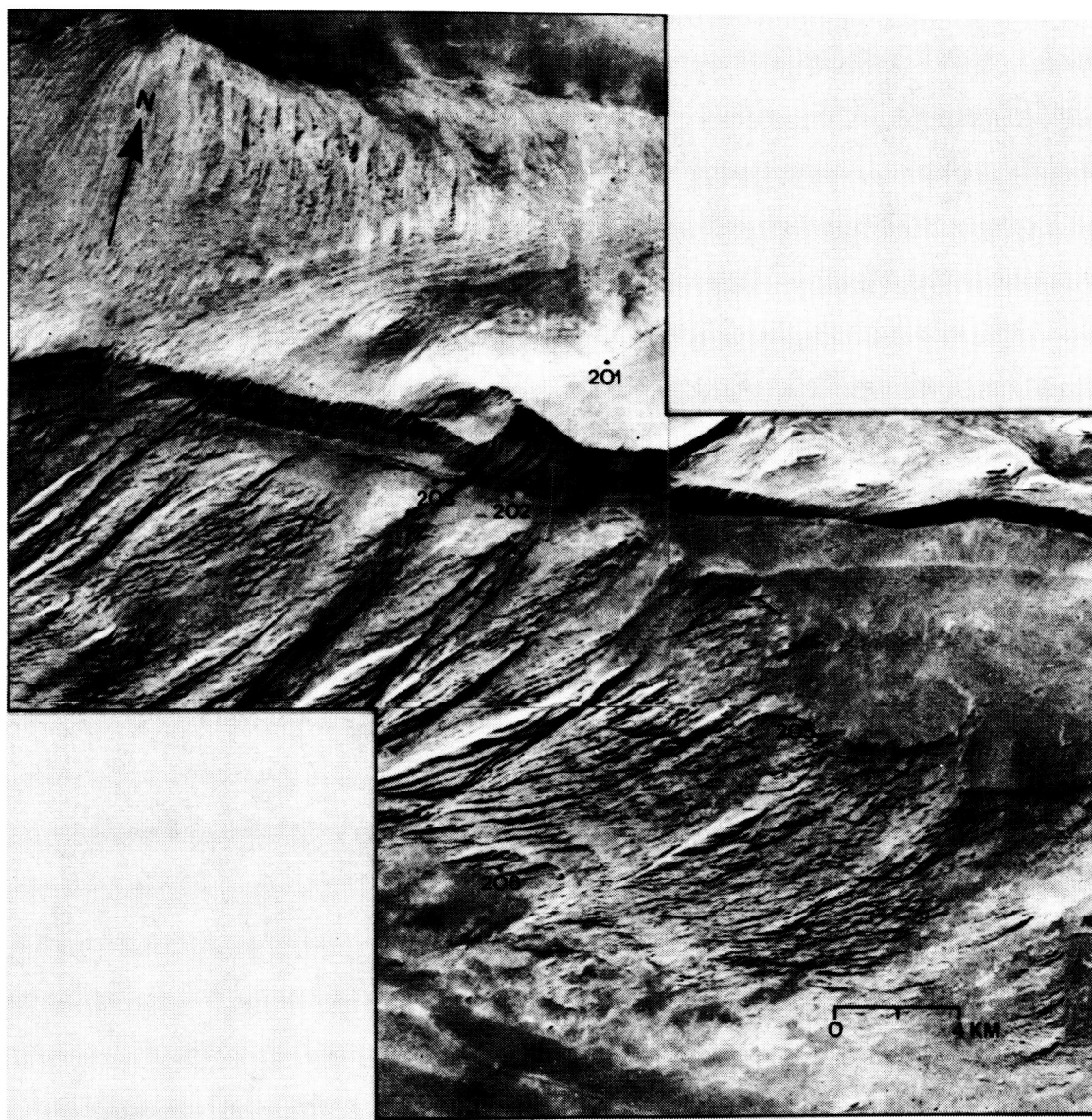


Figure 31: Locations of data points for stereophotogrammetry on a southern cliff face in Candor Chasma. Values for the data points are reported in Table 1 (picture nos. 815A58, 815A60).

ORIGINAL PAGE IS
OF POOR QUALITY



Figure 32: Index map of locations used for stereophotogrammetric measurements on Candor Mensa. The values are reported in Table 1 (picture no. 066A25).

values of the elevations. The average thickness of an individual layer was determined by counting the number of layers between two data points and dividing the thickness of the section by that number. One layer was considered to be a light and dark couplet. The error on each layer thickness measurement was calculated by averaging the standard deviations of the two data point elevations, and dividing that number by the number of layers detected between those two data points. The thickness measurements of individual layers are more accurate for southeast Candor Chasma than for Candor Mensa because the resolution of the images is higher. The resolution for southeast Candor Chasma is approximately 20 m/pixel, versus 80 m/pixel for Candor Mensa.

The cliff face in southeast Candor Chasma has two distinct layering styles that are evident in the images. The upper, narrow portion of the section has a finer layering, which was calculated to be 72 ± 8 m per layer. Individual layers in the lower section (fig. 31, points 205 and 206) are 304 ± 13 m.

The thickness of the layers on the southwest-facing cliff of Candor Mensa was determined from data points 102 and 103 (fig. 32). The average thickness of the exposed layers is 190 ± 4 m per layer. As one can see, layers are not exposed immediately below point 102. The elevation where the layers first appear on this cliff face was determined by assuming the slope was constant, and interpolating between the two data points. This calculated elevation was used to determine the average layer thickness in the manner previously described.

Six layers on the upper portion of the cliff face on the north side of Candor Mensa were calculated to be 106 ± 17 m per layer (fig. 32, points 307 and 308). If one assumes that layers on the north side of the mesa are continuous throughout the entire plateau, the layers that are obscured on the southwest side of the mesa may also be ~ 100 m thick. If this is the case, there are two distinct layer thicknesses for this plateau; thinner beds above, and thicker beds below. Alternatively, the layers throughout the section may thin to the north. It would follow from this hypothesis that a sedimentary source would have been situated southwest of the plateau. However, there appears to be no likely source southwest of Candor Mensa. Another large area of layered chasma deposits

Table 1. Mean elevation measurements above Mars datum for locations in Candor Chasma. Locations are given in figures 31 and 32.

Location	Mean Value (m)	Standard Deviation (m)
101	6429	75
102	7383	99
103	3226	39
104	1614	26
105	4929	53
106	2319	40
201	5621	63
202	5136	60
203	5275	64
204	5924	89
205	4319	106
206	2188	75
305	4340	25
306	3140	27
307	5714	116
308	5075	109
309	3488	41
310	1940	105

is situated in that direction. If the source for Candor Mensa was canyon wall material, a more likely area would be the canyon wall directly north of the plateau. Transport of material from this direction would produce a thinning of layers to the south. Because this is the sense opposite to what appears on the images, there is no good support for the idea that the layers taper.

As postulated for Candor Mensa, and identified in southeast Candor Chasma, the layering is coarse below and finer above. The two localities are separated by a distance of 170 km, a plateau of layered deposits, and two erosional valleys. Hence, there is some evidence for variations in deposition that affected much of the Valles Marineris region. This statement is tentative because the images for Candor Mensa are not good enough to see directly a change in the nature of the layering. If a canyon-wide depositional pattern does exist, it would imply that formation of the layered chasma deposits was controlled by an external process affecting the entire Valles Marineris region. In any case, the data from southeast Candor Chasma suggest that there was a change in the rate of accumulation of light and dark layers in that area.

The thickness of the layers in the layered chasma deposits can be compared with those in the polar layered deposits. Dzurisin and Blasius (1975) determined that the thicknesses of the layers in the polar regions range between 10 m and 50 m, and it is possible that the layering continues below the resolution of the images (Carr, 1981). The layering in the Valles Marineris deposits may also be finer than the resolution that the existing images reveal. The differences in layer thicknesses are consistent with the idea that the layered chasma deposits were formed by a different mechanism than the polar layered deposits.

Regional Slopes

Additional information was derived from the elevation measurements. The average slope angle between data points was calculated from trigonometric relationships. The errors on slope measurements were determined by calculating the slope angles using

data point elevations without the standard deviation, with the addition of two standard deviations, and then minus two standard deviations. The maximum and minimum slope angles then became the standard deviations on the slope measurements. It was found that the slopes of the plateau faces vary. In southeast Candor Chasma, the cliff has two distinct gradients. The upper part of the section where the layers are thinner has a mean slope angle of $21^{\circ} \pm 4^{\circ}$. The lower section has a gentler mean slope angle of $12^{\circ} \pm 1^{\circ}$. This change in slope angle may reveal information on the nature of the upper layers versus the lower layers. A gently dipping slope above a steeper one could be due to compaction from the weight of overlying sediment. The lower portion of the cliff would form a steeper face because it would be stronger. But the cliff face in southeast Candor Chasma changes from a steep to a more gentle slope, suggesting that another mechanism is responsible, such as a decrease in the competence of the deposits from the upper to the lower portion of the plateau.

The slope angles on Candor Mensa appear to change from one face of the plateau to the other, rather than with vertical position on one face. The southeast side has a mean average slope of $23^{\circ} \pm 1^{\circ}$, the northern face ranges between $12^{\circ} \pm 1^{\circ}$ and $16^{\circ} \pm 1^{\circ}$. No obvious change in slope similar to the location in southeast Candor Chasma is detectable.

It is important to note that in both locations the cliff faces of the plateaus have gradients similar to those of the canyon walls, yet there are no landslide scars or landslide deposits associated with the layered plateaus. This observation suggests that the layered deposits are of a different and more competent material than the canyon walls.

Interpretations of the layered deposits from Mariner 9 and early Viking data considered the layers to be horizontal. Although no angular unconformities or disconformities can be detected in the high resolution images, the elevation data reveal that some sequences may not be horizontal. The upper surface of Candor Mensa, between data points 101 and 102 (fig. 32), slopes gently to the east at $2.6^{\circ} \pm 0.5^{\circ}$. The section between points 307 and 305 (fig. 31) also slopes to the east, but at an angle of $4.4^{\circ} \pm 0.4^{\circ}$. The slope between points 101 and 305 is $8.8^{\circ} \pm 0.5^{\circ}$, and between points 102 and 307 is $10.8^{\circ} \pm 1.3^{\circ}$. Because these data points lie on the upper surface of the plateau that

is exposed to the wind, one can not be certain whether this surface represents a recent erosional surface, the original depositional slope, or the upper surface of a tilted fault block. Each of these hypotheses are considered.

An erosional surface would produce light and dark banding. The difference in elevation between the highest and lowest points on the plateau surface is 5- to 10-times greater than the average thickness of a layer. If the layers were flat lying, an angular erosion of the plateau would cut across the light and dark layers. Because no layers are exposed on the upper surface of Candor Mensa, the origin of the slope was probably not due to erosion.

If this upper surface is parallel to the layers below, one possible explanation for the slope would be that it is the original depositional surface. Although a slope of 8° to 10° is geologically feasible, at this image resolution one would expect to see a "grain" on the surface indicating the transport direction. Because no directional indicator can be detected, and because there is no obvious sediment source immediately to the south, the hypothesis that the upper surface is the original depositional slope is not favored.

A final possible explanation for the apparent dip of the surface of Candor Mensa is that it is a fault block that is tilted to the north. If this hypothesis were correct, the previous speculation that thinner layers overlie thicker layers in Candor Mensa would also be favored. Because there is other evidence for faulting within and around the Valles Marineris, this hypothesis is favored. A tilted fault block is also consistent with the tectonic origin of the Valles Marineris.

An apparent dip to the layered deposits is supported by data from southeast Candor Chasma. Two data points that are located on one continuous layer also indicate that the layering may not be strictly horizontal. Points 203 and 202 (fig. 31) mark the separation between the upper, finely layered section and the lower, more coarsely layered section. The apparent dip of the layer between these two points is $2^{\circ} \pm 2^{\circ}$ to the east. Without a third point there is no way of calculating whether the true dip is greater or not. Nevertheless, the slope angle indicates that these layers may not be flat-lying.

Total Thickness and Volume of Deposits

Mapping of the thicknesses of the plateaus was restricted to Coprates NW quadrangle because a sufficiently detailed topographic map presently exists only for that area (U.S. Geological Survey, 1984). The quadrangle encompasses Hebes, Ophir, Candor, Melas, and Tithonium chasmata. An estimated 75 percent of the mapped layered chasma deposits occur within this area. To determine the thickness of an individual plateau, the level of the canyon floor was assumed to be the base of layered deposits. This assumption is fairly reasonable because the canyon floor has a relatively smooth topography, and in most areas does not show textures that are characteristic of the layered deposits. Where the layered deposits lap against the canyon wall, the three-dimensional shape of that plateau was approximated by assuming that the slope of the exposed part of the canyon wall has the same gradient as where it is buried by the layered deposits.

An isopach map of the deposits is shown in figure 33. The greatest thicknesses of layered deposits occur in Hebes, Ophir, and Candor Chasmata. The deposits in Hebes Chasma are ~ 5000 m thick. Layered deposits in Ophir Chasma are between 5300 m and 5500 m thick. Candor Mensa in Candor Chasma is ~ 4300 m thick, and the thickness of other deposits in Candor Chasma range between 2400 m and 4200 m. In contrast, the deposits in Melas Chasma range between 2000 m and 3200 m. The relief on the chasma walls is not as great in Melas Chasma (~ 5000 m), as in the canyons to the north (~ 6000 m in Hebes, ~ 7000 m in Ophir, and 6000 m to 7000 m in Ophir).

The total volume of the layered chasma deposits in Coprates NW Quadrangle was derived from the isopach map, using a planimeter to determine the area within each contour interval and linear interpolation to estimate elevations between contours. The volume of each plateau of layered deposits is presented in Table 2. The total volume of the layered deposits in Coprates NW is $\sim 1.29 \times 10^5$ km³. If these deposits are composed of sediment that once was spread uniformly over the surface of Mars, it would have covered the planet with a layer 90 cm thick. For comparison, ancient terrestrial Lake Gosuite (situated in the southwest corner of Wyoming during Eocene time) accumulated an estimated 2.0×10^4 km³ of deposits over a period of 4 million years (Bradley, 1963). It

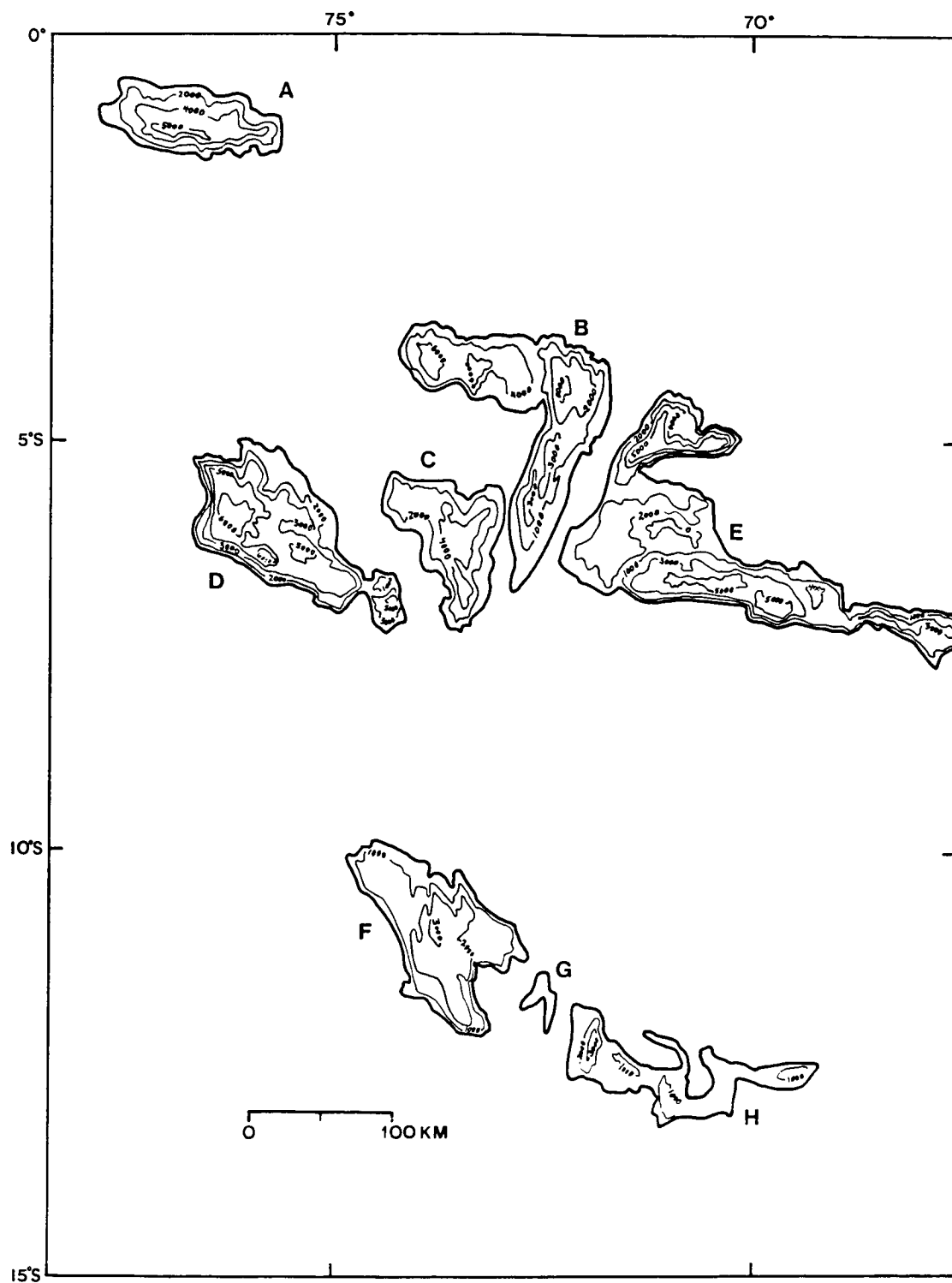


Figure 33: Isopach map of the layered deposits in Coprates NW Quadrangle. Derived from the U.S. Geological Survey (1984) topographic map. Letters correspond to calculated volumes reported in Table 2. Contour interval is irregular; thickness is shown in meters.

Table 2. Volume of individual plateaus of layered deposits. Lettered locations correspond with Figure 33.

Location	Volume (km ³)
A	13,400
B	26,300
C	12,200
D	27,500
E	32,500
F	12,300
G	200
H	4,000
I	200
TOTAL	128,600

is estimated that Mt. Vesuvius in Italy has erupted approximately $1.37 \times 10^3 \text{ km}^3$ of lava since 79 A.D. (Simkin and others, 1981). The Yellowstone Volcanic Field in northwest Wyoming has erupted roughly $6.5 \times 10^3 \text{ km}^3$ of rhyolitic magma in the past 2.25 million years (Christiansen, 1984).

It also is useful to compare the volume of the layered deposits to that of other large deposits on Mars to understand the magnitude of the events that produced this unit. The volume of the north polar layered deposits is roughly $4 \times 10^7 \text{ km}^3$. This figure was arrived at by assuming that the deposits are on the average 2.5 km thick. The volume of Olympus Mons was calculated to be approximately $1.12 \times 10^6 \text{ km}^3$ (Blasius, 1976). In keeping with the fact that volcanic deposits commonly are larger on Mars than on the Earth, the volume of the deposits is not inconsistent with a volcanic origin. In fact, the volume of the layered deposits is an order of magnitude less than the volume of Olympus Mons.

Stratigraphic Relationships and History of the Valles Marineris

Stratigraphic relationships between units were used to construct the sequence of events within the Valles Marineris. Locations that show key stratigraphic information permit the history to be inferred.

The history of the Valles Marineris apparently began with the formation of tectonic fractures or grabens radial to the Tharsis bulge. The graben system was a result of extensional stresses at shallow depths produced by the formation of the Tharsis bulge (Sharp, 1973a; Carr, 1974; McCauley, 1978; Wise and others, 1979). The construction of the main volcanic cones that cap Tharsis occurred after the major portion of the fracture system formed.

Several workers have suggested that the present geometry of the Valles Marineris was largely due to faulting and tectonic subsidence caused by southward movement of the Syria-Solis Planum block, which lies to the south of the Valles Marineris (Allegre and others, 1974; Sengor and Jones, 1975; Courtillot and others, 1975; Masson, 1977). This

hypothesis would imply that opposing canyon walls were once in contact, a situation that seems implausible. Geometric arguments alone allow the possibility that Tithonium, Ius and Coprates chasmata were formed largely by tectonic movement, but the wide and irregularly shaped Hebes, Ophir, Candor, Melas, Juventae, Gangis, Capris, and Eos cannot be explained by tectonic activity alone. To accomodate such a large amount of extension, transform faults, for which there is no evidence, would be required at the east and west ends of the troughs. The irregular geometry also argues strongly that most canyons are not essentially unmodified grabens. Further, if the canyons were purely downfaulted blocks, there would be normal faults at the ends of the canyons, for which there is no evidence. A much more likely hypothesis is that relatively modest extensional faulting provided relief to allow processes such as landsliding, gullying and undermining to enlarge the canyons to their present geometry (Sharp, 1973a; Lucchitta, 1978; Lucchitta, 1981a; Patton, 1981). The spur-and-gully morphology was the dominant wall type to form as a result of the enlargement of the canyons.

The vast quantity of material that was eroded from the walls of the canyons does not coincide with the limited extent of the interior deposits and the enormous size of the present-day canyons. More material than is observed today must have been eroded from the canyon walls. Where is this "missing" material? Because completely enclosed basins like Hebes Chasma exist, the debris could not have simply been carried away. The wall material probably was volatile-rich, and therefore much of the original volume could have been removed by sublimation or carried away as liquid water.

The deep "moat" that commonly separates the layered chasma deposits from the canyon wall probably was not formed by eolian erosion because of its great depth (over 5 km in Ophir and Hebes chasmata) and the difficulty of producing deep erosion along canyon walls while leaving the sediment farther from the walls virtually untouched. Rapid release of ponded water by overtopping divides in the canyon has been suggested by Lucchitta (1982) as a mechanism of forming the outflow channels associated with the Valles Marineris. There are some areas within the canyons that may have been affected by fluvial erosion, such as the valley east of Candor Mensa (fig. 10), and the valley

that connects Ophir and Candor chasmata (fig. 13). However, the draining of lakes accompanied by deep fluvial erosion is not a viable candidate for all moat formation. Hebes Chasma is a completely enclosed basin, but it has a well-developed moat that must have been formed without rapid drainage. The deep moats in cases like Hebes most probably formed subsequent to deposition of the adjacent layers, primarily by collapse and recession of the canyon walls due to removal of large amounts of ground ice. Many workers have stressed the importance of groundwater sapping and sublimation or melting of ground ice in forming the present canyon wall morphology (Sharp, 1973a; Carr, 1981; Lucchitta, 1978, 1982). There also is strong evidence elsewhere in the canyons (for example Noctis Labyrinthus) for substantial enlargement of the canyons by sapping and wall collapse. This collapse and subsequent mass wasting also formed the spur-and-gully topography of the canyon wall.

At the divide between Ophir and Candor chasmata, the layered deposits lap directly against and partially bury canyon walls with spur-and-gully morphology (fig. 16). In this location, the deposition of the layered deposits clearly postdated the enlargement of the canyon walls. Because the spur-and-gully morphology of the canyon walls formed in some places before and in other place after layer deposition, it is inferred that deposition of the layered chasma deposits and canyon enlargement by wall collapse and mass wasting took place during roughly the same period of Martian history.

Continued movement on the faults that initiated the Valles Marineris caused tilting of the layered deposits. The orientation of the layers in Candor Mensa and southeast Candor Chasma is evidence for this post-depositional movement.

Following the formation of the layered deposits and collapse of the canyon wall, the layered chasma deposits were deeply eroded by a mechanism apparently separate from the processes that created many of the moats. The outflow channels associated with the Valles Marineris may date from this epoch of erosion (Lucchitta, 1982). There are two locations in Candor Chasma where the layered deposits are deeply eroded. To the east of Candor Mensa, a V-shaped trough separates the mesa from another plateau of layered deposits to the east (fig. 10). The surface of the narrow valley has streaks

that may be a result of wind or fluvial erosion. The divide between Ophir and Candor chasmata is another location that shows substantial erosion. Two mesas are separated by an erosional valley that connects Ophir Chasma to the north with Candor Chasma to the south (fig. 13). McCauley (1978) and Lucchitta and Ferguson (1983) suggested that ponded water in Ophir Chasma breached the divide to the south, causing catastrophic flooding that eroded the surrounding countryside. Sediment has been identified in Eos Chasma with no layering and a gently undulating surface (fig. 21). These deposits may be products of erosion of the layered chasma deposits. This hypothesis would imply, that when water was flowing through the narrow Coprates Chasma, it lost the capacity to carry much of its load as the canyons widened into Eos and Capri, and it consequently redeposited much of its load.

Landsliding of the canyon walls postdates the erosion of the layered chasma deposits as evidenced by two clear cases. In Ophir Chasma, a landslide was diverted by a plateau of layered deposits (fig. 22). Landslide deposits on the north side of Hebes Chasma abut against the central plateau of layered deposits (fig. 9).

Eolian erosion responsible for fluting along the slopes of the layered deposit plateaus probably has been volumetrically minor. It can not be determined when the eolian erosion began, but it could be continuing up to the present.

Figure 34 summarizes the history of the Valles Marineris. Faulting and graben formation resulted in response to the Tharsis uplift. The troughs were enlarged by collapse, sapping, and weathering of the walls to form the spur-and-gully morphology of the canyon walls. During roughly the same period, the layered chasma deposits were emplaced. Further local canyon wall collapse, and perhaps deep erosion of the deposits in some areas followed, producing the present plateau and canyon-wall geometry. The outflow channels associated with the Valles Marineris may date from this period of erosion. Landsliding postdates the formation and deep erosion of the layered deposits. A minor episode of mafic explosive volcanism occurred after the emplacement of the landslide deposits. Eolian erosion responsible for the fluting could be continuing up to the present.

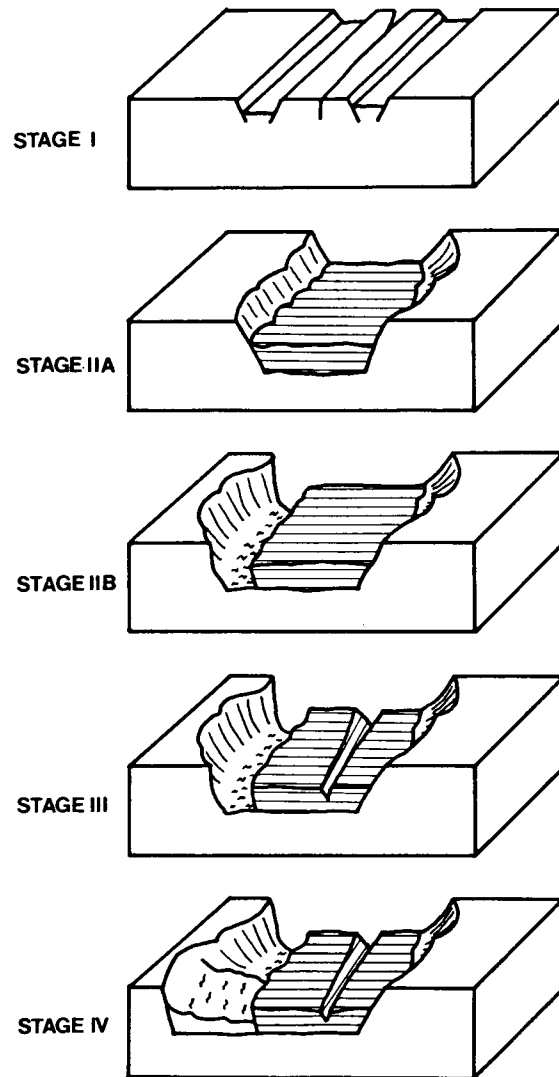


Figure 34: Simplified geologic history of the Valles Marineris. Stage I: graben formation in response to the Tharsis bulge. Stage IIA: Canyon wall enlargement with contemporaneous deposition of the layered deposits. Stage IIB: Further canyon wall collapse in some locations forming “moats”. Stage III: Erosion of the layered deposits. Stage IV: Landsliding of the canyon walls.

Origin of the Layered Deposits

Four hypotheses for the origin of the layered deposits seem to be worthy of consideration: that they are eolian deposits; that they are the same material as the canyon walls; that they are deposits from explosive volcanic eruptions; or that they were deposited in standing bodies of water.

Eolian Hypothesis

Peterson (1981) suggested that the central plateau in Hebes Chasma may have formed by eolian processes. Although present eolian activity in the canyons apparently involves only minor erosion and redistribution, Peterson suggested that the layered deposits may have been produced by global dust storms during a period when the Martian atmosphere was denser. However, the distribution of the layered deposits appears inconsistent with formation by eolian processes. Layered deposits are found only in the lower elevations of the canyons. The higher elevations of the canyon walls and surrounding uplands are completely free of any similar deposits, a situation which would be extremely difficult to produce if layered deposits once covered the entire area.

Canyon Wall Hypothesis

There are a number of indications that the layered chasma deposits are not remnants of the canyon walls. The clear differences in weathering style between the layered deposits and the canyon walls show that the two materials are quite different. The canyon walls commonly have spur-and-gully topography, whereas the slopes of the layered deposits have weathered to a relatively smooth surface characterized in some places by eolian fluting. Although the slopes of the canyon walls and plateaus of layered deposit have similar gradients, the canyon walls have commonly undergone catastrophic failure, producing landslides in many locations. The layered deposit plateaus do not show any evidence for landsliding. The canyon walls do not show the fine, rhythmic layering that

is a prominent characteristic of the layered deposits. The layered deposits also have been found to lap against the canyon wall, showing by their stratigraphic relationship that the two units did not form at the same time.

Volcanic Hypothesis

There is evidence for explosive volcanism on Mars. Morris (1980) proposed that the aureole deposits on Olympus Mons are pyroclastic material. Mouginis-Mark and others (1982) identified deposits west of the summit caldera of Hecates Tholus in the Elysium Planitia region that may have been generated by explosive volcanism. Scott and Tanaka (1982) identified possible ignimbrites southwest of Olympus Mons in the Amazonis Planitia region. Wilson and Head (1983) pointed out that the low atmospheric pressure of Mars would make pyroclastic eruptions more likely than on Earth, other factors being equal. Eruption velocities also will be greater by a factor of about 1.5 for the same volatile content.

The origin of the layered deposits by air-fall volcanic debris is argued against by the same reasoning as for an eolian origin. Because the atmospheric pressure and gravity are low, Martian eruption clouds will rise to heights about 5 times greater than on Earth (Wilson and Head, 1983). One would expect that pyroclastic debris would be widespread. Even if the source of the volcanism was from within the canyons, the clouds would be expected to rise and deposit ash on the surrounding plains. If the source for the material was Olympus Mons, as Peterson (1981) suggested, one would certainly see some evidence of layered deposits on the surrounding plains, and/or in other depressions.

It has been suggested that the layered chasma deposits have an ash-flow origin (Lucchitta, 1981a). Scott and Tanaka (1982) found deposits that they postulated are ignimbrites, or ash-flow tuffs, in the Amazonis, Memnonia, and Aeolis quadrangles. They described them as being flat sheets up to 100 m thick with upper surfaces that are smooth or gently undulating. The deposits cover an area of $\sim 2.2 \times 10^6$ km². When viewed at high resolutions, the putative ignimbrites are massive deposits without visible

bedding. Unlike air-fall tuffs, they do not blanket topography, instead they tend to even out the underlying topography by filling in lows with more material. The greatest thickness of the unit occurs where there are topographic barriers. Scott and Tanaka suggested that, where the flow was unconfined, it spread laterally for large distances in thin sheets. The deposits have several detailed morphologic features in common with terrestrial ignimbrites, including possible welded layers that show joint sets in high-resolution images, and nonwelded ash-flow tuffs that are eroded into conical pinnacles. It was suggested that the source areas of the pyroclastic flows were large collapse structures, such as faults, fissures, and cauldrons, that developed over shallow magma chambers (fig. 35). Possible vents, however, have been identified in only a few places. Perhaps most of them were buried by eruptive material.

The proposed Amazonis Planitia ignimbrites have a morphology most similar to what are classified as large-volume ash-flow deposits on Earth. Fisher and Schmincke (1984) reported that terrestrial deposits in this category have typical volumes between 100 and 1000 km³. The estimated volume of the Amazonis ignimbrite is $\sim 3.85 \times 10^6$ km³ (Scott and Tanaka, 1982). The total volume of the layered deposits in Coprates quadrangle is $\sim 1.29 \times 10^5$ km³. If the layered chasma deposits are volcanic in origin, their volume is consistent with the large magnitude of other proposed volcanic events on Mars.

The thickness of the layered chasma deposits ranges from 2000 m in the southern canyons to 5500 m in the north. These values are greater than the average thickness of the proposed Amazonis ignimbrite, which is approximately 1750 m. Large terrestrial ash-flows typically spread out in aprons from central vents on slopes of a few degrees (Sheridan, 1979). Their thickness is greatest near the source and decreases laterally. Scott and Tanaka (1982) also recognized that the Amazonis ignimbrite was thickest near their proposed volcanic vents.

It could be proposed that the layered chasma deposits are ash-flow sheets with their sources in Ophir and Candor chasmata where the deposits are thickest, but there are severe problems with this hypothesis. First, there are no identifiable volcanic calderas

ORIGINAL PAGE IS
OF POOR QUALITY

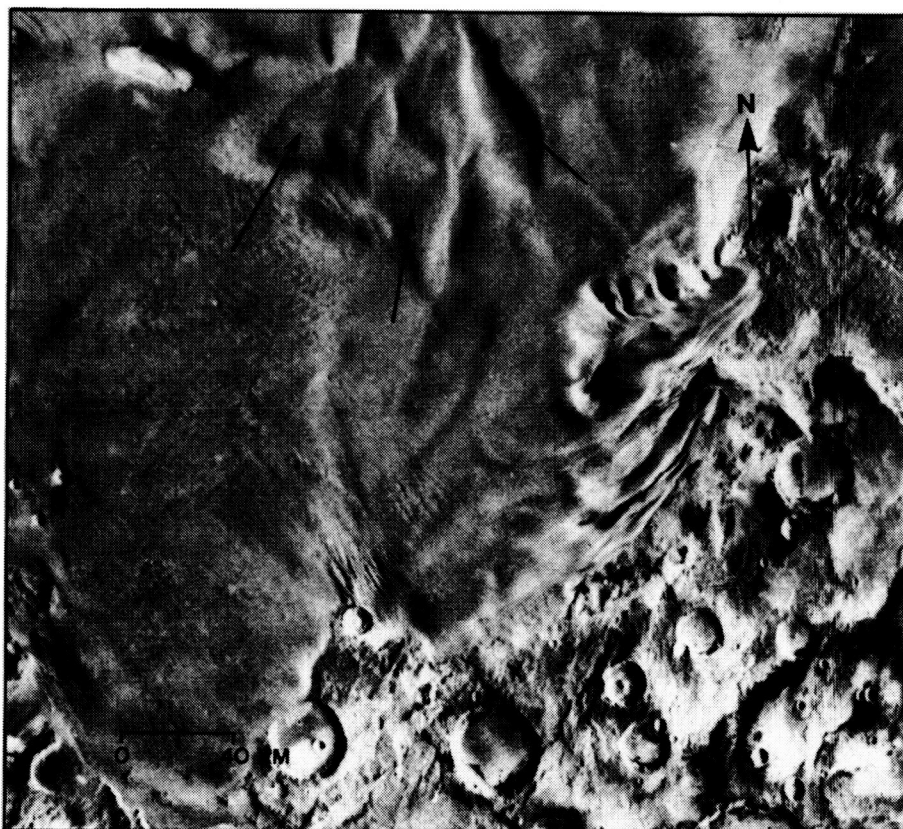


Figure 35: The depressions (arrows) were proposed to be the sources for pyroclastic flows in the Amazonis Planitia region as described by Scott and Tanaka (1982) (picture no. 637A76).

in Ophir and Candor chasmata. No depressions were detected similar to ones that Scott and Tanaka (1982) suggested were sources for volcanic material in Amazonis Planitia (fig. 34). Even if there were major sources there, the chasma wall that separates Candor Chasma from Melas Chasma would have prevented volcanic avalanches from spreading into Melas Chasma. In fact, flows that spread southward would have piled up against the canyon wall, producing thicker deposits. On the contrary, the plateaus of layered deposits are characterized by a fairly uniform thickness. There presently is an opening in the wall, but no evidence of layered deposits can be seen near this entrance. In addition, although the thickness of layered deposits decreases from north to south, there was no systematic thinning of individual layers detected in the highest resolution Viking images. Over a distance of hundreds of kilometers, one would expect to see beds tapering out if they originated from a central source. It is therefore unlikely that there was a major source for volcanism centered in the northern canyons.

Perhaps the plateaus of layered deposits were formed by many smaller, localized eruptions scattered throughout the canyons. One would envision a series of episodes in which each event produced a layer of tuff and ash that subsequently covered the vent. The magma conduits of subsequent events would have had to penetrate the previous layers to erupt another continuous sheet. This might be expected to cause considerable disruption of previous layers. The locations of successive vents probably would have had to have been constantly changing, or else noticable volcanic edifices would have been built. Small explosive events on Earth tend to form central cones similar to Mount St. Helens, Washington, or Mount Mazama at the site of Crater Lake, Oregon (Fisher and Schmincke, 1984). The flows of these smaller-scale pyroclastic eruptions tend to erode channels in the flanks of the volcano (Sheridan, 1979), producing stacks of elongate deposits, instead of the more sheet-like layers of larger flows. Individual layers in the plateaus of layered chasma deposits do not show noticeable variations in thickness. It seems improbable that a continuous series of small eruptions could produce such uniform, rhythmic layering on the scale that is seen in layered chasma deposits.

Subaerial pyroclastic volcanism does not seem to be a viable mechanism for the

deposition of the layered chasma deposits. It has been eliminated for further consideration because there are no identifiable volcanic vents, and because rhythmic, continuous layering in many separated canyons would not likely be produced by a series of small, localized eruptions. Another form of pyroclastic volcanism that has not been previously suggested is subaqueous volcanism. This process will be considered after discussion of the lacustrine hypothesis.

Lacustrine Hypothesis

There have been speculations that the layered chasma deposits may have formed in a low-energy, liquid-water environment (McCauley, 1978; Lucchitta, 1981a; Carr, 1981). The deposition of the layered deposits in standing bodies of water can readily explain the location, horizontality, lateral continuity, great thickness, and stratigraphic relationships with other units within the canyons.

Troughs located in active tectonic settings on earth have produced great thicknesses of water-lain deposits. The east African and the Baikal rifts produced long-lasting lakes with sedimentary deposits 2 to 5 km thick (King, 1976). The great depths of the Valles Marineris canyons and the large thicknesses of the layered deposits, together with the history of tectonism of that area, suggest that lakes on Mars could have had histories similar to those of rift-valley lakes on earth.

As with any planetary photogeologic investigation, the complexity of geologic processes and the limitations of the data available preclude absolute confidence in determining the origin of the layered deposits. Of the four hypotheses considered, it is concluded that only deposition in a lacustrine environment or explosive volcanism merit further consideration. However, because of the problems that exist with subaerial explosive volcanism, it is concluded that the layered chasma deposits probably were formed in standing bodies of liquid water. If the source of the deposits was volcanic, the volcanism was most likely sublacustrine. Alternatively, the sediment that was deposited in the lakes may have come from the atmosphere or the canyon walls. The layered chasma

deposits provide the most convincing evidence for the former existence of standing water bodies on a planet other than the Earth. A decisive determination of their origin will only be reached once they are sampled directly.

Based on our present understanding of the evolution of the Martian atmosphere, lakes on Mars would have been ice-covered (Wallace and Sagan, 1979; Carr, 1983; McKay and others, 1985). The lacustrine hypothesis therefore presents a problem of how to produce thick sedimentary deposits in ice-covered lakes. Three mechanisms will be considered in detail for the emplacement of sediment in the putative lakes: sedimentation through the ice from above, infilling from the lake sides, and volcanic eruption from the lake floor. However, it is difficult to constrain adequately all of the possibilities that may have occurred on Mars with the amount of data we have at this time. It is therefore instructive to gather additional information from possible terrestrial analogs, in the hope of being better able to understand sedimentation in martian lakes. The antarctic Dry Valley Lakes were chosen for study, because they, too, have a perennially frozen ice cover, and it is possible to obtain sediments and other pertinent data from this area. The next section of this thesis will present the information and interpretation of sedimentation in the ice-covered Dry Valley Lakes, and how it can be related to possible lakes on Mars.

ANTARCTIC DRY VALLEY LAKES

Purpose of Investigation

Sedimentation in ice-covered lakes involves processes that are not understood because, unlike temperate lakes, inflow streams are active during only a few months of the year at most, and the permanent ice cover prevents windblown sediment from freely entering the lake. The goals of this investigation are: to determine if sediment on the ice surface can migrate downward through the ice and enter the liquid water system; to resolve the mechanism(s) by which the sediment travels through the ice; and to determine the relative proportions that the inflow streams, lake margins, and sediment in the ice-cover contribute to the deposits on the lake bottom. The answers to these questions may help to constrain processes of sedimentation in ice-covered lakes that may have existed on Mars.

Location and General Geography

The Dry Valleys are in one of the largest ice-free regions within a vast polar desert situated in southern Victoria Land, at the southern extent of the Transantarctic Mountains, which stretch from the Ross Sea northward to the Weddell Sea. The valleys cover an area of $\sim 4000 \text{ km}^2$ (Cartwright and Harris, 1981) between latitudes 160° and 164° east, and longitudes $76^\circ 30'$ and $78^\circ 30'$ south. Ice-covered lakes that are discussed in this study lie west of McMurdo Sound, in Wright and Taylor valleys (fig. 36). Lake Vanda lies in Wright Valley. The Onyx River, the main inflow stream, enters Lake Vanda at its eastern end. There are no streams flowing out of Lake Vanda. Lakes Bonney, Hoare, and Fryxell lie in Taylor Valley. Taylor Glacier dams Lake Bonney at its western end. The Canada Glacier separates Lake Hoare to the west from Lake Fryxell to the east. Although there are numerous inflow streams entering these lakes, the system is

PRECEDING PAGE BLANK NOT FILMED

PAGE 356 INTENTIONALLY BLANK

~~PRECEDING PAGE BLANK NOT FILMED~~

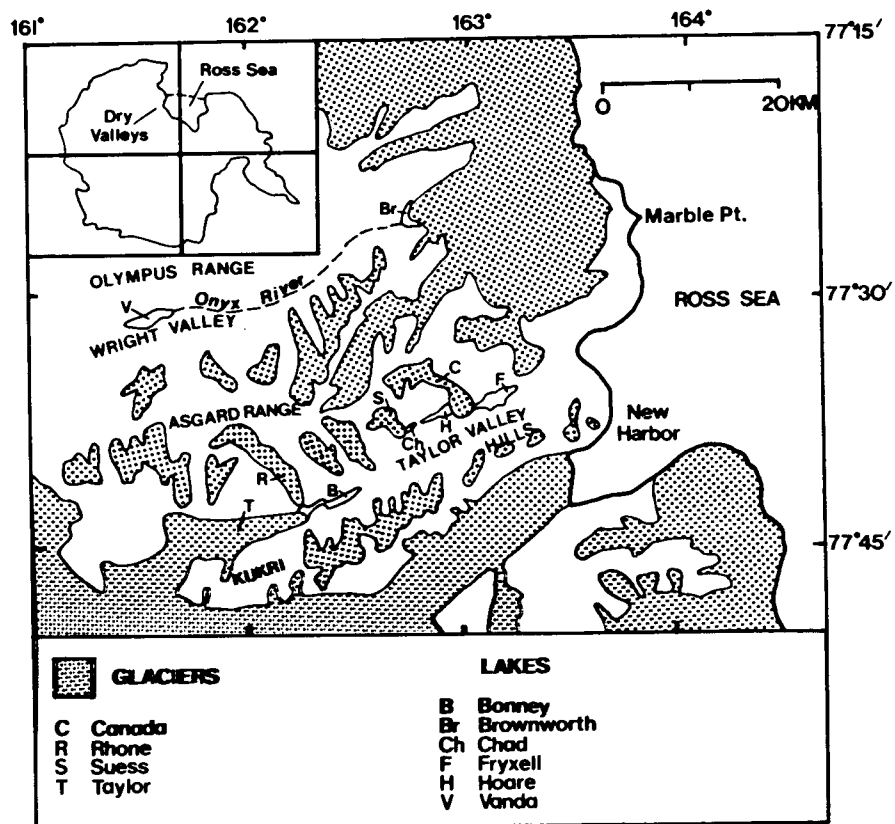


Figure 36: Index map of the Dry Valley area showing lakes within Wright and Taylor Valleys.

separated from the Ross Sea to the east by a low set of hills at the easternmost portion of the valley.

Climate

The Dry Valleys are free of ice chiefly because they are cut off from the main ice-sheet in East Antarctica by the Transantarctic Mountains. Other factors also contribute to their desert environment. Precipitation is low and local ablation rates are high. Snowfall averages 5-10 cm/yr (Thompson and others 1971a), and the sublimation rate for snow is estimated to be ~ 50 cm/yr (Harris, 1981). The lower albedo of rock compared to snow and ice, together with the low proportion of cloud cover, produce an annual net radiation gain in the Dry Valleys (Thompson and others, 1971a). Katabatic winds, which are most common in the winter months, travel down valley from the west. They are warmed by adiabatic compression, producing relative humidities that are typically 10 to 30% (G.D. Clow, 1985, pers. commun.).

Mean wind speeds are 10-15 km/hr, although gale force winds do occur (Bull, 1966). Easterly winds that blow up-valley during the summer months bring most of the precipitation (Bull, 1966; Thompson and others, 1971a). Air temperatures in the Dry Valleys range from -55° C in winter to $+10^{\circ}$ C in midsummer; the annual mean is $\sim -20^{\circ}$ C (Thompson and others, 1971b).

Paleoclimates are considered to have been as severe as the present one. As a result, the permafrost layer is irregular and deep (Cartwright and Harris, 1981). Decker and Bucher (1982) estimated that the permafrost is between 250 and 1000 m thick. During summer months when there are 24 hours of daylight, the soil surface can warm to high enough temperatures (20° C in some areas), to allow for surface water flow (Cartwright and Harris, 1981). During this same period, the lakes also experience the effects of solar radiation. The ice-cover frequently melts at the lake margins, forming a zone of open water up to 3 m wide.

General Geology

The Dry Valleys are located at the southeastern end of the Transantarctic Mountains, which border the Precambrian shield of East Antarctica. The region's geology is typical of the Transantarctic Mountains. The basement consists of upper Precambrian to lower Cambrian medium- to high-grade metasedimentary hornfelses, schists, and marbles that make up the Skelton Group. The original greywackes and limestones were complexly folded during the Ross Orogeny along predominantly north-south axes. The youngest basement rocks are massive dikes of granite and lamprophyre. They crosscut all other basement rocks, and together form the Granite Harbor Intrusives (Gunn and Warren, 1962; Gibson and others, 1983).

Flat-lying Devonian to Triassic sedimentary rocks of the Beacon Supergroup lie unconformably over the basement rocks (Gunn and Warren, 1962). The Beacon rocks are thick sequences of non-marine, fossil-poor sandstones (arkose, subgreywacke, and orthoquartzite), which were deposited in fluvial, lacustrine and eolian environments (Gibson and others, 1983). The basement complex provided the source rock for the sediment of the Beacon Supergroup. A brief period of glaciation during the Jurassic followed the formation of the Beacon sandstones, and glaciers eroded the formation to varying depths. A great thickness of till, named the Mawson Tillite, was deposited on the irregular surface. During the same period, the basement complex and Beacon Supergroup were intruded by the Ferrar Group, a massive formation of thick sills and sheets of dolerite.

A period of volcanic and tectonic quiescence followed the emplacement of the Ferrar Group in the Dry Valleys, during which the only activities were erosive processes (Harris, 1981). This state continued until the Pliocene (4 Ma), when basaltic volcanism began. McMurdo volcanism was minor in the Dry Valley region, and lasted until a few hundred thousand years ago (Gibson and others, 1983). Only a few small cinder cones and scoria patches were produced. In other regions such as Ross Island, volcanism was more extensive, and it has continued up to the present. Continental glaciation was fully developed by the late Miocene (10 Ma). The Dry Valleys are believed to have been eroded by glacial ice from the polar plateau during this period of glaciation (Bockheim,

1979; Harris, 1981). More recent silty till and gravel, which overlie the glacial deposits, may be marine sediment that was deposited in fjords (Vucetich and Topping, 1972). After the marine waters retreated, additional episodes of glaciation affected the valleys (Bockheim, 1979). The present lakes were formed less than 22,000 yr ago, after the most recent retreat of the Ross Ice Shelf (Denton and others, 1970).

Description of Lakes

During the summer field season in 1984/85 (December through January) S. W. Squyres performed field studies and took sediment samples of the areas in and around lakes Vanda and Hoare. All the lake margin, inflow stream, and ice surface samples used for analysis in the following sections were collected by him. Additional data and observations were collected by the author at Lake Hoare during summer 1985 (November and early December).

Wright Valley: Lake Vanda

Lake Vanda is located in Wright Valley, approximately 29 km west of Lower Wright Glacier, and 18 km east of Upper Wright Glacier (fig. 36). It lies in the lowest portion of Wright Valley in an undrained bedrock depression. The lake is approximately 5.5 km wide and 1.5 km long, covering an area of 8.2 km². It is deepest near the center of the western portion, where water depths reach 68 m (Nelson and Wilson, 1972) (fig. 37). The major stream that flows into Lake Vanda is the Onyx River (fig. 38). It originates at the western terminus of the Lower Wright Glacier and flows 25 km westward, away from the Ross Sea, down-valley into Lake Vanda. This reversal of drainage resulted from there having been more glacial erosion in the region of the lake, and less erosion and more deposition near the terminus of Lower Wright Glacier (Nichols, 1962). When measurements were taken during the 1984/85 summer, the Onyx River was flowing at the rate of 7.2 m³/sec, which is near its peak discharge.

The surface of Lake Vanda is perennially frozen, as are the other lakes described

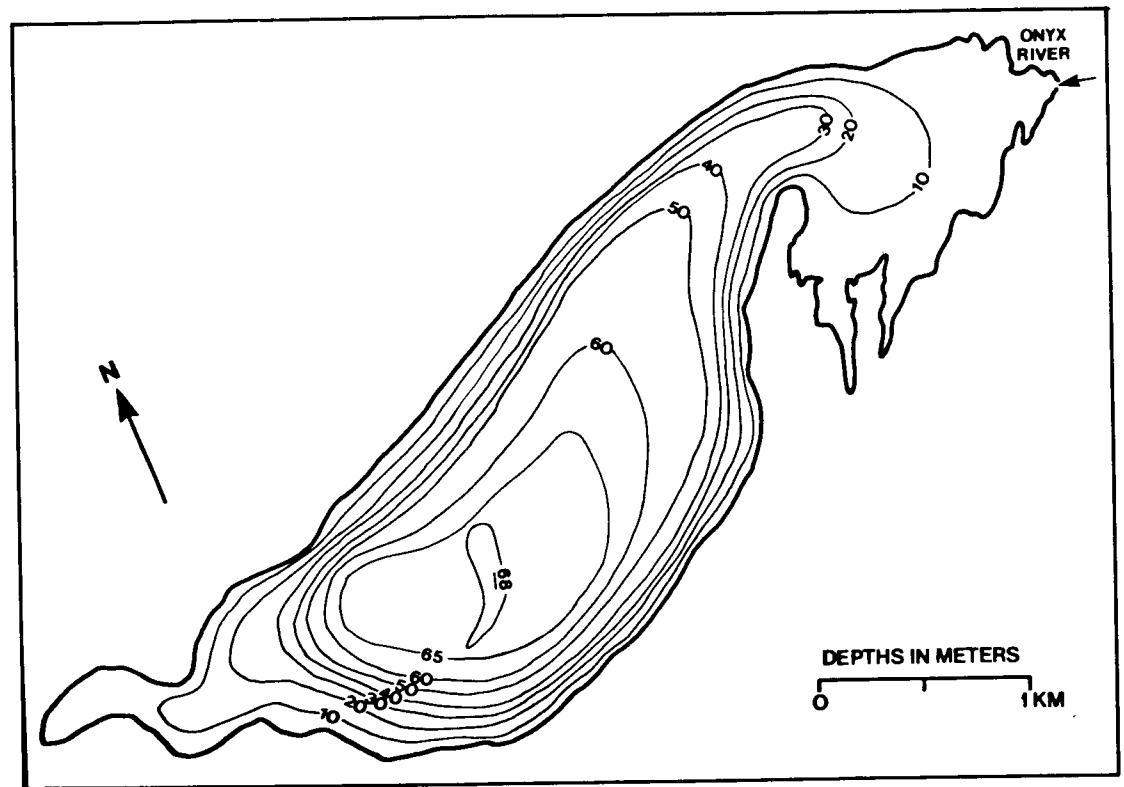


Figure 37: Bathymetric map of Lake Vanda from Nelson and Wilson (1972).

in this study. The ice cover is between 2.5 and 3.5 m thick (Jones and others, 1971; F.G. Love, 1984, pers. commun.). The character of Lake Vanda's ice cover is unique among lakes Vanda, Bonney, Hoare, and Fryxell. There is sediment within the ice cover of all the lakes, but the quantity is much less at Lake Vanda than at the other lakes (fig. 39). In addition, at the other lakes most of the sediment accumulates in discrete horizons within the ice cover, with few or no grains in between the layers, whereas at Lake Vanda grains are scattered throughout the portions of ice between sediment layers (R.A. Wharton, 1985, pers. commun.). The ice also is very porous. Air bubbles released by divers are briefly trapped against the bottom of the ice cover, and then gradually disappear (G.M. Simmons, 1985, pers. commun.). Air channels at the base are up to 10 cm long, and may contribute to a permeable ice structure that allows sediment to work their way through the channel network (F.G. Love, 1984, pers. commun.). The surface of the ice is gently hummocky, has fractures 10-20 cm wide and 20-30 cm deep, and generally is free of sediment except where small amounts of wind-blown sediment have been trapped in the fractures (fig. 40). The fractures are best developed along the lake margins.

During the summer the ice cover melts away from the lake margin exposing 2-3 m of water. At the eastern end where the Onyx River enters the lake, the open area is wider. The temperature of the lake water is close to 0° C directly below the ice, and warms to 25° C at the bottom of the lake (Nichols, 1962; Wilson and Wellman, 1962). It was proposed by Ragotzkie and Likens (1964) that the heating was solely due to solar heating of the water column; subsurface advection from thermal springs was rejected on the basis that water was migrating from the lake into the ground. Because there are no outlet streams, the greatest water loss from Lake Vanda is by evaporation. During this process, salts are left behind, making the water saline. The lake is stratified by density resulting partly from differences in chemical composition. The water just below the ice is very low in dissolved salts, while the bottom water is a saline brine (Wilson and Wellman, 1962). The high bottom temperatures are in part maintained by the lack of mixing in the water column. Very little light penetrates down into the deep region of the lake, but due to the very high stability of the salt-rich layers, the thermal transport

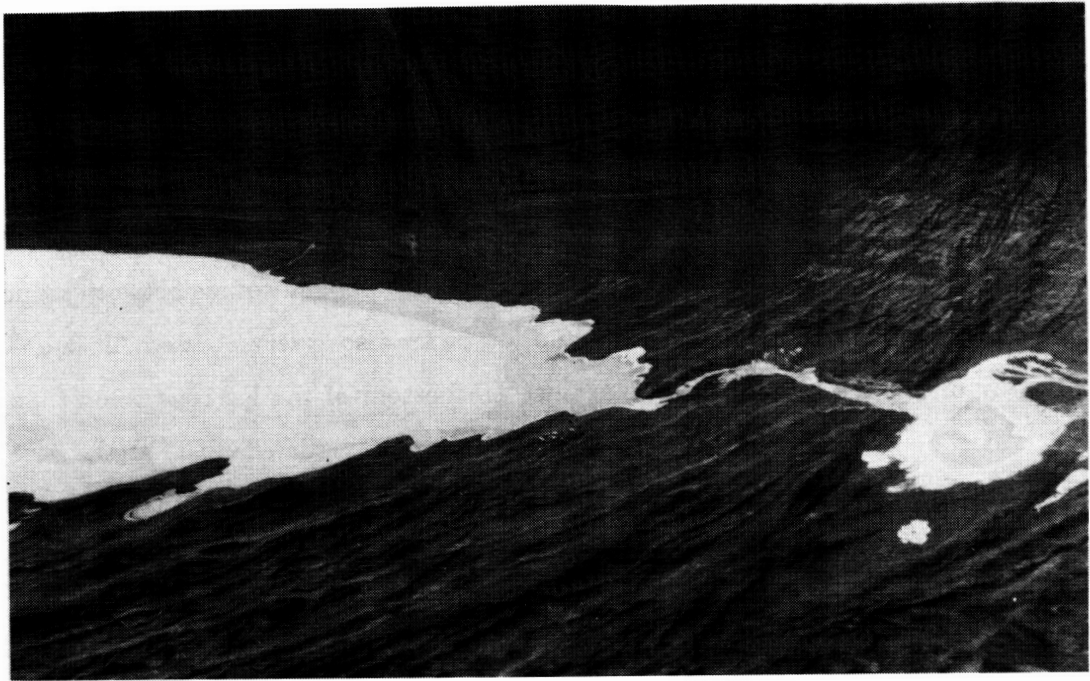


Figure 38: The Onyx River flowing into the eastern end of Lake Vanda.

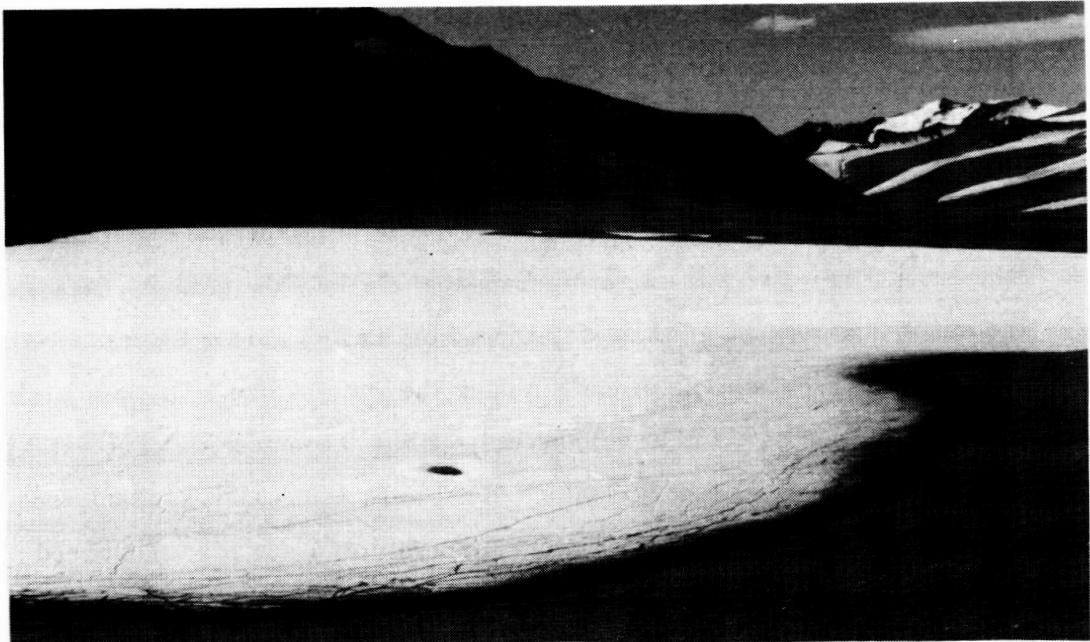
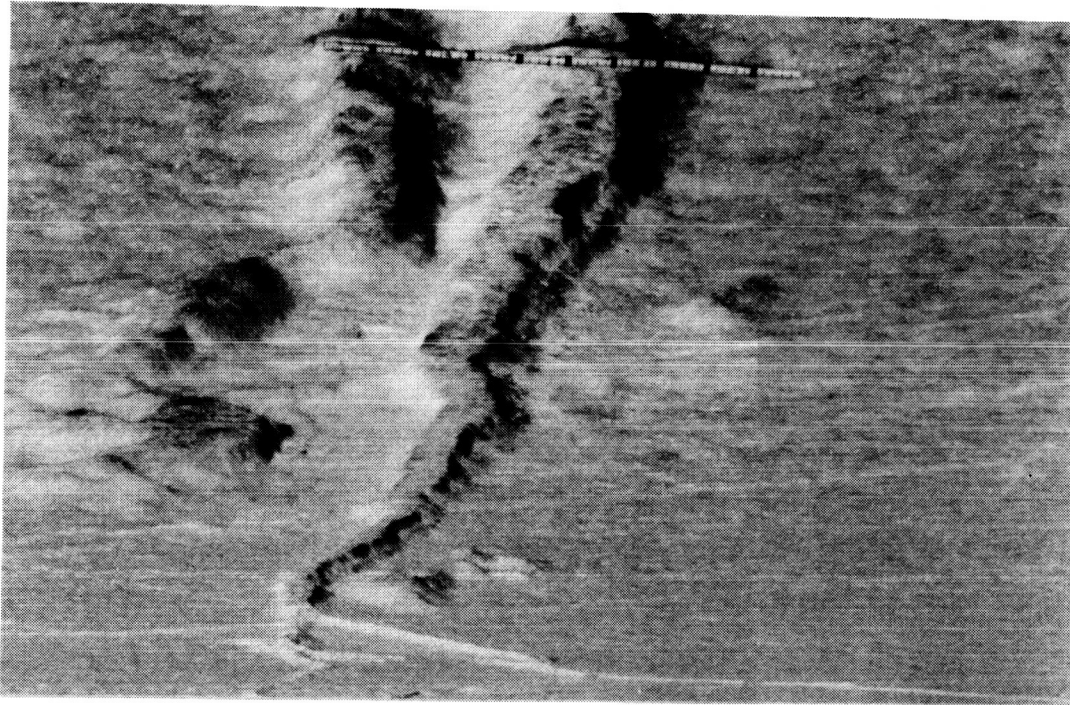


Figure 39: The ice on Lake Vanda is virtually sediment-free.

Figure 40: The ice cover on Lake Vanda is gently hummocky with 10 to 20 cm wide fractures. Scale is 1 m long.



ORIGINAL PAGE IS
OF POOR QUALITY

is very efficient and high temperatures result (C.P. McKay, 1986, person. commun.).

An interesting ecosystem exists on the bottom of Lake Vanda, and other lakes in Wright and Taylor valleys. Algal mat communities have been found to be thriving in this very harsh environment of low light levels, low temperatures (as well as the higher temperatures in Lake Vanda), high salinities, and low to nonexistent water flow. Parker and others (1982) reported that the organisms leave the lake system by first lifting off from the bottom of the lake buoyed with bubbles of photosynthetically produced oxygen. The clumps of algal mat then float upward toward the bottom of the ice cover and become frozen into the ice that forms when the colder season sets in. They migrate upward through the ice as ice is ablated from the upper surface, and new ice is formed on the lower surface. When the algal mat pieces reach the upper surface in 5-10 years, they are freeze-dried and dispersed by winds.

Analysis of sediment from Lake Vanda has been performed by Cartwright and others (1974) and Nelson and Wilson (1972) through the use of cores. Cartwright and others (1974) presented a tentative geologic history of Lake Vanda in which they suggested that there was a marine incursion during which 6.7 m of sediment was deposited over the granitic basement. A period of glaciation followed, and 2.2 m of till was deposited. The till is overlain by 3.5 m of lacustrine sediment. Nelson and Wilson (1972) reported on the character of the lacustrine deposits. They noted that sediment in water shallower than 60 m was deposited in an aerobic environment. The sediment is massive, medium- to coarse-grained, quartzofeldspathic sand (0.24-1.0 mm grain size), overlain by a layer of lighter-colored, biogenic detritus up to 13 cm thick. Below a water depth of 60 m, the environment is anaerobic. The sediment emits a strong H_2S odor and consists of grey to green sandy mud (mean grain size < 0.06 mm) and muddy fine and medium sand (mean grain size 0.125-0.5 mm) with a 6% content (by weight) of fine organic matter, and significant quantities of apparently authigenic calcite. The cores from the deeper portions are also broadly stratified. A white calcite and gypsum crust, found 4 to 10 cm below the surface, commonly separates sediment that consists of poorly laminated organic material and fine- to medium-grained sand above, from thick sandy mud and

muddy sand rich in organic material and calcite below. Locations nearer to the margin of the lake were more difficult to core because they became increasingly gravelly, resembling the sand above the present shore of Lake Vanda. Near the lake margin where the summer melt zone forms, an interesting feature was observed during summer 1984/85. In some locations, a ridge of poorly sorted sediment that is typically 2 m wide and 30-50 cm high formed on the lake bottom close to the edge of the ice and roughly parallel to the shoreline.

Former lake levels were recognized by Jones and others (1971) and Smith and Friedman (1974). Old shorelines produce a stairstep-like pattern on the surrounding moraine. The "risers" have a slope of $\sim 20^\circ$, the "steps" are nearly level. The deposits have no internal stratification. Jones and others (1971) described the ancient beaches as being poorly sorted to very poorly sorted sand with sediment ranging in size from > 4 mm to clay. They concluded that the conditions during the deposition of these higher shorelines were similar to those that exist today. If there was more open water, wave action would have sorted the high-level beach sediment better than the poorly sorted sediment of the present lake shore. Smith and Friedman (1974) described not only former beaches, but also former lacustrine deposits that are perched up to 60 m above the present lake level. They suggested that the ancient shorelines are erosional features that date back to the time of initial lake expansion, when wind-generated waves along the ice-free margins cut into the older colluvium. The lacustrine deposits are mostly poorly sorted, fine to coarse sand with a thin veneer of lag gravel. Bedding is rare, but where it does occur it dips $\sim 5^\circ$ lakeward. No presence of organic matter was mentioned. Smith and Friedman concluded that Lake Vanda, and perhaps other lakes in the Dry Valleys, experienced only one main cycle of lake expansion in response a regional climatic event.

Taylor Valley Lakes

Lake Bonney. Lake Bonney is the westernmost lake in Taylor Valley (fig. 36). Its western shore abuts against Taylor Glacier, and it is within a few hundred meters of the Rhone Glacier terminus to the northwest. The lake covers an area of ~ 3.2

km², and has a mean depth of 18.7 m. The highest water temperature, +2° C, occurs at approximately 15 m below the surface, the temperature then decreases to -4° C towards the lake bottom (Shirtcliffe and Banseman, 1964) . The ice cover is ~ 3.7 m thick, and sand lenses occur at ~ 1.3 m below the ice surface (F.G. Love, 1984, pers. commun.). This lake was not investigated in this study, but it is mentioned here to illustrate its similarities, such as the sediment-filled ice cover, and its differences, such as the temperature regime, compared to other lakes in the Dry Valleys.

Lake Hoare. Lake Hoare is situated west of the Canada Glacier and east of the Suess Glacier and Lake Chad, in Taylor Valley (fig. 36). It is approximately 3200 m long and 550 m wide, covering an area of ~ 1.8×10^6 m². The lake is divided into two basins. The deepest area in the eastern portion of the lake is ~ 1.5 km west of the Canada Glacier, and is 30 m deep. In the western portion of the lake, the deepest location is about midway along the length of the lake, and is also 30 m deep (fig. 41, F.G. Love, 1984, pers. commun.). Lake Hoare has at least five inflow streams during the summer season. The major one enters the lake at its northeastern margin. No streams drain Lake Hoare, because the Canada Glacier blocks the down-valley end of the lake. The water temperature is 0° to 1° C (Wharton others, 1983), which is cooler than the temperatures recorded in the other lakes discussed in this study. As in lakes Vanda, Bonney, and Fryxell, algal mats thrive on the lake bottom.

During the summer months, the surface of the ice cover is extremely irregular. Troughs up to 1 m deep cover the surface (fig. 42). In one location (fig. 42), the ice structure consists of two layers of icicles, each ~ 30 cm thick, separated by a thin layer of solid ice. The top icicle layer also is capped by a thin layer of solid ice. Sand layers with pieces of algal mat mixed in lie on the floors of the troughs. Under overhangs where there are wind shadows, pieces of algal mat tend to concentrate in greater quantities. Depressions in the ice surface in between the troughs also contain sand in layers up to 1 cm thick. Also scattered on the surface are boulders up to 2 m in diameter. An aerial view from 900 m above the lake shows that 40-50% of the ice surface is covered with sediment (fig. 43). The sand was most likely transported onto the ice by wind, and the

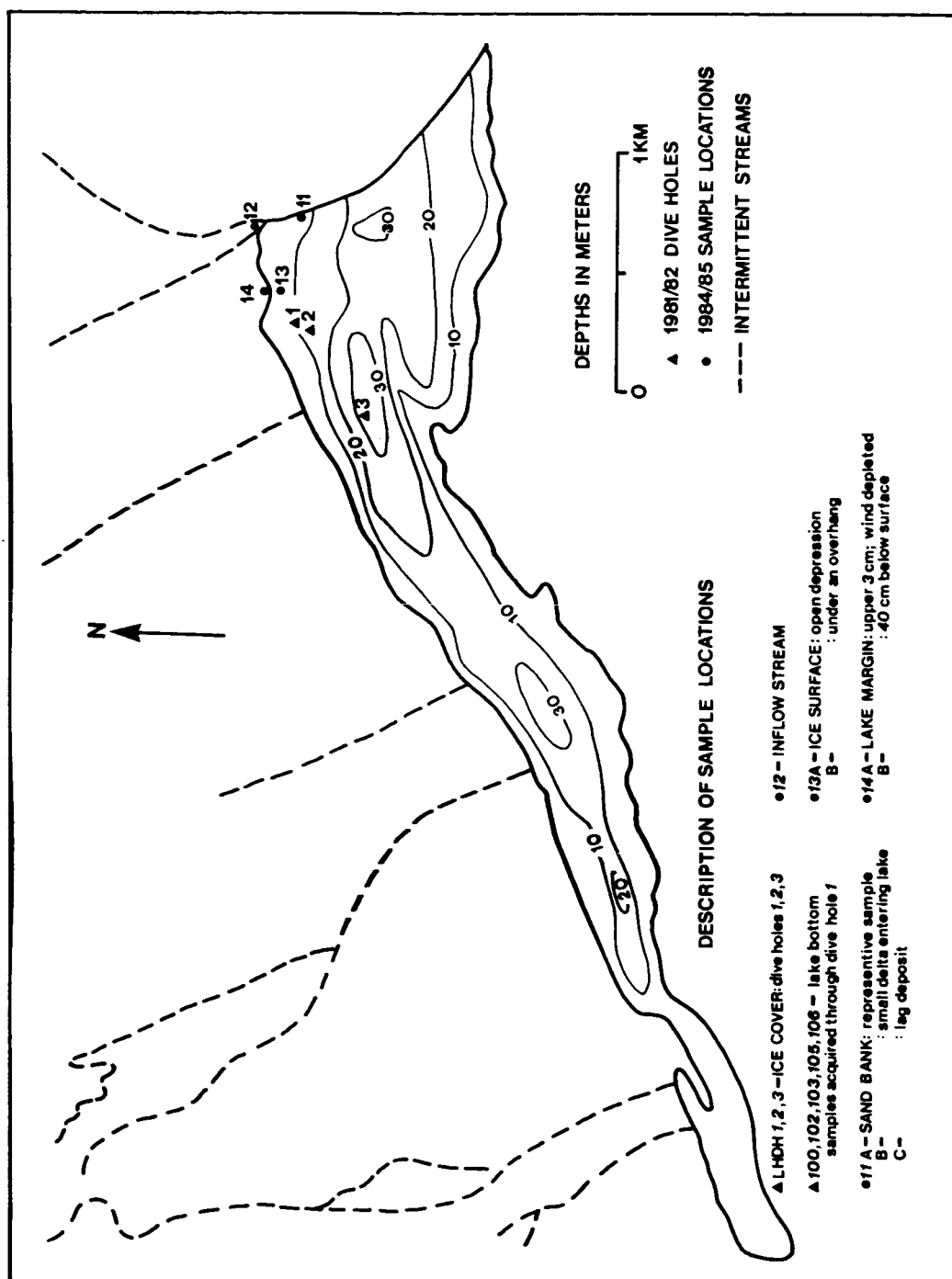


Figure 41: Bathymetric map of Lake Hoare (from F.G. Love, written pers. commun.) showing sample locations and their description.

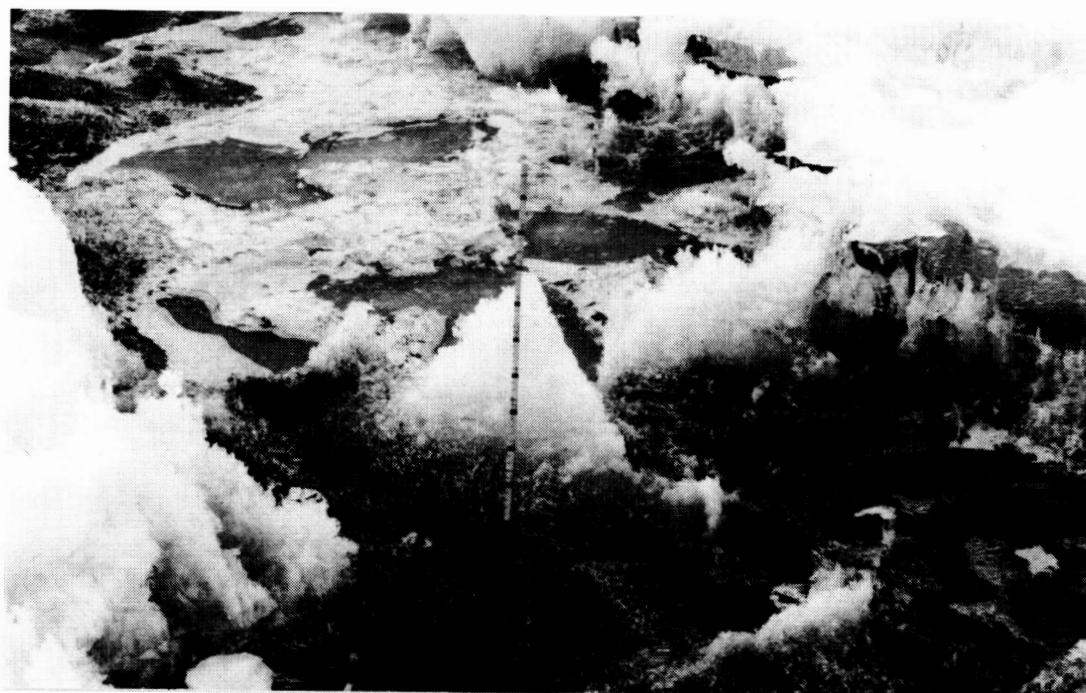


Figure 42: Sediment-filled troughs up to 1 m deep pervade the surface of Lake Hoare.
Scale is 1 m.

ORIGINAL PAGE IS
OF POOR QUALITY

ORIGINAL PAGE IS
OF POOR QUALITY



Figure 43: An aerial view of Lake Hoare looking eastward toward the Canada Glacier, 900 m above the surface. 40-50% of the ice is covered with sediment.

irregularities in the surface provide traps in which the sediment is deposited.

The average thickness of the ice covering Lake Hoare is 4.7 m (F.G. Love, 1984, pers. commun.). Sand and pieces of algal mat occur as ~ 20 cm thick, discontinuous lenses 1-2 m below the ice surface that may extend laterally for meters. Sand also occurs in small, centimeter-sized pockets in the top 1 m of the ice cover. By comparing the stratigraphy of three holes melted in the ice cover, it has been shown that the tabular sand lenses do not correlate from one hole to the next. Above the tabular sand lenses the ice is porous, containing irregular and frothy air bubbles (F.G. Love, 1984, pers. commun.). Below the sand lenses, extended air bubbles form narrow vertical channels up to 1.5 m long (fig. 44) (R.A. Wharton, 1985, pers. commun.). Groups of parallel air channels start and end at the same depths below the surface. These groups may be repeated two to three times in a vertical column of ice. At the top of any one group of air channels, pieces of algal mat are frequently found.

Unlike Lake Vanda, Lake Hoare does not appear to have any remnants of old shorelines. The material at the present shoreline is coarse and poorly sorted, with boulders up to 0.5 m in size (fig. 45). The bank is steeper above the present water level and flattens out to a gentle slope below, as in Lake Vanda, although no ridge near the lake margin where the lake is ice-free was observed.

A sand bank inferred to be of eolian origin lies at the east end of the lake against the Canada Glacier. It is approximately 10-15 m wide and 50 m long and is oriented with its long axis parallel to the glacier. A minor amount of cobbles, which were sloughed off the face of the glacier, are intermixed with the sand. During the summer, several small melt streams flow from the steep, 15 to 20 m high terminus of the glacier onto the sand bank. As the streams flow over the sand bank, they cut channels that expose internal layering and form deltas as they enter the lake. The largest inflow stream flows along the western margin of the glacier (fig. 46). At the location and time when stream gauging data were obtained, it was an approximately 3-m-wide braided stream with a depth < 10 cm. The stream travels more than 100 m from the location where it leaves the glacier to where it enters the lake. On one warm day during the summer 1984/85

ORIGINAL PAGE IS
OF POOR QUALITY

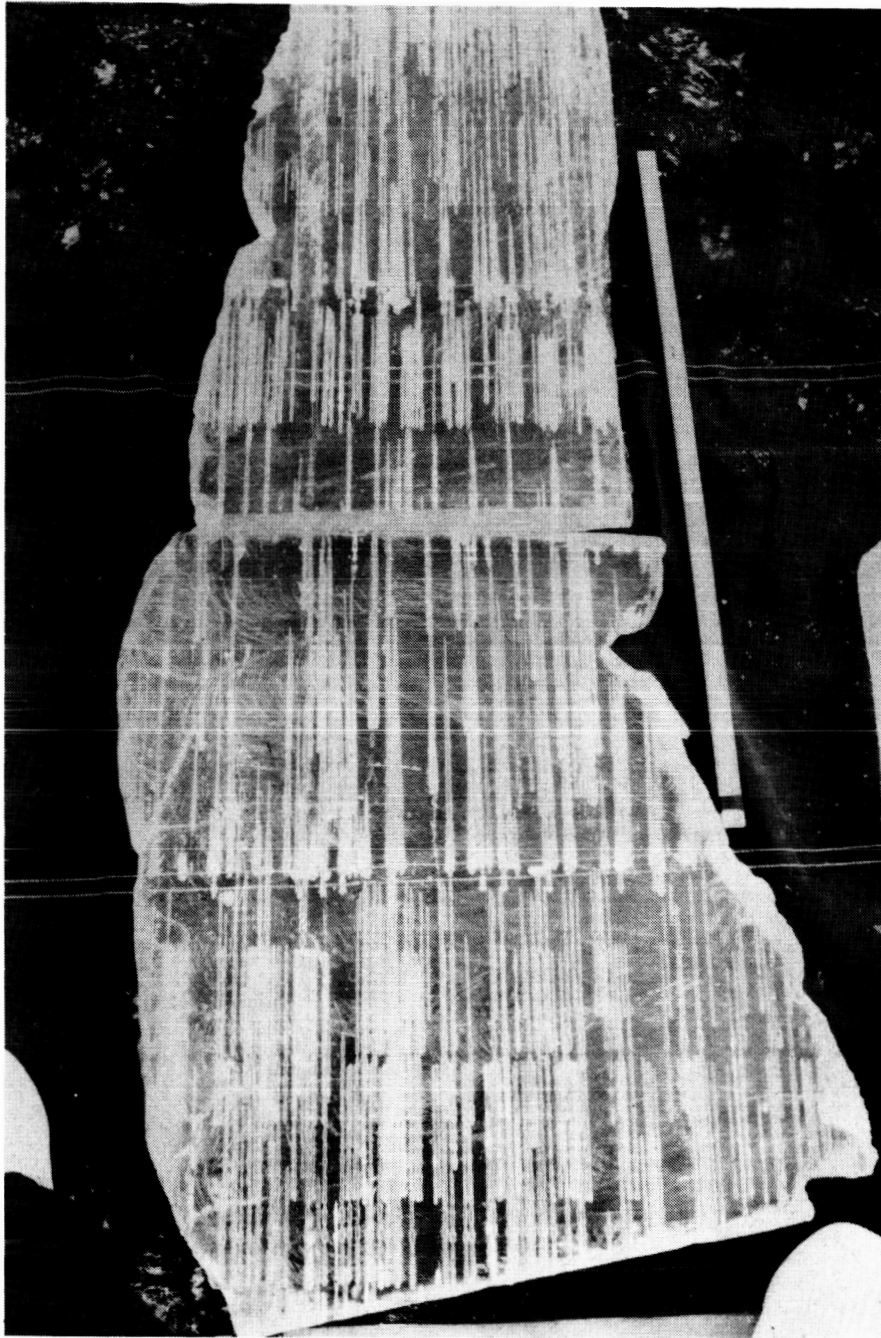


Figure 44: Cross-section of part of the ice cover on Lake Hoare. Air bubbles form vertical channels up to 1.5 m long. Scale is 1 meter.



Figure 45: The shoreline at Lake Hoare is made of poorly sorted sediment. Scale is 1 m.



Figure 46: The largest stream flows into Lake Hoare on the western side of the Canada Glacier.

when data were obtained, the discharge was $0.06 \text{ m}^3/\text{sec}$. Smaller streams to the west flowed during daytime hours, but ceased at night when glaciers or snowfields at their sources no longer were melting.

Sediment samples were collected from locations shown on Figure 41. Samples were collected from the ice cover (LHDH1, LHDH2, LHDH3) and lake bottom (100, 102, 103, 105, and 106) during the summer of 1980/81 by F.G. Love, and from the ice surface (13A and B), inflow stream (12), lake margin (14A and B), and sand bank at the east end of the lake (11A, B, and C) during the summer 1984/85.

Lake Fryxell. Lake Fryxell lies east of Lake Hoare in Taylor Valley, between the Canada Glacier to the west, and the Commonwealth Glacier to the east. The lake is approximately 5 km by 1.5 km, covering an area of $\sim 7.5 \text{ km}^2$, and is 11-18 m deep. The temperature of the lake varies from $\pm 0.01^\circ\text{C}$ directly below the ice cover, to 2.2°C at a depth of 10 m (Hoare and others, 1965). Small, intermittent streams flow into both the north and south sides of the lake during the summer months. A larger, unnamed stream that originates at the Commonwealth Glacier flows into the lake at its eastern end. No information presently exists on its seasonal discharge rate.

The thickness of the ice cover on Lake Fryxell is 4.5 m (Hoare and others, 1965; R.A. Wharton, 1985, pers. commun.). Tabular sand lenses $\sim 5 \text{ cm}$ thick are located $\sim 1.0 \text{ m}$ below the surface. During the summer months, a well-developed melt zone forms at the lake margins. Cores from the bottom sediment reveal coarse sediment (1 cm to 2 mm) that includes pyroclastic material derived from Mt. Erebus, which is on the eastern border of the Ross Sea, calcite grains concentrated in the stromatolites, and Fe-Mg minerals concentrated in between the algal layers. A preliminary radiocarbon age for sediment taken $\sim 70 \text{ cm}$ below the surface of the lake bottom is $10,300 \pm 400$ years (F.G. Love, 1984, pers. commun.). The character of Lake Fryxell's ice cover is similar to that at Lake Hoare.

Grain Size Analysis

Purpose and Procedure

The purpose of comparing grain size distributions of samples taken from different localities within and around Lake Hoare was to determine the dominant mechanism responsible for deposition of lake-bottom sediment. The three possibilities are: downward transport through the ice cover, transport into the lake from the inflowing streams, and slumping of material from the lake margin.

Lake Hoare was chosen for this study because a fairly complete data set was acquired for this lake only. Small cores of sediment from the lake bottom (6-10 cm long and 2 cm in diameter) were obtained from G.M. Simmons at Virginia Polytechnic Institute and State University. Samples of sediment from within the ice cover, which were retrieved in the process of melting dive holes, were provided by F.G. Love, formerly at Virginia Polytechnic Institute. Sediment samples from the surface of the ice, the lake margins, and an inflowing stream were supplied by S.W. Squyres at NASA Ames Research Center. Figure 41 shows the sample locations with brief descriptions.

The samples required only minor preparation for analysis. Suspended sediment was removed by washing each sample in distilled water and pouring off the liquid containing the clay-sized particles into a separate beaker. The wet sample and the beaker containing the suspended sediment were then dried in an oven. The sample was gently mixed in a ceramic mortar with a rubber pestle to break up any clumps that may have formed, and then split and weighed a number of times, depending on how large the original sample was. The suspended sediment was weighed separately, and the weight was added to the weight of the portion of sediment finer than the smallest sieve (4.0ϕ in this study). This procedure was followed for the wet samples, which were in the majority. The few dry samples were merely split and weighed. Each sample was sieved at whole phi intervals, the largest mesh used was -1.99ϕ (3.962 mm), and the smallest 4.0ϕ (0.063 mm). The stack of sieves was placed in a Derrick sieving machine that vibrated the sample for fifteen minutes. Each phi interval was weighed to the nearest 0.01 gm.

The results of the sieving analyses are presented in Table 3 in their raw form, and in Figure 47 as cumulative size-frequency curves (using cumulative-probability plots).

Histograms or cumulative size-frequency graphs using a normal scale were not used for analysis because Folk (1980) argued that the greatest amount of information can be extracted from cumulative log-probability size-frequency graphs. A number of statistical parameters of grain size distribution were then produced from each curve. Graphic mean (M_z), median (Md), inclusive graphic standard deviation (σ_I), inclusive graphic skewness (Sk_I), and kurtosis (K_G), presented in Table 4, were calculated according to the formulas of Folk (1980):

$$M_z = \frac{\phi_{16} + \phi_{50} + \phi_{84}}{3} \quad (1)$$

$$Md = \phi_{50} \quad (2)$$

$$\sigma_I = \frac{\phi_{84} - \phi_{16}}{4} + \frac{\phi_{95} - \phi_5}{6.6} \quad (3)$$

$$Sk_I = \frac{\phi_{16} + \phi_{84} - 2\phi_{50}}{2(\phi_{84} - \phi_{16})} + \frac{\phi_5 + \phi_{95} - 2\phi_{50}}{2(\phi_{95} - \phi_5)} \quad (4)$$

$$K_G = \frac{\phi_{95} - \phi_5}{2.44(\phi_{75} - \phi_{25})}. \quad (5)$$

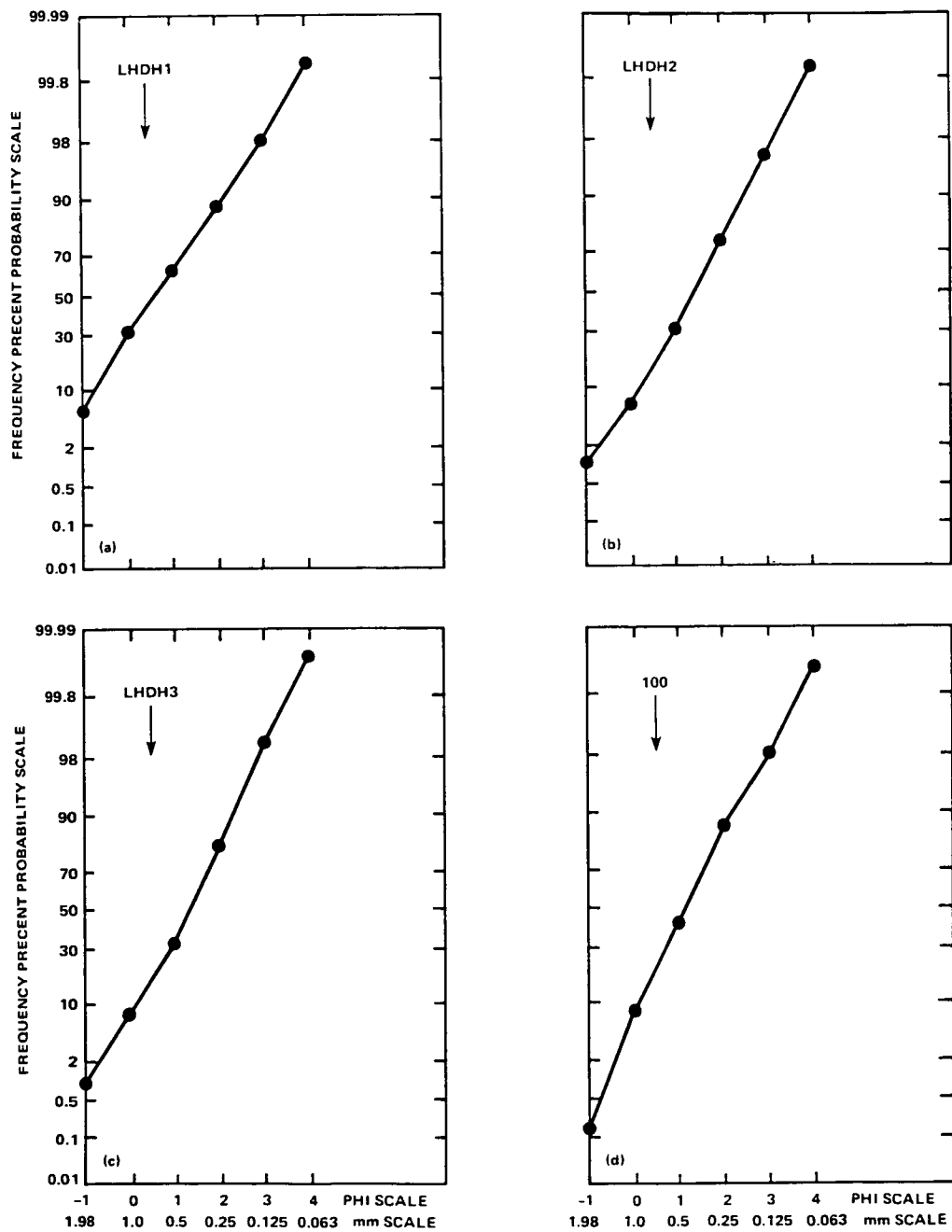


Figure 47: Cumulative size-frequency curves of the grain-size distributions of sample from Lake Hoare.

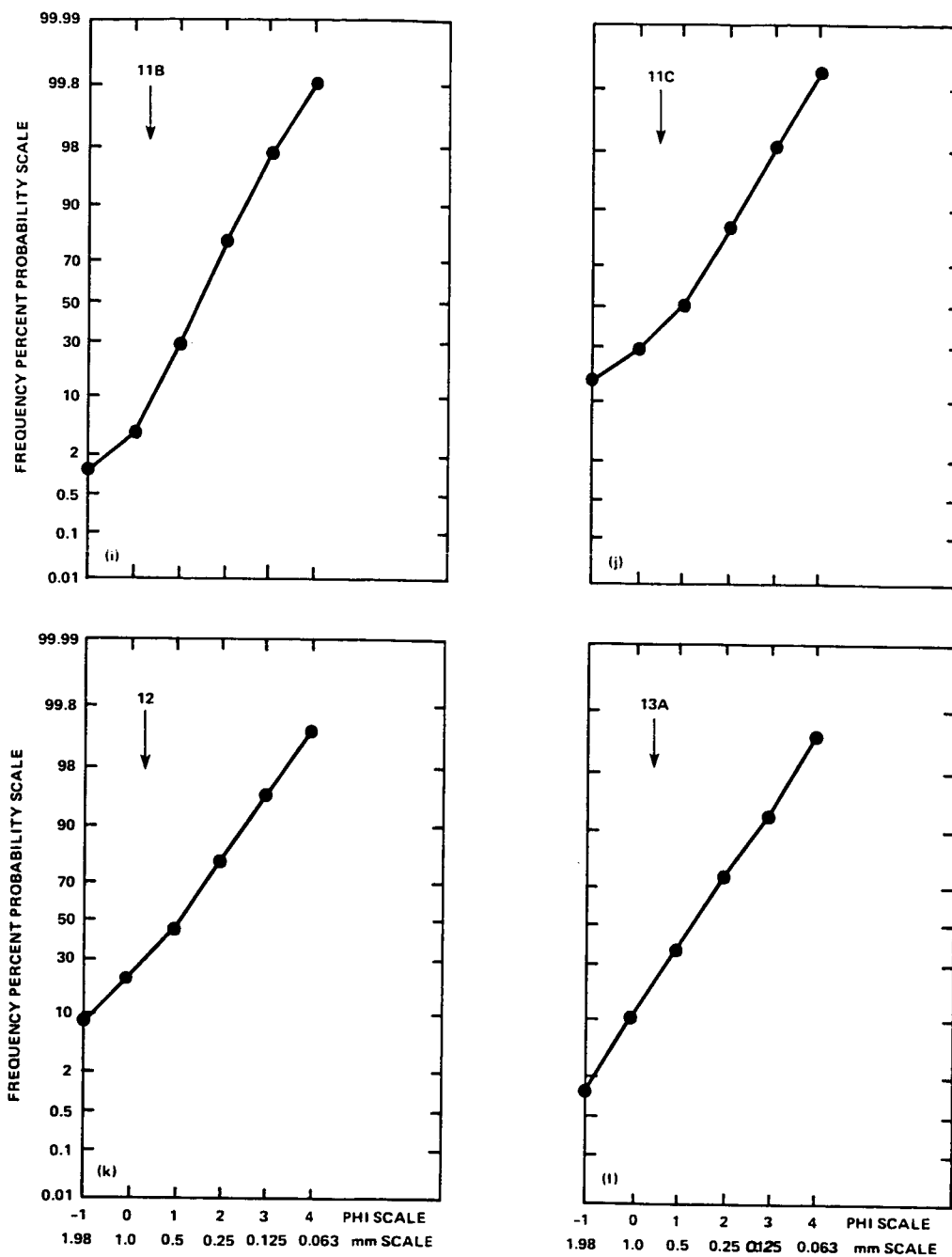


Figure 47: continued.

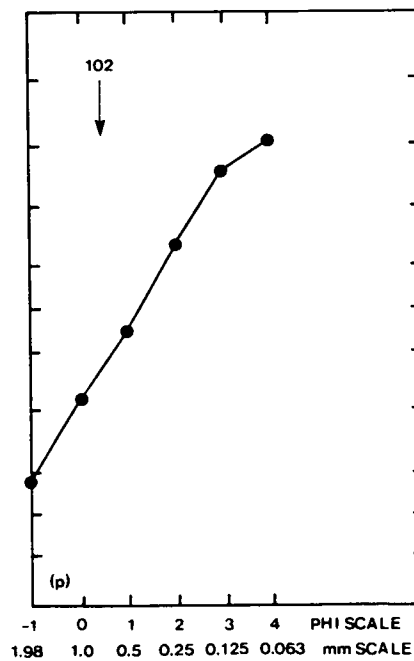
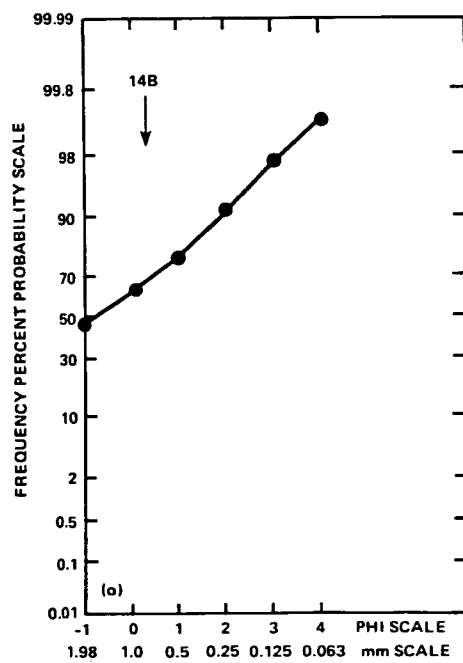
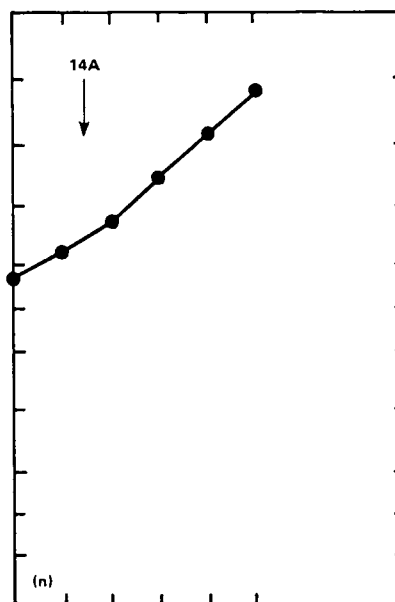
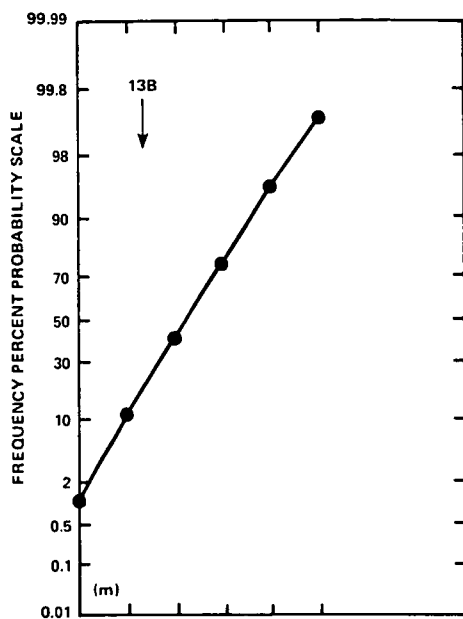


Figure 47: continued.

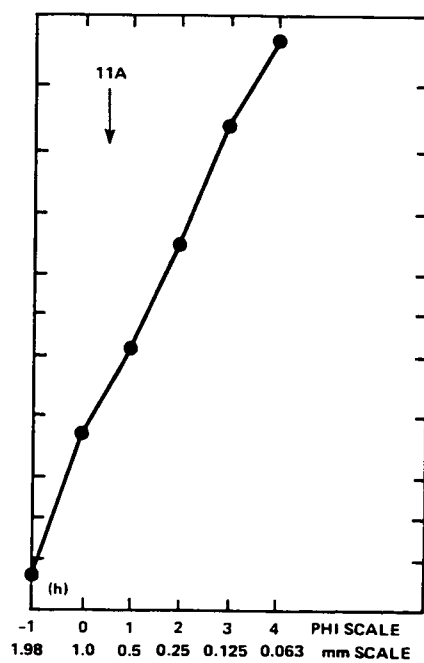
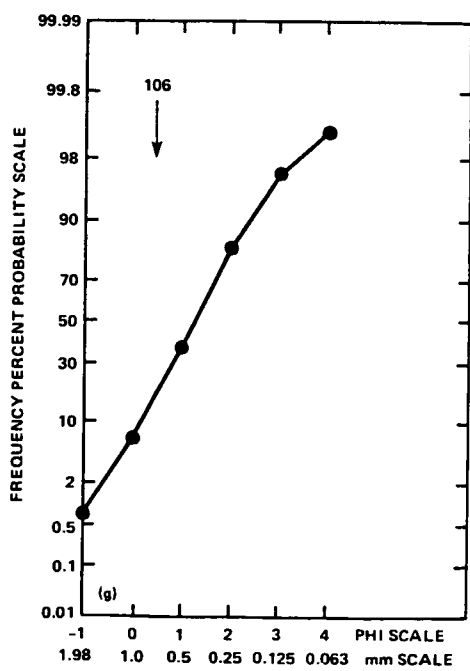
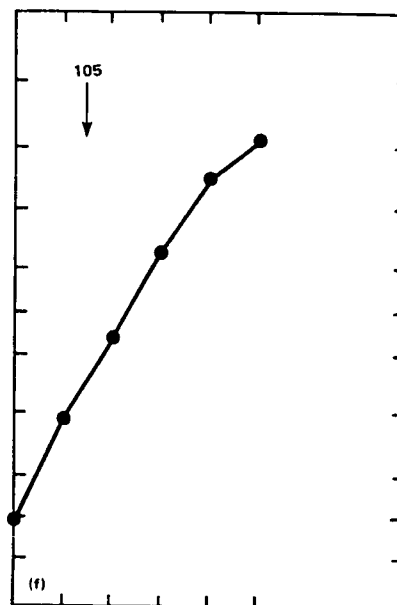
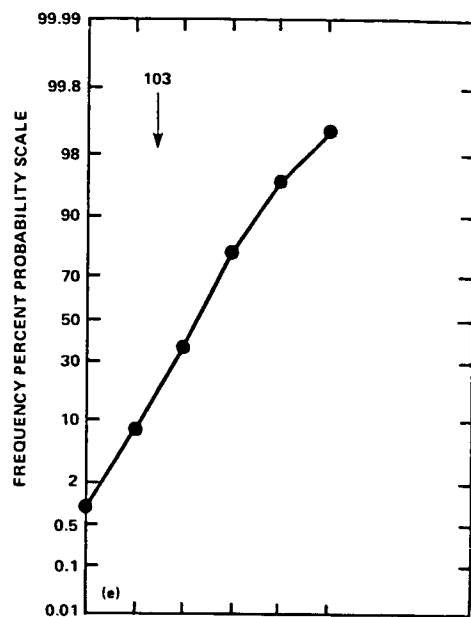


Figure 47: continued.

Weight in Grams									
Location	-1.99 ϕ	-0.99 ϕ	0.0 ϕ	1.0 ϕ	2.0 ϕ	3.0 ϕ	4.0 ϕ	< 4.0 ϕ	TOTAL
	3.96mm	1.98mm	1.0mm	0.5mm	0.25mm	0.125mm	0.06mm	< 0.06mm	
LHDH1	0.82	4.04	18.64	27.17	21.55	8.46	1.68	0.09	82.45
LHDH2	0.36	0.44	4.43	17.93	33.98	16.23	2.58	0.11	76.06
LHDH3	0.0	0.22	1.59	6.56	13.65	5.69	0.38	0.01	28.10
100	0.0	0.02	1.11	4.90	6.92	1.87	0.30	0.01	15.13
102	0.14	0.30	2.84	7.53	10.20	4.37	0.87	0.50	26.75
103	0.0	0.14	1.15	4.39	7.16	2.86	0.50	0.21	16.41
105	0.0	0.11	1.75	6.09	9.10	4.35	0.78	0.42	22.60
106	0.0	0.16	1.20	5.73	8.76	3.16	0.49	0.20	19.70
11A	0.0	0.14	14.72	60.64	118.29	43.84	2.29	0.07	239.99
11B	2.17	0.58	5.42	54.79	115.18	45.83	5.34	0.45	229.76
11C	29.53	8.43	23.37	48.20	78.77	29.69	3.73	0.5	221.92
12	3.64	16.92	31.14	50.70	79.38	39.99	10.90	1.52	234.19
13A	0.0	2.58	18.40	52.52	74.81	44.83	10.08	1.29	204.51
13B	0.24	1.35	15.47	44.10	54.46	30.28	6.37	0.93	153.19
14A	327.53	59.88	61.69	57.75	51.01	21.06	5.80	1.73	586.46
14B	129.53	52.06	56.00	58.25	60.11	27.26	7.71	3.01	393.93

Table 3: Results of sieve analyses for sediment samples from in and around Lake Hoare, Antarctica. Sample locations are shown in Figure 41. Cumulative frequency plots are presented in Figure 47.

Table 4. Statistical analyses of grain-size distributions from samples in and around Lake Hoare. Formulas for statistics are from Folk (1980). Sample locations are presented in Figure 41.

Sample	Mean (ϕ)	Median (ϕ)	Std. Deviation (ϕ)	Skewness	Kurtosis
LHDH1	0.66	0.67	1.21	-0.063	0.97
LHDH2	1.41	1.45	0.85	-0.07	1.06
LHDH3	1.37	1.4	0.82	-0.10	1.29
100	1.17	1.2	0.81	-0.013	1.07
102	1.23	1.25	1.05	-0.01	1.08
103	1.34	1.35	0.94	-0.004	1.13
105	1.02	1.35	0.98	0.03	1.06
106	1.30	1.30	0.88	0.01	0.63
11A	1.32	1.35	0.80	-0.10	1.04
11B	1.43	1.45	0.78	-0.002	1.08
11C	0.32	1.0	1.44	-0.32	1.01
12	1.03	1.2	1.34	-0.17	1.03
13A	1.39	1.35	1.09	0.03	1.02
13B	1.27	1.30	1.02	0.01	0.93
14A	-1.09	-1.99	1.28	0.5	0.89
14B	-0.41	-0.75	1.57	0.23	0.63

Results and Discussion

Visher (1969) proposed that straight line segments separated by discrete points, which mark a change in slope within individual cumulative probability curves of grain-size distribution, can be interpreted as sub-populations. The modes of transportation represented by these characteristic slope changes are inferred to reflect suspension, saltation, and surface creep or rolling processes (Visher, 1969). This explanation has been criticized. Walton and others (1980) showed that cumulative frequency curves with similarly sloped segments can be reproduced by a variety of mixing and truncation models. Nevertheless, Visher (1969) has observed that combinations of characteristic slopes do occur repeatedly in many sedimentary depositional environments, and it is helpful to apply Visher's method of grain-size distribution analysis to the curves from Lake Hoare sediment.

A first look at the curves reveals them to be much simpler than those of shoreline and dune environments (Visher, 1969). Except for samples 11B, 11C, 14A, and 14B, there are no obvious breaks in the slopes of the curves. The length and slope of the simpler curves may be compared to the central portion of common curves, the "saltation population." The curves for Lake Hoare sediment from the ice cover, lake bottom, and sand bank, are most similar to the grain-size curve typical of dunes reported by Visher (1969), although the median grain size is greater by $1-2\phi$, and the sediment more poorly sorted than the sediment reported by Visher (1969). The coarse size is a result of the strong winds that are constantly blowing up or down the Dry Valleys. A stronger wind is capable of moving larger grains than are typically moved in an eolian environment, and it can also transport a larger range of grain sizes. The poor sorting is a result of trapping and mixing of sediment. The resulting grain-size population is not from a single event, but rather it represents a range of wind conditions.

The samples that depart from the dune sand curve are the stream and lake margin deposits, and the delta and lag deposits from the sand bank (sample numbers 12, and 14A and B, 11B and C respectively). The break in slope of the curves from samples 11B and 11C is located in the largest grain sizes. Sample 11B was taken from a small

delta on the sand bank and may represent the concentration of coarser particles in the topset or upper forset beds. Sample 11C is from an eolian lag deposit. The coarse grains presumably fell off the face of the glacier and were later concentrated by the wind. Samples 14A and 14B are from the lake margin. Sample 14A was taken from the surface where it seemed that the smaller grain sizes had been winnowed away by eolian processes. Sample 14B is from ~ 40 cm below the surface. Both samples show evidence of eolian winnowing of fine grains.

The grain-size distributions for lake bottom samples 103, 105, and 106 all show a change in slope at the 3.0ϕ size. The fine-grained sediment population may have been transported into the lake by the inflowing streams, and its abundance may reflect sorting processes within the lake.

The statistical parameters derived from each cumulative-probability curve produce a quantitative method for comparing grain-size distributions. It is important to understand the significance of each parameter. The equation used for determining mean grain size is based upon three points on the curve, and it takes into consideration any deviations from a normal distribution. Differences between mean and median result from these deviations. Standard deviation is a measure of the sorting of the sample. Skewness is a measure of the asymmetry of the grain size distribution. A symmetrical curve has a skewness value of 0.00, and the theoretical extremes have values of +1.00 and -1.00. A positively skewed sample has a tail or excess of fine grains, and a negatively skewed sample has a tail of coarse grains. Kurtosis is a measure of the peakedness of a curve. A normal curve has a kurtosis value of 1.00. Values less than 1.00 are platykurtic, having tails that are better sorted than the central portion. Values greater than 1.00 are leptokurtic; the central portion of the curve is better sorted than the tails. Although skewness is believed to be environment-sensitive, it seems that kurtosis is not (Friedman, 1961). Mason and Folk (1958), on the other hand, found that kurtosis values provided a way to separate eolian flat sediment from dune and beach sediment. It is controversial whether kurtosis values add anything to statistical grain size analysis but confusion (Sedimentation Seminar, 1981).

The statistical parameters in Table 4 reveal the important relationships between the various groups of samples. The lake margin sediment samples (14A and 14B) are coarser and more poorly sorted than the lake bottom sediment samples (100, 102, 103, 105, and 106). Sediment in the inflow stream (12) have a similar grain size, but the sorting (standard deviation) is much poorer than the lake bottom sediment. Sediment from within the ice cover (LHDH2 and LHDH3, excluding LHDH1) and the surface of the ice (13A and 13B) have mean grain size and standard deviation values in the same range as the lake bottom sediment. The representative sample from the sand bank (11A) has a mean grain size also in the same range as the lake bottom sediment, and a standard deviation that is slightly lower. The skewness and sorting values of the sand bank are not typical of eolian sands. In eolian sand skewness values are usually positive, and sorting is usually excellent (McKee, 1979), whereas this sample is slightly negatively skewed, and moderately sorted. Although the sand bank would appear to be a product of eolian processes, the atypical skewness and sorting values may be a result of unusually strong winds.

The grain size analyses are consistent with the hypothesis that transport through the ice is the dominant sedimentation mechanism in Lake Hoare. The sediment on the lake bottom are similar in their size distribution to sediment on the surface and within the ice cover, and less similar to sediment from the lake margins and inflow stream. Because the mean grain size and distribution of the sediment from the ice cover and lake bottom are similar to the sand bank at the east of the lake, it is probable that the dominant mode of transportation and deposition of the grains was eolian with perhaps some fluvial reworking.

Mineralogy

Procedure

The samples from Lake Hoare were analyzed for their mineralogy to test further the hypothesis that the sediment in the ice cover is most similar to that in the lake

bottom. To cut the sediment into thin sections, the disaggregated samples were cast in petro-poxy. The thin sections were each examined for general mineralogical content, and then reexamined in a point-count analysis. From 160 to 200 grains were counted in each sample. Points were grouped into quartz, feldspar, and rock fragments according to the scheme of Folk (1980), in which "quartz" includes all types of monocrystalline and polycrystalline, coarse quartz, but not chert. Monocrystalline "accessory" minerals, including micas and pyroxenes, are listed as "other" grains. The results are presented in Table 5.

Results and Discussion

The entire group of sediment has a very limited range in composition. Using Folk's classification (1980), the samples are considered submature lithic arkosic to feldspathic lithic sand. The feldspar content is between 30-45%, rock fragments 17-41%, and quartz 28-44%. The high feldspar content in these sediment can be attributed to the cold, dry climate of the Dry Valleys, which inhibits feldspar decomposition. Under these conditions, feldspars are eliminated mostly by abrasion. In these samples, the majority of feldspars are plagioclase and orthoclase. The lithic constituent is made of felsic plutonic fragments with subordinate amounts of mafic volcanics, and marble. The majority of quartz is undulatory. The minerals that are grouped under the heading "other" include orthopyroxene and clinopyroxene with lesser, varying amounts of biotite, chlorite, olivine, and hornblende.

There is very little variability in the percentages of quartz, feldspar, rock fragments and "other" grains. A ternary diagram comparing the three essential constituents, quartz, feldspar and rock fragments is presented in figure 48. The most obvious separation among the samples is in their rock fragment percentages. Samples from the inflow stream and lake margin contain more rock fragments than the other samples. In general, the coarser-grained samples also contain more rock fragments. Samples from on and within the ice cover, the lake bottom, and sand bank are mineralogically homogenous, in that the ternary diagram does not separate out any one of these groups.

Table 5. Mineralogical point count data of samples from Lake Hoare. Values are given in percentages.

Sample	Quartz (%)	Feldspar (%)	Rock Frags. (%)	Other (%)
LHDH1	23	26	24	27
LHDH2	33	30	14	23
LHDH3	22	29	20	29
102	23	30	25	22
103	29	26	15	30
105	19	25	20	36
106	23	30	20	27
11A	24	24	17	35
11B	23	28	20	29
11C	21	28	17	34
12	21	23	25	31
13A	29	33	14	24
13B	24	31	17	28
14A	19	20	27	34
14B	24	24	23	29

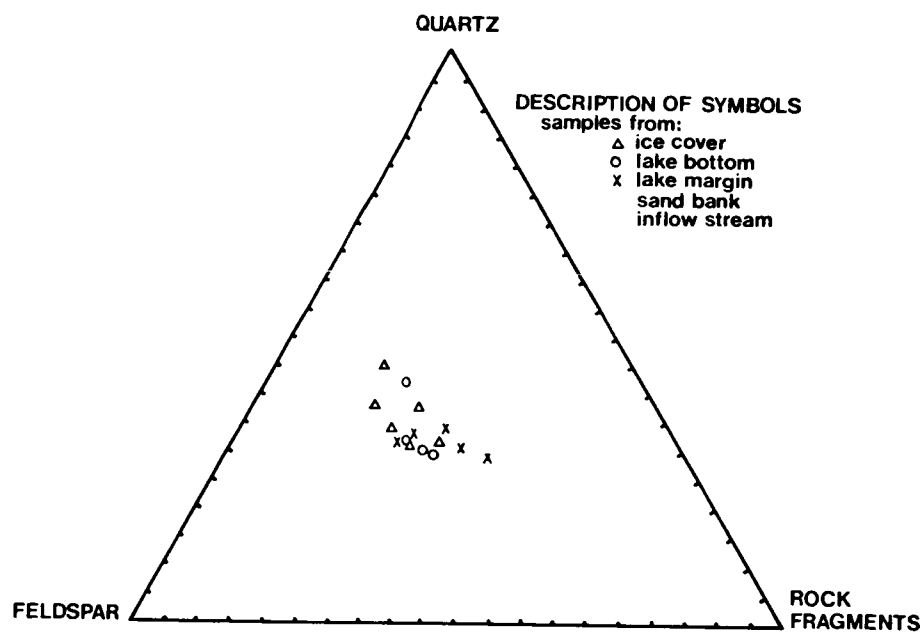


Figure 48: Ternary diagram showing mineralogical relationships among the samples from Lake Hoare.

The mineralogical data alone do not unequivocally show that the lake bottom sediment are most similar to the sediment from the ice cover. They do, however, provide weak support for the hypothesis because the samples from the lake margin and inflow stream differ the most from the lake bottom samples.

Microscopic Analysis of Quartz Grain Textures

Purpose and Procedure

The study of quartz grain surface textures by scanning electron microscopy (SEM) has become a useful method for relating surface features to specific environments of transportation and deposition (Margolis and Krinsley, 1974; Hill and Nadeau, 1984). By recognizing various mechanical and chemical surface markings on a number of grains from the same sample, it is possible to make an environmental interpretation. The major limitation in this method of analysis is that there is no single mechanical feature diagnostic of an environment or of an abrasion process (Krinsley and Doornkamp, 1973). Nevertheless, by producing a semi-quantative analysis of the features on a number of grains, it is usually possible to make conclusions on the origin and transport history of the grains. In this study, it was most important to determine if there is a strong similarity between sediment from the lake bottom, and sediment from the ice cover, lake margin, or inflowing stream.

Samples LHDH2 (ice cover), 12 (inflow stream), 14B (lake margin), and 102 (lake bottom) were chosen for analysis. Preparation of the samples followed the methods described in Krinsley and Doornkamp (1973). Grains from the 0.25-0.50mm ($2 - 1\phi$) size range were selected because that interval includes to the mean of most of the samples. The samples were boiled in a 50% solution of HCl for ten minutes, and then washed in distilled water. Twenty-five grains were randomly chosen from each sample and mounted on metal specimen stubs using double sided tape. The stubs were then coated with a gold-palladium alloy. A Cambridge Stereoscan 250 Mk2 scanning electron microscope was used to examine all the samples. First, each grain was inspected with an X-ray

analyzer to determine that the grain was indeed quartz, and then the entire grain was photographed at a low resolution. Further examination was performed at magnifications up to 8,000X, in order to identify smaller features. Ten grains from each sample were photographed and studied in order to provide enough data for a semi-quantitative analysis of the textures.

Results

The grains were analyzed for three main types of surface features: grain outline and degree of rounding, evidence of mechanical abrasion, and chemical alteration. Because each grain has various degrees and combinations of these features, it was necessary to create five categories to which each grain could be assigned. Examples of the five grain types are presented in Figure 49. The descriptions of the grain types are as follows:

Type A. Grain outline highly angular; fresh conchoidal fractures; high relief; smooth fracture surfaces; features may be slightly rounded by precipitation and solution.

Type B. Grain outline subangular; medium relief; relict conchoidal fractures may appear somewhat abraded; chemical precipitation and solution particularly on faces; some edges show abrasion in the form of large breakage blocks.

Type C. Grain outline subrounded; no angular protrusions; medium to low relief; relict fractures subdued by much abrasion and chemical precipitation and solution; heavily abraded edges show large breakage blocks and some small breakage blocks.

Type D. Grain outline well to very well rounded; low relief; no relict fractures; dish-shaped concavities; grain surface mostly small blocks and upturned cleavage plates that may be smoothed or accentuated by chemical activity.

Type E. Grain with fresh fracture surface making up more than 10% of grain; original surface may be like C or D.

A histogram for each sample is presented in figure 50, which shows the number of grains assigned to each grain type (A-E). These results indicate that all of the samples

ORIGINAL PAGE IS
OF POOR QUALITY

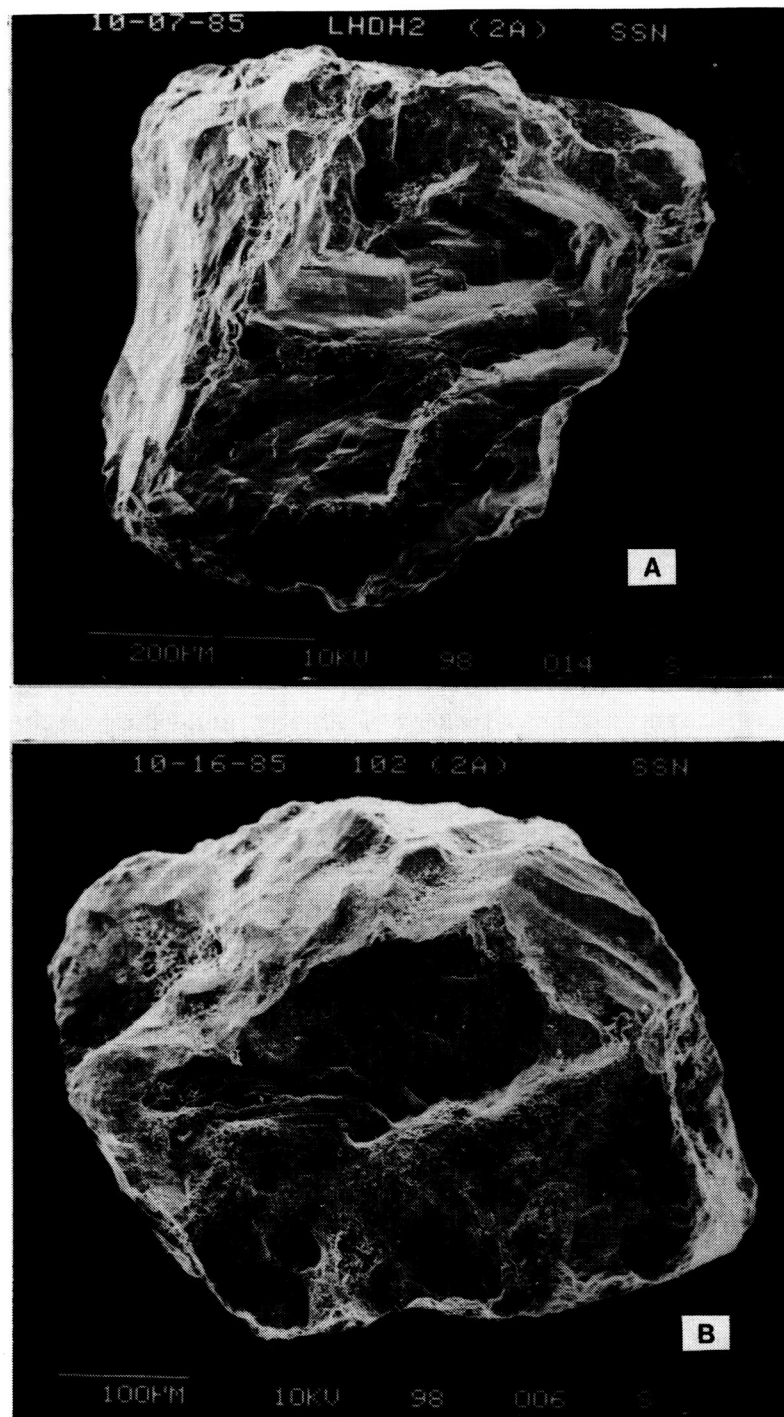


Figure 49: The five quartz grain types used to classify the samples from Lake Hoare (A, B, C, D, E).

ORIGINAL PAGE IS
OF POOR QUALITY

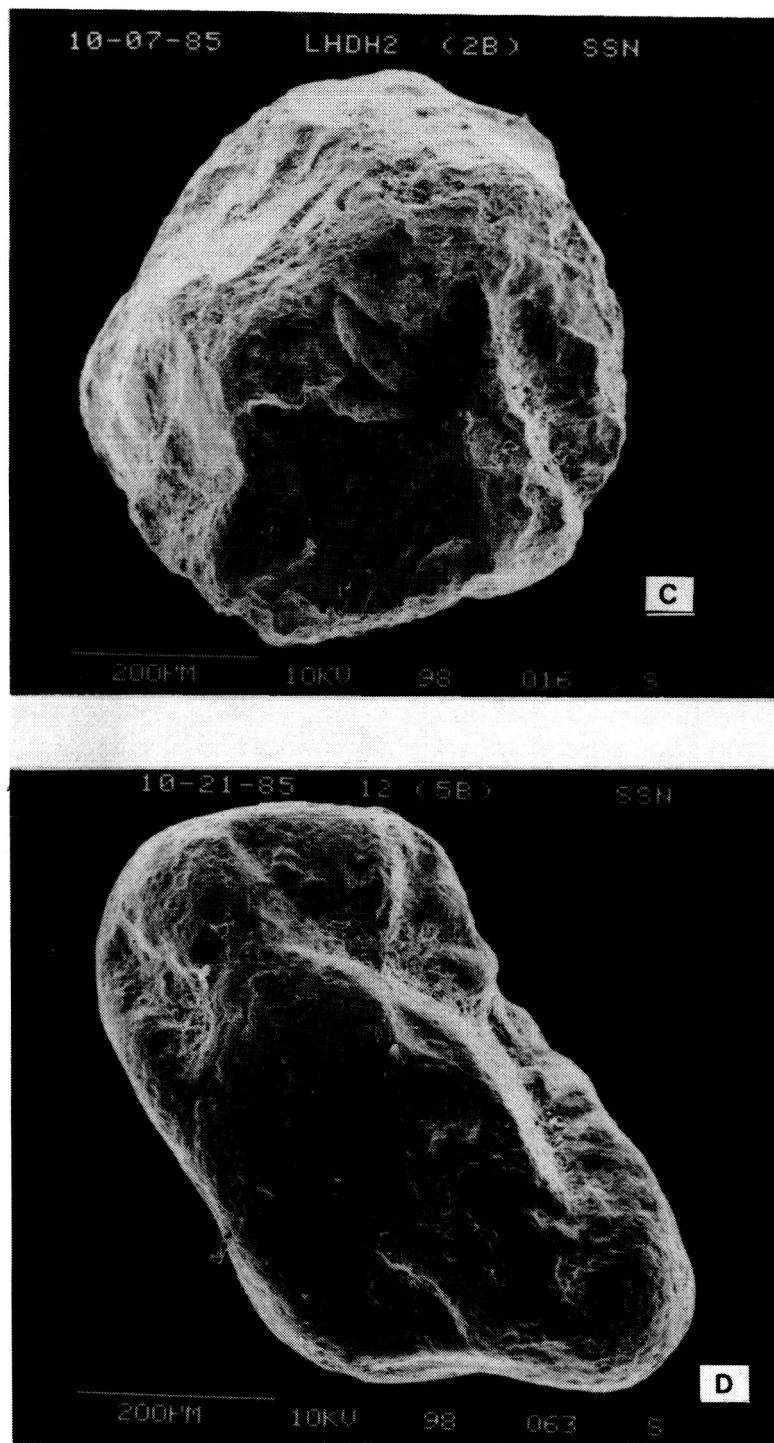


Figure 49: continued

ORIGINAL PAGE IS
OF POOR QUALITY

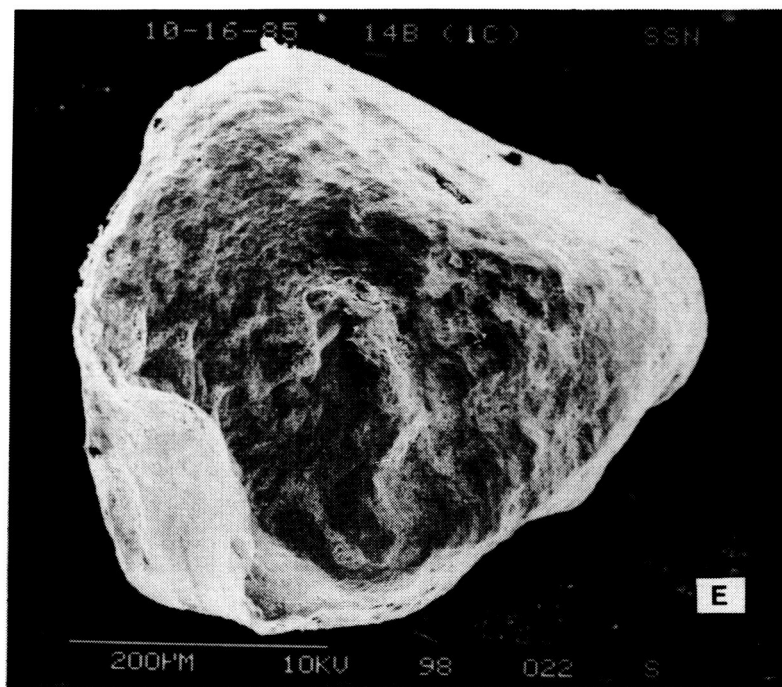


Figure 49: continued

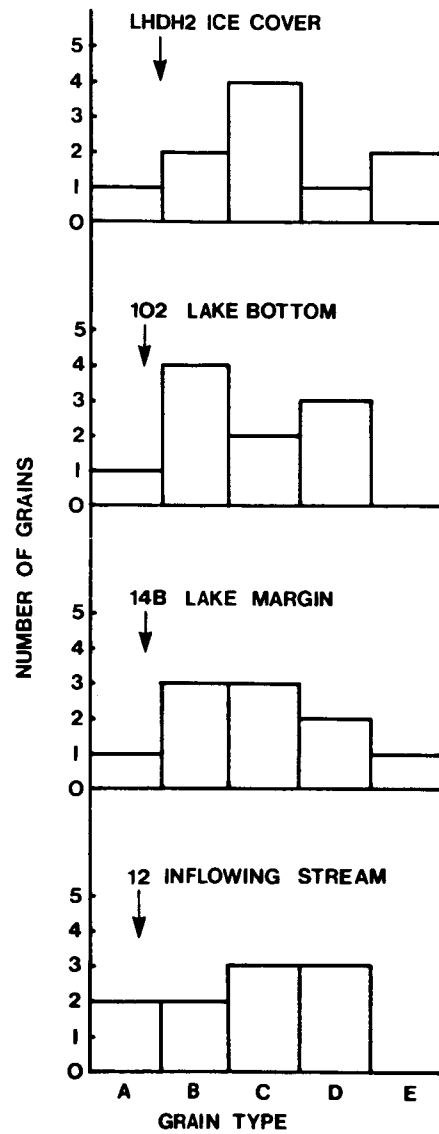


Figure 50: Histograms showing the number of grains in each grain type (A-E) for samples from Lake Hoare.

have the same range of grain textures, but no samples have obvious, striking similarities. The most common type of abrasion throughout these samples is small breakage blocks and upturned cleavage plates (fig. 49). The arrangement of these features is indicative of an eolian environment, which suggests that eolian transport plays an important role in continually redistributing the sediment in all of the subenvironments studied. This part of the study supports the mineralogical results that the sediment seems to represent a single population.

Estimation of Sediment Flux

An estimate of the sedimentation rates from the inflow streams was calculated from discharge rates and the quantity of suspended sediment in the streams. Data were obtained for both lakes Hoare and Vanda during the summer season of 1984/85. It was determined that, at the time of data acquisition, the streams were very near their peak discharge rates for the season (S.W. Squyres, 1985, pers. commun.).

The stream discharge rate for the inflowing stream into Lake Hoare was 0.06 m³/sec during the peak of the summer and there was 2.41×10^{-2} gm/l of suspended sediment in the stream water. The Onyx River at Lake Vanda was discharging at a rate of 7.24 m³/sec, and the quantity of suspended sediment was 5.42×10^{-2} gm/l. If one assumes that the bulk density of the sediment is 2.5 gm/cm³, the volume of sediment in the water for Lake Hoare is 9.6×10^{-6} m³ sediment/m³ H₂O, and 2.2×10^{-5} m³ sediment/m³ H₂O for Lake Vanda.

Chinn (1982) reported that the average annual discharge for the Onyx River over a ten year period (1969/70 to 1979/80) was 2×10^6 m³. There are no similar results reported in the literature for the inflow stream into Lake Hoare. In order to arrive at a similar figure for Lake Hoare, it was assumed that the discharge rate recorded during the summer 1984/85 at Lake Hoare was also at its peak. The ratio of the peak discharge of the Onyx River to its average annual discharge is thus inferred to be equal to the ratio of the peak discharge of the inflow stream into Lake Hoare to its average annual

discharge rate (which is unknown). Using the equality of these two ratios, the average annual discharge of the inflow stream at Lake Hoare was calculated to be $1.6 \times 10^4 \text{ m}^3$.

The sedimentation rate due to the inflow stream is the product of the average discharge and the volume of suspended sediment. For Lake Hoare, the sedimentation rate is $0.15 \text{ m}^3/\text{yr}$, and for Lake Vanda it is $43.4 \text{ m}^3/\text{yr}$. It is evident from these results that there is a great variability between the sedimentation rate of the Onyx River (Lake Vanda), and the inflow stream into Lake Hoare. Not only is there more than twice as much suspended sediment in the Onyx River water, but the discharge rate is also more than one hundred times greater. The two lakes also differ in the basins where the sediment eventually settle. The inflowing stream at Lake Hoare enters near the deepest portion of the lake, the Onyx River enters Lake Vanda at the eastern end in the shallowest part, which is cut off from the main body by a peninsula jutting out from the southern margin. Most of the sediment entering by the Onyx River are prevented from migrating into the deeper portions of Lake Vanda by the land barrier. Contribution of sediment from the ice cover on Lake Vanda also is minimal, because the ice contains very little sediment. Divers investigating west of the peninsula reported that only a thin veneer of sediment covers the bedrock at the lake bottom (F.G. Love, 1984, pers. commun.).

The maximum age of the lakes as determined from the history of recent glaciation in the valleys also constrains the sedimentation mechanisms of the lakes. The Ross Ice Shelf most recently expanded $\sim 22,000$ yr ago, blocking off Taylor Valley to form glacial Lake Washburn (Denton and others, 1970). If one considers Lake Hoare to be no older than 22,000 yr, and the amount of suspended sediment in the inflow stream to be $\sim 10\%$ of the total amount of sediment (bed load and suspended load), an average thickness of only ~ 19 mm of sediment would have accumulated at the bottom of Lake Hoare, if the only sediment input was from the stream. Because sediment cores over 50 cm in length have been retrieved from the lake bottom, it appears that most of the sediment in Lake Hoare was transported into the system by another mechanism.

Lake Vanda, however, does not require another mechanism to produce the thickness of sediment recorded east of the peninsula. Using the same assumptions as for Lake

Hoare (above), an average thickness of 4.8 m of sediment would have been deposited east of the peninsula by the Onyx River. Cartwright and others (1974) drilled through ~ 4 m of lacustrine sediment before reaching glacial deposits. Little sediment is evidently brought into the system from the ice cover on Lake Vanda, because at present the ice is virtually free of debris and there is little sediment at the bottom of the main portion of the lake.

Interpretation

The results from the analyses of grain size distribution, mineralogy, quartz grain textures, and estimation of sediment flux best support the hypothesis that the dominant mode of sedimentation in Lake Hoare is through the ice cover. The mean grain size and sorting of the samples from the lake bottom are most similar to the samples from the ice cover. The point count analyses showed that the mineralogical content varies very little throughout the subenvironments, although the samples from the lake margin and inflow stream differ the most from the other samples, which supports the results from the grain size distributions. The distribution of quartz grain textures does not, however, show any particular differences between the samples. The various subenvironments seem to represent a single, fairly homogeneous population.

The mechanism of sedimentation was further tested by estimating the sediment flux via the inflowing stream throughout the history of Lake Hoare. These results show that the stream contributed only a fraction of the sediment that has been recovered from the lake bottom. Together with the previous results, one can conclude that the majority of sediment presently on the bottom of Lake Hoare most likely entered into the lake system by migrating through the ice cover.

Processes of Sedimentation Through Ice

Two methods were considered for transport of sediment through the ice cover: (1) grains melt their way through the ice by absorbing solar energy, and (2) individual

grains work their way through vertical channels and/or cracks in the ice that form during the summer season. The first method was theoretically analyzed by G.D. Clow and C.P. McKay (person. commun.), and the second method is based on the observational data.

Grains Melting Through Ice

C.P. McKay and G.D. Clow (1985, pers. commun.) theorized whether particles could melt through a 5 m thick ice cover in a Dry Valley lake. They calculated the particle size required to melt the surrounding ice at a various depths within an ice cover, assuming that energy is absorbed by the particle and is conducted away by the ice. The problem was simplified by treating the ice as an infinite slab and the particle a spherically symmetrical heat source. This assumption is reasonable because a grain is much smaller than the thickness of the ice cover. The amount of energy absorbed by the particle on the surface of the ice (including absorption of the reflected upwelling light) is given as

$$q = F_o(1 - \varpi)\pi r^2 \quad (6)$$

where F_o is the energy flux incident on the top of the ice cover, ϖ is the albedo of the particle, and r is the radius of the particle. With depth the flux is approximately reduced by the factor $e^{-\frac{z}{h}}$ where z is the depth and h is the extinction path length. The condition for melting is given by the equation

$$273^\circ K - T(z) = \frac{q}{4\pi r k} \quad (7)$$

where $T(z)$ is the temperature of the ice; and k is the thermal conductivity. Substituting equation (6) into this equation, and solving for r gives

$$r = \frac{4k\Delta T e^{\frac{z}{h}}}{F_o(1 - \varpi)} \quad (8)$$

where ΔT is the temperature increase required to raise the local ice temperature to melting.

During the summer, the temperature of the ice surface warms to near melting temperatures, and ΔT is $\sim 1^\circ\text{C}$; deeper in the ice cover the temperature remains approximately constant throughout the entire year, and ΔT is $10 - 20^\circ\text{C}$. At the bottom

of the ice cover near the ice/water interface, ΔT is also of order 1°C because the water keeps the ice temperature near melting. McKay and Clow calculated the minimum particle size that will cause melting of the surrounding ice under optimum conditions in summer. In their calculations, $h = 1.5 \text{ m}$, $F_o = 600 \text{ W m}^{-2}$, $\varpi = 0.2$, and $k = 2.1 \text{ W K}^{-1}\text{m}^{-1}$. Their results show that at the ice surface, a particle must have a radius of $\sim 2 \text{ cm}$ to cause melting; at 2 m below the surface, the particle radius must be between 60 and 130 cm ; and at the bottom of the cover near the ice/water interface, the particle radius must be between 25 and 50 cm .

Although pebble-sized rocks may be able to melt into the upper surface of the ice cover, only large boulders would be able to melt through the coldest part of the ice cover, $\sim 2 \text{ m}$ below the surface. McKay and Clow's work shows that sand-sized particles will not heat up the ice enough to melt through, even if the ice is within 1°C of melting, and all other variables are optimal.

Percolation Through Vertical Channels or Cracks

During the summer months at Lake Hoare, the ice surface becomes extremely irregular, and sometimes may even melt to form local pockets of ponded water. A cross-section of the ice cover (fig. 44) reveals that, above the sand layer (which is $\sim 1 - 2 \text{ m}$ below the surface), the ice is very porous and frothy, while below the sand layer it is compact and dense. Clumps of sediment and water have been found coexisting in the upper section of the ice cover. It is suggested here that sediment may work its way down to the sand lens in water-filled air channels during the warmest months. The sand lens would continue to collect sediment slowly until a period of climatic warming when the ice becomes thin enough for the sediment layer to fall out of the bottom, or perhaps the ice cover would completely melt, and all the sediment within the ice cover would be released into the lake. There is evidence that the ice thickness undergoes fluctuations. During the 1985/86 field season, the ice cover was thinner by 1 to 2 m than in previous seasons.

Near-vertical cracks in the ice cover were observed during the 1985/86 field season at Lake Hoare. One crack in particular was investigated because it was close to a dive hole. In this instance, sediment was found below the horizontal sand layer. The sediment-filled crack extended laterally for a few meters and probably farther (the lack of visibility within the ice prevented a more accurate estimation). The crack may penetrate the entire ice cover or perhaps will by the end of the summer season, although there is no direct evidence. The creaking and groaning of the ice cover illustrated that cracks are continually forming during the summer months at Lake Hoare. If it could be shown that grains worked their way down to the ice/water interface, the abundance of cracks would provide an efficient and widespread mechanism for getting sediment through the ice cover. This process is attractive because it does not require a major seasonal or regional climatic change.

Remaining Questions

Although the results from this investigation suggest that sediment in the ice cover of Lake Hoare contribute the most to the lake bottom deposits, the limited distribution of the sample localities leaves many questions unanswered. It would be important to determine the compositional and textural variations of the deposits at other locations around the ice cover and bottom of the lake, and how they relate to the surrounding geology. From this information, one may be able to better understand the role of the wind in controlling distribution of sediment. The age of Lake Hoare is also poorly constrained. A sediment core from within the lake that reached bedrock may reveal cyclic sedimentation from which an age estimate could be made. This estimate would greatly improve evaluation of the sedimentation rate and would further indicate whether the ice cover is a major source for the lake bottom sediment. It is not yet understood whether sediment is deposited on the lake bottom in small, steady quantities or in large batches. Widely separated samples from the entire lake bottom would also lead to a better understanding the variation in sediment distribution, which would in turn be a clue to the sedimentation processes. A more comprehensive investigation of Lake Hoare

would clarify processes of sedimentation in perennially ice-covered lakes in general.

SEDIMENTATION PROCESSES ON MARS

Working from the hypothesis that the layered deposits in the Valles Marineris were deposited in ice-covered lakes that existed early in Martian history, one must consider how sediment would enter the liquid part of the system. There are three ways that sediment could have entered the lake: down through the ice cover, up from lake bottom by volcanic eruptions, and in from the sides of the lakes. These mechanisms will be considered, as well as the subject of global dust storms, which would have influenced the amount of sediment available to be deposited in the lake through the ice cover.

Transport of Sediment Through Ice Cover

Four processes for transporting sediment through the ice cover will be considered: (1) that solar energy warmed individual particles, allowing them to melt through the ice; (2) that sediment worked its way down through water-filled channels; (3) that a layer of sediment deposited on the ice was thick enough to form an unstable system that foundered and dumped the load of sediment into the lake; and (4) that a layer of sediment deposited over the ice created a Rayleigh-Taylor instability forming sediment diapirs that penetrated downward through the ice layer.

Solar Warming

The process of melting individual grains through the ice by absorbing solar radiation was found to be unlikely in the Antarctic lakes, and can be considered still more unlikely for the Martian case where the solar flux is less than on Earth, and the ice thickness greater.

Vertical Melt-Channels in Ice

It was suggested above that particles migrate through the ice cover in Antarctic Lake Hoare by the process of individual grains working their way downward through water-filled channels created by air bubbles that form during the summer season when air temperatures rise above freezing. The grains would migrate 1-2 m down to a sand layer, where they may remain until a climatic warming allows the ice to become thin enough that the sand layer drops out, or perhaps the ice cover is completely removed and the entire load of sand in the ice cover is dumped into the lake.

In order for this process to have worked on Mars, at least two conditions must have been met. First, surface temperatures and ablation rates must have been high enough to thin the ice to a thickness of only a few meters. Second, liquid water must have been stable at the surface for periods during the summer, in order to permit short-lived vertical melt channels to form. Neither condition is likely to have been met. There is no evidence that the Martian climate at the time of layered deposit formation was substantially warmer than it is at the present. The primary geologic evidence for a former warmer climate on Mars comes from the valley systems (e.g. Pieri, 1980). These appear to require atmospheric temperatures and pressures high enough to allow liquid water to be stable, or nearly so, at the Martian surface. However, valley systems are found only in ancient cratered terrain, and date from the earliest recorded epoch of Martian history. No valley systems postdate the formation of the Valles Marineris. Outflow channels, which formed during roughly the same epoch as the layered deposits, could form under the current climatic conditions (Carr, 1979, 1983). Any explanation of sedimentation in the Valles Marineris must therefore be applicable to a climate not grossly dissimilar from the present one.

McKay and others (1985) calculated the thickness of ice on Martian lakes under the current climate. In their model, steady-state ice thickness was controlled by ablation at the upper surface of the ice layer, balanced by freezing at the lower surface. Release of latent heat at the lower surface was shown to be an important term in the overall energy budget of the ice. The model required slow inflow of water to replace that lost to

the ice cover by freezing, a condition that is plausible given the widespread evidence for an extensive aquifer system on Mars. It accurately predicted ice thicknesses for the Dry Valley Lakes. Ablation rates on Mars are unknown, but for the plausible but high value of 10 cm/yr, they found an equilibrium ice thickness of 65 m. A fairly low ablation rate of 1 cm/yr would yield an ice thickness of 650 m. Ice thicknesses of a few meters would require ablation rates of over 2 m/yr, which would seem very difficult to achieve. It is unlikely, then, that the ice cover was thin enough, other than for very brief periods, for sediment to percolate downward.

Moreover, even though surface temperatures in the Valles Marineris may briefly exceed 273 K at midday, liquid water cannot exist in equilibrium with the atmosphere. In order for liquid water at a given temperature to be stable, the partial pressure of atmospheric H₂O must exceed the saturation vapor pressure above the liquid at that temperature. The present annual mean H₂O vapor content of the Martian atmosphere is only about 12 precipitable microns, yielding a frost point of about 200 K. Above this temperature, neither liquid water nor ice is stable at the surface. Even short term stability of liquid water at the surface would require a substantial increase in atmospheric H₂O content. Because a major perturbation to the present Martian climate would be required both to thin the ice to a few meters and to allow transient vertical melt channels to form, this mechanism does not appear to be a viable means of getting sediment into former lakes in the Valles Marineris.

Foundering

Another method for sediment to penetrate the ice cover is by foundering. If enough debris is loaded onto the ice surface, the overall density of the ice-sediment layer will become greater than that of the liquid below, causing the ice layer to founder and dump the sediment into the liquid water. In a steady-state condition, the thickness of the ice cover is balanced by the removal of ice by ablation off the upper surface, and growth of the slab at the bottom (McKay and others, 1985). When the surface is covered with a thick layer of sediment, the ice layer will continually thicken because ice can no

longer readily ablate off the top. One must then calculate, for a given ice thickness, how rapidly sediment must be piled onto the ice surface in order to create a condition for foundering.

The first step of this problem is to calculate the maximum thickness (z_i) that the ice must be to create an unstable situation, given a value for the sediment thickness (z_s). The two values used for the thickness of the sediment were $z_s = 150$ m and $z_s = 75$ m. These values are the average thicknesses of the light/dark layer couplet and light layer of the layered deposits in Candor Chasma. The geometry of the problem is given in figure 51. The sediment/ice slab will be in bouyant equilibrium with the water under the following conditions

$$\rho_i z_i + \rho_s z_s = \rho_w (z_i + z_s) \quad (9)$$

where $\rho_i = 0.92$ gm/cm³, $\rho_s = 2.50$ gm/cm³, and $\rho_w = 1.0$ gm/cm³. Solving equation (9) shows that a sediment layer (z_s) 150 m thick will be in equilibrium with an ice slab (z_i) 2.8 km thick. A sediment layer 75 m thick is in equilibrium with a 1.4-km-thick ice layer.

The problem is treated by performing an analytic solution of the one dimensional heat conduction equation. The boundary conditions are such that the upper surface of the ice is held at a fixed temperature ($T_o < 273$ K), and the ice layer is initially at $T = T_o$ throughout. The lower surface migrates downward as freezing takes place. Latent heat effects are included. Following Neumann's solution of this problem (Carslaw and Jaeger, 1959), it is found that:

$$z_i = 2\lambda(Kt)^{\frac{1}{2}} \quad (10)$$

where

$$\lambda e^{\lambda^2} \text{erf} \lambda = \frac{c(273 - T_o)}{L\pi^{1/2}} \quad (11)$$

In these expressions, t is time, K is the thermal diffusivity of ice ($\sim 10^{-2}$ cm²/sec), c is the specific heat of ice (3×10^7 erg/g/K), L is the latent heat of fusion (3.3×10^9 erg/g), and λ is a constant whose value is given by equation (11).

Equation (10) was solved for two temperatures; $T_o = 240$ K and 210 K (which is

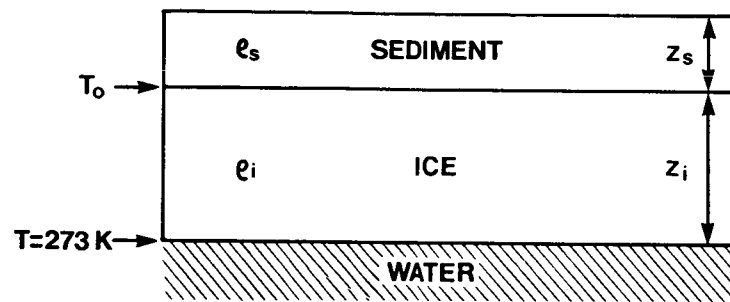


Figure 51: Geometry of the ice cover for the foundering calculation.

reflected in the the value of λ). When the ice slab is at 240 K, it will take 3.8×10^5 yr for the ice cover to grow to 2.8 km thick. In order to create an unstable situation, 150 m of sediment must also accumulate on the surface during the same period of time, which gives a sedimentation rate of 0.39 mm/yr. When the ice slab is 210 K, it will grow to 2.8 km thick in 2×10^5 yr, which gives a sedimentation rate of 0.77 mm/yr.

This series of calculations was also performed for a sediment layer 75 m thick. In this case, when the ice slab is at 240 K, it will take 9.6×10^4 yr for the ice to grow 1.4 km thick. A sedimentation rate of 0.78 mm/yr is required to deposit a 75 m thick sediment layer during the same period of time. When the ice temperature is 210 K, it will take 4.9×10^4 yr to grow to a thickness of 1.4 km. The corresponding sedimentation rate is 1.5 mm/yr.

If a bulk density value of 1.5 gm/cm^3 for the sediment is used instead of the higher 2.5 gm/cm^3 value in equation (9), the relative ice thickness required to produce an unstable geometry is reduced. As a result, the sedimentation rate for each of the calculations increases by a factor of ten. Because the density of the layered deposit material is not well constrained, these values provide upper and lower limits to the sedimentation rates.

The rhythmic nature of the layered deposits suggests that if this mechanism were in operation it must have been repeated a number of times. Although the sedimentation rates derived from these calculations are geologically feasible, the major obstacle to the foundering mechanism would have been to somehow trap a thick pile of sediment on the ice surface.

Rayleigh-Taylor Instability

Even if foundering cannot take place, it is likely that a thick layer of sediment overlying the ice layer would rapidly find its way through the ice. Assuming that there was a mechanism to continually accumulate sediment on top of an ice cover, a situation would have arisen such that relatively dense sediment was superposed on less dense ice,

thus creating favorable conditions for diapiric upwelling of the ice, and in turn, sinking of sediment around the domes of ice. This gravitational instability of a heavy fluid overlying a lighter fluid is called a Rayleigh-Taylor instability.

The assumption is made that the problem can be adequately represented by treating both the soil layer and the ice layer as incompressible viscous fluid. For an incompressible viscous fluid in which pressure p and density ρ vary in the vertical coordinate only, the equation of motion is given by:

$$D \left\{ \left[\rho - \frac{\mu}{n}(D^2 - k^2) \right] Dw - \frac{1}{n}(D\mu)(D^2 + k^2)w \right\} = k^2 \left\{ -\frac{g}{n^2}(D\rho)w + \left[\rho - \frac{\mu}{n}(D^2 - k^2) \right] w - \frac{2}{n}(D\mu)Dw \right\} \quad (12)$$

where g is the acceleration due to gravity, μ is dynamic viscosity, D represents d/dz , D^2 represents d^2/dz^2 , and w describes the boundary conditions which vanish when the thickness $z \rightarrow \pm\infty$ at the bounding surfaces, and it is assumed that the fluid is confined between two rigid plates (Chandrasekhar, 1961). The constants n and k have values such that the solution of (12) is of the form $\exp(ik_x x + ik_y y + nt)$. Motions will therefore be periodic in x with a length scale $1/k$, and will grow exponentially with characteristic time $1/n$.

The geometry of the problem is shown schematically in figure 52. In order to simplify the problem, it was assumed that both layers have a kinematic viscosity equal to that of the coldest part of the ice layer. This is a conservative assumption, and simply means that the problem is considered to be dominated by the highest viscosity material present. The coldest temperatures lie at the top of the ice layer. The boundary condition used is that w and Dw vanish at the upper surface of the sediment and the lower surface of the ice. Modes larger than the thickness of the sediment layer are therefore not considered.

The solution of equation (12) is:

$$- \left[\frac{gk}{n^2}(\alpha_1 - \alpha_2) + 1 \right] (q - k) - \frac{4k^2\nu}{n}(\alpha_1 - \alpha_2)^2(q - k) + \frac{4k^3\nu^2}{n^2}(\alpha_1 - \alpha_2)^2(q - k)^2 - 4k\alpha_1\alpha_2 = 0 \quad (13)$$

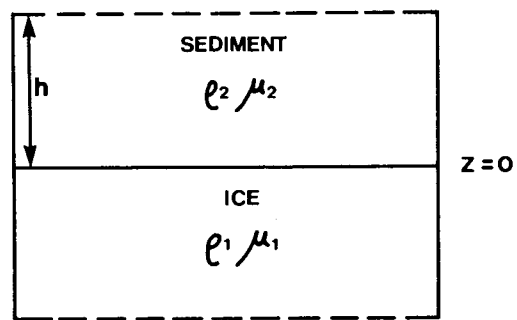


Figure 52: Geometry of the Rayleigh-Taylor instability calculation.

where:

$$\begin{aligned}\alpha_1 &= \frac{\rho_1}{\rho_1 + \rho_2} \\ \alpha_2 &= \frac{\rho_2}{\rho_1 + \rho_2}\end{aligned}\quad (14)$$

$$q = k\sqrt{\left(1 + \frac{n}{k^2\nu}\right)} \quad (15)$$

and kinematic viscosity $\nu = \mu_1/\rho_1 = \mu_2/\rho_2$. Letting

$$c = \frac{n}{k^2\nu} \quad (16)$$

so that

$$q = k\sqrt{(1 + c)} \quad (17)$$

and further substituting

$$y = \frac{q}{k} = \sqrt{1 + c} \quad (18)$$

so that

$$c = y^2 - 1 \quad (19)$$

and defining Q as

$$Q = \frac{g}{k^3\nu^2}. \quad (20)$$

If k and n are measured in the "units" $(g/\nu^2)^{1/3}\text{cm}^{-1}$ and $(g^2/\nu)^{1/3}\text{sec}^{-1}$ respectively, then equations (17) through (20) become:

$$k = Q^{-\frac{1}{3}} \quad (21)$$

and

$$n = (y^2 - 1)Q^{-\frac{2}{3}}. \quad (22)$$

Rewriting (13) with these substitutions:

$$Q = \frac{y - 1}{\alpha_2 - \alpha_1} \left[y^3 + (1 + 4\alpha_1\alpha_2)y^2 + (3 - 8\alpha_1\alpha_2)y - (1 - 4\alpha_1\alpha_2) \right] \quad (23)$$

Equation (23) has only one root when the upper fluid is more dense (i.e., when $\alpha_2 > \alpha_1$). In this case, the root is real, $y > 1$, and n is real and positive (from equation

(22)). The amplitude of the instability will therefore grow exponentially with a characteristic time $1/n$. The asymptotic behavior of n is such that $n \rightarrow 0$ both when $k \rightarrow 0$ and $k \rightarrow \infty$. There exists a value of k for which n is maximized; this is the most unstable mode. The length scale $(1/k)$ is measured by:

$$L = k^{-1}(\nu^2/g)^{\frac{1}{3}} \quad (24)$$

For sediment overlying ice on Mars, the values for $\rho_1 = 0.92 \text{ gm/cm}^3$, $\rho_2 \simeq 2.5 \text{ gm/cm}^3$, $\alpha_1 = 0.27$, $\alpha_2 = 0.73$, and $g \simeq 370 \text{ cm/sec}^2$. The effective viscosity of the ice is given approximately by (Weerman, 1970):

$$\mu = 10^{14} \exp \left[26 \left(\frac{273}{T} - 1 \right) \right] \quad (25)$$

where T is temperature in Kelvins. Taking $T = 240 \text{ K}$, $\nu = 3.9 \times 10^{15} \text{ poise-cm}^3\text{gm}^{-1}$ from equation (25). From equation (24), it is apparent that the most unstable mode operates on a scale that is much larger than the sizes of the lakes. Assuming that the largest mode that can grow is equal in size to the thickness of the sediment layer.

$$k = h^{-1}(\nu^2/g)^{\frac{1}{3}} \quad (26)$$

where h is the thickness of the sediment layer. Solving for $n(k)$ where k is the mode determined from equation (26), and n is calculated from equation (22), the growth time τ is:

$$\tau = n^{-1}(g^2/\nu)^{-\frac{1}{3}} \quad (27)$$

This problem was solved using two different thicknesses for the sediment layer: $h = 1.5 \times 10^4 \text{ cm}$, and $h = 7.5 \times 10^3 \text{ cm}$. These values were chosen because they are the average thicknesses of a light/dark couplet and light layer, respectively, in Candor Chasma of the Valles Marineris. A range of temperatures from 270 to 210 K was used to determine the viscosity of the ice from equation (25).

The growth time τ was calculated for the various temperatures and values of h . The results are presented in figure 53. This model predicts that an instability will develop in tens of years when the ice temperature is near freezing and the sediment layer is 75 m

or 150 m thick. With less favorable conditions, when the ice is at 210 K and the thickness of the sediment layer is 75 m, the instability will grow on the order of 1.4×10^4 yrs. These results indicate that migration of sediment through an ice cover by diapiric instabilities may be possible in very short geologic time periods. The limiting factors are not the thickness nor temperature of the ice, but rather the necessity to accumulate substantial amounts of sediment on the ice surface. If a thin veneer of sediment remained on the ice surface at any one time, the thickness of the sediment would not be great enough to form an instability with respect to the ice. If a sediment layer thick enough to form one of the sediment layers in the canyons formed on top of the ice, it would penetrate it rapidly.

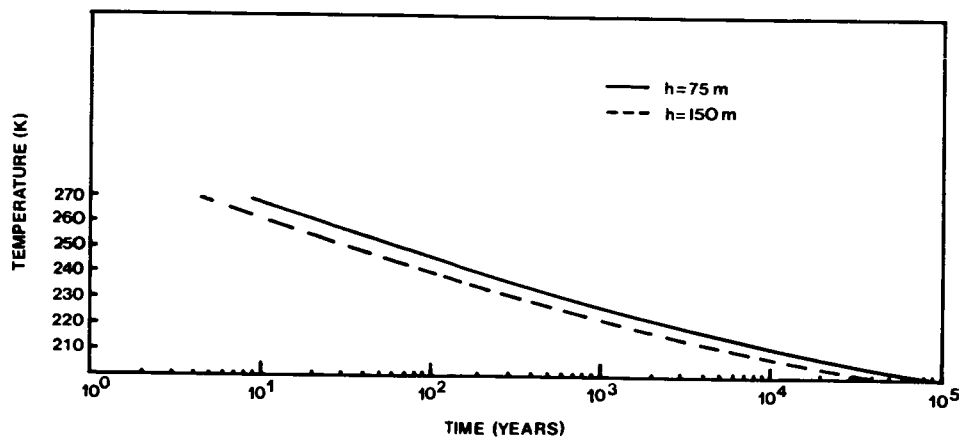


Figure 53: Growth times for Rayleigh-Taylor instabilities where the thickness of the overlying sediment is 75 m and 150 m.

Eolian Deposition onto the Ice Surface

Rayleigh-Taylor instability, and perhaps foundering, may be viable means of allowing a sediment layer that had accumulated on top of an ice cover to be transported to the bottom of a lake. However, in order to produce the thick layered deposits, such accumulation must have taken place repeatedly. The most simple mechanism would be

to build up a layer of sediment on the ice surface until an instability develops and the sediment is transported to the lake bottom. Dust in the atmosphere is the logical source for the sediment. Global dust storms occur annually on Mars when the planet is close to perihelion (Carr, 1981). The intensities of the storms are modulated by variations in atmospheric pressure that occur in response to oscillations in Mars' orbital elements.

The variations in the orbital motions and axial orientation on Mars are caused by gravitational interactions with the other planets and the sun (Ward, 1973; 1974). Precession of the equinoxes occurs on a 5.1×10^4 yr cycle, and it influences which pole points toward the sun at perihelion. The eccentricity of Mars' orbit modulates the amplitude of the hemispheric differences in climate caused by precession. The orbital eccentricity variations occur with two different periodicities. The cycle with larger eccentricities (between 0.14 and 0.01) oscillates with a period of 2×10^6 yr. The superimposed cycle with smaller eccentricities (< 0.06) oscillates with a 9.5×10^4 yr period. During period of low eccentricities, the hemispheric differences in climate are minimized. The obliquity cycle (variations in the angle between the planes of the equator and orbit) has the greatest effect on the Martian climate. The obliquity varies between 15° and 35° , and oscillates with a period of 1.2×10^5 yr modulated by a period of 1.2×10^6 yr. At maximum obliquity, there is much greater insolation at the poles than during low obliquity (Ward, 1974). These variations in the degree of polar insolation are believed to affect the atmospheric CO_2 pressure, and hence the ability to initiate dust storms (Toon and others, 1980; Ward, 1974). The lowest atmospheric pressures may be below the threshold to initiate global dust storms. High atmospheric pressures may cause global dust storms that last for many months, or perhaps years.

The formation of the polar layered deposits may have been controlled by these fluctuations (Murray and others, 1972). The basins of the Valles Marineris may also have received sediment in cycles. Although the eccentricity and obliquity variations of Mars produce climatic changes in an intricate manner whose results are not fully understood, it seems possible that their influence on the magnitude and duration of global dust storms may be reflected in the layered chasma deposits. In the polar regions, it is generally

believed that individual layers correspond to individual periods of deposition from the atmosphere, separated by periods of non-deposition. Because deposition in lakes would be modulated by transport through the ice cover, however, there would not necessarily be a one-to-one correspondence between a period of deposition at the ice surface and an eventual layer on the lake bottom. Recall that the polar layers are substantially thinner than the layers in the Valles Marineris. If this mechanism is viable, it may require a number of periods of deposition to accumulate a sediment layer thick enough to produce an instability and overturn the ice cover.

Pollack and others (1979) estimated the present rate of dust deposition at the polar regions based on the amount of dust in the atmosphere during the 1977 storm. They calculated that there was 4×10^{-3} g/cm² of dust in the atmosphere. If storms occur every other Earth year, and the bulk density of the sediment is 1.5 g/cm³, the annual global redistribution rate would be 1.3×10^{-3} cm of sediment. If there were some way to trap dust on the ice covers of the equatorial lakes, it would take 5.8×10^6 yr to accumulate a 75 m thick layer, which is the thinnest layer detected in the layered chasma deposits. Ten of these layers would take about 60 million years to accumulate. If the highest plateau, which is 6 km, represents the total thickness, it would take roughly 450 million years to form the layered deposits with this sedimentation rate.

Although periodic global dust storms might be a logical source of sediment for the layered chasma deposits, there are major problems with this mechanism. The current Martian climate apparently produces net deposition at the poles. If somehow this process were reversed in the past and there was net deposition at the equator, sediment would have also accumulated on the plateaus surrounding the Valles Marineris. Presently, there is no eolian debris built up on the surrounding uplands. There may be a way to get around these difficulties if there were repeated periods of deposition and erosion near the equator. Sediment built up on the plateaus surrounding the canyons would be swept away during the erosional episodes, while the debris on the lake ice would have been "trapped" by Rayleigh-Taylor instabilities, and thus preserved. This procedure may be theoretically feasible, but a comprehensive model of the deposition/erosion mechanism

is still lacking.

Subaqueous Volcanism

Volcanic debris makes an important contribution to the sediment in rift-valley lakes such as Lake Baikal, and the lakes within the East African Rift (Reading, 1978). The huge volcanic constructs on the Tharsis Bulge, and possible evidence of ash-flow volcanism in Amazonis Planitia suggest that volcanism within the Valles Marineris should not be ruled out, even though no obvious volcanic vents have been detected.

Subaqueous explosive volcanic eruptions are believed to be limited by water depth (Fiske, 1963; Moore and Shilling, 1973; Allen, 1980; Sigurdsson, 1982). The eruption of magma with a finite amount of gas is dependent on the exsolution and expansion of the gas as pressure decreases (Wilson and Head, 1983). Both basaltic and rhyolitic magma dissolve more H_2O with depth, and the efficiency of vesiculation decreases also with depth (Sigurdsson, 1982). Allen (1980) calculated that subglacial basaltic eruptions should change from effusive to explosive activity, due to magma vesiculation, at ice depths between 100 and 200 m. Based on empirical evidence, Sigurdsson (1982) reported that basaltic phreatomagmatic explosions are restricted to water depths less than 300 m. Silicic explosive eruptions may occur in water depths of 500 m (Moore and Schilling, 1973). At shallower water depths, floating pumice, ejecta, and steam that rises considerably higher than the water surface may be produced (Moore and Schilling, 1973). Because the gravity of Mars is less than half that of the Earth, the corresponding water depths for the explosive eruption are about 1300 m for silicic magma and 250 to 500 m for basaltic magma. This value limits the water depth of the putative lakes on Mars if the dominant source of sediment is from pyroclastic sources.

If volcanism were subaqueous rather than subaerial, many of the morphologic arguments against the volcanic hypothesis are weakened or eliminated. Volcanic constructs may have been destroyed by slumping of material off cones as they began to form. Fiske (1963) reported that most of the Ohanapecosh volcaniclastic flows in the eastern part

of Mount Rainier National Park, Washington, probably were caused by large volumes of debris that suddenly slumped into deeper water from the flanks of underwater volcanoes. The flows may have been contemporaneous with large eruptions, or debris from small subaqueous eruptions may have accumulated on slopes, until larger eruptions or earthquake shocks disrupted the deposits, causing them to be redistributed in the deeper water. Floating pumice that eventually becomes water-logged and sinks to the lake floor may also mask volcanic vents or fissures. Eruptions in water would also help to more evenly distribute the effusive material.

Although there is no direct evidence for it, the process of subaqueous volcanism within Valles Marineris lakes is an attractive hypothesis for a number of reasons: it provides additional material to an ice-covered lake system without needing to penetrate or remove the ice cover; the process of sedimentation would still be controlled by a low-energy liquid water environment; the absence of unequivocal volcanic vents can be more easily envisioned, because a subaqueous environment can more efficiently distribute material than a subaerial one; and material from volcanic eruptions is more consistent with the lack of deposition on the surrounding uplands.

Transport of Sediment from Canyon Walls

An obvious source of sediment for the layered chasma deposits could have been the nearby canyon walls. The formerly shallow, narrow tectonic grabens are believed to have been enlarged by removal of interstitial ground ice and subsequent collapse of the canyon walls. Debris from the canyon walls would have been deposited in the interior of the canyons. In a dry environment, the sediment would have formed alluvial fans in close proximity to the canyon walls. With a limited source of water, canyon wall material would have been transported farther into the interior of the canyons by a network of streams. If there was an abundant source of water, such as the confined aquifers that Carr (1979) proposed, lakes may have formed. Sediment could have been transported from the canyon walls into the basins by gravity flows. It seems almost unavoidable that much of the material removed from the canyon walls would have wound up on the deep

parts of the canyon floors, and that it would have been deposited in horizontal layers if significant water were present.

A closer look at this source of sediment for the layered chasma deposits reveals a difficulty, however. The geometry and volume of the layered deposit plateaus are inconsistent with the volume of material that could have originated from the canyon walls. Presently, the top of the major plateaus in Hebes, Ophir, and Candor chasmata are within hundreds of meters of the elevations of the surrounding uplands, and in addition there commonly is a "moat" surrounding the plateaus (fig. 54A). If one could make the ice within a 5 km high and 5 km wide section of canyon wall material instantly melt, the sediment would sink to the bottom and only partially fill the basin (fig. 54B, C). In this scenario there would seem to be no way to extract enough sediment from the canyon walls to fill up the basin to within a few hundred meters of the top. An additional problem would be to form a moat after the water was removed, and the major destruction of the canyon walls was over. Consequently, if the source of material for the layered deposits was the canyon walls, there must have been a mechanism for the present geometry of the plateaus to form as the canyons were enlarging.

If there were some way to preserve cores of canyon wall material within the plateaus of layered deposits, a geometry similar to the present one could have been produced. Figure 55 schematically illustrates the process that may have occurred. In this diagram, the process is illustrated for simplicity as having taken place in a few discrete steps, although in reality it probably would have been more continuous. In the first step, a shallow tectonic depression is filled with water and a small amount of sediment. In each successive step, a volume of material composed partly of soil and partly of water is mobilized. This material is derived from the area adjacent to the existing depression. The solid component sinks to the lowest level present, and the process repeats. The resulting deposit would be mound-shaped, very near the elevation of the surrounding uplands, and separated from the canyon walls by a "moat." The movement of groundwater presumably was the cause for collapse of the canyon wall. Perhaps when the central mound of canyon wall material became isolated from the surrounding

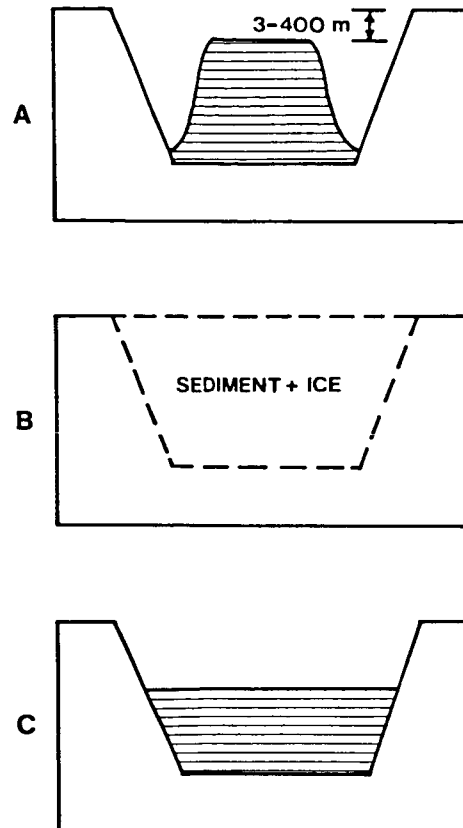


Figure 54: A. Cross-section of the present relationship between the canyon wall and the plateau of layered deposits. B. Material that was the precursor of the canyons consisted of sediment and ice. C. Ice within the dashed area of (B) melted, the sediment sunk to the bottom of the canyon, and the water removed. The process from (B) to (C) does not produce (A).

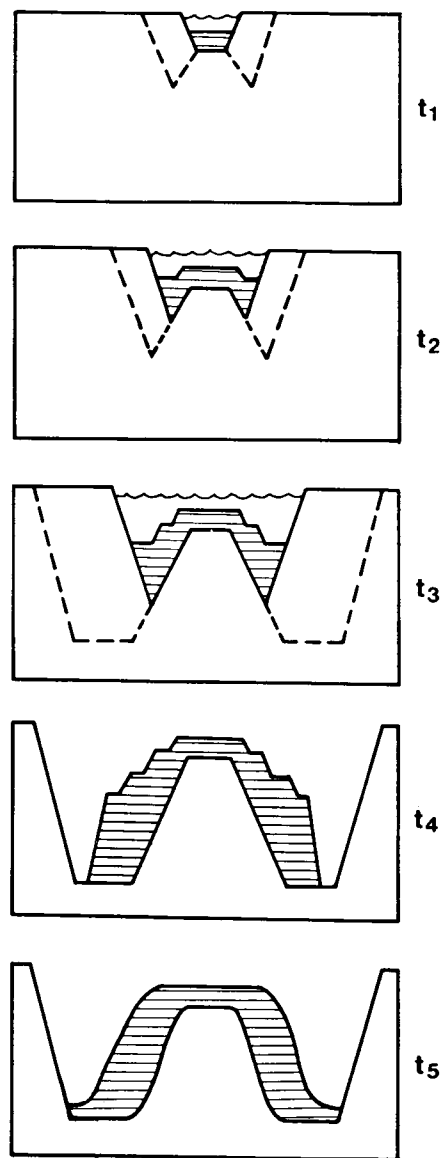


Figure 55: Formation of the layered deposits: t_1 : a depression is made by melting the sediment/ice mixture; the sediment sank to the bottom, and the water rises to the top; t_2 : more material is melted to a greater depth; t_3 : the sediment from the previous melt is deposited in a larger lake, and the process is again repeated; t_4 : in the final step most of the material was removed to form the “moat”; t_5 : the entire process done smoothly instead of step-wise results in a geometry similar to Figure 54A.

uplands after formation of the initial depression, the groundwater system ceased to be replenished in that area. If isolation of the plateau from the canyon wall could somehow have prevented further collapse of the plateau, the core of canyon wall material could have remained essentially intact, while the surrounding material continued to collapse in the presence of groundwater movement. It seems that, without a mechanism for preserving some of the initial volume while forming the canyons, additional sources of material would have been required. Although there are problems with forming the layered chasma deposits entirely by material from the canyon walls, it seems almost unavoidable that sediment derived from the canyon walls has been incorporated into the layered deposits.

DISCUSSION AND SUMMARY

Formation of the Layered Deposits in the Valles Marineris

Four possible origins have been examined for formation of the layered deposits: eolian deposition, erosional isolation of plateaus of canyon wall material, subaerial explosive volcanism within the canyons, and deposition of sediment in standing bodies of water. The first three processes appear inconsistent with geologic evidence in the Viking orbiter images. If the layered deposits were formed by simple deposition of wind-transported sediment, one would expect to see evidence of layered deposits on the surrounding highlands. The uplands are free of any similar deposits. The great differences in weathering styles between the layered deposits and the canyon walls rules out the possibility that the layered deposits are remnants of the canyon walls. In addition, there are locations within the canyons where layered deposits are in contact with the canyon wall, and there is a well-defined difference between their morphologies. A volcanic origin for the layered deposits is not as easily eliminated. Ash fall is argued against by the same reasoning as the eolian hypothesis, and it would be difficult to produce such rhythmic layering with an ash-flow origin. A recurring problem with all forms of volcanism is the lack of evidence for any vents or calderas. The process of subaqueous volcanism has the flexibility that water would play an important role in redistribution of sediment so that the absence of preserved vents would not be as critical an issue.

The lacustrine hypothesis appears to be the most viable mechanism for forming the layered chasma deposits. It has been suggested that water played an important role in Mars' history by other workers. Squyres and others (1986) have found evidence of substantial subsurface flow in an area northeast of Hellas basin. Confined aquifers have been suggested to be the source of water for outflow channels (Carr, 1979). Groundwater probably would have been the source for ancient lakes in the Valles Marineris. As the initial tectonic depressions were enlarged by canyon wall collapse, water derived from

the surrounding area could have filled up the forming basins. A possible source for water may have been seepage from deep aquifers along major faults. Since Mars apparently does not have a hydrologic cycle like Earth's, there would have been no process to replenish the supply of water in the aquifers once it was released onto the surface, and subsequently lost to the atmosphere. In areas such as Hebes Chamsa where the basin is completely enclosed, the lakes would have gradually diminished by sublimation. In other chasmata, such as Ophir and Candor, there is evidence that lakes may have drained rapidly. The lake in Ophir Chasma may have breached the dam separating it from Candor Chasma, causing a catastrophic flood to flow eastward through the canyon system. If the layered deposits once filled the canyons, considerable erosion may have occurred to form the present-day remnants. Alternatively, if the present geometry of the plateaus reflects the original size of the lakes, comparatively minor changes in the Valles Marineris occurred after the lakes were removed. Landsliding of the canyon walls, eolian erosion, small movements on ancient faults, and perhaps localized volcanic eruptions did not significantly alter the geometry of the canyons and the layered deposits. It seems that the particular set of circumstances that formed the layered chasma deposits and the Valles Marineris are unique to that particular location and time period on Mars.

There are only three ways in which material could enter lakes in the canyons: down through the ice cover, in from the canyon walls, or up from the lake floor. Each mechanism has a large degree of uncertainty, and none can be unequivocally considered the best hypothesis for formation of the layered deposits.

Although the mechanisms to transport dust through the ice by foundering or Rayleigh-Taylor instabilities seem physically feasible, it is doubtful whether the geologic circumstances to support these processes would have occurred. It would be most unlikely that 75 m to 150 m of dust from the atmosphere would settle on the ice surface only, and not on the surrounding plateau, but there is no trace of once thick eolian deposits on the highlands surrounding the Valles Marineris. If there was continuous deposition of dust from the atmosphere on the lake ice causing successive instabilities, an enormous amount of debris must have been removed from the surrounding uplands. Alternatively,

periodic deposition over the entire region, followed by erosion would clear the plateaus of debris, but would necessitate an efficient means of "trapping" dust on the ice surface that would lead to an instability. If this process could have happened for one foundering or Rayleigh-Taylor instability event, it must have repeated in the same manner over and over again, in order to build up the successive layers that are now recorded in the layered deposits.

Depositing sediment from the canyon walls presents some geometric complications. Once water was removed from the collapsing canyon wall material, the volume of the remaining sediment would only partially fill the depressions that were forming. Yet, presently the plateaus of layered deposits rise to within a few hundred meters of the top of the canyon walls. The lack of canyon wall-derived sediment would be compensated for if the plateaus of layered deposits had cores of undisturbed canyon wall material, or if volcanic material derived from beneath the base of the canyons were added. Both of these solutions are speculative.

The source of debris could be entirely volcanic. Because there are no obvious volcanic vents within the canyon system, there is no direct evidence to support this hypothesis. Because subaqueous volcanism can produce a variety of sedimentary features, it is possible that vents could have been obscured. Nevertheless, the absence of any compelling volcanic evidence makes this hypothesis also speculative.

Discussions of sedimentation processes in ice-covered lakes on Mars are by nature compartmentalized into distinct mechanisms and do not truly reflect the manner in which geologic processes happen. In reality, the formation of the layered chasma deposits may have involved aspects of all of these hypotheses, which in turn created interactions that we are unaware of at this time, and with these data.

Analogy to the Antarctic Dry Valley Lakes

Investigation of Antarctic lakes provided an opportunity to closely examine sedimentation processes in ice-covered lakes on Earth. At the outset of this study, it was

hoped that an understanding of a terrestrial system would point to processes that may have occurred on Mars. Although specific questions were answered, the results have only a limited application to sedimentation processes in possible Martian lakes.

The Antarctic Dry Valley lakes differ from lakes that may have existed on Mars in a number of ways. Most notably, the Dry Valley lakes are smaller and shallower than the canyons of the Valles Marineris by a factor of a few hundred, they have been in existence for a fraction of the time that any Martian lakes might have existed, the basins they occupy were formed by glaciers rather than enlargement by collapse of the surrounding terrain, and the thicknesses of their ice covers probably are some 10 to 100 times thinner than ice covers on Mars would have been.

Comparison of sediment from various subenvironments in and around Lake Hoare indicated that the sediment at the lake bottom came from the ice cover. Although details how grains are transported through the ice are not yet fully understood, from theoretical studies done in this investigation, it seems that the ways in which sediment may migrate through the ice cover in Martian lakes are quite different from the mechanisms that may occur in ice-covered lakes on Earth.

Recommendations for Future Work

Future work on the layered deposits in the Valles Marineris can be divided into two types of data retrieval: remote sensing and direct sampling. An enormous amount of investigation could be done in both areas.

In the area of remote sensing, many questions could be answered by use of higher resolution images and more precise topographic data. A more detailed stratigraphy, as well as knowledge of the orientation of individual layers, could answer many questions about their formation. Was there any contemporaneous tectonic activity while the layers were being deposited? Is there evidence of folding or faulting? Do layers pinch out or vary in thickness from the centers of the plateaus to the margins? Is there a consistent orientation to the layers that would indicate a canyon-wide depositional pattern? What

are the thicknesses of individual layers in the canyons where the present resolution is too low to allow measurement? Answers to questions such as these would greatly enhance not only the general description of the layered deposits, but would also more tightly constrain the mechanisms of their origin.

The next planned mission to Mars by a U.S. spacecraft will be the Mars Observer. This spacecraft has the potential to send back to Earth vital information on the geology and geochemistry of the layered deposits in the Valles Marineris that will greatly enhance our understanding of their origin. Four instruments that are scheduled to be aboard the spacecraft have particular applications to this study. They are: the imaging camera, the visual and infrared mapping spectrometer, the gamma-ray spectrometer, and the radar altimeter.

The camera will have an imaging resolution of approximately 1 m/pixel, which is 20 times greater than the highest resolution images used in this study. Possible targets for this greatly enhanced imaging would be the layered deposits in Candor chasma, specifically, the areas where detailed studies of the layers were performed in this investigation. The information we have recovered from the Viking images have shown the layer thicknesses to be on the scale of 100 m, but with the present data there is no way to tell if there is layering on a finer scale. If finer layering does exist, its physical characteristics might reveal the processes of formation. One would look for the lateral extent of the layers, whether they are uniform in thickness, thin and thicken, or are wedge-shaped. Do successive layers have similar thicknesses? Are there variations in texture or slope within each layer? Comparison of two or more plateaus of layered deposits would clarify whether there is a canyon-wide depositional pattern. These characteristics were considered while studying the layered deposits from Viking images, but the resolution was not sufficient to accurately answer these questions.

The visual and infrared mapping spectrometer will retrieve information on the mineralogy of the surface, with high spatial and spectral resolution. Because the exposures of layered deposits are hundreds of kilometers in extent, this instrument would allow comparison of the mineralogy of the layered deposits, not only from one plateau to

the next, but also within one plateau. Comparison of the mineralogy of the layered deposits with that of the canyon walls, floors, and surrounding uplands may reveal that one of these subenvironments was a predominant source of material for the layered deposits. Determining the type of clay minerals, the presence or absence of carbonates, sulfates, etc., may clarify the diagenetic history of the layered deposits, and provide evidence as to whether water played an important role in their formation.

The gamma-ray spectrometer will map the elemental composition of the surface of Mars to a depth of tens of centimeters, and will have a spatial resolution of about 300 km. This instrument would provide an effective way of comparing the surface composition from various sub-environments throughout Mars. In this way, possible source areas for the layered deposits could be directly tested. For instance, the elemental composition of the layered deposits could be compared with various volcanic provinces, such as the Tharsis region or the possible pyroclastic material in Amazonis Planitia, and with the dust that is trapped in the polar layered deposits. Each hypothesis could be systematically considered, thereby further constraining the origin of the layered deposits.

The radar altimeter will give surface elevations to an accuracy on the order of 10 m. The regional slope of the canyon floors could be detected using this instrument. The results may be used to investigate the hypothesis that water once flowed from the central canyons to the east. Data from the altimeter would also be useful to map the surface elevations of the plateaus of layered deposits in greater detail. This information, together with the high-resolution images would clarify whether the layered deposits are flat-lying or tilted.

Direct sampling of the layered chasma deposits would immediately answer many of the questions that will be addressed by the Mars Observer. The composition of the deposits would be verified, as well as their relationship to other materials that were sampled. It would be important to test for any evidence of pre-biotic chemistry in the sediment, as well as for primitive life forms such as those that thrive in the Antarctic lakes. Sedimentological data could be gathered on a smaller scale. One would look for even finer layering. If the sediment is consolidated, what is binding it together?

Grain size analyses performed in a manner similar to that for the sediment from Lake Hoare would increase our knowledge of the transport mechanisms. Sediment cores that were taken at the base of the moats would reveal if layered deposits continue to a greater depth than presently is detected. Seismic studies would also help to constrain the overall geometry of the layered deposits.

There seems to be an endless supply of questions at this time about the layered deposits. As geologic investigations go, our understanding of the formation of the layered chasma deposits is in its infancy. Because the Valles Marineris may be a unique location in the solar system (other than Earth) where standing bodies of water may have existed for large time periods, these deposits warrant much more comprehensive data coverage and continued investigation. They should be considered an important possible target site for a future Mars Sample Return mission.

REFERENCES CITED

- Allegre, C.J., Courtillot, V.E., and Matteur, M., 1974, Evidence for lateral movements of the martian crust (abstract): American Geophysical Union (EOS), v. 55, p. 341.
- Allen, C.C., 1980, Icelandic subglacial volcanism: Thermal and physical studies: Journal of Geology, v. 88, p. 107-117.
- Baker, V.R., and Milton, D.J., 1974, Erosion by catastrophic floods on Mars and Earth: Icarus, v. 23, p. 27-41.
- Blasius, K.R., and Cutts, J.A., 1976, Shield volcanism and lithospheric structure beneath the Tharsis plateau, Mars: Proceedings of the Seventh Lunar Science Conference, v.3, p. 3561-3573.
- Bockheim, J.G., 1979, Relative age and origin of salts in eastern Wright Valley, Antarctica: Soil Science, v. 128, p. 142-152.
- Bradley, W.H., 1963, Paleolimnology, in Frey, D.G., ed., Limnology in North America: Madison, University of Wisconsin Press, p. 621-652.
- Bull, C., 1966, Climatological observations in ice-free areas of Southern Victoria Land, Antarctica, in Antarctic Research Series: American Geophysical Union, Washington D.C., v. 9, p. 177-194.
- Carr, M.H., 1974, Tectonism and volcanism of the Tharsis region of Mars: Journal of Geophysical Research, v. 79, p. 3943-3949.
- , 1979, Formation of martian flood features by release of water from confined aquifers: Journal of Geophysical Research, v. 84, p. 2995-3007.
- , 1981, The surface of Mars: New Haven, Yale University Press, 232 p.

- , 1982, Periodic climate changes on Mars: Review of evidence and effects on distribution of volatiles: *Icarus*, v. 50, p. 129-139.
- , 1983, Stability of streams and lakes on Mars: *Icarus*, v. 56, p. 476-495.
- Carr, M.H., Crumpler, L.S., Cutts, J.A., Greeley, R., Guest, J.E., and Masursky, H., 1977, Martian impact craters and emplacement of ejecta by surface flow: *Journal of Geophysical Research*, v. 82, p. 4055-4065.
- Carr, M.H., and Schaber, G.G., 1977, Martian permafrost features: *Journal of Geophysical Research*, v. 82, p. 4039-4054.
- Carslaw, H.S., and Jaeger, J.C., 1959, *Conduction of heat in solids*: London, Oxford University Press, 500 p.
- Cartwright, K., Treves, S.B., and Tetsuya, T., 1974, Geology of DVDP 4, Lake Vanda, Wright Valley, Antarctica: *Dry Valley Drilling Project Bulletin*, n. 4, p. 49-59.
- Cartwright, K., and Harris, H.J.H., 1981, Hydrogeology of the Dry Valley region, Antarctica: *in* Antarctic Research Series: American Geophysical Union, Washington D.C., v. 33, p. 193-214.
- Chandrasekhar, S., 1961, *Hydrodynamics and hydrodynamic stability*: Oxford, Clarendon Press, 652 p.
- Chinn, T.J.H., 1982, Hydrology and climate in the Ross Sea area: *Journal of the Royal Society of New Zealand*, v. 11, n. 4, p. 373-386.
- Christiansen, R.L., 1984, Yellowstone magmatic evolution: Its bearing on understanding large-volume explosive volcanism, *in* *Studies in geophysics and explosive volcanism: Inception, evolution, and hazards*: Washington, D.C., National Academy Press, p. 84-95.
- Courtillot, V.C., Allegre, C.J., and Matteur, M., 1975, On the existence of lateral relative motions on Mars: *Earth and Planetary Science Letters*, v. 25, p. 279-285.

- Decker, E.R., and Bucher, G.J., 1982, Preliminary geothermal studies in the Ross Island-Dry Valley region, in Craddock, C., ed., Antarctic Geoscience: Madison, University of Wisconsin Press, p. 887-894.
- Denton, G.H., Armstrong, R.L., and Stuiver, M., 1970, Late Cenozoic glaciation in Antarctica: The record in the McMurdo Sound region: Antarctic Journal of the U.S.A., v. 5, p. 15-20.
- Dzurisin, D., and Blasius, K.R., 1975, Topography of the polar layered deposits of Mars: Journal of Geophysical Research, v. 82, p. 4225-4248.
- Fisher, R.V., and Schmincke, H.U., 1984, Pyroclastic Rocks: Berlin, Heidelberg, Springer-Verlag, 472 p.
- Fiske, R.S., 1963, Subaqueous pyroclastic flow in Ohanapecosh Formation, Washington: Geological Society of America, Bulletin: v. 74, p. 391-406.
- Folk, R.L., 1980, Petrology of sedimentary rocks: Austin, Texas, Hemphill Publishing Company, 182 p.
- Friedman, G.M., 1961, Distinction between dune, beach, and river sands from their textural characteristics: Journal of Sedimentary Petrology, v.31, n.4, p. 514-529.
- Gibson, E.V., Wentworth, S.J., McKay, D.S., 1983, Chemical weathering and diagenesis of cold desert soil from Wright Valley, Antarctica: An analog of martian weathering processes, Proceedings of the 13th Lunar and Planetary Science Conference, part 2: Journal of Geophysical Research, v. 88, supplement, p. 912-928.
- Gunn, B.M., and Warren, G., 1962, Geology of Victoria Land between the Mawson and Mulock Glaciers, Antarctica: New Zealand Geological Survey Bulletin, n. 71, 157 p.
- Harris, H.J.H., 1981, Hydrology and hydrogeochemistry of the South Fork, Wright Valley, Southern Victoria Land, Antarctica (Ph.D. dissertation): Urbana, University of Illinois, 341 p.

- Hill, P.R., and Nadeau, O.C., 1984, Grain-surface textures of late Wisconsin sands from the Canadian Beaufort shelf: *Journal of Sedimentary Petrology*, v. 54, p. 1349-1357.
- Hoare, R.A., Popplewell, K.B., House, D.A., Henderson, R.A., Prebble, W.M., and Wilson, A.T., 1965, Solar heating of Lake Fryxell, a permanently ice-covered antarctic lake: *Journal of Geophysical Research*, v. 70, p. 1555-1558.
- Jones, L.M., Carver, R.E., McSaveney, E.R., and Tickhill, T., 1971, Sediment analyses of the beaches of Lake Vanda, Wright Valley: *Antarctic Journal of the United States*, v. 6, p. 199-200.
- Kellogg, D. E., Stuiver, M., Kellogg, T.B., and Denton, G.H., 1979, Non-marine diatoms from late Wisconsin perched deltas in Taylor Valley, Antarctic: *Paleogeography, Paleoclimatology, Paleoecology*, v. 30, p. 157-189.
- King, B.C., 1976, The Baikal Rift: *Journal of the Geological Society of London*, v. 132, p. 348-349.
- Krinsley, D.H., and Doornkamp, J.C., 1973, *Atlas of quartz sand surface textures*: London, Cambridge University, 91 p.
- Lucchitta, B.K., 1978, Morphology of Chasma Walls, Mars: *U.S. Geological Survey Journal of Research*, v. 6, p. 651-662.
- , 1979, Landslides in Valles Marineris, Mars: *Journal of Geophysical Research*, v. 84, p. 8097-8113.
- , 1981a, Valles Marineris - faults, volcanic rocks, channels, basin beds: *NASA Technical Memorandum*, no. 84211, p. 419-421.
- , 1981b, More on landslides - Valles Marineris: *NASA Technical Memorandum*, no. 84211, p. 326-328.
- , 1982, Lakes or playas in Valles Marineris: *NASA Technical Memorandum*, no. 85127, p. 233-234.

- , 1986, More on recent (?) dark volcanic patches in the Valles Marineris, Mars: *Lunar and Planetary Science* 17, The Lunar and Planetary Institute, Houston, Texas, p. 496-497.
- Lucchitta, B.K., and Ferguson, H.M., 1983, Chryse basin channels: Low gradients and ponded flows: *Journal of Geophysical Research*, v. 88, p. 553-568.
- Malin, M.C., 1976, Nature and origin of intercrater plains on Mars (Ph. D. dissertation): California Institute of Technology, Pasadena, 176 p.
- Margolis, S.V., and Krinsley, D.H., 1974, Processes of formation and environmental occurrence of microfeatures on detrital quartz grains: *American Journal of Science*, v. 274, p.449-464.
- Mars Channel Working Group, 1983, Channels and valleys on Mars: *Geological Society of America Bulletin*, v. 94, p. 1035-1054.
- Mason, C.C., and Folk, R.L., 1958, Differentiation of beach, dune, and aeolian flat environments by size analysis, Mustang Island, Texas: *Journal of Sedimentary Petrology*, v. 28, n. 2, p. 211-226.
- Masson, P. 1977, Structural pattern analysis of the Noctis Labyrinthus-Valles Marineris regions of Mars: *Icarus*, v. 30, p. 49-62.
- McCauley, J.F., 1978, Geologic map of the Coprates Quadrangle of Mars: U.S. Geological Survey Miscellaneous Investigation Series Map I-897, scale 1:5,000,000.
- McCauley, J.F., Carr, M.H., Cutts, J.A., Hartmann, W. K., Masursky, H., Milton, D.J., Sharp, R.P., and Wilhelms, D.W., 1972, Preliminary Mariner 9 report on the geology of Mars: *Icarus*, v. 17, p. 289-327.
- McKay, C.P., Clow, G.D., Wharton, R.A., and Squyres, S.W., 1985, Thickness of ice on perennially frozen lakes: *Nature*, v. 313, p. 561-562.
- McKee, E.H., 1979, A study of global sand seas: U.S. Geological Survey Professional Paper 1052, 429 p.

- Moore, H.J., and Wu, S.C., 1973, Effect of photogrammetric reading error on slope-frequency distributions: in Apollo 17 Preliminary Science Report, NASA SP-330, p. 26-33.
- Moore, J.G., and Schilling, J.G., 1973, Vesicles, water, and sulfur in Reykjanes Ridge basalts: *Contributions to Mineralogy and Petrology*, v. 41, p. 105-118.
- Morris, E.C., 1980, A pyroclastic origin for the aureole deposits of Olympus Mons (abs.): *Reports of Planetary Geology Program*, NASA Technical Memorandum no. 82385, p. 252-254.
- Mouginis-Mark, P.J., Wilson, L., and Head, J.W., 1982, Explosive volcanism on Hecates Tholus, Mars: Investigation of eruption conditions: *Journal of Geophysical Research*, v. 87, n. B12, p. 9890-9904.
- Murray, B.C., Soderblom, L.A., Cutts, J.A., Sharp, R.P., Milton, D.J., and Leighton, R.B., 1972, Geologic framework of the south polar regions of Mars: *Icarus*, v. 17, p. 328-345.
- Nelson, C.S., and Wilson, A.T., 1972, Bathymetry and bottom sediments of Lake Vanda, Antarctica: *Antarctic Journal of the United States*, v. 7, p. 97-99.
- Nichols, R.L., 1962, Geology of Lake Vanda, Wright Valley, South Victoria Land, Antarctica, in Wexler, H., Rubin, M.J., and Cashey, J.E., eds., *Matthew Fontaine Maury Memorial Symposium*: American Geophysical Union, p. 47-52.
- Parker, B.C., Simmons, G.M., Wharton, R.A., and Love, F.G., 1982, Removal of organic and inorganic matter from Antarctic lakes by aerial escape of bluegreen algal mats: *Journal of Phycology*, v. 18, p. 72-78.
- Patton, P.C., 1981, Evolution of spur and gully topography on the Valles Marineris Wall Scarps: NASA Technical Memorandum, no. 84211, p. 324-325.
- Peterson, C.P., 1981, A secondary origin for the central plateau of Hebes Chasma: *Proceedings of the Lunar and Planetary Science Conference*, v. 12B, p. 145-1471.

- Pieri, D., 1980, Martian valley: Morphology, distribution, age and origin: *Science*, v. 210, p. 895-897.
- Pollack, J.B., Colburn, D.S., Flaser, M., Kahen, R., Carlston, C.E., and Pidek, D., 1979, Properites and effects of dust particles suspended in the martian atmosphere: *Journal of Geophysical Research*, v. 84, p. 2929-2945.
- Pollack, J.B., and Toon, O.B., 1982, Quasi-periodic climatic changes on Mars: A review: *Icarus*, v. 50, p. 259-287.
- Ragotzkie, R.A., and Likens, G.E., 1964, The heat balance of two antarctic lakes: *Limnology and Oceanography*, v. 9, p. 412.
- Reading, H.G., 1978, *Sedimentary environments and facies*: New York, Elsevier North-Holland, 569 p.
- Scott, D.H., and Tanaka, K.L., 1982, Ignimbrites of Amazonis Planitia region of Mars: *Journal of Geophysical Research*, v.87, n. B2, p. 1179-1190.
- Sedimentation Seminar, 1981, Comparison of methods of size analysis for sands of the Amazon-Solimoes Rivers, Brazil and Peru: *Sedimentology*, v. 28, p. 123-128.
- Sengor, A.M.C., and Jones, E.C., 1975, A new interpretation of martian tectonics with special reference to the Tharsis region (abstract): *Geological Society of America, Abstract with Program*, v. 7, p. 1264.
- Sharp, R.P., 1973a, Mars: Troughed terrain: *Journal of Geophysical Research*, v. 78, p. 4063-4072.
- , 1973b, Mars: Fretted and chaotic terrains: *Journal of Geophysical Research*, v. 78, p. 4074-4083.
- Sheridan, M.F., 1979, Emplacement of pyroclastic flows: A review: *Geological Society of America, Special Paper 180*, p. 125-136.
- Shirtcliffe, T.G.L., and Benseman, R.F., 1964, A sun-heated antarctic lake: *Journal of Geophysical Research*, v. 69, p. 3355-3359.

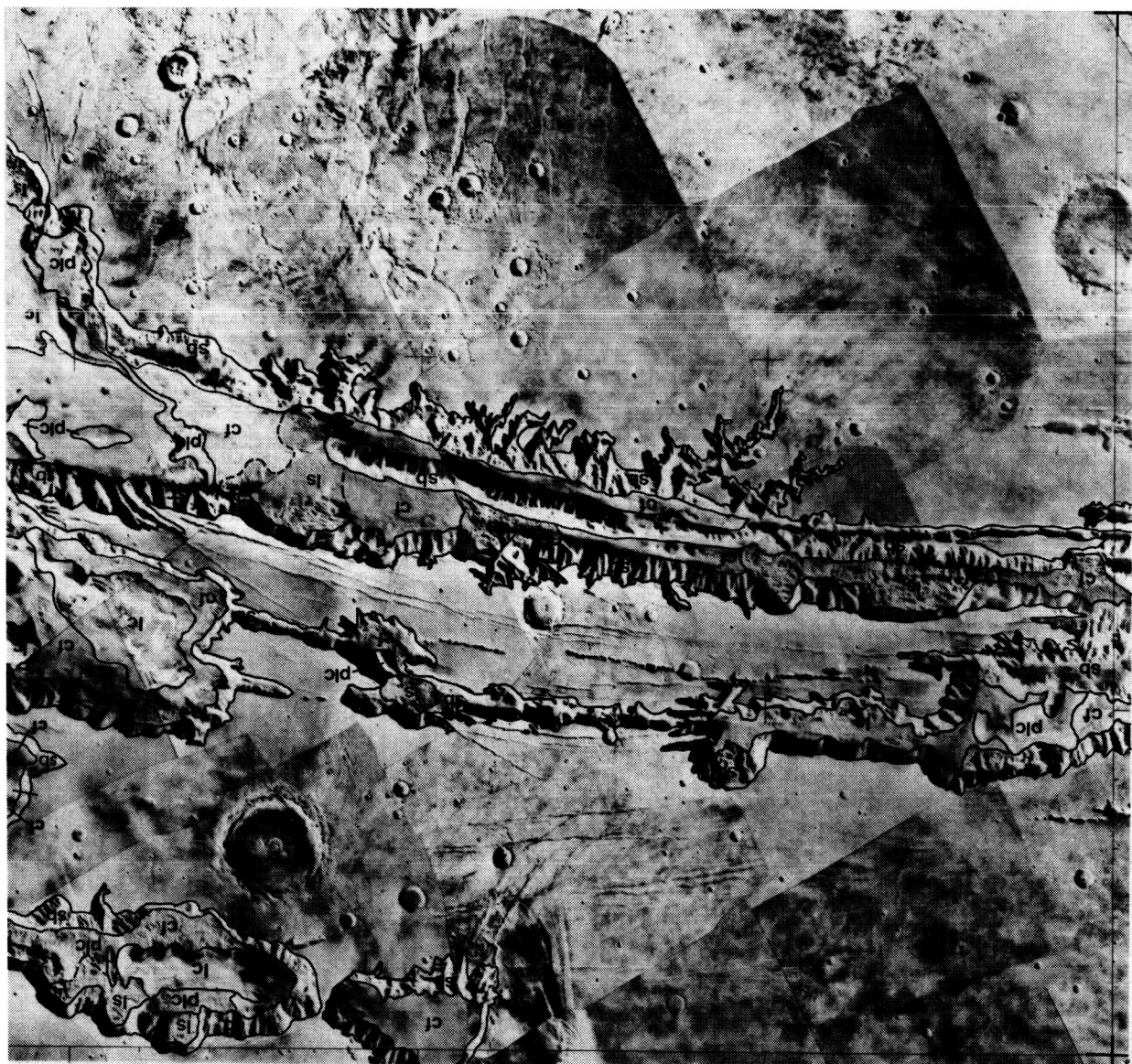
- Shreve, R.L., 1966, Sherman landslide, Alaska: *Science*, v. 154, p. 1639-1643.
- Sigurdsson, H., 1982, Subaqueous volcanogenic sediments in ocean basins: Geological Association of Canada, Short Course Notes, v. 2, p. 294-342.
- Simkin, T., Siebert, L., McClelland, L., Bridge, D., Newhall, C., Latter, J.H., 1981, *Volcanoes of the World*: Stroudsburg, Hutchinson Ross Press, 232 p.
- Smith, G.I, and Friedman, I., 1974, Lacustrine deposits around Lake Vanda and Don Juan Pond, Antarctica: *Dry Valley Drilling Project Bulletin*, n. 3, p. 187-190.
- Soderblom, L.A., and Wenner, D.B., 1978, Possible fossil H₂O liquid-ice interfaces in the martian crust: *Icarus*, v. 34, p. 622-637.
- Squyres, S.W., 1979, The distribution of lobate debris aprons and similar flow on Mars: *Journal of Geophysical Research*, v. 84, p. 8087-8096.
- , 1984, The history of water on Mars: *Annual Review of Earth and Planetary Science*, v. 12, p. 83-106.
- Squyres, S.W., and Carr, M.H., 1986, Geomorphic evidence of the distribution of ground ice on Mars: *Science*, v. 231, p. 249-252.
- Squyres, S.W., Wilhelms, D.E., and Moosman, A.C., 1986, Large-scale volcano - ground ice interactions on Mars: *Icarus*, 19 p., in press.
- Thompson, D.C., Bromley, A.M., and Craig, R.M.F., 1971a, Ground temperatures in and Antarctic Dry Valley: *New Zealand Journal of Geophysics*, v. 14, p. 477-483.
- Thompson, D.C., Craig, R.M.F., Bromley, A.M., 1971b, Climate and surface heat balance in an Antarctic Dry Valley: *New Zealand Journal of Geophysics*, v. 14, p. 245-251.
- Toon, O.B., Pollack, J.B., Ward, W., Burns, J.A., Bilski, K, 1980, The astronomical theory of climatic change on Mars: *Icarus*, v. 44, p. 552-607.

- U.S. Geological Survey, 1976, Topographic map of Mars: U.S. Geological Survey Miscellaneous Investigation Map I-961, scale 1:25,000,000.
- U. S. Geological Survey, 1984, Topographic map of Coprates Northwest quadrangle of Mars, (MC-18 NW): M 2M-7/79, scale 1:2,000,000.
- Visher, G.S., 1969, Grain size distributions and depositional processes: *Journal of Sedimentary Petrology*, v. 39, p. 1074-1106.
- Vucetich, C.G., and Topping, W.W., 1972, A fjord origin for the Pecten deposits, Wright Valley and Taylor Glacier region: *New Zealand Journal of Geology and Geophysics*, v. 6, 361-387.
- Wahrhaftig, C., and Cox, A., 1959, Rock glaciers in the Alaska Range: *Geological Society of America Bulletin*, v. 70, p. 383-436.
- Wallace, D., and Sagan, C., 1979, Evaporation of ice in planetary atmospheres: Ice-covered rivers on Mars: *Icarus*, v. 39, p. 385-400.
- Walton, E.K., Stephens, W.E., and Shawa, M.S., 1980, Reading segmented grain-size curves: *Geological Magazine*, v. 117, n. 6, p. 517-644.
- Ward, W.R., 1973, Large-scale variations in the obliquity of Mars: *Science* v. 181, p. 260-262.
- , 1974, Climatic variations on Mars. I. Astronomical theory of insolation: *Journal of Geophysical Research*, v. 79, p. 3375-3386.
- , 1979, Yardangs on Mars: Evidence of recent wind erosion: *Journal of Geophysical Research*, v. 84, p. 8147-8166.
- Washburn, A.L., 1973, *Periglacial Processes and Environments*: New York, St. Martin's, 320 p.
- Weertman, J., 1970, The creep strength of the Earth's mantle: *Reviews of Geophysics and Space Physics*, v. 8, p. 145-148.

- Wharton, R.A., Parker, B.C., and Simmons, 1983, Distribution, species, composition, and morphology of algal mats in Antarctic Dry Valley lakes: *Phycologia*, v. 22, p. 355-365.
- Wilhelms, D.E., 1972, Geologic mapping of the second planet: Interagency report, *Astrogeology* 55, 36 p.
- Wilson, A.T., and Wellman, H.W., 1962, Lake Vanda: An antarctic lake: *Nature*, v. 196, p. 1171-1172.
- Wilson, A.T., Hendy, C.H., Healy, T.R., Gumbley, J.W., Field, A.B., and Reynolds, C.P., 1974, Dry Valley lake sediments: a record of Cenozoic climatic events: *Antarctic Journal of the U.S.A.*, v. 9, p. 134-135.
- Wilson, L., and Head, J.W., 1983, A comparison of volcanic eruption processes on Earth, Moon, Mars, Io, and Venus: *Nature*, v. 302, m. 5919, p. 663-669.
- Wise, D.U., Golombek, M.P., and McGill, G.E., 1979, Tectonic evolution of Mars: *Journal of Geophysical Research*, v. 84, p. 7934-7939.
- Wu, S.S.C., Schafer, F.J., Nakata, G.M., Jordan, R., 1973, Photogrammetric evaluation of Mariner 9 photography: *Journal of Geophysical Research*, v. 78, p. 4405-4410.

ORIGINAL PAGE IS
OF POOR QUALITY

90°W



EXPLANATION

- ls LANDSLIDE MATERIAL
- lc LAYERED CHASMA DEPOSITS
- plc POSSIBLE LAYERED CHASMA DEPOSITS
- cf CHASMA FLOOR MATERIAL
- sb SLOPE AND BEDROCK MATERIAL
- ch AREAS WHERE THE CANYON WALL AND CHASMA FLOOR ARE INTERMIXED

0 200 KM

Plate 1A: Geologic map of the Valles Marineris. Parts A through D comprise the entire map.

67.5°W

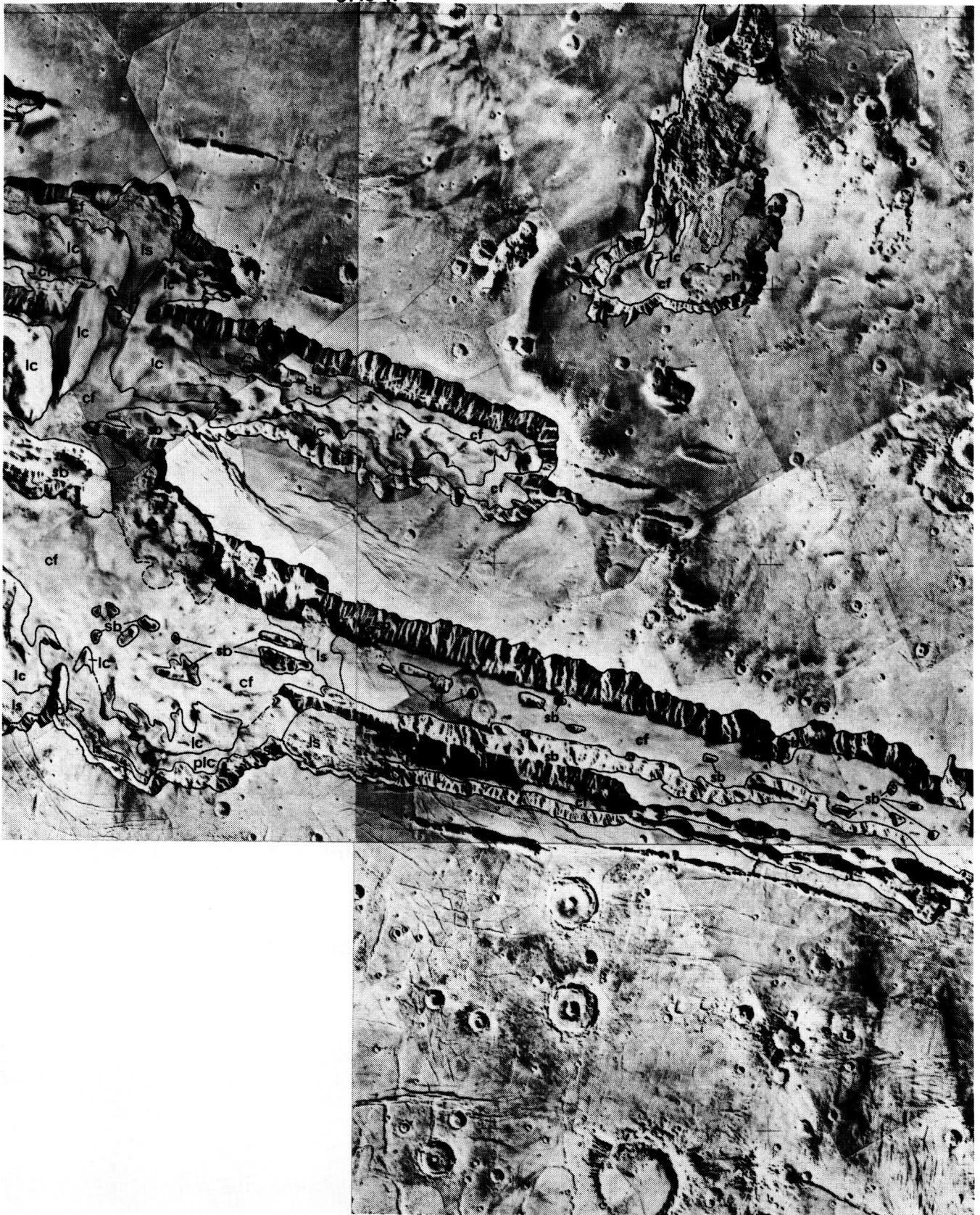


Plate 1B: Geologic map, con't.

ORIGINAL PAGE IS
OF POOR QUALITY

40°W



Plate 1C: Geologic map, con't.

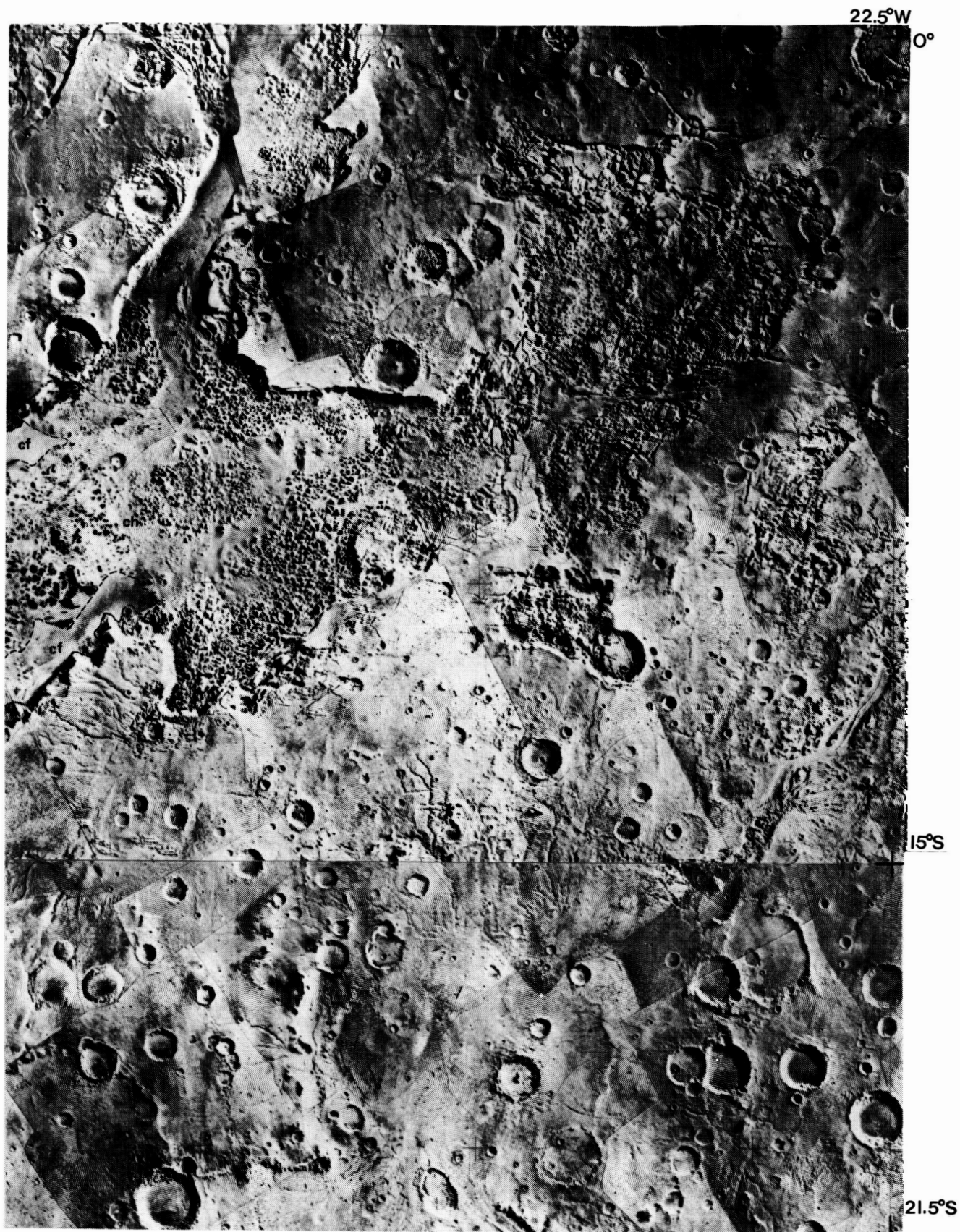


Plate 1D: Geologic map, con't.

Report Documentation Page

1. Report No. NASA TM-89871		2. Government Accession No.		3. Recipient's Catalog No.	
4. Title and Subtitle Advances in Planetary Geology				5. Report Date June 1987	
				6. Performing Organization Code EL	
7. Author(s) John A. Grant III and Susan S. Nedell				8. Performing Organization Report No.	
				10. Work Unit No.	
9. Performing Organization Name and Address Planetary Geoscience Program Solar System Exploration Division Office of Space Science and Applications				11. Contract or Grant No.	
				13. Type of Report and Period Covered Technical Memorandum	
12. Sponsoring Agency Name and Address National Aeronautics and Space Administration Washington, DC 20546				14. Sponsoring Agency Code	
15. Supplementary Notes					
16. Abstract The surface of Mars displays a broad range of channel and valley features. There is as great a range in morphology as in scale. This document examines some of the features Mars' geography. Part 1 uses geomorphic mapping, crater counts on selected surfaces, and a detailed study of drainage basins to trace the geologic evolution of the Margaritifer Sinus Quadrangle. Part 2 describes the layered deposits in the Valles Marineris in detail and analyzes the geologic processes that could have led to their formation.					
17. Key Words (Suggested by Author(s)) Mapping Sapping Etched, Chaotic, and Fretted Terrain Layered Deposits Eolian Deposits Rayleigh-Taylor Instability				18. Distribution Statement Unclassified--Unlimited Subject Category 91	
19. Security Classif. (of this report) Unclassified		20. Security Classif. (of this page) Unclassified		21. No. of pages 444	
				22. Price A19	

National Aeronautics and
Space Administration
Code NTT-4

Washington, D.C.
20546-0001

Official Business
Penalty for Private Use, \$300

SPECIAL FOURTH-CLASS RATE
POSTAGE & FEES PAID
NASA
Permit No. G-27

NASA

POSTMASTER: If Undeliverable (Section 158
Postal Manual) Do Not Return
